

**SYNTHESIS AND CHARACTERIZATION OF NEW
SCHIFF BASE ALKYNES AND THEIR TRIAZOLE
DERIVATIVES, AS POTENTIAL ION SENSORS**

Thesis Submitted for the Award of the Degree of

DOCTOR OF PHILOSOPHY

in

Chemistry

By

Nancy George

Registration Number: 11919699

Supervised By

Dr. Jandeep Singh (19394)

Chemistry (Associate Professor)

Lovely Professional University



**LOVELY PROFESSIONAL UNIVERSITY, PUNJAB
2025**

This thesis is dedicated to my beloved Parents and Grand parents

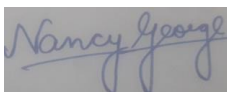
George Masih, Ruby

And

Pastor Mangat Masih, Helin

DECLARATION

I, hereby declared that the presented work in the thesis entitled “**Synthesis and Characterization of new Schiff base alkynes and their triazole derivatives, as potential ion sensors**” in fulfillment of degree of **Doctor of Philosophy (Ph.D.)** is the outcome of research work carried out by me under the supervision of **Dr. Jandeep Singh**, working as **Associate Professor**, in the **School of Chemical Engineering and Physical Sciences, Lovely Professional University**, Punjab, India. In keeping with the general practice of reporting scientific observations, due acknowledgements have been made whenever the work described here has been based on the findings of other investigator. This work has not been submitted in part or full to any other University or Institute for the award of any degree.



(Signature of Scholar)

Nancy George

Registration No.:11919699

Department of Chemistry,

School of Chemical Engineering and Physical Sciences,

Lovely Professional University, Punjab India

CERTIFICATE

This is to certify that the work reported in the Ph.D. thesis entitled “**Synthesis and Characterization of new Schiff base alkynes and their triazole derivatives, as potential ion sensors**” submitted in fulfillment of the requirement for the reward of degree of **Doctor of Philosophy (Ph.D.)** in the **School of Chemical Engineering and Physical Sciences, Lovely Professional University**, is a research work carried out by **Nancy George, 11919699**, is bonafide record of her original work carried out under my supervision and that no part of thesis has been submitted for any other degree, diploma or equivalent course.



(Signature of Supervisor)

Dr. Jandeep Singh

Associate Professor

Department of Chemistry,

School of Chemical Engineering and Physical Sciences,

Lovely Professional University, Punjab India

ABSTRACT

The exorbitant use or erroneous management of metal ions has been incurred with catastrophic pollution of our ecological system, particularly in soil and water bodies, resulting in significant repercussions. Hence, precise identification and analysis of metal ions such as Pb^{2+} , Mn^{2+} , Co^{2+} , Ni^{2+} , Cu^{2+} , Zn^{2+} , Cd^{2+} , Hg^{2+} , Ce^{3+} , Fe^{3+} , Fe^{2+} , Cr^{3+} is required. Therefore, precise detection of these analytes is highly recognized and a subject of significant interest. Scientists from numerous fields, including the environment science, agriculture, food processing, medicinal chemistry, pharmacy, and health sciences, chemical and biochemical sciences are gradually attentive in the quantitative and qualitative sensing of specific analytes, such as cations, anions, and neutral molecules.

The structural diversity of sensors can reveal different features of receptor-analyte interactions in organic and semi-aqueous solvent systems. Thus, the current dissertation titled "Synthesis and Characterization of new Schiff base alkynes and their triazole derivatives, as potential ion sensors" focuses on synthesis of five novel Schiff base linked 1,2,3 triazoles stitched via Cu(I) catalyzed Click cycloaddition of Schiff base terminal alkynes with freshly prepared organic azide employed for chemosensing application during this research work. Schiff bases with strong chromophoric units, possessing decent absorption in the UV-visible region, were sought for and used in the synthesis of Schiff base linked terminal alkynes. The objectives of the research work are as follows

- To synthesize novel 1,2,3–triazole derivatives using terminal alkyne, organic azide and Cu(I) catalyst.
- To characterize the synthesized compounds by spectroscopic techniques like IR, NMR (^1H , ^{13}C) and x-ray (if possible).
- To explore the ion sensing behaviour of synthesized 1,2,3–triazole derivatives using UV–Visible spectroscopy or fluorescence spectroscopy.

The Schiff bases selected as starting molecules contained a hydroxyl group whose proton was nucleophilically replaced with a propynyl group derived from propargyl bromide in suitable solvent system. Following this, Cu(I)-catalyzed reactions were employed to convert the organic azide and newly synthesised Schiff base alkynes into the desired Schiff base linked 1,2,3-triazole derivatives.

The synthesized compounds such as Schiff bases, Schiff base terminal alkynes and Schiff base tethered 1,2,3 triazole linkers denoted as **81c**, **82c**, **83c**, **84c** and **85c** were characterized using FTIR,

NMR, (^1H and ^{13}C) alongwith mass spectrometry. The designed chemosensors are synthesized with excellent yields, high selectivity and sensitivity. These sensors are found to be soluble in aqueous-organic binary solvent mixtures and appropriate for sensing metal ions such as Fe^{3+} , Pb^{2+} , Cu^{2+} and Hg^{2+} ions, exclusively.

For the detection of metal ions, instrumentation techniques such as optical approaches like (fluorescent and colorimetric spectroscopy) compared to traditional detection methods, offer numerous benefits owing to their rich sensitivity, visual detection, exceptional sensitivity, and minimal background interference. Therefore, the developed chemosensors were explored for their optical properties using UV–visible absorption and fluorescent spectroscopy. The synthesized probes exhibit very intense absorption bands in the UV-visible region and generate isosbestic points indicating the binding of metal-ligand complexes. Furthermore, these molecules exhibit a weak fluorescence, which is attributed to photoelectron transfer (PET) resulting from the presence of non-bonding electrons. However, this property proved to be advantageous as it enabled a noticeable increase in fluorescence when it interacted with the metal ions, the mechanism behind this phenomenon is chelation enhanced fluorescence (CHEF), which is accomplished by inhibiting PET. The absorption and emission responses documented for a range of novel Schiff base tethered 1,2,3-triazole linkers, which were synthesised during this course, are illustrated in this thesis through graphs and figures.

The analytical calculations, such as the limit of detection (LOD) from linear calibration curve, binding ratio from Job's plot, and binding efficiency from B-H plot of synthesized receptors towards specific metal ions, have been plotted and presented in the manuscript. Additionally, time and temperature dependent studies have been performed to check the practical efficacy of the developed chemosensors. Thus, the Schiff base tethered 1,2,3-triazole organic chemosensors with substantial chemical architectures have great potential for chemosensing applications. It's important to note that the combination of UV-vis and fluorogenic dual responsive chemosensing, along with sensing mechanism, offers diverse optical signals creating the favourable sensors for detecting analytes. The careful selection of a donor, acceptor, and π -bridge is anticipated to result in certain features, such as improved selectivity, sensitivity, water solubility, and better emission spectra, desirable for practical applications in the field of molecular chemosensors.

Keywords: Click Chemistry, 1,4-disubstituted 1,2,3-triazoles, chemosensing, metal cations, Host-guest binding, supramolecular chemistry

ACKNOWLEDGEMENTS

Though words are seldom sufficient to express gratitude and feelings, it gives me an opportunity to acknowledge those who helped me during the course of my studies.

First, I bow in reverence to **Almighty** the cherisher and sustainer to benediction giving me the required zeal for completion of my research work. The successful completion of any research work is a matter of great endeavourance but, the personal and practical support of numerous people makes the job entirely enjoyable and simple. It is a pleasant aspect that I have now the opportunity to express my gratitude to them.

I wish to express my deepest gratitude and indebtedness to my revered supervisor **Dr. Jandeep Singh, Associate Professor, Department of Chemistry, School of Chemical Engineering and Physical Sciences, Lovely Professional University, Punjab**, for his constant support, kind encouragement, immensely valuable ideas, suggestions and for having an unwavering attention. I have been amazingly fortunate to have a supervisor who gave me the freedom to explore on my own and at the same time the guidance to recover when my steps faltered. I shall remain indebted to him for his confidence in my work and most importantly for his kind affection during my Doctoral research. Simply his contribution is beyond the preview of acknowledgments and I feel very much honored. It has been a real privilege for me to get an opportunity to work under him, a teacher par excellence.

My heartfelt thanks to all my teachers right from school until now and all my well-wishers for their constant encouragement and wishes for my career. I also extend my thanks to all those, who have been directly or indirectly related to my project work.

My parents have been a strong pillar of support for me and my research would not have seen the day's light without their constant motivation. I owe them a lot. Thanks to my mother **Mrs. Ruby** for being my rock and helping me in touch with reality throughout my life. Special thanks to my father **Mr. George Masih** for letting me do it 'my way' and for encouraging and inspiring me to reach my dreams.

I must record my sincere thanks to my esteemed brother **Sahul Masih** for helping me in many ways and cousin siblings for their steady encouragement, timely support, unconditional love, and moral support, without whom I would never have enjoyed so many opportunities.

I particularly thank my colleagues for those sleepless nights, we were working together before deadlines and for all the fun we had during this research work. Without their precious support, it would

not have been possible to conduct this research. I would like to express my gratitude towards their moral and emotional support that helped me in the completion of this thesis and inspired me to work tirelessly to accomplish this task. I also express my gratitude to all who knowingly and unknowingly contributed to the completion of this thesis.

Date: 1-03-2025

(Nancy George)

Place: Lovely Professional University, Punjab

TABLE OF CONTENTS

S. No.	Content	Page No.
1	Title	-
2	Dedication	i
3	Declaration	ii
4	Certificate	iii
5	Abstract	iv-vi
6	Acknowledgements	vii-viii
7	Table of Contents	ix-xiiv
8	List of Figures	xiv-xxv
9	List of Tables	xxv
10	List of Annexures	xxvi-xxviii
11	List of Abbreviations	xxix-xxxii
Chapter 1: Introduction		1-17
1	Exploring the Legacy of ‘Click Chemistry’	2
2	1,3 dipolar cycloaddition reaction	2-3
3	Classical cycloaddition reaction versus Cu(I) catalyzed reaction	3
4	Copper(I)-catalyzed alkyne azide cycloaddition click reaction	3-4
5	Mechanistic insights of CuAAC	5
6	Importance of 1,4 disubstituted 1,2,3-triazoles	6-7
7	Photoluminescence	7
8	Photophysical processes	7-8
8.1	Absorbance	7-8
8.2	Fluorescence	8
9	Analytical Supramolecular chemistry: Host guest relationship	8-9
9.1	Chemosensor	9-10

9.2	Fluorimetric sensors	10-11
9.3	Fluorescence signal mechanism: Photo induced electron transfer (PET)	11-12
10	Chemosensing analysis via UV-vis and Fluorescence spectroscopy	13-14
11	Conclusion	14
12	References	14-17
Chapter 2: Review of literature		18-50
1	Synthesis of hybrids of 1,2,3-triazoles	19
1.1	Chemical reactions for the synthesis of Schiff base	19-21
1.2	Chemical reactions for the synthesis of terminal alkynes	21-24
1.3	Chemical reactions for the preparation of azides	24-26
1.4	Adduct formation of 1,2,3-triazoles from CuAAC reaction	26-31
2	Fluorogenic 1,2,3-triazole chemosensors for metal ions detection	31-44
3	Aim, Objective, and scope of the thesis	44-46
4	Conclusion	46
5	References	46-50
Chapter 3: Experimental data		51-74
1	Materials and instrumentation	52
2	Purification technique of different solvents	52-53
3	Intended research methodology	54-55
3.1	General technique for the synthesis of compounds	54-55
3.2	Synthesis of organic azide	55-56
3.2.1	Synthesis of <i>Azidomethylbenzene</i>	55-56
3.3	Synthesis of Schiff base 81a, Schiff base terminal alkyne 81b and 1,2,3-triazole derivative 81c	56-59
3.3.1	Synthesis and characterization of Schiff base 81a	56-57
3.3.2	Synthesis and characterization of Schiff base alkyne 81b	57-58
3.3.3	Synthesis and characterization of Schiff base 1,2,3-triazole 81c	58-59
3.4	Synthesis of Schiff base 82a, Schiff base terminal alkyne 82b and 1,2,3-triazole derivative 82c	60-65

3.4.1	Synthesis and characterization of Schiff base 82a	60-61
3.4.2	Synthesis and characterization of Schiff base alkyne 82b	61-62
3.4.3	Synthesis and characterization of Schiff base 1,2,3-triazole 82c	62-63
3.5	Synthesis of Schiff base 83a, Schiff base terminal alkyne 83b and 1,2,3-triazole derivative 83c	63-67
3.5.1	Synthesis and characterization of Schiff base 83a	63-64
3.5.2	Synthesis and characterization of Schiff base alkyne 83b	64-65
3.5.3	Synthesis and characterization of Schiff base 1,2,3-triazole 82c	66-67
3.6	Synthesis of Schiff base 84a, Schiff base terminal alkyne 84b and 1,2,3-triazole derivative 84c	67-71
3.6.1	Synthesis and characterization of Schiff base 84a	67-68
3.6.2	Synthesis and characterization of Schiff base alkyne 84b	68-69
3.6.3	Synthesis and characterization of Schiff base 1,2,3-triazole 84c	69-71
3.7	Synthesis of Schiff base 85a, Schiff base terminal alkyne 85b and 1,2,3-triazole derivative 85c	71-74
3.7.1	Synthesis and characterization of Schiff base 85a	71-72
3.7.2	Synthesis and characterization of Schiff base alkyne 85b	72-73
3.7.3	Synthesis and characterization of Schiff base 1,2,3-triazole 85c	73-74
3.8	Depiction of molecules	74
3.9	Metal-Ion recognition	74
Chapter 4: Result and discussion of spectroscopic data		75-100
1	Synthesis and spectral analysis of <i>Azidomethylbenzene</i> 39	76-77
2	Synthesis and spectral analysis of Schiff base 81a	77-78
3	Synthesis and spectral analysis of Schiff base alkyne 81b	78-79
4	Synthesis and spectral analysis of Schiff base 1,2,3-triazole 81c	80-81
5	Synthesis and spectral analysis of Schiff base 82a	81-82
6	Synthesis and spectral analysis of Schiff base alkyne 82a	83-84
7	Synthesis and spectral analysis of Schiff base 1,2,3-triazole 82c	84-86
8	Synthesis and spectral analysis of Schiff base 83a	86-87
9	Synthesis and spectral analysis of Schiff base alkyne 83b	87-89

10	Synthesis and spectral analysis of Schiff base 1,2,3-triazole 83c	89-90
11	Synthesis and spectral analysis of Schiff base 84a	91-92
12	Synthesis and spectral analysis of Schiff base alkyne 84b	92-93
13	Synthesis and spectral analysis of Schiff base 1,2,3-triazole 84c	93-95
14	Synthesis and spectral analysis of Schiff base 85a	95-96
15	Synthesis and spectral analysis of Schiff base alkyne 85b	97-98
16	Synthesis and spectral analysis of Schiff base 1,2,3-triazole 84c	98-100
Chapter 5: Photophysical analysis		101-178
1	Spectroscopic analysis of 81c	102-115
1.1	U.V-visible spectroscopy analysis of chemosensor 81c	102-103
1.2	UV- visible response of chemosensor 81c towards Fe^{3+}	103-105
1.3	Job plot analysis of $[\text{81c-Fe}^{3+}]$ complex	105-106
1.4	Competitive metal ion titrations of 81c	106-107
1.5	B-H plot, time and temperature study of $[\text{81c-Fe}^{3+}]$ complex	107-110
1.6	Fluorescence analysis of chemosensor 81c	110-112
1.7	Limit of Detection of (81c-Fe^{3+}) complex	112-113
1.8	A proposed mechanism for the synthesized probe 81c	114-115
2	Spectral analysis of chemosensor 82c	115-127
2.1	UV-visible spectroscopic studies of 82c	115-118
2.2	Job's plot of chemosensor $[\text{82c-Pb}^{2+}]$ complex	118-119
2.3	Competitive metal ion titrations of chemosensor 82c	119-120
2.4	Time bound and temperature dependent study of $[\text{Pb}^{2+}\text{-82c}]$ complex	120-122
2.5	B-H plot $[\text{82c-Pb}^{2+}]$ complex	122-123
2.6	Fluorescence spectroscopic studies of chemosensor 82c	123-125
2.7	Limit of detection of $[\text{82c-Pb}^{2+}]$ complex	125-126
2.8	Probable binding mode of $[\text{82c-Pb}^{2+}]$ complex	126-127
3	Photophysical properties of chemosensor 83c	128-139
3.1	UV-visible spectral studies of chemosensor 83c	128

3.2	Optical response of 83c in the existence of Cu ²⁺	129-133
3.3	Time bound and temperature dependent study of [83c-Cu ²⁺] complex	133-135
3.4	Fluorescence studies of chemosensor 83c	135-138
3.5	Probable binding mode of [83c-Cu ²⁺] complex	138-139
4	Photophysical properties of chemosensor 84c	139-153
4.1	Absorbance spectra of probe 84c	139-140
4.2	Optical response of 84c towards metal ion Hg ²⁺	140-144
4.3	Competitive metal ion titration of chemosensor 84c	144-145
4.4	Time and Temperature Dependence Study of [84c-Hg ²⁺] complex	145-147
4.5	Fluorescence Emission studies of chemosensor 84c	147-150
4.6	Detection Limit of [84c-Hg ²⁺] complex	151
4.7	Probable binding mode of [84c-Hg ²⁺] complex	152-153
5	Photophysical analysis of chemosensor 85c	153-174
5.1	U.V visible absorption studies of 85c	153-158
5.2	Job's plot of 85c with (Cu ²⁺ and Pb ²⁺) metal ions	158-160
5.3	Selectivity of the probe 85c	160-161
5.4	B-H plot of 85c with (Cu ²⁺ and Pb ²⁺) metal ions	161-163
5.5	Time-dependence study of 85c with (Cu ²⁺ and Pb ²⁺) metal ions	163-165
5.6	Temperature dependence of 85c with (Cu ²⁺ and Pb ²⁺) metal ions	165-167
5.7	Fluorescence emission spectral studies of chemosensor 85c	167-171
5.8	Sensitivity of the probe 85c	171-173
5.9	Plausible binding mode of 85c with (Cu ²⁺ and Pb ²⁺) metal ions	173-174
6	Conclusion	174-177
7	References	177-178
Summary		179-199
Annexure A: Chemicals and Instruments		200-202
Annexure B: ATR-FTIR, NMR (¹H, ¹³C), and MS spectra (GCMS-MS/ LCMS-MS)		203-268
List of Publications		269-270

LIST OF FIGURES

Figure No.	Description	Page No.
Figure 1	The mechanistic pathway for cycloaddition of 1,3 dipolar reaction.	3
Figure 2	A scheme showing the Huisgen 1,3-dipolar cycloaddition reaction of organic azide with terminal alkyne under thermal conditions, leading to 1,4 and 1,5 isomers and Sharpless click reaction in the presence of Cu(I) catalyst, resulted in selective 1,4 regioisomer of 1,2,3-triazole	4
Figure 3	The initially developed CuAAC mechanism, as proposed by Fokin and co-workers	5
Figure 4	Schematic design of Fluorescent chemosensor for sensing of metal ions	7
Figure 5	A schematic illustration of analyte detection via a chemosensor	10
Figure 6	The emission spectra showing the different types of shifts observed during metal-ligand complexation	11
Figure 7	PET mechanism, displaying the modified version of the frontier molecular orbital energy diagram	12
Figure 8	Synthesis of Schiff base in ethanol medium	20
Figure 9	Synthesis of Schiff base in methanol solvent system	20
Figure 10	Synthesis of Schiff base via green synthetic route	21
Figure 11	Reaction pathway for the synthesis of diarylacetylene	21
Figure 12	Synthetic approach for the synthesis of terminal alkynes and alkynyl halides	22
Figure 13	Synthesis of terminal alkyne from 1,1-dibromoolefin	22
Figure 14	Synthesis of phenylacetylene using Bestmann-Ohira reagent	22
Figure 15	Synthetic route for the preparation of substituted bis terminal alkyne	23
Figure 16	The Preparation of terminal alkyne from imines using propargyl bromide	23
Figure 17	Various methods for the preparation of organic azides	24
Figure 18	Synthesis of azido compound from substituted Pyridine	25
Figure 19	Conversion of aromatic hydrazine into aryl azide	25
Figure 20	Synthesis of 8-aminoquinoline from aromatic amine	25

Figure 21	Synthesis of organic azides from primary amines	26
Figure 22	Synthesis of organic azides from non-benzylic alcohol	26
Figure 23	Synthesis of benzyl azide from benzyl chloride and sodium azide	26
Figure 24	Synthetic pathway for the 1,2,3-triazole derivative	27
Figure 25	Illustration of the reaction scheme for synthesising the 1,2,3-triazole derivative	28
Figure 26	Steps for synthesizing Schiff base 1,2,3-triazole	28
Figure 27	Synthesis of 1,2,3-triazole functionalised azo dye silane	29
Figure 28	Synthesis of urea-hybrid 1,2,3-triazole	29
Figure 29	Preparation of 1,2,3-triazole hybrid coumarin derivatives	30
Figure 30	Synthesis of Indole Schiff base hybrid 1,2,3 triazole	30
Figure 31	A plausible mechanism for the ring-opening of the rhodamine-1,2,3-triazole dyad is facilitated by the coordination of Cu^{2+} ions	31
Figure 32	Probable binding mode of click-derived 1,2,3-triazole derivative with Hg^{2+} ions	32
Figure 33	Plausible stoichiometric binding (2:1) of chemosensor 69 with Zn^{2+} complex	33
Figure 34	Fluorometric detection of Fe^{3+} via newly developed chemosensor 70	34
Figure 35	Plausible binding mode of chemosensor 71 and Pb^{2+} ions	34
Figure 36	Possible binding structure of chemosensor 72 with Sn^{2+} ions	35
Figure 37	The plausible sensing mechanism of chemosensor 73 for Pb^{2+} and Cu^{2+} ions	36
Figure 38	Possible binding interaction of Fe^{3+} metal ion with receptor 74	36
Figure 39	The proposed binding mechanism of probe 75 with Pb^{2+} ions	37
Figure 40	Plausible binding structure of Zn^{2+} with chemosensor 76	38
Figure 41	Possible binding structure of probe 77 with Cu^{2+} and Ni^{2+} ions	39
Figure 42	Proposed binding structure of chemosensor 78 with Fe^{2+} ions	40
Figure 43	Depiction of intramolecular interaction of probe 79 with Cu^{2+} ions	41
Figure 44	Representation of Binding of chemosensor 80 with Cu^{2+} and F^- ions	41
Figure 45	General reaction of Schiff base	54

Figure 46	General reaction of Schiff base tethered terminal alkynes	54
Figure 47	General reaction of organic azide	55
Figure 48	General reaction of Schiff base linked 1,4-disubstituted-1,2,3-triazole	55
Figure 49	Schematic representation for the synthesis of <i>Azidomethylbenzene</i>	56
Figure 50	Schematic procedure for <i>(E)-4-((benzylimino)methyl)-2-methoxyphenol</i>	57
Figure 51	Systematic procedure for synthesis of <i>(E)-N-benzyl-1-(3-methoxy-4-(prop-2-yn-1-yloxy)phenyl)methanimine</i>	58
Figure 52	Synthetic procedure for <i>(E)-N-benzyl-1-(4-((1-benzyl-1H-1,2,3-triazol-4-yl)methoxy)-3-methoxyphenyl)methanimine</i>	59
Figure 53	Synthetic route for <i>(E)-4-(((3-hydroxybenzyl)imino)methyl)-2-methoxyphenol</i>	60
Figure 54	Systematic pathway for <i>(E)-1-(3-methoxy-4-(prop-2-yn-1-yloxy)phenyl)-N-(4-(prop-2-yn-1-yloxy)phenyl)methanimine</i>	61
Figure 55	Schematic illustration for <i>(E)-1-(4-((1-benzyl-1H-1,2,3-triazol-4-yl)methoxy)-3-methoxyphenyl)-N-(4-((1-benzyl-1H-1,2,3-triazol-4-yl)methoxy)phenyl)methanimine</i>	62
Figure 56	Synthetic procedure for <i>(E)-2-methoxy-4-((naphthalen-1-ylimino)methyl)phenol</i>	64
Figure 57	Synthetic scheme for the synthesis of <i>(E)-N-(3-methoxy-4-(prop-2-yn-1-yloxy)benzylidene)naphthalen-1-amine</i>	65
Figure 58	Systematic route for the synthesis of <i>(E)-N-(4-((1-benzyl-1H-1,2,3-triazol-4-yl)methoxy)-3-methoxybenzylidene)naphthalen-1-amine</i>	66
Figure 59	Synthetic route for the synthesis of <i>(E)-2-methoxy-4-((phenethylimino)methyl)phenol</i>	67
Figure 60	Synthesis procedure for <i>(E)-1-(3-methoxy-4-(prop-2-yn-1-yloxy)phenyl)-N-phenethylmethanimine</i>	69
Figure 61	Synthetic route for the synthesis of <i>(E)-1-(4-((1-benzyl-1H-1,2,3-triazol-4-yl)methoxy)-3-methoxyphenyl)-N-phenethylmethanimine</i>	70
Figure 62	Synthesis scheme for <i>(E)-2-methoxy-4-((p-tolylimino)methyl)phenol</i>	71
Figure 63	Synthetic procedure for <i>(E)-1-(3-methoxy-4-(prop-2-yn-1-yloxy)phenyl)-N-(p-tolyl)methanimine</i>	72
Figure 64	Synthetic route for the <i>(E)-1-(4-((1-benzyl-1H-1,2,3-triazol-4-yl)methoxy)-3-methoxyphenyl)-N-(p-tolyl)methanimine</i>	73

Figure 65	Structure of Azidomethylbenzene 39	76
Figure 66	Structure of (<i>E</i>)-4-((benzylimino)methyl)-2-methoxyphenol 81a	77
Figure 67	Structure of (<i>E</i>)- <i>N</i> -benzyl-1-(3-methoxy-4-(prop-2-yn-1-yloxy)phenyl)methanimine 81b	79
Figure 68	Structure of (<i>E</i>)- <i>N</i> -benzyl-1-(4-((1-benzyl-1 <i>H</i> -1,2,3-triazol-4-yl)methoxy)-3-methoxyphenyl)methanimine 81c	80
Figure 69	Structure of (<i>E</i>)-4-(((3-hydroxybenzyl)imino)methyl)-2-methoxyphenol 82a	82
Figure 70	Structure of (<i>E</i>)-1-(3-methoxy-4-(prop-2-yn-1-yloxy)phenyl)- <i>N</i> -(4-(prop-2-yn-1-yloxy)phenyl)methanimine 82b	83
Figure 71	Structure of (<i>E</i>)-1-(4-((1-benzyl-1 <i>H</i> -1,2,3-triazol-4-yl)methoxy)-3-methoxyphenyl)- <i>N</i> -(4-((1-benzyl-1 <i>H</i> -1,2,3-triazol-4-yl)methoxy)phenyl)methanimine 82c	85
Figure 72	Structure of (<i>E</i>)-2-methoxy-4-((naphthalen-1-ylimino)methyl)phenol 83a	86
Figure 73	Structure of (<i>E</i>)- <i>N</i> -(3-methoxy-4-(prop-2-yn-1-yloxy)benzylidene)naphthalen-1-amine 83b	88
Figure 74	Structure of (<i>E</i>)- <i>N</i> -(4-((1-benzyl-1 <i>H</i> -1,2,3-triazol-4-yl)methoxy)-3-methoxybenzylidene)naphthalen-1-amine	89
Figure 75	Structure of (<i>E</i>)-2-methoxy-4-((phenethylimino)methyl)phenol	91
Figure 76	Structure of (<i>E</i>)-1-(3-methoxy-4-(prop-2-yn-1-yloxy)phenyl)- <i>N</i> -phenethylmethanimine	92
Figure 77	Structure of (<i>E</i>)-1-(4-((1-benzyl-1 <i>H</i> -1,2,3-triazol-4-yl)methoxy)-3-methoxyphenyl)- <i>N</i> phenethylmethanimine	94
Figure 78	Structure of (<i>E</i>)-2-methoxy-4-((<i>p</i> -tolylimino)methyl)phenol	96
Figure 79	Structure of (<i>E</i>)-1-(3-methoxy-4-(prop-2-yn-1-yloxy)phenyl)- <i>N</i> -(<i>p</i> -tolyl)methanimine	97
Figure 80	Structure of (<i>E</i>)-1-(4-((1-benzyl-1 <i>H</i> -1,2,3-triazol-4-yl)methoxy)-3-methoxyphenyl)- <i>N</i> -(<i>p</i> -tolyl)methanimine	98
Figure 81	A histogram assessing the response of chemosensor 81c (0.2 mM) with various competitive metal ions (1 mM) using EtOH:H ₂ O (9:1 v/v) solvent system, after addition of 10 equiv. of various metal ions added consecutively in 81c solution. The significant change in relative absorbance of Fe ³⁺ was observed as compared to other metal ions	103
Figure 82	Absorption spectra of the 81c probe (0.2 mM) upon successive addition of 1 equiv. of Fe ³⁺ ion solution (1mM) in EtOH:H ₂ O (9:1 v/v) solvent	104

	system, with each addition of 1 equiv. of Fe^{3+} ion solution in 81c solution, hyperchromic shift was observed signifying the $[\text{81c-Fe}^{3+}]$ complexation	
Figure 83	The absorption spectra of probe 81c were analysed by plotting the relative change in absorption against the sequential addition of Fe^{3+} ions (0-15 equiv.) in DMSO solvent system, wherein the absorbance intensity of probe 81c, represented by A_0 and A_n signify the absorbance intensity after the addition of Fe^{3+} ions solution in the 81c solution	105
Figure 84	Job's plot from the absorbance spectrum of chemosensor 81c and Fe^{3+} ions in EtOH:H ₂ O (9:1, v/v) solvent system, the mole fraction of 81c plotted against relative absorption shows maximum absorbance above 6 mole fraction depicting the stoichiometric ratio (1:2) of $[\text{81c+Fe}^{3+}]$ complex	106
Figure 85	UV-vis spectra of chemosensor 81c (0.2 mM) in EtOH:H ₂ O (9:1, v/v) demonstrating selective binding of Fe^{3+} ions in equimolar concentration of multiple metal ions; where M^{n+} represents the mixture of metal ions i.e. equiv. of (Al^{3+} , Sr^{3+} , Mg^{2+} , Co^{2+} , Cr^{2+} , Hg^{2+} , Mn^{2+} , Cu^{2+} , Fe^{3+} , Ce^{2+} , Cd^{2+} , Ni^{2+} , Zn^{2+} , Fe^{2+}) showing the dominance of Fe^{3+} binding with 81c even in presence of other metal ions	107
Figure 86	Absorption titration data of the synthesized probe with Fe^{3+} for the record of Benesi-Hildebrand plot at absorption intensity monitored at 275 nm in EtOH:H ₂ O (9:1, v/v) solvent system	108
Figure 87	Time dependent profile versus absorption of the $[\text{Fe}^{3+}\text{-81c}]$ complex in EtOH:H ₂ O (9:1, v/v) solvent system for 30 minutes	109
Figure 88	Temperature dependent study of the $[\text{Fe}^{3+}\text{-81c}]$ complex in EtOH:H ₂ O (9:1, v/v) solvent system from 30 °C to 52 °C	110
Figure 89	The fluorescence titration spectra of probe 81c (0.02 mM) at $\lambda_{\text{max}} = 346$ nm in (EtOH:H ₂ O::9:1) solvent medium at 25 °C with incremental addition of 1 equiv. of Fe^{3+} ions in 81c solution shows noticeable increase in intensity (hyperchromic shift) depicting chelation of $[\text{Fe}^{3+}\text{-81c}]$ complex	111
Figure 90	The emission spectra showing relative change in intensity (I_n/I_0) at $\lambda_{\text{em}} = 346$ nm plotted against concentration of Fe^{3+} metal ion in (EtOH:H ₂ O::9:1) solvent media. The fluorescence intensity of probe 81c in the absence of Fe^{3+} is represented by I_0 , and I_n denote the fluorescence intensity during the binding of 81c with Fe^{3+} ion solution	112
Figure 91	A linear calibration curve showing the relative absorbance $(I_0-I_n)/I_0$ at different $[\text{Fe}^{3+}]$ ion concentrations in (EtOH:H ₂ O::9:1) solvent media, wherein I_0 = emission intensity of probe 81c in absence of Fe^{3+} ions and I_n = emission intensity observed with each addition of Hg^{2+} solution in 81c solution.	113

Figure 92	Binding mode of the synthesized compound 81c with Fe^{3+} metal ion showing Fe^{3+} sandwiched between ligand molecules as 2:1 (81c- Fe^{3+}) stoichiometric ratio in (EtOH:H ₂ O::9:1) solvent media.	115
Figure 93	The change in absorption spectra of probe 82c (0.05 mM) upon addition of 10 equiv. of different metal ion solutions in DMSO	116
Figure 94	UV-vis spectrum of probe 82c (0.05 mM) with sequential addition of 1 equiv. of Pb^{2+} ions (1 mM) using DMSO as solvent system displaying increase in intensity (hyperchromic shift) at $\lambda_{\text{max}} = 276$ nm, confirming the binding of [82c- Pb^{2+}] complex	117
Figure 95	The relative change in absorption spectra of probe 82c plotted against sequential addition of Pb^{2+} ions fluctuating from 0.16 mM to 0.23 mM in DMSO solvent system, wherein A_0 represent the absorbance intensity of probe 81c and A_n signifies the absorbance intensity after the addition of Pb^{2+} ions solutions in 81c solution	118
Figure 96	Job's plot assessing stoichiometric ratio of [82c- Pb^{2+}] complex showing $\Delta A \cdot X$ v/s mole fraction (X) in DMSO solvent system, the relative absorption (y-axis) shows maximum absorbance at 0.7 mole fraction depicting (2:1) binding ratio [82c- Pb^{2+}] complex	119
Figure 97	UV-vis spectra of probe 82c (0.05 mM) in DMSO illustrating selective binding of Pb^{2+} ions among equimolar concentration of mixture of metal ions such as Al^{3+} , Sr^{2+} , Hg^{2+} , Mg^{2+} , Cr^{3+} , Ni^{2+} , Pb^{2+} , Mn^{2+} , Ca^{2+} , Ba^{2+} , Co^{2+} , and Zn^{2+} , where M^{n+} represent the mixture of metal ions	120
Figure 98	Time bound study of [82c- Pb^{2+}] complex in DMSO solvent system examined for 30 minutes at $\lambda = 276$ and 311 nm	121
Figure 99	Temperature bound analysis of [82c- Pb^{2+}] complex in DMSO solvent system from 32 °C to 44 °C	122
Figure 100	The relative absorbance titration data of probe 82c with the increasing Pb^{2+} ions concentration for the Benesi-Hildebrand plot in DMSO solvent system	123
Figure 101	The fluorescence spectra of probe 82c when titrated with Pb^{2+} ions solution observed at $\lambda = 436$ nm in DMSO solvent system, a significant increase in intensity i.e hyperchromic shift was observed on addition of 1 equiv. of Pb^{2+} ions solution to 82c solution	124
Figure 102	The relative emission intensity ratios (I_n/I_0) of probe 82c at $\lambda = 436$ nm plotted against change in concentration of Pb^{2+} ions in DMSO solvent system, where I_0 signify the emission intensity of 82c in absence of Pb^{2+} ions and I_n represent the emission intensity during the binding of 82c with Pb^{2+} ions with each consecutive addition	125

Figure 103	The linear calibration curve showing relative intensity $(I_o - I_n)/I_o$ with variation in Pb^{2+} ions concentration, wherein I_n = emission intensity with each subsequent addition of Pb^{2+} ions and I_o = emission intensity of free probe 82c	126
Figure 104	The proposed ligand-metal (2:1) binding of probe 82c with Pb^{2+} ions in DMSO solvent system	127
Figure 105	Histogram demonstrating the response of the chemosensor 83c at $\lambda_{max} = 277$ nm in CH_3CN/H_2O (4:1) solvent system towards several competing metal cations such as Na^+ , K^+ , Mg^{2+} , Ba^{2+} , Pb^{2+} , Mn^{2+} , Co^{2+} , Ni^{2+} , Cu^{2+} , Zn^{2+} , Cd^{2+} , Hg^{2+} , Ce^{3+} , Fe^{3+} , Cr^{3+} , Ag^+ comprising 10 equiv. of metal ion solution.	128
Figure 106	The variations in the absorption spectra of 83c (30 μ M) in $CH_3CN:H_2O::4:1$ solvent mixture upon consecutive addition with increasing equivalent of Cu^{2+} ions, change in intensity before and after the isosbestic point at 309 nm, along with 11 nm blue shift and rise in intensity	129
Figure 107	The relative change in absorbance intensity at $\lambda = 277$ nm plotted against the cumulative addition of Cu^{2+} ions (0-11 equiv.) in $CH_3CN:H_2O::4:1$ solvent mixture, wherein A_o = absorbance intensity of free probe 83c without Cu^{2+} ions and A_n = absorbance intensity during binding of 83c with Cu^{2+} ions solution	130
Figure 108	Representation of Job's plot exhibiting the binding ratio of $[83c-Cu^{2+}]$ complex in $CH_3CN:H_2O::4:1$ solvent system, at 0.5 mole fraction maximum relative absorbance value was attained depicting the (1:1) stoichiometric ratio of $[83c-Cu^{2+}]$ complex	131
Figure 109	UV-vis absorption spectra of probe 83c (0.03 mM) in $CH_3CN:H_2O::4:1$ solvent system exhibiting selective binding of Cu^{2+} ions in presence of equal concentrations of assorted metal cations such as Na^+ , K^+ , Mg^{2+} , Ba^{2+} , Pb^{2+} , Mn^{2+} , Co^{2+} , Ni^{2+} , Cu^{2+} , Zn^{2+} , Cd^{2+} , Hg^{2+} , Ce^{3+} , Fe^{3+} , Cr^{3+} , Ag^+ , herein M^{n+} represents the mixture of metal ions in the spectrum	132
Figure 110	The relative absorbance titration data for probe 83c with increase in concentration of Cu^{2+} ions, monitored at 277 nm for the Benesi-Hildebrand plot in $CH_3CN:H_2O::4:1$ solvent system	133
Figure 111	Time bound study of $[83c-Cu^{2+}]$ complex in $CH_3CN:H_2O::4:1$ solvent system for 30 minutes at $\lambda = 277$ nm and 315 nm	134
Figure 112	Temperature dependent study of metal-ligand complex in $CH_3CN:H_2O::4:1$ solvent system from 32 $^{\circ}C$ to 50 $^{\circ}C$	135
Figure 113	Emission spectra of probe 83c when titrated with Cu^{2+} ions solution in $(CH_3CN:H_2O::4:1)$ solvent media illustrating change in intensity at $\lambda = 415$ nm.	136

Figure 114	The linear calibration curve illustrating the relative emission intensity [I_o - I_n/I_o] observed at various concentration of Cu^{2+} ions	137
Figure 115	The relative change in intensity (I_n/I_o) of emission spectrum plotted against variant concentration of Cu^{2+} metal ion at $\lambda = 415$ nm.in ($CH_3CN:H_2O::4:1$) solvent media, where I_o = emission intensity of free 83c and I_n = emission intensity during binding of Cu^{2+} with 83c	138
Figure 116	Plausible binding mode showing 1:1 stoichiometry ratio of [83c- Cu^{2+}] complex	139
Figure 117	The variation in chemosensing response of the probe 84c in ($ACN:H_2O::4:1$) solvent mixture, when 10 equivalents of various metal ions such as Zn^{2+} , Ni^{2+} , Mg^{2+} , Co^{2+} , Ce^{3+} , Mn^{2+} , Cd^{2+} , Hg^{2+} , Cu^{2+} , Cr^{2+} , Ba^{2+} , Pb^{2+} were consecutively added. A noticeable alteration can be observed in the absorbance intensity with Hg^{2+} ions compared to other metal ions for 84c sensor	140
Figure 118	UV-visible graph of 84c showing absorbance responses measured after adding 1 equiv. of 1 mM Hg^{2+} ion solution to 0.05 mM 84c solution in ($ACN:H_2O::4:1$) solvent system. A noticeable change in the intensity of absorbance before and after the isosbestic points at 273 nm, along with hypsochromic shift and substantial rise in intensity	141
Figure 119	Relative absorbance ratios (A_n/A_o) ranging from 273 nm to 267 nm were plotted against Hg^{2+} ion concentrations fluctuating from 0.02 mM to 1.83 mM, wherein A_o = Absorbance intensity of probe 84c in the absence of Hg^{2+} ions and A_n = Absorbance intensity during binding of 84c with Hg^{2+} ions for each consecutive addition	142
Figure 120	Job's plot using the method of continuous variations in ($ACN:H_2O::4:1$) solvent system. The mole fraction of 84c plotted against relative absorption shows at 0.5 mole fraction, the complex attains the maximum absorbance depicting (1:1) binding ratio of 84c and Hg^{2+} ions.	143
Figure 121	Benesi–Hildebrand plot of chemical receptor 84c with Hg^{2+} ions monitored at 273 nm for determining association constant	144
Figure 122	The UV–vis spectra of probe 84c in ($ACN:H_2O::4:1$) demonstrate the specific binding of Hg^{2+} ions among other metal ions such as Zn^{2+} , Ni^{2+} , Mg^{2+} , Co^{2+} , Ce^{3+} , Mn^{2+} , Cd^{2+} , Hg^{2+} , Cu^{2+} , Cr^{2+} , Ba^{2+} , Pb^{2+} at equimolar concentration	145
Figure 123	Time bound profile versus absorption of the [84c- Hg^{2+}] complex in $ACN:H_2O::4:1$ solvent system for 30 minutes at $\lambda = 273$ and 307 nm	146
Figure 124	Effect of temperature on the binding of [84c- Hg^{2+}] complex in $ACN:H_2O::4:1$ solvent system from 32 °C to 44 °C	147

Figure 125	The fluorescence spectra of the sensor 84c (0.005 mM) was observed at $\lambda_{\text{ex}} = 310$ nm. As 1 equiv. of 0.1 mM Hg^{2+} ions solution was added in (ACN:H ₂ O::4:1) solvent mixture, a noticeable increase in the intensity was observed (Hyperchromic shift)	148
Figure 126	The fluorescence intensity ratios (I_n/I_o) at 520 nm plotted against variant concentration of Hg^{2+} ions at $\lambda_{\text{ex}} = 320$ nm. The emission intensity of probe 84c in the absence of Hg^{2+} is denoted as I_o , whereas I_n represents the emission intensity during the binding of 84c with Hg^{2+} ions with each successive addition	149
Figure 127	PET mechanism, displaying the modified version of the frontier orbital energy diagram showing binding based fluorescent metal ion detection when the probe was excited at $\lambda_{\text{ex}} = 310$ nm	150
Figure 128	The co-linear plot, represented by the ratio $[I_o - I_n/I_o]$ plotted against the concentration of Hg^{2+} ions, wherein I_n = Emission intensity seen with each subsequent addition of Hg^{2+} ions, while I_o = Emission Intensity of probe 84c	151
Figure 129	Plausible binding mode of 84c- Hg^{2+} complex (1:1) stoichiometric ratio in (ACN:H ₂ O::4:1) solvent system	152
Figure 130	Bar graph illustrating the response of metal ions such as Ba^{2+} , Cr^{3+} , Mn^{2+} , Na^+ , K^+ , Ce^{3+} , Cu^{2+} , Ni^{2+} , Zn^{2+} , Mg^{2+} , Pb^{2+} , Ag^+ , Cd^{2+} , Th^{4+} towards chemosensor 85c at $\lambda_{\text{max}} = 272$ nm in $\text{CH}_3\text{CN}:\text{H}_2\text{O}::4:1$ solvent system.	154
Figure 131	The UV-vis spectral variations of 85c (0.05 mM) in (ACN:H ₂ O::4:1) after incremental addition (0-19 equiv.) of Cu^{2+} ions. The rise in absorbance intensity (hyperchromic shift) at $\lambda = 272$ nm and the decrease in absorbance intensity at $\lambda = 307$ nm was observed along with the isosbestic point at 392 nm	155
Figure 132	The absorbance spectra of 85c (0.05 mM) displaying the spectral changes after cumulative addition of (0-22 equiv.) Pb^{2+} ions. The upsurge in absorbance intensity (hyperchromic shift) at $\lambda = 272$ nm and the reduction in absorption intensity at $\lambda = 307$ nm alongwith a distinct isosbestic point at 392 nm was observed	156
Figure 133	The linear response of the relative absorbance (A_n/A_o) of 85c plotted against the increase in concentration of Cu^{2+} ions in (ACN:H ₂ O::4:1) solvent medium at $\lambda = 272$ nm, herein A_o denotes the absorbance of free 85c and A_n represent the absorbance of 85c after addition of Cu^{2+} ions	157
Figure 134	The relative absorbance of 85c increases in linear manner with the upsurge in concentration of Pb^{2+} ions at $\lambda = 272$ nm in (ACN:H ₂ O::4:1) solvent medium, wherein A_o = absorbance of free probe 85c and A_n = absorbance of probe 85c in presence of Pb^{2+} ions	158

Figure 135	Job's plot for assessing the stoichiometry ratio of complexation between 85c and Cu^{2+} ions in $\text{ACN}:\text{H}_2\text{O}::4:1$ solution, the maximum absorption value attained at 0.5 mole fraction showing (1:1) ratio of $[\text{85c-Cu}^{2+}]$ complex	159
Figure 136	Job's plot for evaluating the stoichiometric ratio of $[\text{85c-Pb}^{2+}]$ complex in $\text{ACN}:\text{H}_2\text{O}::4:1$ solution at $\lambda = 272$ nm, the maximum value of relative absorbance was attained at 0.5 mole fraction depicting the (1:1) binding ratio of $[\text{85c-Pb}^{2+}]$ complex	160
Figure 137	UV-vis anti-interference spectra of chemosensor 85c depicting the selective sensing of Cu^{2+} and Pb^{2+} in equimolar coexistence of multiple metal ions, where M^{n+} represent the mixture of Ba^{2+} , Cr^{3+} , Mn^{2+} , Na^+ , K^+ , Ce^{3+} , Cu^{2+} , Ni^{2+} , Zn^{2+} , Mg^{2+} , Pb^{2+} , Ag^+ , Cd^{2+} , Th^{4+} metal ions in $\text{ACN}:\text{H}_2\text{O}::4:1$ solution	161
Figure 138	The absorption titration data of the probe 85c with Cu^{2+} measured via Benesi-Hildebrand plot at 272 nm in $\text{ACN}:\text{H}_2\text{O}::4:1$ solution	162
Figure 139	Benesi-Hildebrand plot of 85c binding with the Pb^{2+} metal ion at 272 nm in $\text{ACN}:\text{H}_2\text{O}::4:1$ solution	162
Figure 140	Time dependent study of probe 85c- Cu^{2+} complex nm in $\text{ACN}:\text{H}_2\text{O}::4:1$ solution for 30 minutes	164
Figure 141	Time dependent graph showing influence on 85c- Pb^{2+} binding in $\text{ACN}:\text{H}_2\text{O}::4:1$ solution for 30 minute	165
Figure 142	Temperature dependent study of 85c- Cu^{2+} complex in $\text{ACN}:\text{H}_2\text{O}::4:1$ solution from 32 °C to 48 °C	166
Figure 143	Temperature dependent study of 85c- Pb^{2+} complex in $\text{ACN}:\text{H}_2\text{O}::4:1$ solution from 32 °C to 48 °C	167
Figure 144	Fluorescence spectra of 85c (0.005 mM) with increasing concentration of Cu^{2+} ions (0-9 equiv.) in ($\text{ACN}:\text{H}_2\text{O}::4:1$) solvent medium at $\lambda = 562$ nm. An increase in intensity (hyperchromic shift) was observed with the addition of Cu^{2+} ion solution in free probe 85c solution depicting the binding of $[\text{85c-Cu}^{2+}]$ complex	168
Figure 145	The change in emission intensity of Probe 85c (0.005 mM) upon the addition of Pb^{2+} ions (0-13 equiv.) in ($\text{ACN}:\text{H}_2\text{O}::4:1$) solvent medium at $\lambda = 562$ nm, with the accumulation of Pb^{2+} ions solution in 85c solution, increase in the emission intensity was observed (hyperchromic shift)	169
Figure 146	The relative change in emission intensity (I_n/I_o) of 85c plotted against successive addition of Cu^{2+} ions using ($\text{ACN}:\text{H}_2\text{O}::4:1$) solvent medium at $\lambda = 562$ nm, wherein I_o represents the emission intensity of the free probe 85c and I_n signifies the emission intensity during the binding of 85c with Cu^{2+} ions with each consecutive addition	170

Figure 147	The relative change in emission spectra (I_n/I_o) of 85c with incremental addition of Pb^{2+} ions in (ACN:H ₂ O::4:1) solvent medium at $\lambda = 562$ nm, where I_o stands for emission intensity of probe 85c and I_n represent emission intensity during addition of Pb^{2+} ion solution in probe 85c solution	171
Figure 148	The linear calibration curve of 85c represented by the ratio $[I_o - I_n/I_o]$ plotted against the concentration of Cu^{2+} ions in (ACN:H ₂ O::4:1) solvent medium, wherein I_n represent the fluorescence intensity of receptor of 85c and the fluorescence emission after consecutive addition of Pb^{2+} ions solution in receptor 85c	172
Figure 149	The linear calibration curve demonstrating the relative emission intensity $[I_o - I_n/I_o]$ observed at various concentration of Pb^{2+} ions in (ACN:H ₂ O::4:1) solvent medium	173
Figure 150	Plausible mode of interaction between 85c and metal ions (Cu^{2+} and Pb^{2+}) ions	174
Figure S1	(a) Rolf Huisgen's classical cycloaddition reaction of 1,2,3-triazole isomers (b) Sharpless Cu(I) catalyzed click reaction for regioselective 1,4-disubstituted triazole	181
Figure S2	Various methods for the synthesis of azides	183
Figure S3	Organic azide 39 and Schiff bases (81a-85a)	184
Figure S4	Schiff base terminal alkynes (81b-85b)	184
Figure S5	Schiff base 1,4 disubstituted 1,2,3-triazole (81c-85c)	185
Figure S6	Absorption spectra of the 81c probe upon successive addition of 1 equiv. of Fe^{3+} ion solution in EtOH:H ₂ O::9:1, inset showing stoichiometric (2:1) of $[81c:Fe^{3+}]$ complex	188
Figure S7	Fluorescence titration spectra of probe 81c in EtOH:H ₂ O::9:1 solvent medium with incremental addition of 1 equiv. of Fe^{3+} ions, inset exhibiting relative change in absorption with addition of Fe^{3+} ions (linear calibration curve)	189
Figure S8	UV-vis spectrum of probe 82c with sequential addition of 1 equiv. of Pb^{2+} ions in DMSO solvent, inset displaying the binding ratio of 2:1 for 82c- Pb^{2+} complex	190
Figure S9	Fluorescence spectrum of probe 82c when titrated with Pb^{2+} ions solution in DMSO solvent, inset displaying the stoichiometric ratio (1:1) of 82c- Pb^{2+} complex	191
Figure S10	Absorption spectra of 83c in CH ₃ CN:H ₂ O::4:1 solvent mixture upon consecutive addition with the increasing equivalent of Cu^{2+} ion, inset unveiling the stoichiometric ratio (1:1) of 83c- Cu^{2+} complex via Job's plot	192

Figure S11	Emission spectra of probe 83c when titrated with Cu ²⁺ ions solution in CH ₃ CN:H ₂ O::4:1 solvent media, inset presenting the pattern of relative emission upon addition of Cu ²⁺ ions solution	193
Figure S12	UV-visible graph of 84c showing absorbance responses measured after adding 1 equiv. of Hg ²⁺ ion solution to 84c solution in ACN:H ₂ O::4:1 solvent system, inset exhibiting binding ratio of [84c-Hg ²⁺] complex calculated via job's plot	194
Figure S13	The fluorescence spectra of the sensor 84c titrated against Hg ²⁺ ions in ACN:H ₂ O::4:1 solution, inset exhibited the relative emission intensity with increase in conc. of Hg ²⁺ ion solution	195
Figure S14	The UV-vis spectral variations of 85c after incremental addition of Cu ²⁺ ions in in ACN:H ₂ O::4:1 solvent, inset demonstrating job's plot (1:1) binding ratio of 85c-Cu ²⁺ complex	196
Figure S15	The absorbance spectra of 85c displaying the spectral changes after addition of Pb ²⁺ ions in ACN:H ₂ O::4:1 solvent, inset exhibiting binding ratio (1:1) of 85c-Pb ²⁺ complex	197
Figure S16	Fluorescence spectra of 85c with increasing concentration of Cu ²⁺ ions in (ACN:H ₂ O::4:1) solvent medium, inset exhibiting relative emission against increasing conc. of Cu ²⁺ ions solution	198
Figure S17	The Change in emission spectra of Probe 85c upon the addition of Pb ²⁺ ions in a ACN:H ₂ O::4:1 solvent medium, inset showing change in emission intensity with increasing conc. of Pb ²⁺ ions	199

LIST OF TABLES

Table No.	Description	Page No.
Table 1	The compilation of previously synthesized 1,2,3-triazoles chemosensors for detection of metal ions	42-44

LIST OF ANNEXURES

Annexures	Description	Page No.
Annexure A	Chemicals and Instrumentation	200-202
Annexure B	FTIR, NMR (^1H , ^{13}C), and MS spectra	203-268
1	FTIR spectrum of <i>Azidomethylbenzene 39</i>	204
2	^1H NMR spectrum of <i>Azidomethylbenzene 39</i>	205
3	^{13}C NMR spectrum of <i>Azidomethylbenzene 39</i>	206
4	FTIR spectrum of Schiff base 81a	207
5	^1H NMR spectrum of Schiff base 81a	208
6	^{13}C NMR spectrum of Schiff base 81a	209
7	FTIR spectrum of Schiff base alkyne 81b	210
8	^1H NMR spectrum of Schiff base alkyne 81b	211
9	^{13}C NMR spectrum of Schiff base alkyne 81b	212
10	FTIR spectrum of Schiff base triazole 81c	213
11	^1H NMR spectrum of Schiff base triazole 81c	214
12	^{13}C NMR spectrum of Schiff base triazole 81c	215
13	Mass spectrum of Schiff base triazole 81c	216
14	FTIR spectrum of Schiff base 82a	217
15	^1H NMR spectrum of Schiff base 82a	218
16	^{13}C NMR spectrum of Schiff base 82a	219
17	FTIR spectrum of Schiff base alkyne 82b	220
18	^1H NMR spectrum of Schiff base alkyne 82b	221
19	^{13}C NMR spectrum of Schiff base alkyne 82b	222
20	FTIR spectrum of Schiff base triazole 82c	223
21	^1H NMR spectrum of Schiff base triazole 82c	224
22	^{13}C NMR spectrum of Schiff base alkyne 82c	225
23	Mass spectrum of Schiff base triazole 82c	226

24	FTIR spectrum of Schiff base 83a	227
25	¹ H NMR spectrum of Schiff base 83a	228
26	¹³ C NMR spectrum of Schiff base 83a	229
27	FTIR spectrum of Schiff base alkyne 83b	230
28	¹ H NMR spectrum of Schiff base 83b	231
29	¹³ C NMR spectrum of Schiff base 83b	232
30	FTIR spectrum of Schiff base triazole 83c	233
31	¹ H NMR spectrum of Schiff base triazole 83c	234
32	¹³ C NMR spectrum of Schiff base triazole 83c	235
33	Mass spectrum of Schiff base triazole 83c	236
34	FTIR spectrum of Schiff base 84a	237
35	¹ H NMR spectrum of Schiff base 84a	238
36	¹³ C NMR spectrum of Schiff base 84a	239
37	FTIR spectrum of Schiff base alkyne 84b	240
38	¹ H NMR spectrum of Schiff base alkyne 84b	241
39	¹³ C NMR spectrum of Schiff base alkyne 84b	242
40	FTIR spectrum of Schiff base triazole 84c	243
41	¹ H NMR spectrum of Schiff base triazole 84c	244
42	¹³ C NMR spectrum of Schiff base triazole 84c	245
43	Mass spectrum of Schiff base triazole 84c	246
44	FTIR spectrum of Schiff base 85a	247
45	¹ H NMR spectrum of Schiff base 85a	248
46	¹³ C NMR spectrum of Schiff base 85a	249
47	FTIR spectrum of Schiff base alkyne 85b	250
48	¹ H NMR spectrum of Schiff base alkyne 85b	251
49	¹³ C NMR spectrum of Schiff base alkyne 85b	252
50	FTIR spectrum of Schiff base triazole 85c	253
51	¹ H NMR spectrum of Schiff base triazole 85c	254

52	¹³ C NMR spectrum of Schiff base triazole 85c	255
53	Mass spectrum of Schiff base triazole 85c	256
54	FTIR spectrum of Schiff base triazole 81c-Fe ³⁺ complex	257
55	Mass spectrum of Schiff base triazole 81c-Fe ³⁺ complex	258
56	FTIR spectrum of Schiff base triazole 82c-Pb ²⁺ complex	259
57	Mass spectrum of Schiff base triazole 82c-Pb ²⁺ complex	260
58	FTIR spectrum of Schiff base triazole 83c-Cu ²⁺ complex	261
59	Mass spectrum of Schiff base triazole 83c-Cu ²⁺ complex	262
60	FTIR spectrum of Schiff base triazole 84c-Hg ²⁺ complex	263
61	Mass spectrum of Schiff base triazole 84c-Hg ²⁺ complex	264
62	FTIR spectrum of Schiff base triazole 85c-Pb ²⁺ complex	265
63	Mass spectrum of Schiff base triazole 85c-Pb ²⁺ complex	266
64	FTIR spectrum of Schiff base triazole 85c-Cu ²⁺ complex	267
65	Mass spectrum of Schiff base triazole 85c-Cu ²⁺ complex	268

LIST OF ABBREVIATIONS

STANDARD UNITS

g	Gram(s)
h	Hour(s)
min	Minute(s)
°C	Degree Celsius
K	Kelvin
atm	Atmosphere
B.Pt.	Boiling point
equiv.	Equivalent(s)
M.Pt.	Melting point
Hz	Hertz
MHz	Mega hertz
mol	Mole(s)
mmol	Millimole(s)
ml	Milliliter(s)
ppm	Parts per million
cm	Centimeter
mm	Millimeter
nm	Nanometer
kcal/mol	Kilocalorie per mole
W	Watt

%	Percentage
Å	Angstrom
<i>et al.</i>	Latin words meaning “and others”

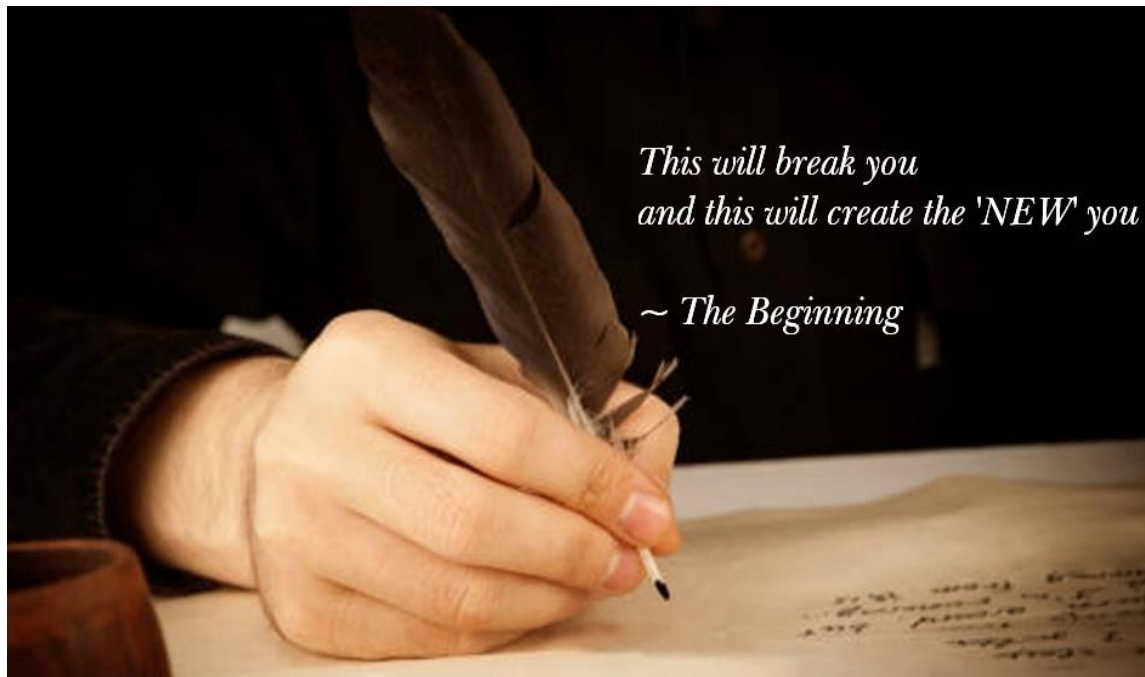
CHEMICALS

DMF	N,N-Dimethylformamide
MeOH	Methanol
AcOH	Acetic acid
DBU	1,8-Diazabicycloundec-7-ene
CDCl ₃	Deuterated chloroform
DMSO-d ₆	Deuterated dimethylsulphoxide
DCM	Dichloromethane
Et ₃ N/TEA	Triethylamine
THF	Tetrahydrofuran
DIPEA	Diisopropylethylamine
PMDETA	Pentamethyldiethyltriamine
HMTETA	Hexamethyltriethyltetraamine
tpy	Tripyridyl
dpy	Dipyridyl
TPMA	Tris(pyridylmethyl)amine
TBTA	Tris(benzyltriazolylmethyl)amine
THPTA	Tris(hydroxypropyltriazolylmethyl)amine
TTTA	Tris(t-butyltriazolylmethyl) amine

Et	Ethyl
Me	Methyl
Ph	Phenyl
<u>OTHERS</u>	
MS	Mass spectrum
GCMS	Gas chromatography3 mass spectrum
LCMS	Liquid chromatography mass spectrum
IR	Infrared
UV	Ultraviolet
stirr	Stirring
rt	Room temperature
M	Molecular mass
H	Hydrogen
μw	Microwave
λ_{max}	Wavelength of maximum absorption
λ_{ex}	Excitation wavelength
μM	Micromolar
ϵ_{max}	Molar absorptivity coefficient
NMR	Nuclear magnetic resonance
s	Singlet

d	Doublet
dd	Double doublet
t	Triplet
m	Multiplet
J	Coupling Constant
δ	Chemical shift
TLC	Thin layer chromatography
CuAAC	Copper catalyzed alkyne-azide cycloaddition
HSAB	Hard-Soft acid base
HOMO	Highest occupied molecular orbital
LUMO	Lowest unoccupied molecular orbital
v/v	Volume/Volume

Chapter 1



*This will break you
and this will create the 'NEW' you
~ The Beginning*

INTRODUCTION

This segment covers the literature pertaining to the research that will be elaborated extensively in the subsequent chapters. This chapter outlines the development of 1,4-disubstituted 1,2,3 triazole chemosensors via click chemistry and their application in cation recognition. The general background about optical sensors that illustrate the overview of chemosensors, different signal mechanisms in the fluorescent chemosensors has been documented in this section. The detailed information on chemosensing via UV-vis and fluorescence spectroscopy has been elaborated in the later section of this chapter

1. Exploring the Legacy of 'Click Chemistry'

The modern era organic synthesis thrives on reactions featuring the quickest and most selective conjugation of molecules possessing extensive features. 'Click Chemistry' was coined by Sir K. B. Sharpless, Nobel Laureate (2022) to describe a set of guiding principles designed to address the challenges of contemporary chemistry and the exigencies of drug discovery.^{1,2} The term "click" refers to the intuitive coupling of molecular building blocks, as in a seat belt locking device. A resilient thermodynamic force drives the click reaction that produces a substantial quantity of the product with no byproducts. The necessary prerequisites for click reactions includes the utilization of easily obtainable precursors and reagents, less hazardous solvents, the consumption of water as a solvent or the avoidance of solvents altogether, and the facilitation of product isolation through the implementation of facile purification techniques.^{3,4} Click chemistry involves four discrete types of reactions, which are summarized as follows:

- (1) Cycloaddition processes such as 1,3-dipolar and Diels-Alder cycloaddition reactions
- (2) Addition to carbon-carbon multiple bonds that include epoxidation and Michael addition
- (3) Nucleophilic Substitution refers to a chemical reaction in which a nucleophile replaces a leaving group in a molecule
- (4) Non-aldol reactions in carbonyl chemistry^{5,6}

The cycloaddition reaction with Cu(I) catalyst is the most renowned and well executed reaction among several Cu-catalyzed reactions. The reaction of organic azide with terminal alkyne via 1,3 dipolar cycloaddition reaction resulting in synthesis of 1,2,3-triazole is considered a very pertinent transformation in the field of synthetic chemistry.^{7,8} Click reactions have been effectively implemented in many of the disciplines such as pharmaceuticals, drug discovery, biochemistry, dye synthesis, antibacterial polymers, corrosion inhibitors, photo-stabilizers, and photographic materials.^{9,10}

2. 1,3 dipolar cycloaddition reaction

1,3-dipolar cycloaddition involves the reaction of 1,3-dipole with a dipolarophile that results in formation of five-membered heterocycle rings. Similar to the Diels-Alder reaction, a 1,3-dipole undergoes a 4π system reaction with a dipolarophile, which has the general formula "ABC" and delivers 2π electrons. This reaction occurs by a (3+2) cycloaddition process, resulting in the

formation of a five-membered cycloadduct. (**Figure 1**) The reaction product exhibits high stereoselectivity with the dipolarophile, wherein a cis-alkene yields a syn-product, and vice versa. This observation provides evidence in favour of an integrated mechanism of cycloaddition.^{11–13}

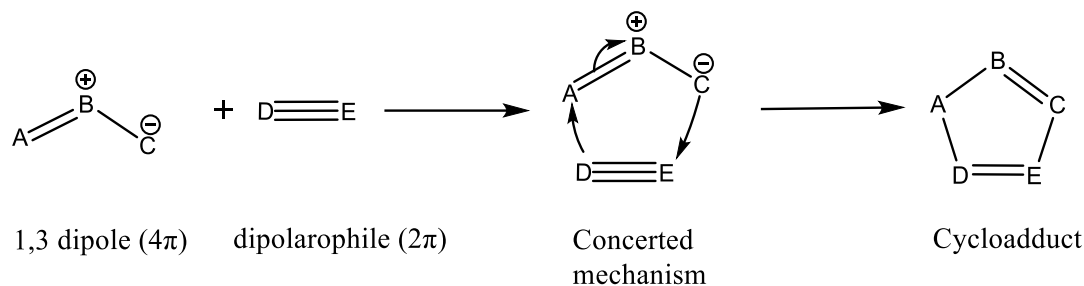


Figure 1. The mechanistic pathway for cycloaddition of 1,3 dipolar reaction

3. Classical cycloaddition reaction versus Cu(I) catalyzed reaction

In 1963, Rolf Huisgen discovered an uncatalyzed thermal 1,3–dipolar cycloaddition reaction of substituted alkyne with substituted azide, leading to the stereoisomers of 1,4 and 1,5–triazole compounds.¹⁴ However, In the era of 2001, Sharpless and his coworkers used Cu(I) in catalytic amounts to dramatically speed up the thermal 1,3–dipolar cycloaddition reaction between substituted alkyne and substituted azide, even under benign conditions with phenomenal regioselectivity.^{15,16} (**Figure 2**) The exclusive isolation of 1,4–disubstituted–1,2,3–triazole is regarded as one of the greatest accomplishments in the field of synthetic chemistry.^{17,18} Since its inception, this methodology has revolutionized the synthesis of physiologically important organic moieties containing 1,2,3-triazole entities and the expansion of their function as pharmacophores, ions detection, polymeric chemistry, and so on. Various cations such as Ni^{2+} , Pt^{2+} , Pd^{2+} , Ir^{1+} , and Ru^{2+} , have also been shown to catalyse the reaction between azides and terminal alkynes, though none of these processes can compete with copper (I)–catalyzed process in the area of efficacy related to reaction time, temperature and yield.^{19,20}

4. Copper(I)-catalyzed alkyne azide cycloaddition click reaction

CuAAC reaction has been widely accepted in the field of organic chemistry following its initial discovery, since the electronic and steric properties of the substituted electron-rich or electron-deficient groups, whether they are aliphatic, aromatic, primary, secondary, or tertiary, on the azide or terminal alkyne do not impede the chemical reaction.^{17,21–23} The literature studies demonstrate the existence of diverse copper sources that offer Cu (I) as an active species, which functions as a catalyst under specific reaction conditions

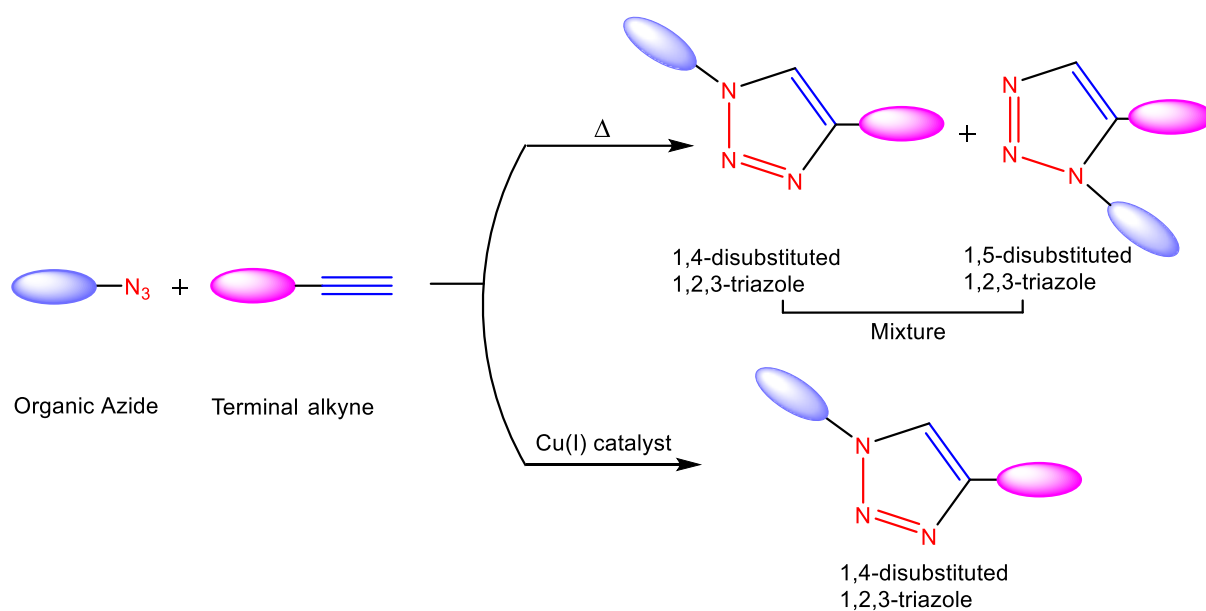


Figure 2. A scheme showing Huisgen 1,3-dipolar cycloaddition reaction of substituted azide and alkyne under thermal conditions, leading to 1,4 and 1,5 isomers and Sharpless click reaction using Cu(I) catalyst, resulted in selective 1,4 regioisomer of 1,2,3-triazole

The preference for direct utilisation of Cu (I) salts has emerged as a strategy to minimise the dependence on reducing agents. The utilisation of the CuAAC reaction presents notable benefits in the field of ligand design and has facilitated the exploration of diverse coordination chemistry. The optimisation of copper(I) catalytic sources has allowed for the tailoring of Cu (II) salts to obtain an active catalyst state that can be recovered. The utilisation of bulky ligands to protect Cu (I) species from oxidation has been demonstrated to be an effective strategy for catalysis, even when used in small amounts and under ambient reaction conditions. The wide range of techniques and catalytic systems have expanded their potential applications, which are contingent upon factors such as the nature of the reactant, prevailing conditions, resource availability, and the suitability of the resulting product. Copper (I) is commonly utilised as a catalyst on various substrates such as carbonaceous materials, inorganic solids, organic polymers, dendrimers, magnetic materials, and metal-organic frameworks. These materials possess the advantageous characteristic of being recyclable, making them highly suitable for applications in biochemical conjugations.^{24–27}

5. Mechanistic insights of CuAAC

The CuAAC reaction exhibits sufficient flexibility, allowing for the utilization of nearly any copper(I) source as catalyst. Sir Fokin and his colleagues proposed a mechanism that involves a mononuclear Cu-alkynyl intermediate, as shown in **Figure 3**. The terminal alkyne (a) is initially reacted with copper(I), resulting in the formation of copper-acetylide (b) (Step A). The alkylation of one of the nitrogen atoms in the azide group, which is coordinated with copper(I), leads to the formation of a complex involving all three components. The π -coordination of terminal alkyne to copper (I) considerably acidifies the terminal hydrogen, allowing for deprotonation in an aqueous media and the formation of an σ -acetylide. Subsequently, the azide is activated by coordinating with copper, generating intermediate (c) (Step B). The initial C–N bond formation occurs in the following phase (Step C), which results in the formation of strained copper metallacycle (d). In this stage, the copper center undergoes formal oxidation from oxidation state +1 to +3. During Step D, copper (III) undergoes reduction to copper(I) while simultaneously undergoing ring contraction, resulting in the formation of cuprous triazolide (e) which is quite facile and easily favourable. The terminal alkyne molecule donates the proton necessary to complete the triazole formation (f) (Step E) while the subsequent copper(I) acetylide is guided into the catalytic cycle. The mechanistic cycle provides insight on the reliance on copper (I) and the regioselectivity attained during the synthesis of triazole, in addition to elucidating the copper's interaction with the alkyne and azide components.^{22,28}

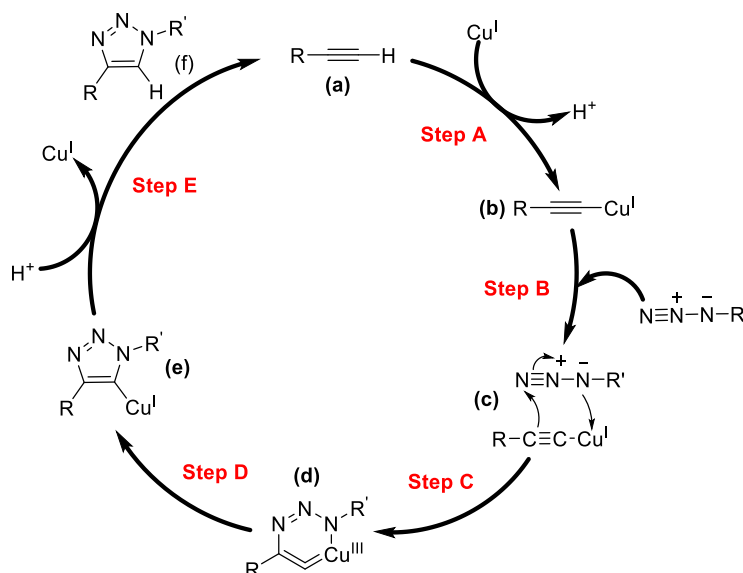


Figure 3. The initially developed CuAAC mechanism, proposed by Fokin and co-workers^{22,29}

6. Importance of 1,4 disubstituted 1,2,3-triazoles

1,4 disubstituted-1,2,3-triazole can also act as a mimetic of amide bond due to its non-reactive chemical nature against oxidation, reduction, and hydrolysis in acidic and basic mediums. Additionally, CuAAC reaction can indulge in effective hydrogen bonding and dipole-dipole interactions due to which it has anticipated demand in various areas like drug discovery, metal ions sensing, biochemistry, polymer chemistry, and material-science.^{30,31} The sensing of cation/anion is possible in 1,4-disubstituted-1,2,3-triazole due to the dipolar nature of triazole, they can aid in the binding of ions, and facilitate a link between the binding site and fluorophore.³² Derivatives of 1,4-disubstituted 1,2,3-triazoles exhibit diverse biological activities such as antiviral, anticancer, anti-inflammatory, and antibacterial effects. Also, CuAAC click reaction doesn't release any undesirable waste or side-products. Therefore, the reaction accomplished the major aspect of atom economy stated as one of the principles of sustainable chemistry.³³

Metal ions like Cd^{2+} , Cu^{2+} , Hg^{2+} , Pb^{2+} , Ni^{2+} , Fe^{2+} , Al^{3+} , and Zn^{2+} cause severe health disorders and also act as the source of environmental pollutants by contaminating the air, water, soil, and environmental surroundings. Hence, the efficient treatment of these hazardous contaminants can only be initiated if they are recognised quantitatively and qualitatively. The Click reaction has been explored for the identification of such probes that can work as fluorescent efficient chemosensors which can aid in the recognition of variant transition metal ions above their concerned toxic levels.³⁴ The chemosensing is generally conducted by techniques like mass spectroscopy (MS), atomic absorption spectroscopy (AAS), time-of-flight mass spectrometry (TOFMS), laser-induced breakdown spectrometry (LIBS) and inductively coupled plasma mass spectrometry (ICP-MS). However, these procedures tend to incur high costs and lack portability, therefore UV-vis, and fluorescence spectroscopy have attained prominence owing to their ease of implementation and their ability to provide ameliorated levels of sensitivity and specificity.³⁵

The CuAAC reaction is a topic of recent interest to scientists all over the globe, as it has been considered for the synthesis of luminophores through facile reaction methods. Several research articles have been cited depicting transition metal ions identification by 1,2,3-triazole derivatives.³⁶ The easiness and self-efficiency of CuAAC reaction to produce 1,2,3-triazoles have allured the synthesis of countless chemosensors. The sensing of a 5-membered heterocycle

inculcates host-guest interaction which can be illustrated as: (1) binding with the analyte (2) linker connecting binder and receptor sites (3) conjugation in fluorophore.³⁷ **(Figure 4)**

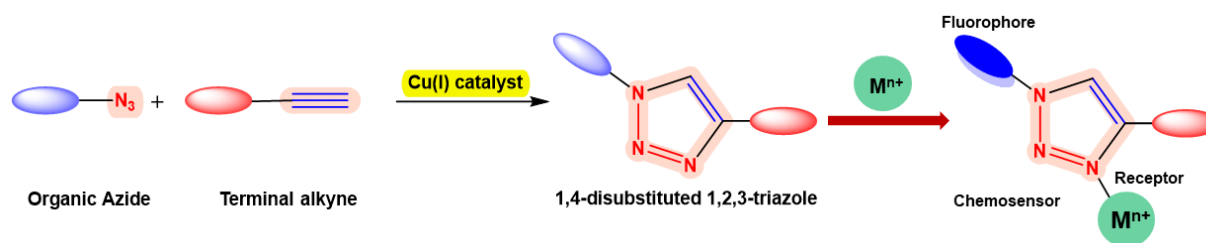


Figure 4. Schematic design of Fluorescent chemosensor for sensing of metal ions

7. Photoluminescence

Photoluminescence refers to the phenomena that occurs when a solid is stimulated by short-wavelength light like UV radiations. The majority of fundamental particles (atoms/molecules) exist at ambient temperature in the ground state. When subjected to electromagnetic irradiation, the particles absorb photon energy. The absorbed energy triggers a quick generation of an electronically excited state, which is subsequently followed by the disposal of the surplus energy in an alternative manner. Photoluminescence is an optical characteristic of the material, when exposed to electromagnetic radiation, absorbs photons and subsequently emits them in a radioactive manner. Photoluminescence is predominantly classified into two distinct types- phosphorescence and fluorescence based on the emission pathway and the electronic orientation of the excited state.

8. Photophysical processes

8.1 Absorbance

Absorbance is the result of the interaction between light and matter. When light strikes an object that absorbs a photon of a specific energy, an electron is excited from a lower energy level to a higher energy level this is referred to as absorbance, occurs in the vicinity of ten to fifteen seconds. Undoubtedly, light that is absorbed is converted to thermal energy or chemical energy when the absorbing molecule undergoes excitation. A spectrophotometer is an instrument that quantifies the amount of light absorption at a particular wavelength (λ) by a material. It is capable of generating a spectrum, which is a graphical representation of absorbance as a function of

wavelength. Absorbance spectroscopy is based on the principle that when ultraviolet or visible light is absorbed, electrons undergo transitions between molecular orbitals, if the energy gaps between the molecules vary, they will exhibit distinct spectra, depending on this phenomenon chemosensing of metal-ligand complex is conducted.³⁸

8.2 Fluorescence

Fluorescence is a type of photoluminescence, which occurs when a substance emits photons in response to light exposure. The emitted light has a wavelength that is longer than the exciting light, which is referred to as the Stokes shift. Electrons have the ability to be excited to higher energy levels, resulting in a change in their quantum state. The addition of any analyte into a solution of fluorescent molecule may alter its emission due to ground-state complex formation between the ligand and the fluorophore(s) in the molecule or excited-state quenching/enhancement in the complex (e.g. energy transfer). This phenomenon defines the metal-ligand interaction via fluorescent spectroscopy.^{39,40}

9. Analytical Supramolecular chemistry: Host guest relationship

Chemical sensing, also known as chemosensor chemistry, ultimately relies on the processes of separation, capture, and signal amplification, which are based on analytical and supramolecular chemistry. Supramolecular chemistry is the field of chemistry that deals with chemical systems consisting discrete number of molecules. Traditional chemistry examines the covalent bond whereas supramolecular chemistry emphasis on the weaker and reversible non-covalent interactions between molecules such as hydrogen bonding, metal coordination, hydrophobic forces, van der Waals forces, π - π interactions, and electrostatic effects. There are several aspects of supramolecular chemistry such as self-assembly, host–guest chemistry, molecular folding, etc. Out of which, host–guest chemistry, also known as molecular recognition chemistry, focuses on the selective recognition of a molecule (guest) by another molecule (host) through the formation of non-covalent interactions. The study of non-covalent interactions is essential for comprehending numerous photophysical processes that heavily rely on these forces for establishing structure and metal-ligand binding. This concept is fundamental and traditional in the design of cation sensors. Supramolecular analytical chemistry is one of the emerging fields of research which integrates analytical and supramolecular chemistry. It analyses recent advances in supramolecular analytical chemistry that make use of optical sensing and primarily focuses on the development and

implementation of sensors. The research goals of supramolecular chemistry include a wide range of molecule classes and aim to create and develop metallacycles and metallacages using metal–ligand coordination chemistry.^{39,41–43}

9.1 Chemosensor

A chemosensor is defined as a chemical entity that is employed to detect molecular species that serve as analytes. Chemosensors are molecular devices that exhibit distinct modifications in their characteristics when exposed to different forms of energy. These sensors can be employed to analyse an analyte of interest qualitatively or quantitatively. An essential characteristic of a chemosensor is the modification of its optical properties that occurs during interaction with a particular analyte. Optical sensor typically comprises three constituent elements: a recognition unit or receptor, a signalling moiety or fluorophore, and a spacer/linker that connects both of them. **(Figure 5)** The electronic characteristics of the host molecule are altered by the recognition unit or binding unit, which is also responsible for initiating optical changes in the chromophoric unit. The receptor plays a meticulous function in selectively recognizing and binding to certain guests. The guest species include neutral molecules, anions, or cations.

For the receptor unit to effectively bind cations, it preferably requires an electron rich atom like oxygen, sulfur, or nitrogen, possessing at least one non-bonded lone pair. This allows for the formation of coordination complex with the metal ions. Optical chemosensors are the molecular investigative tools used to detect variations in light intensity. They alter the receptor's photophysical properties when the analyte (guest) binds to the receptor and can be characterized via UV–visible and fluorescence spectroscopy instrument based on the type of sensor. These are broadly classified as either chromogenic or fluorimetric based on the nature of the signal generated by the signalling unit. The former may be distinguished by the alteration in colour, whereas the latter can be detected by changes in fluorimetric characteristics such as emission intensity or emission wavelength. The existence of lone pair of electrons on the N₂ and N₃ atoms of triazoles allows them to bind with metal ions, making them suitable for applications such as metal sensing or as stabilizing ligands.⁴⁴

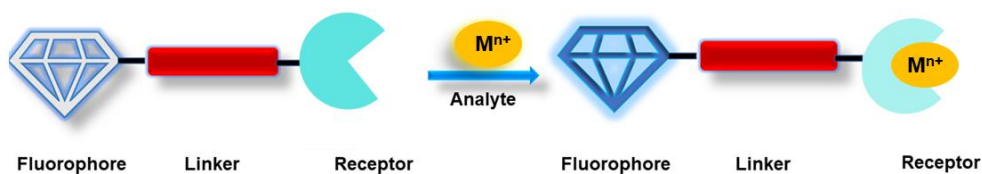


Figure 5. A schematic illustration of analyte detection via a chemosensor

9.2 Fluorimetric sensors

The process of molecular recognition is transduced by fluorescent or fluorogenic chemosensors via a modification in their emission characteristics-e.g., an increase or decrease in emission intensity (fluorescence enhancement or quenching), or a shift in the emission wavelength. Charge transfer, electron transfer, energy transfer, and excimer formation were identified as photoinduced mechanisms accountable for these fluctuations. The implementation of a fluorescence sensor to detect metal ions is often regarded as a very significant analytical technique due to its rapid reaction times, consistent and reliable responses, exceptional selectivity, and substantial sensitivity. In addition to its enhanced sensitivity, fluorimetric chemosensing exhibits a limit of detection (LOD) that is smaller in magnitude when compared to spectrophotometric techniques. The fluorophore and target analytes form specific binding by noncovalent bonding interactions, including π - π stacking, metal complexation, hydrogen bonding, electrostatic connections, and hydrophobic forces.⁴⁵

Fluorescent chemosensors may be categorized into two primary types based on how they respond to analytes: (i) ON-OFF (or OFF-ON) type fluorescent chemosensors, and (ii) ratiometric fluorescent chemosensors. These categories are determined by the changes in the optical signal when the chemosensors interact with analytes. For an ON-OFF type chemosensor, the unbound probe exhibits fluorescence (ON) and converts non-fluorescence (OFF) upon binding to the analyte. If the free probe is initially non-fluorescent (OFF) and then turns fluorescent (ON) upon binding to the analyte, it may be classified as an OFF-ON type. Within the second category, the chemosensor that is not bound by any analyte is capable of fluorescence and emits light at a specific wavelength. This wavelength may shift either towards longer wavelengths (bathochromic shift) or shorter wavelengths (hypsochromic shift) when interacting with an analyte. Also, the increase in intensity of emission (hyperchromic shift) or decrease in intensity of emission (hypochromic shift) can also be observed when ligand interact with specific analyte. (**Figure 6**) In

some cases, the with interaction of analyte. The alterations in emission spectra that are observed when an analyte binds to the chemosensor are attained via one or more prevalent photophysical mechanisms. Significant progress has been made in comprehending these sensing mechanisms, to create highly effective fluorescent chemosensors that can selectively identify analytes. A concise overview of the frequently utilized signal mechanism has been provided in the below section.⁴⁶

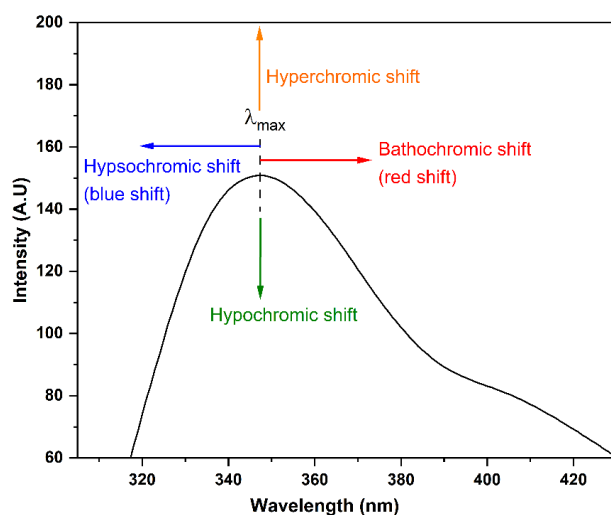


Figure 6. The emission spectra showing the different types of shifts observed during metal-ligand complexation

9.3 Fluorescence signal mechanism: Photo-induced electron transfer (PET)

To develop a highly effective optical chemosensor, it is crucial to have a robust understanding of the receptor's affinity for a particular analyte, as well as a thorough understanding of the photo-physical properties of the signalling component and the process for generating an output signal. Therefore, it is critical to possess an extensive understanding of the various operational principles or mechanisms that comprise the signalling process. The majority of turn-on optical sensors exhibit low fluorescence or non-fluorescence in their unbound state, potentially attributable to the photo-induced electron transfer (PET) effect. The PET mechanism is widely recognized in the field of organic probes that consist primarily of a binding unit and a lone pair of electrons on hetero-atoms (e.g., nitrogen, oxygen, sulphur).⁴⁷

PET is a crucial design for the creation of fluorescent probes that can switch between an "off" and "on" state. PET arises due to the transfer of electrons between the fluorophore and the recognition group. The PET process occurs in the unbound sensor molecule, upon excitation when

it absorbs photons. This causes an electron transfer from highest occupied molecular orbital (HOMO) to the lowest unoccupied molecular orbital (LUMO) of the fluorophore. The energy level of the orbital that contains a non-bonded electron pair (receptor unit) is greater than that of the HOMO of the fluorophore that leads to a rapid transfer of electron from the HOMO of the receptor/binding unit (donor) to fill the partially empty HOMO of the excited fluorophore.

Consequently, a single electron becomes trapped in the fluorophore's LUMO, resulting in the suppression of emission. This process deactivates the excited state in a non-radiative manner, thereby inducing a quenching effect within the fluorescence system. After recognition, the oxidation potential of the activating group rises and it loses its ability to effectively donate electrons. As a result, the PET process is prohibited because of the coordination of the cation/anion with the lone pair of electrons of the binding unit. When the cation/anion attach with the binding unit, the HOMO of the receptor is at a lower energy level than that of the fluorophore. This disturbance in the receptor's redox potential inhibits the process of PET, which in turn activates the emission of fluorescence.⁴⁸ This phenomenon in the context of metal ions binding is known as chelation-enhanced fluorescence (CHEF) as shown in **(Figure 7)**

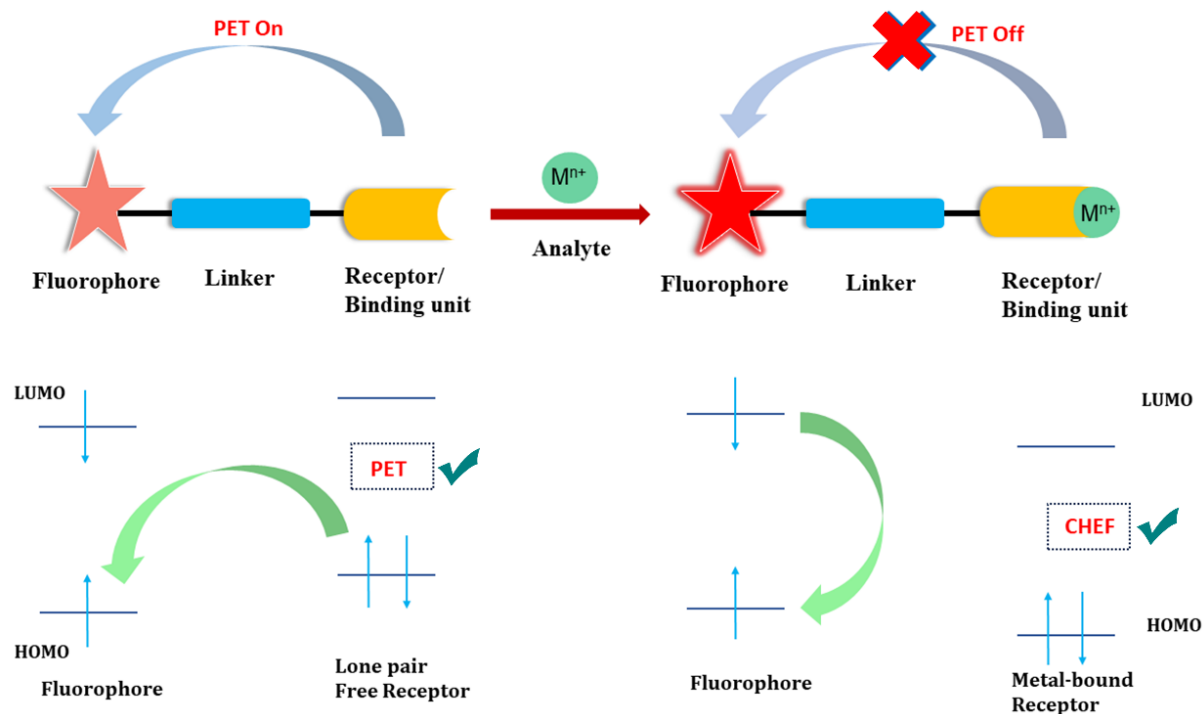


Figure 7. PET mechanism, displaying the modified version of the frontier molecular orbital energy diagram

10. Chemosensing analysis via UV-vis and Fluorescence spectroscopy

UV-visible spectrophotometry is a quantitative analytical method that focuses on measuring the absorption of near-UV (200-400 nm) or visible (400-800 nm) radiation by chemical species dissolved in a solution with emphasis on the electronic transitions operating within molecules in a specified sample. Although commercially accessible since the 1940s, technological advancements in recent years, such as improved detectors and fiber optic sampling, have enabled UV-visible instruments to become more compact, portable, quick, and capable of analyzing ever-smaller sample quantities. This method allows for the quantification of both organic species, mainly in the near-UV range, and inorganic species, mainly in the visible range. The principle of absorption spectroscopy follows Beer-Lambert's law which states that the degree of light absorption increases as the number of molecules capable of absorbing light of a certain wavelength increases and the correlation between absorbance, the concentration of the sample and pathlength is defined in the equation as:

$$A = \log \frac{I_0}{I} = \epsilon \times c \times l$$

A = Absorbance,

I_0 = intensity of light striking upon sample,

I = intensity of light emitted out,

ϵ = molar absorption coefficient,

c = concentration,

l = absorption path length.^{49,50}

UV-vis absorption spectroscopy can be used to demonstrate the absorption spectrum of a sample and may be used to induce fluorescence in the UV-vis region of the electromagnetic spectrum and this fluorescence can then be employed for fluorescence spectroscopy or fluorometry. Similar to UV-vis spectroscopy, the fluorescence spectrum of a sample may also be influenced by the solvent's polarity and pH, as well as the analysis temperature. Intensity is increased with non-polar solvents and at lower temperature. Also, the fluorescence signal can be altered by the proximity of additional molecules to the fluorophore. As a result, fluorescent

spectroscopy can be employed to observe and monitor chemical reactions. Both approaches are cost-effective, efficient, and particularly suitable for analysing forensic samples without causing damage. UV-vis is generally considered a generic approach because many samples are coloured and, therefore, absorb in the UV-vis wavelength range. Therefore, UV-vis is a widespread choice of detector for many quantitative procedures. Fluorescence spectroscopy exhibits higher sensitivity compared to UV-vis because it involves the excitation of numerous fluorescent photons from a single molecule, compared to the absorption of a small amount of light over a short pathlength.^{49,50}

11. Conclusion

The global prominence of research in chemistry has been directed towards the identification and understanding of harmful analytes that impact the biological and pathological progression in living organisms. Therefore, the development of new ions sensor with great selectivity is a crucial endeavour that encompasses enhancing sensor performance, minimizing environmental harm, selectively removing undesired substances, and extracting dangerous chemical species. ‘Click chemistry’ has allured enormous research attention due to the synthetic simplicity for synthesis of 1,2,3-triazole sensors, that act as binding pockets in diverse applications in chemical biology, agrochemical, chemical sensing, dyes, pigments, and so forth. The CuAAC Meldal–Sharpless cycloaddition “click” reaction is attributed to enriching discernible metal ion sensors. The five-membered 1,2,3-triazole ring probe acts as an active donor and has the potential to bind with metal ions due to availability of the electron-rich N and O donor sites. Optical techniques like UV-vis spectroscopy and fluorescence are of paramount importance in analytical chemistry as these determine the solutions of different analytes like metal ions, organic ligands, and biochemical compounds and also scrutinizes the metal ions sensing at low concentrations, binding the metal with ligand probes.

12. References

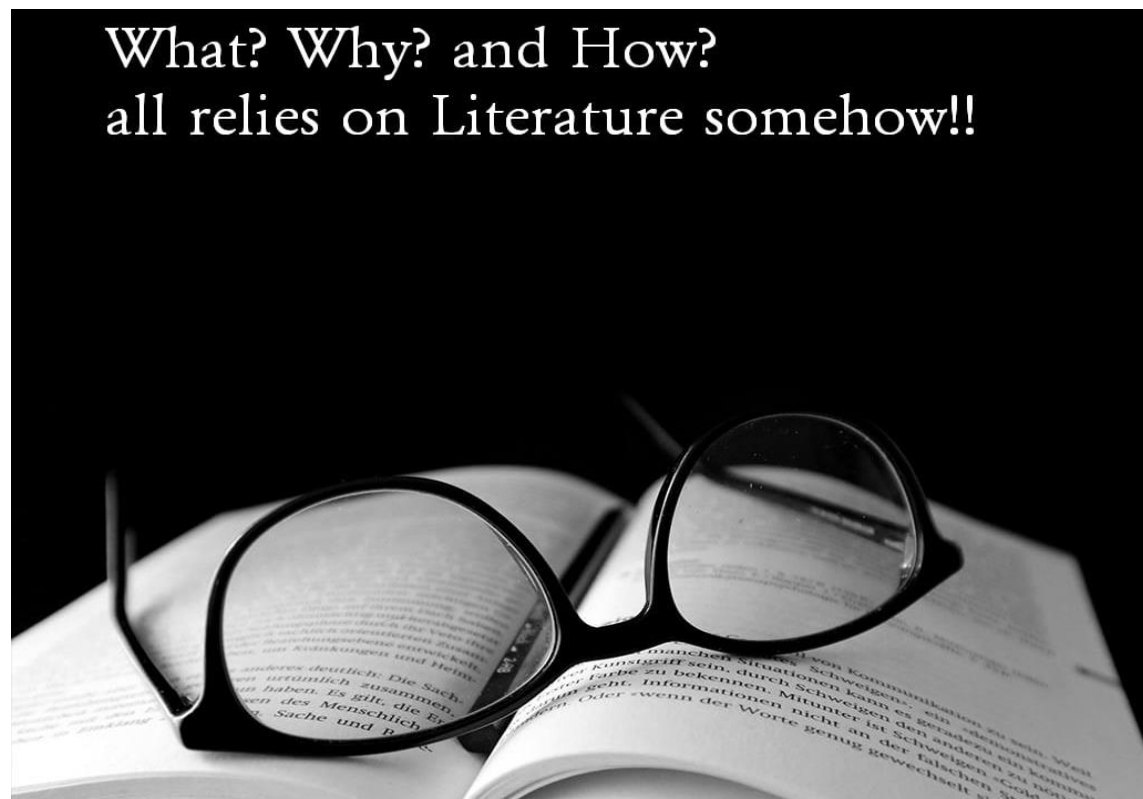
- 1 G. Kaur, G. Singh and J. Singh, *Mater Today Chem*, 2018, **8**, 56–84.
- 2 B. L. Droumaguet and K. Velonia, *Macromol Rapid Commun*, 2008, **29**, 1073–1089.
- 3 S. Gupta, C. Ameta, R. Ameta and P. B. Punjabi, *Elsevier*, 2020, 13–48.

- 4 J. E. Moses and A. D. Moorhouse, *Chem Soc Rev*, 2007, **36**, 1249–1262.
- 5 V. K. Tiwari, B. B. Mishra, K. B. Mishra, N. Mishra, A. S. Singh and X. Chen, *Chem Rev*, 2016, **116**, 3086–3240.
- 6 C. R. Becer, R. Hoogenboom and U. S. Schubert, *Angew Chem Int Ed*, 2009, **48**, 4900–4908.
- 7 A. A. Saikia, R. N. Rao, S. Das, S. Jena, S. Rej, B. Maiti and K. Chanda, *Tetrahedron Lett*, 2020, **61**, 152273.
- 8 M. V. Gil, M. J. Arévalo and Ó. López, *Synthesis (Stuttg)*, 2007, 1589–1620.
- 9 A. Tăbăcaru, B. Furdui, I. O. Ghinea, G. Cârâc and R. M. Dinică, *Inorganica Chim Acta*, 2017, **455**, 329–349.
- 10 H. C. K. and K. B. Sharpless, *Elsevier*, 2008, **8**, 401–422.
- 11 M. Breugst and H. U. Reissig, *Angew Chem Int Ed*, 2020, **59**, 12293–12307.
- 12 W. Carruthers, *Tetrahedron Org. Chem. Ser.*, 1990, **8**, 269–314.
- 13 C. O. Kappe and E. V. D. Eycken, *Chem Soc Rev*, 2010, **39**, 1280–1290.
- 14 V. V. Rostovtsev, L. G. Green, V. V. Fokin and K. B. Sharpless, *Angew Chem Int Ed*, 2002, **114**, 2708–2711.
- 15 L. Liang and D. Astruc, *Coord Chem Rev*, 2011, **255**, 2933–2945.
- 16 B. S. Sumerlin and A. P. Vogt, *Macromol*, 2010, **43**, 1–13.
- 17 P. Saini, Sonika, G. Singh, G. Kaur, J. Singh and H. Singh, *Mol Catal*, 2021, **504**, 111432.
- 18 A. K. Agrahari, P. Bose, M. K. Jaiswal, S. Rajkhowa, A. S. Singh, S. Hotha, N. Mishra and V. K. Tiwari, *Chem Rev*, 2021, **121**, 7638–7956.
- 19 V. Kumar, K. Lal, Naveen and R. K. Tittal, *Catal Commun*, 2023, **176**, 106629.
- 20 P. L. Golas and K. Matyjaszewski, *Chem Soc Rev*, 2010, **39**, 1338–1354.
- 21 V. Kumar, K. Lal, Naveen and R. K. Tittal, *Catal Commun*, 2023, **176**, 106629.

- 22 J. E. Hein and V. V. Fokin, *Chem Soc Rev*, 2010, **39**, 1302–1315.
- 23 S. Song, H. Zhang, C. Kim, L. Sheng, X. He, Y. Long, J. Li and G. Chen, *Tetrahedron*, 2010, **66**, 9974–9980.
- 24 F. Ahmed and H. Xiong, *Dyes Pigm*, 2021, **185**, 108905.
- 25 V. D. Bock, R. Perciaccante, T. P. Jansen, H. Hiemstra and J. H. V. Maarseveen, *Org Lett*, 2006, **8**, 2596–2599.
- 26 *Click Chemistry and Bio Orthogonal Chemistry*, The Nobel Committee for Chemistry, 2022, **50005**, 1-20.
- 27 B. Li, R. Hu, A. Qin and B. Z. Tang, *Polym Chem*, 2020, **11**, 2006–2014.
- 28 P. Kalra, R. Kaur, G. Singh, H. Singh, G. Singh, Pawan, G. Kaur and J. Singh, *J Organomet Chem*, 2021, **944**, 121846.
- 29 N. Z. Fantoni, A. H. E. Sagheer and T. Brown, *Chem Rev*, 2021, **121**, 7122–7154.
- 30 E. Haldón, M. C. Nicasio and P. J. Pérez, *Org Biomol Chem*, 2015, **13**, 9528–9550.
- 31 N. George, G. Singh, R. Singh, G. Singh, Anita Devi, H. Singh, G. Kaur and J. Singh, *Sustain Chem Pharm*, 2022, **30**, 100824.
- 32 N. Khanapurmath, M. D. Prabhu, J. Tonannavar, J. Tonannavar and M. V. Kulkarni, *J Mol Liq*, 2020, **314**, 113620.
- 33 G. Franc and A. Kakkar, *Chem Comm*, 2008, **42**, 5267–5276.
- 34 G. Singh, J. Singh, S. S. Mangat, J. Singh and S. Rani, *RSC Adv*, 2015, **5**, 12644–12654.
- 35 G. Singh, J. Singh, J. Singh and S. S. Mangat, *J Lumin*, 2015, **165**, 123–129.
- 36 N. Kaur, G. Singh, J. Singh, A. Singh, P. Satija, G. Kaur and J. Singh, *RSC Adv*, 2018, **8**, 36445–36452.
- 37 P. Kaur, B. Lal, N. Kaur, G. Singh, A. Singh, G. Kaur and J. Singh, *J Photochem Photobiol A Chem*, 2019, **382**, 111847.
- 38 K. V. R. Murthy and H. S. Virk, *Defect and Diffusion Forum*, 2014, **347**, 1–34.

- 39 C. A. Parker and W. T. Rees, *Analyst*, 1962, **87**, 83–111.
- 40 M. V. D. Weert and L. Stella, *J Mol Struct*, 2011, **998**, 144–150.
- 41 M. C. L. Yeung and V. W. W. Yam, *Chem Soc Rev*, 2015, **44**, 4192–4202.
- 42 G. Fukuhara, *J Photochem Photobiol C Photochem Rev*, 2020, **42**, 100340.
- 43 A. Nangia, *Curr Sci*, 2010, **122**, 35–51.
- 44 T. W. Bell and N. M. Hext, *Chem Soc Rev*, 2004, **33**, 589–598.
- 45 D. Wu, A. C. Sedgwick, T. Gunnlaugsson, E. U. Akkaya, J. Yoon and T. D. James, *Chem Soc Rev*, 2017, **46**, 7105–7123.
- 46 A. P. D. Silva, T. S. Moody and G. D. Wright, *Analyst*, 2009, **134**, 2385–2393.
- 47 H. Niu, J. Liu, H. M. O'Connor, T. Gunnlaugsson, T. D. James and H. Zhang, *Chem Soc Rev*, 2023, **52**, 2322–2357.
- 48 S. Kumar, N. Goswami, S. Naithani, J. Mangalam, T. Goswami, R. Dubey, P. Kumar and P. Kumar, *Dalton Trans*, 2023, **52**, 14704–14732.
- 49 R. Wolstenholme, *Elsevier*, 2021, **6**, 115–143.
- 50 P. J. Worsfold, *Elsevier*, 2005, 318–321.

Chapter 2



LITERATURE REVIEW

This chapter offers the literature on the methodology used in the actual study undertaken during the Ph.D. programme. The document provides a comprehensive overview of the synthesis process for specific molecules as well as an analysis of the optical properties of the synthesised molecules. It also includes a review of the literature on chemosensing. An in-depth comprehension of the binding mode and sensing mechanism was given significant emphasis to gain insights into the future development of the chemosensors. Ultimately, it illustrates the aim, objective, and extent of my investigation

1. Synthesis of hybrids of 1,2,3-triazoles

Heterocycles, particularly those containing nitrogen, are crucial targets in organic synthesis due to their abundant occurrence in natural products and their diverse range of applications in the pharmaceutical sector. Because of their many industrial uses, including the production of dyes, cosmetics, weed killers, antioxidants, and plastics, as well as their medicinal qualities (such as DNA-virus inhibitors, anti-hepatotoxic, and anti-microbial agents), heterocyclic compounds have become a unique class of compounds and have advanced scientific research.¹⁻³ One of the most comprehensive methods for synthesising N-heterocycles is the cycloadditive stitching of a terminal alkyne with an organic azide. This approach allows for the efficient synthesis of molecules, especially the 5-membered 1,2,3-triazole linked compounds.⁴⁻⁷ The 1,2,3-triazole derivatives display wide chemoselectivity as it's tolerant to large number of functional groups. The preparation of terminal alkynes and their connectivity with azide moiety is one of the supreme conversions for the synthesis of 1,4-disubstituted 1,2,3-triazoles.⁸ This reaction involves 4 steps, i.e.

1. Synthesis of Schiff base
2. Synthesis of Schiff base terminal alkynes
3. Synthesis of organic azides
4. Adduct formation from terminal alkyne and organic azide

1.1 Chemical reactions for the Synthesis of Schiff base

Schiff bases, commonly referred to as imines or azomethines, are nitrogen derivatives of aldehydes or ketones in which the carbonyl group is substituted by an imine group. The conventional formula for these compounds is $R_1R_2C = NR_3$, however, in some instances, the carbon atom may be linked with a hydrogen atom, resulting in the formula $R_1CH = NR_2$. In both situations, R_1 , R_2 , and R_3 indicate organic side chains, which may be alkyl or aryl groups.⁹ The reaction involving carbonyl groups (aldehydes or certain ketones) and compounds containing amino groups (NH_2 , NH_2OH , NH_2-NH_2 , etc.) is referred to as the Schiff base reaction, after the German chemist Hugo Schiff.¹⁰

A. Jarrahpour *et al.* reported synthesis of Schiff base using the solution of dimethoxyaniline **1** in 25 ml of ethanol, which was treated sequentially with substituted benzaldehyde **2** in a 50 ml

round bottom flask and the resulting mixture was refluxed for 2-4 h (**Figure 8**). Upon cooling the mixture, the resulting solid precipitate was separated by filtration and further purified by washing with ethanol. This process yielded pure Schiff base **3**, which was obtained as coloured solids or crystals in a remarkably high quantity.¹¹

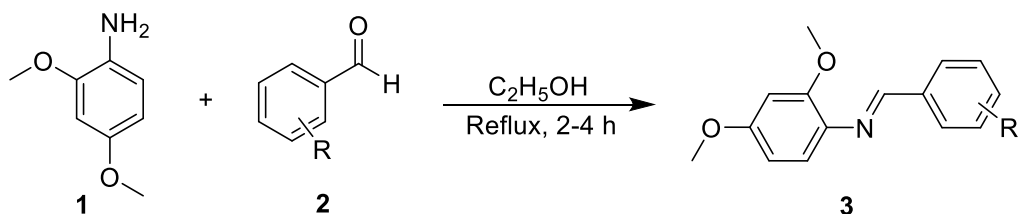


Figure 8. Synthesis of Schiff base in ethanol medium¹¹

M. Sadia *et al.* documented the synthetic pathway of Schiff base as shown in **Figure 9**. A solution of 2-hydroxy-1-naphthaldehyde **4** was prepared by dissolving it in 10 mL of methanol with continuous stirring. After 3-5 minutes, methanolic solution of benzylamine **5** was added to it dropwise. The solution was subjected to reflux for about 8 h at 80 °C, resulting in the formation of yellow solution. To obtain the crystals, the solvent was allowed to slowly evaporate at ambient temperature for several days. The rod-shaped, yellow in colour crystals of Schiff base **6** was obtained after the evaporation of solvent and the crystals was then recrystallized in ethanol.^{12,13}

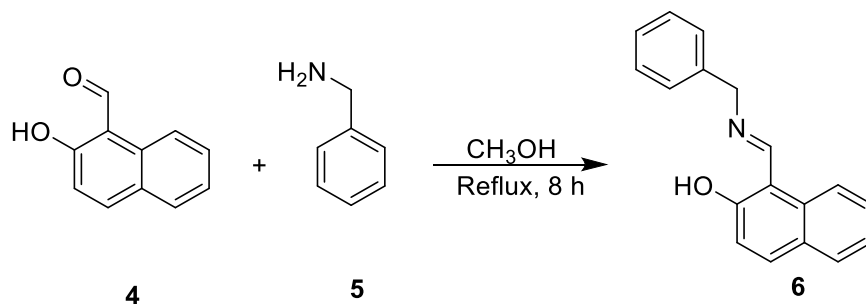


Figure 9. Synthesis of Schiff base in methanol solvent system¹²

V. K. Rao *et al.* developed Schiff base compound by reacting 1,2-diamino benzene **7** with substituted aromatic aldehyde in an aqueous solution. A solution was prepared by adding salicylaldehyde **7** to a solution of 1,2-diaminobenzene **8** in 10 ml of water as a green solvent. The resultant mixture was further agitated for 10 minutes at ambient temperature. The resulting yellow

precipitate was separated by filtration, washed with water, and dried to get yellow needle-shaped crystals Schiff base **10** with a yield of 95%.^{14,15} (**Figure 10**)

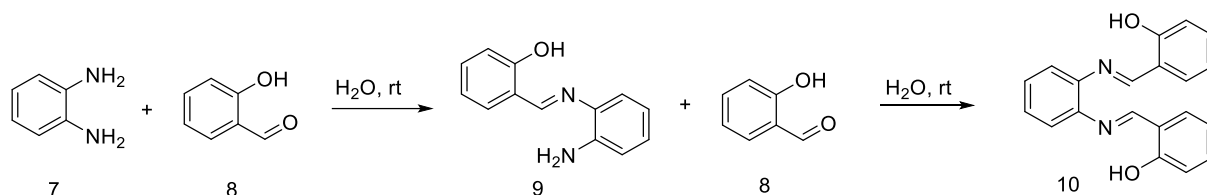


Figure 10. Synthesis of Schiff base via green synthetic route¹⁴

1.2 Chemical reactions for the synthesis of terminal alkynes

Alkynes and their derivatives are an extremely vital class of compounds and are commonly employed by organic chemists as crucial precursors for the assembly of various heterocycles. In recent years, considerable efforts have been devoted to the advancement of synthetic methodologies that facilitate the functionalization of alkynes in an efficient manner. Alkyne compounds are divided into two distinct categories: internal and terminal alkynes. The CuAAC reaction of terminal alkynes offers an easy and effective method for synthesizing 1,4-disubstituted 1,2,3-triazoles. Internal alkynes exhibit much lower reactivity compared to terminal alkynes due to the influence of steric and electronic processes. Therefore, the literature survey enlightens the synthesis of terminal alkynes from diverse initial materials and discrete reaction conditions.^{16,17}

B. C. Ranu *et al.* conducted a reductive debromination reaction of 1,2-dibromo-1,2-diarylethene **11** to produce 1,2-diarylacetylenes **12**. The reaction was carried out in the presence of an equivalent quantity of indium metal in methanol solvent for 8 h under reflux conditions. (**Figure 11**)¹⁸ M. Okutani *et al.* reported a method for synthesizing terminal alkynes **14** by treating vinyl halides **13** with TBAF.3H₂O in DMF at 60 °C for a duration of 1-2 h leading to moderate yield of the desired product. Substituting THF for DMF resulted in a significant increase in the response time, extending it to a duration of 48 h. (**Figure 12**)¹⁶

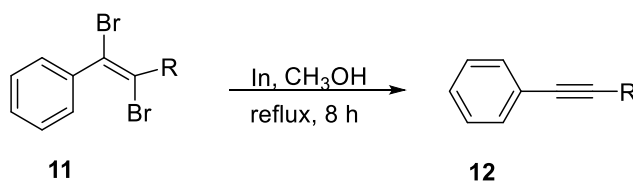


Figure 11. Reaction pathway for the synthesis of diarylacetylene¹⁸

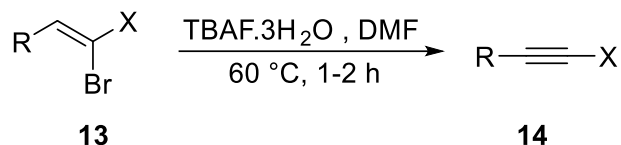


Figure 12. Synthetic approach for the synthesis of terminal alkynes and alkynyl halides¹⁶

The transition metal-free sequential elimination reaction of 1,1-dibromoolefin **15** at room temperature was delineated by A. K. Morri *et al.* to produce terminal alkynes **17**. Initially, DBU facilitates the process of dehydrohalogenation, resulting in the formation of alkynyl bromide **16**. Subsequently, when this compound is treated with triphenylphosphine in water, it undergoes debromination, leading to the production of terminal alkynes **17**. (**Figure 13**) Under these reaction conditions, both electron-rich and electron-deficient substrates were successfully reacted, resulting in the production of aromatic and aliphatic alkynes in moderate to excellent yields.¹⁹ P. Krapf *et al.* synthesized fluorinated phenylacetylene **19** from fluorobenzaldehydes **18** in 20 minutes using their homologation reaction, achieving 40-60% yield and greater than 98% purity. (**Figure 14**)²⁰

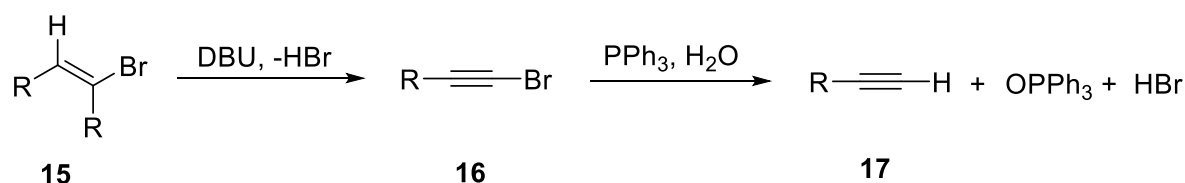


Figure 13. Synthesis of terminal alkyne from 1,1-dibromoolefin¹⁹

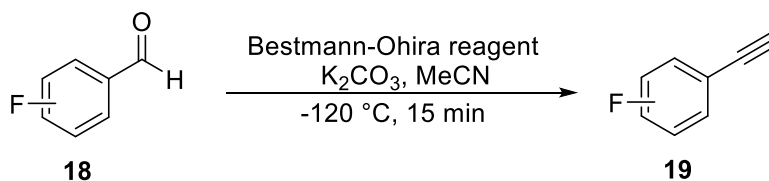


Figure 14. Synthesis of phenylacetylene using Bestmann-Ohira reagent²⁰

P. Rani *et al.* reported the synthesis of terminal alkynes from 4-fluoro phenyl isocyanate and propargyl amine in the presence of triethylamine in dichloromethane at room temperature and the product formed resulted in 81% yield.²¹ A.S.K. Hashmi and co-workers synthesized dialkynes from the propargylation of C-H acidic compounds with propargyl bromide and this method was further applied for the preparation of bis-alkynes from cyclohexanedione and propargyl bromide

in the presence of potassium carbonate by D. Ghosh et al. in their laboratories for 18 h with constant stirring.^{22,23} The bis-terminal alkyne **22** was synthesized by reacting 1H-benzimidazol-2(3H)-one **20** with propargyl bromide **21** using potassium carbonate and DMF as solvent at room temperature with constant stirring for 6 h by N.Khanapurmath *et al.* (**Figure 15**)²⁴

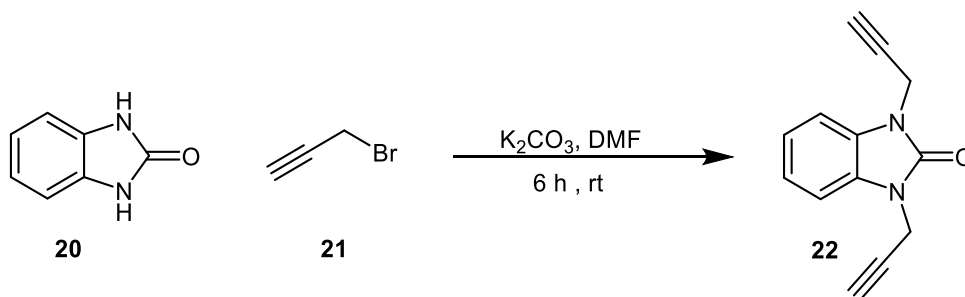


Figure 15. Synthetic route for the preparation of substituted bis terminal alkyne²⁴

Recently, Imines have gained the utmost attention in the research field due to their facile preparation, smooth execution, and swift metal complex formation. From the literature study, it has been observed that aldehydes have proven to be multifaceted to act as fluorescent chemosensor binder with cluster of metal ions. Hence, the fusion of imines and 1,2,3-triazole could be applied as fluorophore framework for various analytes.²⁵ G. Singh *et al.* described the synthesis of Schiff base linked terminal alkyne **24** from imines **23** on reacting with propargyl bromide **21** induced by base potassium carbonate in DMF as solvent at 25 °C and the time taken for the completion of this step was 16 h resulting in excellent yield⁸ as shown in **Figure 16**. Another conversion was observed, where alkyne was synthesized by reacting substituted aldehyde with propargyl bromide **12** using potassium carbonate and DMF as solvent at r.t for 24 h, and the product formed was further treated with the amines in ethanol for 4 h to get the Schiff base terminal alkyne²⁵

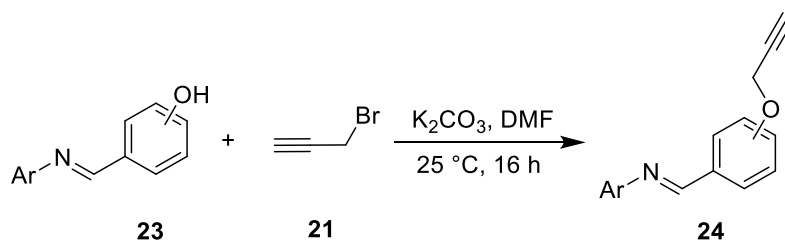


Figure 16. The Preparation of terminal alkyne from imines using propargyl bromide⁸

The intense literature studies shed light on the synthesis of alkynes from various compounds incorporated with functional groups like CHO, C=O, N=C, OH etc. with propargyl bromide using solvents like N,N-dimethylformamide, dichloromethane, and bases like potassium carbonate and triethylamine etc. were spotted. The reaction conditions are determined based on the type of solvent or the base preferred. The reaction with K₂CO₃ as the base can be implemented at room temperature.

1.3 Chemical reactions for the preparation of azides

The significant utilization of acyl, aryl, and alkyl azides in the field of chemistry has caught the heed of the organic azides since the 1950's-1960's. The exploitation of organic azides for the production of heterocycles like triazoles and tetrazoles and as functional groups in pharmaceuticals has gained the attention of industries towards organic azides. The different methods through which organic azides can be synthesized are: addition of the N₃ group (substitution or addition), addition of the N₂ group (diazo-transfer), addition of N atom (diazotization), breakage of triazines, rearrangement of azides. **(Figure 17)** The organic azides can be manipulated to remove their explosive nature when the number of carbon atoms exceeds the number of nitrogen atoms in a molecule.²⁶

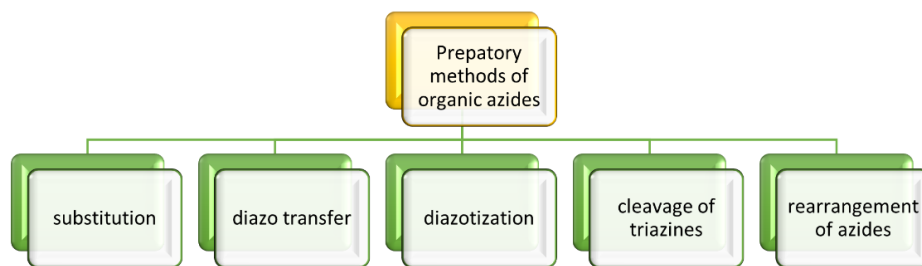


Figure 17. Various methods for the preparation of organic azides²⁶

For the preparation of the azido compound, W. Stadlbauer *et al.* stated tri-substituted pyridine **25** reaction with sodium azide **26** using dimethylformamide (DMF) as a solvent with continuous stirring at room temperature for 24 h and produces 4-azido-2-chloropyridine **27** as 45% yield. **(Figure 18)**²⁷ Y. H. Kim *et al.* documented the formation of aryl azide **29** from aromatic hydrazine **28** and nitrosyl ions at (-30 °C) in the presence of acetonitrile solvent as crucial reaction as it provides 95% isolated and purified yield in 10 minutes. **(Figure 19)**²⁸

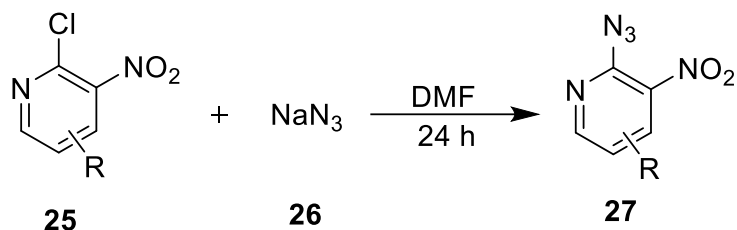


Figure 18. Synthesis of azido compound from substituted Pyridine²⁷

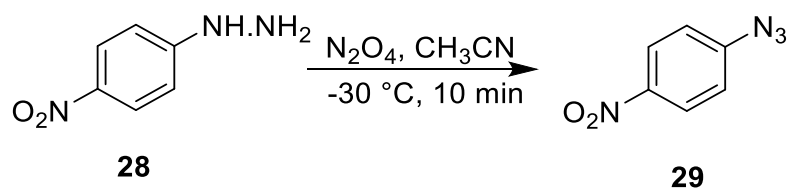


Figure 19. Conversion of aromatic hydrazine into aryl azide²⁸

Q. Liu *et al* reported the synthesis of 8-Azidoquinoline **32** from 8-aminoquinoline **30** and triflyl Azide **31** at room temperature using the mixture of dichloromethane and methanol, in addition to triethylamine and copper sulphate provides 95% yield. (**Figure 20**)²⁹

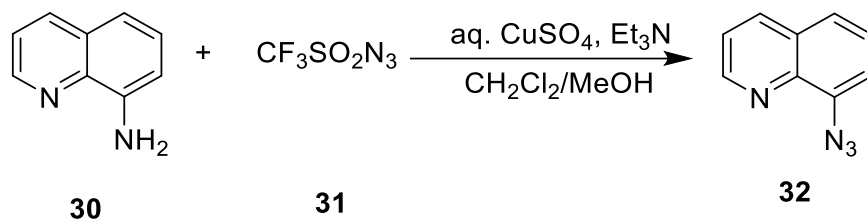


Figure 20. Synthesis of 8-aminoquinoline from aromatic amine²⁹

The reaction of azide ions by nucleophilic substitution mechanism aids in the formation of aliphatic azides. The azide source used for most of the reactions is sodium azide.²⁹ M. Kitamura *et al.* described the diazo conversion of primary amines **33** to organic azides **35** using, ADMP (2-Azido-1,3dimethylimidazolium hexafluorophosphate) **34**, DMAP (N,N-dimethyl-4-aminopyridine), DCM (dichloromethane) as solvent results in quantitative yield of organic azide. (**Figure 21**)³⁰

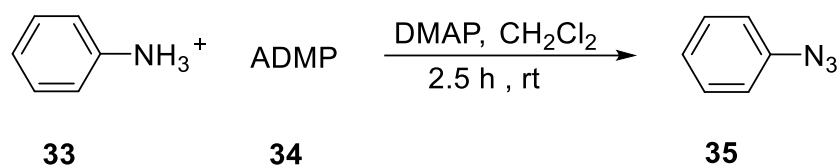


Figure 21. Synthesis of organic azides from primary amines³⁰

Another conversion by M. Kitamura *et al.* depicts the synthesis of organic azides **37** from non-benzylic alcohol **36** with ADMP **34**, DBU in the presence of THF in 15 h at 0 °C granted sufficient yield. (**Figure 22**)³¹ M. D. Lourdes *et al.* synthesized azidomethyl benzene **39** via the nucleophilic substitution of chloromethylbenzene **38** with sodium azide **26**. The resulting mixture was maintained at reflux while being agitated for a duration of 6 h and yellow oil was produced with satisfactory yield. (**Figure 23**)³²

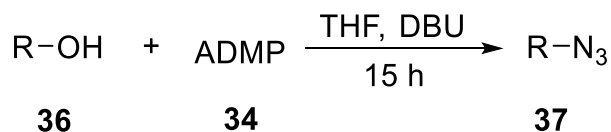


Figure 22. Synthesis of organic azides from non-benzylic alcohol³¹

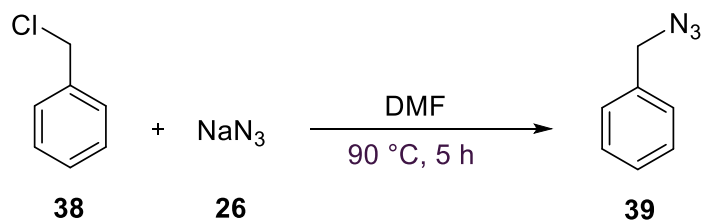


Figure 23. Synthesis of benzyl azide from benzyl chloride and sodium azide³²

Organic azides can also be synthesised by employing extremely volatile, toxic, and explosive substances such as hydrogen azide. However, contemporary techniques for azidation have emerged, circumventing the need for such hazardous substances. The majority of the methods consist of nucleophilic substitution which involves the azidation of alkyl halides, acyl halides, and aryl halides using sodium azide. To synthesize aromatic azides, one may employ the method of diazotization of aromatic amines followed by sodium azide nucleophilic substitution.²⁶

1.4 Adduct formation of 1,2,3-triazoles from CuAAC reaction

Organic azides and alkynes are separately involved in diverse kind of reactions like substitution, cycloaddition, addition etc. The organic azides display a 1,3-dipolar character while reacting with unsaturated compounds to produce triazole and tetrazoles. In recent years, the cycloaddition reaction of alkynes with organic azide aided with copper (I) as catalyst to synthesize 1,2,3-triazole has attracted the attention of the scientific community. Using this approach novel 1,2,3-triazole was developed by G. Senthilkumaran *et al.* from 2-azidophenol reacting with propargyl alcohol using THF as a solvent and Cu(I) as the catalyst and it was obtained in good yield. The fluorescent studies and UV-vis spectrophotometer studies showcase the newly synthesised triazole as a fluorescent chemo- sensor with the ability to detect copper ions.³³

A novel 1,4-disubstituted 1,2,3-triazole derivative **43** was synthesized utilizing CuAAC reaction involving 4-azido-1,2-dichlorobenzene **42** and 2-hydroxy-4-(prop-2-yn-1-yloxy)benzaldehyde **41** by T. Gokturk *et al.* The reaction was aided by copper acetate as a catalyst, sodium ascorbate (NaAsc) as a reducing agent, and the solvent system of CH₂Cl₂/H₂O (1:1) and pure crystals of compound **43** was obtained with 89% yield. (Figure 24)³⁴

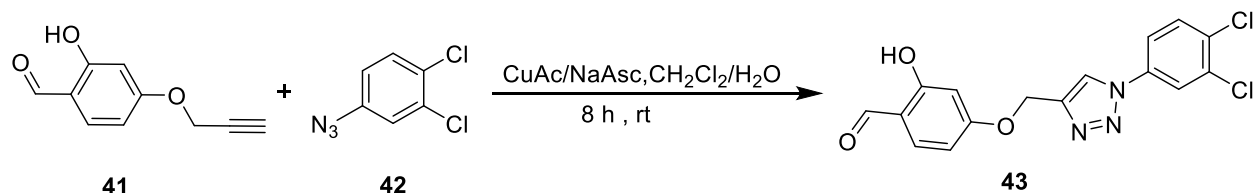


Figure 24. Synthetic pathway for the 1,2,3-triazole derivative³⁴

G. Singh and colleagues attained alkylated product **45** when 2-methyl-8-hydroxyquinoline **44** was nucleophilically substituted with propargyl bromide **21**. The resulting terminal alkyne **45** underwent an azide-alkyne cycloaddition reaction with γ -azidopropyltriethoxysilane, resulting in the formation of 8-methyl-quinolinol-linked triethoxysilane 1,2,3-triazole **46**. The synthesized compound exhibits remarkable photophysical properties for detecting Fe²⁺ and Fe³⁺ ions, demonstrating its ability to effectively sense these two oxidation states of iron. This is evident from the distinct spectral response observed in UV-Vis and fluorescence studies. (Figure 25)³⁵

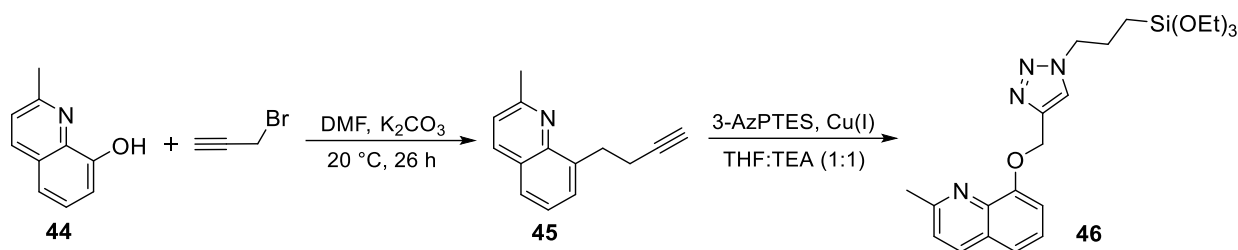


Figure 25. Illustration of the reaction scheme for synthesising the 1,2,3-triazole derivative³⁵

M. Bal and co-workers employed salicylaldehyde derivatives containing an oxypropargyl group **47** which was dissolved in a mixture of water and tetrahydrofuran (THF), with the addition of $\text{CuSO}_4 \cdot 5\text{H}_2\text{O}$, sodium ascorbate and reacted with the azide compound of aniline derivatives **48**. The reaction mixture was stirred at ambient temperature for 24 h. The acquired product of 1,2,3 triazole derivative **49** was dissolved into a methanol-based refluxing solution containing 4-aminobenzoic acid **50**, few drops of glacial acetic acid were added to obtain Schiff base linked 1,2,3 triazole **51**. (**Figure 26**)³⁶

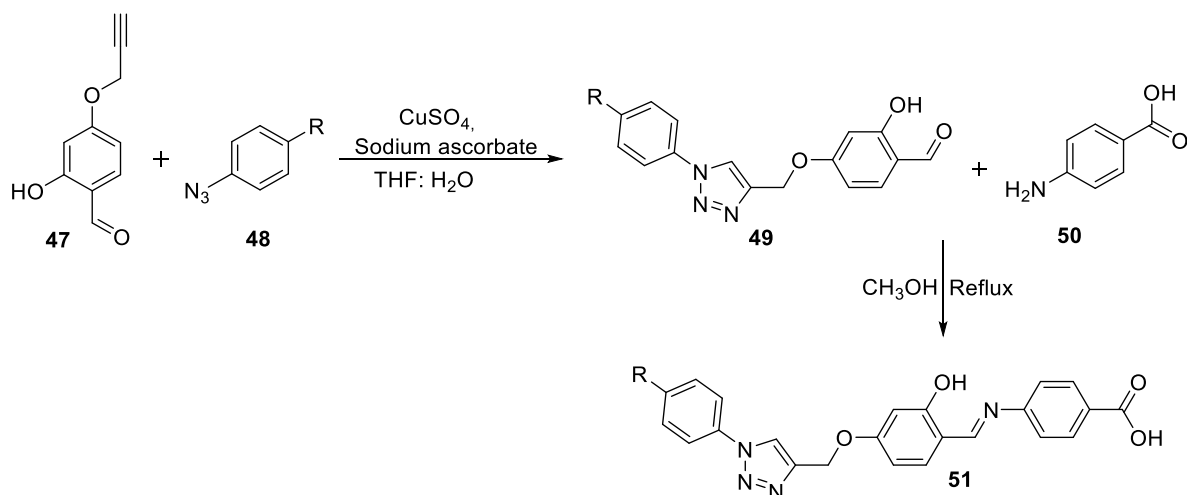


Figure 26. Steps for synthesizing Schiff base 1,2,3-triazole³⁶

G. Singh *et al.* developed azo dye based alkyne **52** by the fusion of azo dyes with propargyl bromide using potassium carbonate which further reacts with azido propyl tri-ethoxy silane **53** in a solvent mixture of ratio 1:1 (THF/ Et_3N) catalysed by $[\text{CuBr}(\text{PPh}_3)_3]$ at 60 °C for 6 h and 1,4 di-substituted 1,2,3-triazole functionalized azo dye organofunctional silane **54** was formed with excellent yield of 98%. This triazole functionalised azo dye silane was set up as an effective chemosensor for the recognition of Fe^{2+} and Cu^{3+} dual cations. (**Figure 27**)³⁷

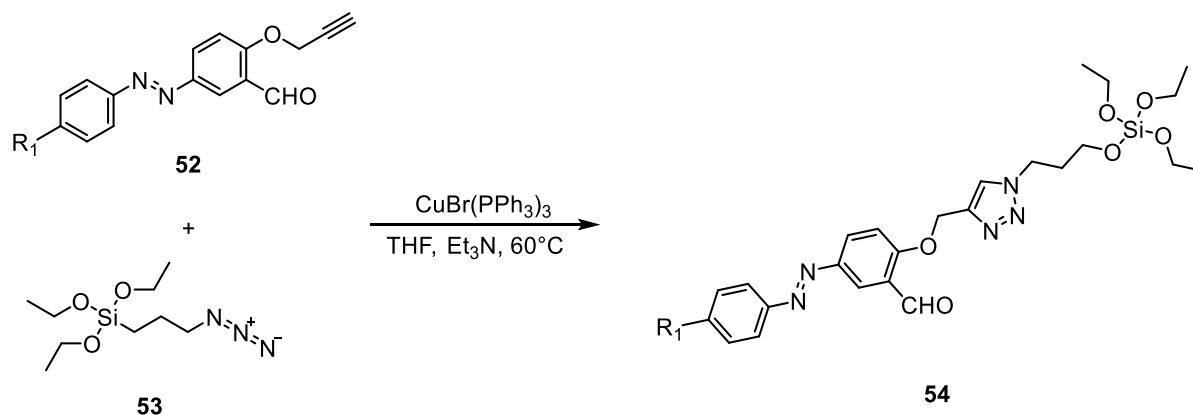


Figure 27. Synthesis of 1,2,3-triazole functionalised azo dye silane³⁷

A report by P. Rani *et al.* presented the preparation of urea linked 1,2,3-triazole **57** from 1-(4-fluorophenyl)-3-(prop-2-yn-1-yl) urea **55** and phenyl azide **56** catalysed by copper sulphate and sodium ascorbate in the presence of Water: DMF as solvent at room temperature in marvellous yield. Also, the urea-linked triazole proved to be chromo-fluorogenic sensor of fluoride ions. (**Figure 28**)²¹ B. Khan *et al.* reported the synthesis of alkyne substituted benzaldehyde from 4-hydroxy benzaldehyde with propargyl bromide and it further reacted with di-azido-propoxycalix [4] arene, using Cu(I) as a catalyst in the presence of sodium carbonate.

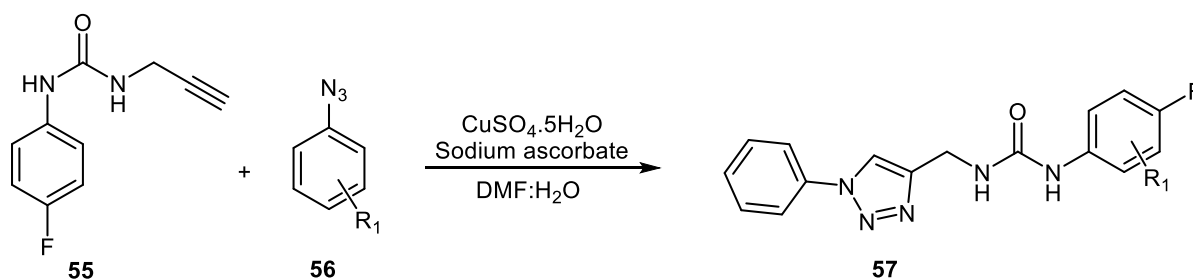


Figure 28. Synthesis of urea-hybrid 1,2,3-triazole²¹

After the purification through silica gel chromatography, a novel bis(triazole)-bis(hexahydroquinoline) was obtained in a moderate yield of 64%. The newly synthesised triazole was counted as a significant optical chemo-sensor as it detected the presence of Hg^{2+} ions.³⁸

The formation of 1,2,3-triazole-based coumarin derivatives has been depicted by P. L. Rojas *et al.* wherein reaction was performed using propargylated coumarin **58** with substituted azide **59** in the presence of copper sulphate and sodium carbonate in DCM/Water as a solvent and coumarin-based 1,2,3-triazole **60** was formed in efficient yield. (**Figure 29**)³⁹

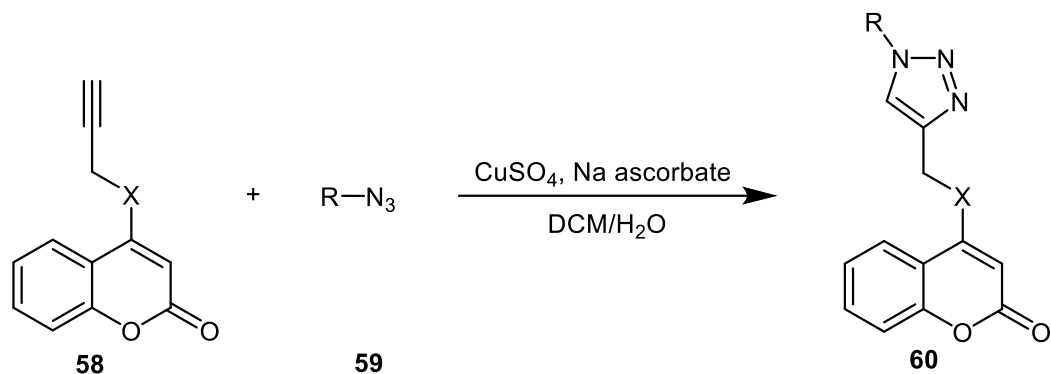


Figure 29. Preparation of 1,2,3–triazole hybrid coumarin derivatives³⁹

G. Singh *et al.* confirmed the synthesis of indole-carboxaldehyde alkyne **62** by fusion of Indole-carboxaldehyde **61** and propargyl bromide **21**, and the Schiff base **64** was formed via the condensation of indole carboxaldehyde alkyne **62** with primary amine **63**. A novel 1,2,3-triazole hybrid molecule **66** was prepared from Schiff base alkyne **64** and 3- azidopropyltriethoxysilane **65** and a magnificent yield was obtained. (Figure 30)⁴⁰ Literature study discloses the various steps involved in the synthesis of terminal alkynes. The preparation of terminal alkynes with propargyl bromide using a nucleophilic substitution mechanism in DMF as a solvent and potassium carbonate as a base at room temperature with constant stirring is a selective technique.

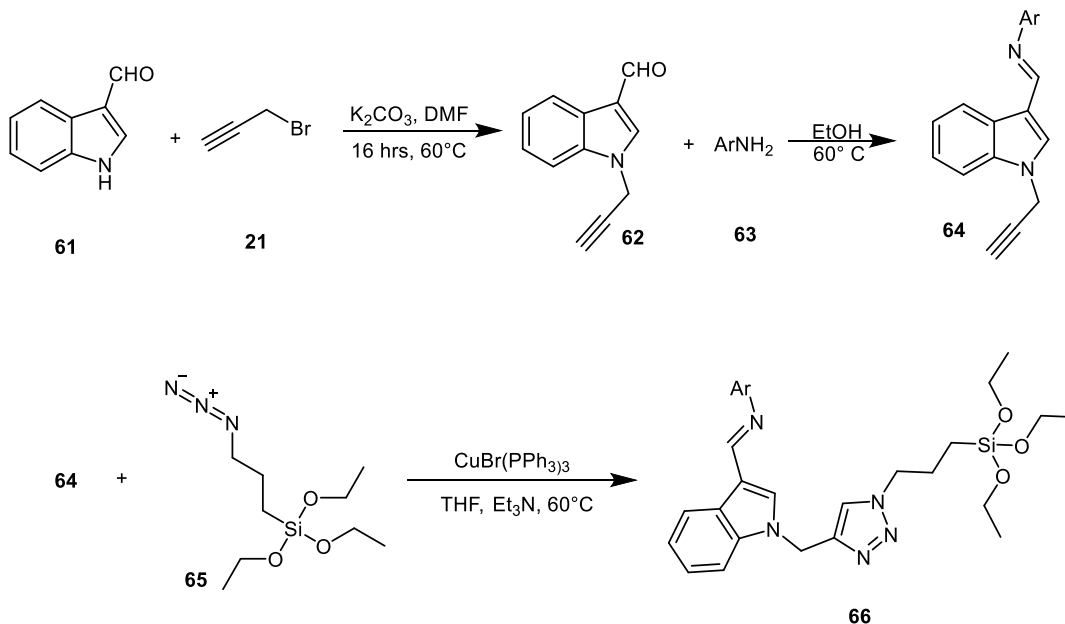


Figure 30. Synthesis of Indole Schiff base hybrid 1,2,3 triazole⁴⁰

The facile separation of catalyst from reaction mixture, smooth isolation, and purification methods of the expected yield provides with determined viewpoint to continue research work through this methodology. Likewise, the potential method for the synthesis of azides comes out to be the azidation of alkyl and aryl halides using sodium azide due to swift reaction conditions and easily accessible reagents. Subsequently, synthesis of 1,2,3-triazoles involving CuAAC click reaction will operate considering its higher stereo-selective nature, benign procedure, easy access, and production of purified and high yield.

2. Fluorogenic 1,2,3-triazole chemosensors for metal ions detection

The spectrophotometric analysis conducted by M. Vadivelu *et al.* to study metal ions detection demonstrated that the rhodamine-triazole dyads **67** exhibited a remarkable selectivity for Cu^{2+} ions. The selective detection of Cu^{2+} is attributed to the unique binding interaction between the triazole ring and hydrazone group with the metal ions. The orange color change upon the addition of Cu^{2+} may be ascribed to the metal-induced delactamization of rhodamine, resulting in the formation of a xanthene ring. The colourless dyads, in their off-state, undergo cross-conjugation enhancement upon binding with Cu^{2+} and transform into a coloured ring-opened form, representing their on-state (**Figure 31**)⁴¹. A novel click-derived 1,2,3 triazole chemosensor **68** was synthesised through the combination of azido and propargylated precursors using the click technique, specifically the 1,3-dipolar cycloaddition reaction for the detection of Hg^{2+} ions.

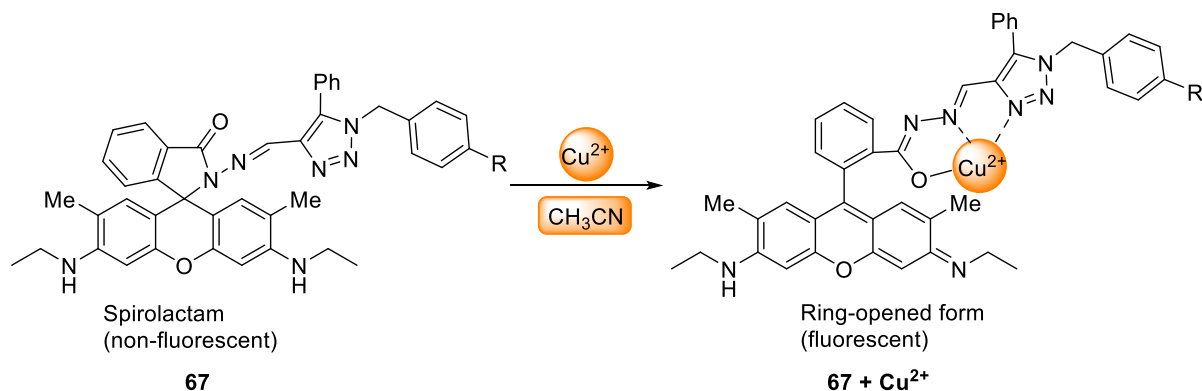


Figure 31. A plausible mechanism for the ring-opening of the rhodamine-1,2,3-triazole dyad is facilitated by the coordination of Cu^{2+} ions⁴¹

The chemosensor **68** demonstrated the capacity to detect Hg^{2+} even at 100 mM limit of detection, demonstrating a higher level of sensitivity towards the specific cation. The equimolar accumulation of Hg^{2+} ions caused a significant sharp rise in the absorption and the fluorescence spectra of compound **68**, indicating that the triazole-based compound **68** selectively interacts with Hg^{2+} ions over other cations. The compound **68** showed the highest chelation with Hg^{2+} at a pH of 5.1, which is slightly acidic. The binding mechanism suggests the stoichiometric ratio of (2:1) for the ligand-metal complex. (**Figure 32**)⁴²

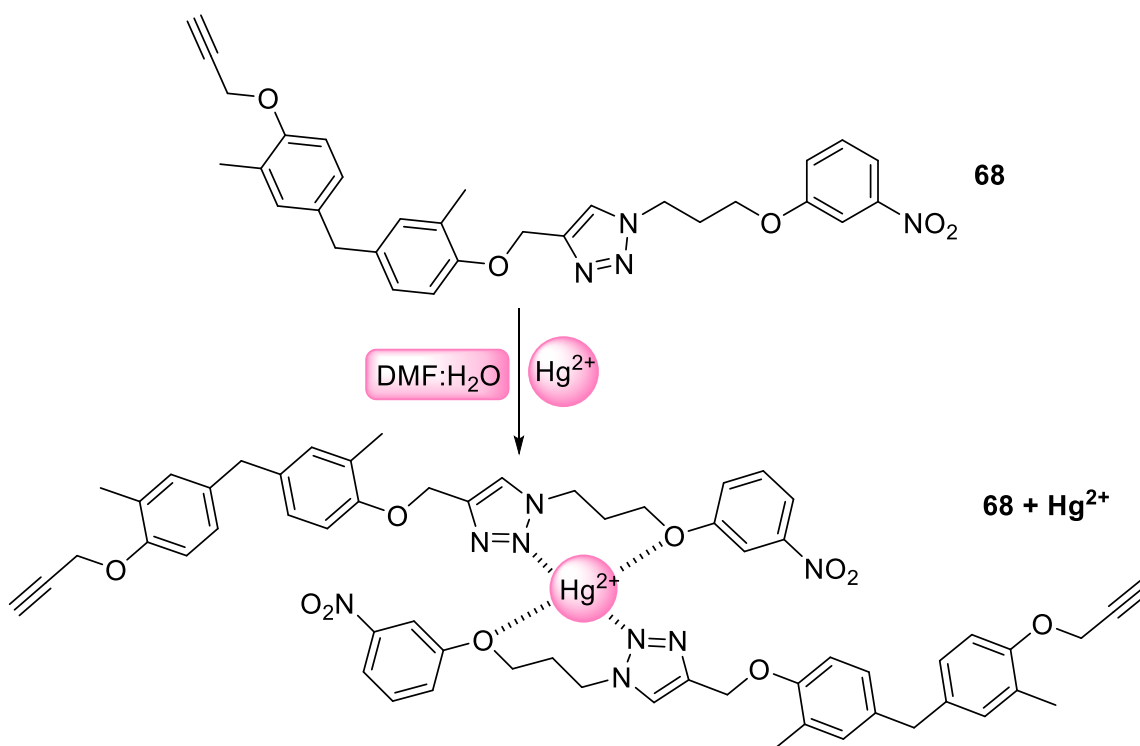


Figure 32. Probable binding mode of click-derived 1,2,3-triazole derivative with Hg^{2+} ions⁴²

S. M. Hashemi *et al.* developed an innovative coumarin-linked 1,2,3-triazole derived fluorescent chemosensor **69** for the rapid and specific detection of Zn^{2+} ions. The Job's plot measurement was used to ascertain the complexation ratio of sensor **69** with the Zn^{2+} cation, revealing the maxima peak that signifies the development of an ML_2 adduct. The binding stoichiometry revealed that the probe **69** and Zn^{2+} ions have a stoichiometric ratio of 2:1. The chemosensor **69** demonstrates a remarkable ability to selectively detect Zn^{2+} ions, outperforming other metal ions, resulting in a significant increase in fluorescence. (**Figure 33**)⁴³

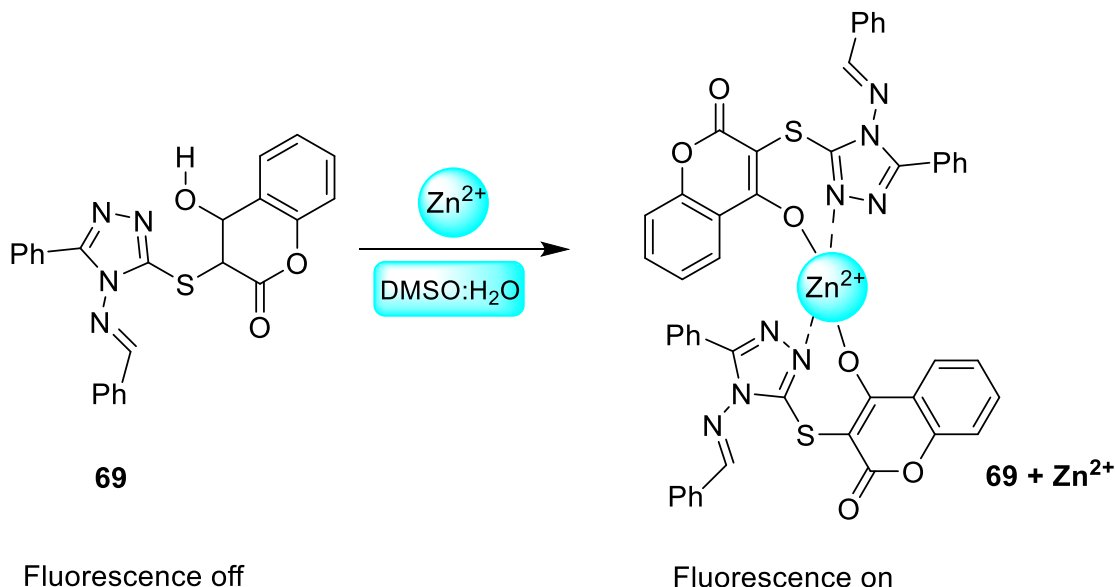


Figure 33. Plausible stoichiometric binding (2:1) of chemosensor **69** with Zn^{2+} complex⁴³

A rhodamine-based 1,2,3-triazole chemosensor **70**, developed by N. R. Chereddy and co-workers, has been synthesised using a click reaction. This chemosensor contains ‘O–N–N–O–N’ binding sites that have been designed to selectively detect Fe^{3+} ions. The selective affinity of Fe^{3+} for chemosensor **70** is attributed to the hydroxyl group of the quinoline group, which forms a chelating moiety with an ‘O–N–N–O’ configuration. This interaction with Fe^{3+} is responsible for the observed colour change. By incorporating the 1,2,3-triazole group into the binding site of the rhodamine derivative, chemosensor **70** was synthesized. This chemosensor exhibited selectivity in forming a complex with Fe^{3+} in existence of different competing metal cations. The addition of the 1,2,3-triazole moiety into a rhodamine-based chemosensor enhanced its selectivity and sensitivity towards Fe^{3+} ions. This is due to the presence of the triazole nitrogen atom in the O–N–N–O–N binding site of chemosensor **70**, which offers suitable coordination sites for Fe^{3+} ions. (**Figure 34**)⁴⁴

G. Wu *et al.* documented the utilisation of click chemistry to synthesize coumarin-linked quinoline-based chemosensor **71**, which was designed to detect Pb^{2+} ions. The fluorescence intensity of **71** at 466 nm is increased by 30-fold after the addition of Pb^{2+} ions. The introduction of other toxic metal ions had no discernible impact on the fluorescence of **71**. Chemosensor **71** exhibits low fluorescence intensity when stimulated at a wavelength of 385 nm. This is due to the PET mechanism taking place between the nitrogen atom of the triazole group and the quinoline

and coumarin components, resulting in the suppression of the fluorescence emitted by chemosensor **71**.

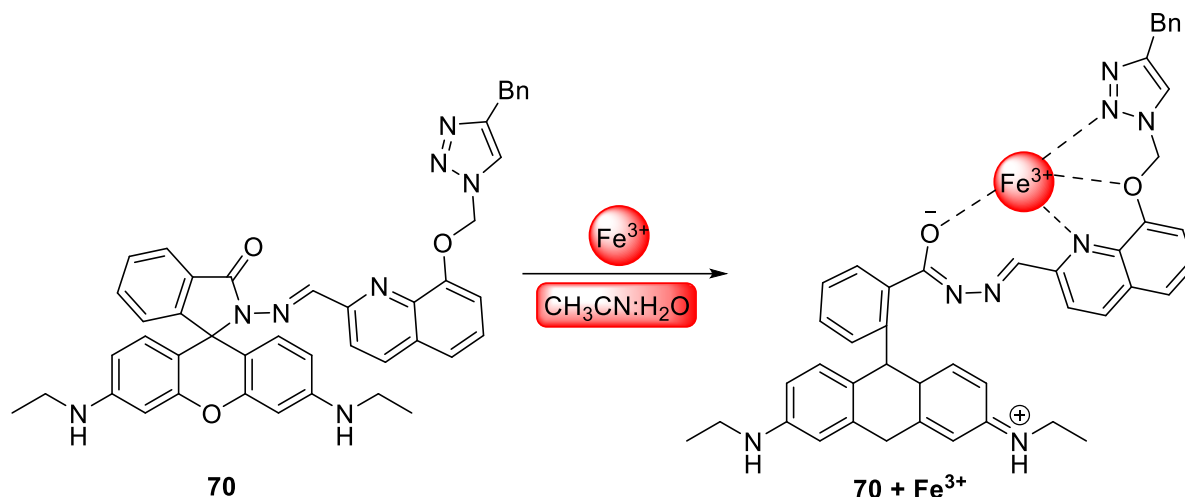


Figure 34. Fluorometric detection of Fe^{3+} via newly developed chemosensor **70**⁴⁴

The PET mechanism, which occurs from the triazole nitrogen atom to the quinoline and coumarin units, is inhibited when complexed with Pb^{2+} . This inhibition leads to a substantial increase in the fluorescence intensity of chemosensor **71**, resulting in an "OFF-ON" response. Based on the findings of ^1H NMR and FTIR spectroscopy, it can be inferred that the nitrogen atom located near to the methylene group, oxygen atom, quinoline nitrogen, and Schiff base nitrogen atom in compound **71** establish a stable complex with Pb^{2+} ions. (Figure 35)⁴⁵

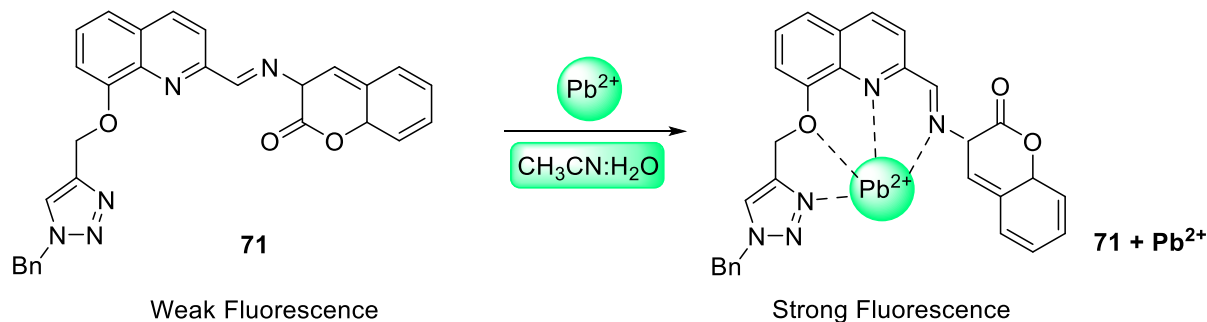


Figure 35. The possible binding interaction of probe **71** with Pb^{2+} ions⁴⁵

For synthesizing a multidentate fluorescent rhodamine triazole **72** for the selective detection of Sn^{2+} was presented by Z. Yan *et al.* Chemosensor **72** exhibits selectivity in detecting Sn^{2+} ions in $\text{ACN}/\text{H}_2\text{O}$ solution by a fluorescence turn-on and colorimetric response. The

chemosensor **72** undergoes a slow transition from colourless to dark pink after the accumulation of Sn^{2+} ions. This transition is accompanied by a significant increase in the fluorescence intensity. The alteration in the colour of the chemosensor after its interaction with Sn^{2+} may be ascribed to the process of ring-opening of the spirolactam molecule inside the rhodamine unit. The hypothesized binding mechanism entails the creation of a 5- or 6-membered ring between sensor **72** and Sn^{2+} . This ring formation stabilises the complex formed between **72** and Sn^{2+} in a 1:1 binding ratio. (**Figure 36**)⁴⁶

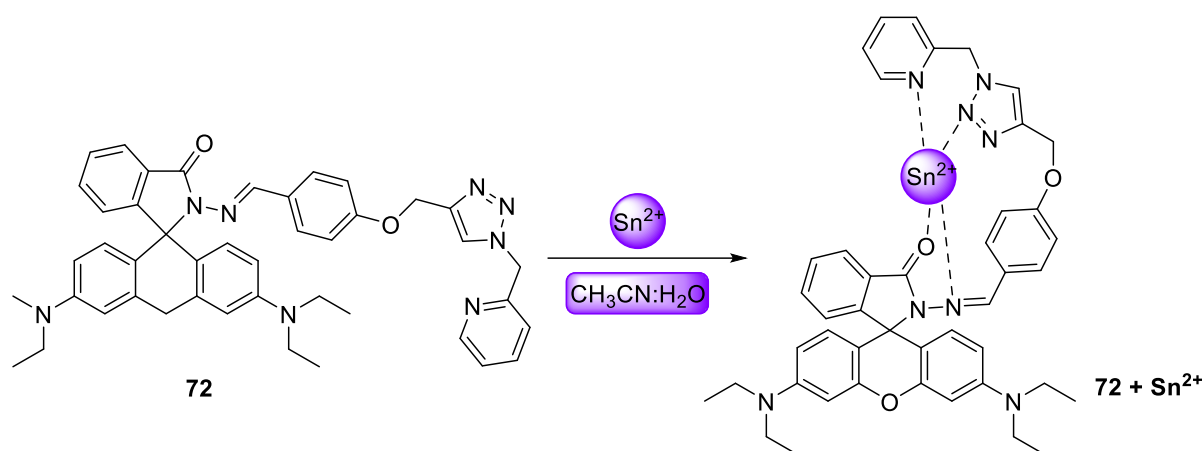


Figure 36. Possible binding structure of chemosensor **72** with Sn^{2+} ions⁴⁶

A novel fluorescent and colorimetric bis Schiff base 1,2,3-triazole chemosensor **73** has been synthesised and designed by K. Rout and co-workers. Receptor **73** exhibited a colorimetric sensing capability that was both selective and sensitive towards Cu^{2+} and Pb^{2+} ions, as evidenced by its colour transition from colourless to yellow and light yellow, respectively, in a CH_3OH –tris-buffer (1:1, v/v). The molecule exhibited a significant increase in fluorescence when both Cu^{2+} and Pb^{2+} ions were added, which may be ascribed to the inhibition of the PET process. The prospective applications of the chemosensor **73** include the detection of Cu^{2+} and Pb^{2+} ions in living cells and the construction of a molecular logic gate of the INHIBIT type. (**Figure 37**)⁴⁷

A fluorescent molecular probe **74** was synthesized using the CuAAC catalysed 'Click' reaction by S. Kumar *et al.* The binding characteristics of chemosensor **74** with various metal ions, including Zn^{2+} , Al^{3+} , Cd^{2+} , Cu^{2+} , Hg^{2+} , Ag^+ , Cr^{3+} , Pb^{2+} , Ni^{2+} , Co^{2+} , Fe^{2+} , and Fe^{3+} were examined using fluorescent spectroscopy. The newly developed fluorescent molecular probe **74** detected Fe^{3+} cations. A significant reduction in intensity at a wavelength of 433 nm was detected in the emission

spectra containing Fe^{3+} ions. The observed attenuation in the presence of Fe^{3+} ions was not detected in the existence with different metal cations. Molecular receptor **74** has a turn-off response, enabling it to selectively detect Fe^{3+} ions in the with the existence of different metal cations

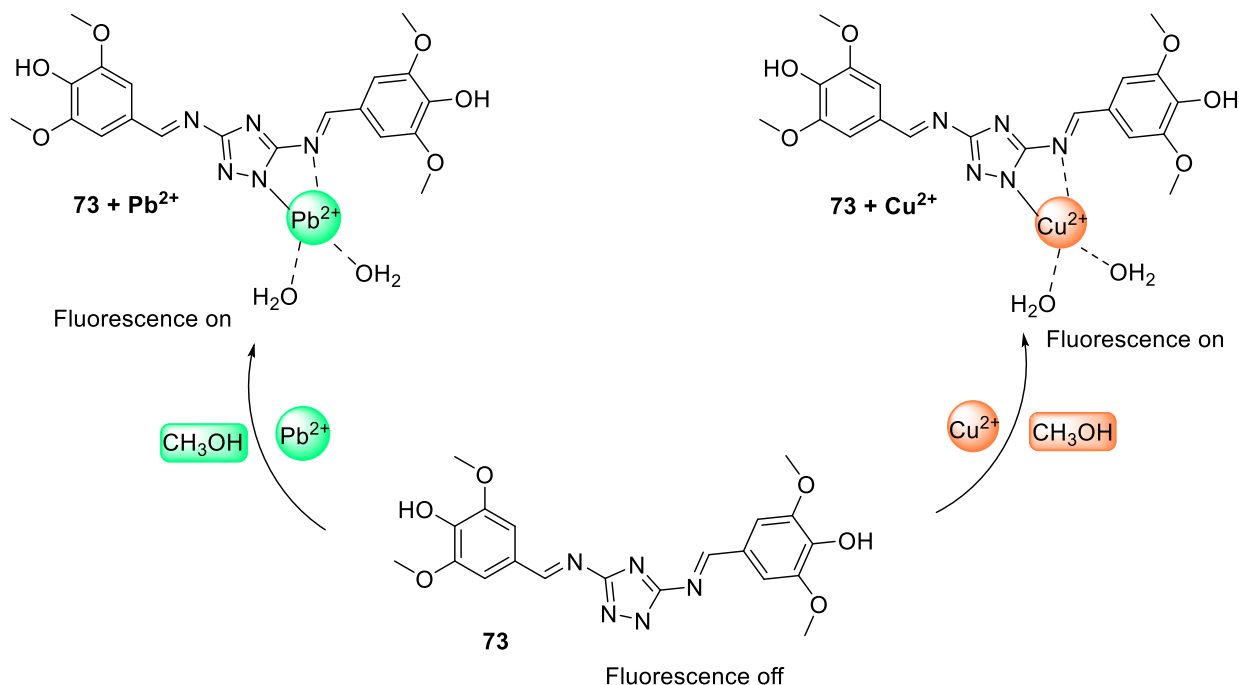


Figure 37. The plausible sensing mechanism of chemosensor **73** for Pb^{2+} and Cu^{2+} ions⁴⁷

The molecular probe **74**, functioning as a paper strip test, can identify and distinguish Fe^{3+} from Fe^{2+} in practical scenarios. (**Figure 38**)⁴⁸

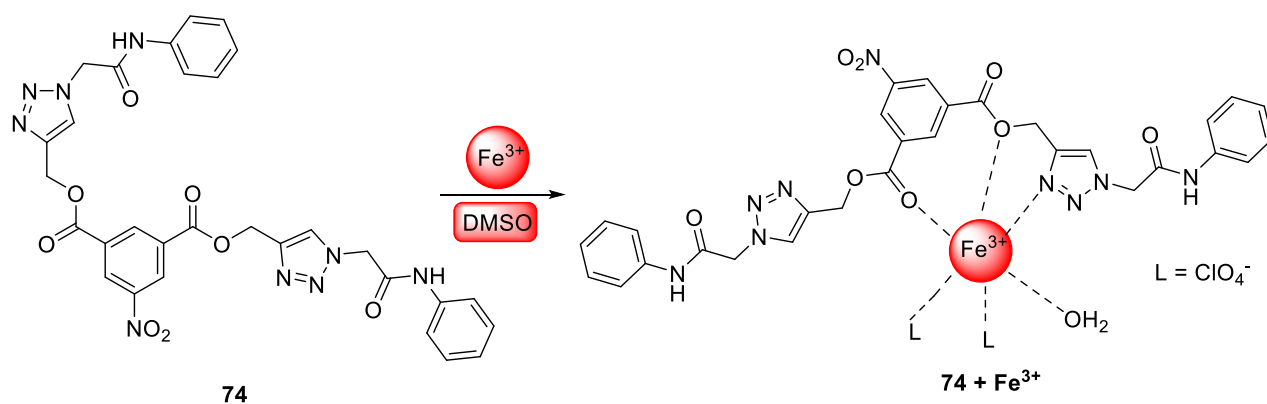


Figure 38. Possible binding interaction of Fe^{3+} metal ions with receptor **74**⁴⁸

The research by P. Saini *et al.* outlines the UV-Vis response of probe **75** when it interacts with Pb^{2+} ions, resulting in a "turn-on" reaction. The proposed receptor was generated using the extremely flexible and stereoselective CuAAC process, which is known for its ability to stitch together various structural components. The ability to detect Pb^{2+} ions is facilitated by the binding of metal ions with heteroatoms in the sensing device, which function as electron donors. The UV-Visible absorption spectrum of **75** was analysed in a solution of ACN- H_2O (4:1, v/v) with various metal ions. The findings demonstrated that the proposed probe **75** is highly sensitive to Pb^{2+} ions, forming a 2:1 stoichiometric complex with chemosensor **75**. (Figure 39)⁴⁹

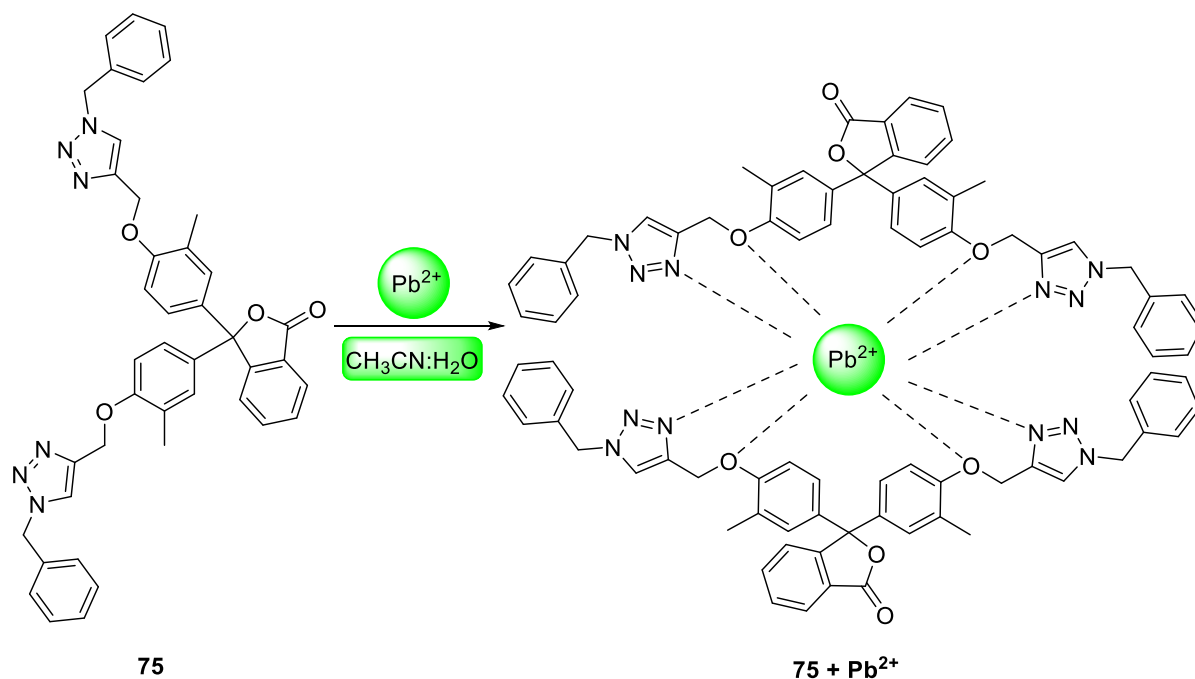


Figure 39. The proposed binding mechanism of probe **75** with Pb^{2+} ions⁴⁹

A novel imino-phenol compound, adorned with a 1,2,3-triazole moiety **76** has been successfully synthesised, characterised, and used to detect metal ions reported by S. Ghosh *et al.* Compound **76** exhibited mild fluorescence in ACN/ H_2O (3:1, v/v) and demonstrates a significant enhancement in emission when it interacts with Zn^{2+} compared to various other metal ions. Out of all the metal ions, only Zn^{2+} specifically and significantly enhances the emission of **76**. The theoretical explanation for emission quenching is due to photoinduced electron transfer. The compound's **76** emission is enhanced by the presence of Zn^{2+} owing to the chelation of the metal ions at the binding site. This chelation causes a change in the rigidity of the structure, thereby

preventing the non-radiative route. The zinc ensemble has been used as an application to specifically identify picric acid (PA) among many other nitroaromatic compounds. **(Figure 40)**⁵⁰

A novel class of fluorescence sensor designated as **77**, has been synthesised by incorporating 1,2,3-triazole groups onto quinoline-based framework by M. Loya and co-workers. The starting material for the synthesis of these sensors is D-glucose. The quinoline moiety's excimer emission was suppressed when Cu^{2+} and Ni^{2+} ions were present in an aqueous methanolic solution.

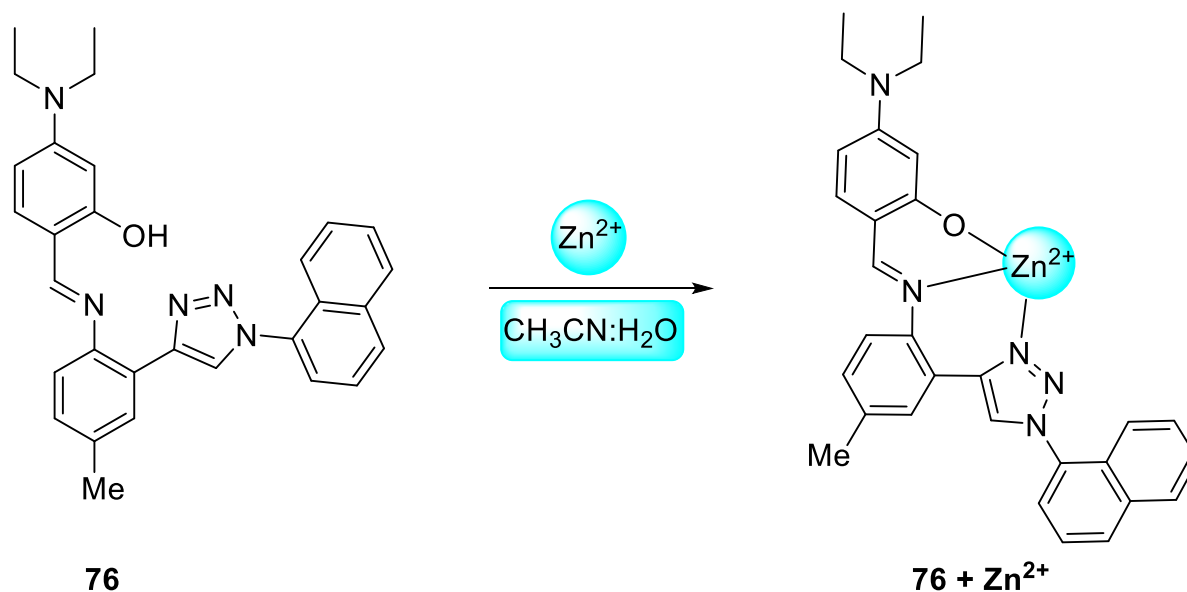


Figure 40. Plausible binding structure of Zn^{2+} with chemosensor **76**⁵⁰

The experimental findings further demonstrated that the generation of excimers is contingent upon the polarity of the solvent. Absorption spectroscopy was used to determine the detection capability of sensor **77** for Cu^{2+} and Ni^{2+} ions. The significance of the quinoline nitrogen in facilitating excimer formation and detecting Cu^{2+} and Ni^{2+} ions was determined using fluorescence analysis of compound **77**. The chemosensor **77** demonstrated a 1:1 stoichiometric ratio for both ions, as confirmed by the mass spectra of the complex. **(Figure 41)**⁵¹

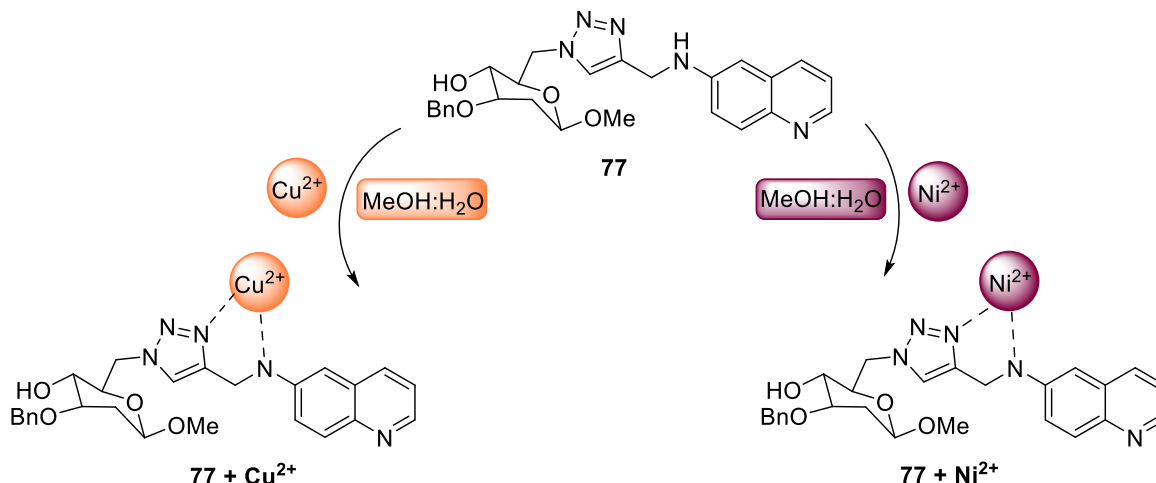


Figure 41. Possible binding structure of probe **77** with Cu^{2+} and Ni^{2+} ions⁵¹

The synthesis of 1,4-dihydroxyanthraquinone based 1,2,3-triazole linker **78** was achieved rapidly and with a high yield using a stereoselective Copper (I)-catalysed alkyne azide cycloaddition (CuAAC) process by P. Saini *et al.* Chemosensor **78** has high efficacy and selectivity in detecting Fe^{2+} ions, which may be analysed using a facile technique such as UV-visible spectroscopy. The UV-visible absorption spectra were measured while adding a 0.5 mM solution of Fe^{2+} ions to the synthesised probes in the $\text{ACN:H}_2\text{O}$ (4:1) solvent system. The intensity of absorption at two specific wavelengths showed a significant change, resulting in the formation of isosbestic points. Fluorescence spectroscopic titrations were conducted using a 0.1 mM solution of the heterocyclic molecule **78**. The introduction of Fe^{2+} ions resulted in a reduction in emission intensity and a shift of the signal towards shorter wavelength values, was observed. The observed variation in the relative change in absorption during UV-visible titrations, indicates that probe **78** has a 1:1 stoichiometry of ligand to metal. (**Figure 42**)⁵²

O. Ozukanar *et al.* reported a new fluorescent dibenzoxanthene derivative, functionalized with anthracene **79**, was synthesised for metal ions sensing in polar aprotic solvent systems.

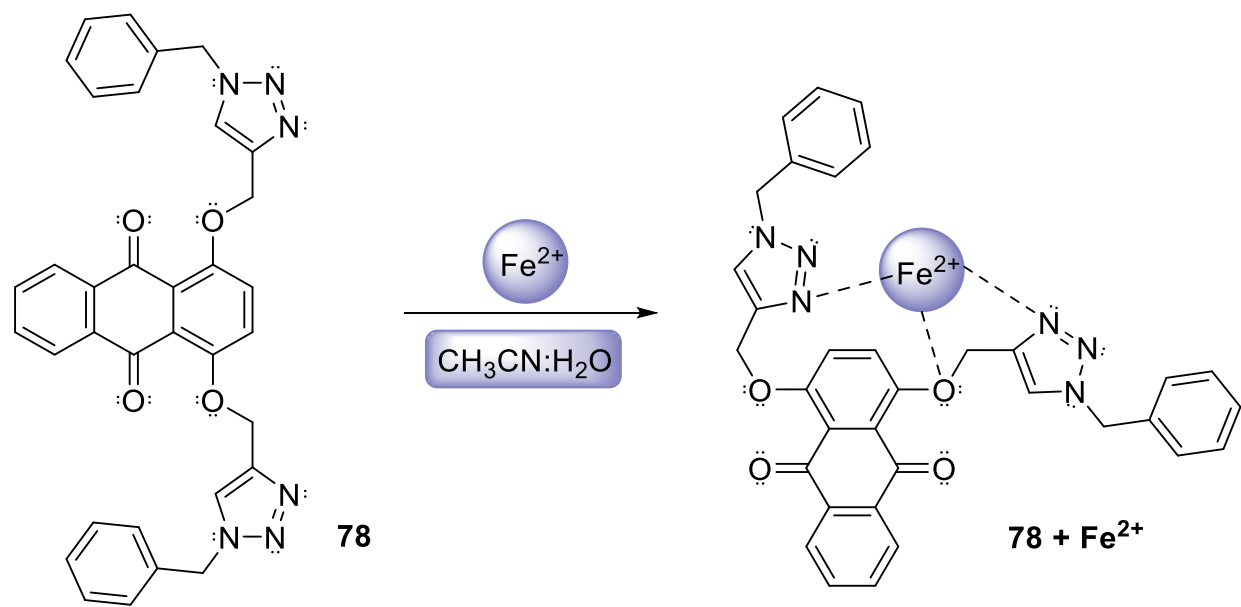


Figure 42. Proposed binding structure of chemosensor **78** with Fe^{2+} ions⁵²

This was achieved via the use of UV-vis spectroscopy and fluorescence spectroscopy. The new anthracenyl-dibenzoxanthene compound **79** exhibited exclusive sensitivity towards Cu^{2+} ions, with a binding capacity of one anthracenyl-dibenzoxanthene molecule to three Cu^{2+} ions because of possessing 1,2,3-triazole rings within the structure. Consequently, the compound's **79** sensitivity to copper was enhanced. The fluorescence measurements were conducted by gradually adding different amounts of Cu^{2+} ions to 5 μM chemosensor's **79** solution. A decrease in fluorescence intensity was observed as the concentration of Cu^{2+} increased. The proximity of the quenching of the sensor's fluorescence to completion increased with the concentration of Cu^{2+} . The geometry of chemosensor **79** was widened by the presence of anthracene, which enabled this compound to capture up to 3 Cu^{2+} ions. Due to the massive and bulky nature of anthracene moieties, exerted pressure on one other, resulting in the expansion of the cavity in chemosensor **79**. (**Figure 43**)⁵³

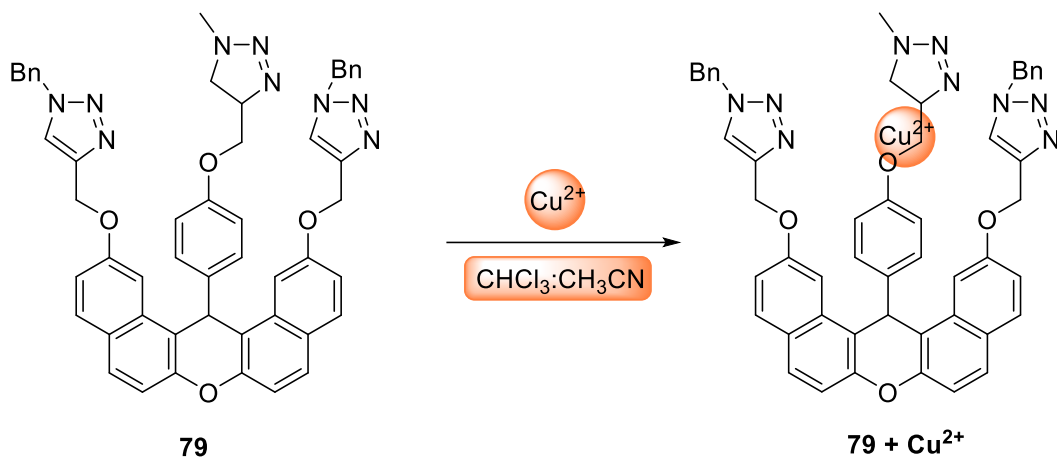


Figure 43. Depiction of intramolecular interaction of probe **79** with Cu^{2+} ions⁵³

Through "click chemistry" and copper (I)-catalyzed azide-alkyne cycloaddition reaction 1,2,3-triazole chemosensor with phenanthrene and phenol groups was successfully synthesised by S. M. Landge and co-workers. Chemosensor **80** proved to be versatile sensor capable of detecting both fluoride and copper ions in a homogeneous medium. The phenolic OH proton is deprotonated by the fluoride ions, resulting in an alteration in colour from blue to yellowish-orange. Additionally, a charge transfer occurs between the triazole nitrogen of the chemosensor and Cu^{2+} , causing a decrease in fluorescence output. Chemosensor **80** demonstrated selective and sensitive recognition of Cu^{2+} ions with cations via spectral modulation in absorption spectroscopy and a fluorescence turn-off response. While studying anions, competitive fluorescence responses were recorded under UV light for acetate and dihydrogen phosphate anions. Chemosensor **80** exhibited two unique binding patterns with the fluoride and copper ions. **(Figure 44)**⁵⁴

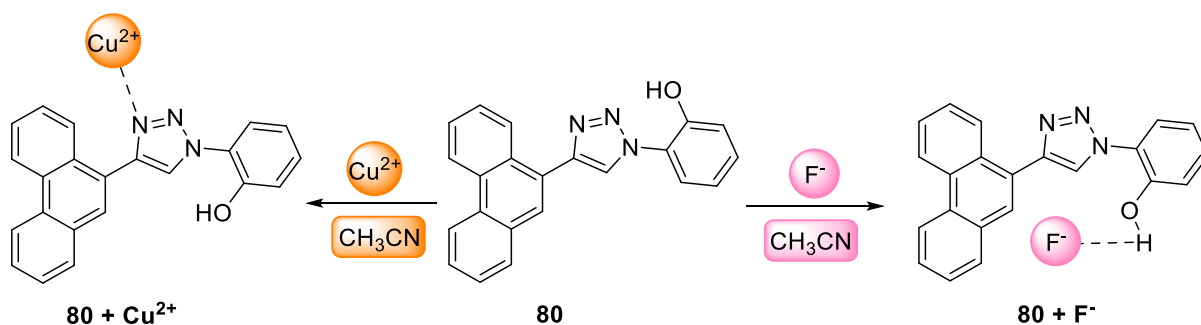


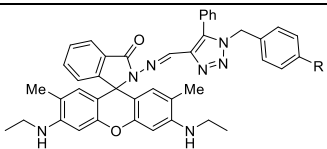
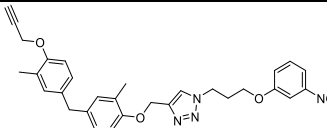
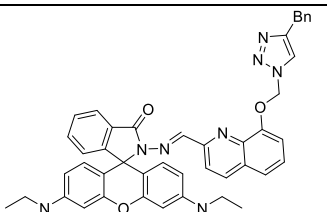
Figure 44. Representation of Binding of chemosensor **80** with Cu^{2+} and F^- ions⁵⁴

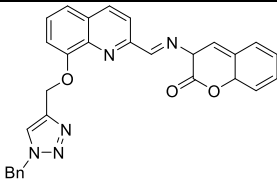
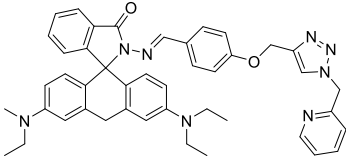
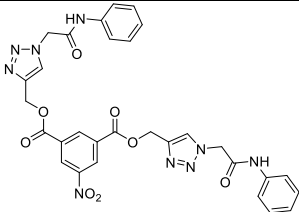
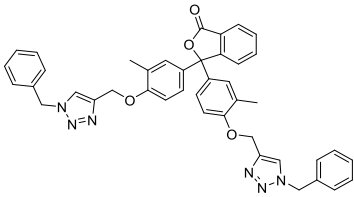
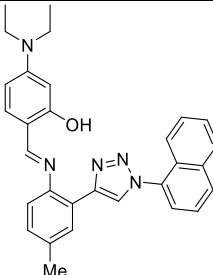
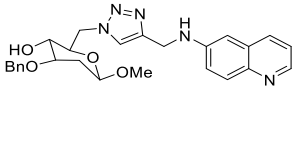
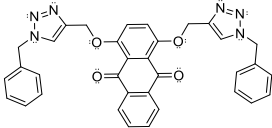
Based on the data acquired, it can be inferred that the synthesis through click reaction is highly efficient, necessitates mild reaction conditions, has a broad range of applicability, and yields

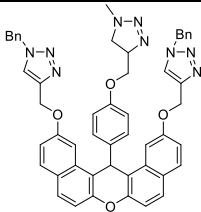
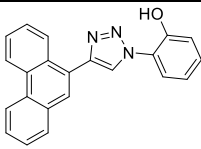
a nearly pure product or harmless by-products that can be easily eliminated using a straightforward procedure under normal and environmentally friendly conditions. Synthesised compounds may be readily characterised using infrared (IR), nuclear magnetic resonance (NMR) spectroscopy (specifically ^1H and ^{13}C), and mass spectrometry. UV-Visible and Fluorescence analyses aid in elucidating the chemosensing characteristics of compounds.

This literature review emphasises the exceptional sensing capabilities of fluorescent 1,2,3-triazoles which have gained recognition as fluorescent chemosensors due to their highly advantageous characteristics such as excellent selectivity, sensitivity, and robust chemical and photochemical stability in solution. Additionally, these chemosensors exhibit remarkable electron/energy transfer properties. A wide variety of interactions, including H-bonding, coordination with heteroatoms, and processes involving electron and photon transmission, have been widely used in the identification, sensing, and detection of diverse anions, cations, and neutral molecules.

Table 1. The compilation of previously synthesized 1,2,3-triazoles chemosensors for detection of metal ions

Sr. No	Type of chemosensor	Structure of compound	Metal ions detected	LOD	Binding ratio (M:L)	Ref.
1.	rhodamine-1,2,3-triazole		Cu^{2+}	152 nM	1:1	⁴¹
2.	click-derived 1,2,3-triazole		Hg^{2+}	0.06 μM	1:2	⁴²
3.	rhodamine-based chemosensor		Fe^{3+}	0.05 μM	1:1	⁴⁴

4.	coumarin-quinoline triazole		Pb^{2+}	33.6 nM	1:1	45
5.	rhodamine-triazole-pyridine		Sn^{2+}	2.6×10^{-8} mol L ⁻¹	1:1	46
6.	5-nitro isophthalate linked bis-triazole		Fe^{3+}	9.18 μM	1:1	48
7.	cresolphthalein appended 1,4-disubstituted 1,2,3-triazole		Pb^{2+}	13 μM	1:2	49
8.	imino-phenol 1,2,3-triazole		Zn^{2+}	1.8×10^{-6} M	1:1	50
9.	quinoline-based 1,2,3-triazole		Cu^{2+} , Ni^{2+}	1 μM , 1.4 μM	1:1	51
10.	dihydroxyanthraquinone based 1,2,3-triazole		Fe^{2+}	10 μM	1:1	52

11.	anthracenyl- dibenzoxanthe ne 1,2,3-triazole		Cu^{2+}	2.19 μM	1:1	⁵³
12.	phenanthrene derivatized triazole		Cu^{2+} , F^-	5.4×10^{-7} mol dm^{-3}	1:1	⁵⁴

4. Aim, Objective, and scope of the thesis

The literature review indicates that there is considerable potential for the development of novel 1,2,3-triazole linkers through the synthesis of additional compounds (organic azides and terminal alkynes). The exploration of organic molecules possessing fluorophoric or chromo functional groups, can have their functional groups modified to produce new terminal alkynes and organic azides amenable to CuAAC reaction, holds considerable promise to synthesise novel molecules linked to 1,2,3-triazoles.

Following the process of characterization, the synthesised molecules may subsequently undergo ions sensing. Based on this observation, the objectives of this study were formulated as follows:

- To synthesize novel 1,2,3–triazole derivatives using terminal alkyne, organic azide and Cu(I) catalyst.
- To characterize the synthesized compounds by spectroscopic techniques like IR, NMR (^1H , ^{13}C) and x-ray (if possible).
- To explore the ion sensing behaviour of synthesized 1,2,3–triazole derivatives using UV–Visible spectroscopy or fluorescence spectroscopy.

The aim of this thesis, entitled, "Synthesis and Characterization of new Schiff base alkynes and their triazole derivatives, as potential ion sensors" was to develop and investigate the viability of 1,2,3-triazole-linked molecules as optical sensors for the quantification of diverse metal ions. 'Click chemistry' has attracted enormous research attention due to the synthetic simplicity for

synthesis of 1,2,3-triazole linkers, that act as binding pockets in diverse applications in chemical biology, agrochemical, dyes, pigments, and so forth. The CuAAC Meldal–Sharpless cycloaddition ‘click’ reaction is attributed to enriching discernible metal ions sensors.^{55,56} Carolyn R. Bertozzia, Morten Meldal, and K. Barry Sharpless were recently awarded the 2022 Nobel Prize in Chemistry for pioneering click chemistry, an eco-sustainable technique of rapidly stitching molecules to generate cancer treatments and materials.⁵⁷ The five-membered 1,2,3-triazole ring probe acts as an active donor and has the potential to bind with metal ions due to the availability of electron-rich N and O donor sites.^{54,58} Schiff bases have been the pioneer leaders as substrates for co-ordination chemistry and thus have found diverse applications in chemical synthesis, ions-sensing, biological activity, and pharmaceuticals.^{59,60} Hence, the aforementioned molecules and the methodologies employed to investigate their capacity for sensing diverse metal ions exhibit a level of excellence surpassing that of traditional approaches.

The exorbitant use and erroneous management of metal ions has been incurred with catastrophic pollution of our ecological system, particularly in soil and water bodies, resulting in significant repercussions. Hence, precise identification and analysis of heavy-metal ions in intricate hydrological environments is imperative.^{61,62} For the detection of metal ions, instrumentation techniques such as atomic absorption and emission spectroscopy, chromatography, polarography, voltammetry, and X-ray photoelectron analysis need sophisticated sample handling, expensive to operate, lengthy processing times, and corrosive solvents. Henceforth, optical approaches like UV-vis spectroscopy and fluorescence are now preferred over traditional techniques for detecting metal ions because they are facile to use, economical, selective, and delicately responsive to metal ions recognition. The ions recognition properties of these compounds have been assessed via UV-vis absorption, and fluorescence emission studies.^{64–66} The chemosensing studies has been conducted to examine the particular interaction between the host and guest molecules, the potential binding mode, the mechanism of signal transduction, and the impact of molecular structure on reactivity. This analysis has used UV-vis, fluorescence, and NMR spectroscopy to observe any changes in the spectra.^{66–69} Within the scope of this thesis, it is not feasible to provide a comprehensive overview of the wide range of applications in materials science, drug discovery, environmental studies, catalysis, chemosensing, and more. Considering this perspective, several 1,2,3-triazole derivatives have been developed using the Cu(I)-catalyzed

alkyne-azide cycloaddition reaction procedure. These compounds have been investigated for their ability to detect different metal ions.

5. Conclusion

Click chemistry, offers significant advantages as a tool in ligand design, and has enabled access to a vast array of coordination chemistry. Click generated 1,2,3-triazole-based chemosensors have become an essential structural motif in the realm of chemical sensing due to their quick synthesis and high selectivity towards certain analytes of interest. Thoroughly reviewing the literature on Schiff base 1,2,3-triazole chemosensors for selective metal ions detection reveals that the ligand structure plays a pivotal role in achieving selectivity. The design of the receptor contains strategically positioned donor atoms that facilitate the efficient coordination of metal ions through host-guest interactions. Hence, this thesis aims to investigate suitable structural modifications that could induce selectivity and sensitivity in a system in which the signalling parameters are determined by efficient coordination in response to electronic states in the Schiff base 1,2,3 triazole.

6. References

- 1 D. R. Mishra, S. Nayak, B. P. Raiguru, S. Mohapatra, M. B. Podh, C. R. Sahoo and R. N. Padhy, *J Heterocycl Chem*, 2021, **58**, 111–126.
- 2 D. Ashok, M. R. Reddy, N. Nagaraju, R. Dharavath, K. Ramakrishna, S. Gundu, P. Shravani and M. Sarasija, *Med Chem Res*, 2020, **29**, 699–706.
- 3 R. Dharavath, N. Nagaraju, M. R. Reddy, D. Ashok, M. Sarasija, M. Vijjulatha, T. Vani, K. Jyothi and G. Prashanthi, *RSC Adv*, 2020, **21**, 11615–11623.
- 4 H. H. López, S. L. Ramos, C. F. A. G. Durán, A. P. Alvarez, I. R. R. Gutiérrez, M. A. L. Peralta and R. S. R. Hernández, *ACS Omega*, 2020, **5**, 14061–14068.
- 5 G. Singh, Sanchita, S. Rani, G. Sharma, P. Kalra, N. Singh and V. Verma, *Sens Actuators B Chem*, 2018, **266**, 861–872.
- 6 M. O. M'Hamed, *Synth Commun*, 2015, **45**, 2511–2528.
- 7 S. Kumar, B. Sharma, V. Mehra and V. Kumar, *Eur J Med Chem*, 2021, **212**, 113069.

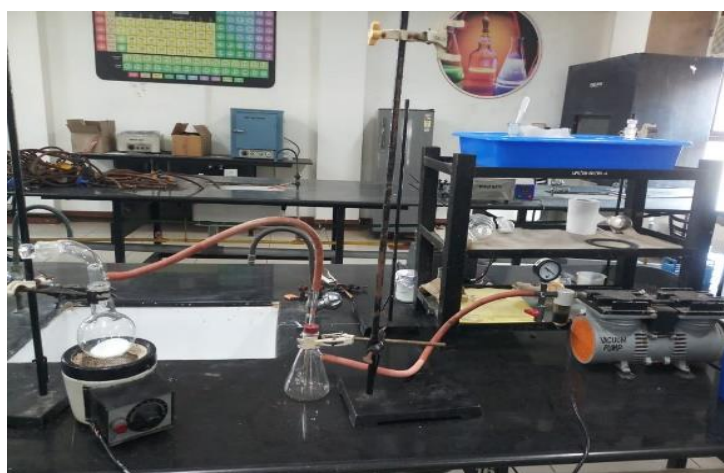
- 8 G. Singh, A. Arora, S. S. Mangat, J. Singh, S. Chaudhary, N. Kaur and D. C. Lazarte, *J Mol Struct*, 2015, **1079**, 173–181.
- 9 N. Kumari, S. Singh, M. Baral and B. K. Kanungo, *J Fluoresc*, 2023, **33**, 859–893.
- 10 S. Omid and A. Kakanejadifard, *RSC Adv*, 2020, **10**, 30186–30202.
- 11 A. Jarrahpour, M. Aye, V. Sinou, C. Latour and J. M. Brunel, *J Iran Chem Soc*, 2015, **12**, 2083–2092.
- 12 M. Sadia, R. Naz, J. Khan and R. Khan, *J Fluoresc*, 2018, **28**, 1281–1294.
- 13 V. K. Gupta, A. K. Singh and L. K. Kumawat, *Sens Actuators B Chem*, 2014, **204**, 507–514.
- 14 V. K. Rao, S. S. Reddy, B. S. Krishna, K. R. M. Naidu, C. N. Raju and S. K. Ghosh, *Green Chem Lett Rev*, 2010, **3**, 217–223.
- 15 S. Nagar, S. Raizada and N. Tripathy, *Results Chem*, 2023, **6**, 101153.
- 16 R. Shaw, A. Elagamy, I. Althagafi and R. Pratap, *Org Biomol Chem*, 2020, **18**, 3797–3817.
- 17 F. Wei, W. Wang, Y. Ma, C. H. Tung and Z. Xu, *Chem Comm*, 2016, **52**, 14188–14199.
- 18 B. C. Ranu, S. K. Guchhait and A. Sarkar, *Chem Comm*, 1998, **19**, 2113–2114.
- 19 A. K. Morri, Y. Thummala and V. R. Doddi, *Org Lett*, 2015, **17**, 4640–4643.
- 20 P. Krapf, R. Richarz, E. A. Urusova, B. Neumaier and B. D. Zlatopolskiy, *European J Org Chem*, 2016, **2016**, 430–433.
- 21 P. Rani, K. L. Aruna, R. Shrivastava and V. D. Ghule, *J Mol Struct*, 2020, **1203**, 127437.
- 22 A. S. K. Hashmi, T. Häffner, M. Rudolph and F. Rominger, *Chem Eur J*, 2011, **17**, 8195–8201.
- 23 D. Ghosh, S. Rhodes, D. Winder, A. Atkinson, J. Gibson, W. Ming, C. Padgett, S. Landge and K. Aiken, *J Mol Struct*, 2017, **1134**, 638–648.
- 24 N. Khanapurmath, M. D. Prabhu, J. Tonannavar, J. Tonannavar and M. V. Kulkarni, *J Mol Liq*, 2020, **314**, 113620.

- 25 G. Singh, J. Singh, A. Singh, J. Singh, M. Kumar, K. Gupta and S. Chhibber, *J Organomet Chem*, 2018, **871**, 21–27.
- 26 S. Bräse, C. Gil, K. Knepper and V. Zimmermann, *Angew Chem*, 2005, **44**, 5188–5240.
- 27 W. Stadlbauer, W. Fiala, M. Fischer and G. Hojas, *J Heterocyclic Chem*, 2000, **37**, 1253.
- 28 G. Mayra, *J Chem Inf Model*, 2013, **53**, 1689–1699.
- 29 Q. Liu and Y. Tor, *Org Lett*, 2003, **5**, 2571–2572.
- 30 M. Kitamura, M. Yano, N. Tashiro, S. Miyagawa, M. Sando and T. Okauchi, *European J Org Chem*, 2011, **3**, 458–462.
- 31 M. Kitamura, T. Koga, M. Yano and T. Okauchi, *Synlett*, 2012, **23**, 1335–1338.
- 32 M. D. L. G. Ferreira, L. C. S. Pinheiro, O. A. S. Filho, M. D. S. Peçanha, C. Q. Sacramento, V. Machado, V. F. Ferreira, T. M. L. Souza and N. Boechat, *Med Chem Res*, 2014, **23**, 1501–1511.
- 33 G. Senthilkumaran and S. Senthil, *Mater Today Proc*, 2020, **22**, 3–6.
- 34 T. Göktürk, E. S. Çetin, T. Hökelek, H. Pekel, Ö. Şensoy, E. N. Aksu and R. Güp, *ACS Omega*, 2023, **8**, 31839–31856.
- 35 G. Singh, J. Singh, J. Singh and S. S. Mangat, *J Lumin*, 2015, **165**, 123–129.
- 36 M. Bal, M. Tümer and M. Köse, *J Fluoresc*, 2022, **32**, 2237–2256.
- 37 G. Singh, P. Satija, A. Singh, Diksha, Pawan, Suman, Sushma, Mohit and S. Soni, *Mater Chem Phys*, 2020, **249**, 123005.
- 38 B. Khan, A. Hameed, A. Minhaz and M. R. Shah, *J Hazard Mater*, 2018, **347**, 349–358.
- 39 P. L. Rojas, M. Janeczko, K. Kubiński, Á. Amesty, M. Masłyk and A. E. Braun, *Mol*, 2018, **23**, 1–18.
- 40 G. Singh, P. Kalra, A. Arora, Sanchita, G. Sharma, A. Singh and V. Verma, *Inorganica Chim Acta*, 2018, **473**, 186–193.

- 41 M. Vadivelu, A. A. Raheem, B. Shankar, K. Karthikeyan and C. Praveen, *Chem Asian J*, 2023,**18**, 202300098.
- 42 R. Ujan, N. Arshad, F. Perveen, P. A. Channar, B. Lal, M. Hussain, Z. Hussain, A. Saeed and S. A. Shehzadi, *Chem Pap*, 2021, **75**, 6377–6388.
- 43 S. M. Hashemi, S. E. Moradi, R. M. Ahangar, D. Farmanzadeh and S. Emami, *J Fluoresc*, 2023, 1-9.
- 44 F. Ahmed and H. Xiong, *Dyes Pigm*, 2021, **185**, 108905.
- 45 G. Wu, M. Li, J. Zhu, K. W. C. Lai, Q. Tong and F. Lu, *RSC Adv*, 2016, **6**, 100696–100699.
- 46 Z. Yan, G. Wei, S. Guang, M. Xu, X. Ren, R. Wu, G. Zhao, F. Ke and H. Xu, *Dyes Pigm*, 2018, **159**, 542–550.
- 47 K. Rout, A. K. Manna, M. Sahu, J. Mondal, S. K. Singh and G. K. Patra, *RSC Adv*, 2019, **9**, 25919–25931.
- 48 S. Kumar, S. Gadiyaram, R. K. Tittal, G. Vikas D and R. Sharma, *J Mol Struct*, 2023, **1290**, 135940.
- 49 P. Saini, G. Singh, G. Kaur, J. Singh and H. Singh, *J Mol Struct*, 2022, **1251**, 131985.
- 50 S. Ghosh, N. Baildya and K. Ghosh, *New J Chem*, 2021, **45**, 10923–10929.
- 51 M. Loya, S. I. Hazarika, P. Pahari and A. K. Atta, *J Mol Struct*, 2021, **1241**, 130634.
- 52 P. Saini, Sushma, G. Singh, G. Kaur, J. Singh and H. Singh, *Inorg Chem Commun*, 2022, **141**, 109524.
- 53 O. Ozukanar, H. Gunduz, C. Unlu and V. Kumbaraci, *Opt Mater*, 2021, **119**, 111370.
- 54 S. M. Landge, D. Y. Lazare, C. Freeman, J. Bunn, J. I. Cruz, D. Winder, C. Padgett, K. S. Aiken and D. Ghosh, *Spectrochim Acta A Mol Biomol Spectrosc*, 2020, **228**, 117758.
- 55 C. Wu, C. Z. Wang, Q. Zhu, X. Zeng, C. Redshaw and T. Yamato, *Sens Actuators B Chem*, 2018, **254**, 52–58.

- 56 D. Ghosh, S. Rhodes, K. Hawkins, D. Winder, A. Atkinson, W. Ming, C. Padgett, J. Orvis, K. Aikena and S. Landge, *New J Chem*, 2015, **39**, 295–303.
- 57 *Scientific Background on the Nobel Prize in Chemistry, Click Chemistry and Bioorthogonal chemistry, The Nobel Committee for Chemistry*, 2022, **50005**, 1-20
- 58 R. Joseph, *ACS Omega*, 2020, **5**, 6215–6220.
- 59 P. Kaur, B. Lal, N. Kaur, G. Singh, A. Singh, G. Kaur and J. Singh, *J Photochem Photobiol A Chem*, 2019, **382**, 111847.
- 60 B. xing Shen and Y. Qian, *Sens Actuators B Chem*, 2018, **260**, 666–675.
- 61 P. Purushothaman and S. Karpagam, *ACS Omega*, 2022, **7**, 41361–41369.
- 62 P. Rasin, V. Manakkadan, V. N. V. Palakkeezhillam, J. Haribabu, C. Echeverria and A. Sreekanth, *ACS Omega*, 2022, **7**, 33248–33257.
- 63 S. Pattaweepai boon, W. Foytong, N. Phiromphu, T. Nanok, N. Kaewchangwat, K. Suttisintong and W. Sirisaksoontorn, *ACS Omega*, 2022, **7**, 18671–18680.
- 64 W. Zhong, L. Wang, D. Qin, J. Zhou and H. Duan, *ACS Omega*, 2020, **5**, 24285–24295.
- 65 C. A. S. Pothulapadu, A. Jayaraj, N. Swathi, R. N. Priyanka and G. Sivaraman, *ACS Omega*, 2021, **6**, 24473–24483.
- 66 Q. Ye, S. Ren, H. Huang, G. Duan, K. Liu and J. B. Liu, *ACS Omega*, 2020, **5**, 20698–20706.
- 67 P. S. Umabharathi and S. Karpagam, *ACS Omega*, 2022, **7**, 24638–24645.
- 68 S. Sasan, T. Chopra, A. Gupta, D. Tsering, K. K. Kapoor and R. Parkesh, *ACS Omega*, 2022, **7**, 11114–11125.
- 69 Z. Qin, W. Su, P. Liu, J. Ma, Y. Zhang and T. Jiao, *ACS Omega*, 2021, **6**, 25040–25048.

CHAPTER 3



EXPERIMENTAL DATA

This section contains comprehensive information regarding the experimental procedures followed to synthesise a wide range of novel molecules, as well as their thorough structural characterization, which encompasses several physical, chemical, spectroscopic examination including yield, colour, CHN analysis, IR, NMR, and mass spectrometry

1. Materials and instrumentation

Commercially available high purity reagents and solvents such as 4-hydroxy-3-methoxy benzaldehyde (LOBA), 4-amino-phenol (LOBA), benzylamine (LOBA), 1-naphthylamine (LOBA), 2-phenylethylamine (LOBA), p-toluidine (LOBA), propargyl bromide (80% in toluene) (Spectro-chem), potassium carbonate (LOBA), dimethylformamide (DMF) (CDH), benzyl chloride (LOBA), tetrahydrofuran (THF) (CDH), triethylamine (CDH), sodium azide, bromotris(triphenylphosphine)copper(I) [CuBrPPh₃]₃] (Merck), hexane, ethyl acetate were used as received. The Metal salts were acquired from LOBA and without any purification used for solution preparation. The glassware used for reaction purposes was oven dried at 100–120 °C.

FTIR spectra of synthesized compounds were recorded in Diamond attenuated total reflection (ATR) mode from PERKIN ELMER Spectrum 2 Spectrometer (pellet accessories) covering field 4000–500 cm⁻¹ with sensitivity including peak to peak for 1 min scan. The detector used in the record of the IR spectra is pyroelectric detector with material Lithium tantalate [LiTaO₃]. NMR spectra were obtained on BRUKER-ADVANCE-II FT-NMR-AL 500 MHz and 126 MHz for (¹H and ¹³C) spectrometer respectively using CDCl₃ and DMSO as solvents and chemical shifts were recorded against tetramethylsilane as an internal standard. Gas Chromatograph-Mass spectrometer (GCMS/ MS Shimadzu TQ8040) was used for recording mass of the compounds and Mel Temp II device for determining melting point of the compounds using sealed capillary. CHN elemental studies were performed using a Perkin Elmer Model 2400 CHNS elemental analyzer. The electronic absorption spectra were measured using a SHIMADZU UV-1800 UV-Spectrophotometer for chemosensing studies. The solutions were generated using a microbalance with an accuracy of ±0.1 mg and volumetric glassware. Subsequently, these solutions were transferred into quartz cuvettes in order to conduct measurements. The emission spectra were generated from Perkin Elmer LS6500 Fluorescence Spectrometer using quartz cuvettes and standard solutions.

2. Purification technique of different solvents

2.1 Methanol

Methanol (SDFCL) was purified by distillation using glass equipment at a temperature of 64.7 °C (760 mm Hg) and was then stored in a sealed container to prevent air exposure. The

contents are distilled at temperature of 64.7 °C and a pressure of 760 mm Hg in a separate flask with calcium hydride. The contents were distilled to yield pure methanol.

2.2 Ethanol

Ethanol (CYCC) underwent distillation using a glass apparatus, and the fraction that evaporated at a temperature of 77.5 °C (at a pressure of 760 mm Hg) was collected in a round-bottomed flask that contained calcium hydride.

2.3 Dichloromethane

The solvent dichloromethane (MERCK) was subjected to reflux for a duration of 15 to 20 h. The solvent was treated with phosphorus pentoxide and then subjected to distillation. The fraction obtained at a temperature of 40 °C/750 mm Hg was collected and stored on activated molecular sieves with a pore size of 40 Å for a period of 48 h before being used.

2.4 Tetrahydrofuran

Tetrahydrofuran (Merck) was stored for 48 h over anhydrous CaCl₂. The mixture was filtered, the filtrate was collected in a flask that contain sodium fragments and benzophenone and attached to reflux cum distillation apparatus and were refluxed until it obtained a blue hue.

2.5 Dimethyl sulfoxide

The solvent dimethyl sulfoxide (Merck) was stored over molecular sieves for a duration of one week. The decanted liquid was subjected to distillation under decreased pressure in order to collect the portion that had a boiling point of 75–76 °C/12 mm Hg. The fraction underwent further purification using a process of partial freezing at 18 °C. The solvent was stored in a well-sealed container with molecular sieves (3 Å) to maintain its purity.

2.6 N,N-Dimethylformamide

N,N-Dimethylformamide (SDFCL) was kept on molecular sieves. The liquid was subjected to distillation at a lower pressure in order to obtain the fraction at 80–85 °C (16 mm Hg). The fraction underwent further purification using a process of partial freezing at 18 °C. The clean solvent was stored over molecular sieves (3 Å) in a securely sealed container.

3. Intended research methodology

3.1 General technique for the synthesis of compounds

The literature study made us familiar with a handful of precursor molecules which can be synthesized for the synthesis of 1,2,3-triazole hybrid molecules. The labile proton attached to the functional groups in the structures of initiating molecules is a necessity so as to convert it into terminal alkyne following the authentic procedure. The synthesis of 1,2,3-triazoles comprises of following steps:

Step I: General procedure of Schiff base

Primary amine (1 mol) was reacted with aromatic aldehyde (1 mol) in polar solvent like methanol or ethanol and the reaction mixture was refluxed for 4-5 h for the synthesis of Schiff base. The solvent mixture was quenched with crushed ice and the product was filtered, dried and washed with water to obtain Schiff bases. (Figure 45)

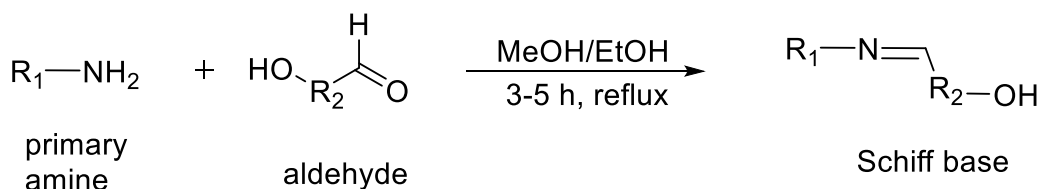


Figure 45. General reaction of Schiff base

Step II: General procedure of Schiff base tethered terminal alkynes

The solution of the starting material (1 mol) was prepared in DMF and dried base such as potassium carbonate (5 mol) was added. Propargyl bromide (1.3mol) was injected dropwise and the reaction mixture was maintained at room temperature with constant stirring for 12-48 h. The separation of the product was done with ice cold water and air dry to obtain solid product. The solvent extraction process is followed if the product is in liquid state. (Figure 46)

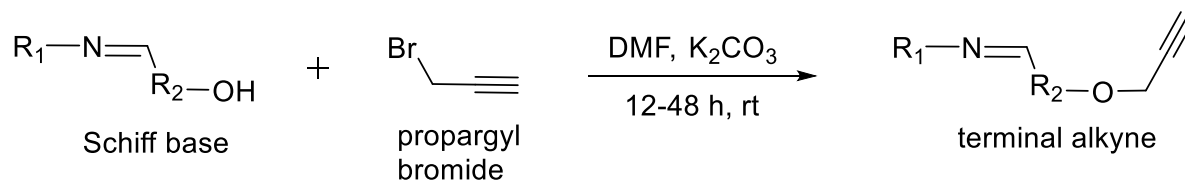


Figure 46. General reaction of Schiff base tethered terminal alkynes

Step III: General procedure of organic azide

To the solution of organic halide (1 mol), sodium azide (5 mol) was added using DMF as the solvent and the stirring was continued for 4-5 h at 85–90 °C temperature conditions. The product was quenched using ice cold water and ethyl acetate was used for solvent extraction method with liquid state of product. (**Figure 47.**)

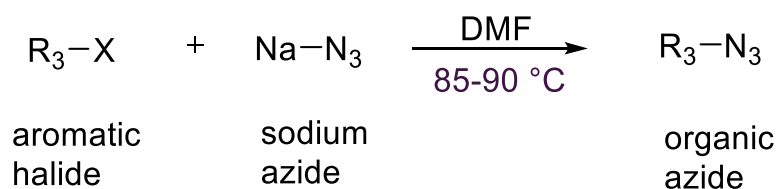


Figure 47. General reaction of organic azide

Step IV: General procedure of Schiff base linked 1,4-disubstituted-1,2,3-triazole

The newly synthesised alkyne was blend with azide in the 1:1 mol ratio in solvent and base (THF: TEA::1:1) respectively. The reaction mixture was loaded with sufficient amount of $[\text{Cu}(\text{PPh}_3)_3\text{Br}]$ catalyst and stirring was performed for 4-6 h at about 60 °C. The separation of product was done using cold water and dried in the air till the constant weight was obtained (solid). In case of liquid state, the solvent extraction method was preferred. (**Figure 48**)

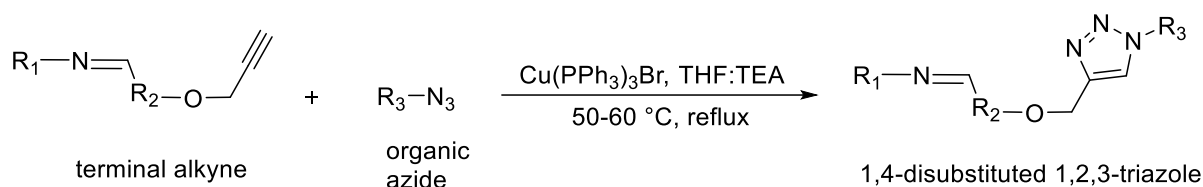


Figure 48. General reaction of Schiff base linked 1,4-disubstituted-1,2,3-triazole

3.2 Synthesis of organic azide

3.2.1 Synthesis of Azidomethylbenzene

In a 50 ml round bottom flask, dried sodium azide (12.87 g, 197.9 mmol) was slowly added to a solution of benzyl chloride (5 g, 4.54 ml, 39.5 mmol) in DMF (50 ml), and the reaction mixture was refluxed for 5 h at 90 °C. The reaction was monitored and the completion of the reaction was determined by taking TLC (ethyl acetate:hexane::1:4) at regular intervals. After the reaction

completion, the product was extracted using ethyl acetate, and the organic layer obtained in the separating funnel was dried over sodium sulfate (in anhydrous form) and the organic solvent present in the sample was eliminated by employing vacuum evaporation. The synthesis technique of compound **39** has been shown in **Figure 49**.

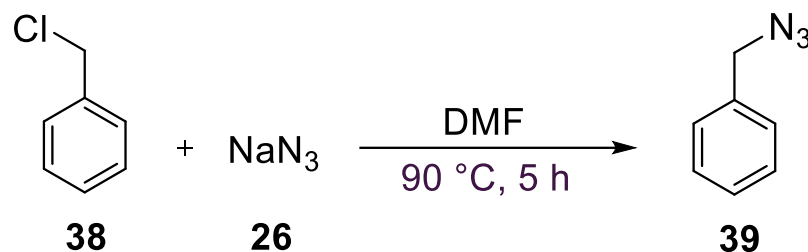


Figure 49. Schematic representation for the synthesis of *Azidomethylbenzene*

Yield: 60%;

Color/texture: light yellow oil

Empirical formula: C₇H₇N₃

Elem. anal. calculated (%): C = 63.14, H = 5.30, N = 31.56

Found (%): C = 63.12, H = 5.31, N = 31.57

FTIR (neat, cm⁻¹): 3032, 2929, 2089, 1495, 1452, 1252, 876, 739

¹H NMR (500 MHz, CDCl₃) δ (ppm) = 7.33 – 7.24 (m, 5H), 4.22 (s, 2H)

¹³C NMR (126 MHz, CDCl₃) δ (ppm) = 135.5, 128.9, 128.4, 128.3, 54.8

3.3 Synthesis of Schiff base **81a**, Schiff base terminal alkyne **81b** and 1,2,3-triazole derivative **81c**

3.3.1 Synthesis and characterization of (*E*)-4-((benzylimino)methyl)-2-methoxyphenol **81a**

A solution of substituted amine (0.5 g, 20 mmol) in 10 ml of ethanol, was treated sequentially with substituted benzaldehyde (0.7 g, 20 mmol) in a 50 ml round bottom flask and the resulting mixture was refluxed for 4 h. (**Figure 50**) TLC was employed to monitor and detect the completion of the reaction, with 10% (ethylacetate:hexane::1:9) accommodating as the mobile phase solvent. The acquired product was quenched in the ice-cold water with constant stirring of

15-20 min. The precipitate formed was filtered, washed with distilled water, and dried in a sealed laboratory desiccator under vacuum pressure to afford solid peach dust powder **81a**.

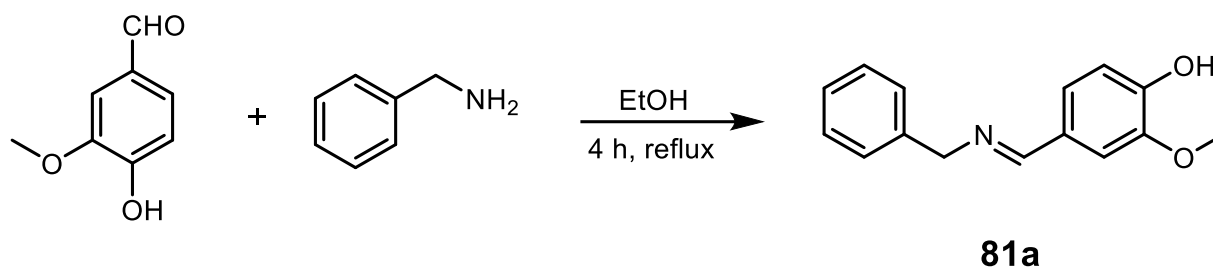


Figure 50. Schematic procedure for *(E)*-4-((benzylimino)methyl)-2-methoxyphenol

Yield: 82%

Color: peach dust

Texture: fine powder

M.pt: 65-67 °C

Empirical formula: C₁₅H₁₅NO₂

Elem. anal. calculated (%): C = 74.67, H = 6.27, N = 5.81

Found (%): C = 74.70, H = 6.25, N = 5.83

FTIR (neat, cm⁻¹): 3055, 2963, 1620, 1580, 1502, 1462, 1380, 1260, 1089, 1007, 858, 785

¹H NMR (500 MHz, CDCl₃) δ (ppm) = 9.82 (s, 1H), 8.27 (s, 1H), 7.48 (s, 1H), 7.33 (d, J = 6.3 Hz, 4H), 7.25 (s, 1H), 7.13 (d, J = 8.1 Hz, 1H), 6.93 (d, J = 8.1 Hz, 1H), 4.79 (s, 2H), 3.90 (s, 3H).

¹³C NMR (126 MHz, CDCl₃) δ (ppm) = 161.8, 148.5, 147.10, 139.40, 128.8, 128.6, 128.4, 128.0, 127.2, 127.0, 124.2, 114.0, 108.3, 64.8, 56.0.

3.3.2 Synthesis and characterization of alkyne *(E)*-*N*-benzyl-1-(3-methoxy-4-(prop-2-yn-1-yloxy)phenyl)methanimine **81b**

Schiff base (0.5g, 2.0 mmol) was dissolved in DMF (4 ml) taken in a 25 ml round bottom flask, followed by the addition of dried potassium carbonate (1.43g, 10.34 mmol), dropwise injecting of propargyl bromide (0.25ml, 2.6 mmol) into the reaction mixture with continuous

stirring at room temperature on a magnetic stirring for 18 h. TLC (ethyl acetate:hexane::1:4) was applied to monitor the reaction conditions to attain the maximum yield. The synthesized material was extracted by pouring the reaction content in the 250 ml beaker containing crushed ice, stirred for 15-20 min till the solid ppt appears at the bottom of the beaker, filtered and dried in a vacuum desiccator overnight to gain ivory dust solid powder as the product. **(Figure 51)**

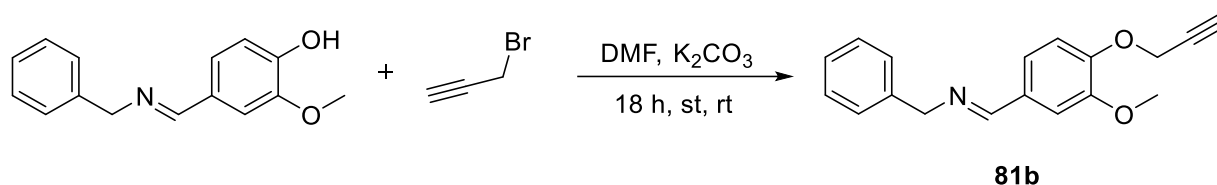


Figure 51. Systematic procedure for synthesis of *(E)-N-benzyl-1-(3-methoxy-4-(prop-2-yn-1-yloxy)phenyl)methanimine*

Yield: 91%

Color: ivory dust

Texture: fine powder

M.pt: 58-60 °C

Empirical formula: C₁₈H₁₇NO₂

Elem. anal. calculated (%): C = 77.40, H = 6.13, N = 5.01

Found (%): C = 77.42, H = 6.15, N = 5.00

FTIR (neat, cm⁻¹): 3190, 3021, 2120, 1636, 1588, 1505, 1453, 1265, 1228, 1016, 864

¹H NMR (500 MHz, CDCl₃) δ (ppm) = 8.28 (s, 1H), 7.49 (d, J = 1.6 Hz, 1H), 7.32 (d, J = 5.8 Hz, 4H), 7.25 (dt, J = 6.1, 3.1 Hz, 1H), 7.17 (dd, J = 8.2, 1.7 Hz, 1H), 7.02 (d, J = 8.2 Hz, 1H), 4.78 (s, 2H), 4.77 (d, J = 2.3 Hz, 2H), 3.89 (s, 3H), 2.51 (s, 1H)

¹³C NMR (126 MHz, CDCl₃) δ (ppm) = 161.4, 149.9, 149.1, 139.4, 130.6, 128.5, 128.0(2C), 127.0(2C), 122.9, 113.2, 109.3, 78.1, 76.2, 64.9, 56.6, 56.0

3.3.3 Synthesis and characterization of *(E)*-*N*-benzyl-1-(4-((1-benzyl-1*H*-1,2,3-triazol-4-yl)methoxy)-3-methoxyphenyl) methanimine **81 c**

Schiff base functionalized alkyne (0.4 g, 1.43 mmol) was treated with the synthesized benzyl azide **39** using equimolar ratio THF:TEA (5 ml)) solvent system, in the presence of $[\text{CuBr}(\text{PPh}_3)_3]$ as catalyst (0.001 mmol) and refluxed at 60 °C for 5 h. TLC (ethyl acetate: hexane::1:4) was used at regular intervals to monitor the completion of the reaction. The product was extracted by pouring the reaction mixture on crushed ice, ppt appeared which was filtered, and dried to attain the dry solid product **81c** with excellent yield. (**Figure 52**)

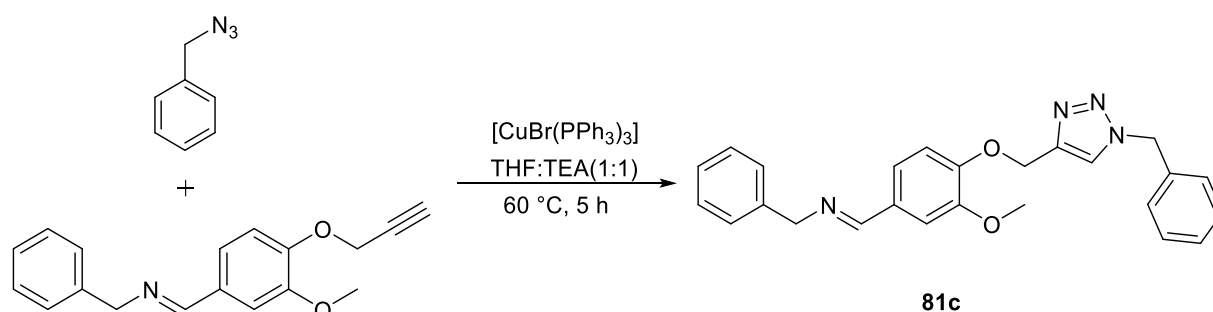


Figure 52. Synthetic procedure for *(E)*-*N*-benzyl-1-(4-((1-benzyl-1*H*-1,2,3-triazol-4-yl)methoxy)-3-methoxyphenyl) methanimine

Yield: 96%

Color: tangelo-cream

Texture: fine powder

M.pt: 84–86 °C

Empirical formula: $\text{C}_{25}\text{H}_{24}\text{N}_4\text{O}_2$

Elem. anal. calculated (%): C = 72.80, H = 5.86, N = 13.58

Found (%): C = 72.79, H = 5.84, N = 13.56

FTIR (neat, cm^{-1}): 3137, 3022, 2960, 1640, 1585, 1513, 1452, 1263, 1120

¹H NMR (500 MHz, CDCl₃) δ (ppm) = 8.18 (s, 1H), 7.45 (s, 1H), 7.37 (s, 1H), 7.23 (d, J = 2.9 Hz, 7H), 7.14 (t, J = 9.0 Hz, 3H), 7.05 (d, J = 7.9 Hz, 1H), 6.96 (d, J = 8.2 Hz, 1H), 5.37 (s, 2H), 5.18 (s, 2H), 4.69 (s, 2H), 3.75 (s, 3H).

¹³C NMR (126 MHz, CDCl₃) δ (ppm) = 161.4, 149.9, 149.7, 144.1, 139.3, 134.3, 130.1, 129.0, 128.7(2C), 128.4(2C), 128.0(2C), 127.9(2C), 126.9, 123.1, 122.9, 113.0, 109.1, 64.8, 62.9, 55.8, 54.1.

GCMS-MS: m/z (actual) = 412.19; m/z (reported) = 412.15.

3.4 Synthesis of Schiff base 82a, Schiff base terminal alkyne 82b and 1,2,3-triazole derivative 82c

3.4.1 Synthesis and characterization of (*E*)-4-(((3-hydroxybenzyl)imino)methyl)-2-methoxyphenol 82a

In a 25 ml round bottom flask, substituted aldehyde (0.69 g, 4.0 mmol) was added to a stirred solution of substituted primary amine (0.50 g, 4.0 mmol) in distilled water (10 ml), and the resulting mixture was shaken for 60 min at room temperature. The reaction was monitored and detected by using TLC in which (ethyl acetate:hexane::1:4) was used as mobile phase solvent. The crude product obtained after filtration was washed with distilled water and dried to gain the dry brown dust powder. (**Figure 53**)

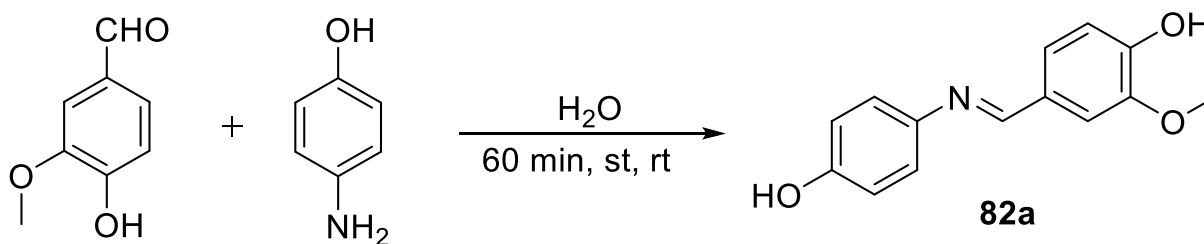


Figure 53. Synthetic route for (*E*)-4-(((3-hydroxybenzyl)imino)methyl)-2-methoxyphenol

Yield: 83%

Color: brown

Texture: fine powder

M.pt: 180–182 °C

Empirical formula: C₁₄H₁₃NO₃

Elem. anal. calculated (%): C = 70.02, H = 5.88, N = 5.44

Found (%): C = 70.05, H = 5.90, N = 5.83

FTIR (neat, cm⁻¹): 3275, 2958, 1622, 1587, 1508, 1429, 1280, 1240, 1024, 781

¹H NMR (500 MHz, CDCl₃) δ (ppm) = 9.43 (s, 2H), 8.40 (s, 1H), 7.49 (s, 1H), 7.13 (d, J = 8.8 Hz, 2H), 6.87 (d, J = 8.1 Hz, 1H), 6.78 (d, J = 8.8 Hz, 2H), 6.52 – 6.44 (m, 1H), 3.80 (s, 3H)

¹³C NMR (126 MHz, CDCl₃) δ (ppm) = 157.0, 155.7, 149.7, 147.9, 143.1, 128.3, 123.6, 122.1, 115.7, 115.6, 115.4, 115.3, 110.1, 55.4

3.4.2 Synthesis and Characterization of *(E)*-1-(3-methoxy-4-(prop-2-yn-1-yloxy)phenyl)-N-(4-(prop-2-yn-1-yloxy)phenyl)methanimine **82b**

Schiff base (0.50 g, 2.0 mmol) was dissolved in DMF (6 ml) and 1.4 g (10 mmol) of dried potassium carbonate as a base was added to it followed by dropwise addition of propargyl bromide (0.50 ml, 6.0 mmol) into the reaction mixture with continuous stirring at room temperature on a magnetic stirrer for 20 h. TLC (ethyl acetate:hexane::1:4) was taken at regular intervals to monitor and examine the synthesis of the desired product. Further, the product was filtered and dried to gain good yield. (**Figure 54**)



Figure 54. Systematic pathway for *(E)*-1-(3-methoxy-4-(prop-2-yn-1-yloxy)phenyl)-N-(4-(prop-2-yn-1-yloxy)phenyl)methanimine

Yield: 89%

Color: ivory

Texture: fine powder

M.pt: 114–117 °C

Empirical formula: C₂₀H₁₇NO₃

Elem. anal. calculated (%): C = 75.22, H = 5.37, N = 4.39

Found (%): C = 75.26, H = 5.30, N = 4.43

FTIR (neat, cm⁻¹): 3255, 3193, 2127, 1620, 1587, 1504, 1418, 1268, 1019, 831

¹H NMR (500 MHz, CDCl₃) δ (ppm) = 8.37 (s, 1H), 7.61 (d, J = 1.9 Hz, 1H), 7.28 (dd, J = 8.3, 1.9 Hz, 1H), 7.21 (d, J = 2.2 Hz, 1H), 7.18 (d, J = 2.3 Hz, 1H), 7.06 (d, J = 8.2 Hz, 1H), 7.00 (d, J = 2.3 Hz, 1H), 6.98 (d, J = 2.2 Hz, 1H), 4.82 (d, J = 2.4 Hz, 2H), 4.70 (d, J = 2.4 Hz, 2H), 3.96 (s, 3H), 2.53 (q, J = 2.5 Hz, 1H)

¹³C NMR (126 MHz, CDCl₃) δ (ppm) = 158.4, 156.0, 150.0, 149.5, 146.0, 130.8, 123.8, 122.1, 115.5, 113.1, 109.3, 78.6, 78.0, 76.3, 75.6, 56.6, 56.2, 56.1

3.4.3 Synthesis and Characterization of (*E*)-1-(4-((1-benzyl-1*H*-1,2,3-triazol-4-yl)methoxy)-3-methoxyphenyl)-*N*-(4-((1-benzyl-1*H*-1,2,3-triazol-4-yl)methoxy)phenyl)methanimine 82c

The head group (N₃) of benzyl azide was reacted with schiff base functionalized alkyne tail groups (0.40 g, 1.0 mmol) in an equimolar ratio of THF: TEA (1:1(v/v), 3 ml)) solvent solution, with [CuBr(PPh₃)₃] as catalyst (0.001 mmol), and refluxed at 60 °C for 5 h. The reaction was monitored using TLC (ethyl acetate:Hexane::1:4) for completion of the reaction. Precipitation occurs when the reaction mixture was put into crushed ice and continued constant stirring for 15 min, the heavy particles settle down and the liquid form of water containing undesired mixture was decant off and the remaining part was then filtered using glass funnel, the moist compound was dried in a glass vacuum desiccator to obtain the dry pure solid product. (**Figure 55**)

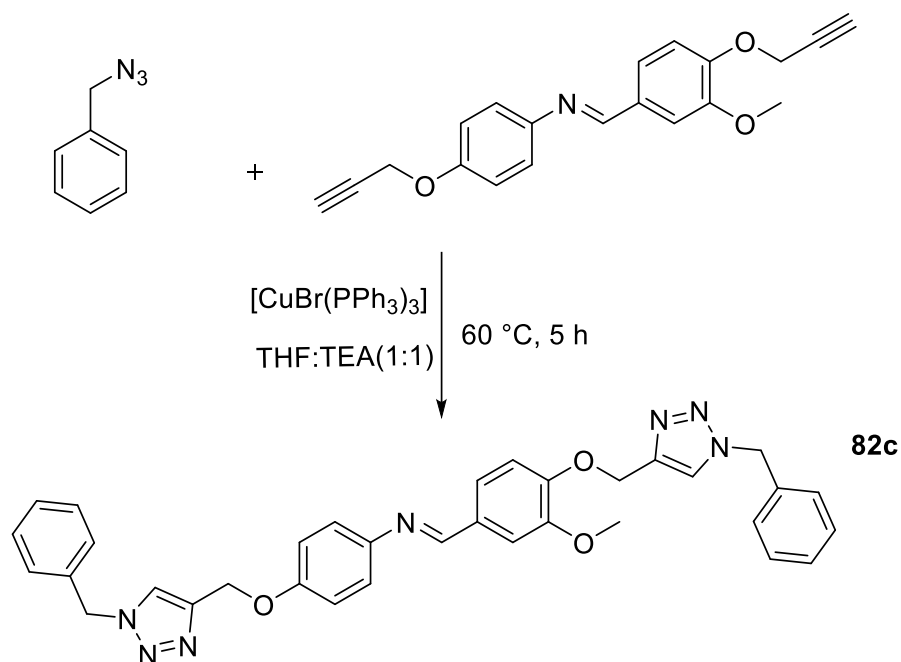


Figure 55. Schematic illustration for *(E)*-1-(4-((1-benzyl-1H-1,2,3-triazol-4-yl)methoxy)-3-methoxyphenyl)-N-(4-((1-benzyl-1H-1,2,3-triazol-4-yl)methoxy)phenyl) methanimine

Yield: 99%

Color: beige

Texture: fine powder

M.pt. 174–176 °C

Empirical formula: C₃₄H₃₁N₇O₃

Elem. anal. Calculated (%): C = 69.73, H = 5.34, N = 16.74

Found (%): C = 69.60, H = 5.38, N = 16.78

FTIR (neat, cm⁻¹): 3094, 2961, 1623, 1599, 1510, 1459, 1264, 1223, 1010, 804

¹H NMR (500 MHz, CDCl₃) δ (ppm) = 8.34 (s, 1H), 7.58 (d, J = 6.5 Hz, 2H), 7.54 (s, 1H), 7.36 (t, J = 6.1 Hz, 5H), 7.28 – 7.22 (m, 6H), 7.18 (d, J = 8.8 Hz, 2H), 7.11 (d, J = 8.3 Hz, 1H), 6.99 (d, J = 8.8 Hz, 2H), 5.53 (d, J = 10.3 Hz, 4H), 5.31 (s, 2H), 5.19 (s, 2H), 3.92 (s, 3H)

¹³C NMR (126 MHz, CDCl₃) δ (ppm) = 158.2, 156.6, 150.3, 149.9, 145.6, 134.5, 134.4, 130.4, 129.1, 128.8, 128.2, 128.1, 124.0, 123.0, 122.6, 122.1, 115.4, 113.1, 109.2, 63.1, 62.4, 56.0, 54.2

GCMS-MS: m/z (actual) = 585.25; m/z (reported) = 585.20

3.5 Synthesis of Schiff base 83a, Schiff base terminal alkyne 83b and 1,2,3-triazole derivative 83c

3.5.1 Synthesis and characterization of (*E*)-2-methoxy-4-((naphthalen-1-ylimino)methyl)phenol 83a

In a 50 ml round bottom flask, 1-naphthylamine (0.50 g, 3.0 mmol) was dissolved in absolute methanol (10 ml) and mixed with an methanolic solution of vanillin (0.50 g, 3.0 mmol) and the reaction mixture was refluxed for 3h. The reaction was monitored via TLC with 10% (ethyl acetate:hexane::1:4) as solvent medium. The resultant mixture was quenched in ice-cold water for 15 min. with constant shaking. The ppt was then filtered off from the mixture and dried for 8 h to afford beige precipitate of the Schiff base. (**Figure 56**)

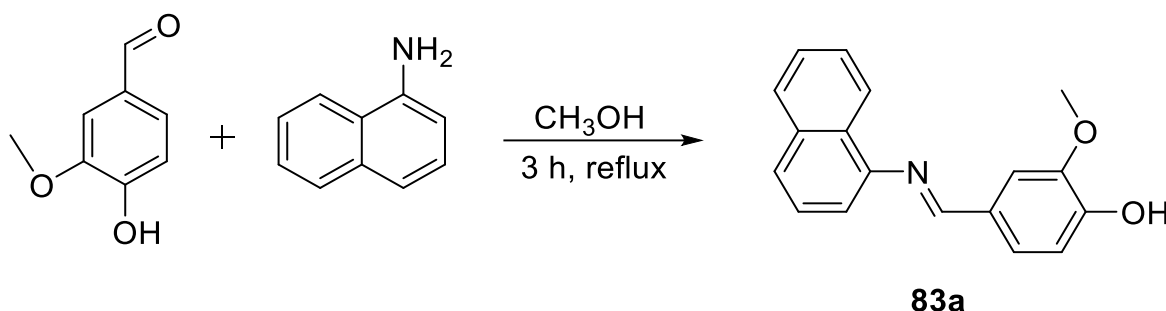


Figure 56. Synthetic procedure for (*E*)-2-methoxy-4-((naphthalen-1-ylimino)methyl)phenol 83a

Yield: 81%

Color: beige

Texture: solid powder

M.pt: 77–79 °C

Empirical formula: C₁₈H₁₅NO₂

Elem. anal. Calculated (%): C = 77.96, H = 5.45, N = 5.05

Found (%): C = 77.92, H = 5.42, N = 5.02

FTIR (neat, cm⁻¹): 3050, 2929, 1620, 1587, 1512, 1424, 1281, 1188, 1024, 772

¹H NMR (500 MHz, CDCl₃) δ (ppm) = 9.86 (s, 1H), 8.53 (s, 1H), 8.35 (s, 1H), 7.91 (s, 1H), 7.75 (d, *J* = 10.3 Hz, 2H), 7.54 – 7.47 (m, 4H), 7.15 (d, *J* = 7.2 Hz, 1H), 7.02 (d, *J* = 8.1 Hz, 1H), 3.91 (s, 3H)

¹³C NMR (126 MHz, CDCl₃) δ (ppm) = 160.3, 150.4, 148.8, 148.0, 133.4, 128.4, 128.1, 127.5, 126.2 (2C), 125.5, 124.9, 124.2, 123.5, 115.5, 112.6, 110.7, 55.5

3.5.2 Synthesis and characterization of *(E)*-*N*-(3-methoxy-4-(prop-2-yn-1-yloxy)benzylidene)naphthalen-1-amine **83b**

A total of (0.50 g, 1.8 mmol) of compound **83a** was dissolved in (11 ml) DMF, then (1.2 g, 8.9 mmol) of dried potassium carbonate was added as base, proceeded by consecutive addition of propargyl bromide (0.21 ml, 2.3 mmol) via 1 ml glass syringe in the reaction mixture while continuously stirring at ambient conditions for 18 h on a magnetic stirrer. The reaction was monitored via TLC taken in (ethyl acetate:hexane::1:4) as the developing mixture verifying the complete conversion of starting material into the product. To extract the synthesized material, the reaction mixture was decanted into a 250 ml beaker containing crushed ice, stirred for 15 minutes, until solid precipitation appeared, filtered, and then dried overnight in a silica gel desiccator to produce yellowish sand fine powder as the desired product **83b**. (Figure 57)

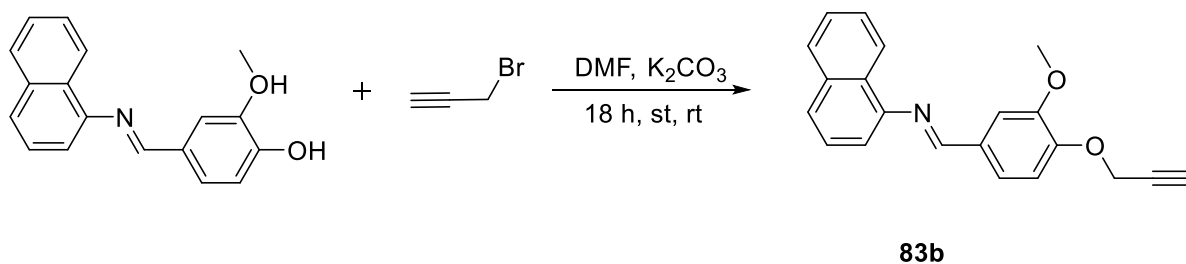


Figure 57. Synthetic scheme for the synthesis of *(E)*-*N*-(3-methoxy-4-(prop-2-yn-1-yloxy)benzylidene)naphthalen-1-amine **83b**

Yield: 86%

Color: yellowish powder

Texture: solid precipitate

M.pt: 60–62 °C

Empirical formula: C₂₁H₁₇NO₂

Elem. anal. Calculated (%): C = 79.98, H = 5.43, N = 4.44

Found (%): C = 79.92, H = 5.41, N = 4.40

FTIR (neat, cm⁻¹): 3190, 2995, 2928, 2105, 1623, 1583, 1508, 1418, 1261, 1130, 1014, 756

¹H NMR (500 MHz, CDCl₃) δ (ppm) = 8.39 (s, 1H), 8.34 – 8.32 (m, 1H), 7.73 (s, 1H), 7.73 (d, *J* = 1.5 Hz, 1H), 7.68 (d, *J* = 8.2 Hz, 1H), 7.49 – 7.48 (m, 2H), 7.41 (t, *J* = 7.7 Hz, 1H), 7.34 (dd, *J* = 8.2, 1.6 Hz, 1H), 7.06 (d, *J* = 8.2 Hz, 1H), 6.98 (d, *J* = 7.1 Hz, 1H), 4.79 (d, *J* = 2.3 Hz, 2H), 3.96 (s, 3H), 2.54 (t, *J* = 2.2 Hz, 1H)

¹³C NMR (126 MHz, CDCl₃) δ (ppm) = 159.8, 150.1, 149.8, 149.4, 134.0, 130.8, 128.8, 127.7, 126.4, 126.1, 125.7, 125.6, 124.0(2C), 113.2, 112.9, 109.8, 78.1, 76.4, 56.6, 56.1

3.5.3 Synthesis and characterization of (*E*)-*N*-(4-((1-benzyl-1*H*-1,2,3-triazol-4-yl)methoxy)-3-methoxybenzylidene)naphthalen-1-amine **83c**

Compound **83b** (0.70 g, 2.2 mmol) was solubilize in 10 ml of a (THF:TEA::1:1) solution in a 100 ml round bottom flask. After the alkyne **83b** was completely dissolved, benzyl azide (0.28 g, 0.28 ml, 2.1 mmol) was injected, followed by [CuBr(PPh₃)₃] catalyst loading (0.04 mmol), and the reaction mixture was refluxed at 60 °C for 18 h. TLC was employed (ethyl acetate:Hexane::1:4) to confirm the complete conversion of the reacting materials into the desired product. After the reaction was completed, the assembly was allowed to cool at room temperature, the mixture was poured on crushed ice, stirred for 15 minutes, and left undisturbed till the precipitate settled down, the undesired liquid portion was decanted off and the remaining mixture was filtered, dried to yield the solid off-white compound **83c**. (**Figure 58**)

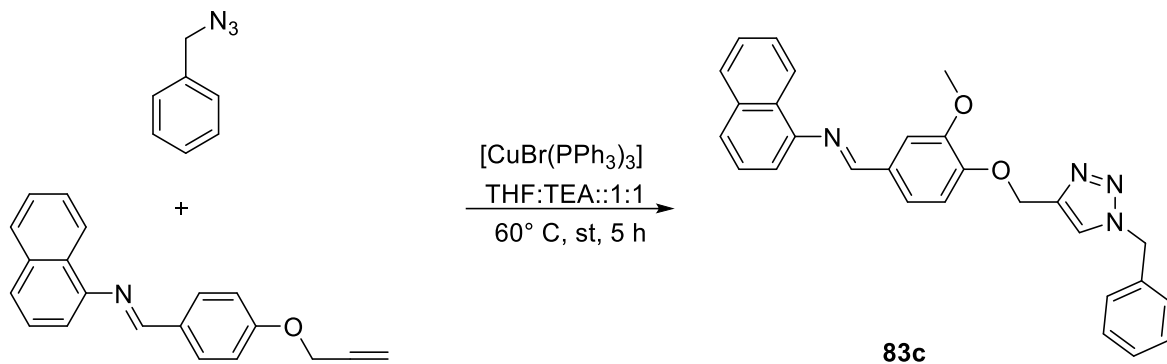


Figure 58. Systematic route for the synthesis of *(E)-N-(4-((1-benzyl-1H-1,2,3-triazol-4-yl)methoxy)-3-methoxybenzylidene)naphthalen-1-amine*

Yield: 82%

Color: off white

Texture: fine solid

M.pt: 112-114 °C

Empirical formula: C₂₈H₂₄N₄O₂

Elem. anal. calculated (%): C = 74.98, H = 5.39, N = 12.49

Found (%): C = 74.90, H = 5.32, N = 12.43

FTIR (neat, cm⁻¹): 3010, 2962, 1623, 1580, 1503, 1411, 1258, 1140, 1002, 790, 729

¹H NMR (500 MHz, CDCl₃) δ (ppm) = 8.38 (s, 1H), 8.31 (d, *J* = 8.5 Hz, 1H), 7.79 (d, *J* = 8.4 Hz, 1H), 7.70 (s, 1H), 7.65 (d, *J* = 8.2 Hz, 1H), 7.53 (s, 1H), 7.47 – 7.45 (m, 2H), 7.40 (t, *J* = 7.7 Hz, 1H), 7.31 (t, *J* = 8.2 Hz, 4H), 7.21 (d, *J* = 6.3 Hz, 2H), 7.10 (d, *J* = 8.2 Hz, 1H), 6.98 (d, *J* = 7.2 Hz, 1H), 5.45 (s, 2H), 5.29 (s, 2H), 3.91 (s, 3H)

¹³C NMR (126 MHz, CDCl₃) δ (ppm) = 159.7, 150.6, 149.9, 149.4, 144.0, 134.3, 133.9, 130.4, 129.1(2C), 128.8, 128.7, 128.1(2C), 127.6, 126.3, 126.1, 125.6, 125.5, 124.3, 123.9, 123.0, 113.1, 112.8, 109.5, 63.0, 56.0, 54.2
GCMS-MS: m/z (calcd.) = 448.19; m/z (found) = 448.10.

3.6 Synthesis of Schiff base 84a, Schiff base terminal alkyne 84b and 1,2,3-triazole derivative 84c

3.6.1 Synthesis and characterization of (*E*)-2-methoxy-4-((phenethylimino)methyl)phenol 84a

A mixture of 2-phenylethylamine (1.03 ml, 1.0 mmol) and 4-Hydroxy-3-methoxy benzaldehyde (1.25 g, 1.0 mmol) was dissolved in dry methanol (MeOH) with a volume of 10 mL and subjected to reflux for a duration of 4 h. The progress of the reaction was monitored by using thin-layer chromatography (TLC) composed of (ethylacetate:Hexane::1:4) as developing solvent. The reaction mixture was carefully transferred into a beaker filled with crushed ice and was then vigorously stirred for 10 to 15 min. Afterward, the mixture was subjected to filtration in order to isolate precipitates of light orange hue. (**Figure 59**)

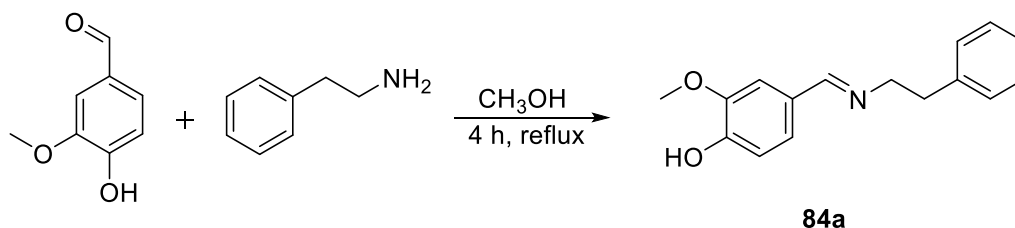


Figure 59. Synthetic route for the synthesis of (*E*)-2-methoxy-4-((phenethylimino)methyl)phenol

Yield: 88%

Color: coffee cream

Texture: dry powder

M.pt: 72–74 °C

Empirical formula: C₁₆H₁₇NO₂

Elem. anal. calculated (%): C = 75.27, H = 6.71, N = 5.49

Found (%): C = 75.32, H = 6.02, N = 5.32

FTIR (neat, cm⁻¹): 3017, 1640, 1593, 1513, 1433, 1278, 1154, 1023

¹H NMR (500 MHz, DMSO) δ (ppm) = 8.12 (s, 1H), 7.32 (s, 1H), 7.29 – 7.24 (m, 4H), 7.18 (t, *J* = 6.8 Hz, 1H), 7.07 (d, *J* = 9.9 Hz, 1H), 6.82 (d, *J* = 8.0 Hz, 1H), 3.79 (s, 3H), 3.74 (t, *J* = 7.1 Hz, 2H), 2.91 (d, *J* = 7.5 Hz, 2H)

¹³C NMR (126 MHz, DMSO) δ (ppm) = 160.4, 149.1, 147.7, 139.9, 128.7 (2C), 128.0(2C), 127.7, 125.8, 122.4, 115.0, 109.7, 61.7, 55.5, 37.0.

3.6.2 Synthesis and characterization of (*E*)-1-(3-methoxy-4-(prop-2-yn-1-yloxy)phenyl)-*N*-phenethylmethanimine **84b**

A solution containing 1.0 g (1.9 mmol) of compound **84a**, 2.7 g (1.9 mmol) of dried potassium carbonate, and 0.53 ml (19.5 mmol) of propargyl bromide was injected via 1 ml glass syringe in 10 mL of N,N-dimethylformamide (DMF). The reaction underwent stirring at ambient temperature for a duration of 43 h, until the starting substrates were fully consumed, as determined by TLC analysis (ethylacetate:Hexane::1:4). Subsequently, the reaction mixture was carefully transferred onto a bed of crushed ice, resulting in the formation of solid precipitates which was then subjected to filtration and then thoroughly washed with distilled water, ensuing in the acquisition of light peach colored product **84b**. (**Figure 60**)

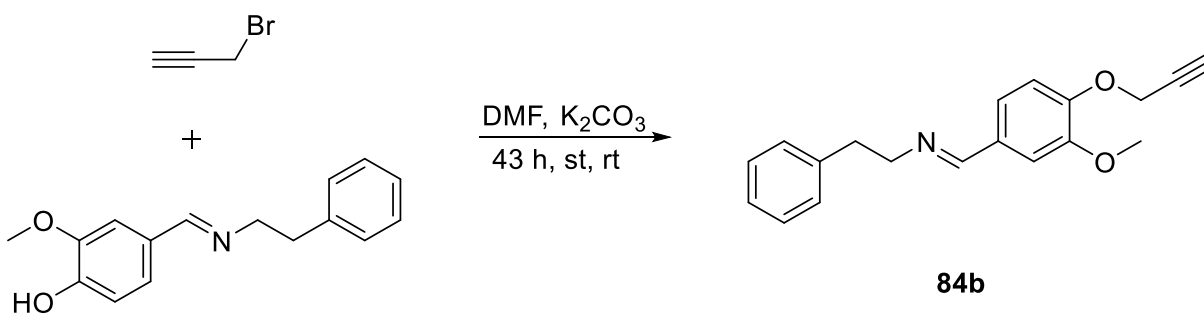


Figure 60. Synthesis procedure for (*E*)-1-(3-methoxy-4-(prop-2-yn-1-yloxy)phenyl)-*N*-phenethylmethanimine

Yield: 92%

Color: light peach

Texture: fine particles

M.pt: 60–62 °C

Empirical formula: C₁₉H₁₉NO₂

Elem. anal. calculated (%): C = 77.79, H = 6.53, N = 4.77

Found (%): C = 77.82, H = 6.51, N = 4.69

FTIR (neat, cm⁻¹): 3182, 3024, 2837, 2101, 1634, 1586, 1504, 1418, 1259, 1014

¹H NMR (500 MHz, CDCl₃) δ (ppm) = 7.99 (s, 1H), 7.34 (s, 1H), 7.18 (d, *J* = 7.4 Hz, 2H), 7.15 (d, *J* = 6.5 Hz, 2H), 7.10 (d, *J* = 7.2 Hz, 1H), 7.02 (d, *J* = 8.3 Hz, 1H), 6.94 (d, *J* = 8.3 Hz, 1H), 4.69 (s, 2H), 3.84 (s, 3H), 3.76 – 3.73 (m, 2H), 2.91 (t, *J* = 7.6 Hz, 2H), 2.44 (t, *J* = 2.4 Hz, 1H)

¹³C NMR (126 MHz, CDCl₃) δ (ppm) = 160.8, 149.9, 149.0, 139.9, 130.6, 129.0(2C), 128.3(2C), 126.1, 122.5, 113.1, 109.2, 78.1, 76.1, 63.0, 56.6, 55.9, 37.6.

3.6.3 Synthesis and characterization of *(E)*-1-(4-((1-benzyl-1*H*-1,2,3-triazol-4-yl)methoxy)-3-methoxyphenyl)-*N* phenethylmethanimine **84c**

A solution containing compound **84 b** (0.80 g, 2.72 mmol), azide **39** (0.34 ml, 2.72 mmol), [CuBr(PPh₃)₃] (0.001 mmol) as catalyst, in a mixture of (THF:TEA::1:1) was subjected to reflux at 55-60 °C for 5 h. The progression of the reaction was monitored by TLC (ethylacetate:Hexane::1:4). After completion of the reaction, the liquid mixture was rapidly quenched on ice-cold water and stirred for 15 minutes to obtain off-white solid precipitates. Subsequently, the solution was filtered, followed by washing with hexane, air-dried, resulting in the acquisition of the desired solid compound **84c**. (Figure 61)

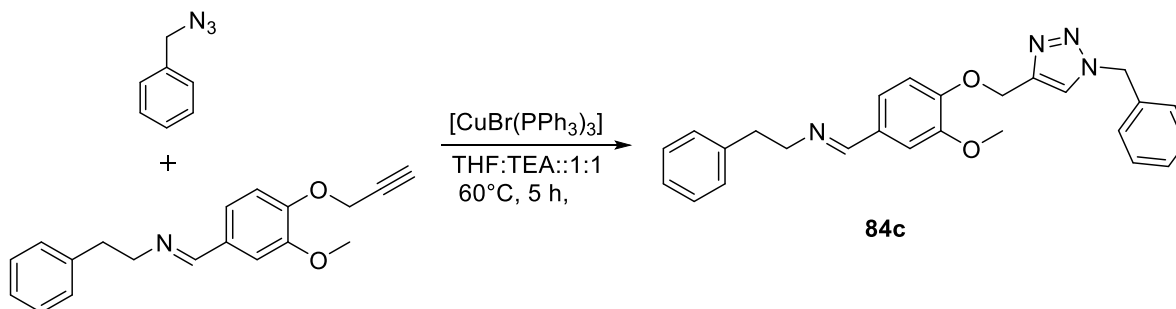


Figure 61. Synthetic route for the synthesis of *(E)*-1-(4-((1-benzyl-1*H*-1,2,3-triazol-4-yl)methoxy)-3-methoxyphenyl)-*N* phenethylmethanimine

Yield: 95%

Color: off-white

Texture: dry bulk powder

M.pt: 92–94 °C

Empirical formula: C₂₆H₂₆N₄O₂

Elem. anal. calculated (%): C = 73.22, H = 6.14, N = 13.14

Found (%): C = 73.30, H = 6.12, N = 13.20

FTIR (neat, cm⁻¹): 3074, 2948, 2838, 1645, 1585, 1510, 1459, 1263, 1140, 1026

¹H NMR (500 MHz, CDCl₃) δ (ppm) = 7.98 (s, 1H), 7.46 (s, 1H), 7.31 (s, 1H), 7.25 (s, 3H), 7.18 – 7.14 (m, 7H), 6.96 (s, 2H), 5.39 (s, 2H), 5.19 (s, 2H), 3.78 (s, 3H), 3.73 (t, *J* = 7.6 Hz, 2H), 2.90 (t, *J* = 7.6 Hz, 2H)

¹³C NMR (126 MHz, CDCl₃) δ (ppm) = 160.9, 149.8, 144.2, 139.9, 134.4, 130.2, 129.1, 129.0, 128.8, 128.3, 128.1, 126.1, 123.0, 122.9, 113.1, 109.0, 63.0, 63.0, 55.9, 54.2, 37.6

LCMS-MS: *m/z* (actual) = 426.20; *m/z* (reported) = 427.21

3.7 Synthesis of Schiff base 85a, Schiff base terminal alkyne 85b and 1,2,3-triazole derivative 85c

3.7.1 Synthesis and characterization of (*E*)-2-methoxy-4-((*p*-tolylimino)methyl)phenol 85a

A solution of *p*-toluidine (0.996 ml, 2 mmol) was prepared by dissolving it in 10 mL of anhydrous methanol. To this solution, 4-Hydroxy-3-methoxy benzaldehyde (1.41 g, 2 mmol) in methanol (10 mL) was added slowly with continuous stirring. The reaction mixture was subjected to reflux for a duration of 4 h at 65 °C, while ensuring that the conditions remained dry, in presence of catalytic quantity of dichloromethane. The progress of the reaction was monitored using TLC using a solvent mixture of (ethyl acetate:hexane::1:4). The reaction mixture was quenched using crushed ice, chalk white-colored precipitate was formed, which was then filtered, washed many

times with water, and then air dried to obtain the desired product **85a**. The synthesis technique of compound **85a** has been shown in **Figure 62**.

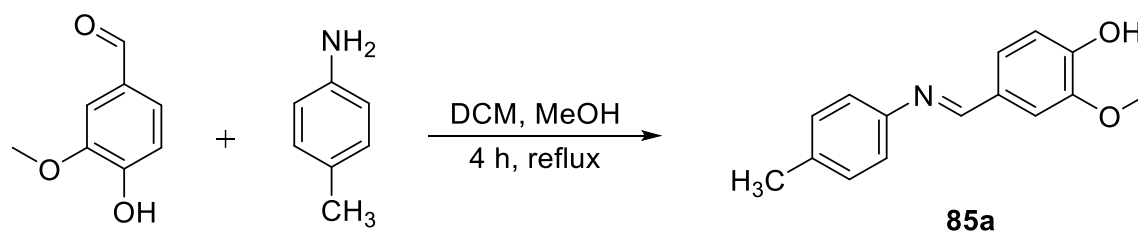


Figure 62. Synthesis scheme for *(E)*-2-methoxy-4-((*p*-tolylimino)methyl)phenol

Yield: 91%

Color: chalk white

Texture: solid powder

M.pt: 90–92 °C

Empirical formula: C₁₅H₁₅NO₂

Elem. anal. calculated (%): C = 74.98, H = 5.87, N = 5.83

Found (%): C = 74.36, H = 5.22, N = 5.65

FTIR (neat, cm⁻¹): 3015, 2933, 1623, 1582, 1507, 1427, 1269, 1147, 1030

¹H NMR (500 MHz, CDCl₃) δ (ppm) = 9.80 (s, 1H), 8.34 (s, 1H), 7.62 (s, 1H), 7.22 (d, *J* = 9.9 Hz, 1H), 7.17 (d, *J* = 8.1 Hz, 2H), 7.12 (d, *J* = 8.3 Hz, 2H), 6.96 (d, *J* = 8.1 Hz, 1H), 3.90 (s, 3H), 2.35 (s, 3H).

¹³C NMR (126 MHz, CDCl₃) δ (ppm) = 159.5, 149.1, 147.3, 135.5, 129.8(2C), 129.0, 125.2, 120.8 (2C), 115.3, 114.3, 108.6, 56.0, 21.0

3.7.2 Synthesis and characterization of *(E)*-1-(3-methoxy-4-(prop-2-yn-1-yloxy)phenyl)-*N*-(*p*-tolyl)methanimine **85b**

In a 50 ml round bottom flask, compound **85a** (0.85 g, 3.0 mmol) was dissolved in DMF with the addition of a strong base, such as K₂CO₃ (2.43 g, 17.5 mmol). The solution was swirled for 15 minutes. After adding propargyl bromide (0.50 mL, 4.2 mmol), the mixture was agitated for

48 h at room temperature. The progress of the reaction was observed developing TLC using (ethyl acetate:hexane::1:4) as solvent mixture. After the reaction completion, the product was extracted using crushed ice, filtered, and then evaporated under vacuum until it was completely dry to obtain the solid product **85b**. (**Figure 63**)

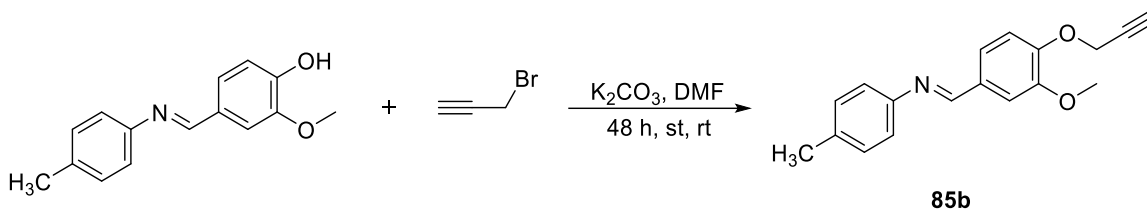


Figure 63. Synthetic procedure for *(E)*-1-(3-methoxy-4-(prop-2-yn-1-yloxy)phenyl)-*N*-(*p*-tolyl)methanimine

Yield: 94%

Color: orange peach

Texture: solid powder

M.pt: 83-85 °C

Empirical formula: C₁₈H₁₇NO₂

Elem. anal. calculated (%): C = 77.40, H = 6.13, N = 5.01

Found (%): C = 77.22, H = 6.10, N = 5.09

FTIR (neat, cm⁻¹): 3254, 3006, 2924, 2127, 1623, 1580, 1505, 1453, 1266, 1138, 1002

¹H NMR (500 MHz, CDCl₃) δ (ppm) = 8.35 (s, 1H), 7.41 (s, 1H), 7.29 (d, *J* = 9.5 Hz, 1H), 7.17 (d, *J* = 8.0 Hz, 2H), 7.10 (d, *J* = 8.2 Hz, 2H), 7.05 (d, *J* = 8.3 Hz, 1H), 4.80 (s, 2H), 3.95 (s, 3H), 2.55 (s, 1H), 2.35 (s, 3H)

¹³C NMR (126 MHz, CDCl₃) δ (ppm) = 158.9, 152.1, 149.9, 149.5, 135.5, 130.9, 130.7, 129.7, 126.2, 123.7, 120.8, 113.1, 109.4, 78.0, 76.3, 56.6, 56.0, 20.9

3.7.3 Synthesis and characterization of *(E)*-1-(4-((1-benzyl-1*H*-1,2,3-triazol-4-yl)methoxy)-3-methoxyphenyl)-*N*-(*p*-tolyl)methanimine **85c**

A clear solution of Compound **85b** (0.50 g, 1.8 mmol) and benzyl azide (0.22 mL, 1.8 mmol) was prepared in dried THF (3 mL). Subsequently, a base such as Et₃N (3 mL) was added to the mixture, which was then stirred for 10 minutes. A catalytic amount of [CuBr(PPh₃)₃] (0.04 mmol) was introduced to the mixture after 15 minutes; agitation persisted for an additional 5 h at 55-60 °C. The progress of the reaction was observed using TLC till the reaction was completed. The reaction mixture was quenched with crushed ice, filtered and dried under vacuum to attain solid product **85c**. (Figure 64)

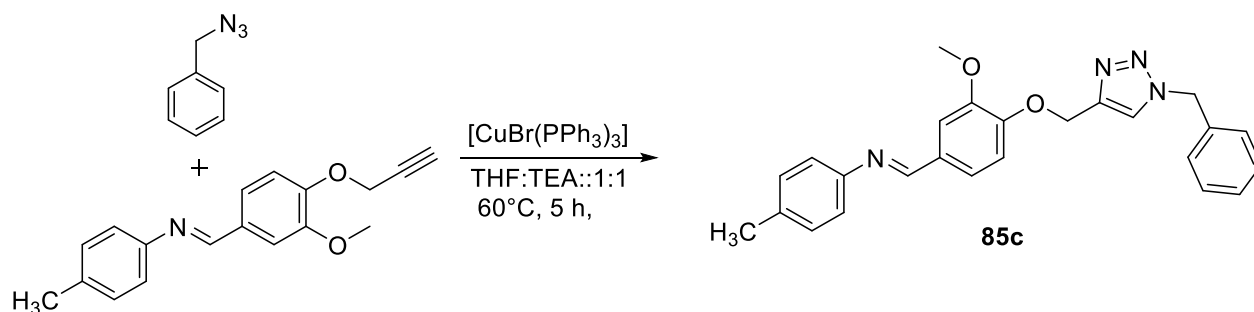


Figure 64. Synthetic route for the *(E)*-1-(4-((1-benzyl-1H-1,2,3-triazol-4-yl)methoxy)-3-methoxyphenyl)-N-(p-tolyl)methanimine

Yield: 97%

Color: ivory

Texture: solid powder

M.pt: 110–112 °C

Empirical formula: C₂₅H₂₄N₄O₂

Elem. anal. calculated (%): C = 72.80, H = 5.86, N = 13.58

Found (%): C = 72.91, H = 5.95, N = 13.22

FTIR (neat, cm⁻¹): 3085, 2950, 1626, 1580, 1508, 1460, 1266, 1138, 1020

¹H NMR (500 MHz, CDCl₃) δ (ppm) = 8.34 (s, 1H), 7.58 (s, 1H), 7.34 (s, 4H), 7.24 (s, 4H), 7.16 (d, *J* = 7.9 Hz, 2H), 7.10 (d, *J* = 8.6 Hz, 2H), 5.48 (s, 2H), 5.30 (s, 2H), 3.90 (s, 3H), 2.35 (s, 3H)

^{13}C NMR (126 MHz, CDCl_3) δ (ppm) = 158.9, 152.9, 150.4, 149.8, 135.5, 134.3, 134.2, 130.5, 129.7, 129.0, 128.8, 128.7, 128.1, 126.6, 124.2, 123.0, 120.7, 113.0, 112.6, 109.2, 109.2, 62.9, 55.9, 54.1, 20.9

GCMS-MS: m/z (actual) = 412.18; m/z (reported) = 412.20

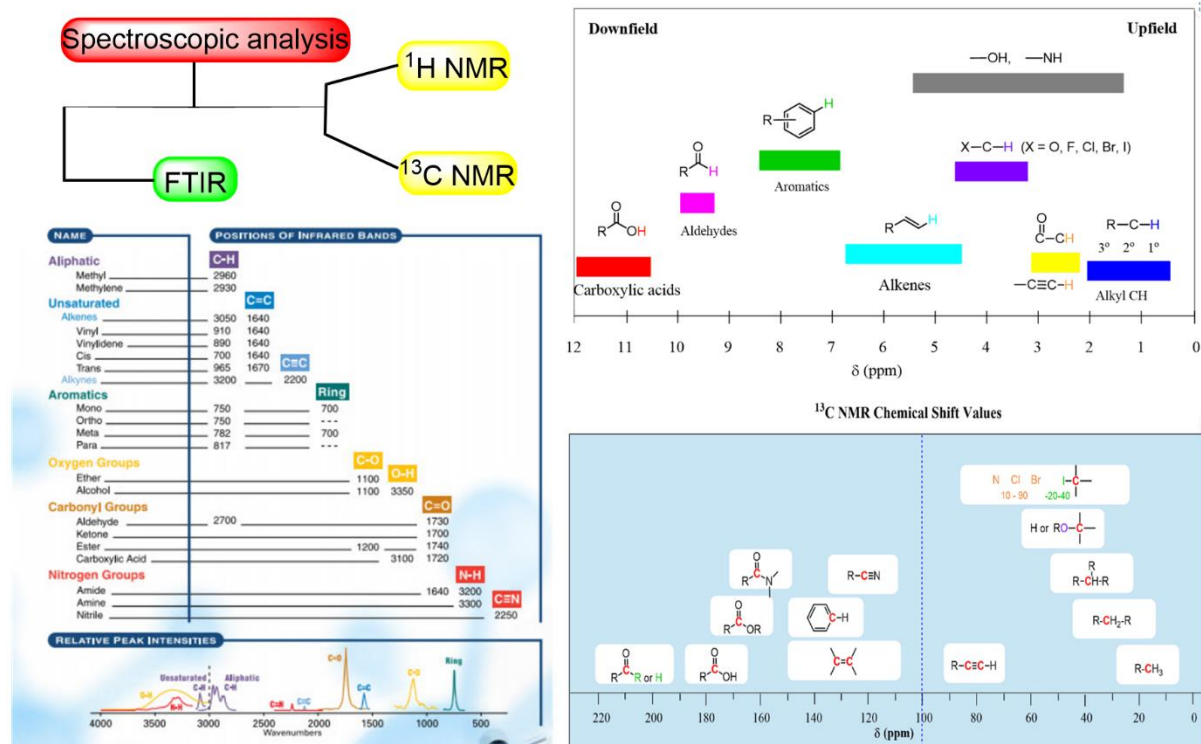
3.8 Depiction of molecules:

The spectroscopic tools like IR, NMR and Mass spectrometric studies will be used for the exact characterisation of the synthesized molecules.

3.9 Metal-ions recognition:

The synthesised 1,2,3-triazole hybrid moiety will be analysed for its chemo-sensing properties using UV-Visible and Fluorescence spectroscopy.

Chapter 4



Result and discussion of spectroscopic data

The results and discussion section offers a thorough and comprehensive explanation of the spectroscopic data such as IR, NMR (^1H , ^{13}C), and MS acquired from the synthesised Schiff bases, Schiff base terminal alkynes and Schiff base tethered 1,4-disubstituted 1,2,3-triazole. This chapter provides an exposition of the findings and outcomes of the current research contribution, together with an explanation for the specific results, presented in the form of textual descriptions

1. Synthesis and spectral analysis of Azidomethylbenzene

1.1 Synthesis

Caution! Azide compounds may be explosive when exposed to heat, pressure, and/or shock, thus handle them with utmost care.

Benzyl chloride was nucleophilic substituted with dried sodium azide in DMF as solvent medium and the reaction mixture was refluxed for 5 h at 90 °C for the synthesis of benzyl azide **39**. Since the azides can be very reactive and explosive at high temperatures, the reaction conditions were carefully maintained to prevent any accidents. After the reaction was completed, the product was extracted using ethyl acetate, the organic layer was dried, and the organic solvent was eliminated to obtain pale yellow oil as product **39**. (**Figure 65**) The sample was characterized via FTIR, NMR (^1H and ^{13}C) and CHN analysis.

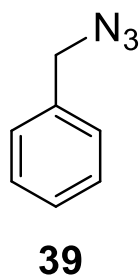


Figure 65. Structure of Azidomethylbenzene 39

1.2 ATR-FTIR spectroscopic analysis

FTIR spectroscopy was employed for the characterization of the benzyl azide in the range 4000-500 cm^{-1} and the results correspond with the expected values. A sharp peak at 2089 cm^{-1} attributed to the ($-\text{N}_3$) group of the azide, the peak at 3032 cm^{-1} represents the vibration mode of the aromatic ($\text{C}-\text{H}$) bond, whereas the peak at 2929 cm^{-1} correspond to the aliphatic stretch of the ($\text{C}-\text{H}$) bond at the benzylic carbon. The typical ($-\text{CH}_2$) bending appears at 1452 cm^{-1} in the IR spectrum. All these values are in accordance with the spectrum of benzyl azide and confirms the substitution of benzyl chloride with benzyl azide.

1.3 NMR (^1H and ^{13}C) spectroscopic analysis

The ^1H NMR spectra of compound **39** exhibit singlet at $\delta = 4.22$ ppm due to methylene ($-\text{CH}_2$) group and the aromatic ring protons in the domain $\delta = 7.33$ - 7.24 ppm supports the synthesis of benzyl azide. The ^{13}C NMR spectra of compound **39** shows singlet at $\delta = 54.8$ ppm due to the methylene ($-\text{CH}_2$) group and the carbon atoms of the aromatic ring in the range $\delta = 128.3, 128.4, 128.9, 135.5$ ppm corresponds to benzyl azide.

1.4 Elemental analysis

CHN analytical study was performed on compound **39**. Empirical formula: $\text{C}_7\text{H}_7\text{N}_3$ elem. anal. calculated (%): C = 63.14, H = 5.30, N = 31.56, found (%): C = 63.12, H = 5.31, N = 31.57. The elemental analysis conducted on compound **39** validated the synthesis of benzyl azide with high purity.

2. Synthesis and spectral analysis of (*E*)-4-((benzylimino)methyl)-2-methoxyphenol

2.1 Synthesis

A solution of substituted primary amine in ethanol, was treated sequentially with substituted benzaldehyde and the resulting mixture was refluxed at 75°C for 4 h. The acquired solution was quenched in ice cold water with constant stirring of 15-20 min. The precipitate formed was filtered, washed with distilled water, and air dried to afford solid peach dust powder. (**Figure 66**)

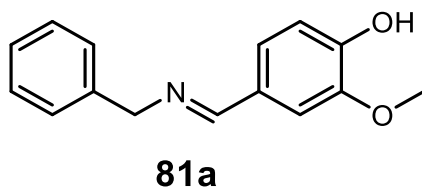


Figure 66. Structure of (*E*)-4-((benzylimino)methyl)-2-methoxyphenol **81a**

2.2 ATR-FTIR spectroscopic analysis

FTIR spectroscopy was employed for the characterization of the compound **81a** in the range 4000 - 500 cm^{-1} and the results laid down the strong foundation with the expected values. The molecule displays strong absorption peak at 1620 cm^{-1} designated to ($-\text{C}=\text{N}$) of the imine group with the disappearance of singlet peak at 1660 cm^{-1} ($-\text{C}=\text{O}$) of aldehyde group, also disappearance

of the doublet peak of (-NH) stretching at 3371 cm^{-1} and 3292 cm^{-1} confirm the modification into imine group. The stretching vibration of aromatic (-C=C) group occurs at 1580 cm^{-1} and 1502 cm^{-1} , whereas the (-CH_2) and (-CH_3) bending vibrations were observed at 1462 and 1380 cm^{-1} in the spectrum.

2.3 NMR (^1H and ^{13}C) spectroscopic analysis

Data interpretation of NMR clearly indicates the formation of acetylenic alkyne. In ^1H -NMR spectrum of compound **81a**, the singlet peak at $\delta = 8.27\text{ ppm}$ is due to the (-N=CH) imine proton, and the aromatic ring protons in the range $\delta = 7.48\text{-}6.91\text{ ppm}$ affirms the synthesis of Schiff base moiety. The methoxy protons (-OCH_3) linked to aromatic ring appeared as singlet at high upfield value of $\delta = 3.90\text{ ppm}$, a singlet due to methylene protons (-CH_2) was observed at $\delta = 4.79\text{ ppm}$ and the secondary group (-OH) was found in the high downfield region at $\delta = 9.82\text{ ppm}$. In the ^{13}C -NMR of compound **81a**, the carbon of Schiff base (-C=N) found in the region at $\delta = 161.8\text{ ppm}$ and the ring protons appears around at $\delta = 148.5\text{-}108.3\text{ ppm}$ confirming synthesis of compound **81a**. The carbon peak of (-OCH_3) methoxy group and methylene (-CH_2) was found at $\delta = 56.0$ and $\delta = 64.8\text{ ppm}$ respectively.

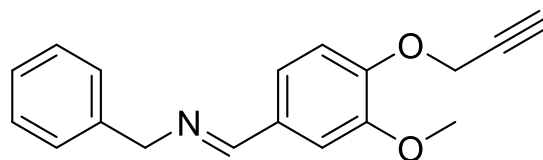
2.4 Elemental analysis

The CHN analytical study was conducted on compound **81a**. Empirical formula: $\text{C}_{15}\text{H}_{15}\text{NO}_2$, elem. anal. calculated (%): C = 74.67, H = 6.27, N = 5.81, found (%): C = 74.70, H = 6.25, N = 5.83. Compound **81a** was analysed by elemental analysis, confirming the purity of the synthesized product.

3. Synthesis and spectral analysis of (*E*)-*N*-benzyl-1-(3-methoxy-4-(prop-2-yn-1-yloxy)phenyl)methanimine

3.1 Synthesis

Schiff base **81a** was further exposed to react with propargyl bromide, the reaction was facilitated with moderate base such as K_2CO_3 for facile proton extraction in DMF solvent media for 18 h at room temperature to obtain Schiff base alkyne **81b**. The synthesized material was extracted by pouring the reaction content in the 250 ml beaker containing crushed ice, stirred for 15-20 min till the solid ppt appears at the bottom of the beaker, filtered and dried overnight to gain ivory dust solid powder as the product **81b**. (Figure 67)



81b

Figure 67. Structure of (*E*)-*N*-benzyl-1-(3-methoxy-4-(prop-2-yn-1-yloxy)phenyl)methanimine **81b**

3.2 ATR-FTIR spectroscopic analysis

A sharp peak at 3190 cm^{-1} in the FTIR spectrum of compound **81b** ascertain the acetylenic proton ($\equiv\text{C-H}$) stretching mode and the stretching frequency of ($-\text{C}\equiv\text{C}$) appears in the domain 2120 cm^{-1} confirms the formation of Schiff base alkyne **81b**. The molecule has a prominent absorption peak at 1636 cm^{-1} attributed to the ($-\text{C}=\text{N}$) bond of the imine group. The aromatic ($-\text{C}=\text{C}$) group exhibits stretching vibrations at 1588 cm^{-1} and 1505 cm^{-1} , whereas the bending vibrations of ($-\text{CH}_2$) and ($-\text{CH}_3$) were detected at 1453 cm^{-1} and 1381 cm^{-1} in the spectrum.

3.3 NMR (^1H and ^{13}C) spectroscopic analysis

In the ^1H -NMR spectrum, a triplet in the highly upfield region at $\delta = 2.51\text{ ppm}$ is due to the ($\equiv\text{C-H}$) proton of the alkynyl group, the signal at $\delta = 4.76\text{--}4.78\text{ ppm}$ is due to ($-\text{CH}_2$) methylene protons, methoxy protons ($-\text{OCH}_3$) attached to aromatic ring shows signal at $\delta = 3.89\text{ ppm}$, whereas the chemical shift from $\delta = 7.01\text{ ppm}$ to 7.49 ppm is due to aromatic protons and the singlet peak at $\delta = 8.28\text{ ppm}$ is due to the ($-\text{N}=\text{CH}$) imine proton confirming formation of the terminal alkyne **81b**. In the ^{13}C -NMR spectrum, for the alkyne moiety **81b**, the imine carbon ($-\text{N}=\text{C}$) appears in the region $\delta = 161.4\text{ ppm}$ as highly deshielded carbon and the two carbons of alkynyl group ($\text{C}\equiv\text{C}$) appears in the range of $\delta = 78.1\text{--}76.2\text{ ppm}$. The aromatic ring carbons appear in the range $\delta = 149.9\text{--}109.3\text{ ppm}$, the methoxy carbon ($-\text{OCH}_3$) was detected at $\delta = 56.0\text{ ppm}$, and the methylene carbons ($-\text{CH}_2$) was found at 56.6 ppm and 64.9 ppm .

3.4 Elemental analysis

The CHN analysis was done on compound **81b**. Empirical formula: $\text{C}_{18}\text{H}_{17}\text{NO}_2$, elem. anal. calculated (%): C = 77.40, H = 6.13, N = 5.01, found (%): C = 77.42, H = 6.15, N = 5.00. Elemental analysis of compound **81b**, validates the purity of the synthesized product.

4. Synthesis and spectral analysis of *(E)*-*N*-benzyl-1-(4-((1-benzyl-1*H*-1,2,3-triazol-4-yl)methoxy)-3-methoxyphenyl) methanimine

4.1 Synthesis

Schiff base alkyne **81b** proceeded a ‘click reaction’ with benzyl azide **39** using ‘[CuBr(PPh₃)₃]/THF-TEA’ system refluxed at 60 °C for 5 h to yield 96% of Schiff base conjugated di-substituted 1,2,3-triazole **81c**. The product was extracted by pouring the reaction mixture into crushed ice, ppt appeared which was filtered, dried in open air to attain the solid product **81c** with excellent yield. (Figure 68)

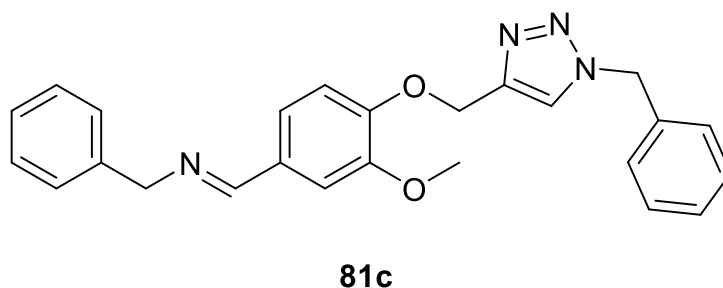


Figure 68. Structure of *(E)*-*N*-benzyl-1-(4-((1-benzyl-1*H*-1,2,3-triazol-4-yl)methoxy)-3-methoxyphenyl) methanimine **81c**

4.2 ATR-FTIR spectroscopic analysis

IR peak appeared at 1640 cm⁻¹ showing (–C=N) of the imine group with the disappearance of the peak at 2089 cm⁻¹ due to (–N=N=N) stretching vibration. Subsequently, the absence of 3190 cm⁻¹ of acetylenic proton (≡C–H) stretching band alongwith the disappearance of (–C≡C) stretching vibration at 2120 cm⁻¹ indicates the formation of 1-4 di-substituted 1,2,3-triazole **81c**.

The spectrum shows stretching vibrations of the aromatic (–C=C) group at 1585 cm⁻¹ and 1513 cm⁻¹, and bending vibrations of (–CH₂) and (–CH₃) at 1452 cm⁻¹ and 1328 cm⁻¹, respectively.

4.3 NMR (¹H and ¹³C) spectroscopic analysis

In case of Schiff base functionalized 1,2,3-triazole, disappearance of the peak at δ = 2.43 ppm representing (≡C–H) proton of the alkynyl group signifies the modification of alkyne and the appearance of the peak at 7.45 ppm of triazole proton ascertain the cyclization of alkynyl moiety

into triazole unit **81c**. The signal of methoxy protons ($-\text{OCH}_3$) was detected at $\delta = 3.75$ ppm, the 3 group of methylene protons ($-\text{CH}_2$) were found at $\delta = 4.69$ ppm, $\delta = 5.18$ ppm and $\delta = 5.37$ ppm, imine proton ($-\text{HC}=\text{N}$) is observed at $\delta = 8.18$ ppm, meanwhile the aromatic ring protons appears from $\delta = 7.37$ – 6.95 ppm.

In the ^{13}C -NMR spectrum, the appearance of 1,2,3-triazole carbon around $\delta = 122.9$ ppm and $\delta = 144.1$ ppm confirms the conversion of the alkyne to 1,2,3-triazole unit **81c**. The signal detected for methoxy carbon ($-\text{OCH}_3$) at $\delta = 54.1$ ppm, the chemical shift value for 3 group of methylene carbons appears ($-\text{CH}_2$) at $\delta = 55.8$ ppm, $\delta = 62.9$ ppm, $\delta = 64.8$ ppm, whereas the signal for the aromatic ring carbons can be seen at $\delta = 149.9$ – 109.1 ppm and the signal for imine carbon ($-\text{C}=\text{N}$) is shown in highly deshielded (downfield) at $\delta = 161.4$ ppm.

4.4 Elemental analysis and Mass spectrometry

The CHN analysis of compound **81b** was performed. Empirical formula: $\text{C}_{25}\text{H}_{24}\text{N}_4\text{O}_2$, elem. anal. calculated (%): C = 72.80, H = 5.86, N = 13.58, found (%): C = 72.79, H = 5.84, N = 13.56. GCMS-MS: m/z (actual) = 412.19; m/z (reported) = 412.15. Purity of the synthesised product is confirmed through elemental analysis. The actual m/z molecular mass of the compound is 412.19 and the reported m/z is 412.15 via GCMS-MS which strongly proves the formation of the desired compound **81c**.

5. Synthesis and spectral analysis of *(E)*-4-(((3-hydroxybenzyl)imino)methyl)-2-methoxyphenol

5.1 Synthesis

The formation of an azomethine compound involves the condensation reaction of an aromatic amine with an aldehyde derivative in presence of water as solvent, and the resulting mixture was stirred for 60 min at room temperature. The crude product obtained after filtration was washed with distilled water and air dried to gain the dry brown dust powder **82a**. (**Figure 69**)

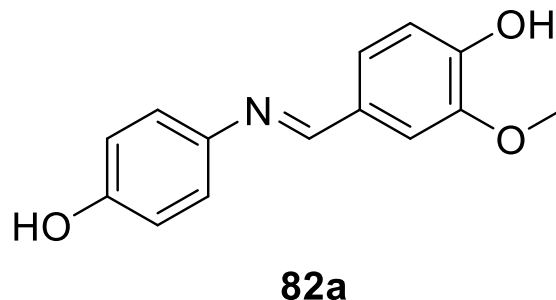


Figure 69. Structure of (*E*)-4-(((3-hydroxybenzyl)imino)methyl)-2-methoxyphenol **82a**

5.2 ATR-FTIR spectroscopic analysis

FTIR spectroscopy was used to record IR spectrum of the compound **82a** in the range 4000–500 cm^{-1} . The resulting data obtained from the FTIR spectra confirms synthesis of desired compound **82a**. The major peak at 1620 cm^{-1} corresponds to ($-\text{C}=\text{N}$) of azomethine group. The aromatic ($-\text{C}=\text{C}$) group exhibits stretching vibrations at 1587 cm^{-1} and 1508 cm^{-1} , whereas the bending vibrations of ($-\text{CH}_2$) and ($-\text{CH}_3$) were detected at 1429 cm^{-1} and 1373 cm^{-1} in the spectrum. Also, the broad peak of hydroxy group ($-\text{OH}$) can be seen at 3275 cm^{-1} in the spectrum.

5.3 NMR (^1H and ^{13}C) spectroscopic analysis

Precisely, NMR data elucidated the synthesis of azomethine group. The singlet peak at $\delta = 8.40$ ppm in the ^1H NMR spectrum of molecule **82a** is attributed to the ($-\text{N}=\text{CH}$) imine proton, the signal at $\delta = 9.43$ ppm is of the secondary ($-\text{OH}$) group, and the ring protons in the range $\delta = 7.49$ – 6.44 ppm confirm the synthesis of Schiff base moiety. The methoxy protons ($-\text{OCH}_3$) associated to the aromatic ring emerged as singlet at high upfield value of $\delta = 3.80$ ppm, and aromatic ring protons were identified at $\delta = 7.49$ – 6.44 ppm. In the ^{13}C NMR spectrum of compound **82a**, the Schiff base carbon ($-\text{C}=\text{N}$) appears around $\delta = 157.0$ ppm at the highly deshielded area, while the ring protons appear around $\delta = 155.7$ – 110.1 ppm. A sharp singlet due to methoxy ($-\text{OCH}_3$) carbon appears at $\delta = 55.4$ ppm.

5.4 Elemental analysis

CHN analysis of the synthesized compound **82a** was performed. Empirical formula: $\text{C}_{14}\text{H}_{13}\text{NO}_3$, elem. anal. calculated (%): C = 70.02, H = 5.88, N = 5.44; found (%): C = 70.05, H = 5.90, N = 5.83. The purity of the synthesised compound **82a** was validated via elemental analysis.

6. Synthesis and spectral analysis of *(E)*-1-(3-methoxy-4-(prop-2-yn-1-yloxy)phenyl)-N-(4-(prop-2-yn-1-yloxy)phenyl)methanimine

6.1 Synthesis

Schiff base **82b** was reacted with propargyl bromide with the addition of a base, like K_2CO_3 , which enables proton extraction from the OH group and speeds up the reaction in the forward direction. When the reaction was completed, the resulting mixture was quenched with acidic ice-cold water. Further, the product was filtered and air dried to gain exceptional yield of compound **82b**. After the reaction completion, the mixture was quenched with ice-cold water. Furthermore, the product was filtered and air dried to attain acceptable yield of compound **82b**. (Figure 70)

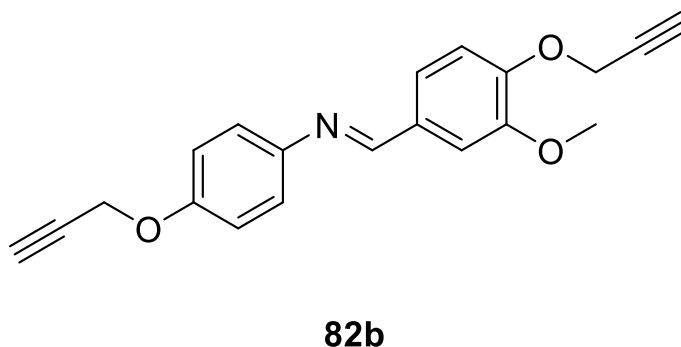


Figure 70. Structure of *(E)*-1-(3-methoxy-4-(prop-2-yn-1-yloxy)phenyl)-N-(4-(prop-2-yn-1-yloxy)phenyl)methanimine **82b**

6.2 ATR-FTIR spectroscopic analysis

The FTIR spectra data verifies the successful synthesis of the compound **82b**. The prominent peak at 1620 cm^{-1} corresponds to the (--C=N) bond of the azomethine group. Similarly, the absorption peaks at 3193 and 2127 cm^{-1} indicate the acetylenic proton ($\text{--C}\equiv\text{C--H}$) and the ($\text{--C}\equiv\text{C}$) bond of the Schiff base alkyne **82b**. The stretching vibrations of the aromatic (--C=C) group appear at 1587 cm^{-1} and 1504 cm^{-1} , whereas the bending vibrations of (--CH_2) and (--CH_3) have been identified at 1454 cm^{-1} and 1373 cm^{-1} in the spectrum.

6.3 NMR (^1H and ^{13}C) spectroscopic analysis

In ^1H NMR spectra of the synthesized terminal alkyne **82b**, quartet peaks at $\delta = 2.54\text{--}2.52$ ppm assigned to the ($\text{--C}\equiv\text{C--H}$) proton of the alkynyl group, the peak observed in domain $\delta = 6.97$

ppm to 7.61 ppm demonstrate the aromatic region and ($\text{N}=\text{CH}$) imine proton appears at $\delta = 8.37$ ppm as singlet peak. The two signals at $\delta = 4.69$ and $\delta = 4.82$ ppm corresponds to the methylene protons ($-\text{CH}_2$) attached to the oxygen atom of the aromatic ring. The methoxy protons ($-\text{OCH}_3$) associated with the aromatic ring exhibit a signal at $\delta = 3.96$ ppm.

In the ^{13}C NMR of terminal alkyne **82b**, the chemical shift in the region $\delta = 158.0$ ppm observed as highly de-shielded ($\text{N}=\text{C}$) imine carbon, the peaks appear at $\delta = 75.6, 76.3, 78.0, 78.6$ ppm corresponds to carbon atoms of two alkyne moiety ($\text{C}\equiv\text{C}$). The aromatic ring carbons range from $\delta = 156.0\text{--}109.3$ ppm, while the methoxy carbon ($-\text{OCH}_3$) was identified at $\delta = 56.13$ ppm and the two methylene group carbons ($-\text{CH}_2$) occurred at 56.2 ppm and 56.6 ppm.

6.4 Elemental analysis

The CHN analysis was conducted on the synthesized compound **82b**. Empirical formula: $\text{C}_{20}\text{H}_{17}\text{NO}_3$, elem. anal. calculated (%): C = 75.22, H = 5.37, N = 4.39; found (%): C = 75.26, H = 5.30, N = 4.43. The purity of compound **82b** was confirmed using elemental analysis.

7. Synthesis and spectral analysis of (*E*)-1-(4-((1-benzyl-1*H*-1,2,3-triazol-4-yl)methoxy)-3-methoxyphenyl)-*N*-(4-((1-benzyl-1*H*-1,2,3-triazol-4-yl)methoxy)phenyl) methanimine

7.1 Synthesis

Pure Schiff base linked terminal alkyne **82b** was reacted with benzyl azide **39** in presence of $[\text{CuBr}(\text{PPh}_3)_3]/\text{THF-TEA}$ system. The reaction was operated for 4 h at 60 °C to obtain the compound **82c** in high yield. Precipitation occurs when the reaction mixture was put into crushed ice and continued constant stirring for 15 min, the heavy particles settle down and filtered, the moist compound was air dried to obtain the dry pure solid product **82c**. (**Figure 71**)

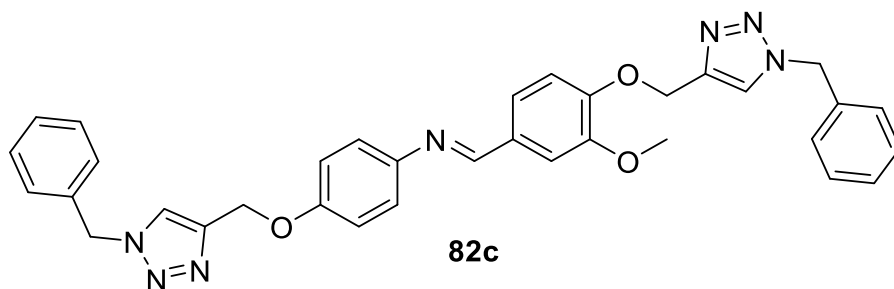


Figure 71. Structure of (*E*)-1-(4-((1-benzyl-1*H*-1,2,3-triazol-4-yl)methoxy)-3-methoxyphenyl)-*N*-(4-((1-benzyl-1*H*-1,2,3-triazol-4-yl)methoxy)phenyl) methanimine **82c**

7.2 ATR-FTIR spectroscopic analysis

The absorption band at 3094 cm^{-1} reveals ($-\text{C}=\text{C}-\text{H}$) of the triazole ring along with the disappearance of the IR peak at 2089 , 3255 and 2117 cm^{-1} due to ($\text{N}=\text{N}=\text{N}$), acetylenic proton ($-\text{C}\equiv\text{C}-\text{H}$) and ($-\text{C}\equiv\text{C}$) respectively which specify the conversion of alkynyl fragment **82b** into the triazole probe **82c**. The spectra display peak at 1623 cm^{-1} of ($\text{N}=\text{C}$) imine group, stretching vibrations of the aromatic ($-\text{C}=\text{C}$) group at 1599 cm^{-1} and 1510 cm^{-1} , as well as bending vibrations of ($-\text{CH}_2$) and ($-\text{CH}_3$) at 1459 cm^{-1} and 1384 cm^{-1} , respectively.

7.3 NMR (^1H and ^{13}C) spectroscopic analysis

The signal observed due to two triazole proton at $\delta = 7.57$, $\delta = 7.58$ ppm and also the disappearance of peak at $\delta = 2.43$ ppm due to ($-\text{C}\equiv\text{C}-\text{H}$) proton of the alkyne moiety confirming the transformation of alkyne moiety to triazole unit. The chemical shift at $\delta = 3.92$ ppm was identified as the methoxy protons ($-\text{OCH}_3$) attached to the aromatic ring. The four groups of methylene protons ($-\text{CH}_2$) were located at chemical shifts of $\delta = 5.19$ ppm, $\delta = 5.31$ ppm, $\delta = 5.50$ ppm and $\delta = 5.53$ ppm, the signal due to imine proton ($-\text{HC}=\text{N}$) was found at $\delta = 8.34$ ppm as the highly de-shielded area of the spectrum and the aromatic ring protons was detected in the range $\delta = 7.54\text{--}6.97$ ppm.

In the ^{13}C NMR of compound **82c**, the imine carbon ($-\text{HC}=\text{N}$) was seen at a chemical shift of $\delta = 158.2$ ppm and the carbon atoms of the aromatic ring appeared in the range of $\delta = 156.6\text{--}109.2$ ppm. The appearance of signal $\delta = 122.6$ ppm and $\delta = 134.5$ ppm due to the 1,2,3-triazole ring carbon affirms the conversion of alkyne moiety to 1,2,3 triazole derivative. The methoxy carbon ($-\text{OCH}_3$) is identified at a chemical shift value of 54.2 ppm. The chemical shift values for the four groups of methylene carbons ($-\text{CH}_2$) are 56.0 ppm, 56.0 ppm, 62.4 ppm, and 63.1 ppm.

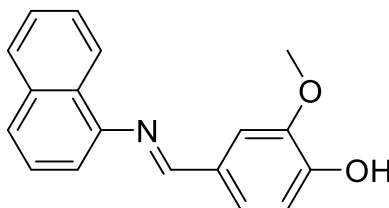
7.4 Elemental analysis and Mass spectrometry

The CHN assay of the synthesised compound **82c** was conducted. Empirical formula: $\text{C}_{34}\text{H}_{31}\text{N}_7\text{O}_3$, elem. anal. calculated (%): C = 69.73, H = 5.34, N = 16.74. found (%): C = 69.60, H = 5.38, N = 16.78. Utilising elemental analysis, the purity of compound **82c** was verified. The mass of the compound **82c** actual $m/z = 585.25$ and the reported $m/z = 585.20$ via GCMS-MS that confirms the synthesis of compound **82c**.

8. Synthesis and spectral analysis of (*E*)-2-methoxy-4-((naphthalen-1-ylimino)methyl)phenol

8.1 Synthesis

1-naphthylamine was dissolved in absolute methanol and mixed with an methanolic solution of 4-hydroxy-3-methoxy benzaldehyde and the reaction mixture was stirred, heated and refluxed for 3h. The resultant mixture was quenched in ice-cold water for 15 minutes with constant shaking. The precipitates were then filtered off from the mixture and air dried to afford beige color compound Schiff base **83a**. (**Figure 72**)



83a

Figure 72. Structure of (*E*)-2-methoxy-4-((naphthalen-1-ylimino)methyl)phenol **83a**

8.2 ATR-FTIR spectroscopic analysis

The FTIR spectra of the chemical scaffold **83a** was recorded in the region 4000–500 cm^{-1} and the data acquired validates the successful synthesis of the target molecule. The prominent peak at 1620 cm^{-1} coincides with the ($\text{C}=\text{N}$) of the azomethine group **83a**. The stretching vibrations of the aromatic ($\text{C}=\text{C}$) group are seen at 1587 cm^{-1} and 1512 cm^{-1} , whereas the bending vibrations of (CH_2) and (CH_3) were found at 1424 cm^{-1} and 1380 cm^{-1} in the spectrum.

8.3 NMR (^1H and ^{13}C) spectroscopic analysis

The analysis of NMR data explicitly confirmed the synthesis of the azomethine moiety **83a**. Regarding the ^1H NMR spectrum of compound **83a**, the signal originating at $\delta = 3.91$ ppm is due to the (OCH_3) methoxy group, whereas the chemical shift at $\delta = 8.53$ ppm of ($\text{C}=\text{N}$) group corroborates the synthesis of azomethine moiety, besides the peak arising at $\delta = 9.86$ ppm allocates to the proton of (OH) group and the aromatic ring protons lies within the range $\delta = 8.35\text{--}7.01$ ppm. In the ^{13}C NMR, the carbon of ($\text{C}=\text{N}$) Schiff base was detected in the area $\delta = 160.34$ ppm strongly de-shielded area, and the aromatic ring protons apparent at $\delta = 150.4\text{--}110.7$ ppm, also

the signal due to methoxy group ($-\text{OCH}_3$) appears at $\delta = 55.6$ ppm. All these chemical shift values validate the synthesis of **83a**.

8.4 Elemental analysis

The CHN analysis was performed on the synthesised chemical **83a**. Empirical formula: $\text{C}_{18}\text{H}_{15}\text{NO}_2$, elem. anal. calculated (%): C = 77.96, H = 5.45, N = 5.05; found (%): C = 77.92, H = 5.42, N = 5.02. The purity of compound **83a** was confirmed by elemental analysis.

9. Synthesis and spectral analysis of *(E)*-*N*-(3-methoxy-4-(prop-2-yn-1-yloxy)benzylidene)naphthalen-1-amine

9.1 Synthesis

The interaction of adduct **83b** with propargyl bromide ($\text{HC}\equiv\text{C}-\text{CH}_2\text{Br}$) and dry K_2CO_3 , a non-nucleophilic base that aids in the deprotonation of the $-\text{OH}$ group at room temperature yielded **83b** in excellent quantity. To extract the synthesized material, the reaction mixture was poured in beaker containing crushed ice, stirred for 15 minutes, until solid precipitation appeared, filtered, and then air dried overnight to produce yellowish sand fine powder as the desired product **83b**. (Figure 73)

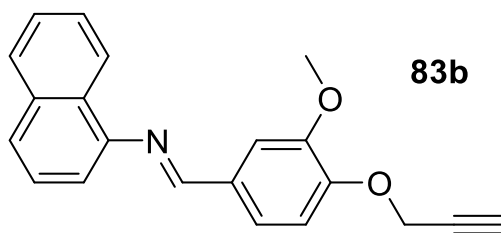


Figure 73. Structure of *(E)*-*N*-(3-methoxy-4-(prop-2-yn-1-yloxy)benzylidene)naphthalen-1-amine **83b**

9.2 ATR-FTIR spectroscopic analysis

The absorption maxima observed at 3190 and 2105 cm^{-1} represent the $(-\text{C}\equiv\text{C}-\text{H})$ of acetylenic proton and $(-\text{C}\equiv\text{C})$ bond of azomethine tailored alkyne **83b**. The IR signal at a frequency of 2995 cm^{-1} and 2928 cm^{-1} corresponds to the stretching vibrations of aliphatic $(-\text{C}-\text{H})$ bond. The aromatic $(-\text{C}=\text{C})$ group exhibits stretching vibrations at 1583 cm^{-1} and 1508 cm^{-1} ,

whereas the bending vibrations of ($-\text{CH}_2$) and ($-\text{CH}_3$) are seen at 1458 cm^{-1} and 1369 cm^{-1} in the spectrum and the sharp peak of imine ($-\text{C}=\text{N}$) was identified at 1623 cm^{-1} .

9.3 NMR (^1H and ^{13}C) spectroscopic analysis

A triplet appeared at $\delta = 2.54\text{--}2.53\text{ ppm}$ is anticipated to alkynyl proton ($\equiv\text{C}-\text{H}$) and $\delta = 4.79\text{ ppm}$ corresponding to ($-\text{CH}_2$) methylene group in the vicinity of oxygen atom linked to alkyne validated the synthesis of adduct **83b**. Additionally, the proton of the ($-\text{OH}$) group in the spectrum of preliminary compound **83a** is missing in the spectrum of **83b** confirming alkyne synthesis. Moreover, the methoxy protons ($-\text{OCH}_3$), imine proton ($-\text{C}=\text{N}$) and the aromatic protons were identified at $\delta = 3.96\text{ ppm}$, $\delta = 8.39\text{ ppm}$ and $\delta = 8.34\text{--}6.98\text{ ppm}$ respectively.

In the ^{13}C NMR of compound **83b**, the appearance of signals at $\delta = 76.4$ and 78.1 ppm are due to the acetylenic carbon ($-\text{C}\equiv\text{C}$) and at $\delta = 56.6\text{ ppm}$ due to methylene carbon ($-\text{CH}_2$) attached to acetylene group assures the synthesis of azomethine tethered alkyne **83b**. The aromatic carbon atoms appeared at $\delta = 109.8\text{--}150.1\text{ ppm}$, the imine carbon ($-\text{C}=\text{N}$) found at $\delta = 159.81\text{ ppm}$ and the methoxy carbon ($-\text{OCH}_3$) identified at $\delta = 56.1\text{ ppm}$.

9.4 Elemental analysis

The CHN analysis was conducted on the synthesized compound **83b**. Empirical formula: $\text{C}_{21}\text{H}_{17}\text{NO}_2$, elem. anal. calculated (%): C = 79.98, H = 5.43, N = 4.44; found (%): C = 79.92, H = 5.41, N = 4.40. Elemental analysis validates the purity of compound **83b**.

10. Synthesis and spectral analysis of (*E*)-*N*-(4-((1-benzyl-1*H*-1,2,3-triazol-4-yl)methoxy)-3-methoxybenzylidene)naphthalen-1-amine

10.1 Synthesis

Schiff base linked terminal alkyne **83b** undergoes [2 + 3] cycloaddition reaction process with azidomethyl benzene **39** in the presence of the $[\text{CuBr}(\text{PPh}_3)_3]/\text{THF-TEA}$ system for 5 h at 60°C in an inert conditions to generate compound **83c** in high yield. Once the reaction completed, the resulting mixture was poured on crushed ice and stirred for 15 minutes, the remaining mixture was filtered and air dried, resulting in the formation of a solid off-white compound **83c**. (Figure 74)

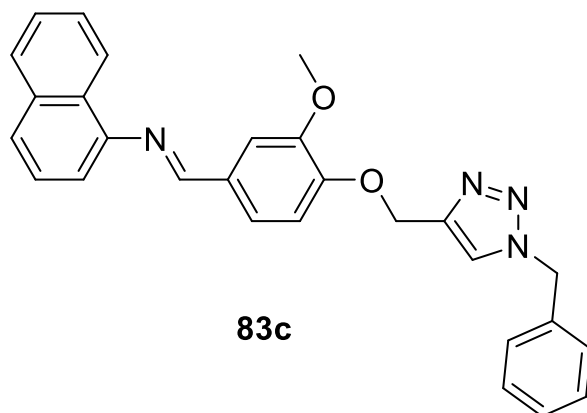


Figure 74. Structure of *(E)-N-(4-((1-benzyl-1H-1,2,3-triazol-4-yl)methoxy)-3-methoxybenzylidene)naphthalen-1-amine*

10.2 ATR-FTIR spectroscopic analysis

The absorption peak at 2962 cm^{-1} confirms ($-\text{C}=\text{C}-\text{H}$) of the heterocyclic 1,2,3-triazole, whereas the peaks at 2089 , 3190 , and 2105 cm^{-1} dissipate owing to ($\text{N}=\text{N}=\text{N}$), acetylenic proton ($\equiv\text{C}-\text{H}$), and ($-\text{C}\equiv\text{C}$), thereby indicating the chemical transformation of alkynyl fragment **83b** to the 1,2,3-triazole unit **83c**. The spectrum exhibits a prominent peak at 1623 cm^{-1} corresponding to the ($\text{N}=\text{C}$) imine group. Additionally, stretching vibrations of the aromatic ($-\text{C}=\text{C}$) group are seen at 1580 cm^{-1} and 1503 cm^{-1} . Bending vibrations of ($-\text{CH}_2$) and ($-\text{CH}_3$) are also present at 1457 cm^{-1} and 1385 cm^{-1} , respectively.

10.3 NMR (^1H and ^{13}C) spectroscopic analysis

The chemical shift at $\delta = 4.79\text{ ppm}$ due to ($-\text{CH}_2-\text{O}$) shifts downfield ($\delta = 5.29\text{ ppm}$) and the signal observed at $\delta = 7.46\text{ ppm}$ owing to the 1,2,3-triazole ring formation, and the chemical shift of azomethine tethered alkynyl proton at $\delta = 2.54\text{ ppm}$ has disappeared since it now constitutes an integral component of the aromatic 1,2,3-triazole ring confirming the formation of compound **83c**. The chemical shift at $\delta = 3.91\text{ ppm}$ is due to methoxy protons ($-\text{OCH}_3$) linked to the aromatic ring. The chemical shifts of the two groups of methylene protons ($-\text{CH}_2$) were observed at $\delta = 5.29\text{ ppm}$, and $\delta = 5.45\text{ ppm}$. The signal from the imine proton ($-\text{HC}=\text{N}$) was found at $\delta = 8.38\text{ ppm}$, which is a highly de-shielded region of the spectrum. The aromatic ring protons were detected in the range of $\delta = 7.70\text{--}7.11\text{ ppm}$.

In the ^{13}C spectrum of **83c**, the peak at $\delta = 56.6$ ppm owing to the carbon of ($-\text{CH}_2-\text{O}$) moves downfield ($\delta = 63.0$ ppm), indicating that it has been linked to the triazole ring. Due to the ($-\text{CH}_2$) of the benzyl group, an additional peak at $\delta = 56.0$ ppm emerged. The signals in the spectrum at $\delta = 76.4, 78.1$ reflect the ($-\text{C}\equiv\text{C}$) shift towards the aromatic area since these carbons now formulate a triazole ring at peak value $\delta = 123.0$ and 144.0 ppm. The signal at $\delta = 54.2$ ppm, $\delta = 159.7$ and $\delta = 150.6-109.5$ ppm corresponds to methoxy carbon ($-\text{OCH}_3$), imine carbon ($-\text{HC}=\text{N}$) and aromatic ring carbon atoms respectively. Therefore, NMR spectra of compound **83c** firmly support the cycloaddition of alkyne **83b** with benzyl azide **39**.

10.4 Elemental analysis and Mass spectrometry

The CHN assay of the synthesised compound **83c** was conducted. Empirical formula: $\text{C}_{28}\text{H}_{24}\text{N}_4\text{O}_2$, elem. anal. calculated (%): C = 74.98, H = 5.39, N = 12.49; found (%): C = 74.90, H = 5.32, N = 12.43. Analysis of elements verifies the purity of compound **83c**. The mass analysis of compound **83c** was done via GCMS-MS where the m/z calculated = 448.19 and the experimental $m/z = 448.10$ signifies the synthesis of compound **83c**.

11. Synthesis and spectral analysis of (*E*)-2-methoxy-4-((phenethylimino)methyl)phenol

11.1 Synthesis

The initial step involves coupling reaction of substituted aldehyde and primary amine for 4 h at 60°C results in the formation of the imine-based moiety **84a** with high yield. The reaction mixture was carefully transferred into a beaker filled with crushed ice and was then vigorously stirred for a duration of 15 minutes. Afterward, the mixture was subjected to filtration in order to isolate pure precipitates of **84a**. (Figure 75)

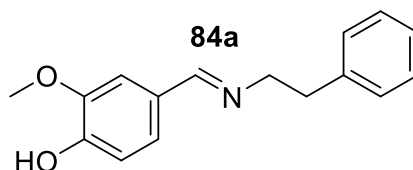


Figure 75. Structure of (*E*)-2-methoxy-4-((phenethylimino)methyl)phenol

11.2 ATR-FTIR spectroscopic analysis

The Fourier transform infrared spectroscopy technique was utilized to record the ATR-FTIR spectra of chemical scaffold **84a** within the spectral range of 4000–500 cm^{-1} . The data obtained serves as confirmation for the successful synthesis of the aforementioned compound. The spectral data reveals a notable peak at 1640 cm^{-1} , which aligns precisely with the characteristic vibrational range associated with the ($\text{C}=\text{N}$) bond within the imine group **84a**. The spectral analysis reveals that the stretching vibrations of the aromatic ($\text{C}=\text{C}$) group occur at 1593 cm^{-1} and 1513 cm^{-1} , whereas the bending vibrations of (CH_2) and (CH_3) are seen at 1433 cm^{-1} and 1345 cm^{-1} , respectively. The IR signal at 3017 cm^{-1} represents aromatic (C-H) stretching vibrations in the aromatic moiety of synthesised molecule **84a**, whereas 2858 cm^{-1} indicates aliphatic (C-H) stretching.

11.3 NMR (^1H and ^{13}C) spectroscopic analysis

The analysis of NMR data explicitly confirmed the synthesis of the azomethine moiety. Regarding the ^1H NMR spectrum of compound **84a**, the signal originating at $\delta = 3.79$ ppm is due to the (OCH_3) methoxy group, and the peak at $\delta = 2.90$ ppm, $\delta = 3.74$ ppm are designated as the two methylene groups (CH_2), whereas the chemical shift at $\delta = 8.12$ ppm of imine proton ($\text{HC}=\text{N}$) and the aromatic ring protons in the range $\delta = 7.32$ – 6.80 ppm corroborates the synthesis of azomethine moiety **84a**. In the ^{13}C NMR, the carbon of ($\text{C}=\text{N}$) Schiff base was detected in the area $\delta = 160.4$ ppm strongly deshielded proton, and the aromatic ring protons apparent at $\delta = 149.1$ – 109.7 ppm, validating the synthesis of compound **84a**. The methoxy carbon (OCH_3) appear at $\delta = 55.5$ ppm, the two methylene groups (CH_2) carbon were stipulated at $\delta = 37.0$ and $\delta = 61.7$ ppm.

11.4 Elemental analysis

The CHN analysis of compound **84a** was performed. Empirical formula: $\text{C}_{16}\text{H}_{17}\text{NO}_2$, elem. anal. calculated (%): C = 75.27, H = 6.71, N = 5.49; found (%): C = 75.32, H = 6.02, N = 5.32. Elemental analysis confirms the purity of compound **84a**.

12. Synthesis and spectral analysis of (*E*)-1-(3-methoxy-4-(prop-2-yn-1-yloxy)phenyl)-N-phenethylmethanimine

12.1 Synthesis

The chemical process involves adduct **84a** and propargyl bromide injected in milieu of non-nucleophilic base such as K_2CO_3 that facilitates the deprotonation of the labile proton, leads to formation of compound **84b** in a satisfactory yield at ambient temperature. Subsequently, the reaction mixture was carefully transferred on crushed ice, resulting in the formation of solid precipitates, filtered and washed, ensuing in the acquisition of light peach coloured product **84b**. (Figure 76)

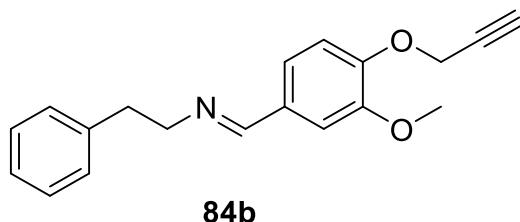


Figure 76. Structure of *(E)*-1-(3-methoxy-4-(prop-2-yn-1-yloxy)phenyl)-*N*-phenethylmethanimine

12.2 ATR-FTIR spectroscopic analysis

The observed peaks at 3182 cm^{-1} and 2101 cm^{-1} correspond to the vibrational modes of the acetylenic proton ($-\text{C}\equiv\text{C}-\text{H}$) and ($-\text{C}\equiv\text{C}$) of the imine geared terminal alkyne **84b**, respectively. Stretching vibrations of the aromatic ($-\text{C}=\text{C}$) group are detected at 1586 cm^{-1} and 1504 cm^{-1} , whereas bending vibrations of ($-\text{CH}_2$) and ($-\text{CH}_3$) were observed at 1457 cm^{-1} and 1388 cm^{-1} in the spectrum, and a strong peak of imine ($-\text{C}=\text{N}$) is recognised at 1634 cm^{-1} .

12.3 NMR (^1H and ^{13}C) spectroscopic analysis

The triplet at $\delta = 2.44\text{--}2.43\text{ ppm}$ suggests the presence of an alkynyl proton ($\equiv\text{C}-\text{H}$) in the spectrum. Similarly, the shift observed at $\delta = 4.69\text{ ppm}$ belongs to a ($-\text{CH}_2\text{O}$) methylene group attached to acetylenic chain and the two other methylene ($-\text{CH}_2$) peaks can be seen at $\delta = 2.91\text{ ppm}$ and $\delta = 3.75\text{ ppm}$. The proton of methoxy group was identified at $\delta = 3.84\text{ ppm}$, the aromatic ring protons lies within the range $\delta = 6.92\text{--}7.34\text{ ppm}$ and the imine proton ($-\text{C}=\text{N}$) can be found at $\delta = 7.99\text{ ppm}$. These outcomes provide evidence of the successful synthesis of compound **84b**. The existence of peaks at $\delta = 76.1$, 78.2 , and 56.6 in the ^{13}C NMR spectrum of **84b** can be attributed to the carbon atoms in the ($-\text{C}\equiv\text{C}-$) and ($-\text{CH}_2\text{O}$) functional groups, which indicate the synthesis

of the imine tethered alkyne **84b**. The methylene carbon ($-\text{CH}_2$) atoms are found at $\delta = 37.6$ ppm, $\delta = 55.6$ ppm, $\delta = 63.0$ ppm, the carbon atoms of methoxy group ($-\text{OCH}_3$) is seen at $\delta = 55.9$ ppm, the signal due to imine carbon ($-\text{C}=\text{N}$) is visible at $\delta = 160.89$ ppm in the highly de-shielded area and the chemical shift value of aromatic carbons found at $\delta = 149.9$ – 109.2 ppm.

12.4 Elemental analysis

Compound **84b** was subjected to CHN analysis. Empirical formula: $\text{C}_{19}\text{H}_{19}\text{NO}_2$, Elem. anal. calculated (%): C = 75.27, H = 6.71, N = 5.49; found (%): C = 75.32, H = 6.02, N = 5.32. Element analysis verifies that compound **84b** is pure.

13. Synthesis and spectral analysis of (E)-1-(4-((1-benzyl-1H-1,2,3-triazol-4-yl)methoxy)-3-methoxyphenyl)-N phenethylmethanimine

13.1 Synthesis

Click derived probe was synthesized by the copper(I)-catalyzed azide-alkyne cycloaddition (CuAAC) reaction between compound **84b** and compound **39** with the addition of $[\text{CuBr}(\text{PPh}_3)_3]$ as a catalyst using (THF:TEA::1:1) as a solvent system at 60°C for 5 h. After completion of the reaction, the liquid mixture was rapidly quenched on ice-cold water and stirred for 15 minutes to obtain off-white solid precipitates. Subsequently, the solution was filtered, followed by washing with hexane, air-dried, resulting in the acquisition of the desired solid compound **84c**. (Figure 77)

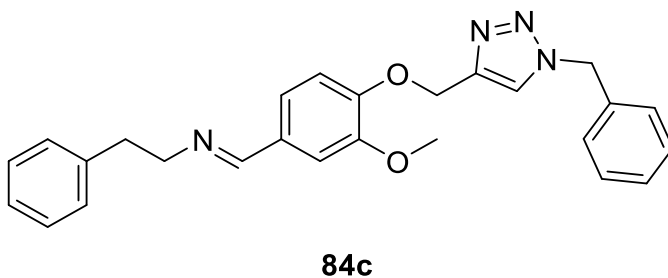


Figure 77. Structure of (E)-1-(4-((1-benzyl-1H-1,2,3-triazol-4-yl)methoxy)-3-methoxyphenyl)-N phenethylmethanimine

13.2 ATR-FTIR spectroscopic analysis

The peaks at 2089, 3182, and 2101 cm^{-1} due to ($\text{N}=\text{N}=\text{N}$), acetylenic proton ($\equiv\text{C}-\text{H}$), and ($-\text{C}\equiv\text{C}$) functionalities disappear and the signal at 2948 cm^{-1} provides confirmation of the ($-\text{C}=\text{C}-\text{H}$) functional group in the heterocyclic 1,2,3-triazole compound. These changes in the peak values suggest a chemical transformation of the alkynyl moiety **84b** to 1,2,3-triazole chemosensor **84c**. The observed peak at 3074 cm^{-1} signifies aromatic ($-\text{C}-\text{H}$) stretching vibration and the signal at 2838 cm^{-1} designates aliphatic ($-\text{C}-\text{H}$) stretching. The stretching vibration at 1645 cm^{-1} corresponds to imine group ($-\text{C}=\text{N}$). Furthermore, stretching vibrations of the aromatic ($-\text{C}=\text{C}$) group observed at 1585 cm^{-1} and 1510 cm^{-1} and the bending vibrations of ($-\text{CH}_2$) and ($-\text{CH}_3$) was found at 1459 cm^{-1} and 1384 cm^{-1} , respectively.

13.3 NMR (^1H and ^{13}C) spectroscopic analysis

The chemical shift seen at $\delta = 4.69$ ppm, which is attributed to ($-\text{CH}_2-\text{O}-$), experiences downfield shift ($\delta = 5.19$ ppm) due to the association with triazole ring and the appearance of signal at $\delta = 7.46$ ppm owing to triazole proton confirms the transformation of alkyne moiety into triazole unit. Additionally, the peak of the alkynyl proton at $\delta = 2.44$ – 2.43 ppm is no longer detectable, as it is now a vital part of the substituted 1,2,3-triazole ring. The methoxy protons ($-\text{OCH}_3$) connected to the aromatic ring displayed a singlet at $\delta = 3.78$ ppm, due to the two methylene groups ($-\text{CH}_2-$) chemical shift was recorded at $\delta = 2.90$ and $\delta = 3.73$ ppm, whereas $\delta = 5.39$ ppm appeared due to the ($-\text{CH}_2-$) of the benzyl group. The imine proton ($-\text{HC}=\text{N}$) signal was detected at $\delta = 7.98$ ppm and the aromatic protons were identified at $\delta = 7.46$ – 6.96 ppm.

In the ^{13}C NMR, the peak at $\delta = 56.6$ ppm owing to the carbon of ($-\text{CH}_2\text{O}$) moves downfield ($\delta = 63.0$ ppm), indicating that it has been linked to the triazole ring. Due to the ($-\text{CH}_2$) of the benzyl group, an additional peak at $\delta = 55.9$ ppm emerged. The signals in the spectrum at $\delta = 76.4$, 78.1 reflect the ($-\text{C}\equiv\text{C}-$) shift towards the aromatic area since these carbons now formulate a triazole ring and displayed new peaks $\delta = 123.0$ and 139.9 ppm in the concluded product. The methoxy carbon ($-\text{OCH}_3$) atoms appears at $\delta = 54.2$ ppm, the other methylene carbon atoms can be seen at $\delta = 37.6$, $\delta = 63.0$, $\delta = 63.0$ ppm, the imine carbon ($-\text{HC}=\text{N}$) shows the signal at $\delta = 160.9$ ppm and the ring protons was found in the range $\delta = 149.8$ – 109.0 ppm.

13.4 Elemental analysis and Mass spectrometry

CHN analysis of compound **84c** was performed. Empirical formula: $C_{26}H_{26}N_4O_2$, elem. anal. calculated (%): C = 73.22, H = 6.14, N = 13.14; found (%): C = 73.30, H = 6.12, N = 13.20. Element analysis confirms the purity of compound **84c**. The mass of compound m/z (actual) = 426.20 and the m/z (reported) = 427.21 $[M + 1]$ via LCMS-MS validates the synthesis of compound **84c**.

14. Synthesis and spectral analysis of *(E)*-2-methoxy-4-((*p*-tolylimino)methyl)phenol

14.1 Synthesis

The synthesis of toluidine linked Schiff base **85a** included a condensation reaction between substituted aldehyde and toluidine in the presence of methanol and a catalytic quantity of DCM. After completion of the reaction, the reaction mixture was then transferred to crushed ice, stirred continuously for 15-20 minutes. The solution was then filtered to attain the desired product **85a**. (Figure 78)

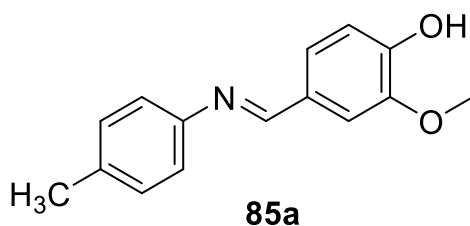


Figure 78. Structure of *(E)*-2-methoxy-4-((*p*-tolylimino)methyl)phenol

14.2 ATR-FTIR spectroscopic analysis

The FTIR spectra of chemical scaffolds **85a** was recorded using the Fourier transform infrared spectroscopy technique, within the spectral range of $4000\text{--}500\text{ cm}^{-1}$. The peak at 3015 , 2933 cm^{-1} represent the ($-\text{C}-\text{H}$) stretching of the aromatic and aliphatic bonds respectively. A prominent peak observed at 1623 cm^{-1} , coincides with the distinctive peak range ($-\text{C}=\text{N}$) of the imine group. The stretching vibrations of the aromatic ($-\text{C}=\text{C}$) group occur at 1582 cm^{-1} and 1507 cm^{-1} , whereas the bending vibrations of ($-\text{CH}_2$) and ($-\text{CH}_3$) are visible at 1461 cm^{-1} and 1391 cm^{-1} , respectively.

14.3 NMR (^1H and ^{13}C) spectroscopic analysis

In the ^1H NMR spectrum of compound **85a**, the signal at $\delta = 3.90$ ppm and $\delta = 2.35$ ppm is due to the ($-\text{OCH}_3$) methoxy group, and ($-\text{CH}_3$) methyl group whereas the chemical shift at $\delta = 8.34$ ppm of the ($-\text{HC}=\text{N}$) group confirms the synthesis of the azomethine moiety, also the signal from $\delta = 7.62$ to 6.96 ppm range coincide with ring protons and the peak at $\delta = 9.80$ ppm allocates to the proton of the ($-\text{OH}$) group. The carbon of ($-\text{C}=\text{N}$) Schiff base was observed in the region $\delta = 159.5$ ppm highly de-shield proton, peak at $\delta = 21.0$ and $\delta = 56.0$ correspond to carbon of ($-\text{CH}_3$) methyl group and ($-\text{OCH}_3$) methoxy group respectively, the aromatic ring protons appeared at $\delta = 149.1$ – 108.6 ppm verifying the synthesis of compound **85a**.

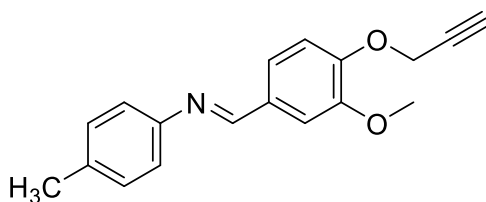
14.4 Elemental analysis

CHN analysis of compound **85a** was carried out. Empirical formula: $\text{C}_{15}\text{H}_{14}\text{NO}_2$, elem. anal. calculated (%): C = 74.98, H = 5.87, N = 5.83; found (%): C = 74.36, H = 5.22, N = 5.65. Element analysis validates the purity of compound **85a**.

15. Synthesis and spectral analysis of (*E*)-1-(3-methoxy-4-(prop-2-yn-1-yloxy)phenyl)-N-(*p*-tolyl)methanimine

15.1 Synthesis

The synthetic procedure includes reaction of compound **85a** with propargyl bromide injected dropwise in presence of K_2CO_3 as base that enables the deprotonation of the labile proton, resulting to synthesis of compound **85b** in good yield at room temperature. The reaction mixture was deposited onto crushed ice, resulting in solid precipitates, filtered and washed with distilled water, yielding the orange-peach coloured product **85b**. (Figure 79)



85b

Figure 79. Structure of (*E*)-1-(3-methoxy-4-(prop-2-yn-1-yloxy)phenyl)-N-(*p*-tolyl)methanimine

15.2 ATR-FTIR spectroscopic analysis

The peaks at 3254 and 2127 cm^{-1} are the stretching vibrations of the acetylenic proton ($\text{C}\equiv\text{C-H}$) and ($\text{-C}\equiv\text{C}$) of the imine tailored terminal alkyne **85b**, respectively. The spectrum exhibits stretching vibrations of the aromatic (-C=C) group at 1580 cm^{-1} and 1505 cm^{-1} , bending vibrations of (-CH_2) and (-CH_3) at 1453 cm^{-1} and 1380 cm^{-1} , respectively, and an identifiable strong peak of imine (-C=N) at 1623 cm^{-1} . The peaks at 3006 and 2924 cm^{-1} show (-C-H) stretching of the aromatic and aliphatic bonds, respectively.

15.3 NMR (^1H and ^{13}C) spectroscopic analysis

The triplet signal at $\delta = 2.55$ ppm indicates the existence of an alkynyl ($\text{C}\equiv\text{C-H}$) proton. Similarly, the chemical shift at $\delta = 3.95$ ppm, $\delta = 2.35$ and $\delta = 4.80$ corresponds to proton of (-OCH_3) methoxy group, (-CH_3) methyl group and (-CH_2) methylene group respectively. Additionally, the signal from $\delta = 7.41$ to 7.05 ppm coincides the aromatic ring protons and the peak at $\delta = 8.35$ allocates to the (-HC=N) imine group.

The peaks at $\delta = 76.3$, 78.0, 56.0, 56.6 and 20.9 in the ^{13}C NMR spectra of **85b** may be ascribed to the two carbon atoms in the ($\text{-C}\equiv\text{C-}$) and methoxy group (-OCH_3), methylene (-CH_2) and methyl group (-CH_3) respectively. Moreover, the carbon of aromatic region lies in the region from $\delta = 152.1$ to 109.4 ppm and the imine carbon (-C=N) situated at $\delta = 158.9$ ppm. All these results indicating the formation of the imine tethered alkyne **85b**.

15.4 Elemental analysis

Elemental analysis of compound **85b** was done using CHN technique. Empirical formula: $\text{C}_{18}\text{H}_{17}\text{NO}_2$, elem. anal. calculated (%): C = 77.40, H = 6.13, N = 5.01; found (%): C = 77.22, H = 6.10, N = 5.09. The purity of Compound **85a** is verified by element analysis.

16. Synthesis and spectral analysis of *Synthesis and characterization of (E)-1-(4-((1-benzyl-1H-1,2,3-triazol-4-yl)methoxy)-3-methoxyphenyl)-N-(p-tolyl)methanimine*

16.1 Synthesis

The copper(I)-catalyzed azide-alkyne cycloaddition (CuAAC) reaction involving compounds **85b** and **39**, with the addition of $[\text{CuBr}(\text{PPh}_3)_3]$ as a catalyst and (THF:TEA::1:1) as a solvent mixture, resulted in the click-derived probe **85c**. Following the reaction completion, the

liquid mixture was quickly extracted with crushed ice and agitated for 15 minutes to produce ivory colour solid precipitates. (Figure 80)

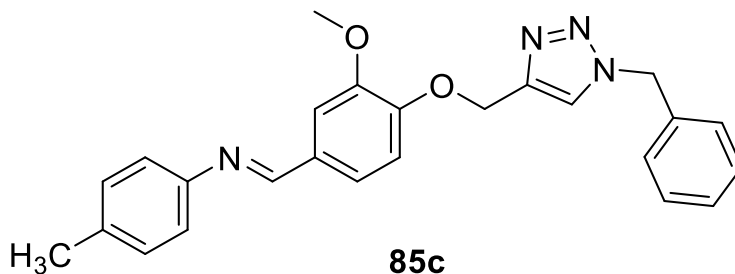


Figure 80. Structure of (*E*)-1-(4-((1-benzyl-1H-1,2,3-triazol-4-yl)methoxy)-3-methoxyphenyl)-N-(*p*-tolyl)methanimine

16.2 ATR-FTIR spectroscopic analysis

The stretching vibration at 3085 cm^{-1} confirms the ($-\text{C}=\text{C}-\text{H}$) group of the heterocyclic 1,2,3-triazole molecule **85c**. The absence of peaks at 2089 , 3254 and 2127 cm^{-1} due to azide ($\text{N}=\text{N}=\text{N}$), acetylenic proton ($\equiv\text{C}-\text{H}$), and ($-\text{C}\equiv\text{C}$), respectively shows disappearance of alkyne and azide group and transformation into imine base 1,2,3-triazole moiety **85c**. The ($\text{C}-\text{H}$) stretching vibration peak of aliphatic compound was detected at 2950 cm^{-1} and the ($\text{C}-\text{H}$) stretching peak of aromatic ring was observed at 3085 cm^{-1} . The bending vibration due to ($-\text{CH}_2$) methylene group and ($-\text{CH}_3$) methyl group and the stretching vibrations of ($\text{C}=\text{C}$) was identified at 1460 cm^{-1} , 1381 cm^{-1} and 1580 cm^{-1} , 1508 cm^{-1} respectively. A prominent peak of imine ($-\text{C}=\text{N}$) group appeared at 1626 cm^{-1} in the spectrum.

16.3 NMR (^1H and ^{13}C) spectroscopic analysis

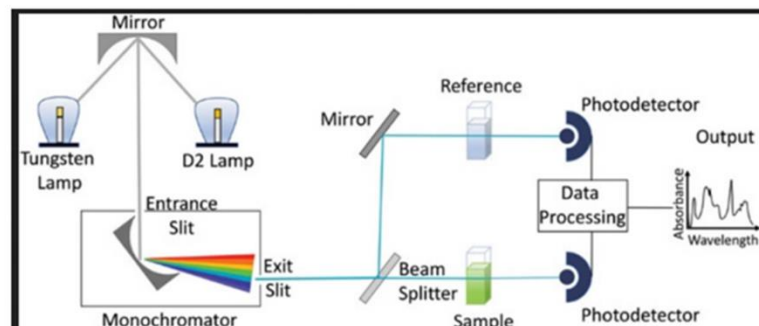
The signal at $\delta = 4.80\text{ ppm}$, assigned to ($-\text{CH}_2-\text{O}-$), undergoes a downfield shift ($\delta = 5.30\text{ ppm}$) and the proton of the triazole ring was found at $\delta = 7.61\text{ ppm}$ owing to the connection with the triazole ring. Furthermore, the alkynyl proton signal at $\delta = 2.55\text{ ppm}$ is no longer visible, since it is now a crucial component of the substituted 1,2,3-triazole ring. The signal of methylene group ($-\text{CH}_2$) at $\delta = 5.48\text{ ppm}$ is due to the benzyl group. The chemical shift of methyl group ($-\text{CH}_3$) protons, methoxy group ($-\text{CH}_3$) protons and another methylene group ($-\text{CH}_2$) protons can be observed at $\delta = 2.35$, $\delta = 3.90$ and 5.30 ppm , respectively. The ring protons and the imine group protons can be duly noted at $\delta = 7.61-7.10\text{ ppm}$ and $\delta = 8.34\text{ ppm}$.

In the ^{13}C NMR spectrum, the signal at $\delta = 56.6$ ppm is due to the carbon of ($-\text{CH}_2\text{O}$) moving downfield ($\delta = 62.9$ ppm), showing that it is connected to the triazole ring. The ($-\text{CH}_2$) of the benzyl group resulted in an additional signal at $\delta = 54.1$ ppm. The signals in the spectrum at $\delta = 76.31, 78.09$ represent the ($-\text{C}\equiv\text{C}-$) shift towards the aromatic region as these carbons now form a triazole ring showing new peaks $\delta = 120.7$ and 134.3 ppm. The methoxy carbon ($-\text{OCH}_3$) atoms are observed at a chemical shift of $\delta = 54.1$ ppm and the methyl carbon ($-\text{CH}_3$) atoms can be detected at chemical shifts of $\delta = 20.9$ ppm. The imine carbon ($-\text{HC}=\text{N}$) exhibits a signal at $\delta = 158.9$ ppm. The protons of the aromatic ring were identified within the range of chemical shifts from $\delta = 109.2$ to $\delta = 152.9$ ppm.

16.4 Elemental analysis and Mass spectrometry

The elemental analysis of compound **85c** was performed using the CHN method. Empirical formula: $\text{C}_{25}\text{H}_{24}\text{NO}_2$, elem. anal. calculated (%): C = 72.80, H = 5.86, N = 13.58; found (%): C = 72.88, H = 5.36, N = 13.21. Elemental analysis validated the purity of the compound **85c**. The mass of compound m/z (actual) = 412.18 and m/z (reported) = 412.20 obtained using GCMS-MS supports the synthesis of compound **85c**.

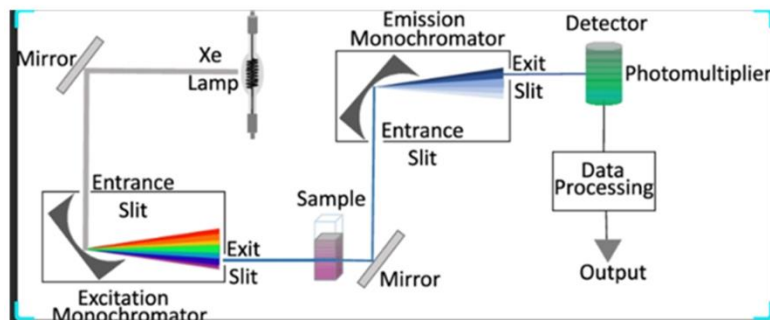
CHAPTER- 5



UV-Visible
spectroscopy

Photophysical
analysis

Fluorescence
spectroscopy



Photophysical analysis

In this segment of chapter 5, a thorough analysis is provided on the photophysical characteristics of recently developed Schiff base conjugated 1,4-disubstituted 1,2,3-triazole derivatives. These attributes were investigated using UV-visible and Fluorescence spectroscopy. The molecules are investigated to identify their ability to chemosense different metal ions

1. Spectroscopic Analysis of **81c**

1.1 U.V-visible spectroscopy analysis of chemosensor **81c**

The newly synthesized compound **81c** have been ornamented with oxygen and nitrogen atoms on its arms. Therefore, the sensor can interact effectively with diverse metal ions. The UV-visible experiment was executed to inspect the sensing ability of the synthesized sensor against different metal ions. Different combinations of the solvent mixture were scrutinized for the selection of the suitable solvent, such as methanol, methanol-water, ethanol, ethanol-water, acetonitrile, and acetonitrile-water for the clear solubility and excellent UV-response of the analyte. Although the implementation of the aqueous medium was imperative for the chemosensing studies, owing to the limited solubility of sensor **81c** in the aqueous medium, the applicability of the organic solvent was inevitable. Considering, the clear solubility of **81c** in EtOH:H₂O (9:1 v/v) and the sharp absorption maxima at 275 nm and 308 nm contemplate the aforementioned solvent as the ‘ideal solvent system’ for the constructive chemosensing response of compound **81c**. Therefore the chemosensing studies of **81c** was carried in EtOH:H₂O (9:1 v/v), the solution of the probe used to detect metal ions and also the solution of metal ions were prepared in the same solvent system to avoid any interference with the results of absorption spectra.

Consequently, metal chloride salts such as Al³⁺, Sr²⁺, Mg²⁺, Co²⁺, Cr³⁺, Hg²⁺, Mn²⁺, Cu²⁺, Fe³⁺, Ce³⁺, Cd²⁺, Ni²⁺, Zn²⁺, Fe²⁺ were investigated for the binding interaction with the designed probe **81c**, none but Fe³⁺ out of the metal ions aforesated showed a selective hyperchromic shift in the absorption spectra contrast to the observed hypochromic shift of remaining metal ions depicting the anomalous behaviour of the ferric ions as compared to other tested metal ions. To ascertain selective binding by sensor **81c**, absorbance titrations were performed with different metal ions solutions of Al³⁺, Sr³⁺, Mg²⁺, Co²⁺, Cr²⁺, Hg²⁺, Mn²⁺, Cu²⁺, Fe³⁺, Ce²⁺, Cd²⁺, Ni²⁺, Zn²⁺, Fe²⁺. The results concluded that there was an insignificant change in intensity enhancement for all metal ions except the Fe³⁺ ions solution which is exhibited in the bar graph (**Figure 81**) thereby confirming strong affinity of **81c** towards ferric ions.

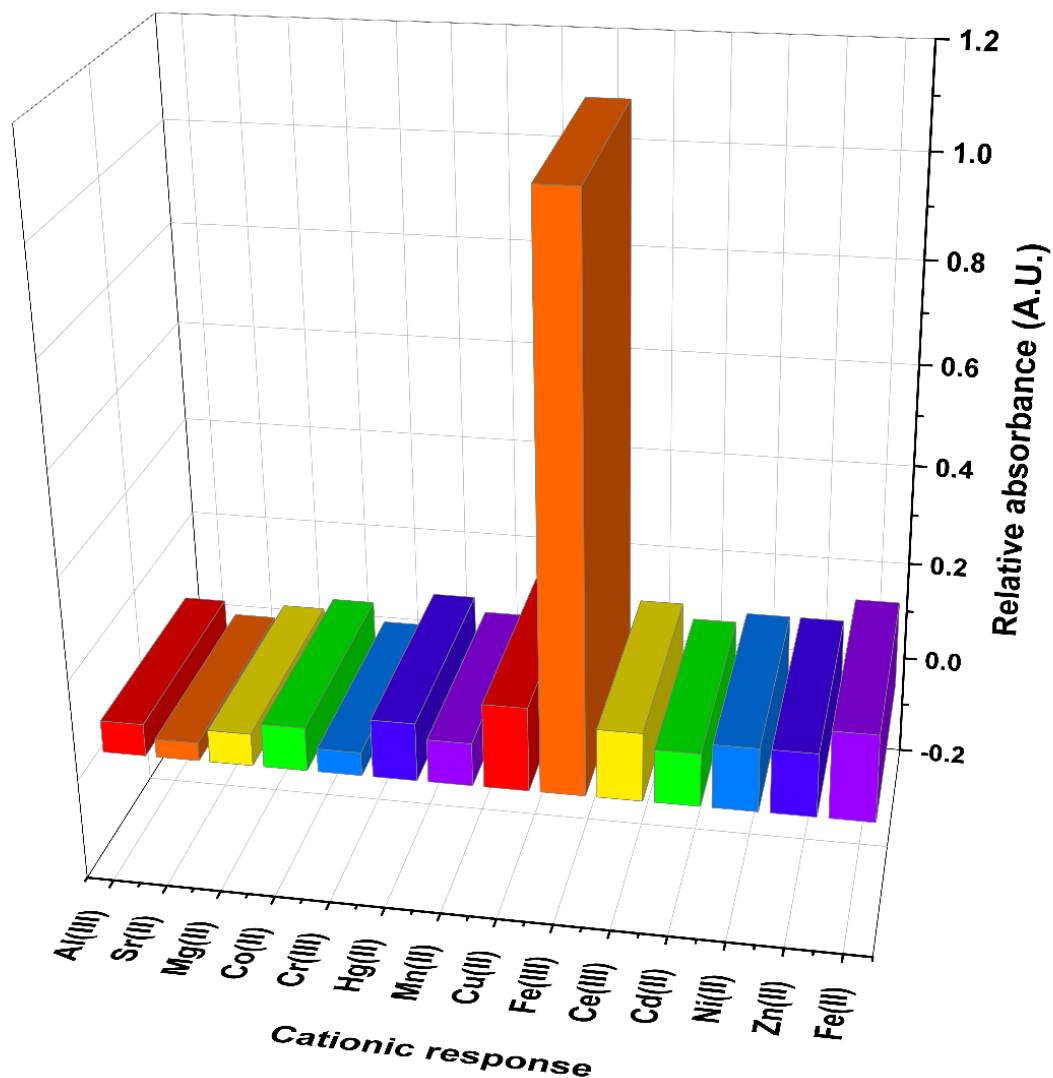


Figure 81. A histogram assessing the response of chemosensor **81c** (0.2 mM) with various competitive metal ions (1 mM) using EtOH:H₂O (9:1 v/v) solvent system, after addition of 10 equiv. of various metal ions added consecutively in **81c** solution. The significant change in relative absorbance of Fe³⁺ was observed as compared to other metal ions

1.2 UV- visible response of chemosensor **81c** towards Fe³⁺

UV-visible titrations were conducted through stepwise addition of 1 equiv. of 1mM of the metal ions solution to the solution of receptor probe (0.2 mM) as shown in **Figure 82** and the spectrum in **Figure 83** displays the correlation between the relative absorption of **81c** with the increase in metal ions concentration from UV-visible data at 275 nm wavelength. The electronic

transitions, like π - π^* and n - π^* manifested two absorptions bands within range 275 nm and 307 nm when titrated against the Fe^{3+} ions. The strong absorption band at 275 nm is exhibited by the analyte **81c** in the UV-visible spectrum in eco-friendly ethanol-aqueous solution (EtOH:H₂O::9:1). A significant change was observed at 275 nm with a noticeable increase in the intensity of the primary peak indicating the binding of the metal ions with the analyte showing the hyperchromic shift in the absorption spectra.

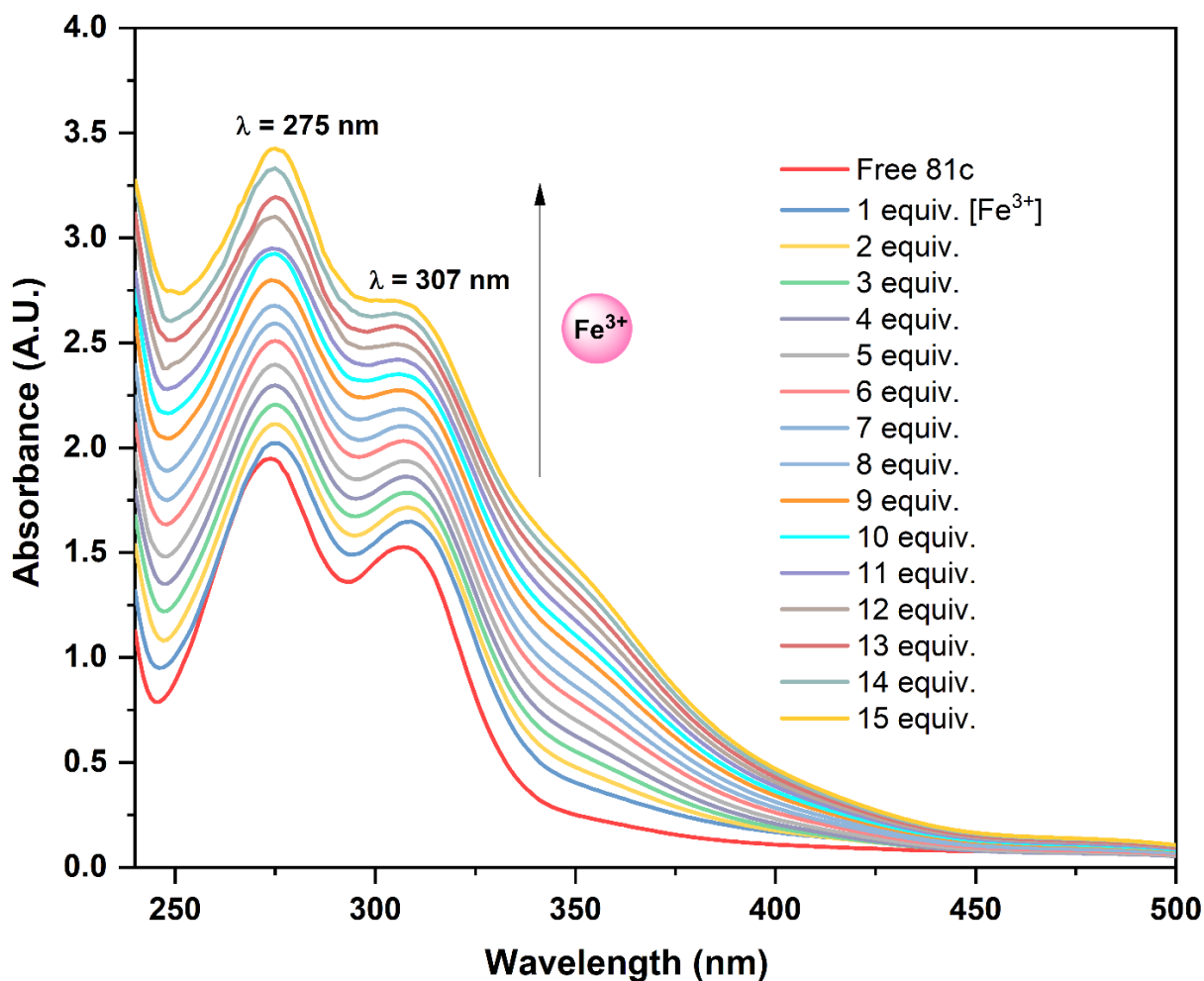


Figure 82. Absorption spectra of the **81c** probe (0.2 mM) upon successive addition of 1 equiv. of Fe^{3+} ions solution (1mM) in EtOH:H₂O (9:1 v/v) solvent system, with each addition of 1 equiv. of Fe^{3+} ions solution in **81c** solution, hyperchromic shift was observed signifying the [**81c**- Fe^{3+}] complexation

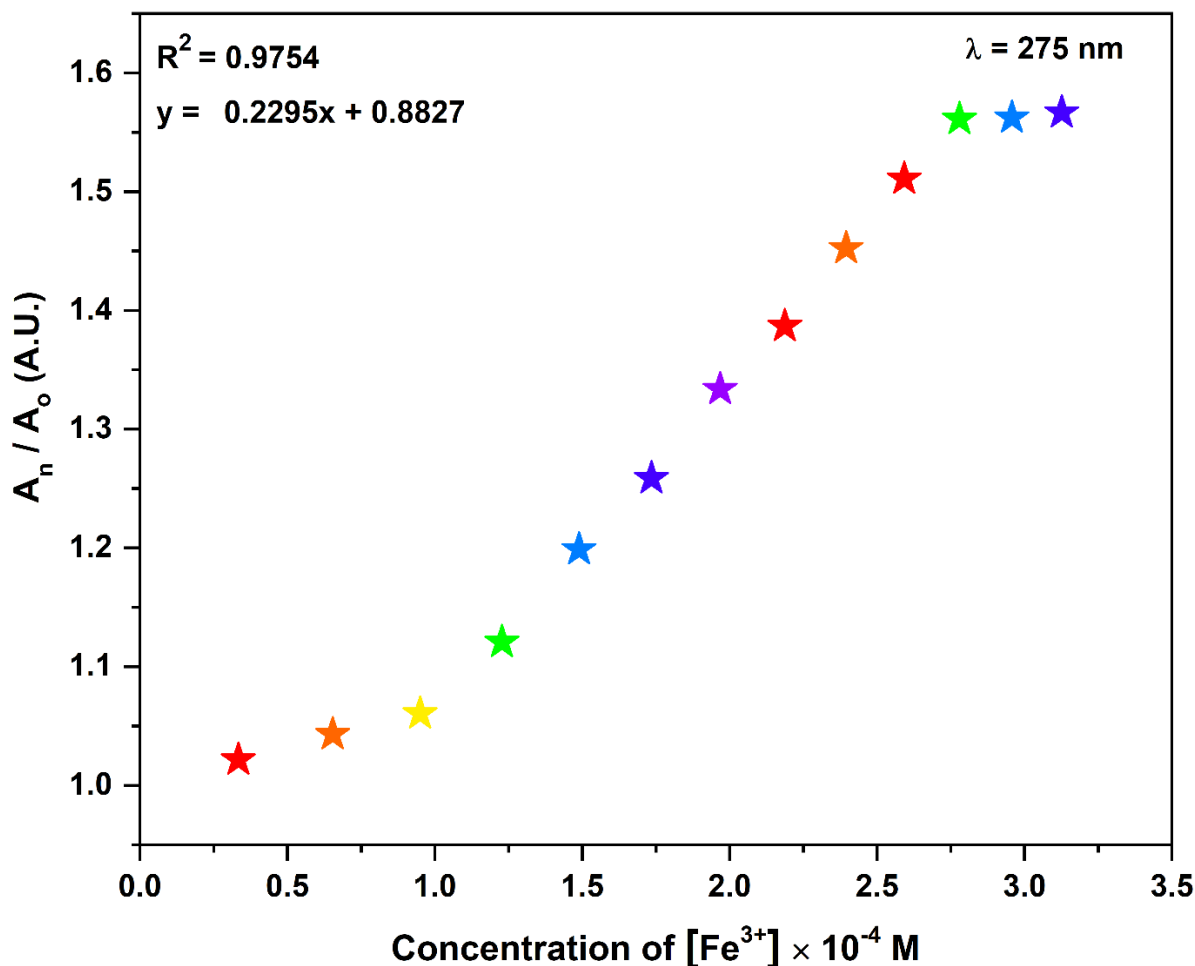


Figure 83. The absorption spectra of probe **81c** were analysed by plotting the relative change in absorption against the sequential addition of Fe^{3+} ions (0-15 equiv.) in DMSO solvent system, wherein the absorbance intensity of probe **81c**, represented by A_o and A_n signify the absorbance intensity after the addition of Fe^{3+} ions solution in the **81c** solution

1.3 Job plot analysis of $[81c-Fe^{3+}]$ complex

Job's plot experiment (the model of continuous variations) was conducted to evaluate the stoichiometry ratio of the metal-ligand complex, by mixing equal concentrations of the host and guest solutions in different ratios. The prepared solutions were kept at room temperature for 1 hour with intermittent shaking. Afterward, the absorption of the mixtures of the various compositions was recorded from UV-visible data at 275 nm. The concentration of the complex i.e., $[81c+Fe^{3+}]$ was determined following the equation $[81c+Fe^{3+}] = \Delta A \cdot X$ where ΔA indicates the relative absorption intensity and X is the mole fraction of $[81c] / [81c+Fe^{3+}]$ as shown in **Figure 84**. The

stoichiometry ratio of the complex is shown by the mole fraction of $[81c]/[81c+Fe^{3+}]$ at which the concentration of the host-guest complex reaches maximum from the graph. Consequently, the binding ratio from the recorded graph indicates Fe^{3+} consistent with (2:1) stoichiometry with **81c**.

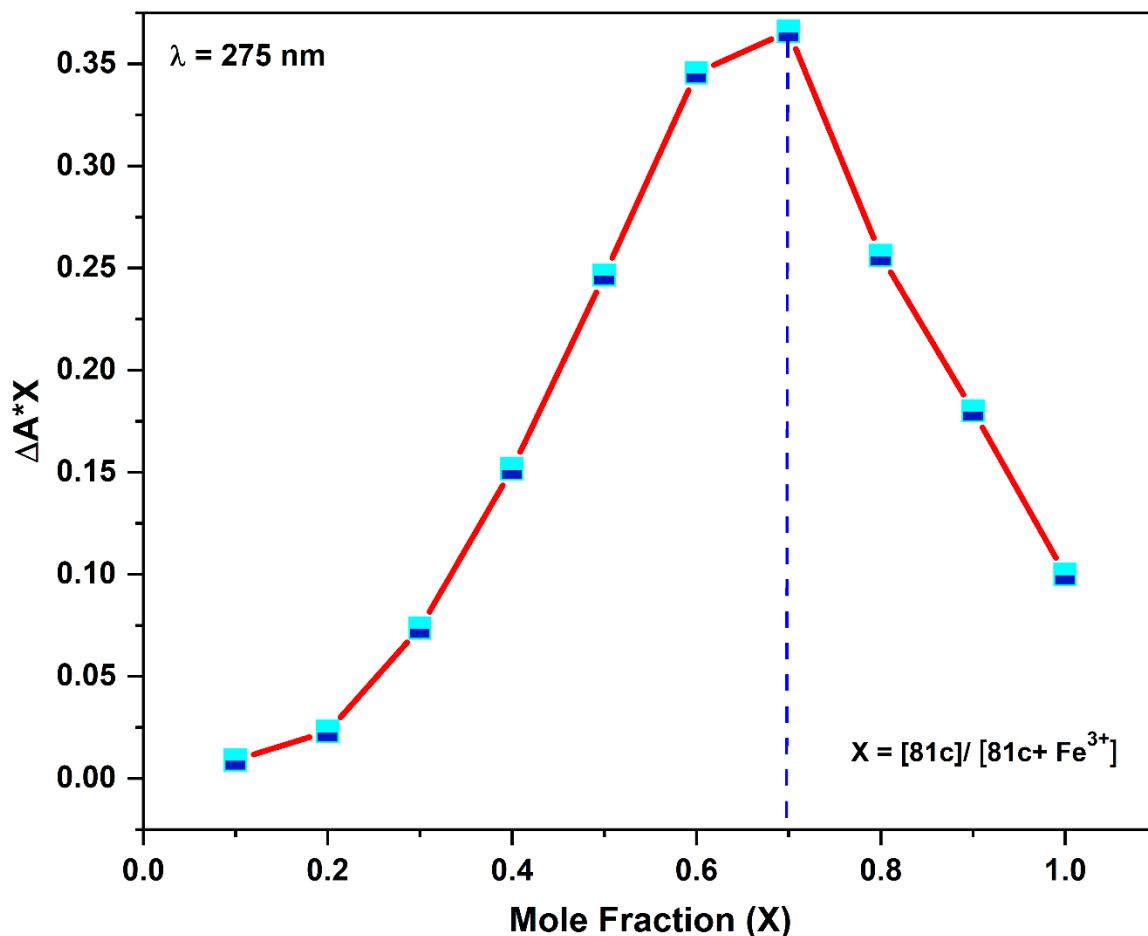


Figure 84. Job's plot from the absorbance spectrum of chemosensor **81c** and Fe^{3+} ions in EtOH:H₂O (9:1, v/v) solvent system, the mole fraction of **81c** plotted against relative absorption shows maximum absorbance above 6 mole fraction depicting the stoichiometric ratio (1:2) of $[81c+Fe^{3+}]$ complex

1.4 Competitive metal ions titrations of **81c**

The ability of various potential metal ions sensors to preferentially detect metal ions selectively regardless of other competing metal ions is a crucial and desired feature in the practical applicability of the chemosensors. To investigate chemosensor **81c** as Fe^{3+} ions selective sensor, competitive metal ions titrations were performed with 0.2 mM probe solution in EtOH:H₂O (9:1 v/v) binary solvent system comprising an equimolar mixture of variant metal ions. (**Figure 85**)

The UV-visible spectrum recorded remains unaltered and nearly identical to [**81c**-Fe³⁺] spectra, indicating the uniqueness of the newly constructed chemosensor **81c** for non-interfering sensing of Fe³⁺ metal ions.

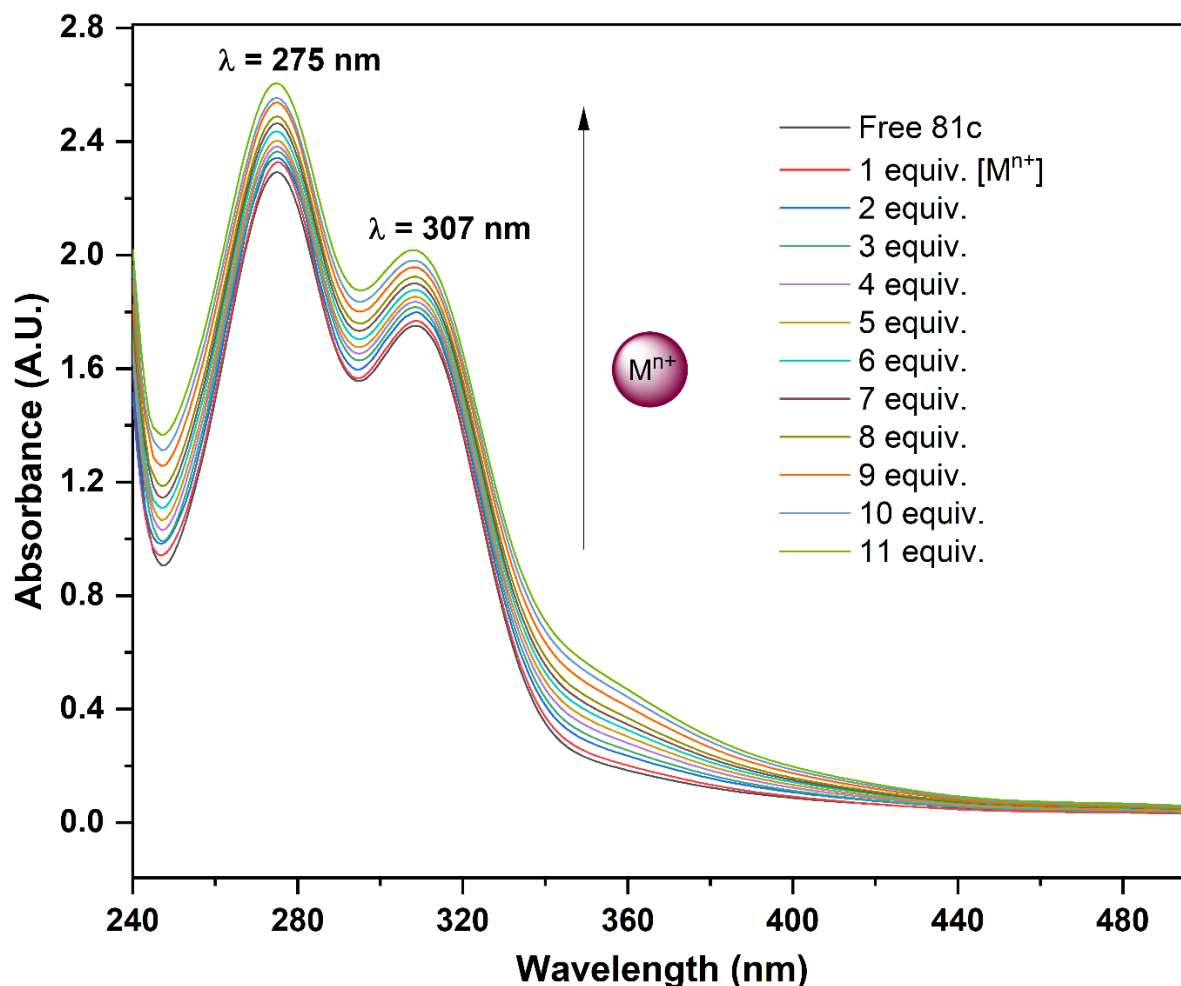


Figure 85. UV-vis spectra of chemosensor **81c** (0.2 mM) in EtOH:H₂O (9:1, v/v) demonstrating selective binding of Fe³⁺ ions in equimolar concentration of multiple metal ions; where Mⁿ⁺ represents the mixture of metal ions i.e. equiv. of (Al³⁺, Sr³⁺, Mg²⁺, Co²⁺, Cr²⁺, Hg²⁺, Mn²⁺, Cu²⁺, Fe³⁺, Ce²⁺, Cd²⁺, Ni²⁺, Zn²⁺, Fe²⁺) showing the dominance of Fe³⁺ binding with **81c** even in presence of other metal ions

1.5 B-H plot of [**81c**-Fe³⁺] complex

The binding efficiency of the metal-ligand complex is a vital practical parameter and thus the association constant (K_a) value was evaluated using the Benesi-Hildebrand plot applying the equation:

$$\frac{1}{A-A_0} = \frac{1}{A'-A_0} + \frac{1}{K_a (A'-A_0)[M^{n+}]} \quad (1)$$

wherein, A_0 = absorbance of the synthesized probe without metal, A = absorbance with specific conc. of metal ions, A' = absorbance of the fully formed complex at maximum conc. of metal, K_a = binding constant, M = specific concentration of the metal ion. The binding constant value was calculated from the graphical method and obtained as $2.6 \times 10^4 \text{ M}^{-1}$ (**Figure 86**) with a correlation coefficient ($R^2 = 0.9754$) disclosing a satisfactory association ability of the chemosensor with the ferric metal ion. Additionally, the B-H plot verifies the stability between the sensor and the metal ion depending upon their association constant values.

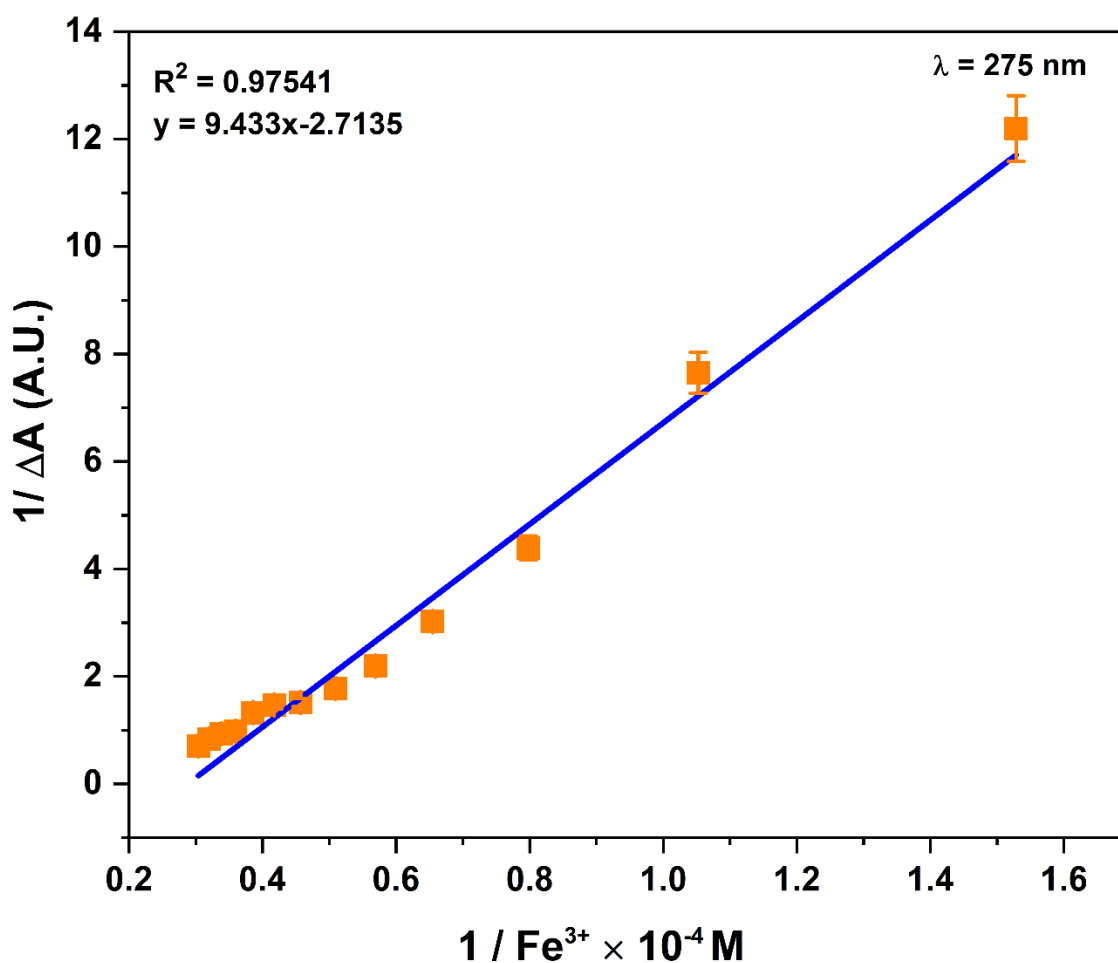


Figure 86. Absorption titration data of the synthesized probe with Fe^{3+} for the record of B-H plot at absorption intensity monitored at 275 nm in EtOH:H₂O (9:1, v/v) solvent system

The quick response time is a necessity for a reliable chemosensor probe. To investigate the effect of reaction time on the metal-ligand binding, the time-dependent experiment was anticipated. The study was conducted in the EtOH:H₂O (9:1,v/v) solvent medium comprising Ferric ions and the synthesized probe as indicated in **Figure 87**, the graph was plotted between absorption V/s time shows the intensity of the target chemosensor reached the constant value confirms the metal-ligand complex formation. The data depicted the enhancement in the intensity of the **81c** ceased after binding and the constant absorption values were attained showing the rational response time of the synthesized chemosensor **81c**.

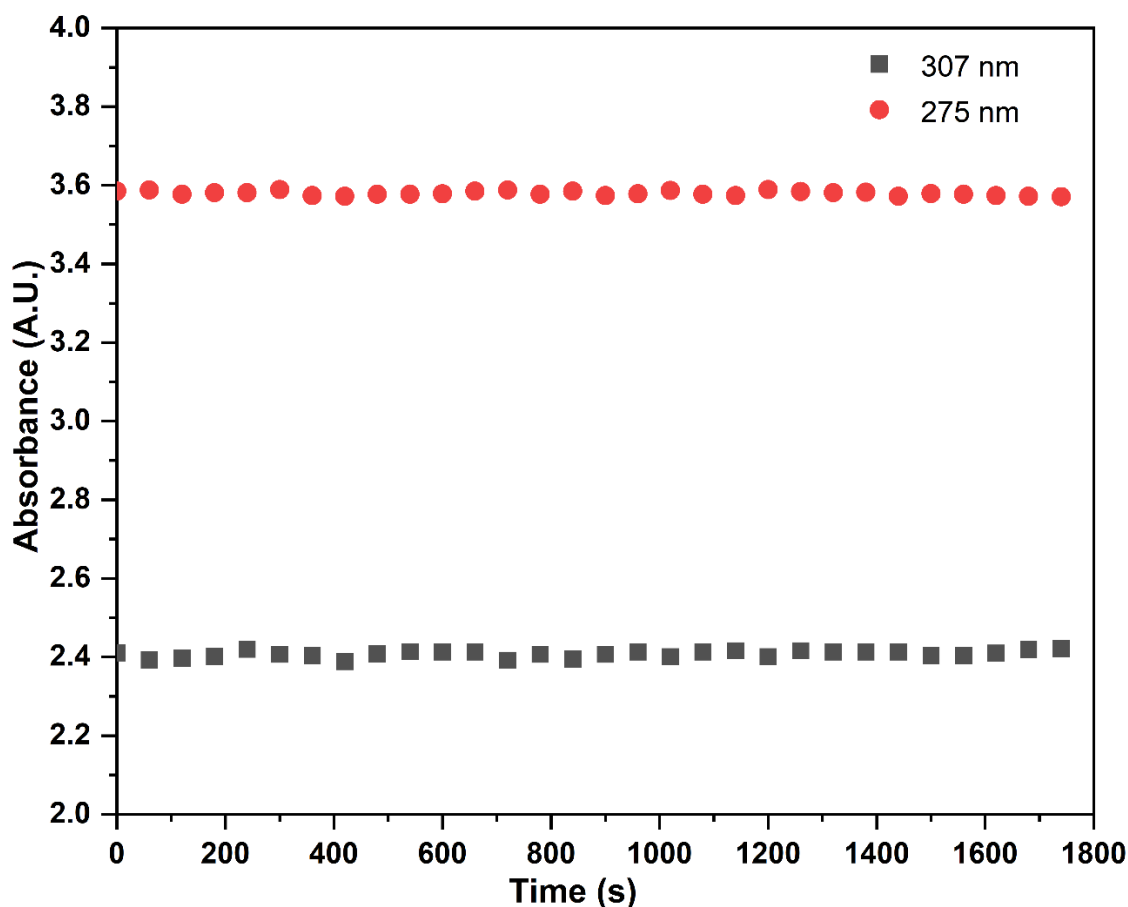


Figure 87. Time dependent profile versus absorption of the [Fe³⁺-**81c**] complex in EtOH:H₂O (9:1, v/v) solvent system for 30 minutes

Furthermore, temperature-dependent experiment was carried out within a certain temperature range to investigate the effect of temperature on the metal-ligand interaction. The absorption values were recorded with progressive increase of 2 °C as the temperature from 30 °C

to 52 °C. The acquired data was plotted and is shown as **Figure 88**, illustrating the enhanced absorption resulting from a temperature increase.

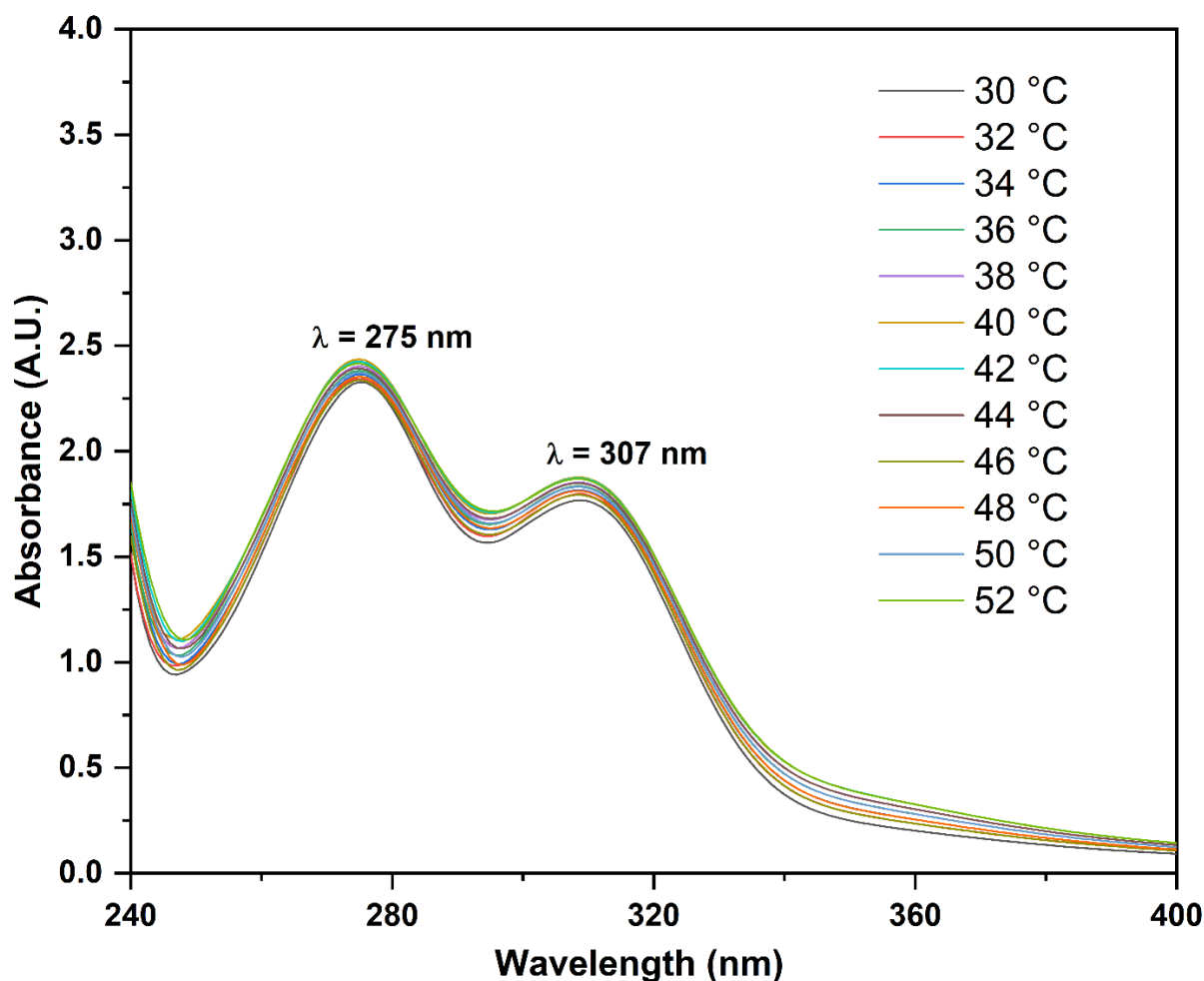


Figure 88. Temperature dependent study of the $[\text{Fe}^{3+}\text{-81c}]$ complex in EtOH:H₂O (9:1, v/v) solvent system from 30 °C to 52 °C

1.7 Fluorescence analysis of chemosensor **81c**

Chemosensor **81c** was developed specifically to detect ecologically significant cations via fluorescence spectroscopy. Fluorescence spectra of the compound **81c** was recorded in (EtOH:H₂O::9:1) solvent medium and upon excitation at $\lambda_{\text{ex}} = 290 \text{ nm}$ the probe (0.02 mM) displayed fluorescence emission at $\lambda_{\text{em}} = 346 \text{ nm}$. The fluorescence data exhibited a significant increase in the fluorescence emission of sensor **81c** only in response to Fe^{3+} (0.1 mM) metal ions. (**Figure 89**) The considerable rise in the relative emission intensity of probe **81c** when exposed to

Fe^{3+} may be ascribed to the inhibition of PET mechanism. The weak fluorescence response of the probe **81c** was due to PET mechanism and with the addition of Fe^{3+} ions solution (0-16 equiv.), there was enhanced fluorescent intensity due to CHEF mechanism, accompanied by the inhibition of PET mechanism in (EtOH:H₂O::9:1) solvent system.

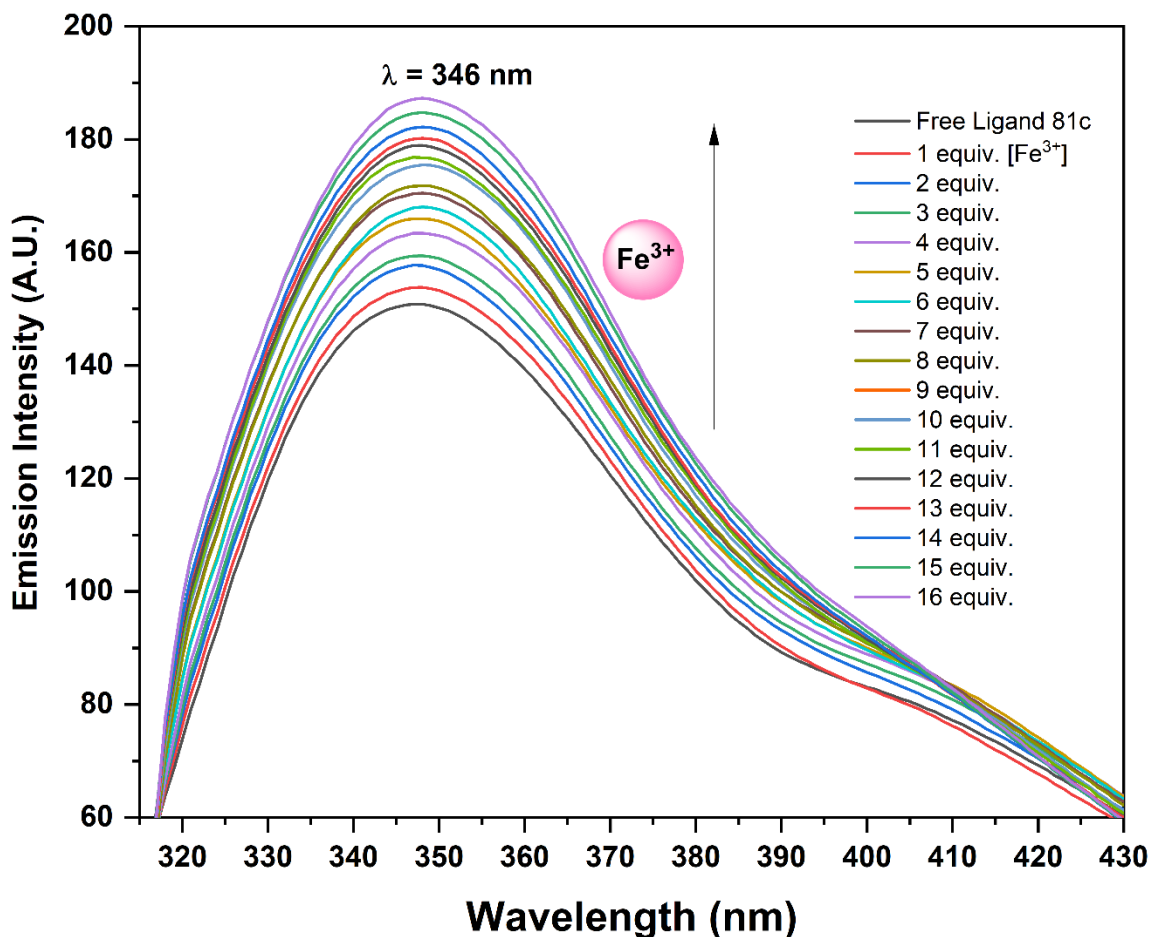


Figure 89. The fluorescence titration spectra of probe **81c** (0.02 mM) at $\lambda_{\text{max}} = 346$ nm in (EtOH:H₂O::9:1) solvent medium at 25 °C with incremental addition of 1 equiv. of Fe^{3+} ions in **81c** solution shows noticeable increase in intensity (hyperchromic shift) depicting chelation of $[\text{Fe}^{3+}\text{-81c}]$ complex

Moreover, **figure 9** shows a rise in the emission intensity ratio I_0/I , where I_0 represents the emission intensity of sensor **81c** in the absence of Fe^{3+} ions and I represents the emission intensity after **81c** bound with Fe^{3+} ions, with each successive addition.

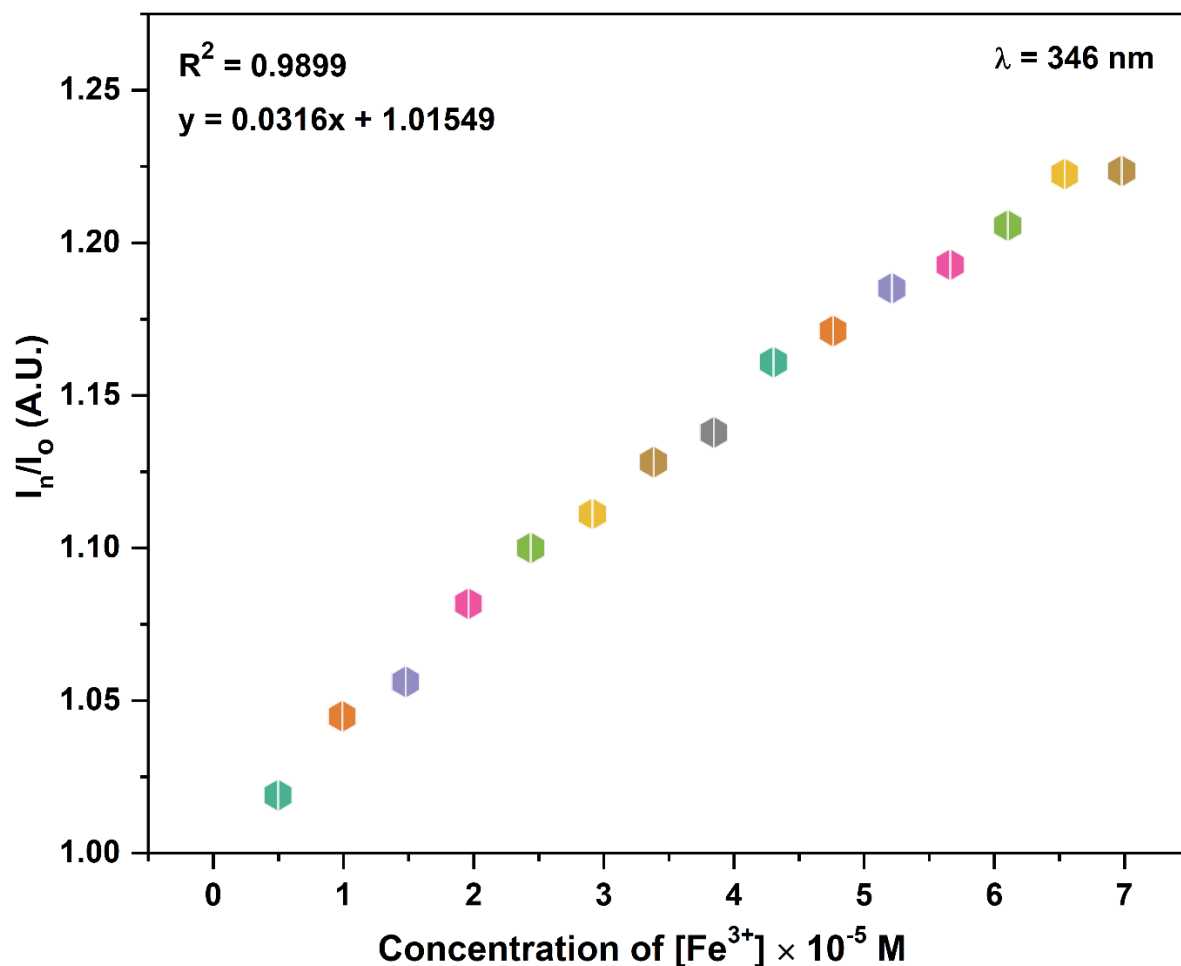


Figure 90. The emission spectra showing relative change in intensity (I_n/I_o) at $\lambda_{\text{em}} = 346 \text{ nm}$ plotted against concentration of Fe^{3+} metal ions in (EtOH:H₂O::9:1) solvent media. The fluorescence intensity of probe **81c** in the absence of Fe^{3+} is represented by I_o , and I_n denote the fluorescence intensity during the binding of **81c** with Fe^{3+} ions solution

1.8 Limit of Detection of (81c- Fe^{3+}) complex

The limit of detection is a crucial variable in chemosensing so, the linear calibration curve was employed for investigating the limit of detection from of the synthesized probe for Fe^{3+} metal ions from the equation:

$$\text{Limit of Detection} = \frac{3\sigma}{K} \quad (2)$$

where (σ) = standard deviation, K = slope of the graph. The graphical data was abstracted by plotting the concentration of Fe^{3+} on the X-axis versus the relative intensity $(I_o - I_n)/I_o$ on the Y-axis. The value of the Limit of detection was established as 1.3×10^{-7} M from the linear calibration curve by evaluating the standard deviation (σ) and the slope from the graph. (**Figure 91**) Limit of quantification was evaluated from the following equation (3) for the newly designed triazole derivative and found to be 4.5×10^{-6} M

$$\text{Limit of quantification} = 10\sigma/K \quad (3)$$

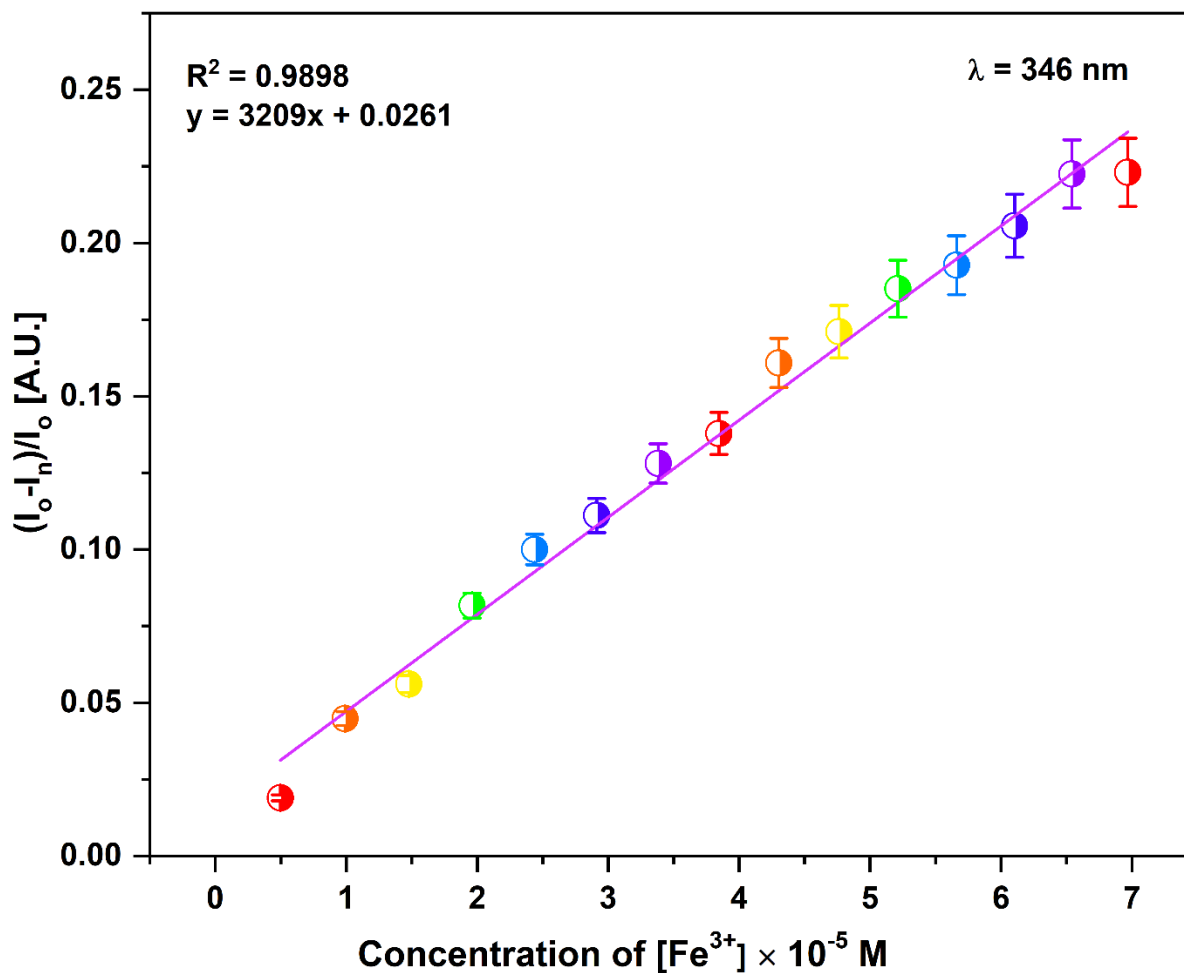


Figure 91. A linear calibration curve showing the relative absorbance $(I_o - I_n)/I_o$ at different $[\text{Fe}^{3+}]$ ions concentrations in (EtOH:H₂O::9:1) solvent media, wherein I_o = emission intensity of probe **81c** in absence of Fe^{3+} ions and I_n = emission intensity observed with each addition of Hg^{2+} solution in **81c** solution

1.8 A proposed mechanism for the synthesized probe **81c**

CuAAC 'Click' reaction yielding 1,2,3-triazole framework loaded with nitrogen atoms coordinate effectively with Fe^{3+} ions. Schiff base moiety equipped with oxygen atoms contributes as additional binding site with the ionic species assisting the binding of Fe^{3+} ions to the sensor **81c**. The prior research on the chemosensing of ferric ions revealed a few ligands containing nitrogen and oxygen atoms as donor sites that bind with Fe^{3+} ions stably.¹ The single crystals of the 2:1 [**81c**- Fe^{3+}] complex could not be generated after repeated attempts. However, the relative change in absorption recorded during UV-visible titrations performed resulted with an increase in the concentration of Fe^{3+} ions, confirming a 2:1 stoichiometry of ligand with the metal. The Fe^{3+} ions can incorporate itself by binding with N-atoms of the heterocycle 1,2,3-triazole ring, the O-atom of the methoxy group, and the oxygen atom linked within close vicinity with the triazole ring. (Figure 92) Thereafter, considering the six coordinating sites of the detected metal ions, the ligand coordination mode often can bind with the methoxy O donor site, following a homoleptic approach of (-O,O,N-) donor arm towards Fe^{3+} in stabilizing the metal-ligand complex, as a sandwich structure²⁻⁴

The plausible mode of interaction amongst **81c** and Fe^{3+} has been validated using FTIR spectroscopy analysis. In the IR spectra of **81c** with Fe^{3+} , the distinctive peak of the (-C-N) group of 1,2,3-triazole ring shifts from 1263 cm^{-1} to 1276 cm^{-1} respectively, which may be attributed to its coordination with this group. Furthermore, the shift in vibrations in area of 1120 cm^{-1} to 1139 cm^{-1} shows that oxygen atoms play a significant role in binding.

The LCMS-MS analysis of the complex [**81c**- Fe^{3+}] was also conducted. The anticipated mass spectrum m/z of [**81c**-**81c**- Fe^{3+}] calculated as 880.22 appeared at $m/z = 881.22$ [$M + 1$]. The m/z value aligns strongly with the postulated stoichiometry.

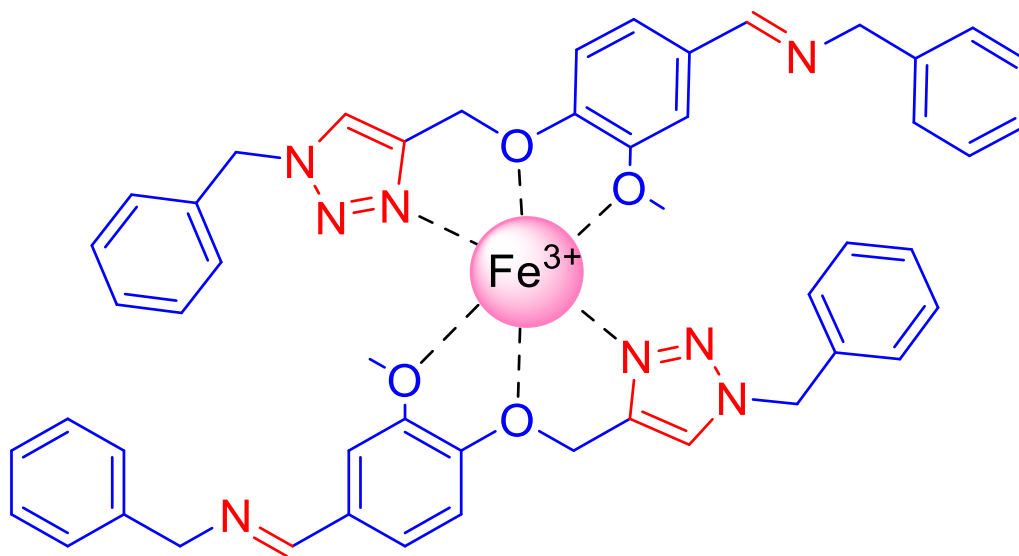


Figure 92. Binding mode of the synthesized compound **81c** with Fe^{3+} metal ion showing Fe^{3+} sandwiched between ligand molecules as 2:1 (**81c**- Fe^{3+}) stoichiometric ratio in (EtOH:H₂O::9:1) solvent media

2. Spectral analysis of chemosensor **82c**

2.1 UV-visible spectroscopic studies of **82c**

Schiff based functionalized 1,2,3-triazole **82c** (0.05 mM) was explored for the chemosensing behavior of the ligand via UV-visible studies. The choice of the solvent was determined on the basis of fine spectrum and solubility observed in various solvents such as methanol, ethanol, acetonitrile and DMSO. The clear solubility of the probe **82c** in DMSO solvent, associated with significant intense absorption peaks at 276 and 311 nm leads to the selection of DMSO as the solvent system. The studies of UV-vis interaction of receptor **82c** in DMSO were conducted against environmentally relevant cations such as Al^{3+} , Sr^{2+} , Hg^{2+} , Mg^{2+} , Cr^{3+} , Ni^{2+} , Pb^{2+} , Mn^{2+} , Ca^{2+} , Ba^{2+} , Co^{2+} , and Zn^{2+} indicating a selective response of probe **82c** towards Pb^{2+} metal ions. The bar graph depicted the binding capacity of the developed probe towards various metal ions in **Figure 93**. However, no substantial effect on the absorption spectra in the presence of other competitive metal ions was observed.

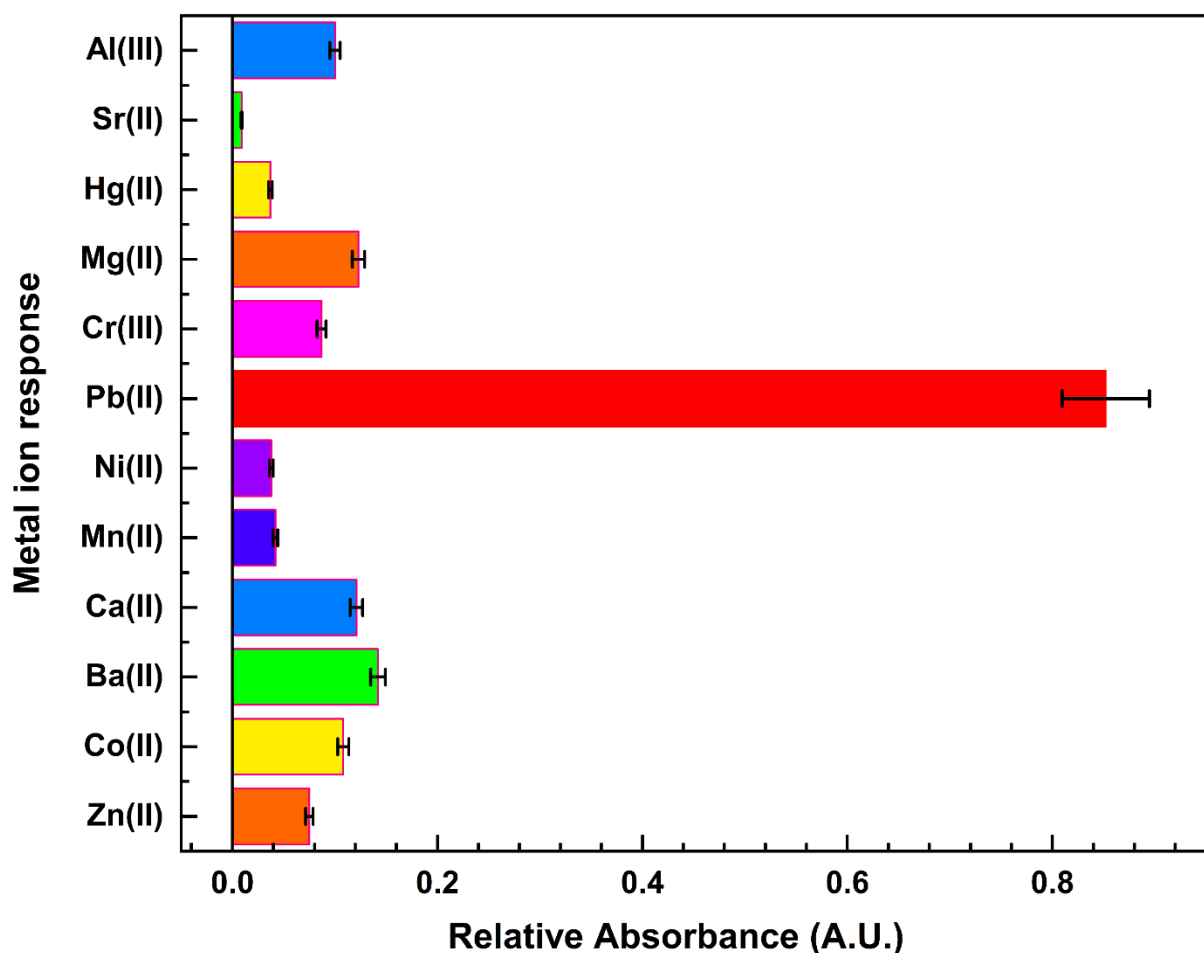


Figure 93. The change in absorption spectra of probe **82c** (0.05 mM) upon addition of 10 equiv. of different metal ions solutions in DMSO

The variations in the UV-vis absorption spectrum of sensor **82c** in DMSO owing to the sequential addition of Pb^{2+} ions were depicted in **Figure 94**. When 1 equiv. of Pb^{2+} ions solution was added to ligand **82c** solution, absorbance bands at 276 nm and 311 nm were observed due to $\pi\text{-}\pi^*$ and $n\text{-}\pi^*$ electronic transitions. With increasing the Pb^{2+} ions concentration from 0.16 mM to 0.23 mM the absorption maxima at 276 nm shifted to wavelength value of 268 nm, resulting in an 8 nm hypsochromic shift and confirming the complexation between the analyte **82c** and Pb^{2+} ions, this was further supported by the presence of distinct isosbestic point at 284 nm. This extraordinary response of receptor **82c** with Pb^{2+} ions in contrast to other metal ions demonstrates their sensitivity and selectivity for the cationic detection.

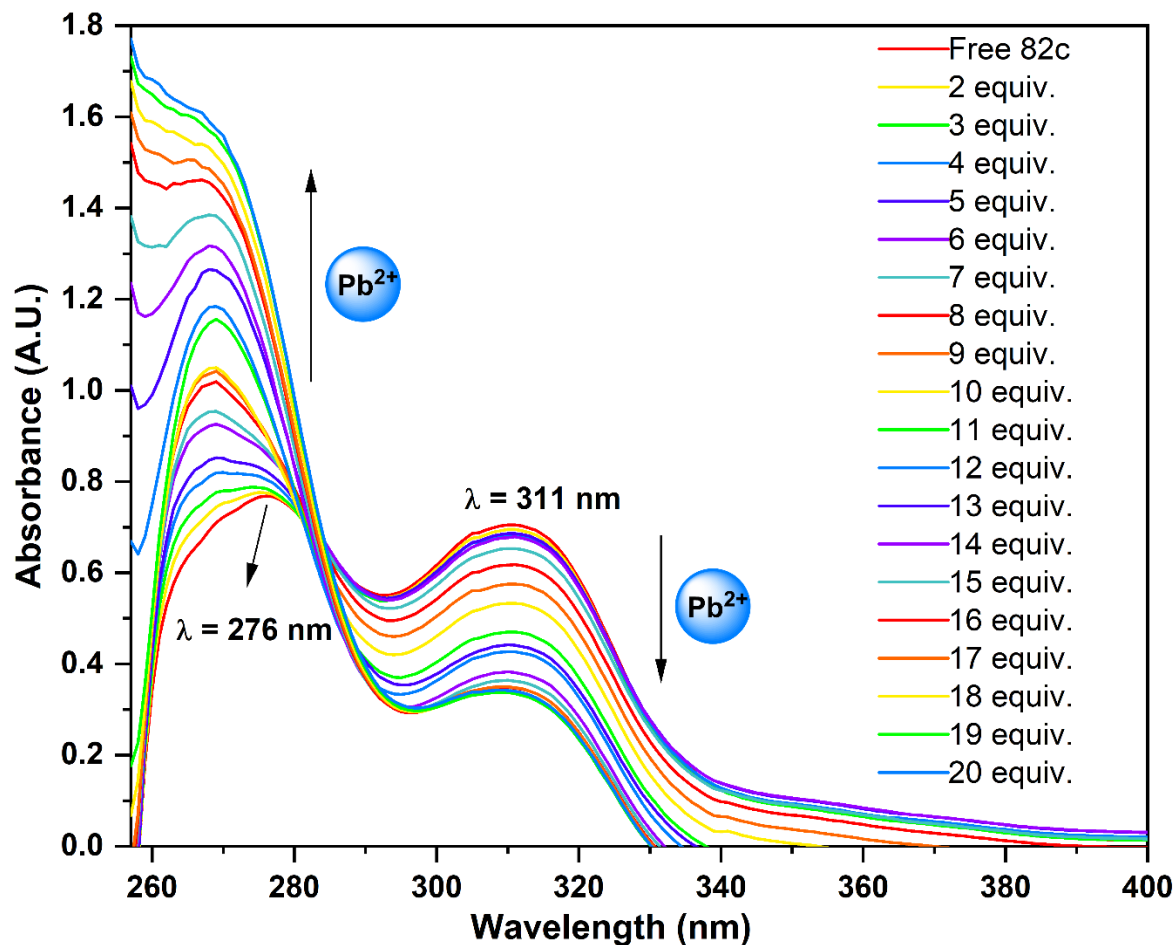


Figure 94. UV-vis spectrum of probe **82c** (0.05 mM) with sequential addition of 1 equiv. of Pb²⁺ ions (1 mM) using DMSO as solvent system displaying increase in intensity (hyperchromic shift) at $\lambda_{\text{max}} = 276$ nm, confirming the binding of [**82c**-Pb²⁺] complex

Figure 95 depicts the correlation between the variation in absorbance maxima (A_n/A_o) and the molar ions concentration at $\lambda_{\text{max}} = 276$ nm, while the concentration of Pb²⁺ ions is incrementally raised. In this context, A_n refers to the absorbance maxima obtained after each addition of Pb²⁺ ions, whereas A_o represents the absorbance maxima observed for **82c** in DMSO solvent system.

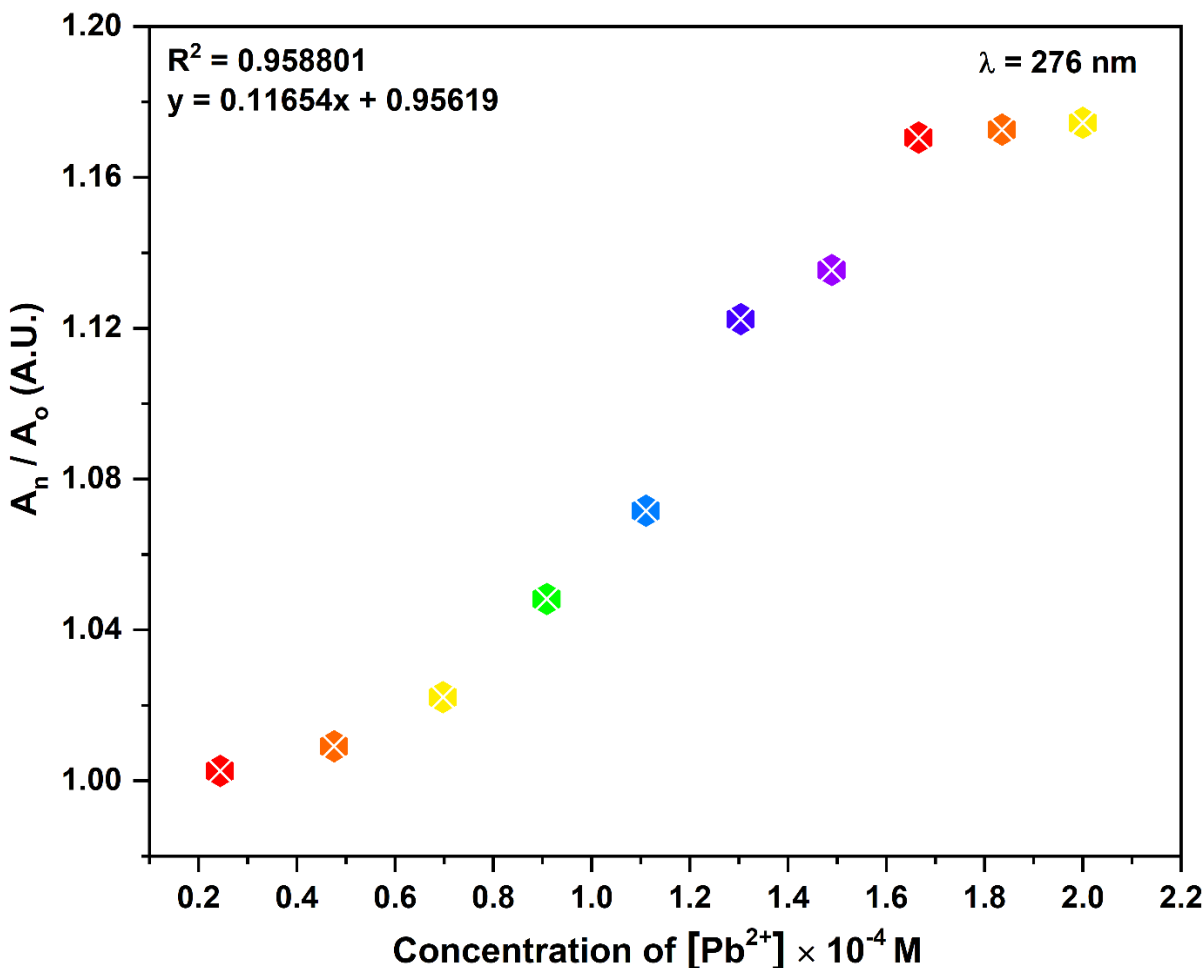


Figure 95. The relative change in absorption spectra of probe **82c** plotted against sequential addition of Pb^{2+} ions fluctuating from 0.16 mM to 0.23 mM in DMSO solvent system, wherein A_o represent the absorbance intensity of probe **81c** and A_n signifies the absorbance intensity after the addition of Pb^{2+} ions solutions in **81c** solution

2.2 Job's plot of chemosensor $[82c-Pb^{2+}]$ complex

The stoichiometric ratio of the metal-ligand binding was determined from UV- visible absorbance data at 276 nm using a model of continuous variations. The Job's plot experiment was conducted for probe $[82c-Pb^{2+}]$ complex similarly, as mentioned in the **section 1.3**. In order to verify the complex's stoichiometry, the graph was plotted with the molar fraction of Probe **82c** on x-axis against $\Delta A \times X$ concentration on y-axis, as shown in **Figure 96**. Furthermore, the binding ratio for the host-guest complex from the job plot was subjected to be 1:2 (Metal-ligand).

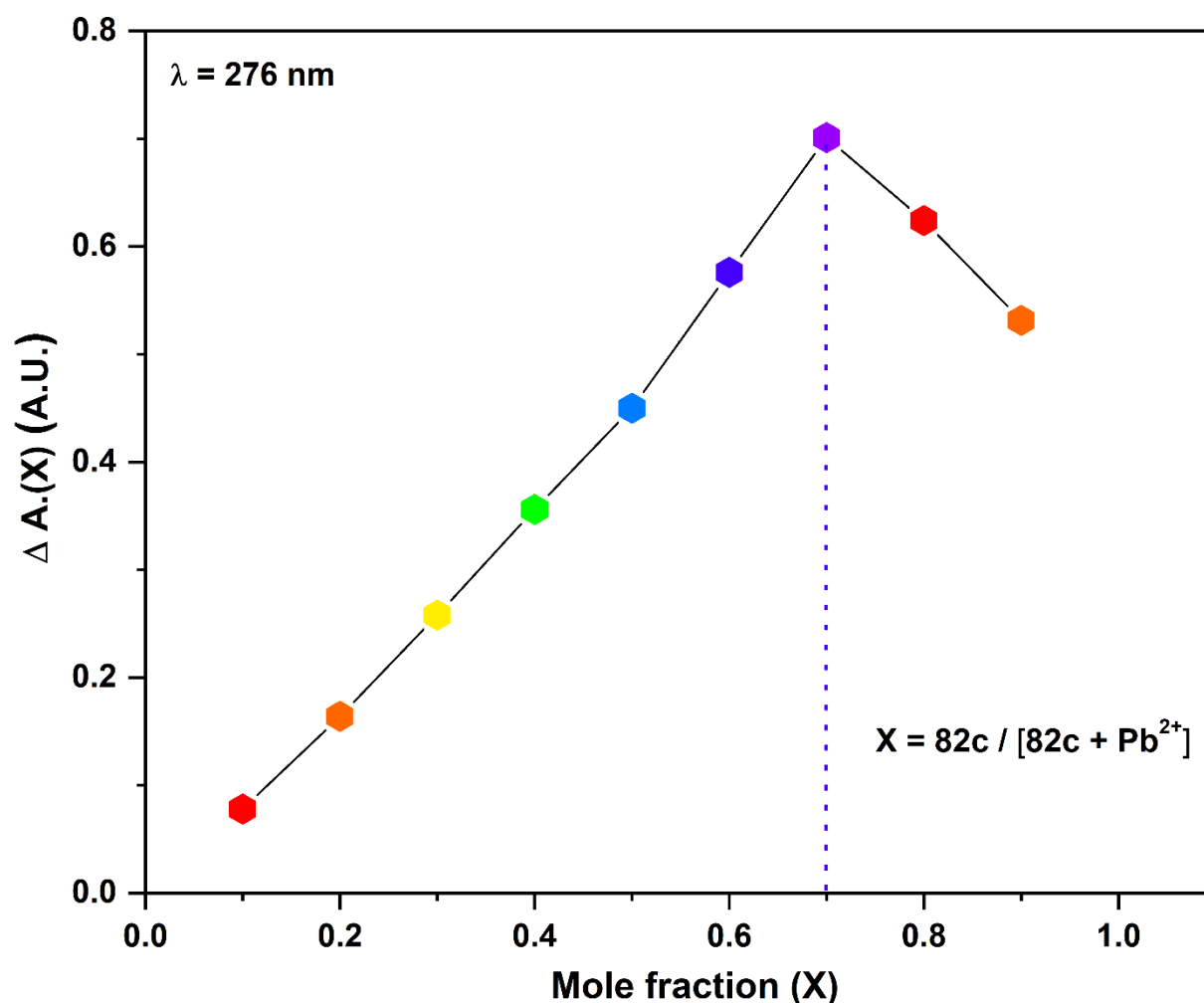


Figure 96. Job's plot assessing stoichiometric ratio of $[82\mathbf{c}\text{--Pb}^{2+}]$ complex showing $\Delta A.X$ v/s mole fraction (X) in DMSO solvent system, the relative absorption (y-axis) shows maximum absorbance at 0.7 mole fraction depicting (2:1) binding ratio $[82\mathbf{c}\text{--Pb}^{2+}]$ complex

2.3 Competitive metal ion titrations of chemosensor **82c**

The competitive metal ions titration was also conducted with the synthesized probe **82c** comprising of an equimolar mixture of Al^{3+} , Sr^{2+} , Hg^{2+} , Mg^{2+} , Cr^{3+} , Ni^{2+} , Pb^{2+} , Mn^{2+} , Ca^{2+} , Ba^{2+} , Co^{2+} , and Zn^{2+} metal ions. The UV-visible spectrum recorded was remarkably close to the spectrogram of Pb^{2+} ions, the absorption intensity $[(82\mathbf{c} + \text{Pb}^{2+}) + \text{M}^{n+}]$ was unaltered and almost similar to $\{82\mathbf{c} + \text{Pb}^{2+}\}$ demonstrating the peculiarity of newly developed chemosensor **82c** for the non-interfering sensing of Pb^{2+} metal ions as shown in **Figure 97**. Thus, we reached the conclusion that the developed chemo-sensor **82c** is highly selective towards lead metal ions without

interacting with any other metal ions. Thus, we reached the conclusion that the developed chemosensor **82c** is highly selective towards Pb^{2+} metal ions without interacting with any other metal ions.

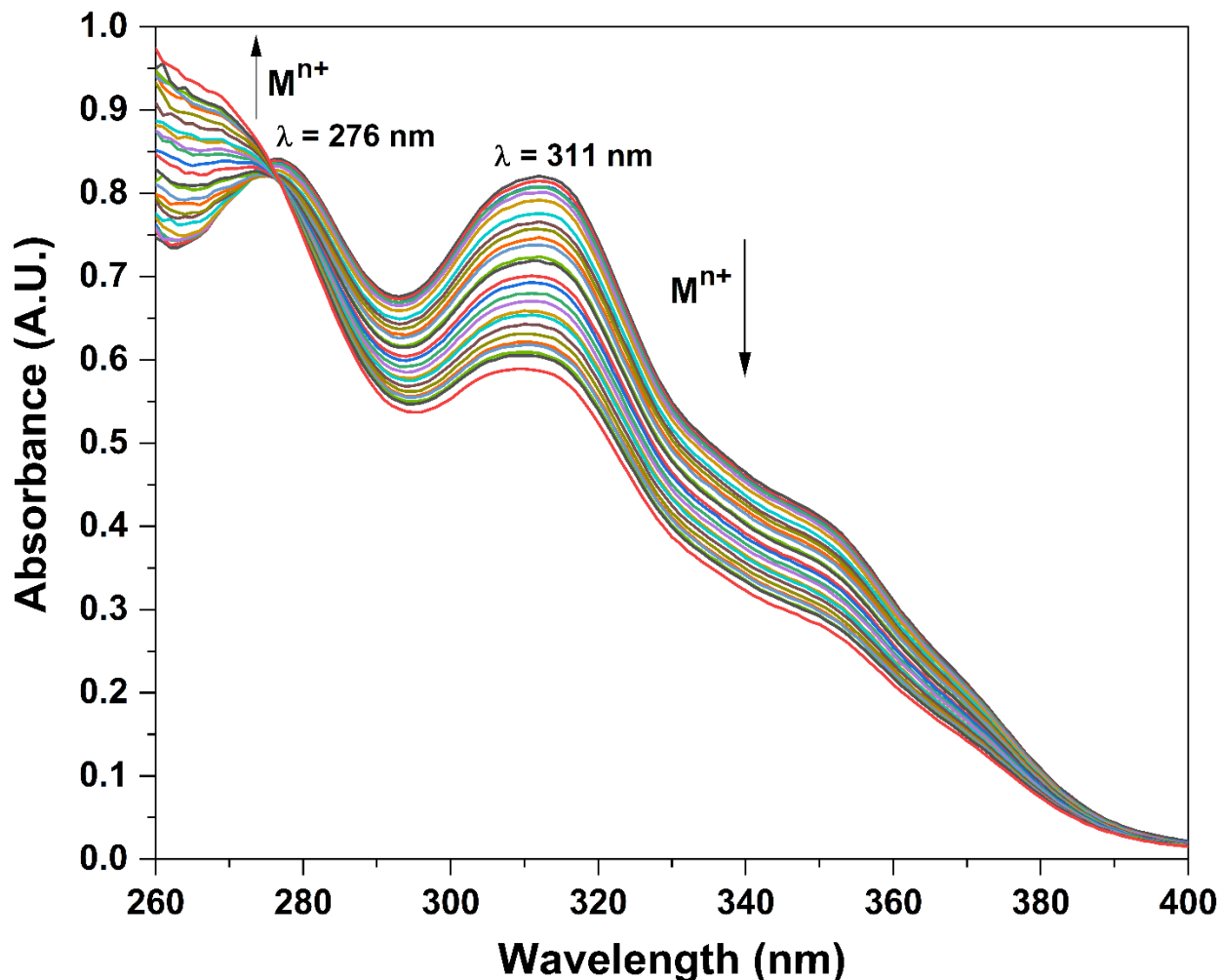


Figure 97. UV-vis spectra of probe **82c** (0.05 mM) in DMSO illustrating selective binding of Pb^{2+} ions among equimolar concentration of mixture of metal ions such as Al^{3+} , Sr^{2+} , Hg^{2+} , Mg^{2+} , Cr^{3+} , Ni^{2+} , Pb^{2+} , Mn^{2+} , Ca^{2+} , Ba^{2+} , Co^{2+} , and Zn^{2+} , where M^{n+} represent the mixture of metal ions

2.4 Time bound and temperature dependent study of $[\text{Pb}^{2+}\text{-82c}]$ complex

Efficiency is crucial when it comes to the practical application of chemosensors. Therefore, time-dependent experiment was conducted to investigate how the reaction time affects the interaction of metal-ligand complex. The experiment was conducted for 30 minutes to determine the impact of time on the interaction between chemosensor **82c** and copper ions.

The results, shown in **Figure 98**, indicate that the absorbance of the chemosensor **82c** reached a constant value, indicating a strong chelation of probe **82c** with lead ions.

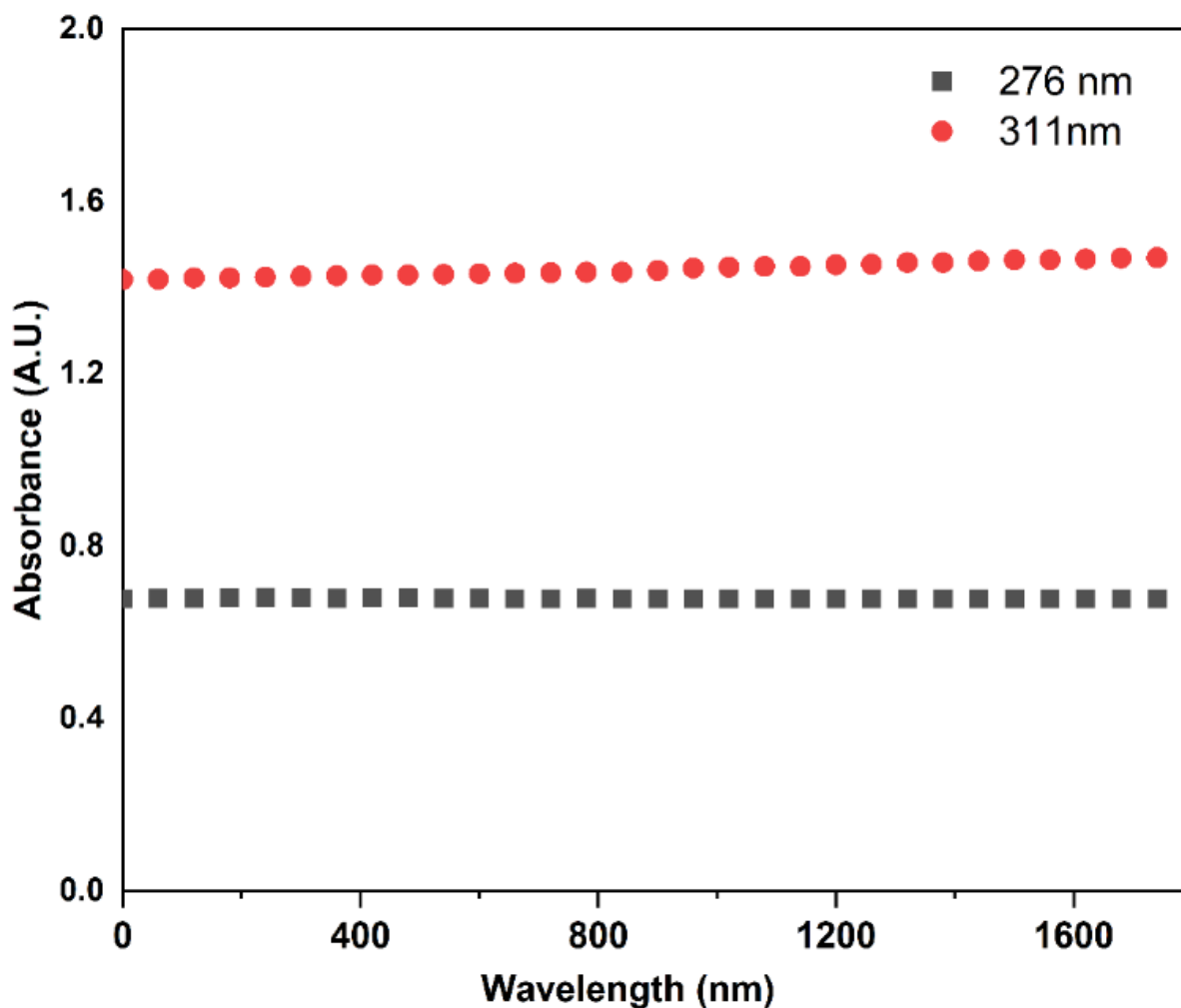


Figure 98. Time bound study of [**82c**–Pb²⁺] complex in DMSO solvent system examined for 30 minutes at $\lambda = 276$ and 311

Furthermore, the temperature-dependent analysis was performed within a defined temperature range to assess the impact of temperature on the interaction between the metal and ligand. The absorption spectra were measured at regular intervals as the temperature increased from 32 °C to 44 °C. The acquired data is shown graphically in **Figure 99**, illustrating the enhanced absorption resulting from a temperature rise.

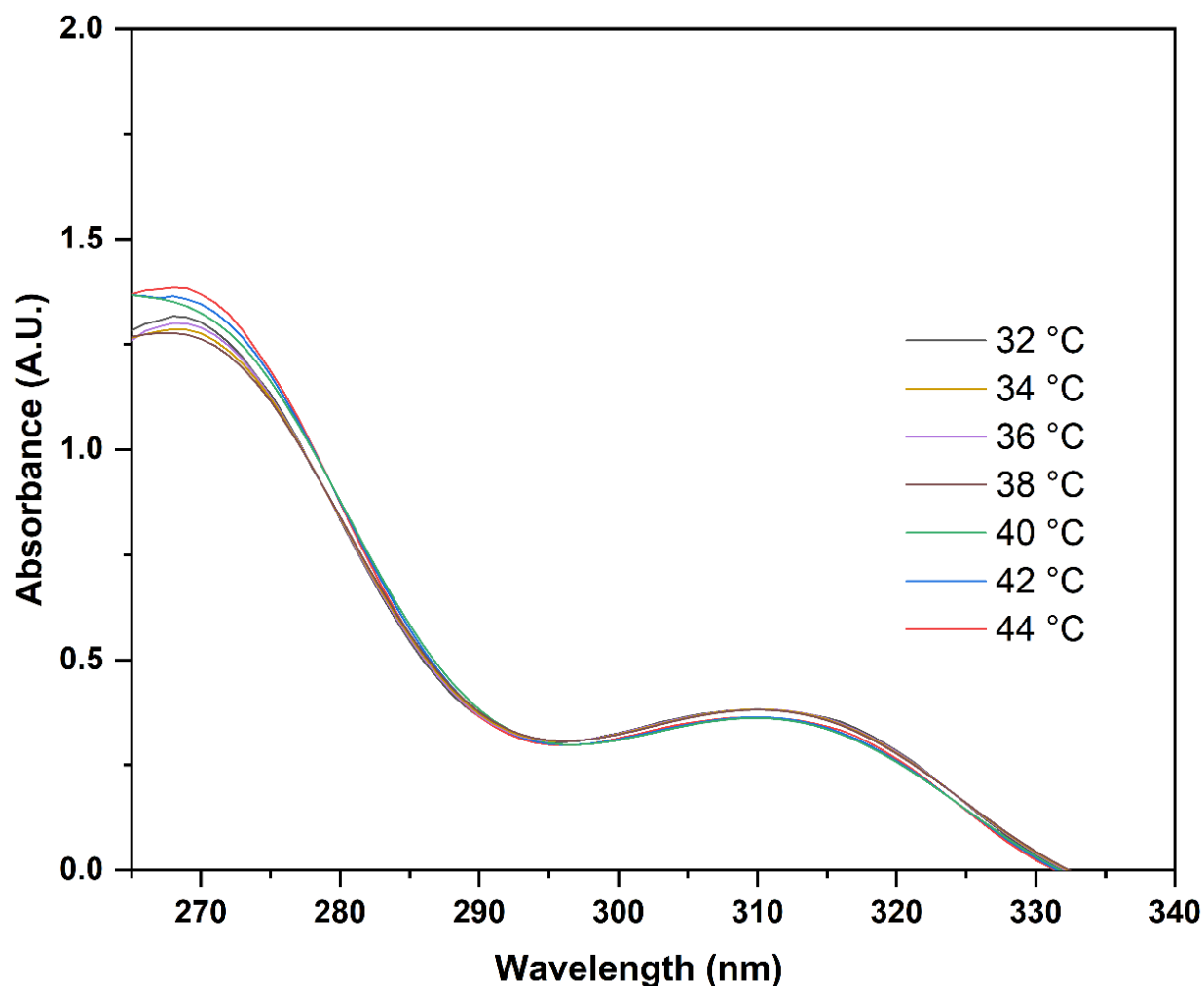


Figure 99. Temperature bound analysis of [82c-Pb²⁺] complex in DMSO solvent system from 32 °C to 44 °C

2.5 B-H plot [82c-Pb²⁺] complex

The Benesi-Hildebrand (B-H plot) was applied to determine the value of the association constant (K_a). The slope of the graph between ΔA and $1/[Pb^{2+}]$ was employed to calculate the binding constant by using the equation as mentioned in the section 1.5. The association constant was found to be $4.1 \times 10^4 \text{ M}^{-1}$ with a good correlation coefficient ($R^2 = 0.9981$), indicating that the developed chemo sensor has a strong association binding with the lead metal ions from **Figure 100** shown below.

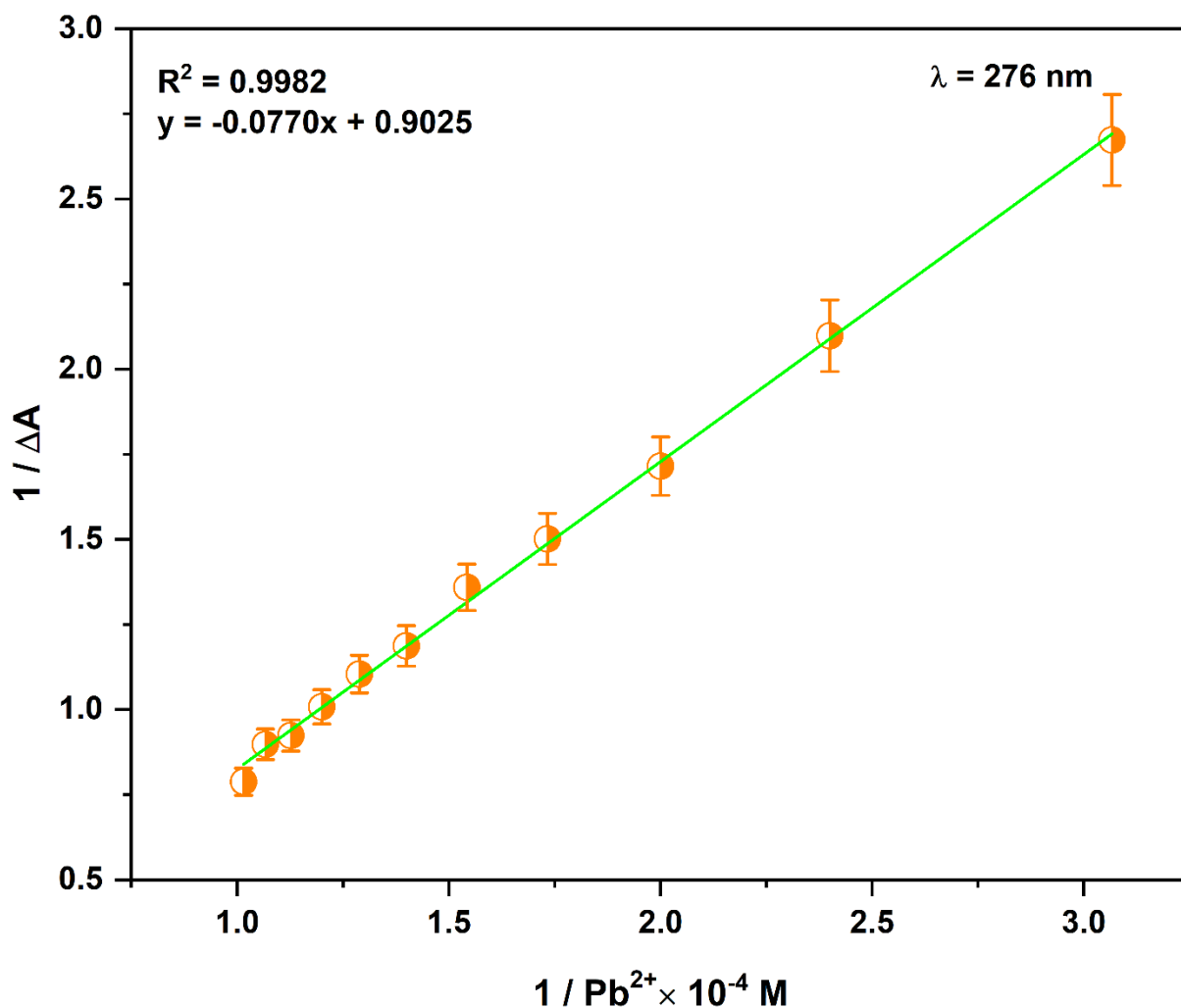


Figure 100. The relative absorbance titration data of probe **82c** with the increasing Pb^{2+} ions concentration for the Benesi-Hildebrand plot in DMSO solvent system

2.6 Fluorescence spectroscopic studies of chemosensor **82c**

The fluorescence spectrum was recorded with the addition of 0.23 μM to 2.36 μM concentration of the metal ions in receptor solution to investigate the interaction of receptor **82c** with Pb^{2+} ions. The emission spectra of probe **82c** indicated excitation frequency (λ_{ex}) of 290 nm and an emission maximum (λ_{em}) of 436 nm. On gradually increasing the Pb^{2+} metal ions concentration in stock solution of the probe **82c**, fluorescence intensity also increased. The typical emission bands at 342 nm, 411 nm, 436 nm were observed in the emission spectrum of the probe **82c** and the bands at 411, 436 exhibited hyperchromic shift after progressive addition of Pb^{2+} ions to the receptor as shown in **Figure 101**. The probe **82c** exhibited weak fluorescence that can be

ascribed to PET mechanism, however with the addition of Pb^{2+} ion solution to **82c** solution (0-11 equiv.), the fluorescence intensity increases (Hyperchromic shift) without causing any peak shift that can be due to chelation enhanced fluorescence (CHEF) mechanism accompanied by inhibition of PET mechanism.

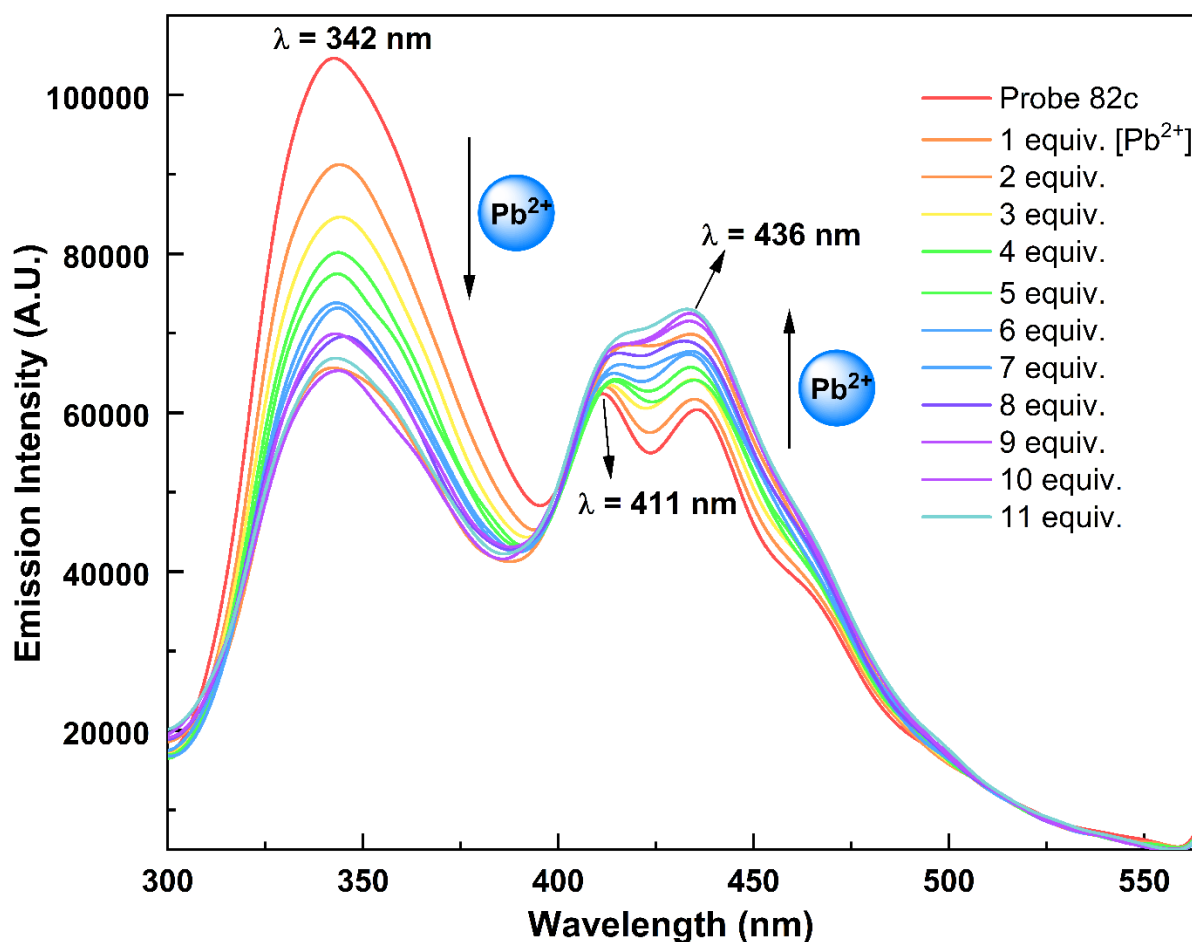


Figure 101. The fluorescence spectra of probe **82c** when titrated with Pb^{2+} ions solution observed at $\lambda = 436$ nm in DMSO solvent system, a significant increase in intensity i.e hyperchromic shift was observed on addition of 1 equiv. of Pb^{2+} ions solution to **82c** solution

The noteworthy changes can be attributed to the lead metal ions chelation with O and N atoms of probe **82c**. Furthermore, **figure 102** depicted a rise in the emission intensity ratio I_o/I_n , where I_o represents the emission intensity of sensor **82c** in the absence of Pb^{2+} ions and I_n represents the emission intensity after **82c** bound with Pb^{2+} ions, with each successive addition.

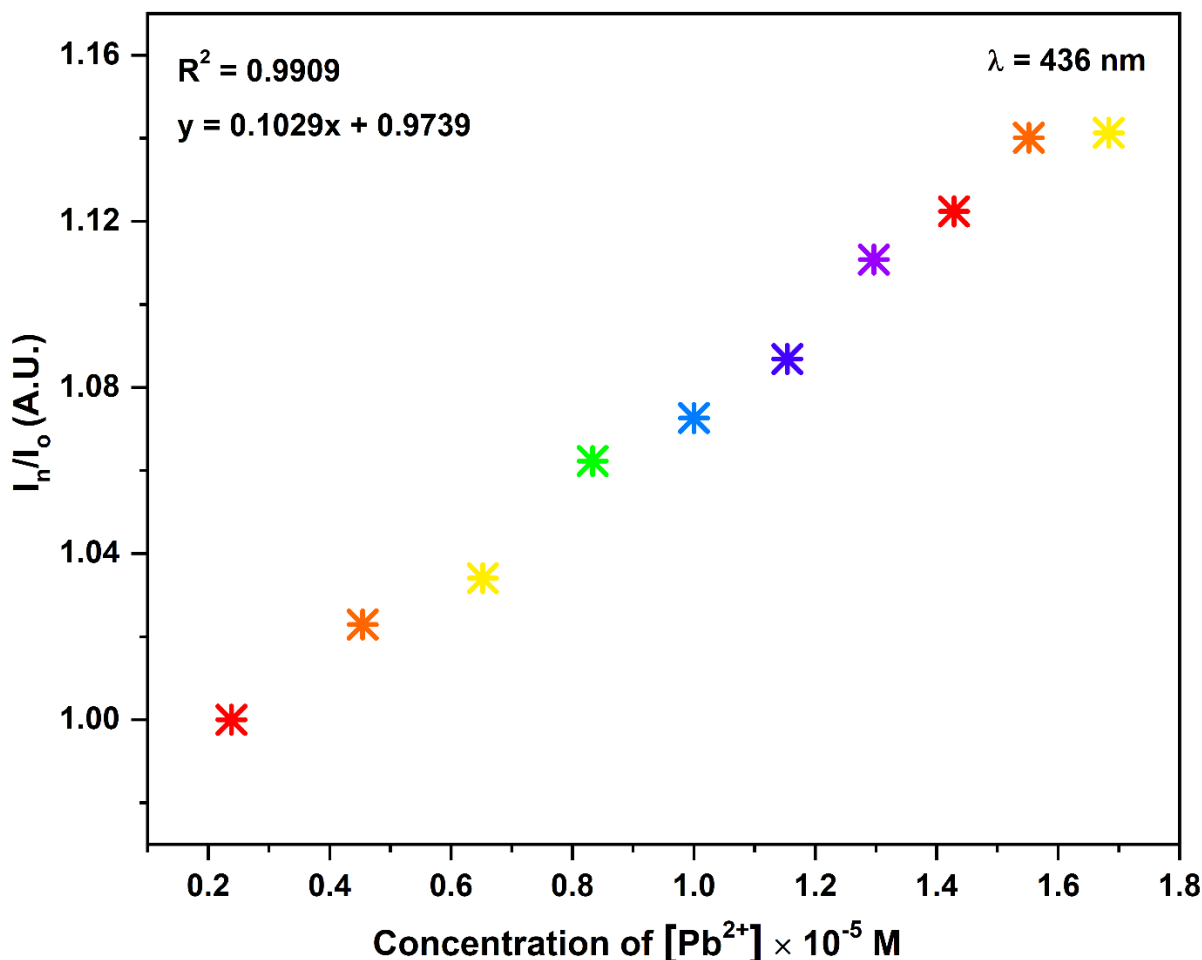


Figure 102. The relative emission intensity ratios (I_n/I_o) of probe **82c** at $\lambda = 436$ nm plotted against change in concentration of Pb^{2+} ions in DMSO solvent system, where I_o signify the emission intensity of **82c** in absence of Pb^{2+} ions and I_n represent the emission intensity during the binding of **82c** with Pb^{2+} ions with each consecutive addition

2.7 Limit of detection of [82c- Pb^{2+}] complex

The detection limit of the developed probe is of prime significance in chemosensing for calculating detection limit of the developed probe, $3\sigma/k$ formula was used, wherein (σ) is the standard deviation and k is the value of slope from the graph, the linear calibration plot was employed by plotting the absorbance values at 436 nm against the concentration of Pb^{2+} ions on the X-axis (**Figure 103**). The thorough analysis from the linear calibration plot was done, thereby the detection limit and limit of quantification of newly developed 1,2,3-triazole probe was evaluated to be 0.25 μM and 0.83 μM respectively.

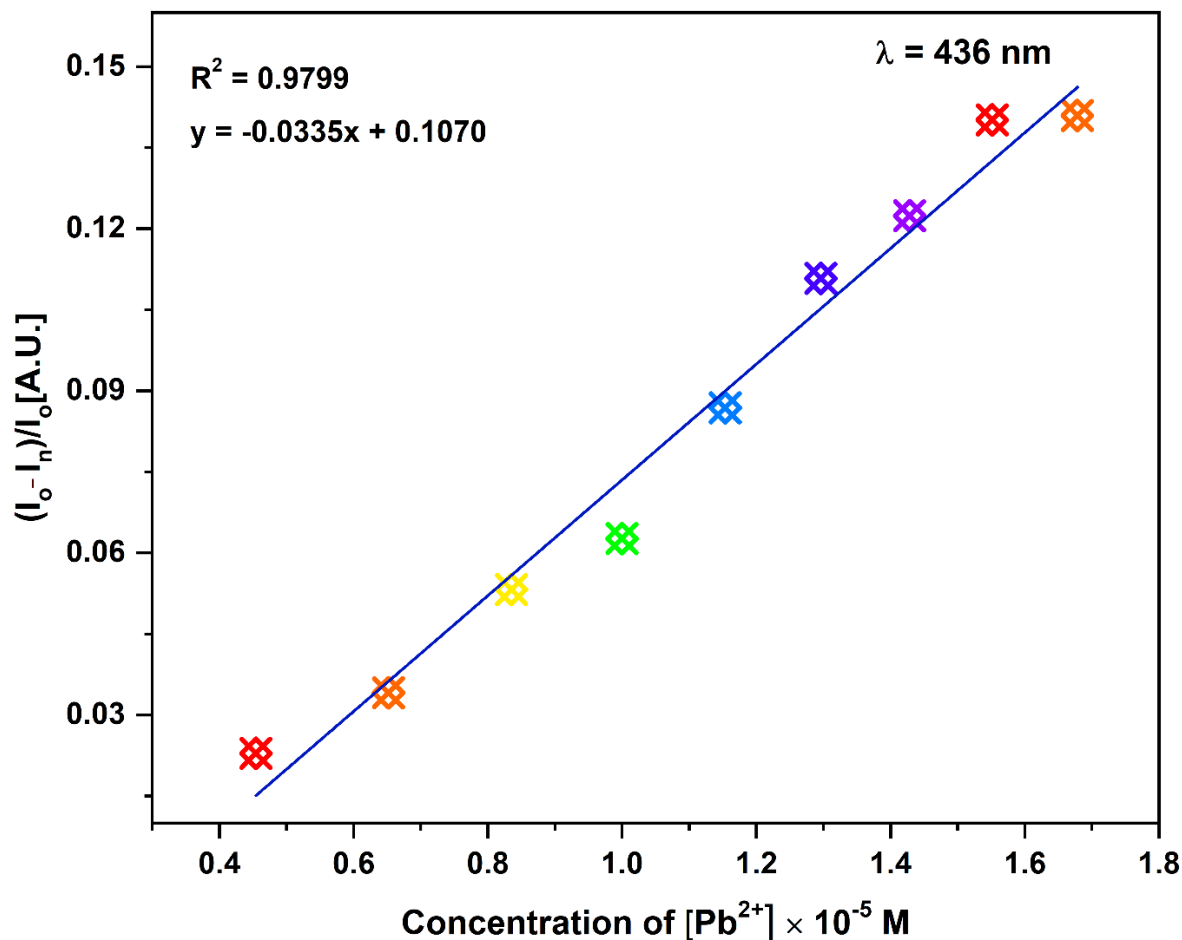


Figure 103. The linear calibration curve showing relative intensity $(I_0 - I_n)/I_0$ with variation in Pb^{2+} ions concentration, wherein I_n = emission intensity with each subsequent addition of Pb^{2+} ions and I_0 = emission intensity of free probe **82c**

2.8 Probable binding mode of $[82c-Pb^{2+}]$ complex

The HSAB hypothesis states that soft acids choose to interact with soft bases and hard acids with hard bases. In view of the fact that the synthesized chemosensor **82c** possess several nitrogen and oxygen atoms, which act as hard base and lead ion is a hard acid, therefore they firmly bond to establish a stable complex. The ring size and structure of the chemosensor indicated a perfect fit of the metal ions in the cavity generated by the ligand. According to previous study on the chemosensing behavior of lead ions, a few ligands with nitrogen and oxygen atoms as donor sites persistently bind with Pb^{2+} ions. The proportionate change in absorbance seen during UV-visible titrations with increasing concentrations of Pb^{2+} ions demonstrate (2:1) ligand-metal ions stoichiometry. In addition, previous research has led researchers to the conclusion that lead

ions are large, may stabilize higher coordination numbers, and efficiently interact with ligands that have cage-like geometries.⁵⁻⁷ The Pb^{2+} ions may embed itself between two ligands, binds to the N-atoms of heterocyclic triazole ring, functionalized Schiff base, and with the oxygen atoms attached to the triazole ring (**Figure 104**).

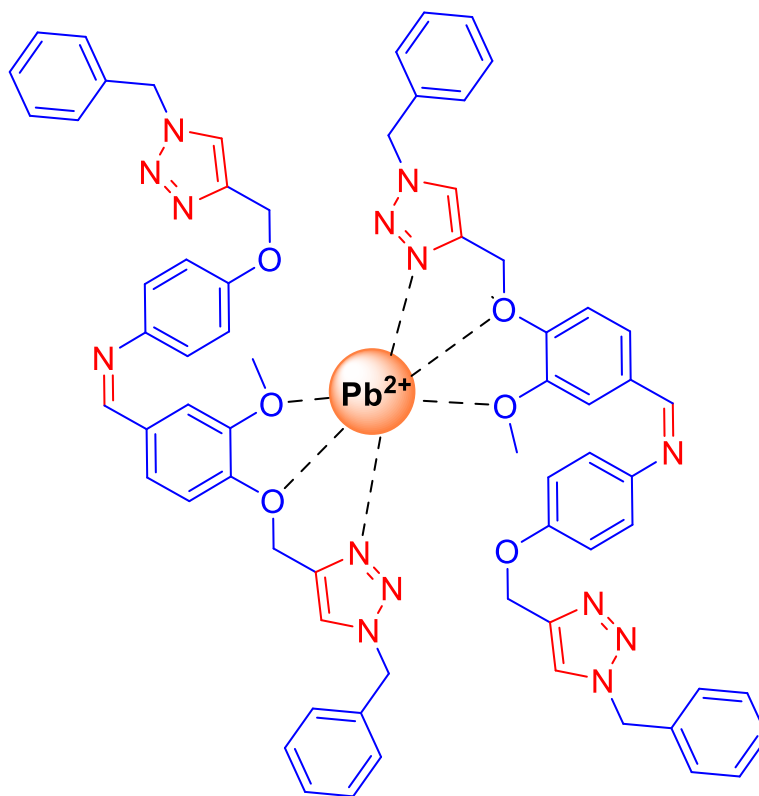


Figure 104. The proposed ligand-metal (2:1) binding of probe **82c** with Pb^{2+} ions in DMSO solvent system

FTIR spectra of both **82c** and the 82c-Pb^{2+} complex was effectively recorded. After complexation of $[\mathbf{82c-Pb}^{2+}]$, the peak associated with the (-C-O) group exhibited a decrease in wavenumber from 1123 to 1110, while the characteristic peak of the C-N group displayed decrease in intensity and shifts from 1264 to 1211 cm^{-1} . This observation suggests the coupling of Pb^{2+} metal ions with (C-O) and (C-N) groups of the 1,2,3- triazole moiety.

The LCMS-MS analysis of the complex $[\mathbf{82c-Pb}^{2+}]$ was also conducted. The anticipated mass spectrum m/z of $[\mathbf{82c+82c+Pb}^{2+}+2\text{Cl}^{-}+\text{K}^{+}+\text{H}_2\text{O}]$ calculated as 1505.70 appeared at $m/z = 1505.70$. The m/z value aligns with the postulated stoichiometry

3. Photophysical properties of chemosensor **83c**

3.1 UV-visible spectral studies of chemosensor **83c**

UV-visible absorption studies were employed to extensively investigate the cation-binding characteristics of chemosensor **83c** that itself comprises different binding sites at the arms of 1,4-disubstituted 1,2,3-triazole. Owing to the evident solubility of **83c** in (ACN:H₂O::4:1) and the strong absorption peaks (λ_{max}) at 277 and 314 nm with intensity 0.8 and 0.7 A.U. respectively, the aforementioned binary solvent system was considered as the 'optimal solvent' system for prolific chemosensing activity of the developed sensor. Absorption titrations studies of receptor **83c** were executed in ACN:H₂O::4:1 by adding 10 equiv. aliquots salts of metal cations Na⁺, K⁺, Mg²⁺, Ba²⁺, Pb²⁺, Mn²⁺, Co²⁺, Ni²⁺, Cu²⁺, Zn²⁺, Cd²⁺, Hg²⁺, Ce³⁺, Fe³⁺, Cr³⁺, Ag⁺ (**Figure 105**). Distinguished metal ions solutions were infused into the synthesized chemosensor **83c** solutions exclusively, and UV-visible absorption spectra were recorded. Apart from the Cu²⁺ ions, no metal ions resulted into substantial alteration of the absorption spectra.

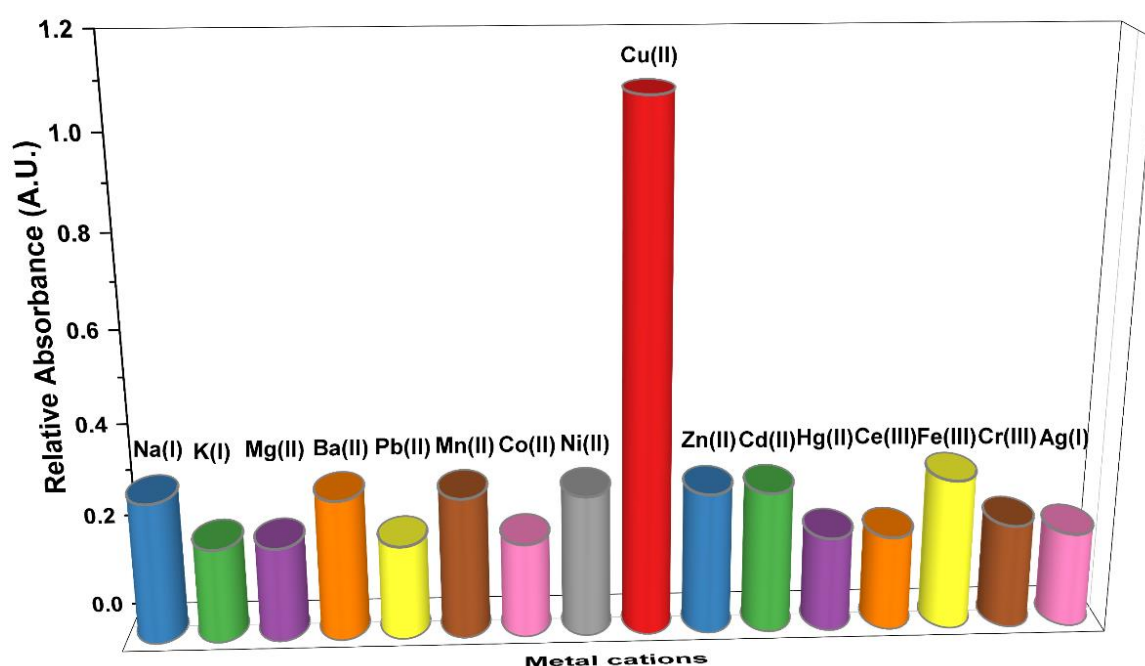


Figure 105. Histogram demonstrating the response of the chemosensor **83c** at $\lambda_{\text{max}} = 277$ nm in ACN/H₂O (4:1) solvent system towards several competing metal cations such as Na⁺, K⁺, Mg²⁺, Ba²⁺, Pb²⁺, Mn²⁺, Co²⁺, Ni²⁺, Cu²⁺, Zn²⁺, Cd²⁺, Hg²⁺, Ce³⁺, Fe³⁺, Cr³⁺, Ag⁺ comprising 10 equiv. of metal ions solution.

3.2 Optical response of **83c** in the existence of Cu^{2+}

To acquire an insight into the optical properties, absorption titration of chemosensor **83c** (30 μM) with Cu^{2+} ions was executed. The relative addition of minute quantity of Cu^{2+} resulted in a noteworthy alteration in the UV-Vis spectrum. **Figure 106** depicted the variations in the UV-Vis absorbance spectra of receptor **83c** in (ACN:H₂O::4:1) solvent media due to the gradual accumulation of Cu^{2+} ions (1 mM). The UV-vis spectra of probe **83c** reveal an intense absorption peak at $\lambda_{\text{max}} = 277 \text{ nm}$ (perhaps owing to a $\pi-\pi^*$ excitation) and a low-energy absorption peak at $\lambda_{\text{max}} = 315 \text{ nm}$ (due to $n-\pi^*$ transition).

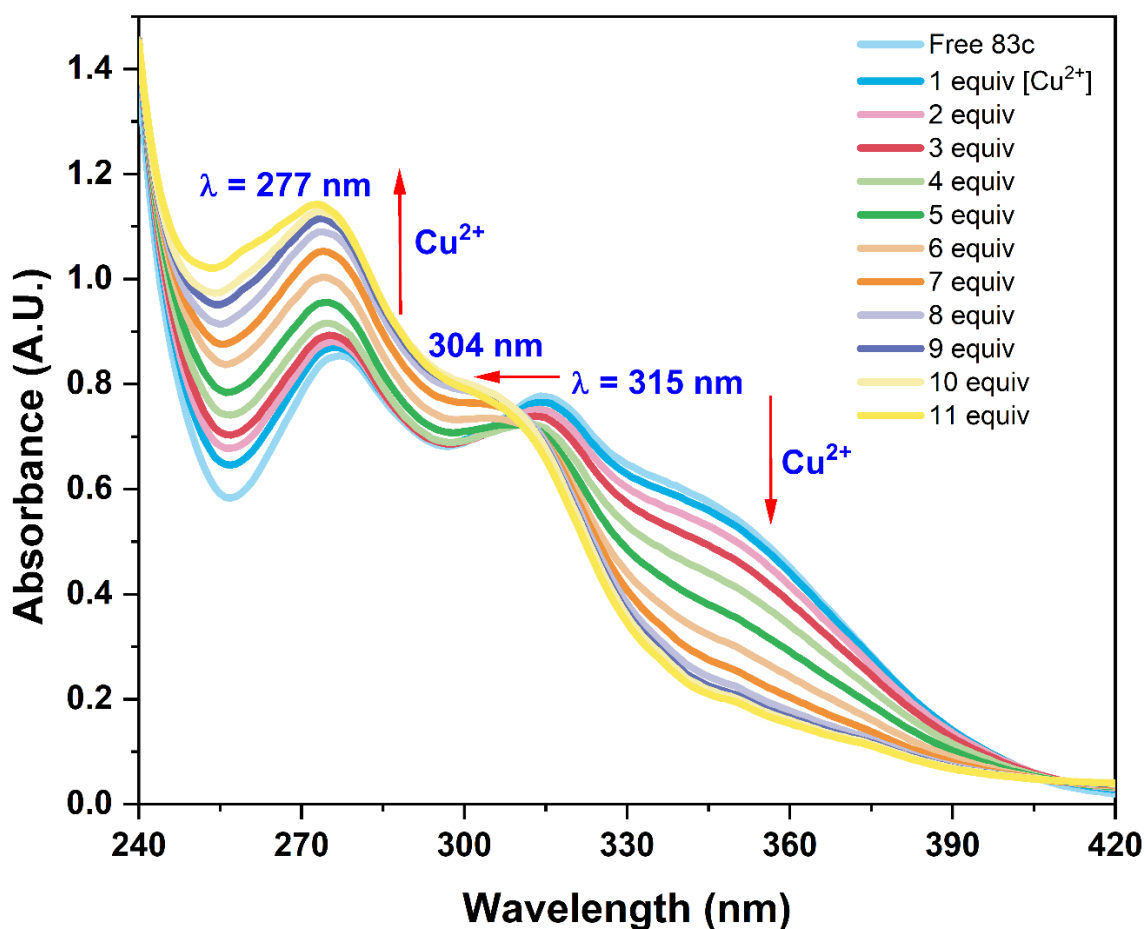


Figure 106. The variations in the absorption spectra of **83c** (30 μM) in ACN:H₂O::4:1 solvent mixture upon consecutive addition with increasing equivalent of Cu^{2+} ions, change in intensity before and after the isosbestic point at 309 nm, along with 11 nm blue shift and rise in intensity

After the incremental addition of 1 equiv. of Cu^{2+} to **83c**, the low-energy absorption bands at $\lambda = 315 \text{ nm}$ decreased, but one high-energy band at $\lambda = 277 \text{ nm}$ increased concomitantly. At

around 309 nm, a well-defined isosbestic site emerged, illustrating the net interconversion and equilibrium between the non-complexed and complexed moieties. Furthermore, when Cu^{2+} ions solution was gradually added to **83c**, the absorption bands at 315 nm shifted hypsochromically by 11 nm to 304 nm.

The comparative change in the absorbance maxima (A_n/A_o) versus molar ions concentration at 277 nm upon incremental augmentation of Cu^{2+} ions concentration is shown in **Figure 107**, wherein A_n = absorbance maxima observed upon the successive addition of Cu^{2+} ions, A_o = absorbance maxima observed for **83c**.

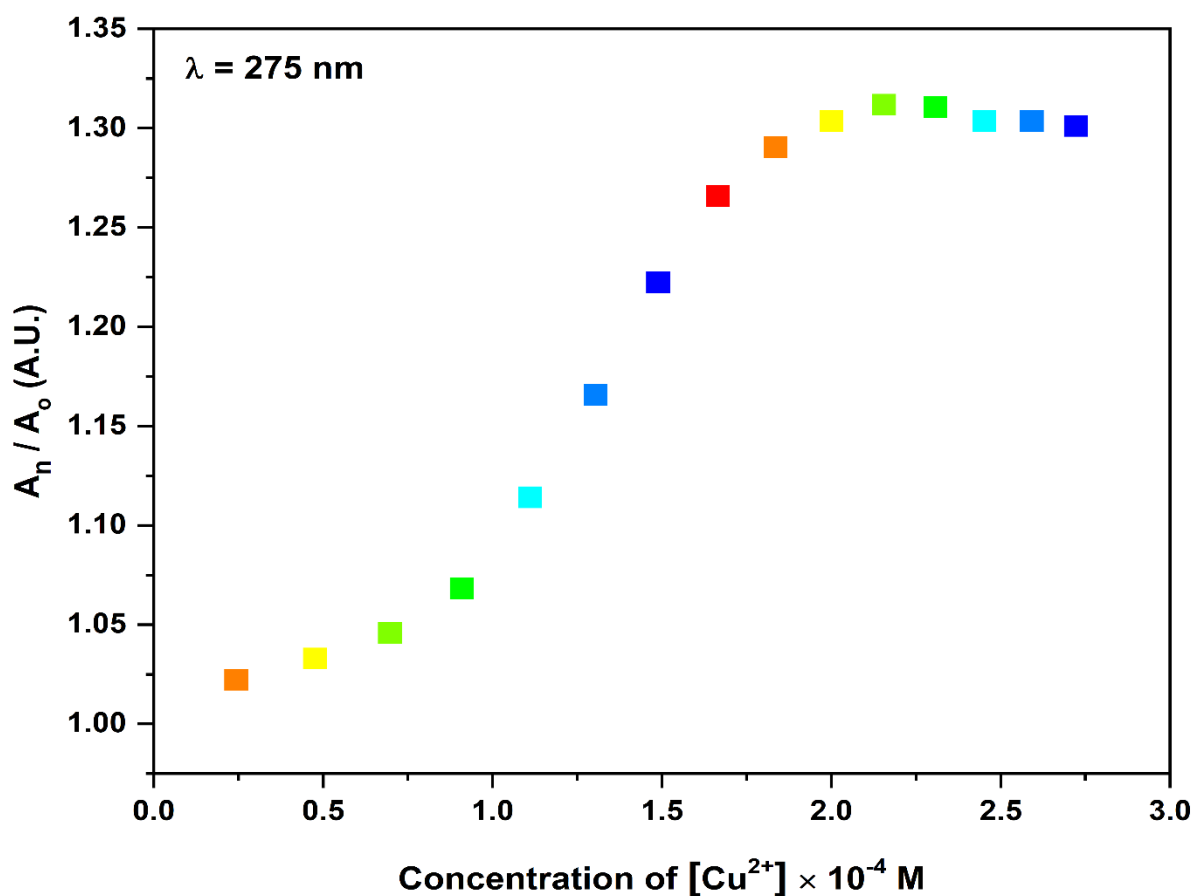


Figure 107. The relative change in absorbance intensity at $\lambda = 277$ nm plotted against the cumulative addition of Cu^{2+} ions (0-11 equiv.) in $\text{ACN:H}_2\text{O}:4:1$ solvent mixture, wherein A_o = absorbance intensity of free probe **83c** without Cu^{2+} ions and A_n = absorbance intensity during binding of **83c** with Cu^{2+} ions solution

By employing the method of continuous variations (Job's plot), binding assays imply a 1:1 binding mode of [83c-Cu²⁺]. The experimental procedure consisted of generating a plot that depicted the relative absorbance of [83c-Cu²⁺], the at a specific wavelength of 277 nm as a function of the molar fractions of 83c and Cu²⁺. It's important to note that the total concentration was kept constant throughout the experiment. At a mole fraction of 0.5, the maximum point was attained, indicating a 1:1 stoichiometry between 83c-Cu²⁺ (Figure 108)

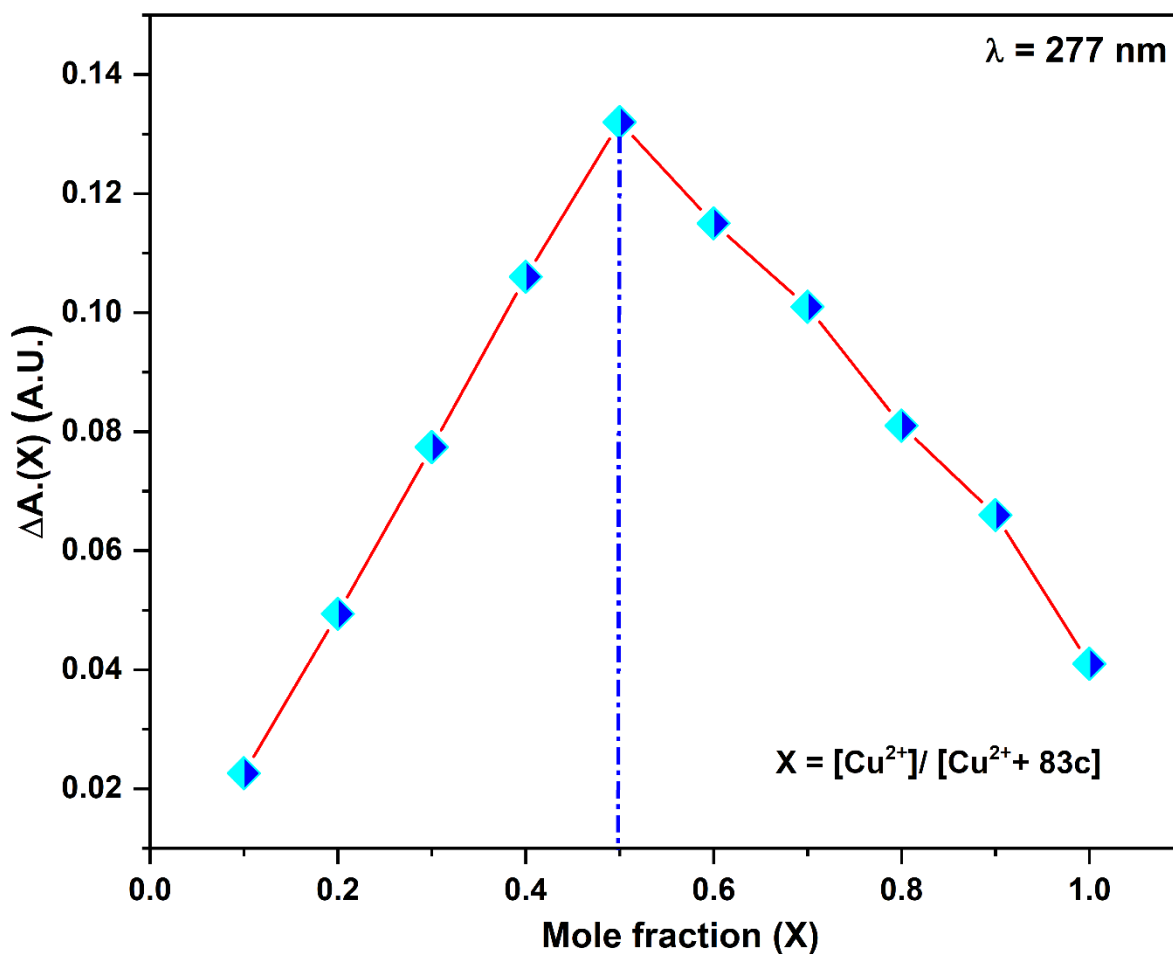


Figure 108. Representation of Job's plot exhibiting the binding ratio of [83c-Cu²⁺] complex in ACN:H₂O::4:1 solvent system, at 0.5 mole fraction maximum relative absorbance value was attained depicting the (1:1) stoichiometric ratio of [83c-Cu²⁺] complex

Additionally, interference assays were conducted to evaluate the practical utility of (83c) as a highly selective probe for Cu²⁺ ions. Consequently, a solution of (83c) was treated sequentially with equimolar concentration of Cu²⁺ and other interfering metal ions such as Na⁺, K⁺, Mg²⁺, Ba²⁺,

Pb^{2+} , Mn^{2+} , Co^{2+} , Ni^{2+} , Cu^{2+} , Zn^{2+} , Cd^{2+} , Hg^{2+} , Ce^{3+} , Fe^{3+} , Cr^{3+} , Ag^+ . Based on the intriguing titrations, as depicted in **Figure 109**, minimal to negligible interference was visible with the detection of Cu^{2+} ions. Clearly, these results illustrate the superior selectivity of Cu^{2+} over all other metal ions.

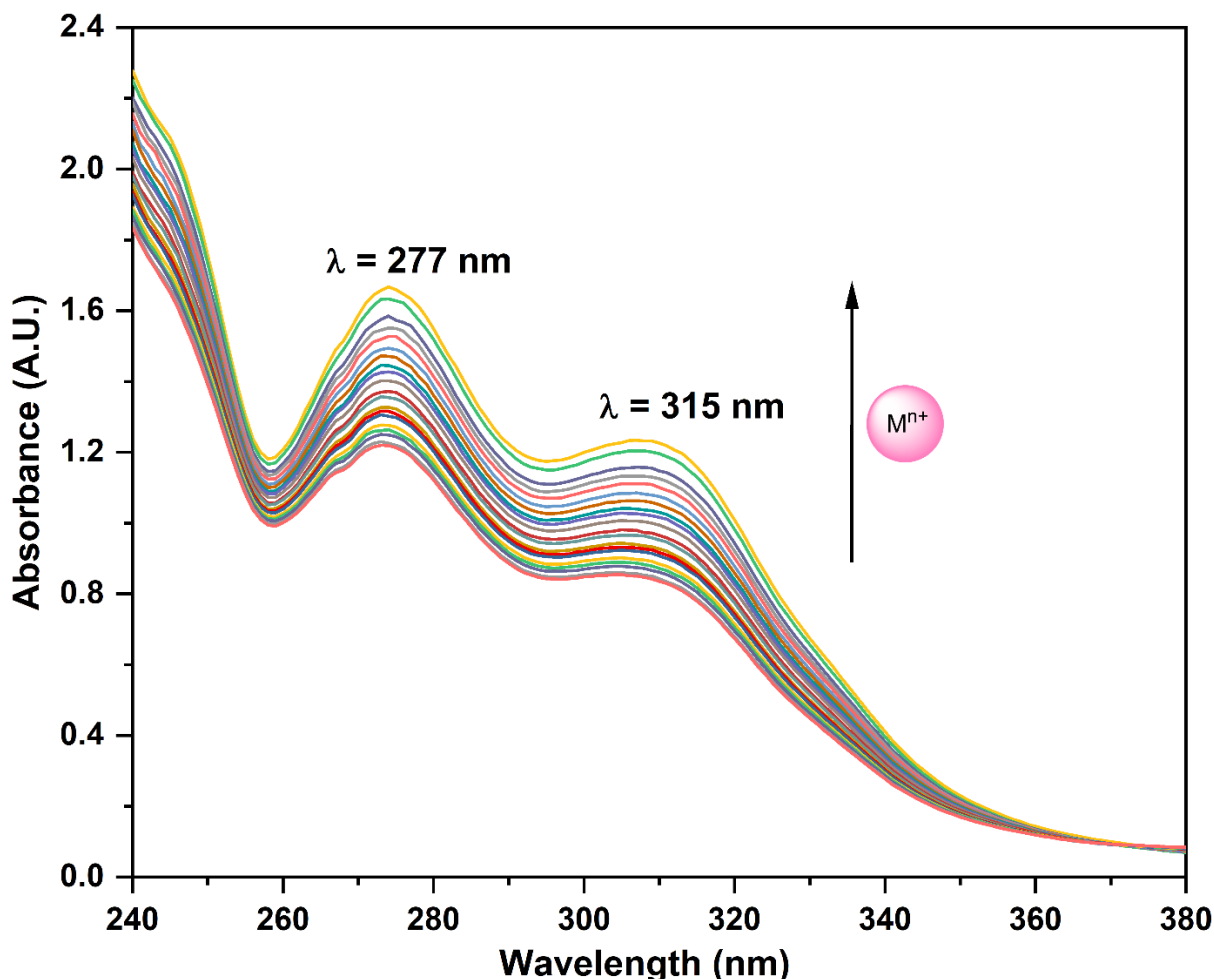


Figure 109. UV-vis absorption spectra of probe **83c** (0.03 mM) in ACN:H₂O::4:1 solvent system exhibiting selective binding of Cu^{2+} ions in presence of equal concentrations of assorted metal cations such as Na^+ , K^+ , Mg^{2+} , Ba^{2+} , Pb^{2+} , Mn^{2+} , Co^{2+} , Ni^{2+} , Cu^{2+} , Zn^{2+} , Cd^{2+} , Hg^{2+} , Ce^{3+} , Fe^{3+} , Cr^{3+} , Ag^+ , herein M^{n+} represents the mixture of metal ions in the spectrum

The association constant of Cu^{2+} with (**83c**) was analyzed based on the absorbance spectra data, adopting the Benesi-Hildebrand equation (1) from **section 1.5**, wherein, A , A_0 and A' represent the absorbance intensity observed at an intermediate Cu^{2+} concentration, in the absence of Cu^{2+} , and at a concentration of complete conversion, respectively, while K represents the

association constant, and M^{n+} represents the concentration of Cu^{2+} . From the plot of $1/\Delta A$ against $1/[\text{Cu}^{2+}]$, the value of K_a was extricated from the slope to be $6.0 \times 10^4 \text{ M}^{-1}$ for **(83c)** with Cu^{2+} . (Figure 110)

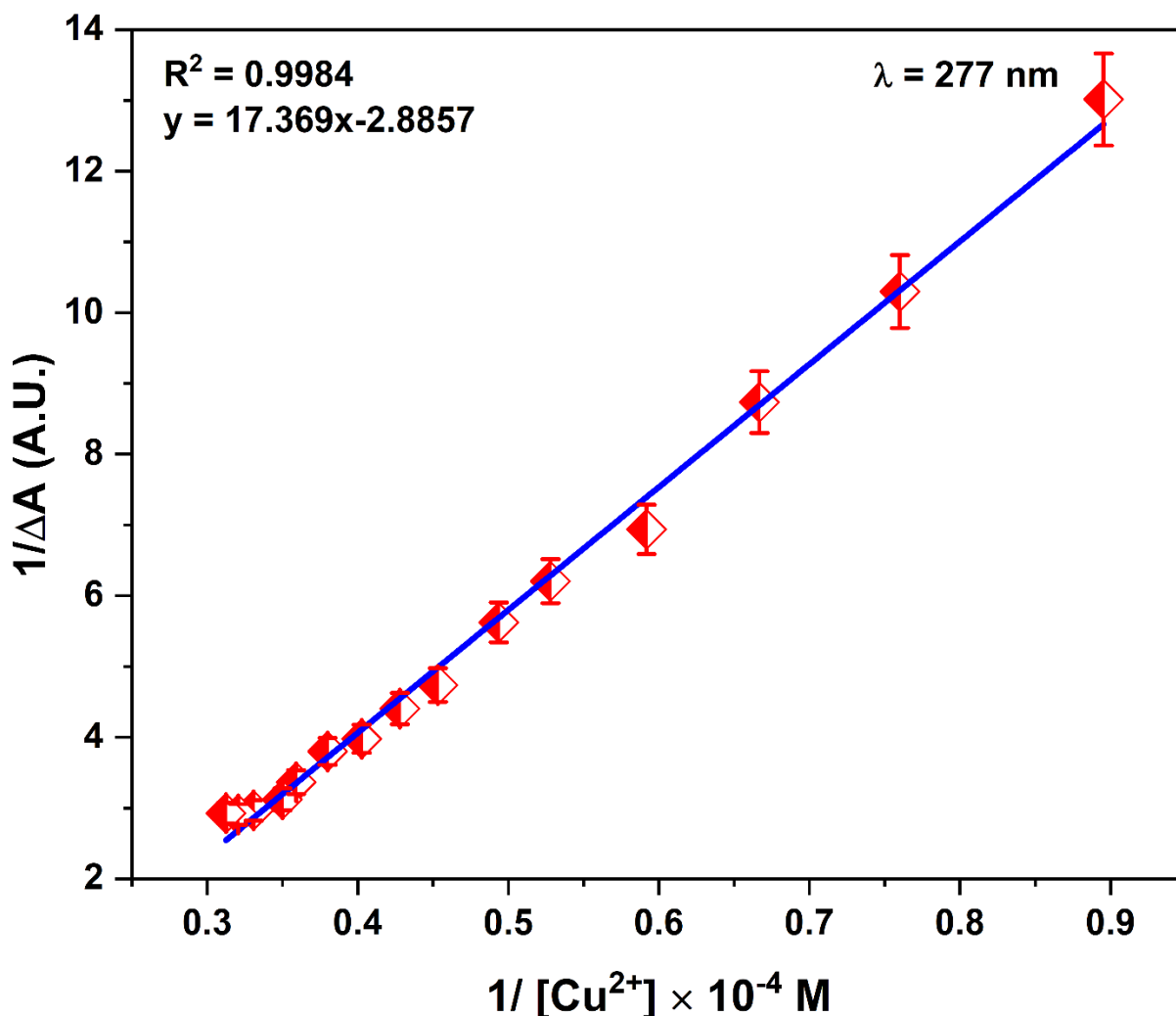


Figure 110. The relative absorbance titration data for probe **83c** with increase in concentration of Cu^{2+} ions, monitored at 277 nm for the Benesi-Hildebrand plot in $\text{ACN}:\text{H}_2\text{O}::4:1$ solvent system

3.3 Time bound and temperature dependent study of $[\text{83c}-\text{Cu}^{2+}]$ complex

A rapid response time is essential for the practical utility of chemosensor, hence a time-dependent experiment was performed to explore the influence of reaction time on interaction of $[\text{83c}-\text{Cu}^{2+}]$ complex. The experiment was carried for 30 minutes to conclude the influence of time on the binding of chemosensor **83c** with copper ion, as shown in (Figure 111), and the spectrum

data demonstrated the absorbance of the target chemosensor attained constant value that exhibited no effect on the **[83c-Cu²⁺]** interaction confirming strong chelation of **(83c)** with Cu²⁺ ions.

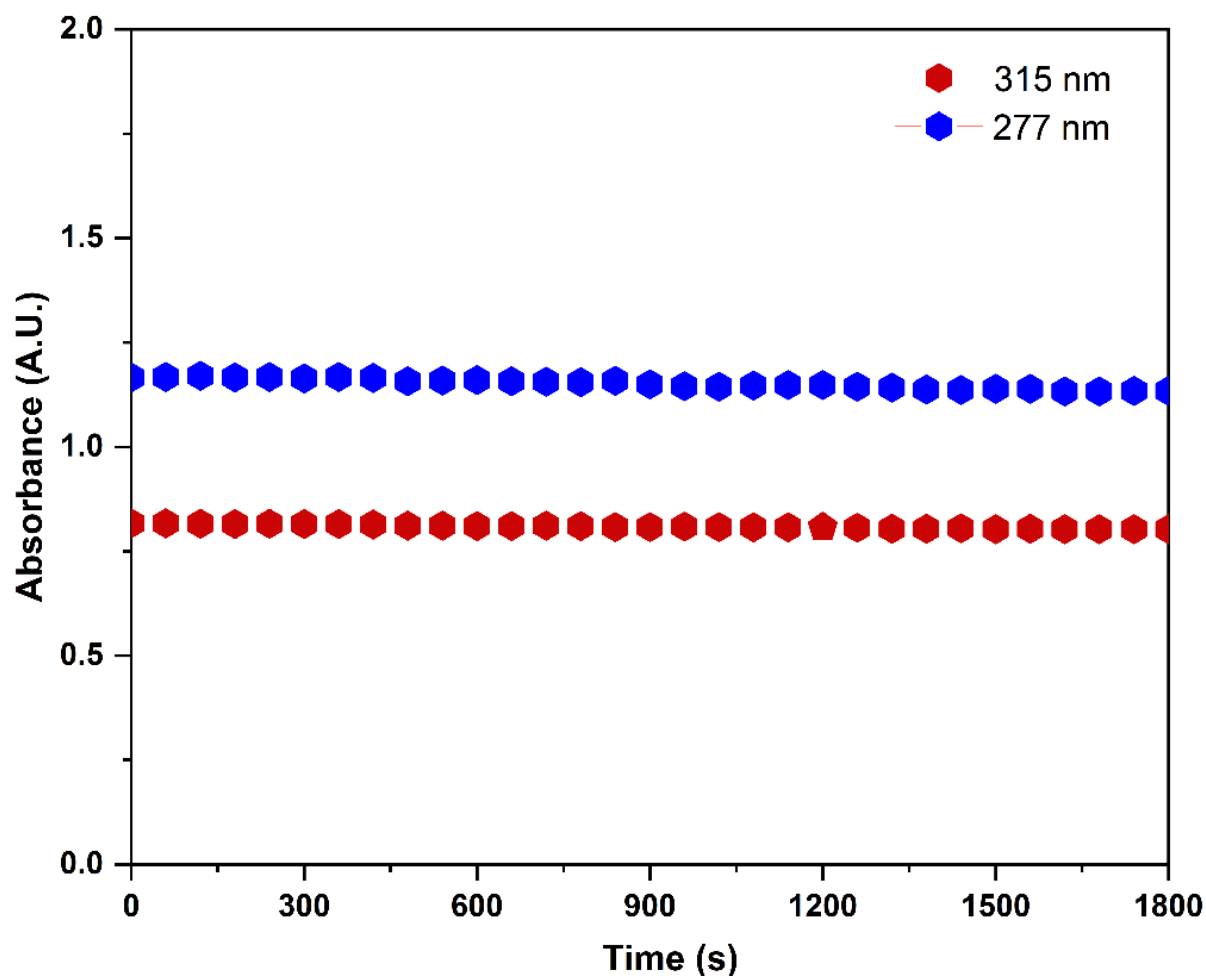


Figure 111. Time bound study of **[83c-Cu²⁺]** complex in ACN:H₂O::4:1 solvent system for 30 minutes at $\lambda = 277$ nm and 315 nm

Moreover, temperature-dependent investigation was conducted within specific temperature range to examine the influence of temperature on the metal-ligand interaction. The absorption spectra were recorded after every 2 °C rise in temperature within the allocated range of temperature from 32 °C to 50 °C. The data obtained is given in graphical form in **(Figure 112)**, which demonstrated the increased absorption that occurred as a consequence of an upsurge in temperature.

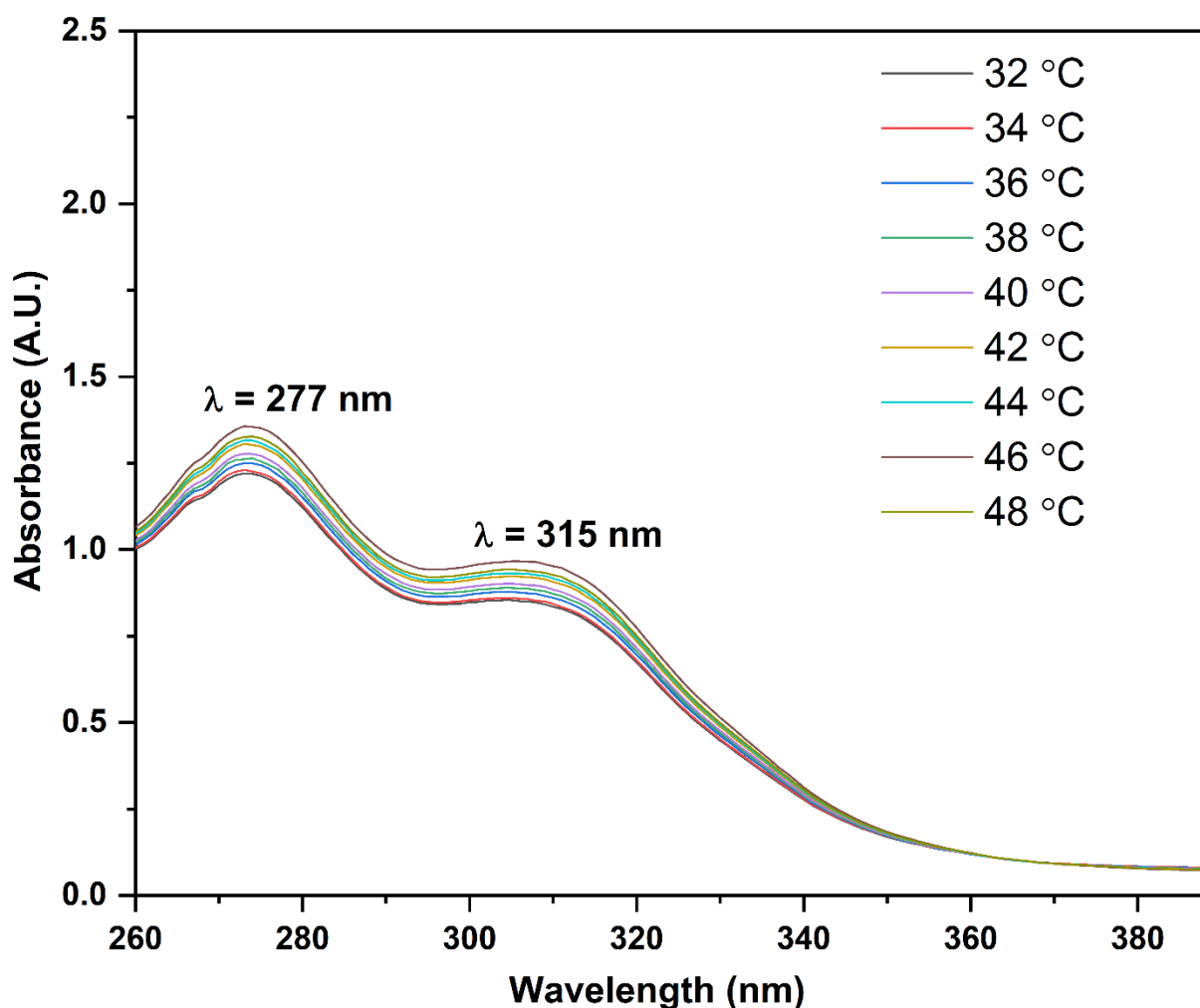


Figure 112. Temperature dependent study of metal-ligand complex in ACN:H₂O::4:1 solvent system from 32 °C to 50 °C

3.4 Fluorescence studies of chemosensor **83c**

The fluorescent recognition sensing was utilized on receptor in CH₃CN:H₂O::4:1 solution of **83c** (0.003 mM) revealing weak fluorescence emission at approximately 415 nm as an outcome of photoelectron transfer process upon excitation at $\lambda_{\text{ex}} = 280$ nm. The addition of Cu²⁺ (0.1 mM) to **83c** during the titration process leads to increase in the emission intensity, which was directly proportional to the concentration of metal ions [Cu²⁺] added. (**Figure 113**) The significant upsurge in the relative emission intensity of probe **83c** when exposed to Cu²⁺ can be attributed to the inhibition of the photoinduced electron transfer (PET) mechanism. It is important to note that the

process of PET typically exhibits a switching behaviour characterized by ON-OFF or OFF-ON transitions.

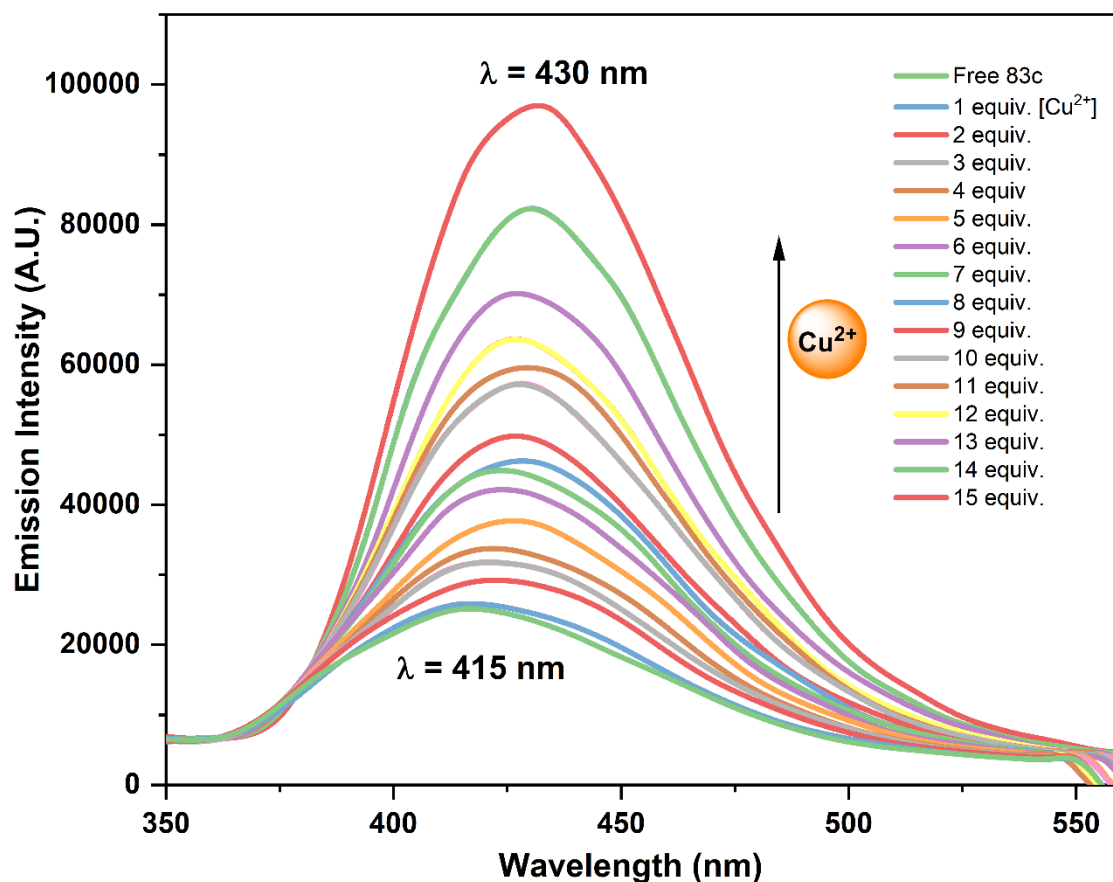


Figure 113. Emission spectra of probe **83c** when titrated with Cu^{2+} ions solution in (ACN:H₂O::4:1) solvent media illustrating change in intensity at $\lambda = 415 \text{ nm}$.

The benzyl ring linked to 1,2,3-triazole unit participates in the intramolecular PET mechanism. The hyperchromic shift was observed by probe **83c** after addition of Cu^{2+} ions that can be described due to CHEF mechanism alongwith inhibition of PET mechanism. Using fluorescence spectroscopy, the extent to which the selected cation affected the fluorescence intensities of receptor **83c** was evaluated. The findings of this experiment indicated that the lower limit of detection is 20.6 nM for Cu^{2+} . To assess the LOD, a linear regression analysis was performed using the data obtained from **Figure 114**. The widely accepted criterion was used for LOD calculation, pursuing the formula stated in **section 1.8**,

Wherein σ represents the standard deviation of the blank sample, and S corresponds to the slope of the calibration curve. The quantification limit for probe **83c** is determined to be 6.0×10^{-8} M for Cu^{2+} ions using the following equation stated in **section 1.8**.

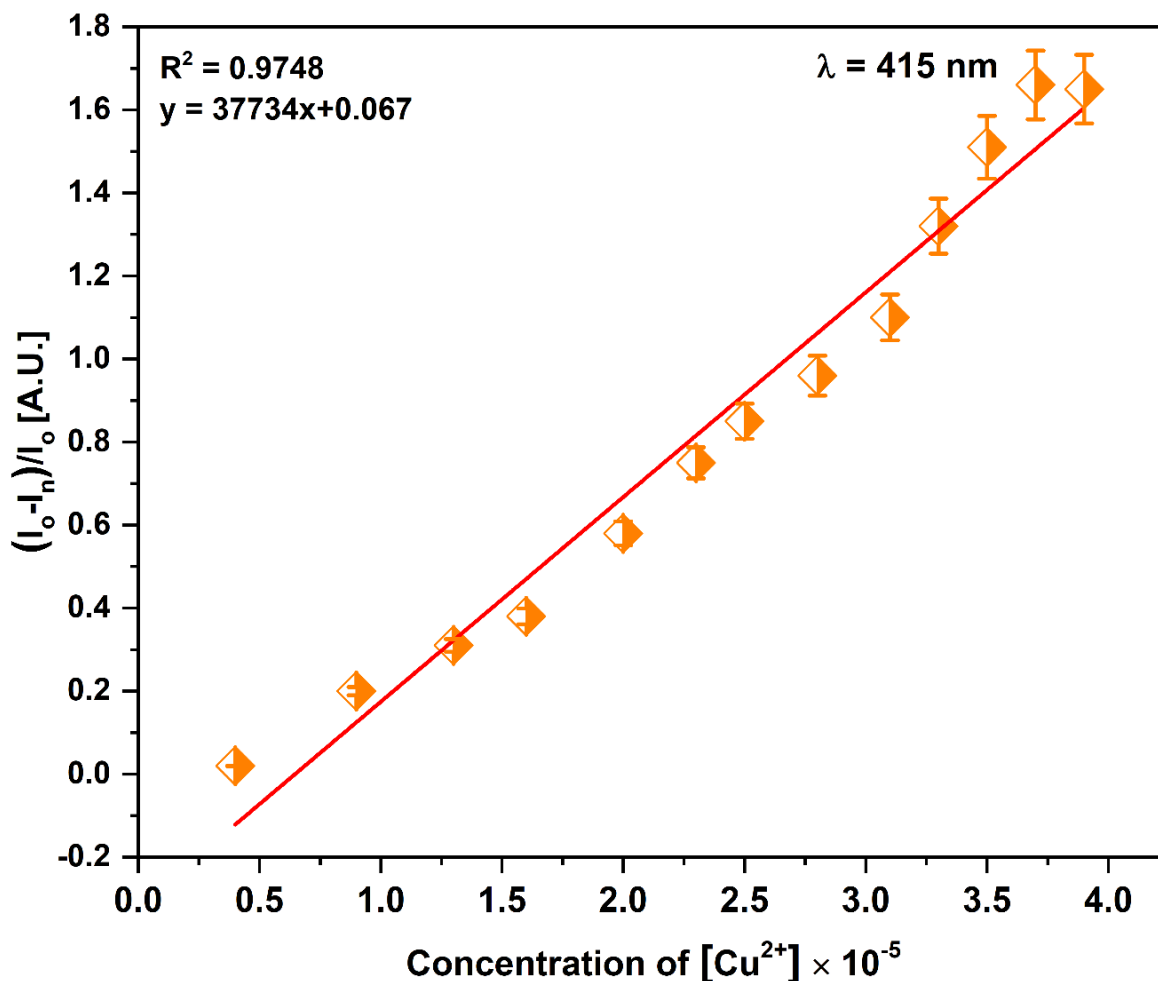


Figure 114. The linear calibration curve illustrating the relative emission intensity $[I_0 - I_n/I_0]$ observed at various concentration of Cu^{2+} ions.

Also, **Figure 115** illustrates the increase in the emission intensity ratio I_0/I , where I_0 represent the emission intensity of probe **83c** in the absence of Cu^{2+} ions and I represents the emission intensity during the binding of **83c** with Cu^{2+} ions, with each subsequent addition.

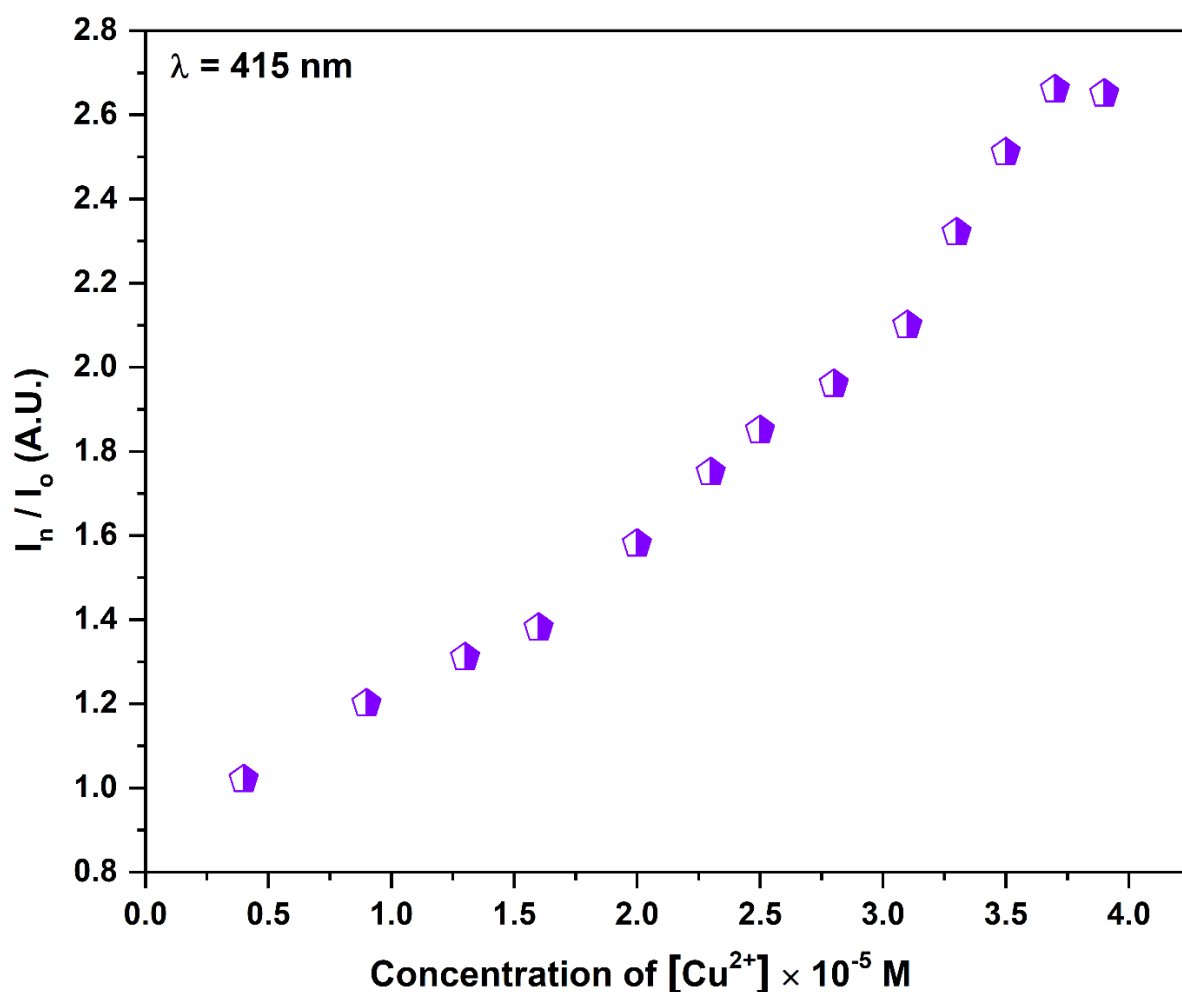


Figure 115. The relative change in intensity (I_n/I_o) of emission spectrum plotted against variant concentration of Cu^{2+} metal ions at $\lambda = 415$ nm.in (ACN:H₂O::4:1) solvent media, where I_o = emission intensity of free **83c** and I_n = emission intensity during binding of Cu^{2+} with **83c**

3.5 Probable binding mode of [83c-Cu²⁺] complex

The copper (II) metal ions have been categorised as a borderline acid according to the HSAB hypothesis. It has the ability to interact with receptor units that possess both hard and soft basic regions. The literature review has identified many intricate units that exhibit interaction with Cu^{2+} ions via oxygen and nitrogen donor sites.⁸⁻¹⁰ The structural units of the synthesised probe Schiff base 1,2,3-triazole derivative, contain nitrogen and oxygen atoms that coordinate with Cu^{2+} ions. Based on the ligand/metal association ratio (Job's plot), the proposed binding mode of **83c** with Cu^{2+} exhibit a 1:1 stoichiometry. The Schiff base 1,2,3-triazole-linked molecules formed an arrangement that encapsulated the Cu^{2+} ions within a cavity surrounded by two water

molecules and associate with (O-O-N) atoms. The interaction depicted in **Figure 116** represent the potential binding mechanism for the $[83c-Cu^{2+}]$ complex.

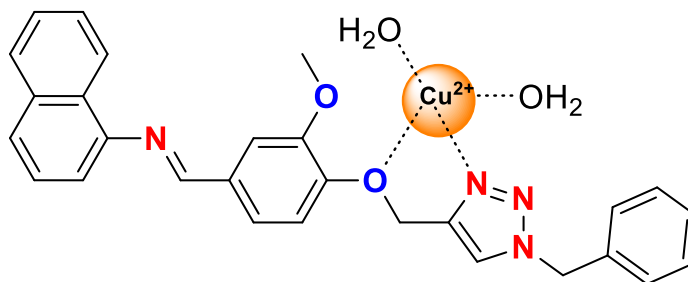


Figure 116. Plausible binding mode showing 1:1 stoichiometry ratio of $[83c-Cu^{2+}]$ complex

FTIR spectra of both **83c** and the $81c-Cu^{2+}$ complex was effectively recorded. After complexation of $[83c-Cu^{2+}]$, a new peak corresponds to OH group at 3334 cm^{-1} appeared that signifies the attachment of H_2O molecules with the metal-ligand complex. The peak associated with the $(-C-O)$ group exhibited a decrease in wavenumber from 1140 to 1127 cm^{-1} , while the characteristic peak of the $C-N$ group displayed an increase in intensity and a shift from 1258 to 1269 cm^{-1} . This observation suggests the coupling of Cu^{2+} metal ions with $(C-O)$ and $(C-N)$ groups of the 1,2,3- triazole moiety.

The LCMS-MS analysis of the complex $[83c-Cu^{2+}]$ was also conducted. The anticipated mass spectrum m/z of $[83c-Cu^{2+}-(H_2O)_2]$ calculated as 547.1 appeared at $m/z = 549.0502 [M + 2]$. The m/z value aligns strongly with the postulated stoichiometry

4. Photophysical properties of chemosensor **84c**

4.1 Absorbance spectra of probe **84c**

The UV-vis spectra of probe **84c** (0.05 mM) was recorded at ambient temperature in a partially aqueous ($ACN:H_2O::4:1$) solvent mixture. ACN was chosen as the preferred solvent to prevent the interference caused by the higher polarity of other solvents (DMF, DMSO) on the electronic transitions that generate the UV pattern of the compound **84c** being studied, also owing to its capability of freely dissolving the probe **84c**. The aqueous media is essential for chemosensing experiment, however the limited solubility of **84c** demands the mixture of organic-aqueous solvent system. The chemosensor **84c** exhibited an absorption spectrum with two

prominent band at around 273 and 307 nm in (ACN:H₂O::4:1). To evaluate the selectivity of chemo-sensor for metal ions, the UV response of **84c** towards distinct metal ions was investigated. Out of all the cations tested (Zn²⁺, Ni²⁺, Mg²⁺, Co²⁺, Ce³⁺, Mn²⁺, Cd²⁺, Hg²⁺, Cu²⁺, Cr³⁺, Ba²⁺, Pb²⁺), only Hg²⁺ showed a conspicuous increase in absorption and no notable alterations were observed in the UV spectra for other metal ions exhibited in bar graph (Figure 117)

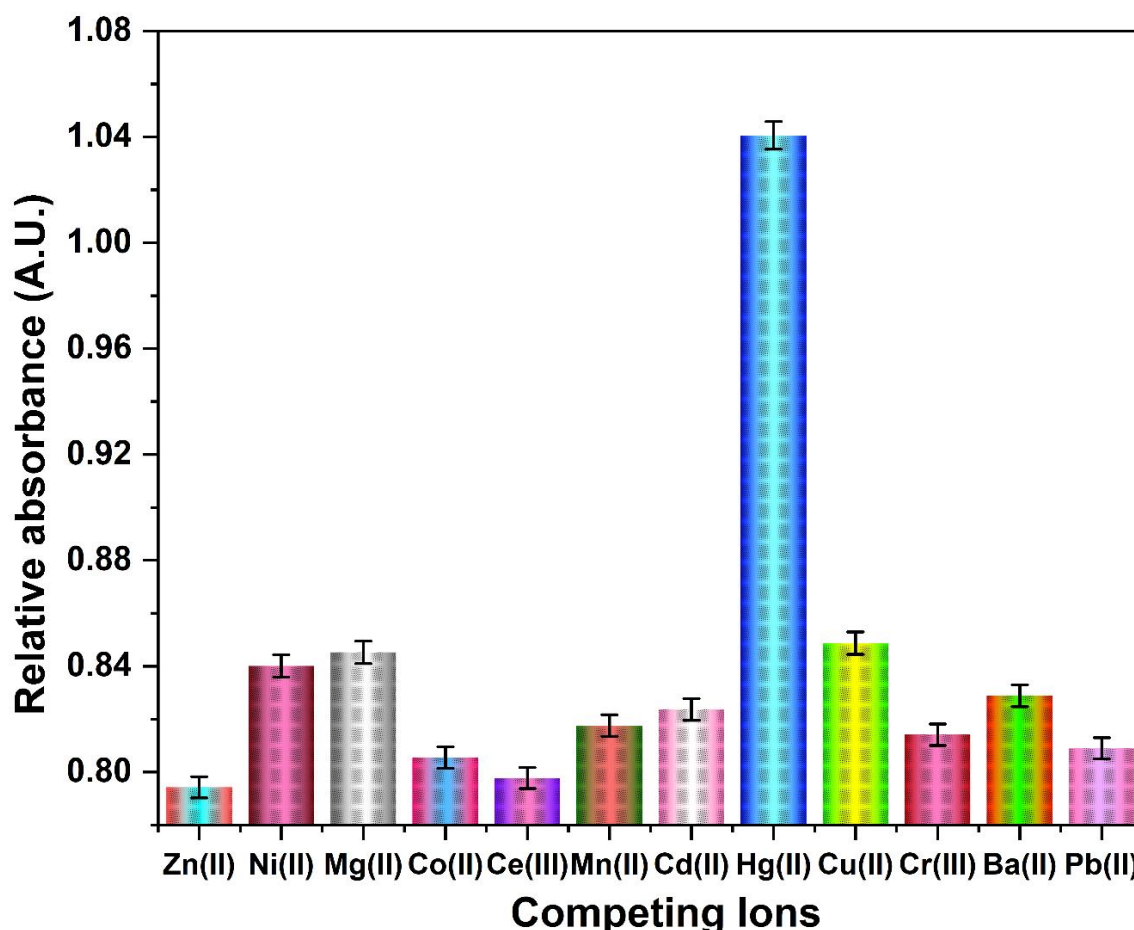


Figure 117. The variation in chemosensing response of the probe **84c** in (ACN:H₂O::4:1) solvent mixture, when 10 equivalents of various metal ions such as Zn²⁺, Ni²⁺, Mg²⁺, Co²⁺, Ce³⁺, Mn²⁺, Cd²⁺, Hg²⁺, Cu²⁺, Cr³⁺, Ba²⁺, Pb²⁺ were consecutively added. A noticeable alteration can be observed in the absorbance intensity with Hg²⁺ ions compared to other metal ions for **84c** sensor

4.2 Optical response of **84c** towards metal ion Hg²⁺

The UV titration of the chemosensor **84c** with Hg²⁺ (1mM) revealed that as the concentration of metal ions (0–9 equiv.) increased, resulted in a decrease in intensity at 307 nm

alongwith the absorption band at 273 nm gradually diminished while the absorbance concomitantly increased and a new absorption band emerges at 267 nm. (**Figure 118**) This indicates the formation of complex between Hg^{2+} and the organic moiety **84c**.

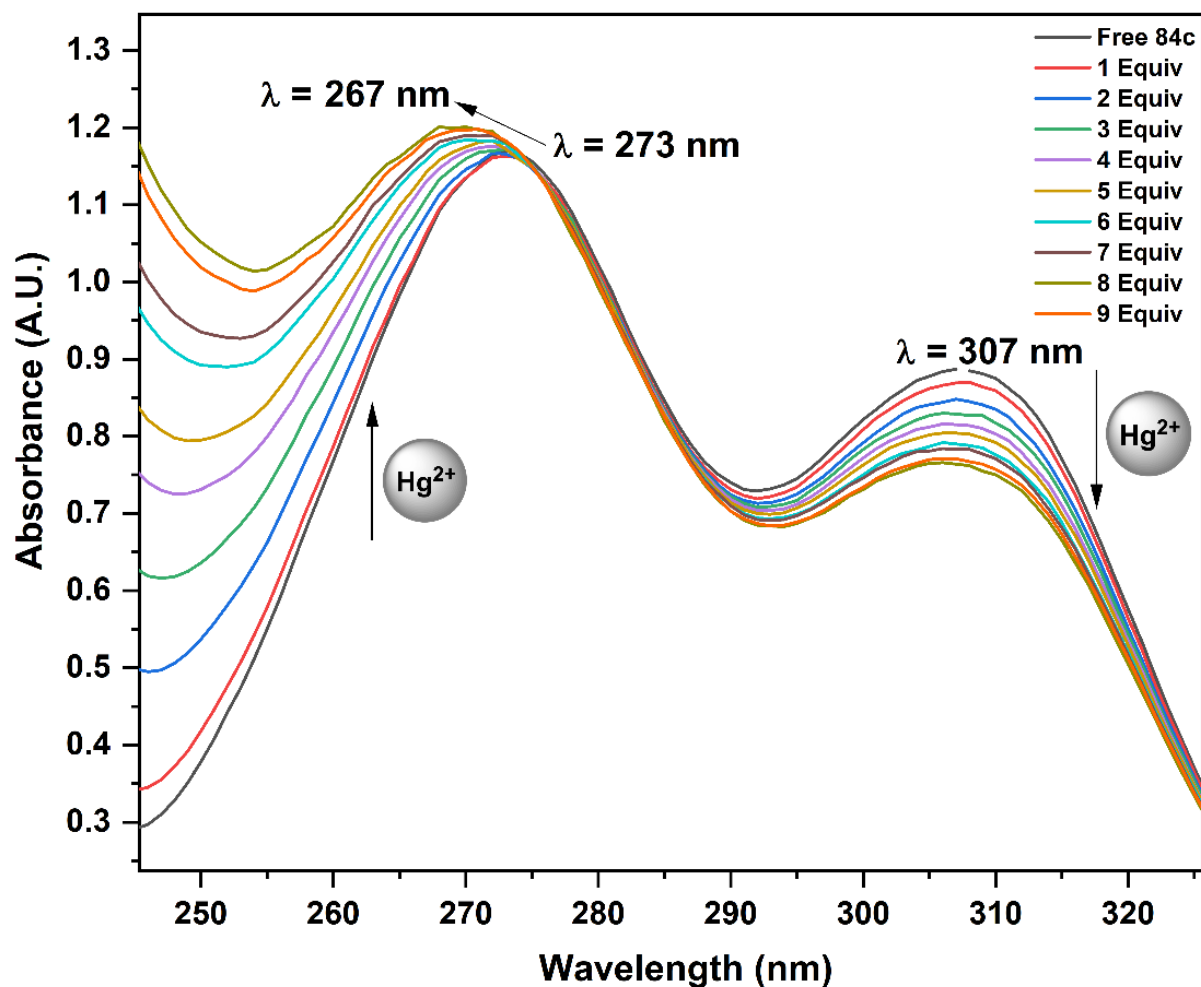


Figure 118. UV-visible graph of **84c** showing absorbance responses measured after adding 1 equiv. of 1 mM Hg^{2+} ion solution to 0.05 mM **84c** solution in (ACN:H₂O::4:1) solvent system. A noticeable change in the intensity of absorbance before and after the isosbestic points at 273 nm, along with hypsochromic shift and substantial rise in intensity

Figure 119 illustrates the relationship between the change in absorbance maxima (A_n/A_o) and the molar ions concentration from 273-267 nm as the concentration of Hg^{2+} ions gradually increase. In this context, A_n refers to the observed absorbance maxima after each addition of Hg^{2+} ions, while A_o represents the absorbance maxima observed for **84c**.

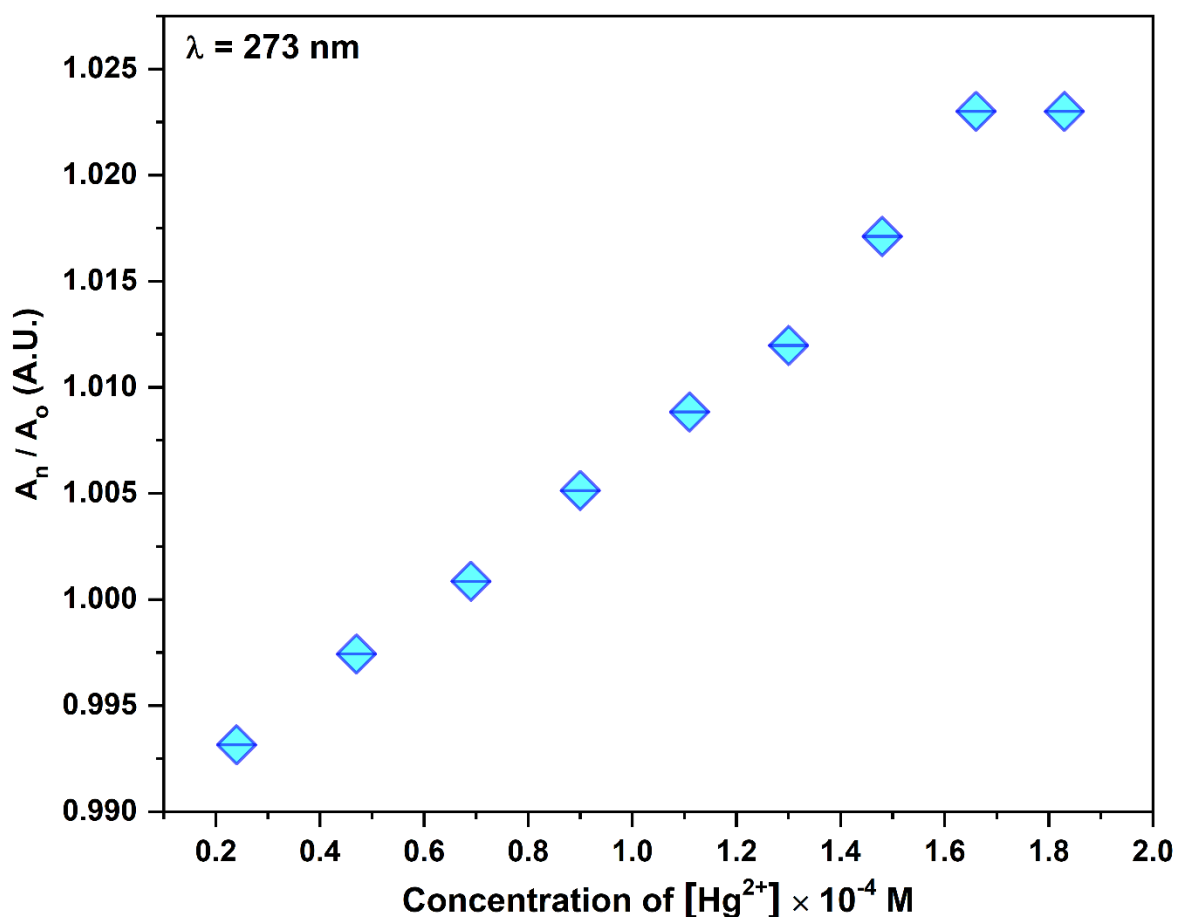


Figure 119. Relative absorbance ratios (A_n/A_o) ranging from 273 nm to 267 nm were plotted against Hg^{2+} ion concentrations fluctuating from 0.02 mM to 1.83 mM, wherein A_o = Absorbance intensity of probe **84c** in the absence of Hg^{2+} ions and A_n = Absorbance intensity during binding of **84c** with Hg^{2+} ions for each consecutive addition

The stoichiometric ratio between [**84c**- Hg^{2+}] was confirmed using the approach of continuous variation (Job's plot analysis). This included altering the mole fraction of metal ions between 0.1 to 0.9, while maintaining a constant overall concentration of the chemosensor and metal in $ACN:H_2O::4:1$. The maximum values for [**84c**- Hg^{2+}] were observed at a molar fraction of 0.5, suggesting a 1:1 complexation stoichiometry ratio. (**Figure 120**)

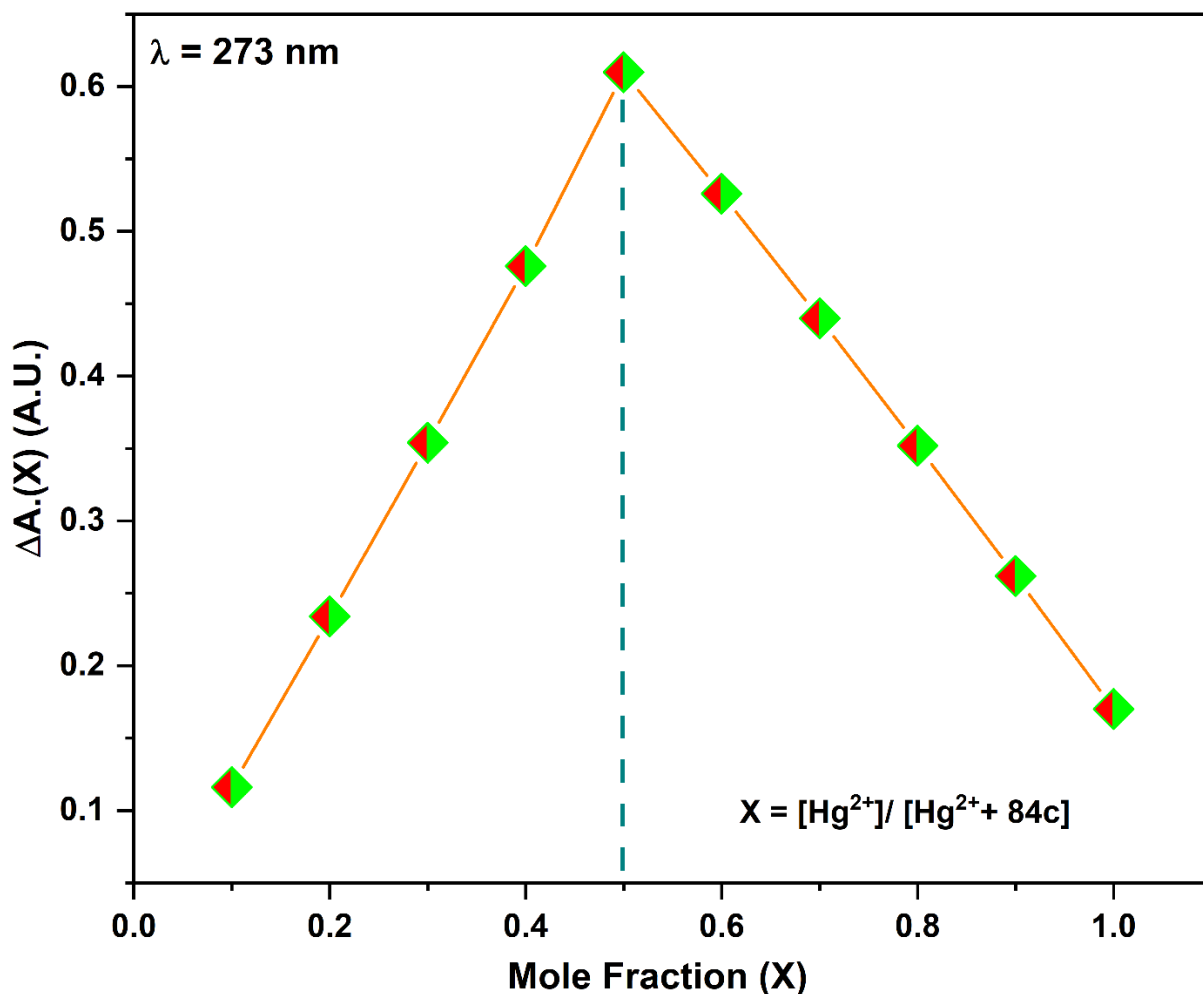


Figure 120. Job's plot using the method of continuous variations in (ACN:H₂O::4:1) solvent system. The mole fraction of **84c** plotted against relative absorbance shows at 0.5 mole fraction, the complex attains the maximum absorbance depicting (1:1) binding ratio of **84c** and Hg²⁺ ions

Furthermore, the binding constant was calculated using UV-Visible titration data. (**Figure 121**) The association constant was determined by analyzing the Benesi-Hildebrand plot for the establishment of [**84c**-Hg²⁺] complex from equation mentioned in **section 1.5**, where A denotes the absorbance intensity at a certain concentration of the (Hg²⁺) ions added, A' signifies the maximum absorbance intensity when (Hg²⁺) is added and A_0 is the absorbance intensity of the free probe at 273 nm. The association constant K_a for the binding of Hg²⁺ ions by **84c** was determined via absorption titration experiments to be $2.93 \times 10^4 \text{ M}^{-1}$

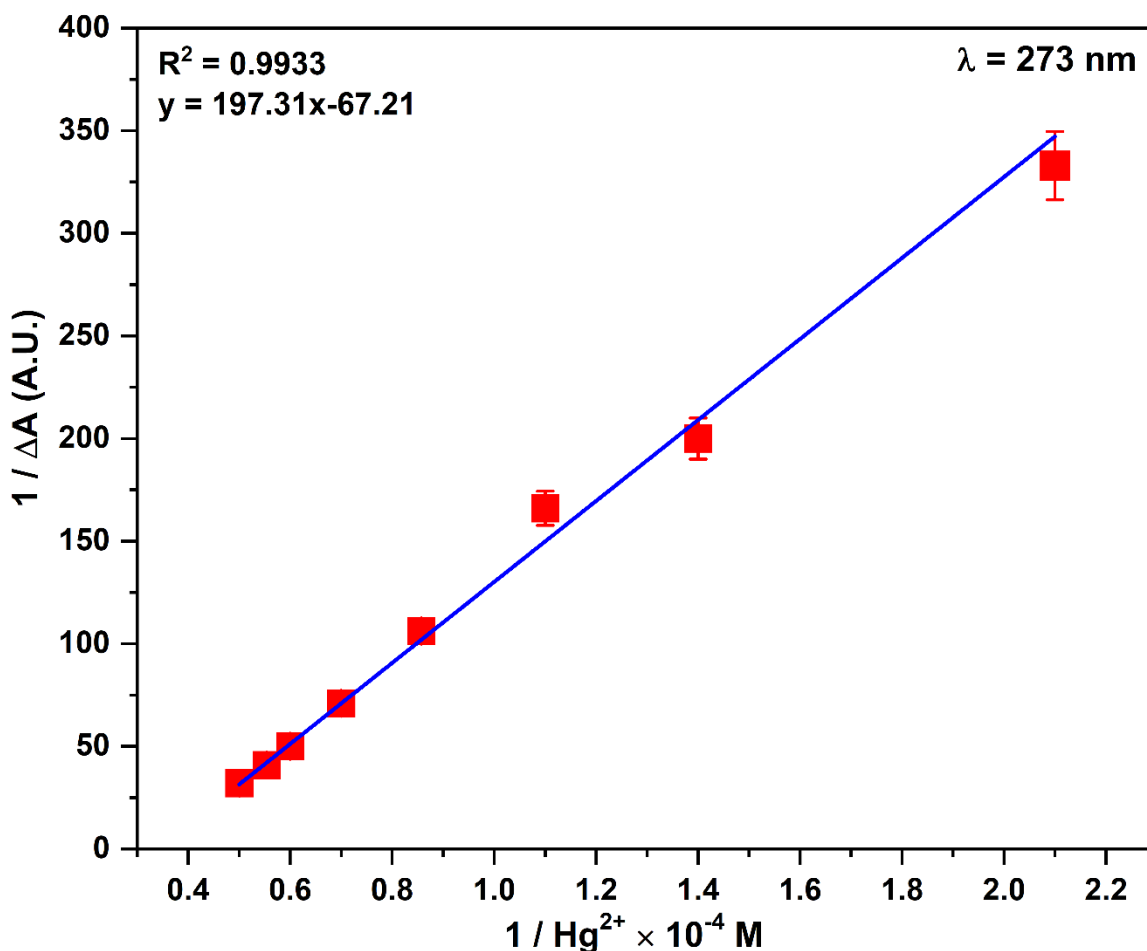


Figure 121. Benesi–Hildebrand plot of chemical receptor **84c** with Hg^{2+} ions monitored at 273 nm for determining association constant

4.3 Competitive metal ion titration of chemosensor **84c**

To demonstrate the practical application of **84c** in selective detection of Hg^{2+} even in the presence of other metal ions, competitive metal ion titrations was conducted. The research investigation display that the increase in absorbance intensity induced by Hg^{2+} remained unaltered in presence of alkaline earth (Mg^{2+} and Ba^{2+}), first row transition (Mn^{2+} , Zn^{2+} , Co^{2+} , Ni^{2+} , Cu^{2+} , Cr^{2+}), and hazardous metal ions (Cd^{2+} , Pb^{2+}). Therefore, it is noteworthy that **84c** may function as a selective Hg^{2+} chemosensor even in presence of other metal ions. (**Figure 122**)

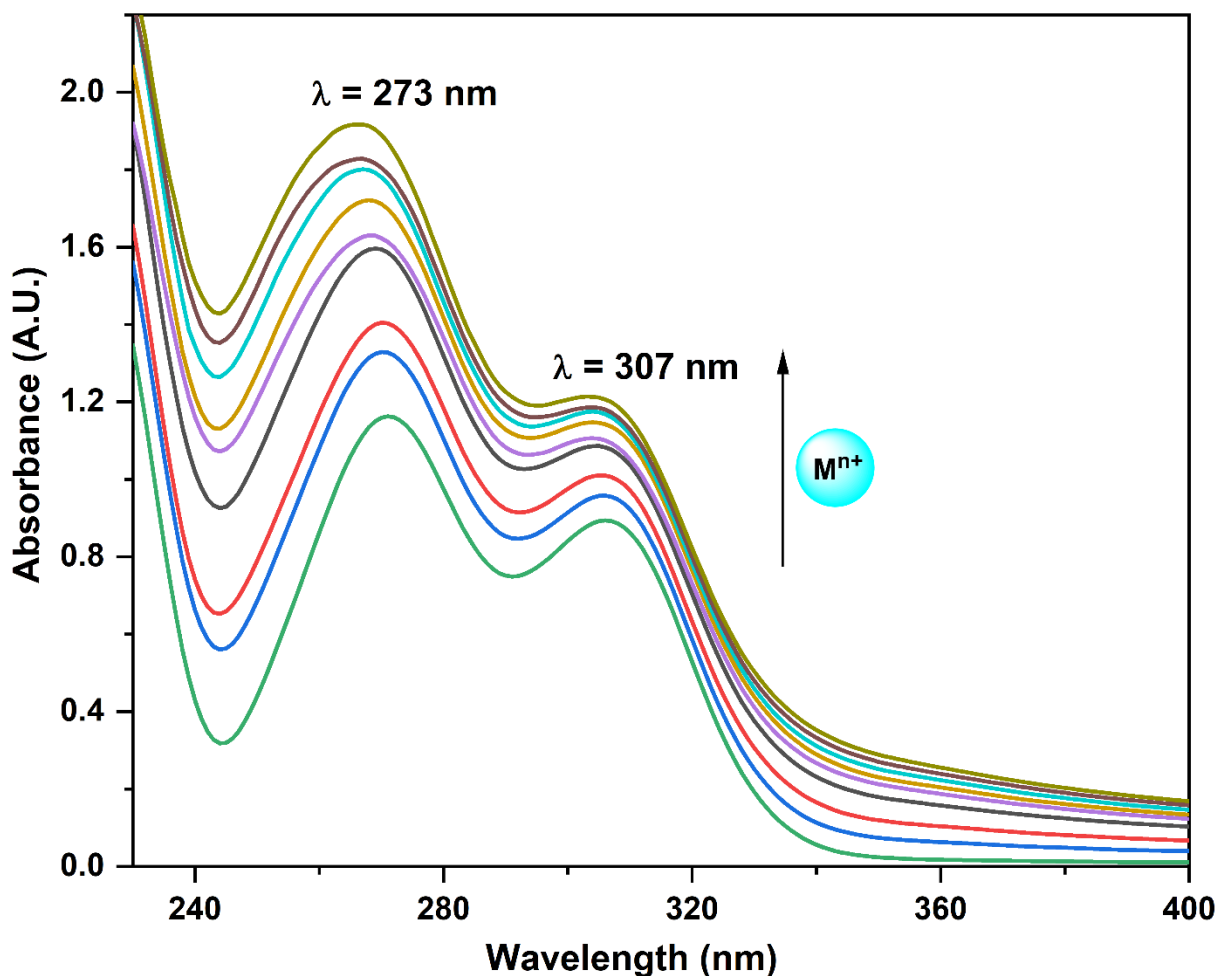


Figure 122. The UV–vis spectra of probe **84c** in (ACN:H₂O::4:1) demonstrate the specific binding of Hg²⁺ ions among other metal ions such as Zn²⁺, Ni²⁺, Mg²⁺, Co²⁺, Ce³⁺, Mn²⁺, Cd²⁺, Hg²⁺, Cu²⁺, Cr²⁺, Ba²⁺, Pb²⁺ at equimolar concentration

4.4 Time and Temperature dependence Study of [84c-Hg²⁺] complex

A time-dependent investigation was conducted using UV-visible spectrophotometry to explore the potential utility of the **84c** sensor in the detection of Hg²⁺ ions. In order to conduct the experiment, the **84c** sensor was added to Hg²⁺ ions, and subsequent UV-visible spectra was obtained at consistent time intervals ranging from 0 to 30 minutes. **(Figure 123)** The outcomes indicate that there was no statistically significant difference in the fluorescence intensity across different time periods. This suggests that **84c** may be considered as an efficient method for rapidly detecting Hg²⁺ ions.

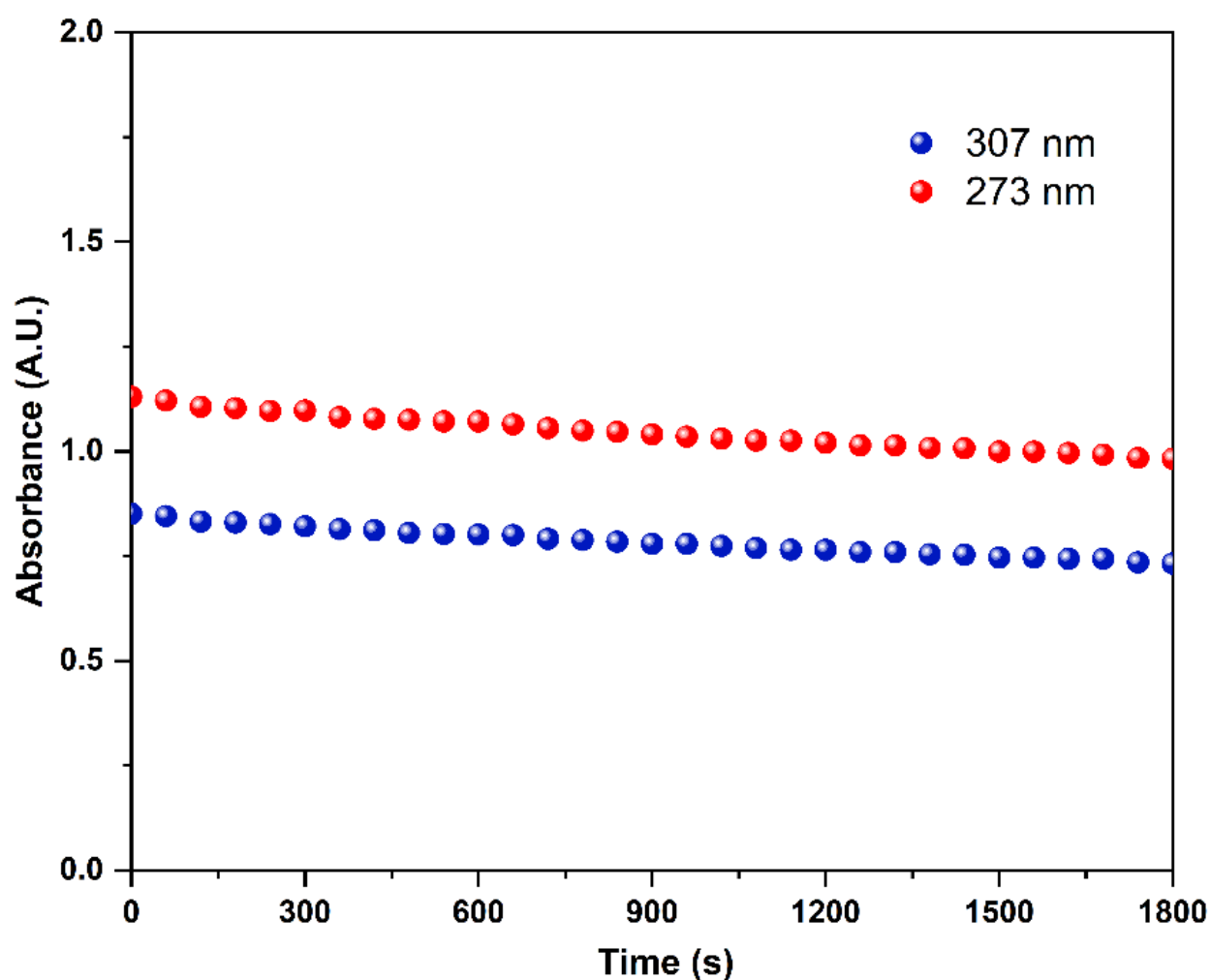


Figure 123. Time bound profile versus absorption of the $[84\mathbf{c}\text{-Hg}^{2+}]$ complex in ACN:H₂O::4:1 solvent system for 30 minutes at $\lambda = 273$ and 307 nm

Moreover, an investigation was carried out within a specific temperature range to examine the impact of temperature on the interaction between the probe $[84\mathbf{c}\text{-Hg}^{2+}]$. The absorption intensity was recorded at regular intervals as the temperature increased from 32 °C to 44 °C. The data is presented in graphical form in (Figure 124), illustrating the decrease in absorption resulting from an increase in temperature.

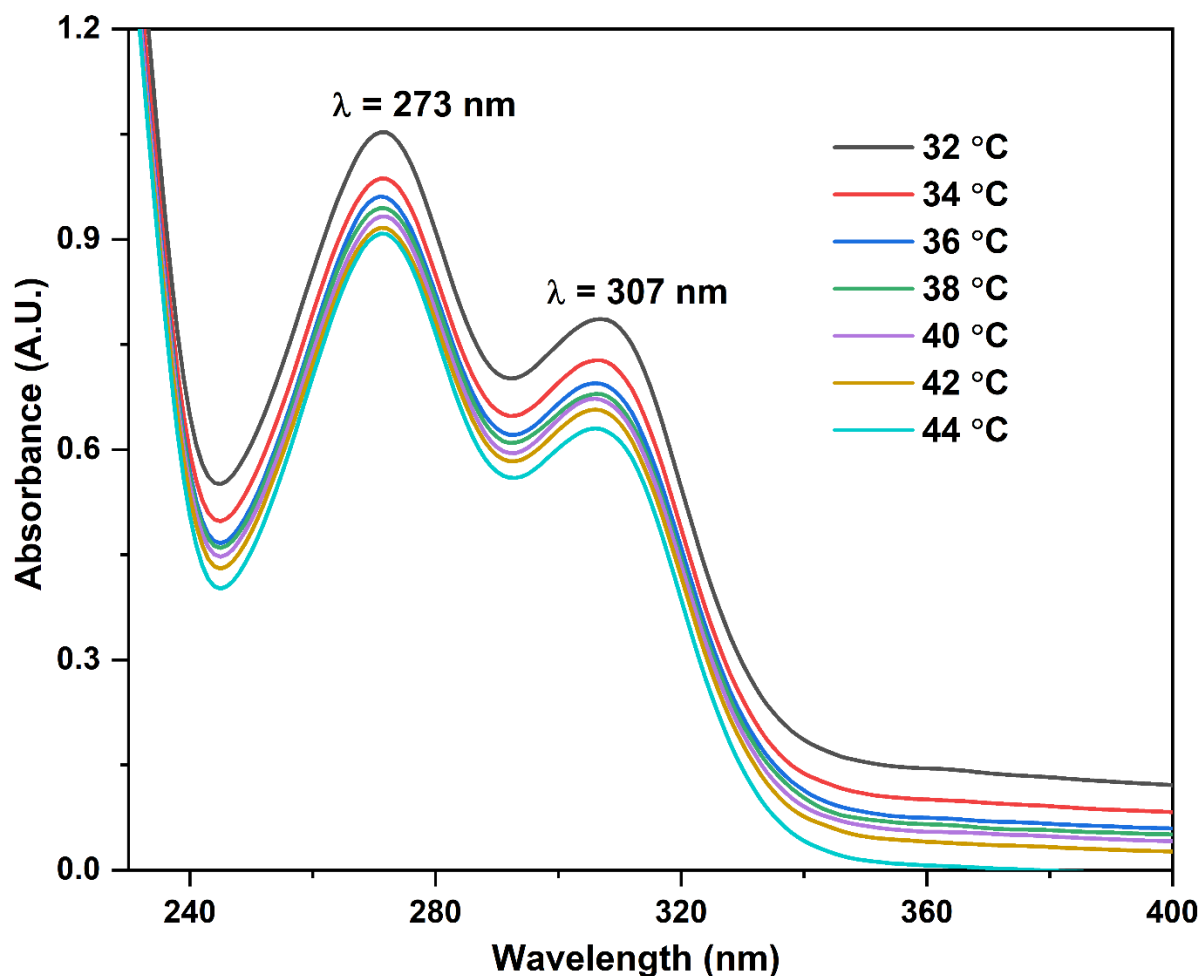


Figure 124. Effect of temperature on the binding of [84c-Hg²⁺] complex in ACN:H₂O::4:1 solvent system from 32 °C to 44 °C

4.5 Fluorescence emission studies of chemosensor 84c

Fluorescence emission spectrum studies were conducted to explore the sensing capability of probe **84c** towards Hg²⁺ ions in a mixed aqueous media (ACN:H₂O::4:1). The spectrum outcomes are illustrated in **Figure 125** where an emission band with wavelength $\lambda_{em} = 520$ nm was observed for probe **84c** when excited at $\lambda_{ex} = 310$ nm in (ACN:H₂O::4:1) solvent mixture. The changes in the emission band at 520 nm were noted while introducing various concentrations of Hg²⁺ ions into the chemosensor **84c** solution.

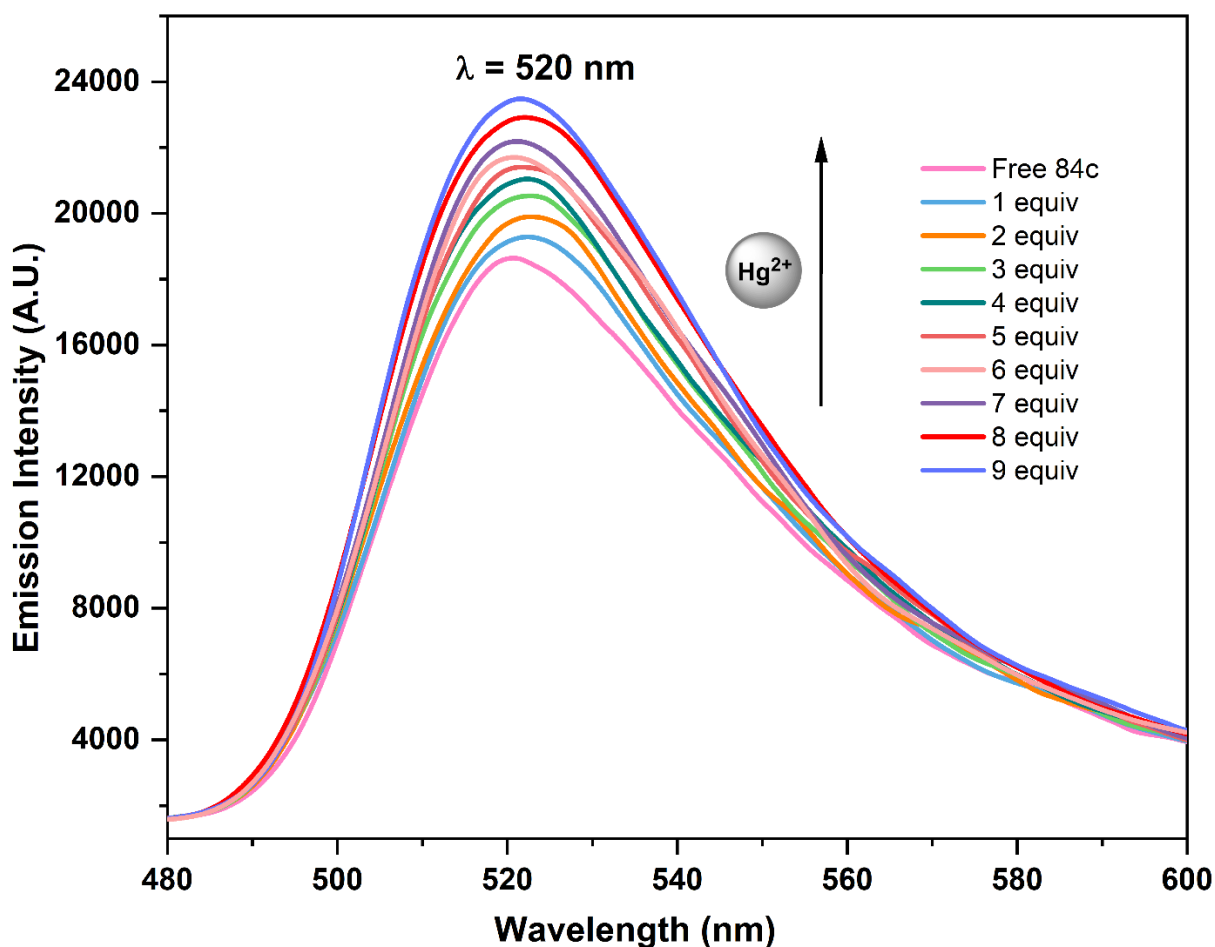


Figure 125. The fluorescence spectra of the sensor **84c** (0.005 mM) was observed at $\lambda_{\text{ex}} = 310$ nm. As 1 equiv. of 0.1 mM Hg^{2+} ions solution was added in (ACN:H₂O::4:1) solvent mixture, a noticeable increase in the intensity was observed (Hyperchromic shift)

Furthermore, **Figure 126** demonstrated an increase in the emission intensity ratio I_0/I , where I_0 symbolize the emission intensity of sensor **84c** without the presence of Hg^{2+} ions and I represents the emission intensity after the binding of **84c** with Hg^{2+} ions, with each consecutive addition. Probe **84c** exhibited feeble fluorescence that can be attributed to photoinduced electron transfer (PET) mechanism that can proceed from the 1,2,3-triazole moiety (Nitrogen atom) to the π -benzyl ring. However, the fluorescence intensity has been progressively increased by the addition of Hg^{2+} in (ACN:H₂O::4:1) solution.

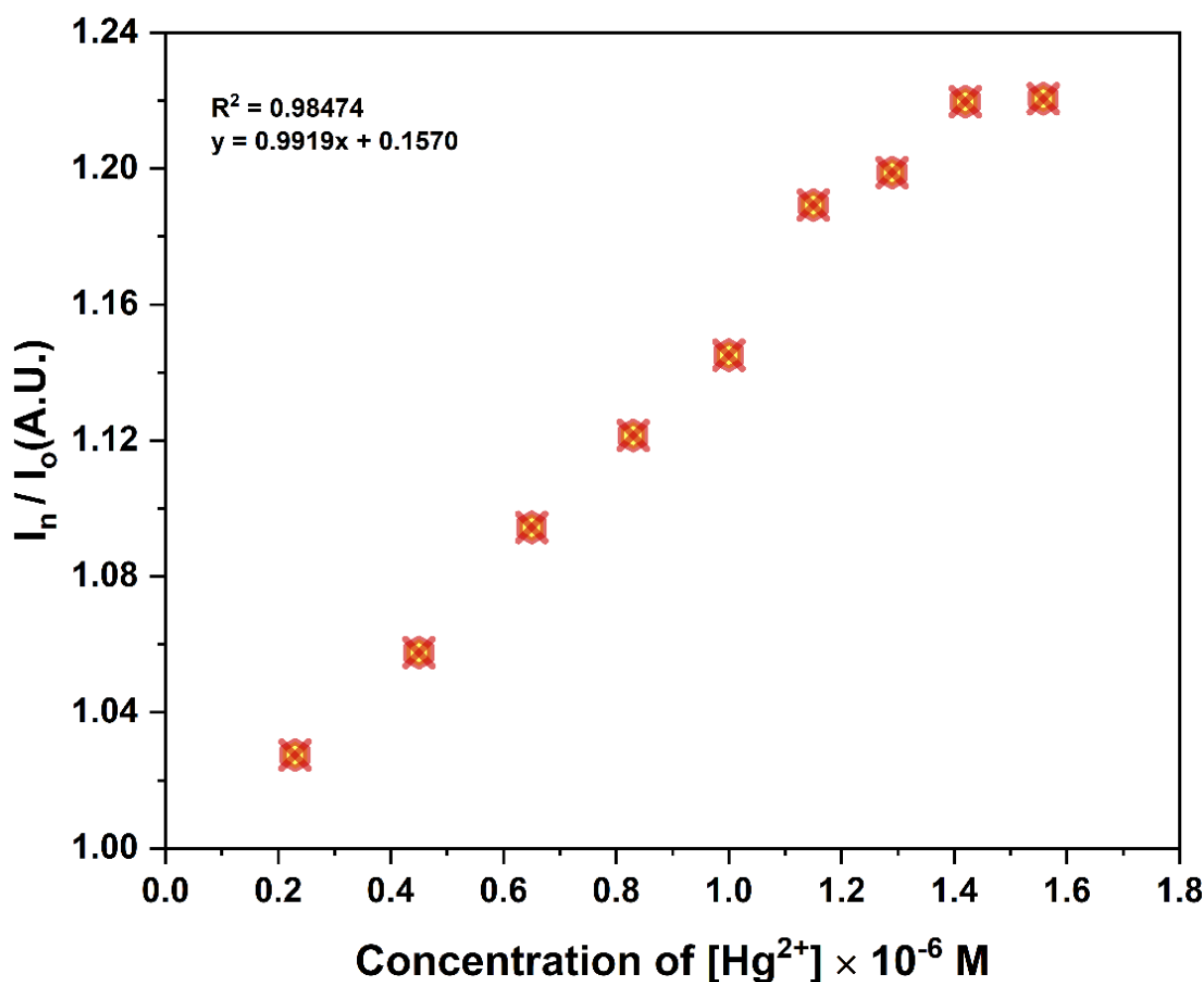


Figure 126. The fluorescence intensity ratios (I_n/I_o) at 520 nm plotted against variant concentration of Hg^{2+} ions at $\lambda_{ex} = 320$ nm. The emission intensity of probe **84c** in the absence of Hg^{2+} is denoted as I_o , whereas I_n represents the emission intensity during the binding of **84c** with Hg^{2+} ions with each successive addition

PET is a crucial design for the creation of fluorescent probes that can switch between a "OFF" and "ON" state. PET arises due to the transfer of electrons between the fluorophore and the recognition group. During the recognition process, the activating group forms a bond with a specific target analyte (Hg^{2+}), resulting in a-PET off and the activation of fluorescence, known as "OFF-ON" response. (**Figure 127**) After recognition, the oxidation potential of the activating group rises and it loses its ability to effectively donate electrons.¹¹ As a consequence, a-PET is prevented from occurring after binding with the Hg^{2+} ions. The fluorophore is excited at $\lambda_{ex} = 310$ nm, causing the promotion of one electron from its highest occupied molecular orbital (HOMO)

to its lowest unoccupied molecular orbital (LUMO). The energy level of the receptor's HOMO is slightly greater than that of the fluorophore's HOMO therefore electron transfer occurs from the receptor's HOMO to the fluorophore's HOMO via photoinduced electron transfer (PET). Consequently, a single electron becomes trapped in the fluorophore's LUMO, resulting in the suppression of emission. The interaction between the analyte and receptor reduces the energy of the receptor's HOMO compared to that of the fluorophore's HOMO. The decrease in energy level of the receptor's HOMO ultimately hinders the PET phenomenon and reestablishes the initial emission of the probe. Fluorescence recovery is often associated with the relaxation of excited $\pi \rightarrow \pi^*$ states in fluorophores, especially organic ones.¹²

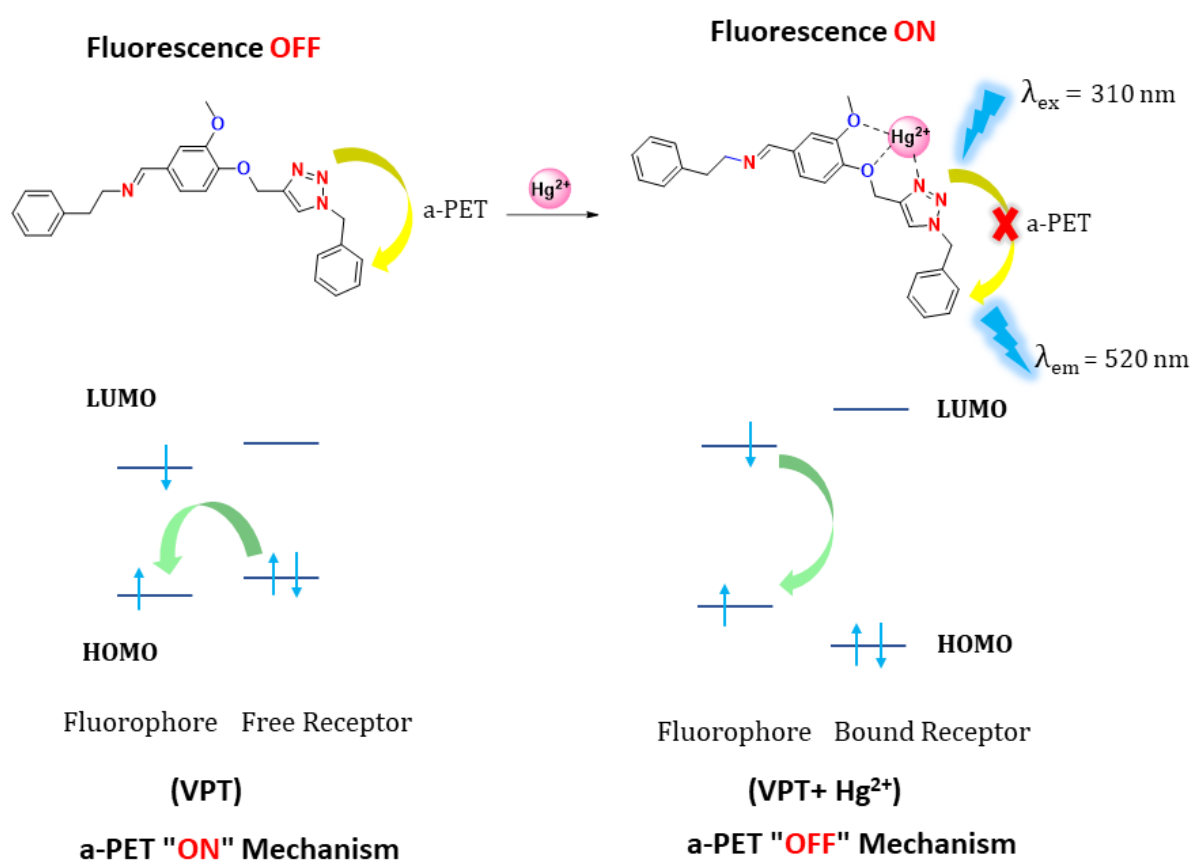


Figure 127. PET mechanism, displaying the modified version of the frontier orbital energy diagram showing binding based fluorescent metal ions detection when the probe was excited at $\lambda_{\text{ex}} = 310 \text{ nm}$

4.6 Detection Limit of [84c-Hg²⁺] complex

The evaluation of the limit of detection (LOD) and limit of quantification (LOQ) for Hg²⁺ ions was calculated using equation (2) and (3) respectively from **section 1.8**, where the variable K represents the slope of the plot that depicts the relationship between the ratio of absorbance intensity and conc. of mercuric ions. On the other hand, the variable σ represents the standard deviation of the blank measurement, which is determined using the Co-Linear plot. (**Figure 128**) The calculated limit of detection (LOD) of mercuric ions in drinking water is significantly lower than the permissible levels. The calculated detection limit and limit of quantification for probe **84c** in determining Hg²⁺ ions were found to be 0.5×10^{-9} M and 1.7×10^{-9} M respectively.

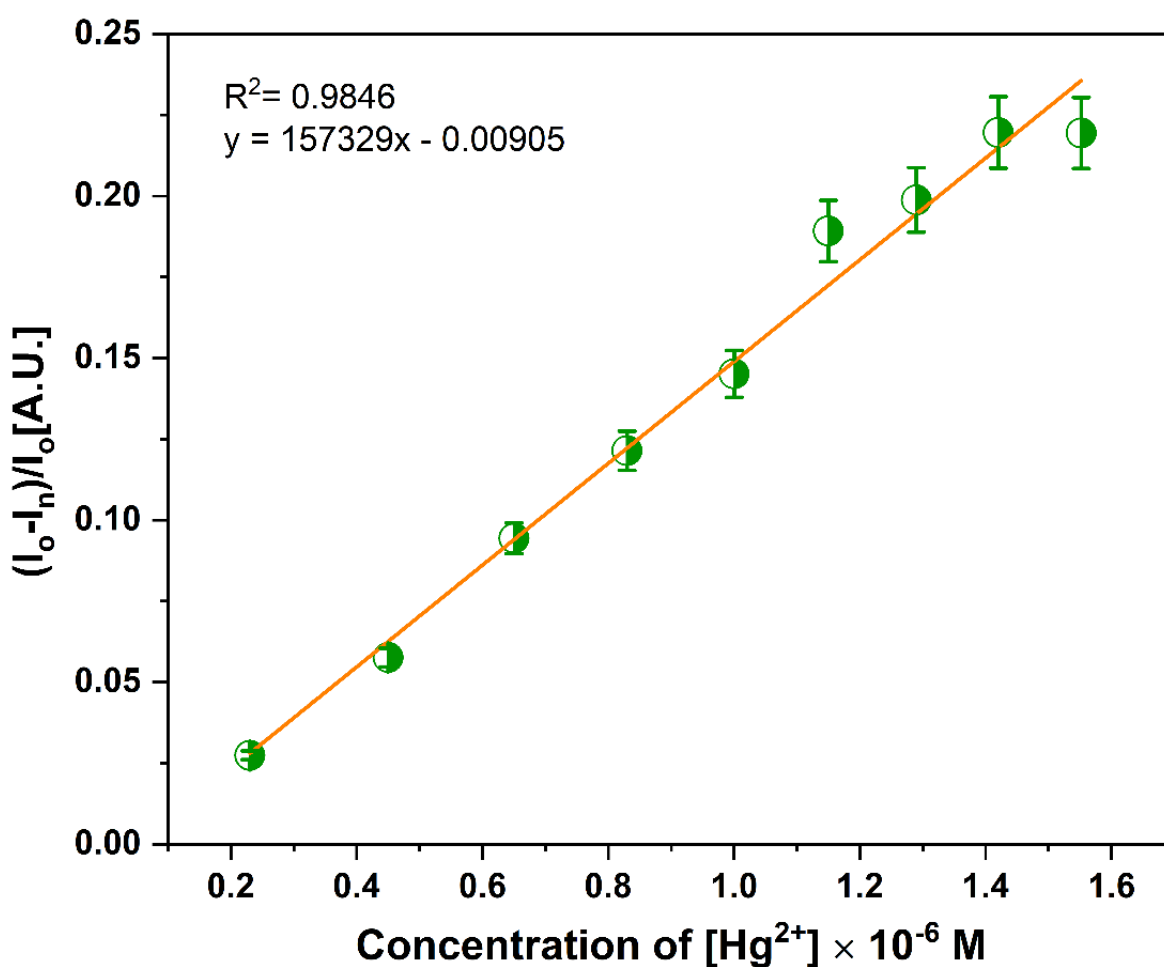


Figure 128. The co-linear plot, represented by the ratio $[I_o - I_n / I_o]$ plotted against the concentration of Hg²⁺ ions, wherein I_n = Emission intensity seen with each subsequent addition of Hg²⁺ ions, while I_o = Emission Intensity of probe **84c**

4.7 Probable binding mode of [84c-Hg²⁺] complex

The HSAB theory postulates that soft acids have a preference for interacting with soft bases, whereas hard acids tend to associate with hard bases.¹³ Prior research on Mercuric ions chemo-sensing has identified a few ligands containing nitrogen and oxygen atoms as donor sites that exhibit strong interaction with Hg²⁺ ions.^{14,15} Enriched with nitrogen and oxygen heteroatoms, the structural constituents of the newly synthesized probe **84c** facilitate its complexation with Hg²⁺ ions. The stoichiometry of the **84c**: Hg²⁺ complex as determined from the job's plot indicates a 1:1 ratio, illustrating the plausible binding mode as shown in **Figure 129**. Through the transfer of a lone pair of electrons into the vacant orbitals of the metal ion's outermost shell, sensor **84c** may bind with Hg²⁺ ions via nitrogen atoms on triazole rings and oxygen atoms in close proximity.

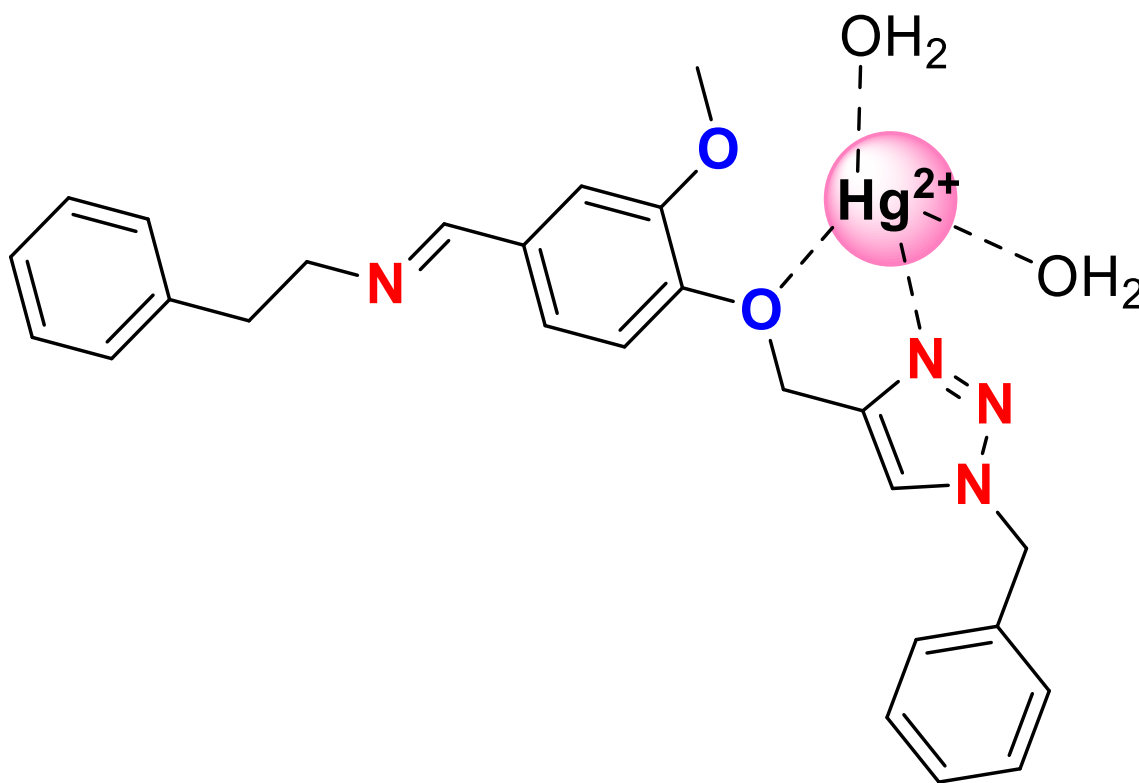


Figure 129. Plausible binding mode of **84c**-Hg²⁺ complex (1:1) stoichiometric ratio in (ACN:H₂O::4:1) solvent system

The plausible mode of interaction amongst **84c** and Hg^{2+} has been validated using FTIR spectroscopy analysis. In IR spectra of **84c** with Hg^{2+} , the broad peak of OH group at 3386 cm^{-1} represent the linkage of H_2O molecules with Hg^{2+} metal ion, the distinctive peak of the (C–N) group of 1,2,3-triazole ring shifts from 1266 cm^{-1} to 1257 cm^{-1} , which may be attributed to its coordination with this group. Furthermore, the shift in vibrations in area of 1138 cm^{-1} to 1127 cm^{-1} shows that oxygen atoms play a significant role in binding. This observation suggests the coupling of Hg^{2+} metal ions with OH_2 , (C–O) and (C–N) groups of the 1,2,3- triazole moiety.

The LCMS-MS analysis of the complex [**84c**- Hg^{2+}] was also conducted. The anticipated mass spectrum m/z of [**84c**- Hg^{2+} - $\text{Na}^+(\text{H}_2\text{O})_2$] calculated as 684.98 appeared at $m/z = 685.52$ [$M + 1$]. The m/z value aligns strongly with the postulated stoichiometry

5. Photophysical analysis of chemosensor **85c**

5.1 U.V visible absorption studies of **85c**

Absorption spectroscopy was employed to investigate effect of various metal ions on the photophysical characteristics of sensor **85c**. The cation sensing capability of the ligand **85c** (0.05 mM) was evaluated in (ACN: H_2O ::4:1) solution at ambient temperature. The probe **85c** exhibited higher energy absorption band at $\lambda_{\text{max}} = 272\text{ nm}$, resulting from the π – π^* transition, and lower energy absorption band at $\lambda_{\text{max}} = 307\text{ nm}$ owing to n – π^* transition. The receptor **85c** was exposed to titration using several metal ions, including Na^+ , K^+ , Mg^{2+} , Cr^{3+} , Mn^{2+} , Co^{2+} , Ni^{2+} , Cu^{2+} , Zn^{2+} , Ba^{2+} , Ag^+ , Pb^{2+} , Ce^{3+} and Cd^{2+} ions. Out of the various metal ions examined, the probe **85c** exhibited significant alterations in the absorption spectra specifically with the Cu^{2+} (0.1 mM) and Pb^{2+} ions (0.1 mM) while the other metal ions did not display any significant changes in their spectra as shown in bar graph. (**Figure 130**)

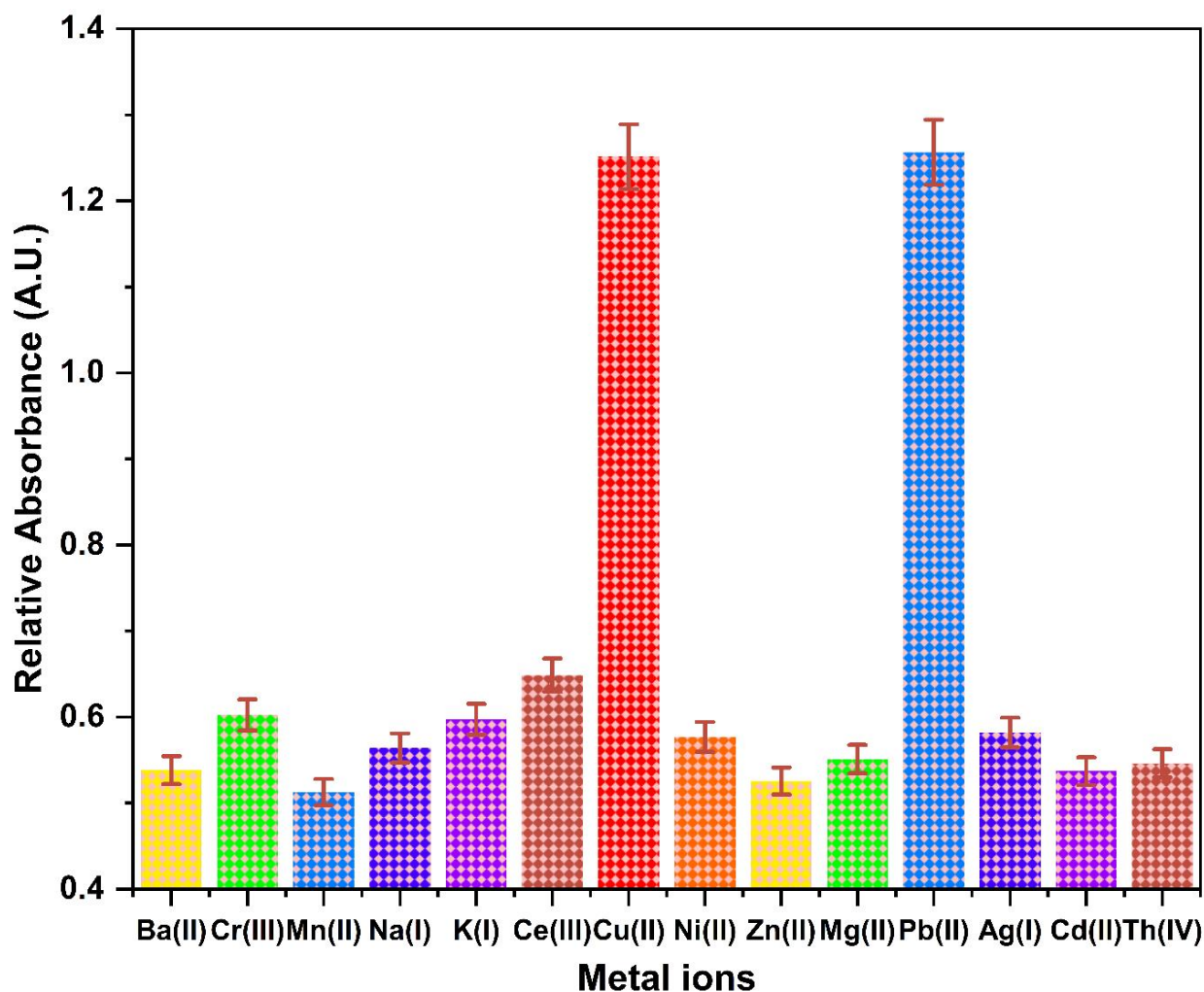


Figure 130. Bar graph illustrating the response of metal ions such as Ba^{2+} , Cr^{3+} , Mn^{2+} , Na^+ , K^+ , Ce^{3+} , Cu^{2+} , Ni^{2+} , Zn^{2+} , Mg^{2+} , Pb^{2+} , Ag^+ , Cd^{2+} , Th^{4+} towards chemosensor **85c** at $\lambda_{\text{max}} = 272 \text{ nm}$ in $\text{CH}_3\text{CN}:\text{H}_2\text{O}::4:1$ solvent system

When Cu^{2+} or Pb^{2+} metal ions were added into the **85c** solution, the higher energy band experiences an enhancement, while the lower energy band is reduced (**Figure 131, 132**). When the Cu^{2+} metal ions solution (0-19 equiv.) was added to solution of **85c**, the absorbance intensity increases at 272 nm, also the isosbestic point at 392 nm for Cu^{2+} was observed in the spectra.

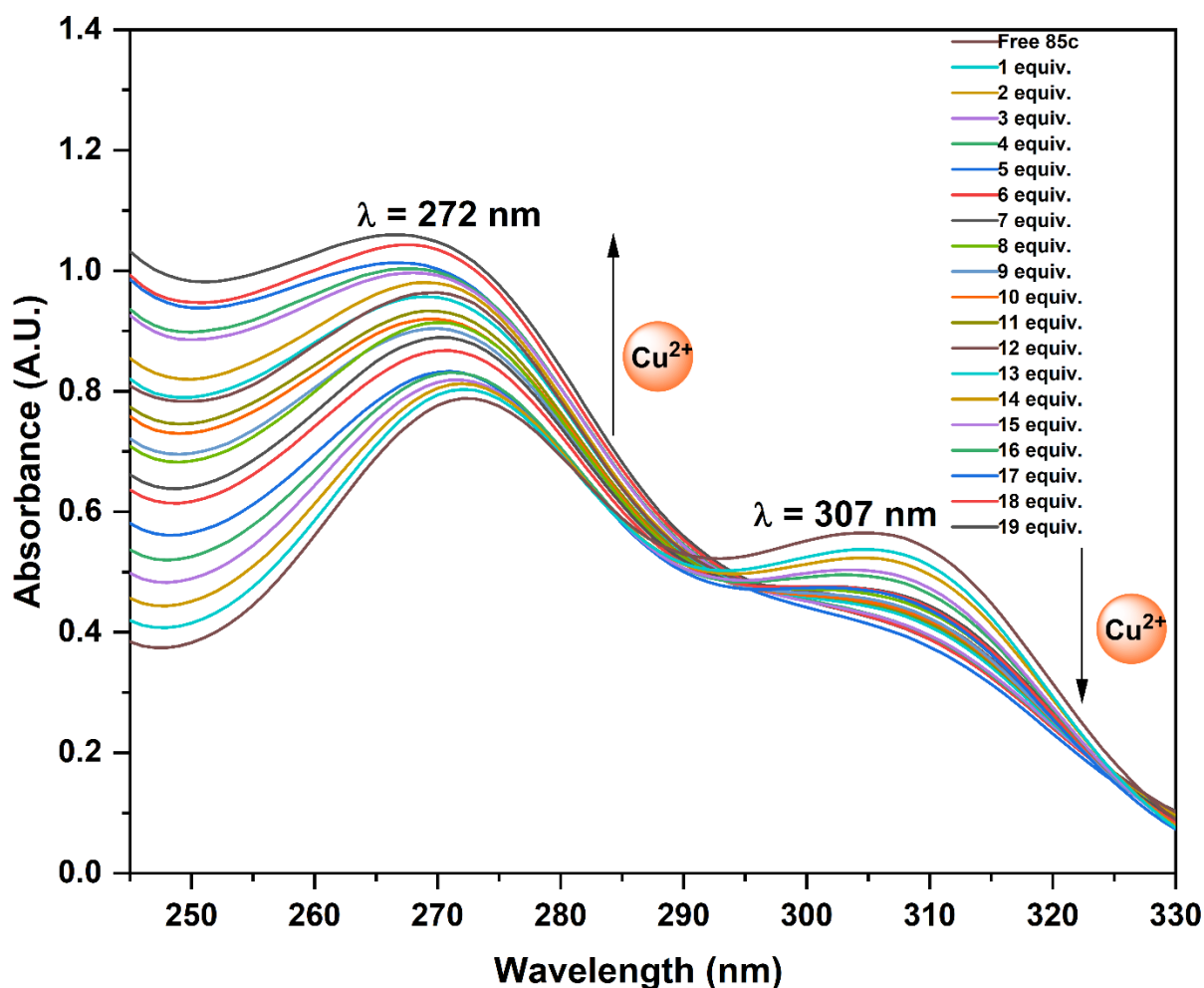


Figure 131. The UV-vis spectral variations of **85c** (0.05 mM) in (ACN:H₂O::4:1) after incremental addition (0-19 equiv.) of Cu²⁺ ions. The rise in absorbance intensity (hyperchromic shift) at $\lambda = 272$ nm and the decrease in absorbance intensity at $\lambda = 307$ nm was observed along with the isosbestic point at 307 nm

Also, on the addition of Pb²⁺ ion solution (0 to 22 equiv.) to the **85c** solution, the similar pattern was seen as observed for Cu²⁺ ions, the absorbance intensity at 272 increases alongwith the emergence of isosbestic point at 396 nm for Pb²⁺ ions. This observation clearly indicated the seamless transformation of the free ligand into a metal-ligand complex for both Cu²⁺ and Pb²⁺ ions.

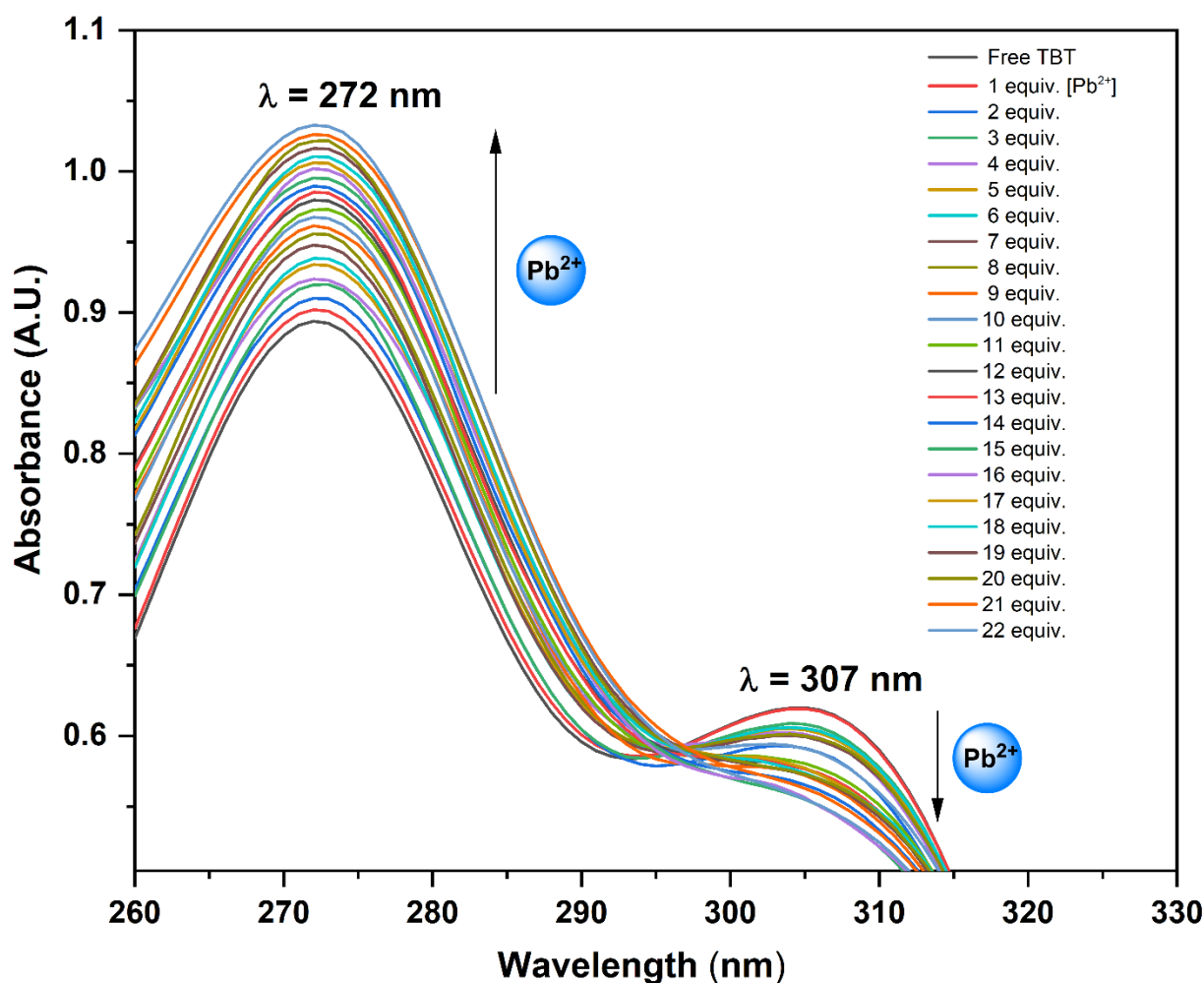


Figure 132. The absorbance spectra of **85c** (0.05 mM) displaying the spectral changes after cumulative addition of (0-22 equiv.) Pb^{2+} ions. The upsurge in absorbance intensity (hyperchromic shift) at $\lambda = 272$ nm and the reduction in absorption intensity at $\lambda = 307$ nm alongwith a distinct isosbestic point at 312 nm was observed

The relative change in the absorbance (A_n/A_o) versus concentration of molar ion at 272 nm following incremental augmentation of metal ions concentration, where A_n = the absorbance maxima observed upon successive addition of metal ions, and A_o = the absorbance maxima observed for **85c**. The relative absorption graph versus the concentration of the metal ions (Cu^{2+} and Pb^{2+}) is presented as **Figure 133** and **Figure 134**

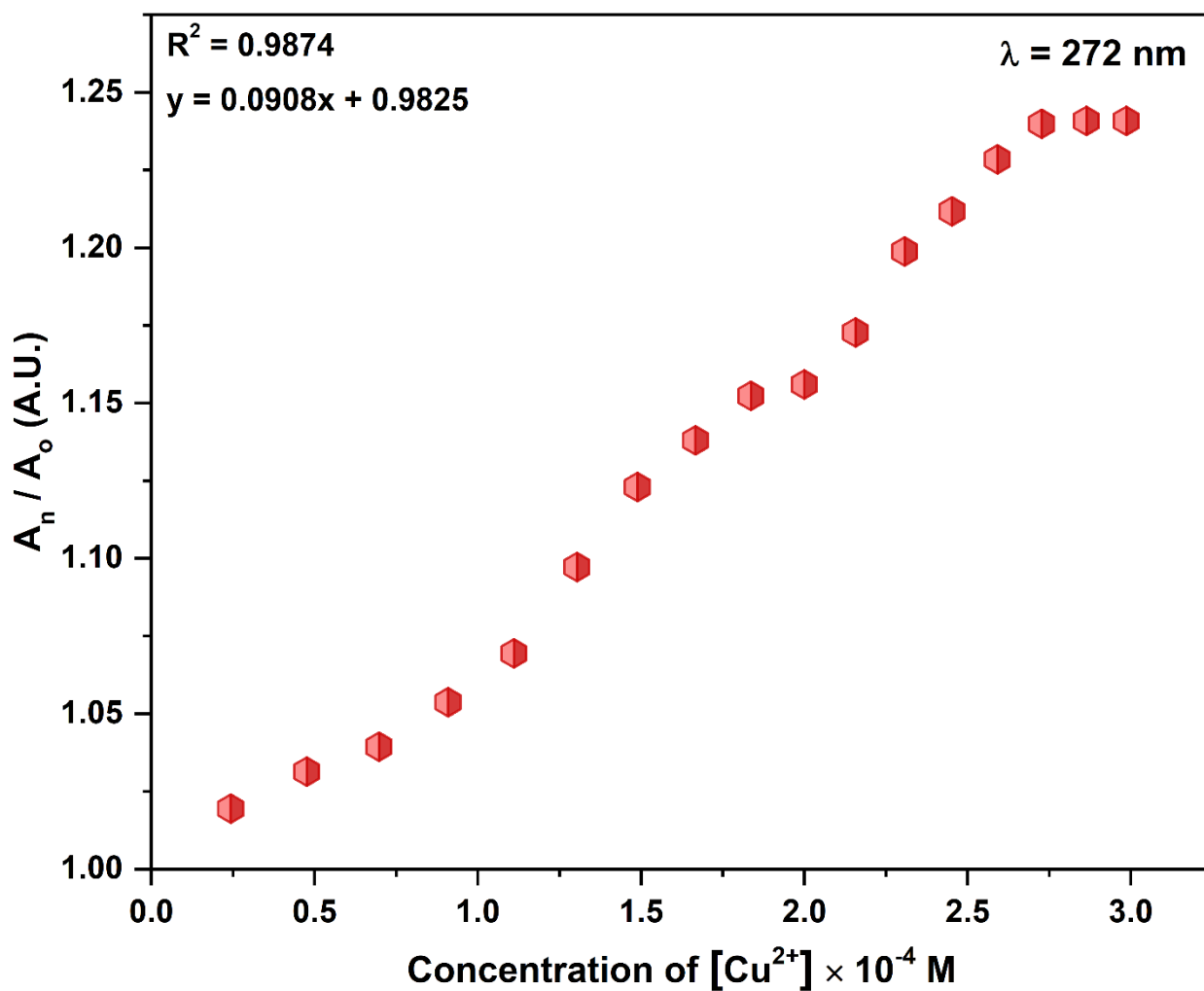


Figure 133. The linear response of the relative absorbance (A_n/A_o) of **85c** plotted against the increase in concentration of Cu^{2+} ions in (ACN:H₂O::4:1) solvent medium at $\lambda = 272 \text{ nm}$, herein A_o denotes the absorbance of free **85c** and A_n represent the absorbance of **85c** after addition of Cu^{2+} ions

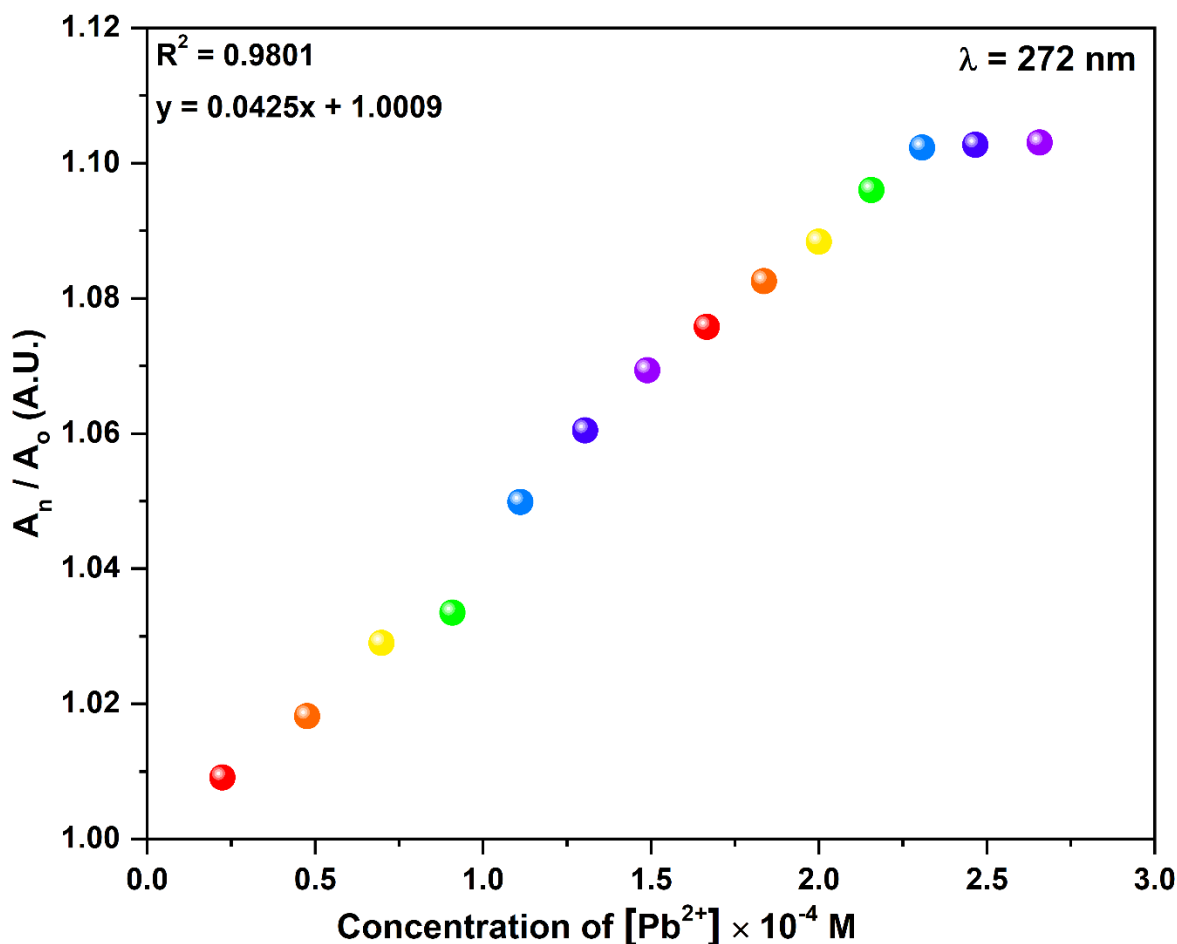


Figure 134. The relative absorbance of **85c** increases in linear manner with the upsurge in concentration of Pb^{2+} ions at $\lambda = 272$ nm in (ACN:H₂O::4:1) solvent medium, wherein A_o = absorbance of free probe **85c** and A_n = absorbance of probe **85c** in presence of Pb^{2+} ions

5.2 Job's plot of **85c** with (Cu^{2+} and Pb^{2+}) metal ions

The method of continuous variation was employed for the complexation stoichiometry of probe **85c** with metal (Cu^{2+} and Pb^{2+}) ions, respectively. The equimolar solutions of probe **85c** and metal ions (Cu^{2+} and Pb^{2+}) were obtained with varying mole fractions, and Job's plots were established using the absorbance at 272 nm for Cu^{2+} and Pb^{2+} , as depicted in **Figure 135** and **136**, respectively

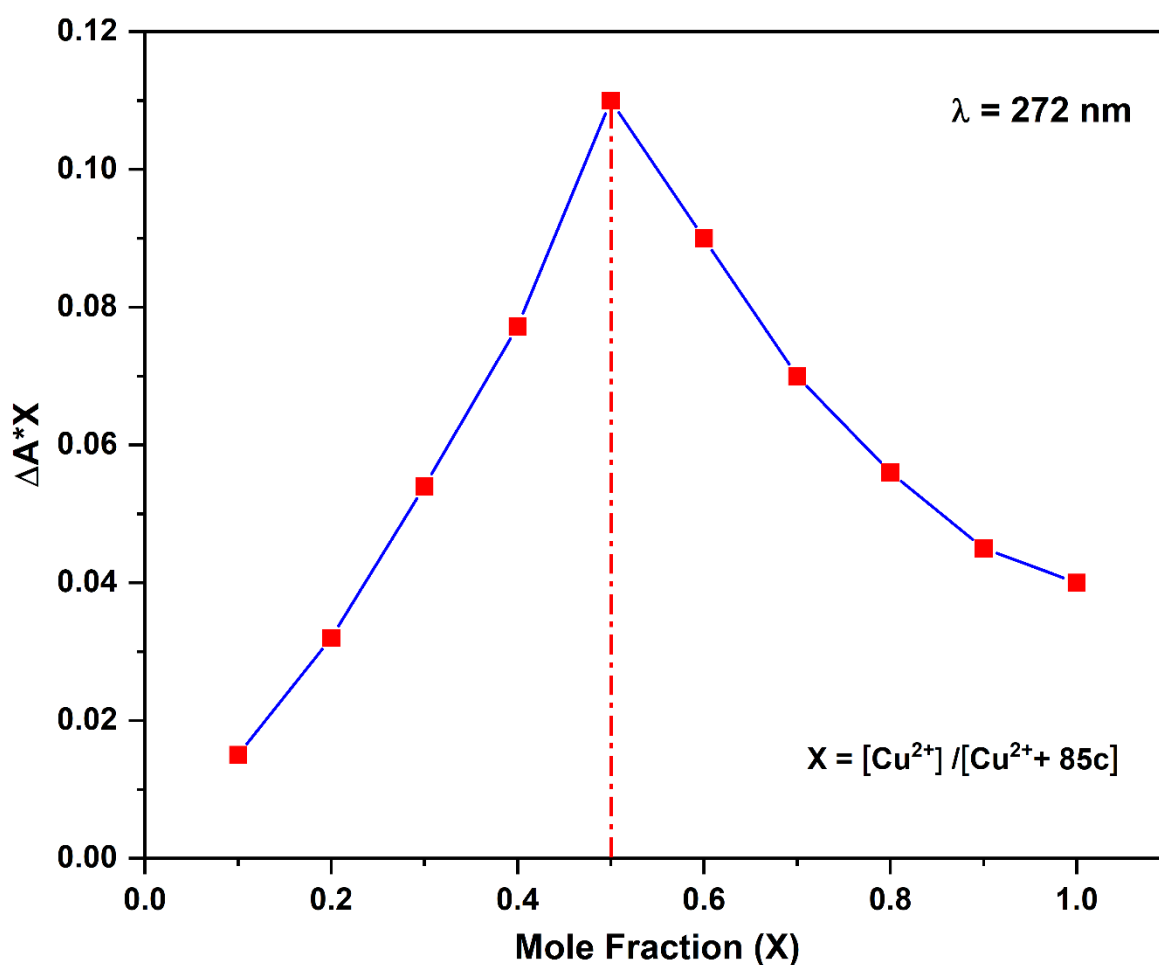


Figure 135. Job's plot for assessing the stoichiometry ratio of complexation between **85c** and Cu^{2+} ions in $\text{ACN}:\text{H}_2\text{O}::4:1$ solution, the maximum absorption value attained at 0.5 mole fraction showing (1:1) ratio of **[85c- Cu^{2+}]** complex

The highest relative absorbance observed at a mole fraction of 0.5 in both cases indicates that the metal-**85c** complex forms in a 1:1 stoichiometric ratio. Hence, the binding structure for the **85c** in the presence of Cu^{2+} or Fe^{3+} (denoted as M^{n+}) was postulated, relying on the formation of a 1:1 complex.

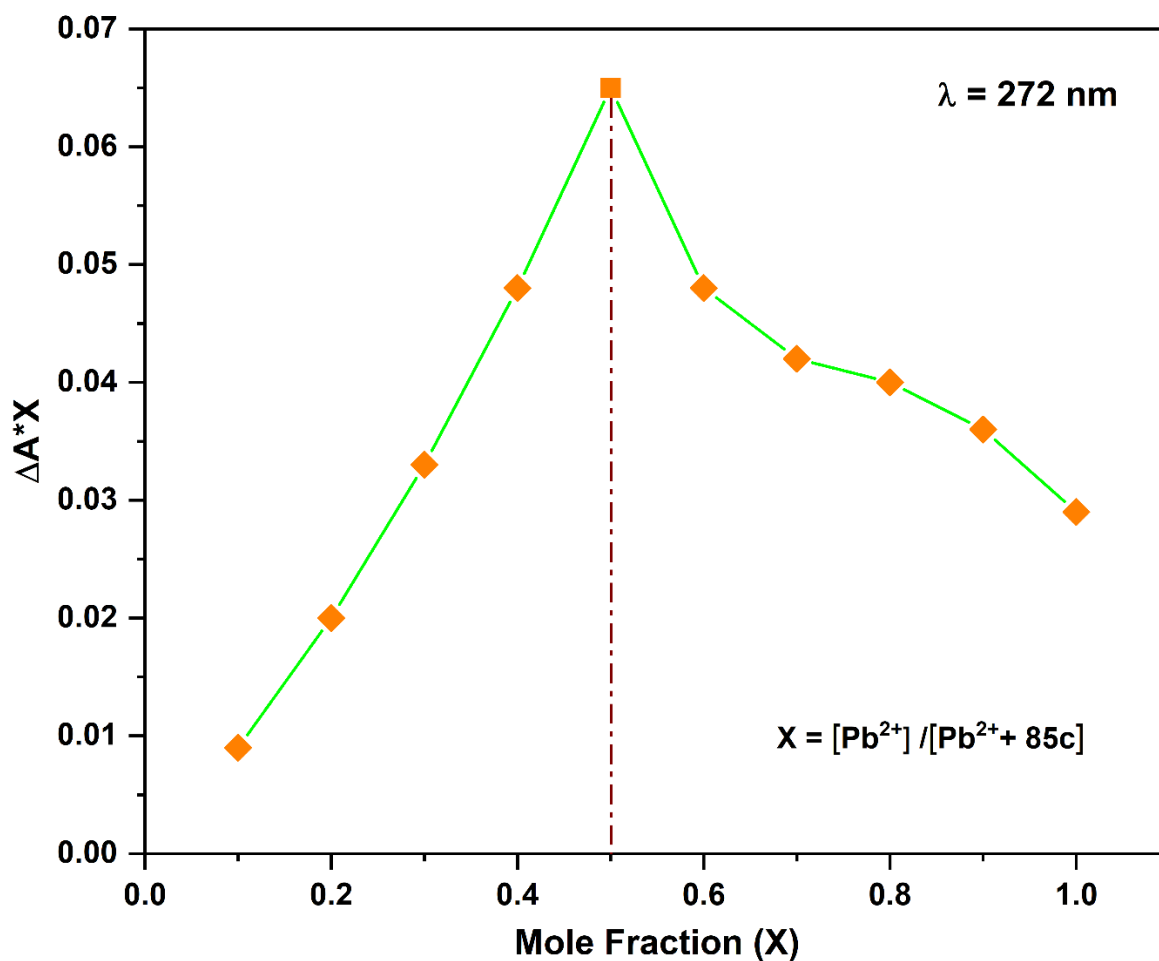


Figure 136. Job's plot for evaluating the stoichiometric ratio of $[85c-Pb^{2+}]$ complex in ACN:H₂O::4:1 solution at $\lambda = 272$ nm, the maximum value of relative absorbance was attained at 0.5 mole fraction depicting the (1:1) binding ratio of $[85c-Pb^{2+}]$ complex

5.3 Selectivity of the probe 85c

In order to assess the selectivity of the probe **85c** for detecting Cu^{2+} and Pb^{2+} , competitive assays were conducted in (ACN:H₂O::4:1) solution in the presence of various interfering metal ions. The absorbance spectrum obtained for all metal ions closely matched the sensing spectrogram of Pb^{2+} ions. The absorbance range of all metal ions titration falls in the same range as of (**85c** + Pb^{2+}) sensing.

The hyperchromic shift observed was identical to the spectra of Pb^{2+} sensing respectively, indicating the unique capability of the newly developed chemo-sensor **85c** for detecting Pb^{2+} metal

ions without interference as shown in **Figure 137** that indicates that the presence of other metal ions has a negligible impact on the sensing capabilities of **85c** towards Pb^{2+} ions.

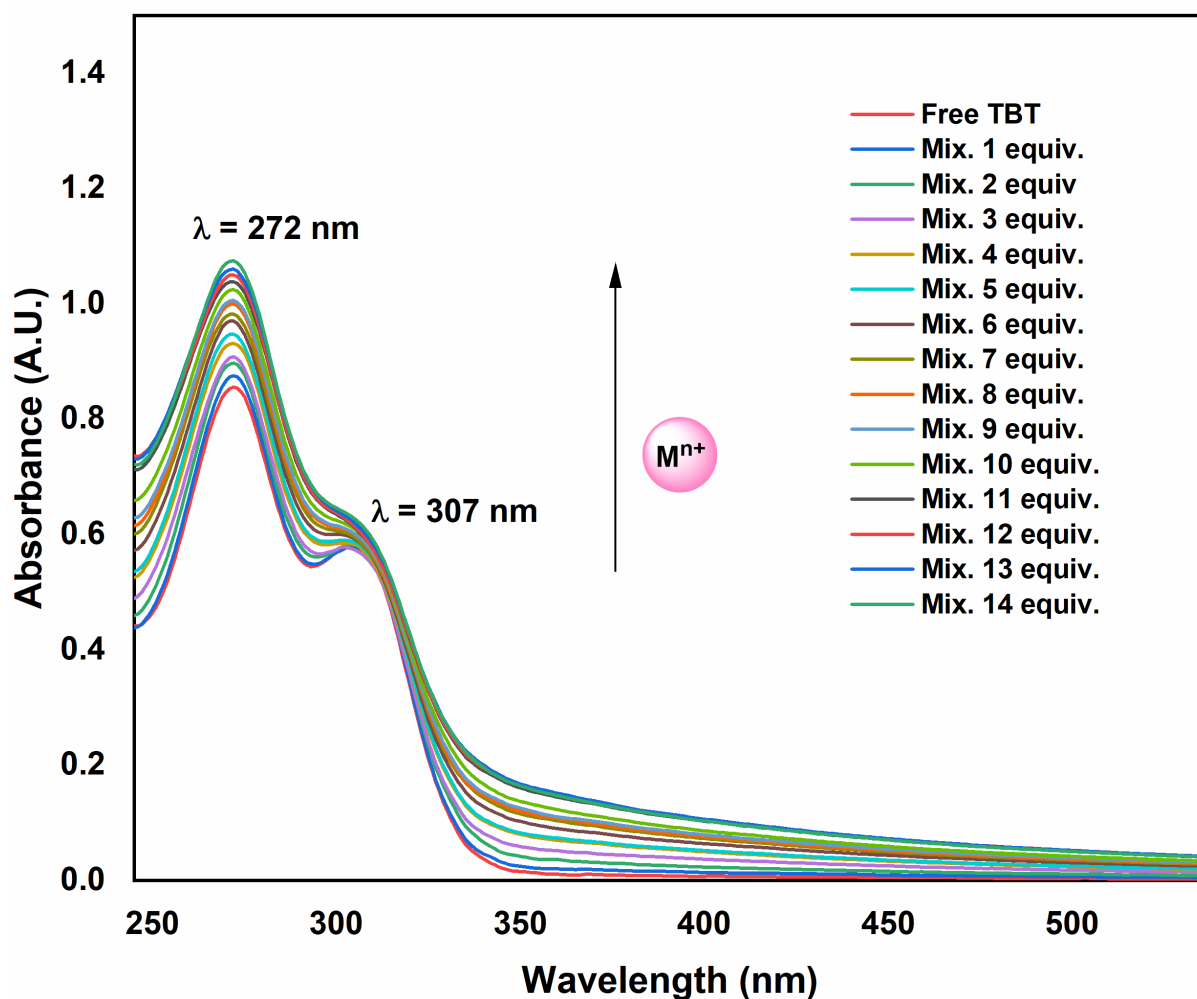


Figure 137. UV-vis anti-interference spectra of chemosensor **85c** depicting the selective sensing of Cu^{2+} and Pb^{2+} in equimolar coexistence of multiple metal ions, where M^{n+} represent the mixture of Ba^{2+} , Cr^{3+} , Mn^{2+} , Na^+ , K^+ , Ce^{3+} , Cu^{2+} , Ni^{2+} , Zn^{2+} , Mg^{2+} , Pb^{2+} , Ag^+ , Cd^{2+} , Th^{4+} metal ions in $\text{ACN}:\text{H}_2\text{O}::4:1$ solution

5.4 B-H plot of **85c** with (Cu^{2+} and Pb^{2+}) metal ions

The association constants for the probe **85c** with both Cu^{2+} and Pb^{2+} ions have been determined by applying the Benesi–Hildebrand equation (1) as stated in **section 1.5**, where the absorbance intensities of **85c** are represented by A_0 , A , and A' , which correspond to the absence

of any metal ions, the intermediate metal ions concentration, and the saturation concentration of M^{n+} , while K_a represents the binding constant. (Figure 138, 139)

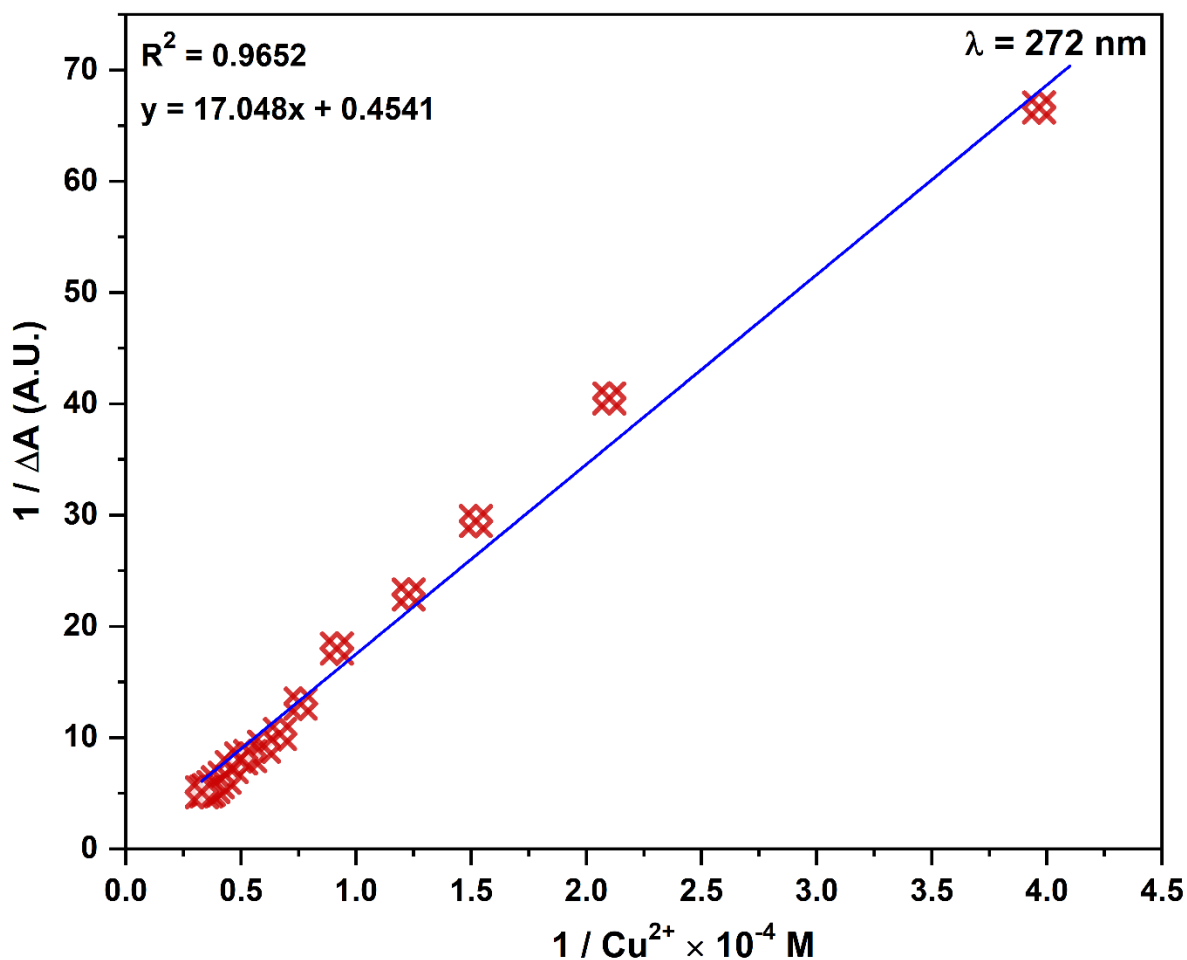


Figure 138. The absorption titration data of the probe **85c** with Cu^{2+} measured via Benesi-Hildebrand plot at 272 nm in ACN:H₂O::4:1 solution

The absorbance titration data was plotted for both the metal ions to obtain the linear fit of the graphical values for calculation of association constant. The binding constant (K_a) values have been estimated to be 3.75×10^5 and $1.02 \times 10^5 M^{-1}$ for Cu^{2+} and Pb^{2+} ions, respectively. The values attained from the graph depicts the strong binding of ligand **85c** with metal (Cu^{2+} and Pb^{2+} ions) complexes.

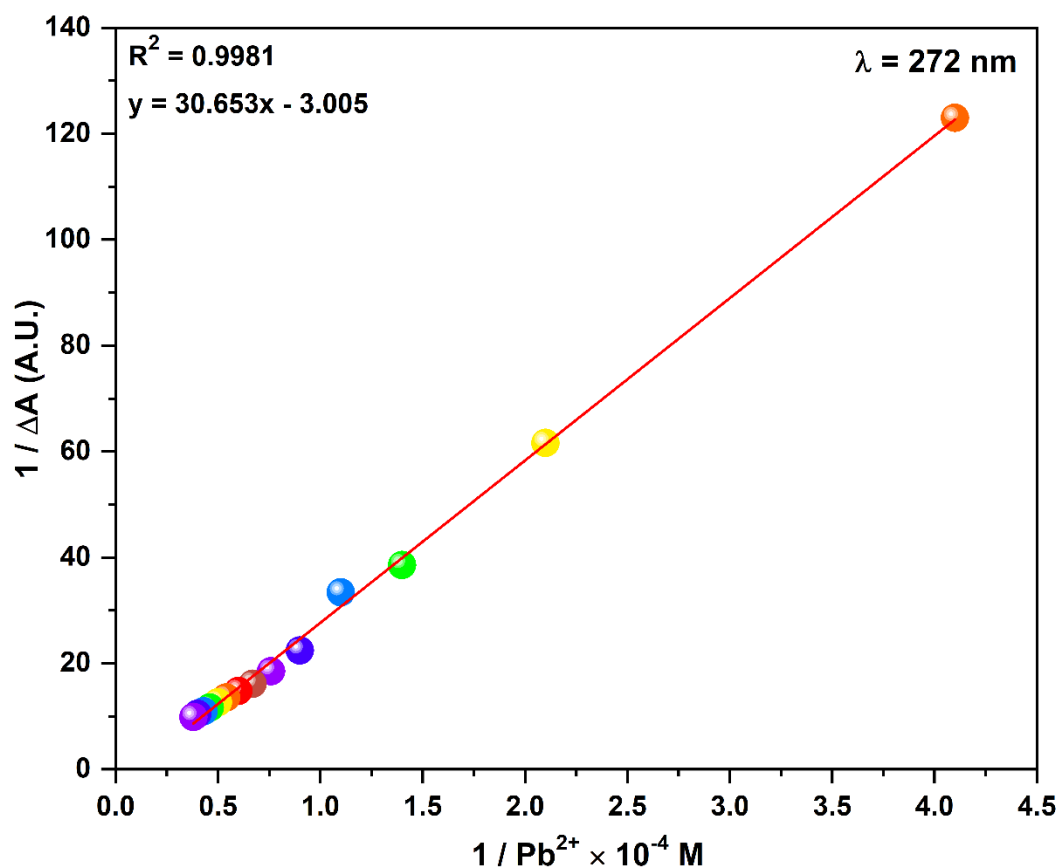


Figure 139. Benesi–Hildebrand plot of **85c** binding with the Pb^{2+} metal ion at 272 nm in ACN:H₂O::4:1 solution

5.5 Time-dependence study of **85c** with (Cu^{2+} and Pb^{2+}) metal ions

The time-dependent investigation was conducted utilising UV-vis spectrophotometry to evaluate the practical utility of sensor **85c** for detecting Cu^{2+} and Pb^{2+} metal ions (**Figure 140**). This investigation was performed by adding Cu^{2+} ions solution in the sensor **85c** solution and then the Pb^{2+} ions solution to sensor **85c** solution to measure the absorbance spectra at regular intervals for 30 minutes at $\lambda = 272 \text{ nm}$ and $\lambda = 306 \text{ nm}$.

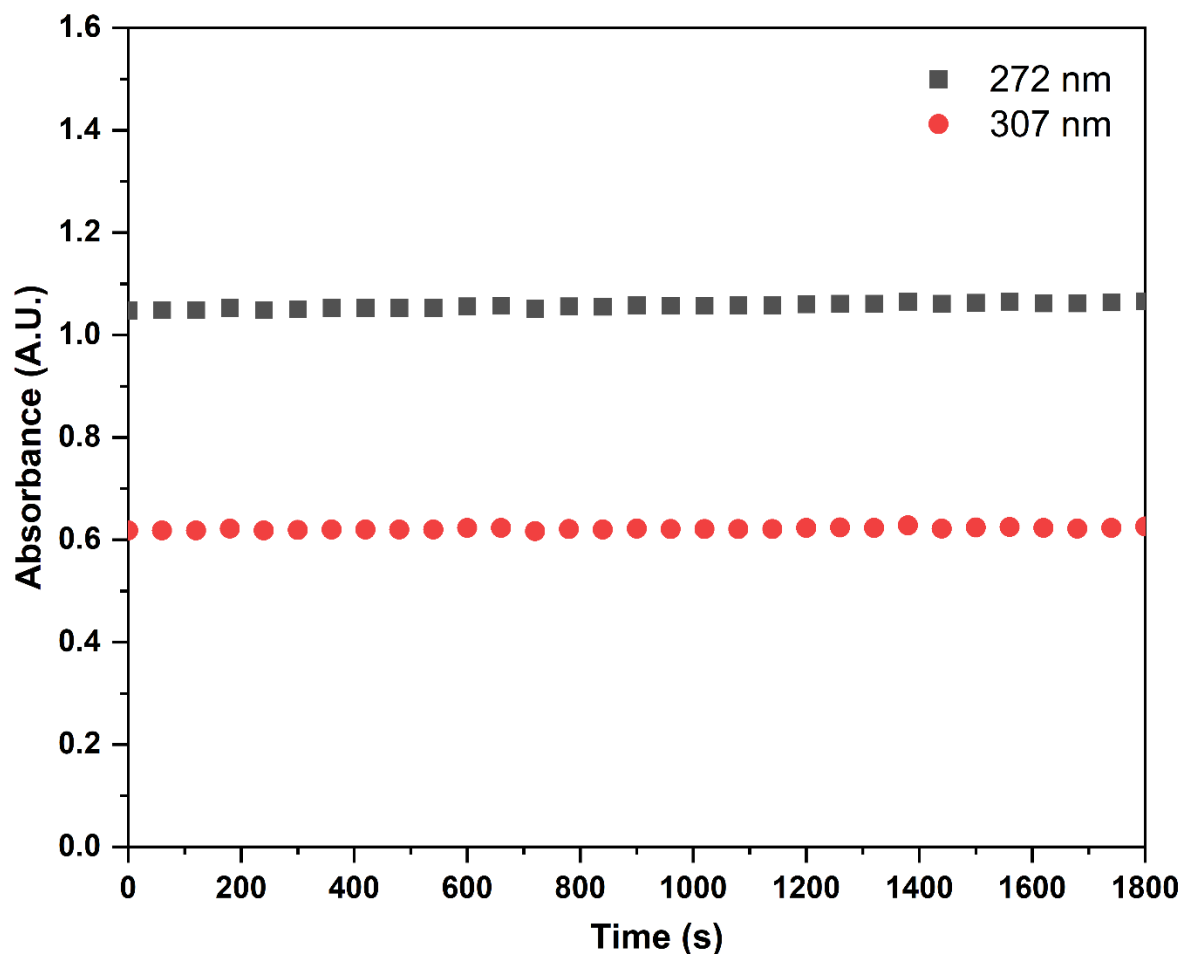


Figure 140. Time dependent study of probe **85c**-Cu²⁺ complex nm in ACN:H₂O::4:1 solution for 30 minutes

The outcomes indicated that there was no notable fluctuation in the absorbance intensity over different time periods (0-30 minutes) for Cu²⁺ ions (and similar changes were observed for Pb²⁺ ions (**Figure 141**) under similar conditions which suggests that **85c** is an effective probe for rapid detection of Cu²⁺ and Pb²⁺ ions. The absorbance intensity remains constant at $\lambda = 272$ nm and $\lambda = 306$ nm for both the metal-ligand complexes i.e [85c-Cu²⁺] and [85c-Pb²⁺] in (ACN:H₂O::4:1) solvent system.

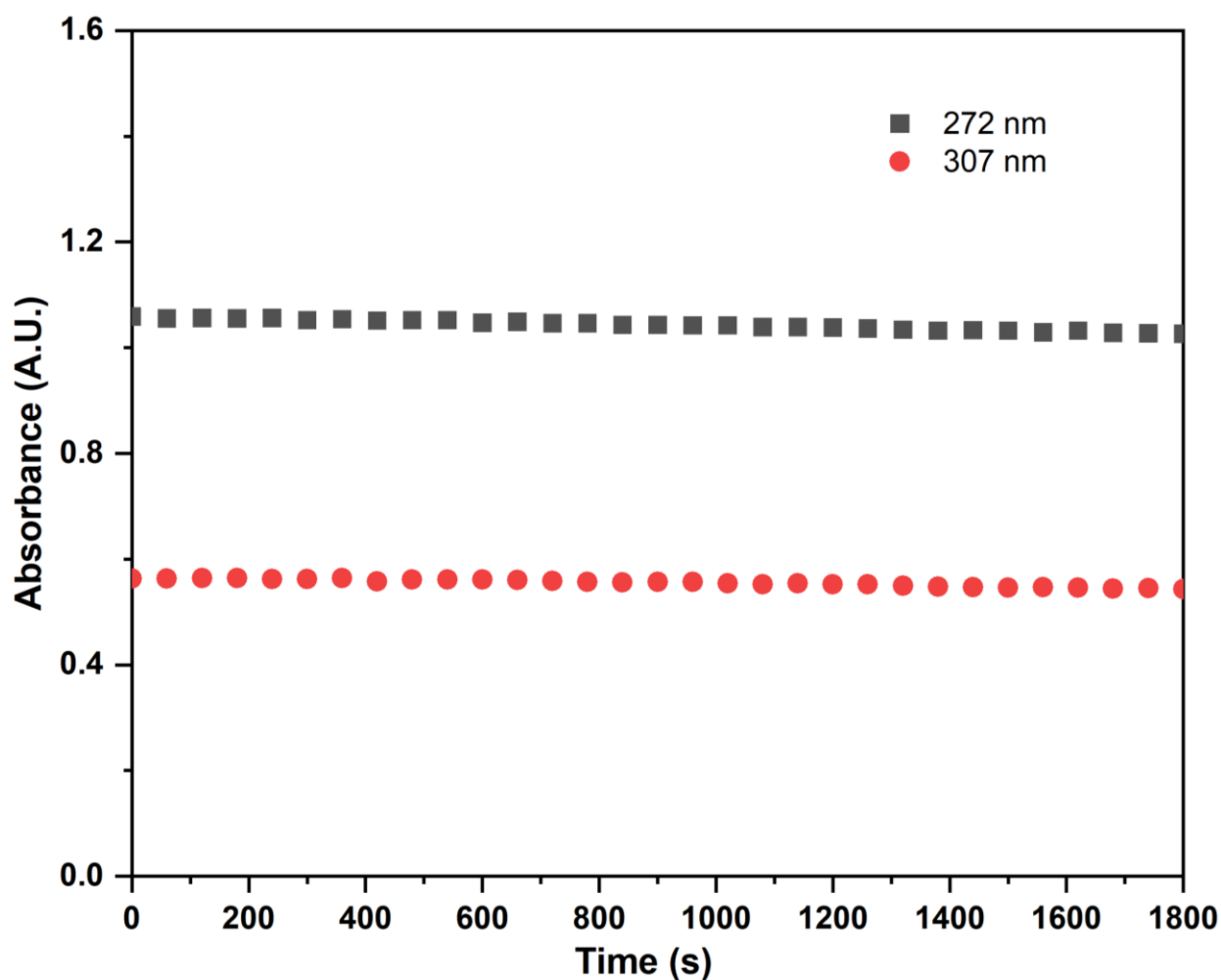


Figure 141. Time dependent graph showing influence on **85c**-Pb²⁺ binding in ACN:H₂O::4:1 solution for 30 minutes

5.6 Temperature dependence of **85c** with (Cu²⁺ and Pb²⁺) metal ions

Furthermore, a temperature-dependent investigation was conducted within a certain temperature range to explore the influence of temperature on metal-ligand interactions. The absorption values were measured after every 2 °C as the temperature increases from 32 °C to 48 °C for [**85c**-Cu²⁺] complex. The data obtained as shown in **Figure 142**, illustrate enhanced absorption resulting from temperature increase for Cu²⁺ ions

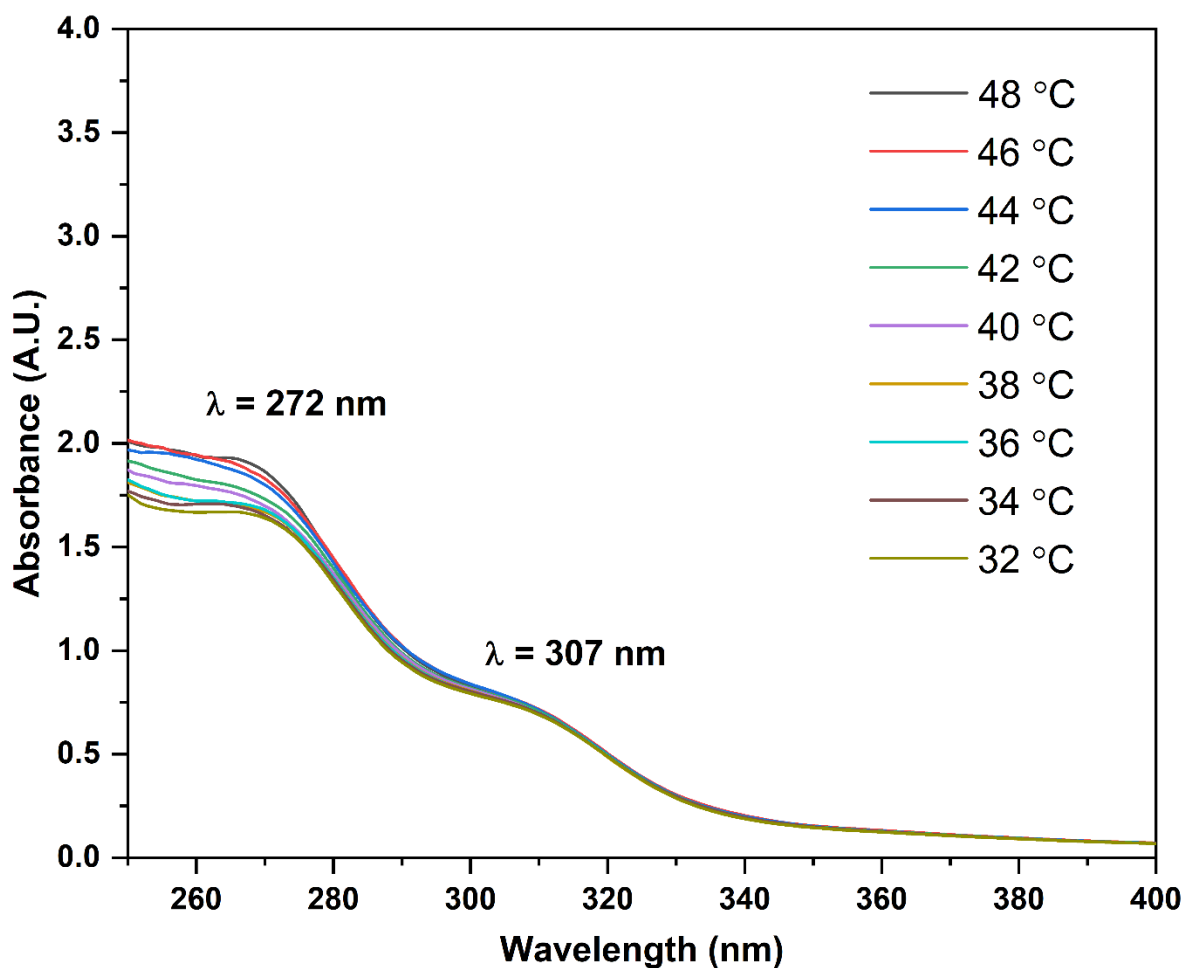


Figure 142. Temperature dependent study of **85c**-Cu²⁺ complex in ACN:H₂O::4:1 solution from 32 °C to 48 °C

Temperature dependent study was also conducted for [**85c**-Pb²⁺] complex using UV-vis spectroscopy. The absorption values were observed after every 2 °C rise in temperature within the range from 32 °C to 48 °C for [**85c**-Pb²⁺] complex. The spectra obtained from the experimental studies as presented as **figure 143** depicts the decrease in absorption values with increase in temperature for Pb²⁺ ions.

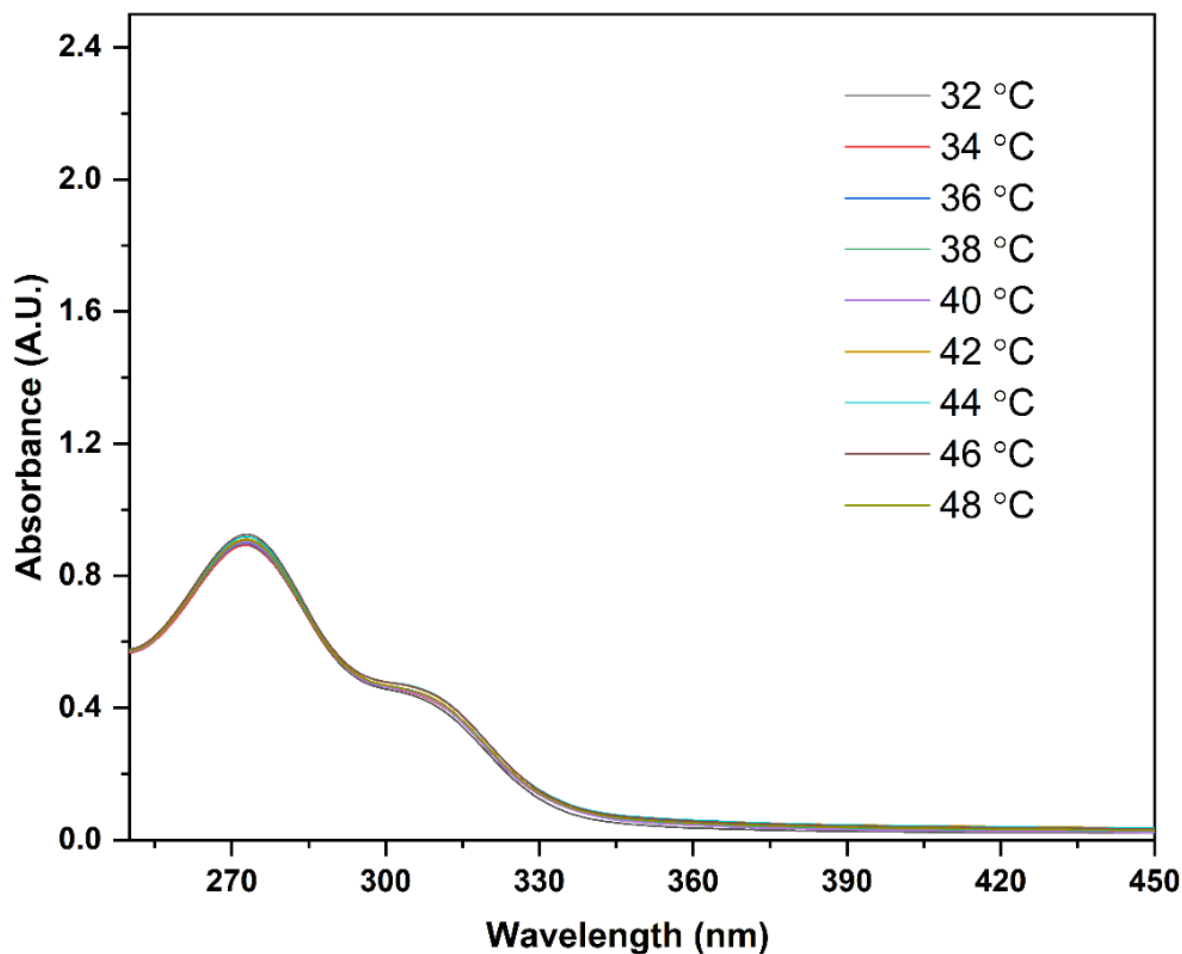


Figure 143. Temperature dependent study of **85c**- Pb^{2+} complex in ACN:H₂O::4:1 solution from 32 °C to 48 °C

5.7 Fluorescence emission spectral studies of chemosensor **85c**

Fluorescence titration studies were conducted for attaining comprehensive knowledge of the molecular-level interaction between the sensor **85c** and with both of the metal ions (Cu^{2+} , Pb^{2+}). Fluorescence emission studies were performed for probe **85c** (5 μM) with metal Cu^{2+} and Pb^{2+} ions (100 μM) in (ACN:H₂O::4:1) solvent medium at ambient temperature. The sensor **85c** has a distinct emission peak at $\lambda_{\text{max}} = 562 \text{ nm}$, which corresponded to the monomer emission intensity of **85c** when it is stimulated at $\lambda_{\text{max}} = 290 \text{ nm}$. The fluorescence emission intensity progressively increased when Cu^{2+} ions were added in incremental amounts to **85c** in ACN/H₂O (4/1, v/v) medium, as shown in **Figure 144**.

Also, under same conditions when Pb^{2+} ions were added to **85c**, similar trend as Cu^{2+} metal ions were observed (**Figure 145**). After the addition of Cu^{2+} ions (0-9 equiv.) and Pb^{2+} ions (0-13 equiv.) to the **85c** solution, the fluorescence emission intensity arose progressively without causing any peak shift. The observed alterations in the spectra indicated that the PET process was hindered in both the complexes

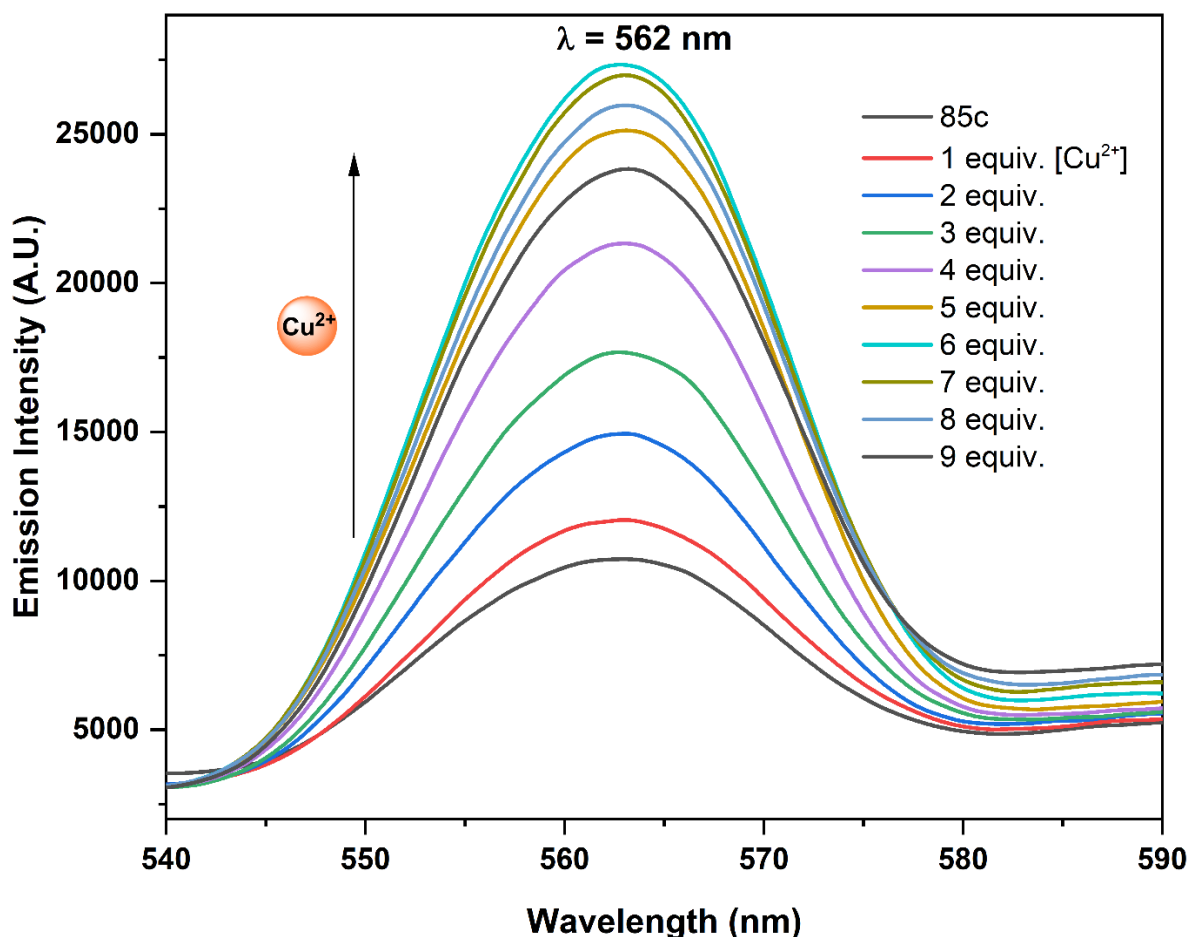


Figure 144. Fluorescence spectra of **85c** (0.005 mM) with increasing concentration of Cu^{2+} ions (0-9 equiv.) in (ACN: H_2O ::4:1) solvent medium at $\lambda = 562 \text{ nm}$. An increase in intensity (hyperchromic shift) was observed with the addition of Cu^{2+} ion solution in free probe **85c** solution depicting the binding of [**85c**- Cu^{2+}] complex

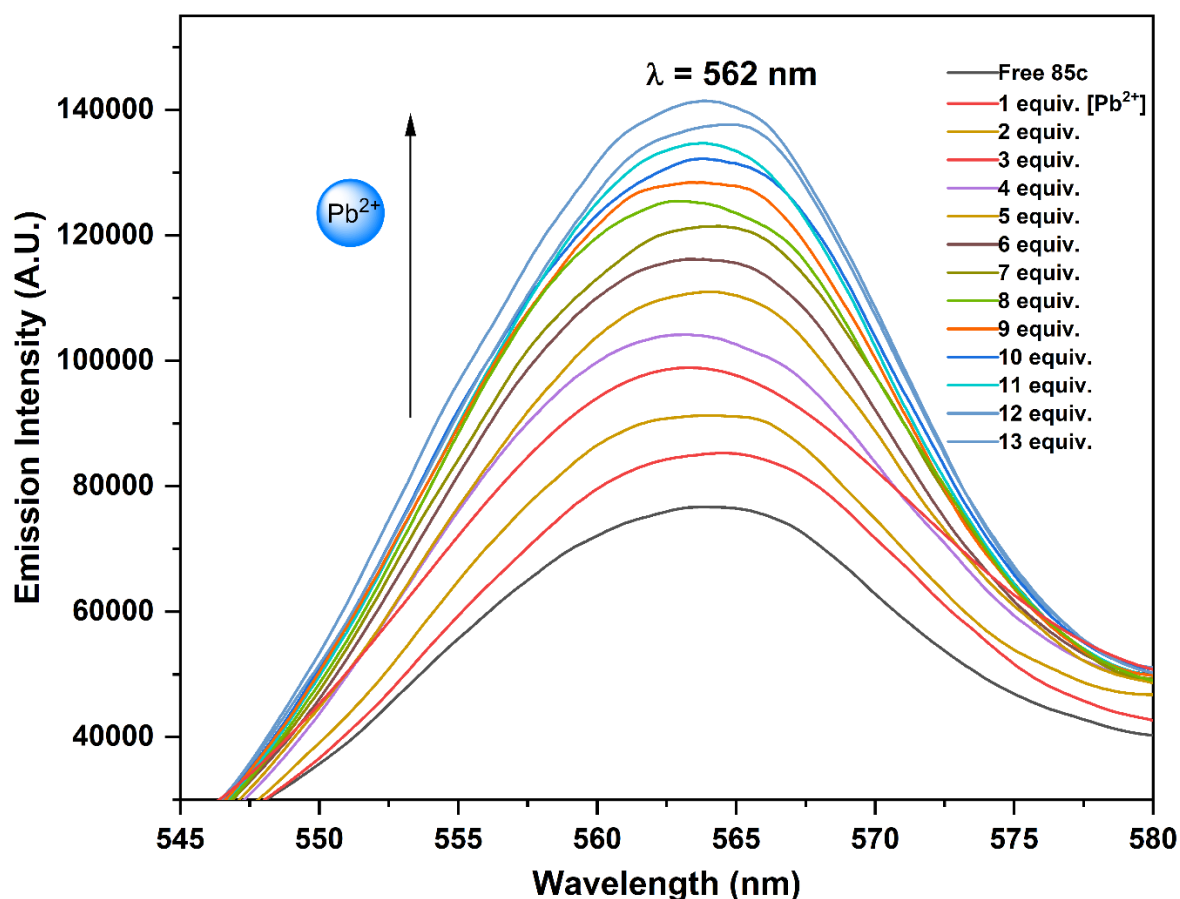


Figure 145. The change in emission intensity of Probe **85c** (0.005 mM) upon the addition of Pb^{2+} ions (0-13 equiv.) in (ACN:H₂O::4:1) solvent medium at $\lambda = 562$ nm, with the accumulation of Pb^{2+} ions solution in **85c** solution, increase in the emission intensity was observed (hyperchromic shift)

Furthermore, **Figure 146** shows a rise in the emission intensity ratio I_0/I , where I_0 represents the emission intensity of sensor **85c** in the absence of Cu^{2+} ions whereas I represent the emission intensity after **85c** is bound with Cu^{2+} ions with each successive addition. At higher concentrations of Cu^{2+} ions, the rise in relative emission intensities halted owing to the complexation saturation with **85c**.

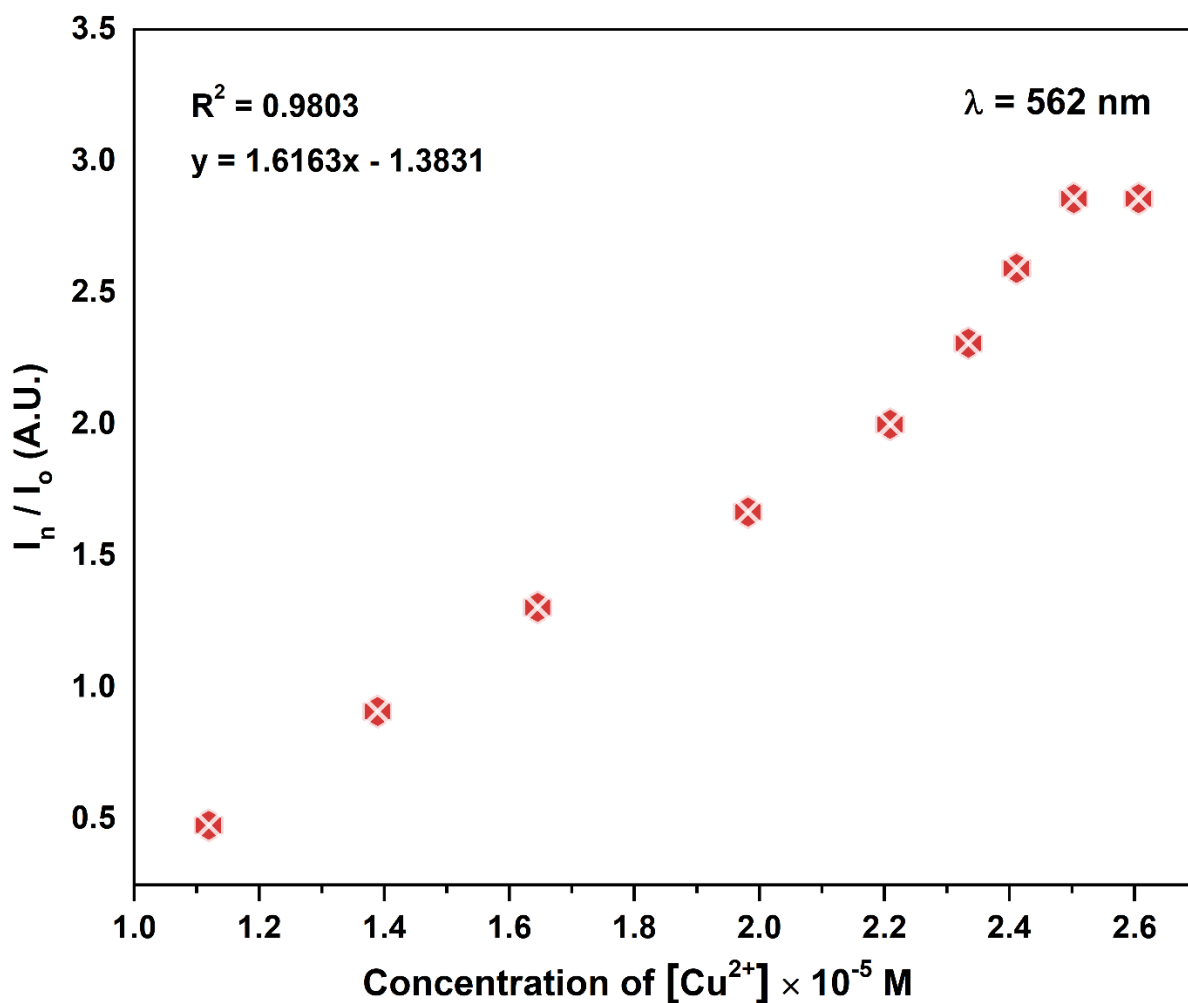


Figure 146. The relative change in emission intensity (I_n/I_o) of **85c** plotted against successive addition of Cu^{2+} ions using (ACN:H₂O::4:1) solvent medium at $\lambda = 562 \text{ nm}$, wherein I_o represents the emission intensity of the free probe **85c** and I_n signifies the emission intensity during the binding of **85c** with Cu^{2+} ions with each consecutive addition

The relative emission intensity was increased with increase in concentration of Pb^{2+} ions solution in Probe **85c** solution as shown in **Figure 147**. The increase in relative emission intensities ceased at higher concentrations of Cu^{2+} ions due to the complexation saturation with **85c**.

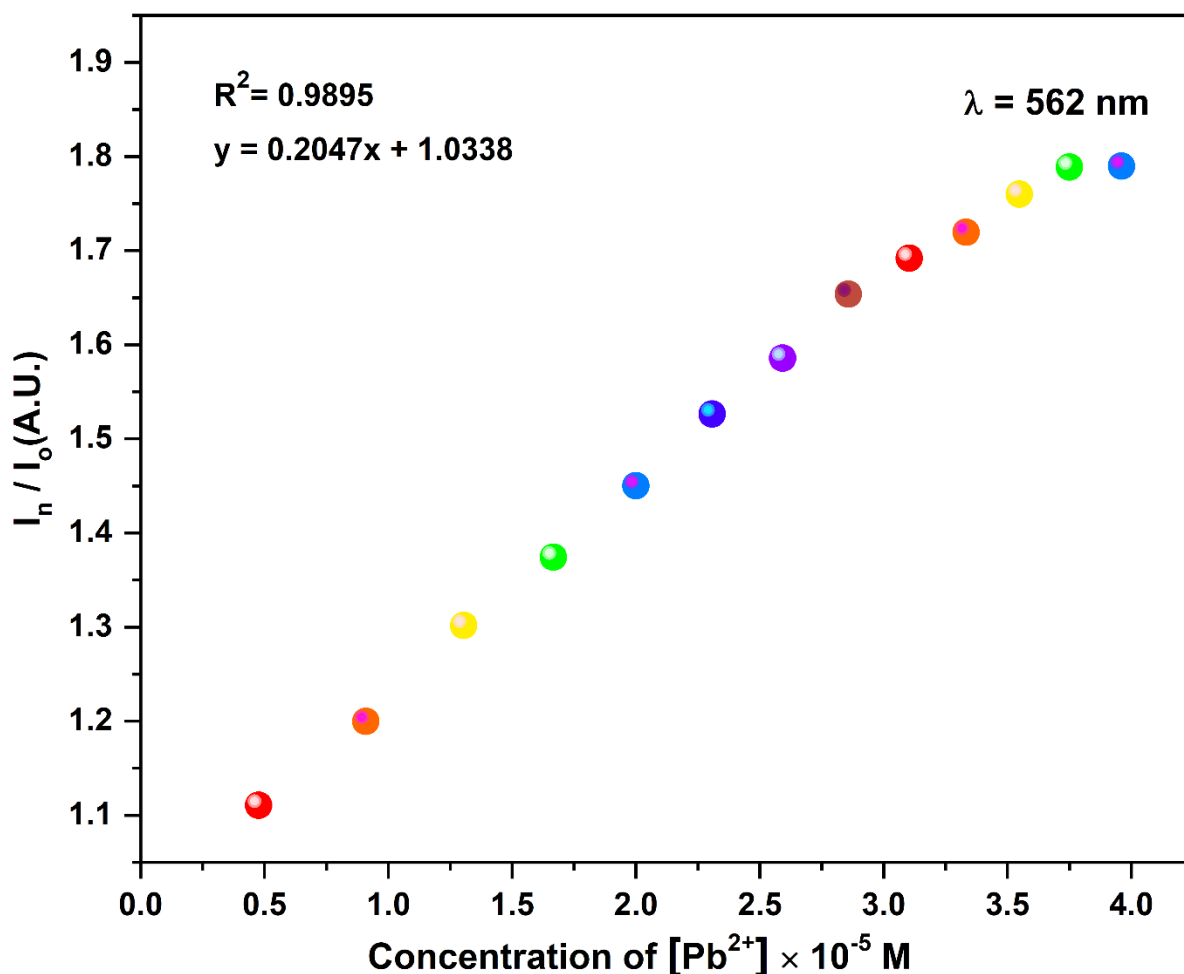


Figure 147. The relative change in emission spectra (I_n/I_o) of **85c** with incremental addition of Pb^{2+} ions in (ACN:H₂O::4:1) solvent medium at $\lambda = 562$ nm, where I_o stands for emission intensity of probe **85c** and I_n represent emission intensity during addition of Pb^{2+} ion solution in probe **85c** solution

5.8 Sensitivity of the probe **85c**

The sensitivity of a probe is contingent upon the limit of detection (LOD) and limit of quantification (LOQ) value. The lower LOD value indicates a higher sensitivity of the probe. The LOD and LOQ of ligand **85c** for both metal ions have been calculated using the $3\sigma/K$ and $10\sigma/K$ equation from the linear calibration graphs respectively plotted for relative absorption versus concentration of metal ions. (**Figure 148** and **Figure 149**)

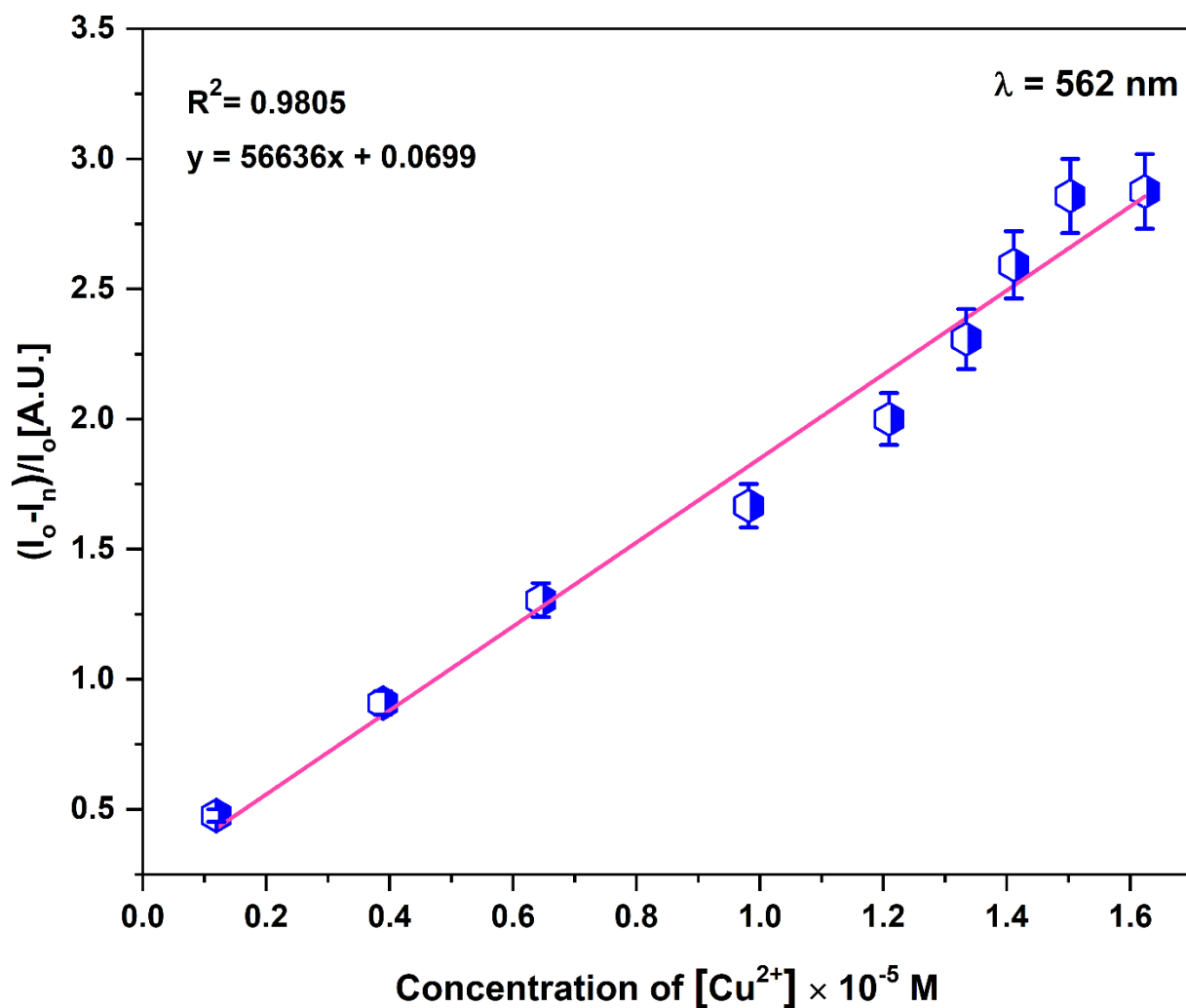


Figure 148. The linear calibration curve of **85c** represented by the ratio $[I_0 - I_n/I_0]$ plotted against the concentration of Cu^{2+} ions in (ACN:H₂O::4:1) solvent medium, wherein I_n represent the fluorescence intensity of receptor of **85c** and the fluorescence emission after consecutive addition of Pb^{2+} ions solution in receptor **85c**

The limit of detection values for Cu^{2+} ions and Pb^{2+} ions have been found to be 0.19 nM, and 0.39 nM respectively. Also, the limit of quantification was also calculated for both Cu^{2+} ions and Pb^{2+} ions and found to be 0.95 nM, and 1.3 nM respectively. This suggests that the probe **85c** exhibits a high level of sensitivity towards both metal (Cu^{2+} and Pb^{2+}) ions.

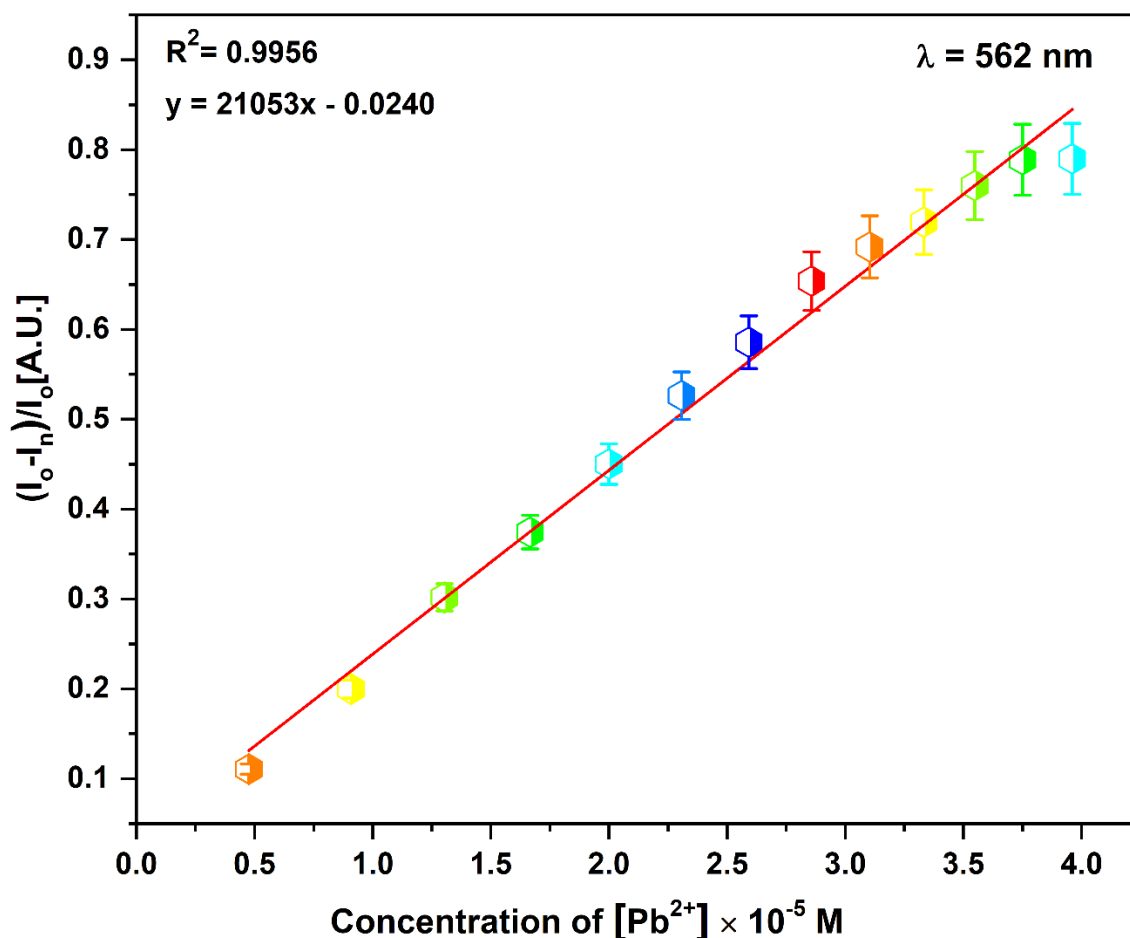


Figure 149. The linear calibration curve demonstrating the relative emission intensity $[I_0 - I_n/I_0]$ observed at various concentration of Pb^{2+} ions in (ACN:H₂O::4:1) solvent medium

5.9 Plausible binding mode of **85c** with (Cu^{2+} and Pb^{2+}) metal ions

CuAAC 'Click' reaction produces a 1,2,3-triazole framework enriched with nitrogen atoms that efficiently coordinate with Cu^{2+} or Pb^{2+} ions. The HSAB hypothesis states that soft acids have a propensity for associating with soft bases, whereas hard acids have a tendency to associate with hard bases. Due to the presence of several nitrogen and oxygen atoms on the synthesised chemosensor **85c**, which function as hard bases, and the hard acid nature of lead ions and copper ions, forms the stable complex by firm bonding. The stoichiometry of the $[85c-Cu^{2+}]$ and $[85c-Pb^{2+}]$ complexes, as estimated from the job's plots, suggests a 1:1 ratio, demonstrating the probable binding mode in Figure **150**. Previous research investigations on the detection of copper or lead

ions have revealed few ligands that include nitrogen and oxygen atoms as donor sites that revealed the significant dual interaction with copper or lead ions.

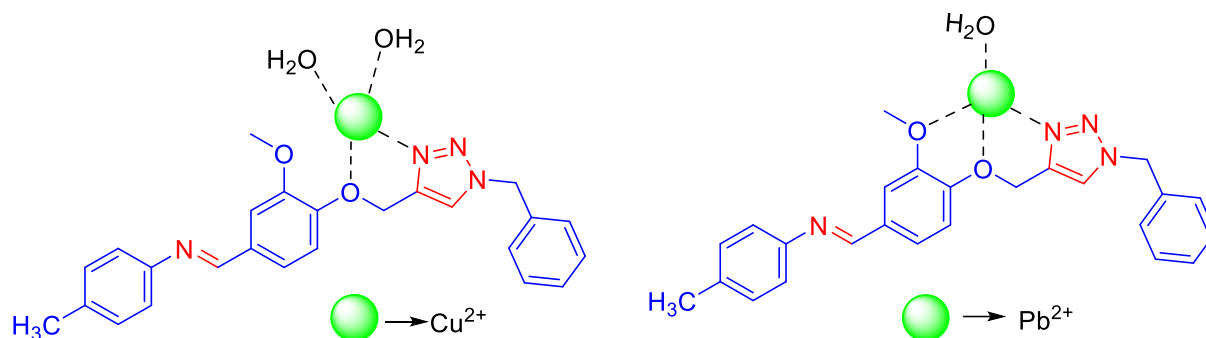


Figure 150. Plausible mode of interaction between **85c** and metal ions (Cu^{2+} and Pb^{2+}) ions

FTIR spectra of both **85c**- Pb^{2+} and the **85c**- Cu^{2+} complex was effectively recorded. After complexation of **85c**- Pb^{2+} and **85c**- Cu^{2+} , new peaks corresponding to OH group at 3343, 3362 cm^{-1} appeared respectively that signifies the attachment of H_2O molecules with the metal-ligand complexes. The peaks associated with the ($-\text{C}-\text{O}$) group exhibited a decrease in wavenumber from 1138 to 1127, while the characteristic peak of the $\text{C}-\text{N}$ group also displayed decrease in intensity and a shift from 1266 to 1257 and 1266 to 1254 cm^{-1} respectively for Pb^{2+} and Cu^{2+} complexes. This observation suggests the coupling of Pb^{2+} and Cu^{2+} metal ions with ($\text{C}-\text{O}$) and ($\text{C}-\text{N}$) groups of the 1,2,3- triazole moiety.

The LCMS-MS analysis of the complex [**85c**- Pb^{2+}] and [**85c**- Cu^{2+}] was also conducted. The anticipated mass spectrum m/z of [**85c**- Pb^{2+} -(H_2O)] and [**85c**- Cu^{2+} -(H_2O)₂] calculated as 641.30 and 511.74 appeared at $m/z = 641.39$ and 512.18 ($M+1$) respectively. The m/z value aligns strongly with the postulated stoichiometry

The spectroscopic analysis of metal ligand complexes via FTIR spectroscopy and mass spectrometry prove the successful binding of metal ligand complexes

6. Conclusion

The Schiff base appended 1,2,3-triazole linkers discussed in this thesis were heterocyclic compounds containing three nitrogen atoms in the 1,2,3-triazole ring, two oxygen atoms from the Schiff base adduct creating an ideal moiety for coordination with metal ions. The current research work focussed on synthesizing several chemosensors namely, **81c**, **82c**, **83c**, **84c** and **85c** possessed different Schiff base, benzyl unit and 1,2,3 triazole ring serving as chromophores to convert molecular recognition events into clear optical signals as these probes with different structures exhibited distinct characteristics during interactions between analytes and receptors.

Since the synthesized molecules are equipped with reliable chromophoric unit in their structure, which allows for exceptional absorption in the UV-visible region. This absorption property was beneficial for studying the molecule's sensing behaviour using UV-visible and fluorescence spectroscopic techniques. The thesis presents the chemosensing investigations conducted on a range of novel Schiff base 1,4-disubstituted 1,2,3-triazole derivatives. These compounds were synthesised using the CuAAC methodology, which included coupling of novel synthesised Schiff base terminal alkynes with benzyl azide. The spectral responses of different probes were shown in various figures to assess their specificity towards certain metal ions. This research investigation presents the analytical calculations used to determine the limit of detection of metal ions, the binding ratio of metal-ligand complexes, and the binding constant for several novel synthesised Schiff base 1,2,3-triazole linker.

The key outcomes of the thesis entitled "Synthesis and Characterization of new Schiff base alkynes and their triazole derivatives, as potential ion sensors" are as follows.

1. The Schiff base tethered 1,4-disubstituted 1,2,3-triazole chemosensors were synthesized and purified via using facile experimental techniques, resulting in high yields. These chemosensors showed high solubility in aqueous-organic binary solvent solutions such as **81c** in (EtOH:H₂O::9:1), **83c**, **84c**, **85c** in (CH₃CN:H₂O::4:1), and **82c** in DMSO because of its low solubility in any other solvent.
2. The synthesized molecules were characterized via FTIR, NMR, (¹H and ¹³C) alongwith mass spectrometry. The peculiar peak of H-atom of 1,2,3-triazole was observed in the range $\delta = 7.45-7.61$, and the two C-atom of 1,2,3-triazole found at $\delta = 120.7-123.0$ and $\delta = 134.3-144.1$

in the ^1H and ^{13}C -NMR, along with the expected m/z of compounds correspond to observed m/z for the synthesized probes **81c-85c** confirmed the synthesis of 1,2,3-triazole derivatives.

3. The chemosensors were carefully examined to determine their ability to recognise specific ions by analysing any changes in UV-vis absorption and fluorescence spectral behaviour. The sensitivity of the synthesized probes to detect metal ions was evaluated via limit of detection and the association constant of metal ligand complexes was calculated via B-H plot.
4. Benzylamine based Schiff base tethered 1,2,3-triazole **81c** containing a (O-N-N) binding unit in its donor site exhibited Fe^{3+} selective response in an aqueous-ethanol mixture. Conversely, **81c** exhibited significant turn-on fluorescence response selectively for Fe^{3+} ion along with hyperchromic shift in emission intensity, ascribed to CHEF through inhibition of PET and also to the formation of (2:1) stoichiometric ratio of [**81c**- Fe^{3+}] complex.
5. Similarly, 4-aminophenol based Schiff base tethered 1,2,3-triazole **82c** was found to selectively detect Pb^{2+} in organic solvent. Also, turn-off fluorescent sensing behavior was observed for the chemosensor **82c**, attributed to the arrest of PET through the formation of a (2:1) binding ratio of [**82c**- Pb^{2+}] complex.
6. Naphthylamine linked Schiff base tethered chemosensor **83c**, demonstrated cation selective recognition of Cu^{2+} in acetonitrile water mixture. Fluorimetric OFF-ON-type response to Cu^{2+} has been established due to the selective binding of **83c** with these ions. The weak fluorescent behavior was observed for the ligand **82c**, after the binding with Cu^{2+} enhancement in fluorescence was detected. A combined effect of PET and CHEF modulation was responsible for the prominent fluorescence enhancement via 1:1 binding ratio of [**83c**- Cu^{2+}] complex.
7. Another chemosensor phenylethylamine linked Schiff base tethered chemosensor **84c** selectively detected Hg^{2+} in acetonitrile mixture. The fluorescent sensor exhibited hyperchromic shift after binding to the metal due to suppression of PET in 1:1 stoichiometric ratio of [**83c**- Hg^{2+}]
8. Toulidine based Schiff base 1,2,3-triazole dual chemosensor detected Cu^{2+} and Pb^{2+} ions in acetonitrile mixture. This chemosensor **85c** shows feeble fluorescent but on binding with Cu^{2+} or Pb^{2+} ions in 1:1 binding ratio showed enhancement in emission intensity ascribed to CHEF process and inhibition of PET mechanism.

9. These chemosensors demonstrated the robust absorption bands in the UV-visible region, and their fluorescence was feeble because of the existence of non-bonding electrons in close proximity to the chromophore component, which suppresses emission via PET.

Overall, these chemosensors based on Schiff base tethered 1,2,3 triazoles provide many benefits, including (i) reduced dependence on non-aqueous solvents, and (ii) improved limit of detection (LOD) that surpasses the WHO's recommended safe concentration for specific analytes. simple one-pot straight method of preparation, (iv) Anti-interference from other common ions, (v) dual sensing response, and (vi) tunable characteristics. Thus, these organic chemosensors based on Schiff base tethered 1,2,3-triazole having modest chemical structures revealed great potential for chemosensing applications. Furthermore, the inclusion of both PET and CHEF mechanisms within the chemosensors was advantageous, as their synergistic impact induced fluorescence enhancement, thereby substantially amplifying the recognition signal. In addition, to optimise the performance of a chemosensor to achieve the desired result, it is critical to examine the effect of the donor, π -network, and acceptor groups in order to determine the structure-activity relationship. Therefore, Understanding the causes and modes of binding in distinct receptors may help build probe molecules with specialised features for certain research and technological applications.

7. References

- 1 R. Kagit, M. Yildirim, O. Ozay, S. Yesilot and H. Ozay, *Inorg Chem*, 2014, **53**, 2144–2151.
- 2 S. Joshi, S. Kumari, R. Bhattacharjee, A. Sarmah, R. Sakhuja and D. D. Pant, *Sens Actuators B Chem*, 2015, **220**, 1266–1278.
- 3 H. Singh, M. Rajeshwari and J. M. Khurana, *J Photochem Photobiol A Chem*, 2018, **353**, 424–432.
- 4 G. Singh, Sushma, A. Singh, P. Satija, Shilpy, Mohit, Priyanka, J. Singh and A. Khosla, *Inorganica Chim Acta*, 2021, **514**, 120028.
- 5 A. Thakur, D. Mandal and S. Ghosh, *Anal Chem*, 2013, **85**, 1665–1674.
- 6 H. Na Kim, W. Xiu Ren, J. Seung Kim and J. Yoon, *Chem Soc Rev*, 2012, **41**, 3210–3244.
- 7 P. Saini, G. Singh, G. Kaur, J. Singh and H. Singh, *J Mol Struct*, 2022, **1251**, 131985.
- 8 H. Kang, C. Fan, H. Xu, G. Liu and S. Pu, *Tetrahedron*, 2018, **74**, 4390–4399.

- 9 M. Loya, S. I. Hazarika, P. Pahari and A. K. Atta, *J Mol Struct*, 2021.130634.
- 10 B. Dolai, S. I. Hazarika, S. Giri and A. K. Atta, *Inorganica Chim Acta*, 2018, **483**, 496–503.
- 11 H. Niu, J. Liu, H. M. O'Connor, T. Gunnlaugsson, T. D. James and H. Zhang, *Chem Soc Rev*, 2023, **52**, 2322–2357.
- 12 S. Kumar, N. Goswami, S. Naithani, J. Mangalam, T. Goswami, R. Dubey, P. Kumar and P. Kumar, *Dalton Transactions*
- 13 R. G. Pearson and D. H. Busch, *Hard and Soft Acids and Bases*, 1963.
- 14 W. Zhong, L. Wang, D. Qin, J. Zhou and H. Duan, *ACS Omega*, 2020, **5**, 24285–24295.
- 15 A. Thakur, S. Sardar and S. Ghosh, *Inorg Chem*, 2011, **50**, 7066–7073.

Summary

Thesis overview

This section provides a concise summary of the entire thesis and provides succinct descriptions of all experimental data and results.

The research work was conducted to synthesize highly effective probes for the detection of physiologically significant cations. The outcomes of this study are outlined in the thesis, which focuses on the synthesis of Schiff based 1,4-disubstituted 1,2,3-triazole, their analysis using various spectroscopic techniques, and their photophysical properties to identify different metal ions. The introductory chapter presents the background of Schiff base 1,4-disubstituted 1,2,3-triazole synthesized via click chemistry and the host-guest analytical chemistry of fluorescent chemosensors. Chapter 2 provides the literature review that sheds light on the evolution of chemosensors and their practical application in the detection of anions and cations while the third chapter deals with the spectroscopic experimental data of synthesized chemosensors. The detailed results and discussions of spectroscopic data is presented in Chapter 4 and Chapter 5 describes the photophysical analysis of the synthesized Schiff based 1,4-disubstituted 1,2,3-triazole moieties. The objectives of this research have been achieved as shown from the results obtained by some of the chemosensors.

Chapter 1. Introduction

This chapter specifically focuses on the historical background of Schiff base 1,4-disubstituted 1,2,3-triazole. It also includes various subsections that highlight the recent methods for synthesising Schiff base linked 1,4-disubstituted 1,2,3-triazole and their applications in photophysical studies. The first section explores the legacy of click chemistry, covers the guiding principles of Click Chemistry, and mentioned the types of click reactions such as: 1,3-dipolar and diels-alder cycloaddition reactions, epoxidation and michael addition, nucleophilic substitution, non-aldol reactions

The next section includes the classical cycloaddition reaction proceeding with the uncatalyzed thermal 1,3-dipolar cycloaddition reaction of terminal alkyne with organic azides, leading to the stereoisomers of 1,4 and 1,5-triazole compounds discovered by Rolf Huisgen in 1963. Further section made us familiar with Sharpless Copper(I)-catalyzed alkyne azide cycloaddition click reaction that leads to formation of selective 1,4 regioisomer of 1,2,3-triazole (**Figure S1**), supported by another section describing the mechanistic insights of CuAAC reaction showing the reliance on copper (I) catalyst and the regiospecificity attained during the synthesis of 1,2,3-triazole.

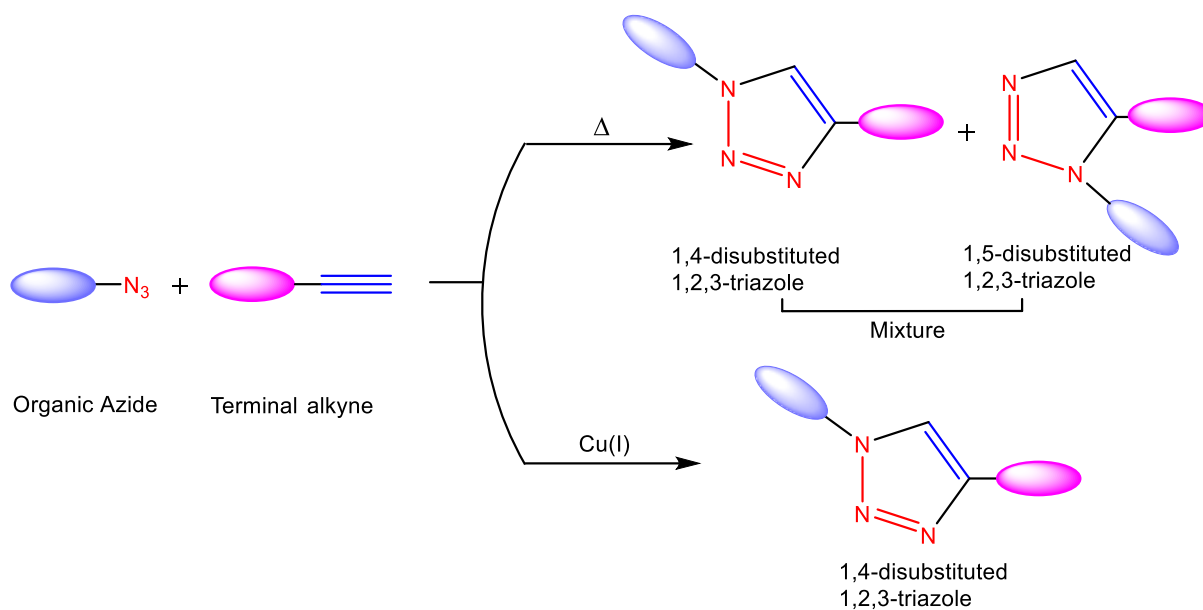


Figure S1. (a) Rolf Huisgen's classical cycloaddition reaction of 1,2,3-triazole isomers (b) Sharpless Cu(I) catalyzed click reaction for regioselective 1,4-disubstituted triazole

This section explains CuAAC reaction can indulge in effective hydrogen bonding and dipole-dipole interactions due to which it has anticipated demand in various areas like drug discovery, metal ion sensing, biochemistry, polymer chemistry, and material-science. The Click reaction has been explored for the probes that can work as fluorescent chemosensors that can aid in the recognition of variant transition metal ions above their concerned toxic levels. The chemosensing is generally conducted by UV-vis spectrophotometer and fluorescence spectroscopy that provides the enhancement or quenching of maxima values. The next section provides brief discussion of photophysical processes covering absorbance and fluorescence phenomenon that will aid in understanding of UV-vis and Fluorescence spectroscopy. A separate section has been illustrated as analytical supramolecular chemistry explaining the host guest relationship that focuses on the selective recognition of a molecule (guest) by another molecule (host) through the formation of non-covalent interactions, this concept sheds light on the chemosensing behavior of probe and analyte. The fluorescence signal mechanism i.e. photo-induced electron transfer (PET) has been vividly mentioned in the next section to get an insight into molecular level interactions of metal-ligand binding. Fluorescence spectroscopy exhibits high sensitivity because it involves the excitation of numerous fluorescent photons from a single molecule, compared to the absorption of a small amount of light over a short path length. Therefore, UV-vis and fluorescence spectroscopy was chosen for the detection of metal ions.

Chapter 2. Literature review

This chapter is organised into sections and subsections to facilitate the discussion of recent literature concerning the synthesis and evolution of 1,4-disubstituted 1,2,3-triazole as fluorescent probes. The document provides an elaborate narrative regarding the progression of 1,4-disubstituted 1,2,3-triazole as colorimetric and fluorometric chemosensors capable of detecting various metal ions, anions, and neutral molecules. The binding mechanism of analytes with the receptors and the kinds of receptor sites have been described in depth. The first section comprises the synthesis of 1,4 di-substituted 1,2,3-triazole that involves 4 steps mentioned as follows:

1. Synthesis of Schiff base
2. Synthesis of Schiff base terminal alkynes
3. Synthesis of organic azides
4. Synthesis of 1,4-disubstituted 1,2,3-triazole from terminal alkyne and organic azide

The subsection initiates with the chemical reactions for the synthesis of Schiff base utilizing variant solvent systems such as ethanol, methanol, or water as green solvent undergoing reaction of substituted aldehyde and aromatic/ aliphatic amines under reflux with good yields and facile reaction conditions. The next subsection involves the chemical reactions for the synthesis of terminal alkynes from various compounds incorporated with functional groups like CHO, C=O, N=C, OH, etc. with propargyl bromide using solvents like N,N-dimethylformamide, dichloromethane, and bases like potassium carbonate and triethylamine. The reaction conditions are based on the type of solvent or base preferred in the reaction. Next to this, another subsection mentions the methods for the synthesis of organic azides as follows: substitution or addition, diazo-transfer, diazotization, breakage of triazines, and rearrangement of azides. (**Figure S2**)

This section made us familiar with the exceptional sensing capabilities of fluorescent 1,4-disubstituted 1,2,3-triazoles which have gained recognition as fluorescent chemosensors due to their highly advantageous characteristics such as excellent selectivity, sensitivity, and robust chemical and photochemical stability in solution.

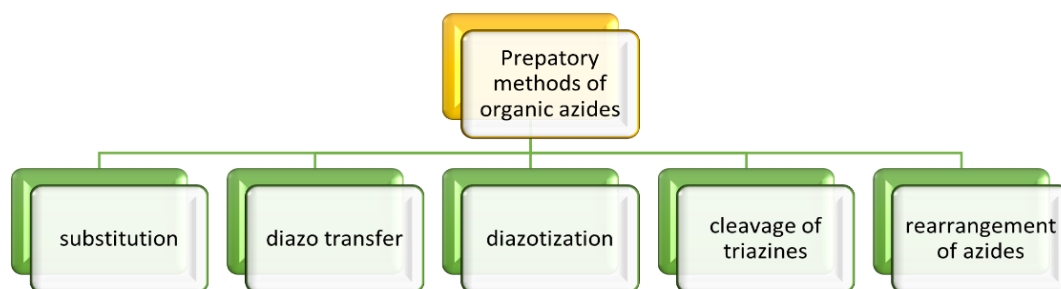


Figure S2. Various methods for the synthesis of azides

Chapter 3. Experimental data

In Chapter 3, the materials, procedures, methodology, and instrument utilised at each stage of the research have been described in detail, in addition to specific details of characterization data for the synthesised compounds such as melting points, IR, NMR, CHN analysis, and mass spectroscopic investigations. The first part of this chapter deals with the practical steps used to produce organic azide, specifically azidomethylbenzene **39** comprising the reaction conditions, physical properties such as the yield, color/texture, and characterization data obtained from FTIR and NMR (^1H , ^{13}C) analysis of the synthesised azide.

Next, the synthesis of Schiff bases (**81a-85a**) shown in **Figure S3** has been described, starting from precursors substituted aldehyde and aromatic amine. The experimental reaction conditions for each synthesis process with reaction scheme have been thoroughly described in separate sections. Interpretation of the results regarding the FTIR and NMR (^1H , ^{13}C) of each Schiff base is provided in detail to support the synthesis of these products. Additionally, the yield, colour, and melting points of each Schiff base were also recorded.

The following section described the synthesis of the Schiff base terminal alkynes (**81b-85b**), which have been illustrated in **Figure S4**, synthesized from the precursors (**81a-85a**).

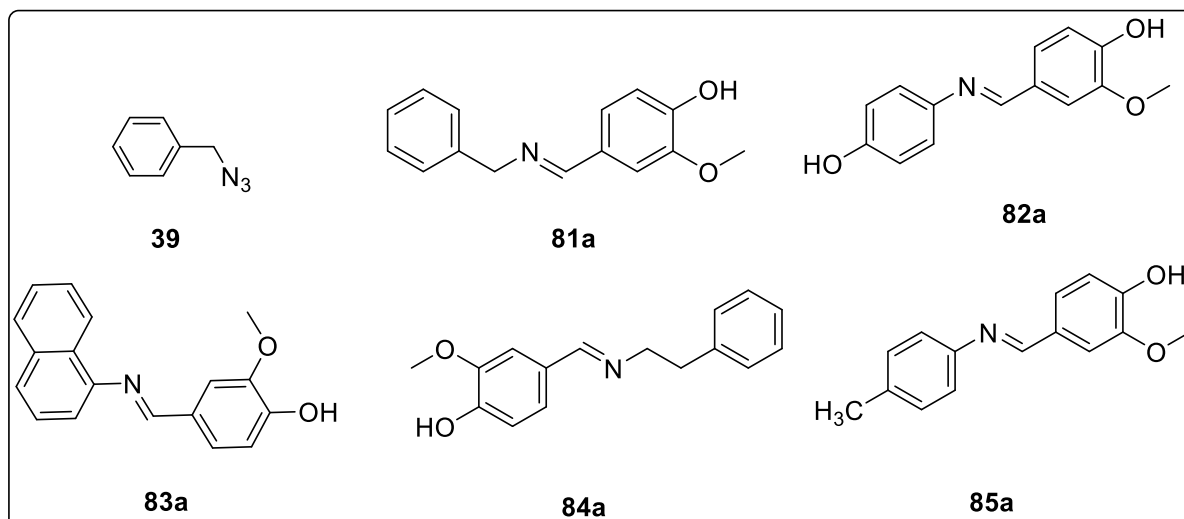


Figure S3. Organic azide **39** and Schiff bases (**81a-85a**)

In distinct sections, the experimental conditions for each synthesis have been described in detail. FTIR, NMR (^1H , ^{13}C) data for each Schiff base terminal alkyne was provided to support the synthesis of these moieties. Furthermore, the section includes information on the yield, color, and melting point of each synthesized Schiff base terminal alkyne.

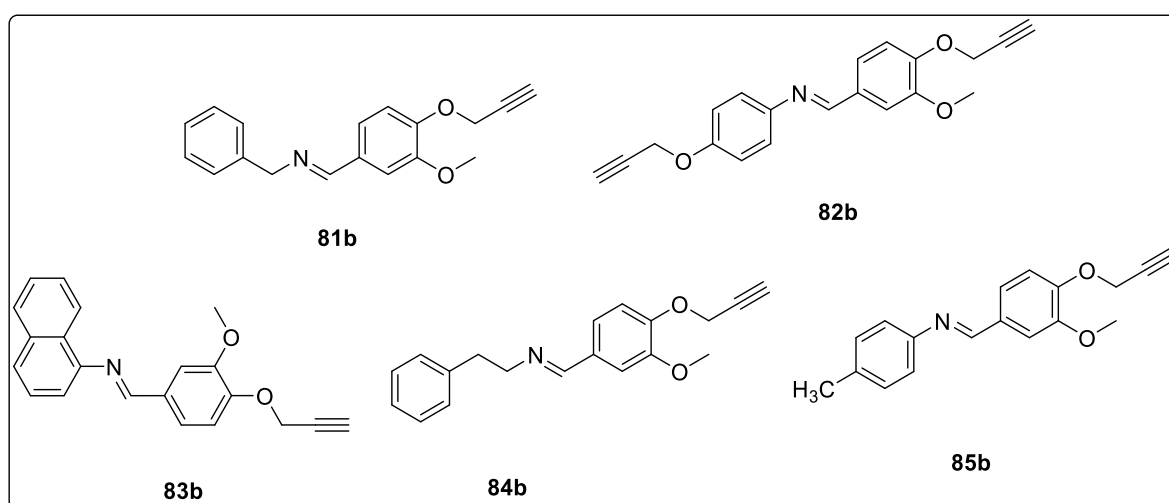


Figure S4. Schiff base terminal alkynes (**81b-85b**)

In the proceeding synthesis section, the next step involved [3+2] cycloaddition reactions of the synthesized Schiff base terminal alkyne with organic azides to obtain 1,2,3-triazole linked molecules and (**81c-85c**) (**Figure S5**) have been thoroughly described, including all the conditions of experimentation for each reaction. The product yield, melting point, color/texture, elemental

analysis, IR, NMR (^1H , ^{13}C), and mass spectrum of each 1,2,3-triazole derivative were measured using appropriate instruments. The data was provided in this chapter as needed. The materials and methods, as well as instrument specifications, utilised in the course of this research has been detailed in the starting section of this chapter. Appendix B contains the FTIR spectra the NMR spectra (^1H and ^{13}C), and the mass spectra.

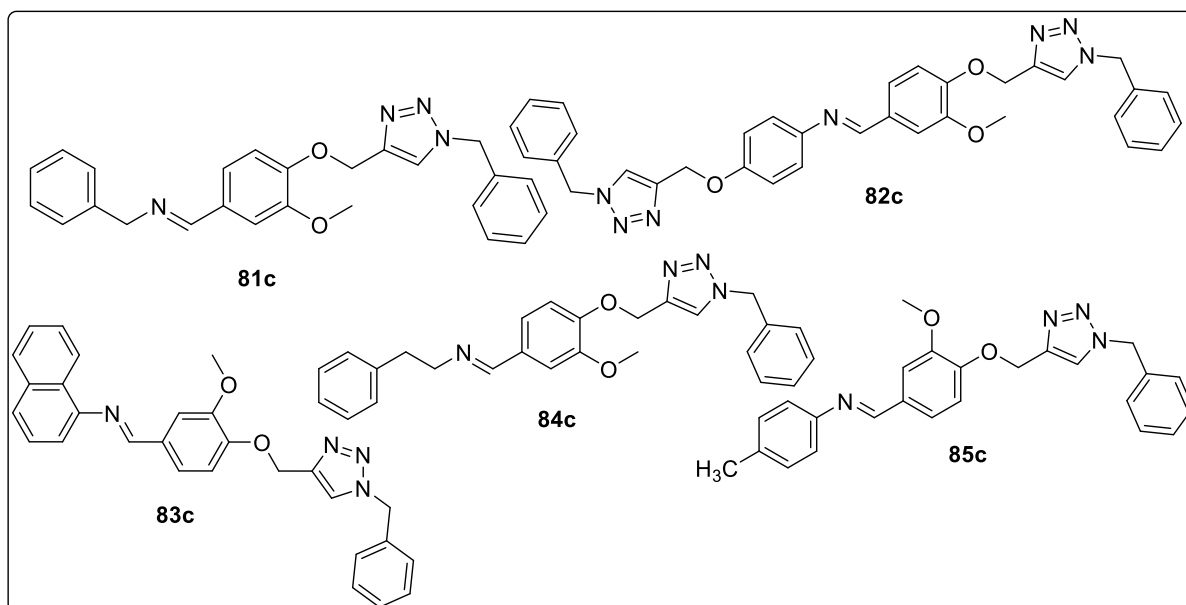


Figure S5. Schiff base 1,4 disubstituted 1,2,3-triazole (**81c-85c**)

Chapter 4. Result and discussion of spectroscopic data

This chapter deal with the spectroscopic results i.e FTIR, NMR (^1H , ^{13}C), and CHN analysis of azide **39**, Schiff base **81a-85a**, Schiff base terminal alkynes **81b-85b**, Schiff base tethered 1,2,3-triazoles **81c-85c**.

The first section deals with the synthesis and characterization of benzyl azide **39** which was synthesized by the substitution reaction of benzyl chloride and sodium azide at 90 °C. The product was oily and was characterized by a sharp peak at 2089 cm^{-1} corresponding to the ($-\text{N}_3$) group in the FTIR spectrum of benzyl azide. ^1H NMR of benzyl azide shows a prominent peak at $\delta_{\text{H}} = 4.22$ ppm of the CH_2 group and $\delta_{\text{H}} = 7.33\text{-}7.24$ ppm corresponding to aromatic ring protons of benzyl azide. ^{13}C NMR of benzyl azide shows singlet at $\delta_{\text{C}} = 54.84$ ppm due to the ($-\text{CH}_2$) group and the carbon atoms of the aromatic ring at $\delta_{\text{C}} = 128.33\text{-}135.58$ ppm.

The FTIR spectra of Schiff bases (**81a-85a**) were recorded in the range 4000-500 cm^{-1} in neat conditions following a similar trend for the synthesized Schiff bases showing the strong peak of (-C=N) of the imine group in the range 1660-1620 cm^{-1} . The ^1H NMR of Schiff bases shows the prominent signal in the range $\delta_{\text{H}} = 8.53\text{-}7.98$ ppm due to (-C=N) of the imine group and the secondary group (-OH) was found in the range $\delta_{\text{H}} = 9.86\text{-}9.43$ ppm. In the ^{13}C NMR of Schiff bases, the chemical shift in the range $\delta_{\text{C}} = 161.8\text{-}157.0$ ppm allocated to the (-C=N) of imine group. All these spectroscopic values from the FTIR and NMR (^1H , ^{13}C) confirms the synthesis of Schiff bases.

Schiff base terminal alkynes (**81b-85b**) were analysed and compared to their respective precursors using FTIR spectroscopy in the range of 4000-500 cm^{-1} . The recorded results confirmed the successful synthesis of the anticipated products. The FTIR spectra of Schiff base terminal alkynes shows the sharp peak in the range 3254-3182 cm^{-1} of acetylenic proton (=C-H) and the stretching vibration of ($\text{-C}\equiv\text{C}$) group appears in the range 2127-2101 cm^{-1} . ^1H NMR of Schiff base terminal alkynes shows the triplet and quartet in the range $\delta_{\text{H}} = 2.54\text{-}2.53$ and $\delta_{\text{H}} = 2.54\text{-}2.52$ due to mono and bis alkynes respectively assigned to (=C-H) proton of the alkynyl group. In the ^{13}C NMR spectra, the signal of the two carbons in the region $\delta_{\text{C}} = 76.41\text{-}75.67$ and $\delta_{\text{C}} = 78.15\text{-}76.35$ ppm due to ($\text{C}\equiv\text{C}$) of the alkynyl group.

Schiff base tethered 1,4-disubstituted 1,2,3 triazole (**81c-85c**) were synthesized via the cycloaddition reaction of benzyl azide with Schiff base terminal alkynes in catalytic amount of $[\text{CuBr(PPh}_3)_3]$ utilising THF:TEA (v/v, 1:1) as solvent system. The characterization of these compounds (**81c-85c**) via IR, NMR, and mass spectroscopic analyses demonstrated the unequivocal synthesis of the aforementioned compounds. In the FTIR spectra of Schiff base tethered 1,4-disubstituted 1,2,3 triazole, the disappearance of the peak at 2089 cm^{-1} due to (-N=N=N) stretching vibration and the absence of 3190 cm^{-1} of acetylenic proton (=C-H) alongwith ($\text{-C}\equiv\text{C}$) stretching vibration at 2120 cm^{-1} indicates the conversion to Schiff base 1-4 disubstituted 1,2,3-triazole. In the ^1H NMR spectra, the spectra show the disappearance of the (=C-H) proton of the alkynyl group in the range $\delta_{\text{H}} = 2.54\text{-}2.53$ and the appearance of triazole proton in the range $\delta_{\text{H}} = 7.61\text{-}7.45$ ppm. The ^{13}C NMR spectra illustrate the appearance of two carbons of Schiff base linked 1,2,3-triazole in the range $\delta_{\text{C}} = 123.0\text{-}120.7$ ppm and $\delta_{\text{C}} = 144.1\text{-}134.3$ ppm confirms the synthesis of Schiff base linked 1,2,3-triazole units.

Chapter 5. Photophysical analysis

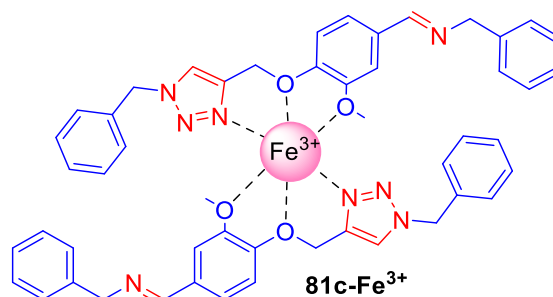
The details of photophysical properties of Schiff base 1,4-disubstituted 1,2,3-triazole (**81c-85c**) via UV-visible/Fluorescence spectroscopy to detect metal ions was described in this section. Aromatic compounds are highly captivating chromophores because of their low-lying p-orbitals, which result in quick electronic transitions. Therefore, the aromatic conjugated system was selected for the synthesis of chemosensors that can incorporate the metal ions and showed effective response in UV-vis region and emission in fluorescence.

In the first section, UV-visible study was conducted of the synthesized sensor **81c** against different metal ions in EtOH:H₂O (9:1 v/v) considering the clear solubility of **81c** and the sharp absorption bands at 275 and 308 nm. The absorbance titrations were conducted through stepwise addition of 1 equiv. of 1mM of the metal ions solution to the solution of receptor probe (0.2 mM) (**Figure S6**).

A noticeable increase in the intensity of the primary peak at 275 nm indicates the binding of the metal ions with the analyte showing the hyperchromic shift. Job plot experiment was depicted binding ratio (1:2) of metal with **81c**.

Fluorescence spectra of the compound **81c**

(0.02 mM) displayed fluorescence emission at $\lambda_{em} = 346$ nm, exhibiting significant increase (hyperchromic shift) by sensor **81c** only in response to Fe³⁺ (0.1 mM) metal ions. (**Figure S7**) The limit of detection of probe **81c** was calculated as 1.3×10^{-7} M.



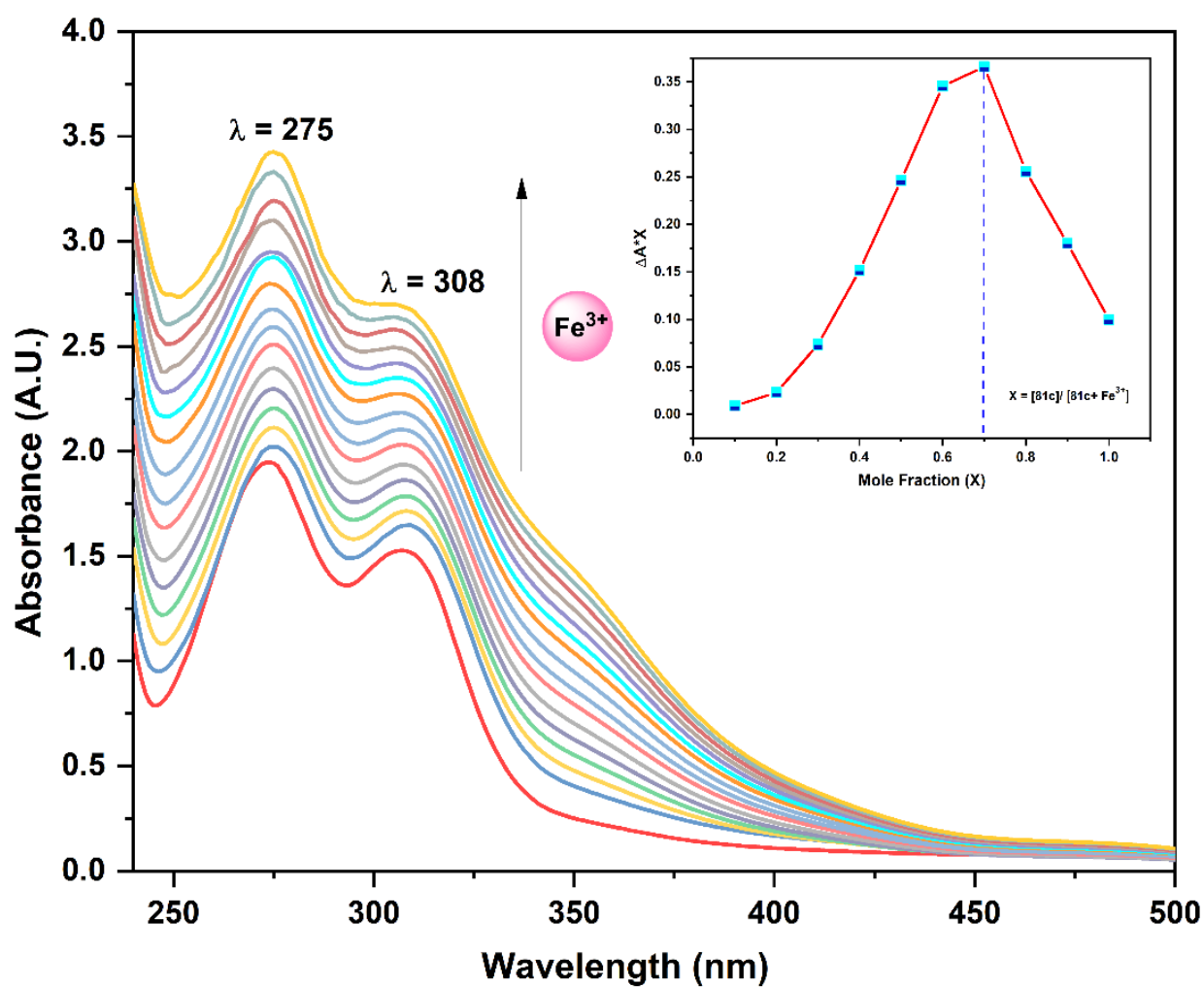


Figure S6. Absorption spectra of the **81c** probe upon successive addition of 1 equiv. of Fe³⁺ ions solution in EtOH:H₂O::9:1 , inset showing stoichiometric (2:1) of [81c:Fe³⁺] complex

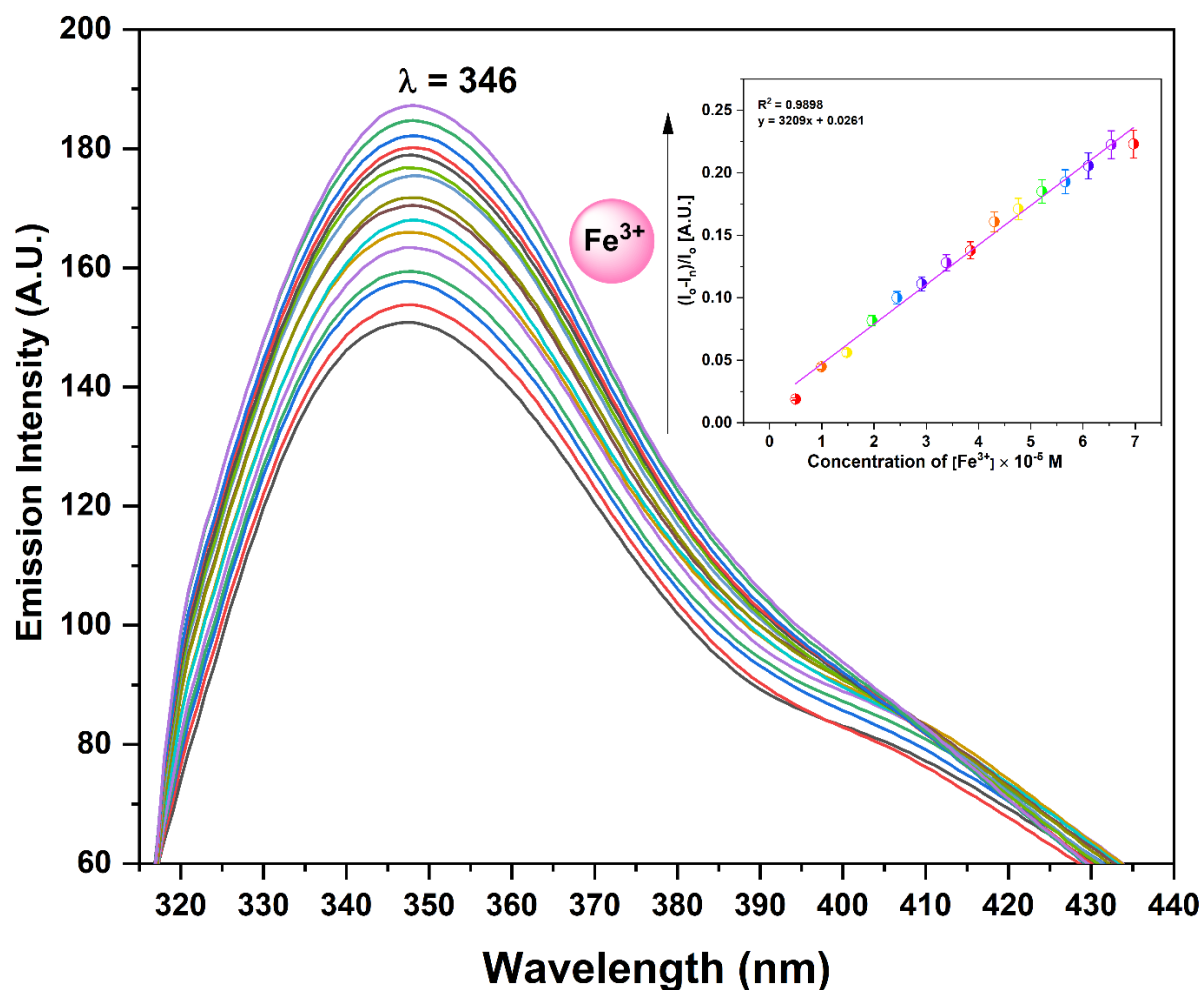


Figure S7. Fluorescence titration spectra of probe **81c** in EtOH:H₂O::9:1 solvent medium with incremental addition of 1 equiv. of Fe³⁺ ions, inset exhibiting relative change in absorption with addition of Fe³⁺ ions (linear calibration curve)

Similarly, probe **82c** (0.05 mM) was explored for the chemosensing behavior of the ligand via UV-visible studies. The clear solubility of the probe **82c** in DMSO solvent, as well as the significant absorption peaks at 276 and 311 nm leads to the selection of DMSO as the solvent. UV-vis interaction of receptor **82c** in DMSO were conducted against environmentally relevant cations indicating a selective response of probe **82c** towards Pb²⁺ metal ions.

The enhancement in the UV-vis absorption spectrum of sensor **82c** was observed in DMSO owing to the sequential addition of Pb²⁺ ions shown in **Figure S8**.

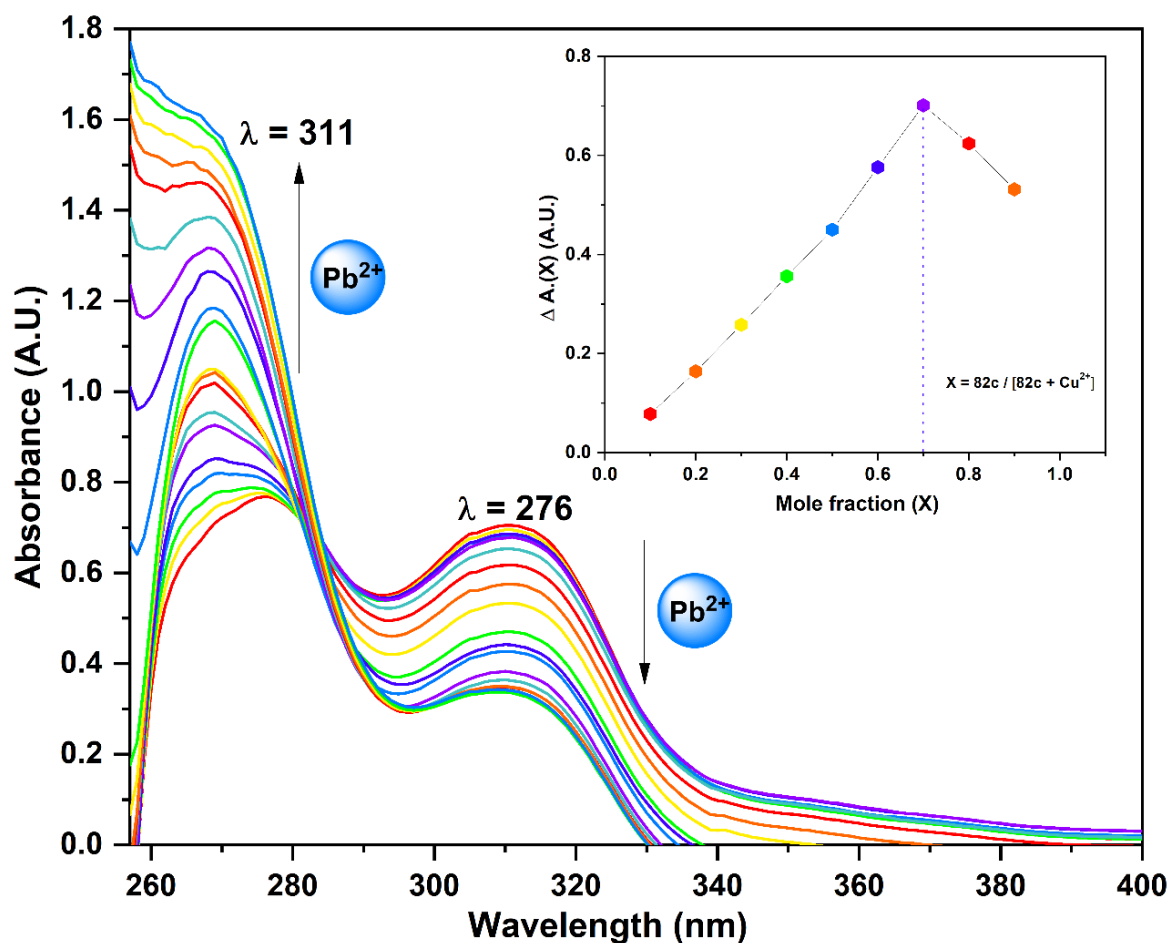
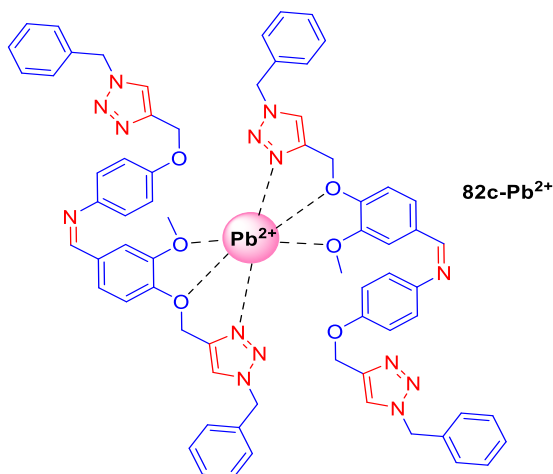


Figure S8. UV-vis spectrum of probe **82c** with sequential addition of 1 equiv. of Pb^{2+} ions in DMSO solvent, inset displaying the binding ratio of 2:1 for **82c**- Pb^{2+} complex

Furthermore, the binding ratio for the host-guest complex was found to be 1:2 (Metal-ligand) from Job's plot. The association constant was found to be $4.1 \times 10^4 \text{ M}^{-1}$ indicating **82c** having strong association binding with the lead metal ions. The hyperchromic shift observed with addition of Pb^{2+} ions in **82c** confirms the binding of **82c**- Pb^{2+} complex



The fluorescence spectrum was recorded with the addition the metal ion at $\lambda_{em} = 436$ nm. On gradually increasing the Pb^{2+} metal ions, fluorescence intensity exhibits hyperchromic effect with detection limit be 0.25 μM (**Figure S9**)

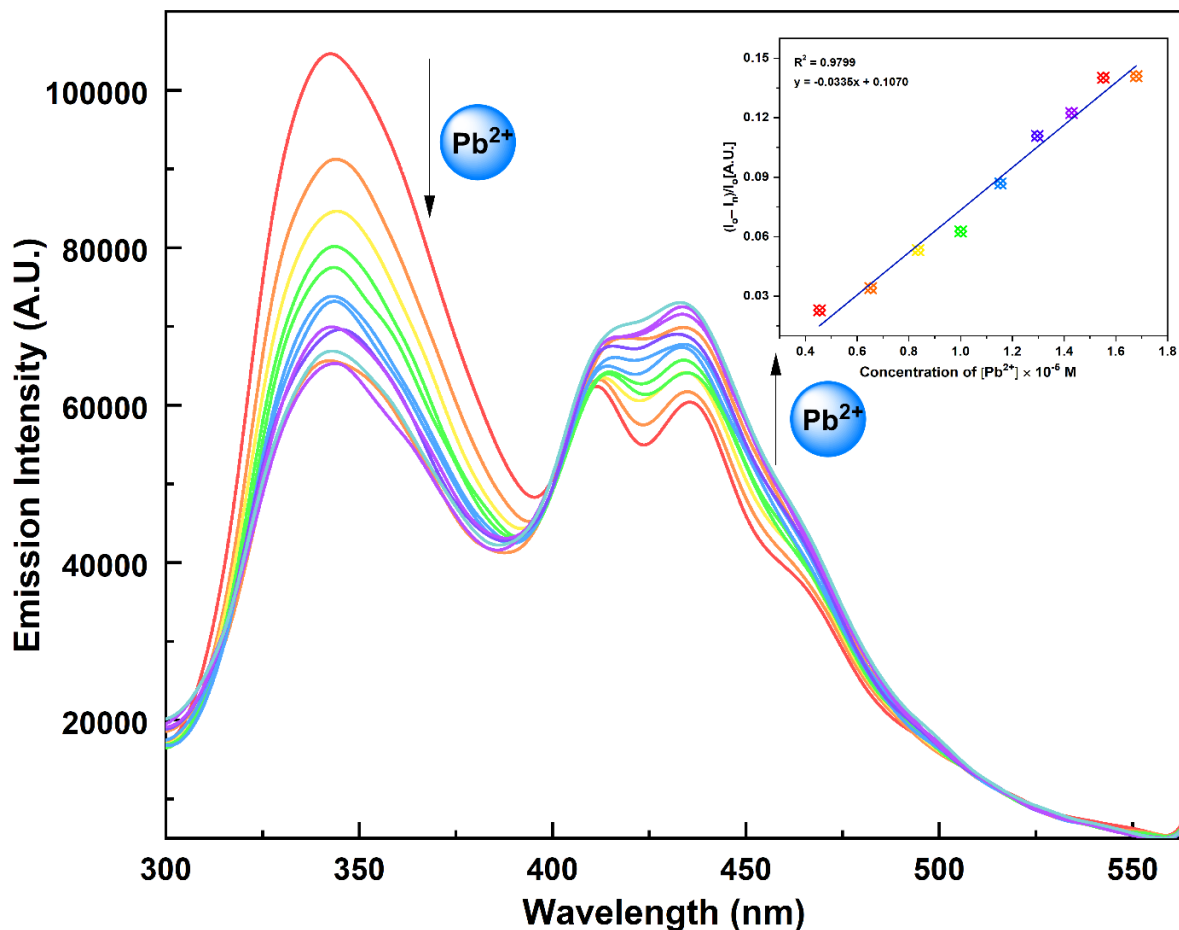


Figure S9. Fluorescence spectrum of probe **82c** when titrated with Pb^{2+} ions solution in DMSO solvent, inset displaying the stoichiometric ratio (1:1) of **82c**- Pb^{2+} complex

To acquire an insight into the optical properties of chemosensor **83c** (30 μM) absorption titration with Cu^{2+} ions were performed. On increasing the concentration of Cu^{2+} ions in probe **83c**, the value of intensity increased (hyperchromic shift). At around 309 nm, a well-defined isosbestic point was observed illustrating the net interconversion between the non-complexed and complexed entities. Furthermore, when Cu^{2+} ions were gradually added to **83c**, the absorption bands at 315 nm shifted hypsochromically by 11 nm (**Figure S10**).

The job's plot implies a 1:1 binding mode of [**83c**- Cu^{2+}]. The value of binding constant (K_a) of metal-ligand complex was found to be $6.0 \times 10^4 \text{ M}^{-1}$ calculated from B-H plot.

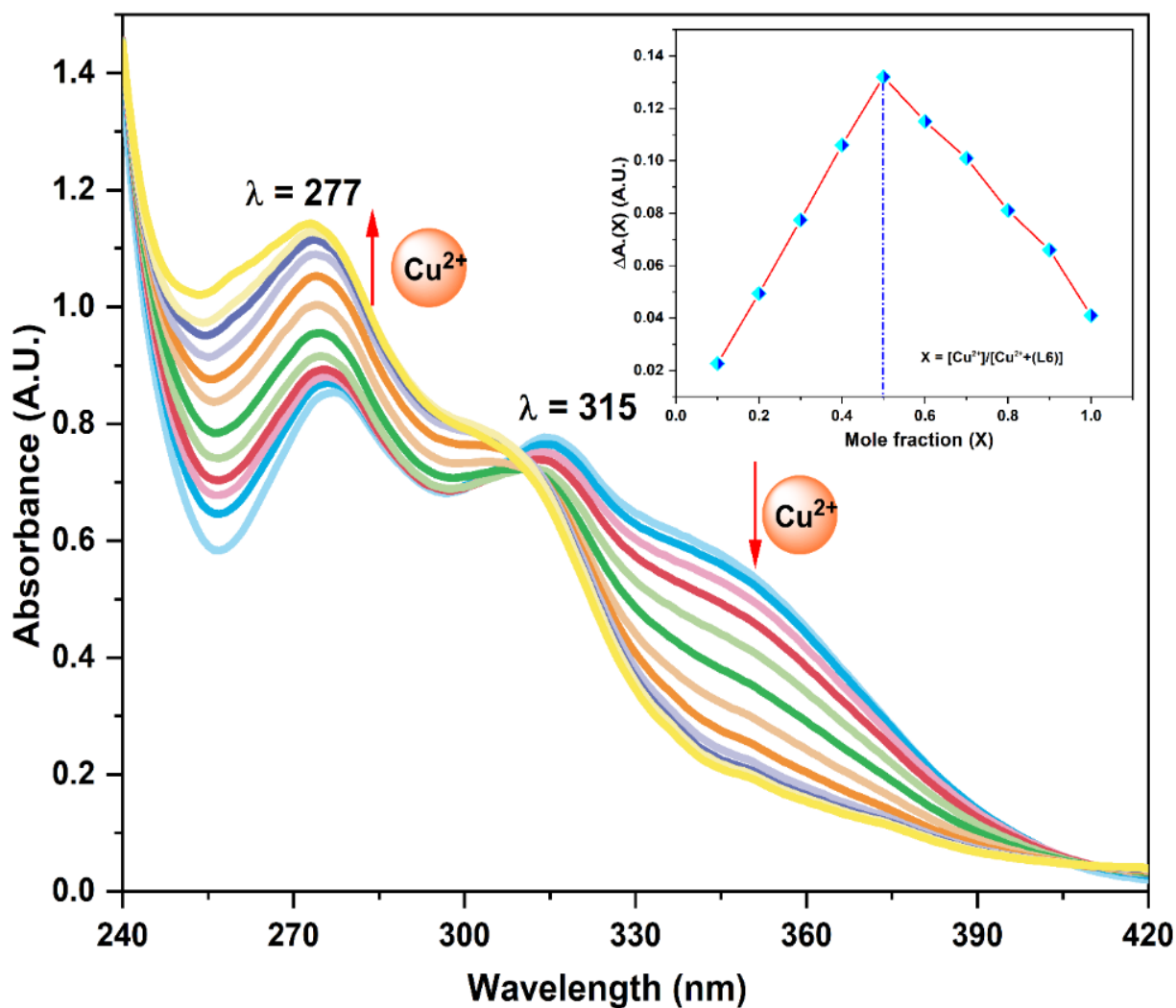
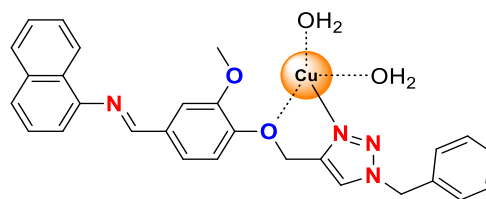


Figure S10. Absorption spectra of **83c** in $\text{CH}_3\text{CN}:\text{H}_2\text{O}::4:1$ solvent mixture upon consecutive addition with the increasing equivalent of Cu^{2+} ions, inset unveiling the stoichiometric ratio (1:1) of **83c**- Cu^{2+} complex via Job's plot

The fluorescent recognition sensing was in ACN:H₂O::4:1 solution system revealing weak fluorescence emission at $\lambda = 415$ nm upon excitation at $\lambda_{\text{ex}} = 280$ nm. The addition of Cu²⁺ (0.0001 mM) to **83c** during the titration process led to an increased in the emission intensity, which was directly proportional to the concentration of metal ions [Cu²⁺] added. (**Figure S11**) The values of Job's plot experiment indicated that the lower limit of detection of chemosensor **83c** for detecting Cu²⁺ ions was 20.6 nM turning it into an effective chemosensor for detection of copper ions.

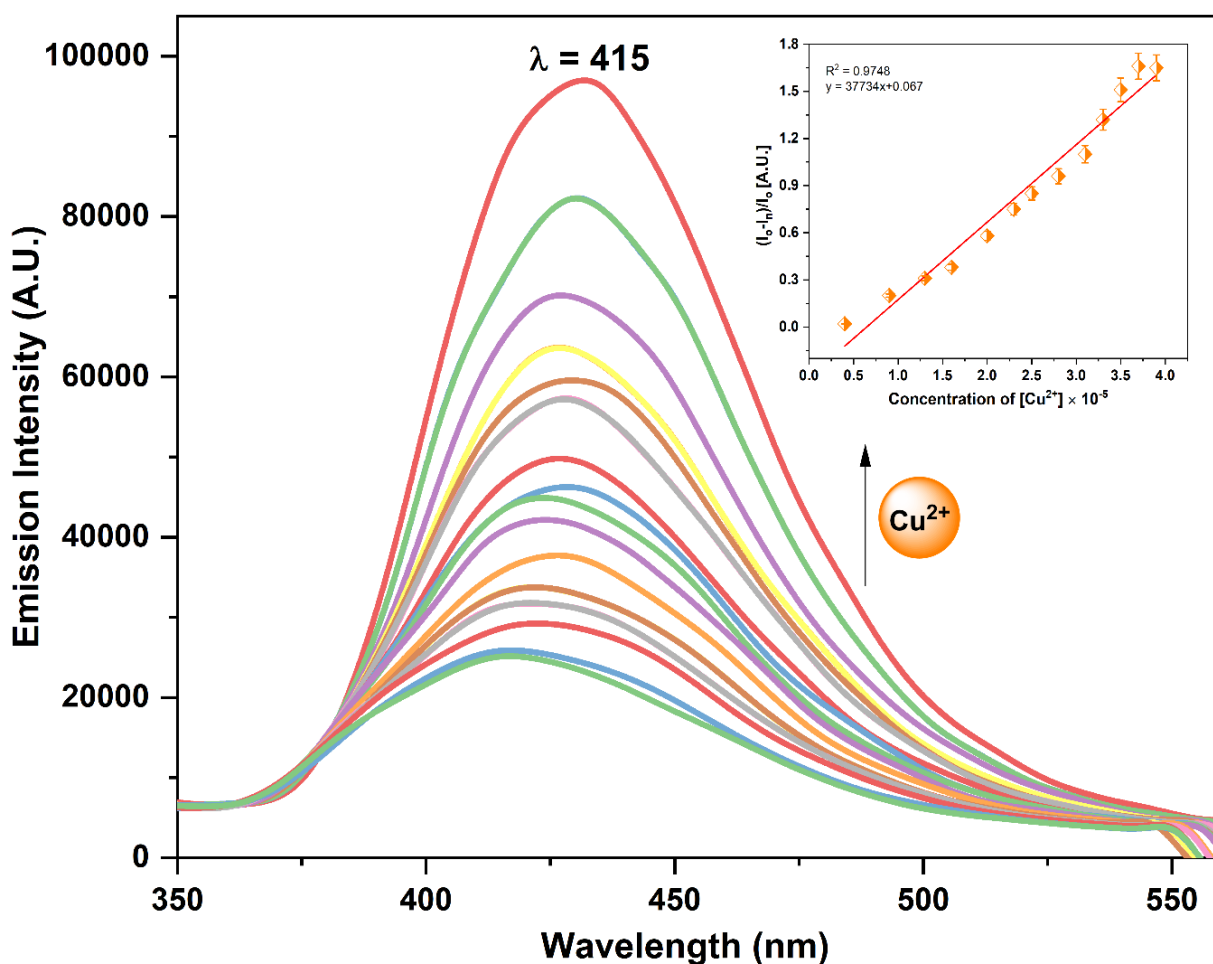


Figure S11. Emission spectra of probe **83c** when titrated with Cu²⁺ ions solution in CH₃CN:H₂O::4:1 solvent media, inset presenting the pattern of relative emission upon addition of Cu²⁺ ions solution

Similarly, UV-vis spectra of probe **84c** (0.05 mM) were recorded at ambient temperature in partially aqueous (ACN:H₂O::4:1) solvent mixture with the addition of Hg²⁺ ions. The UV titration of the chemosensor **84c** with Hg²⁺ (1mM) revealed that as the concentration of metal ions

(0–9 equiv.) increased, resulted in a decrease in intensity at 307 nm along with the absorption band at 273 nm gradually diminished while the absorbance concomitantly increased and a new absorption band emerges at 267 nm (**Figure S12**).

The stoichiometric ratio (1:1) between [**84c**-Hg²⁺] was confirmed using the approach of Job's plot. The association constant K_a for the binding of Hg²⁺ ions with **84c** was determined from B-H plot as $2.93 \times 10^4 \text{ M}^{-1}$.

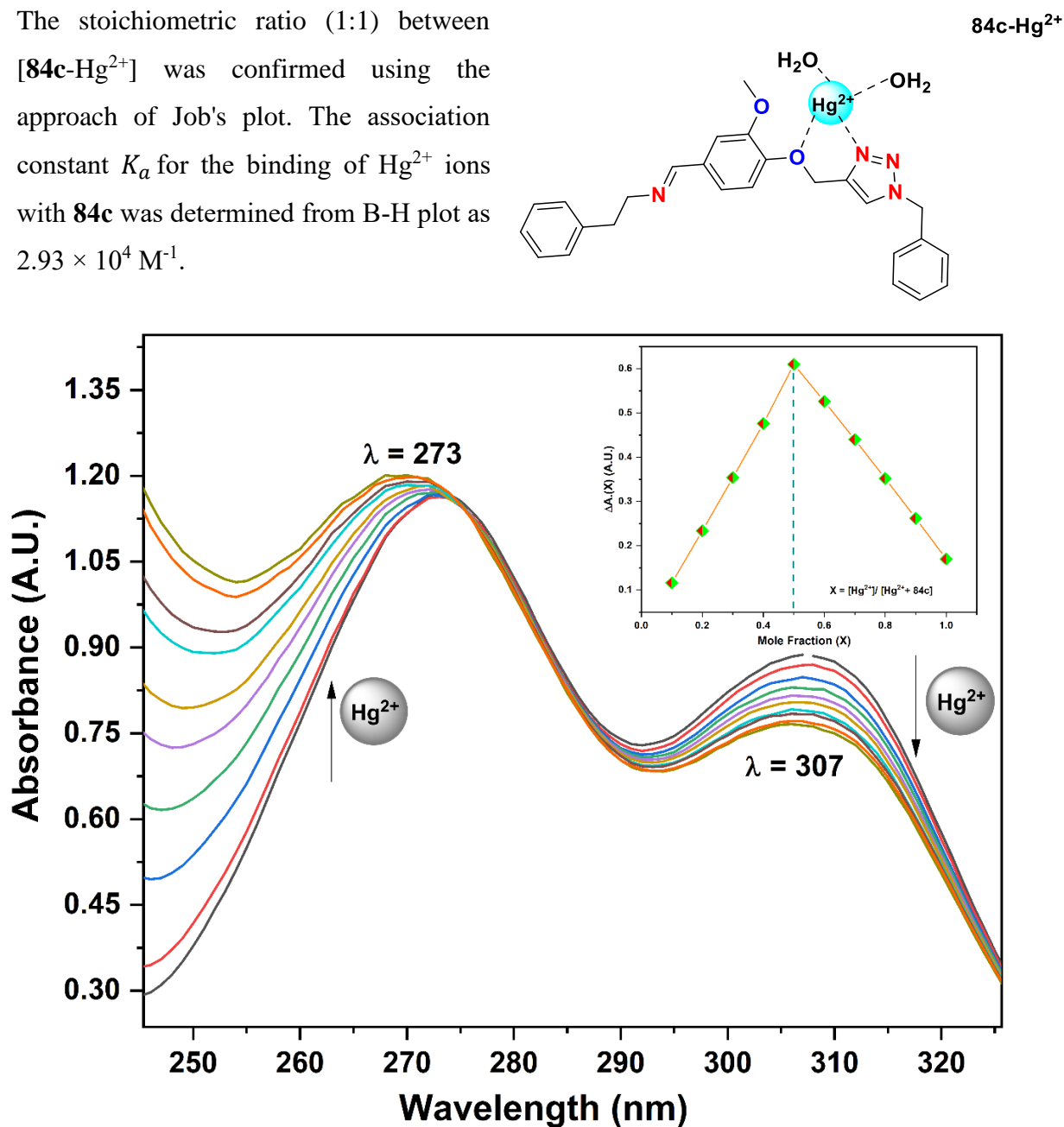


Figure S12. UV-visible graph of **84c** showing absorbance responses measured after adding 1 equiv. of Hg²⁺ ions solution to **84c** solution in ACN:H₂O::4:1 solvent system, inset exhibiting binding ratio of [**84c**-Hg²⁺] complex calculated via job's plot

Fluorescence emission spectrum studies were conducted to explore the sensing capability of probe **84c** towards Hg^{2+} ions in a mixed aqueous media ($\text{ACN}:\text{H}_2\text{O}::4:1$). An emission band with wavelength $\lambda_{\text{em}} = 520$ nm was observed for probe **84c** in ($\text{ACN}:\text{H}_2\text{O}::4:1$) solvent mixture. The fluorescence intensity has been progressively increased by the addition of Hg^{2+} in **84c** solution when excited at $\lambda_{\text{ex}} = 310$ nm (**Figure S13**), attributed to CHEF mechanism along with the inhibition of PET mechanism

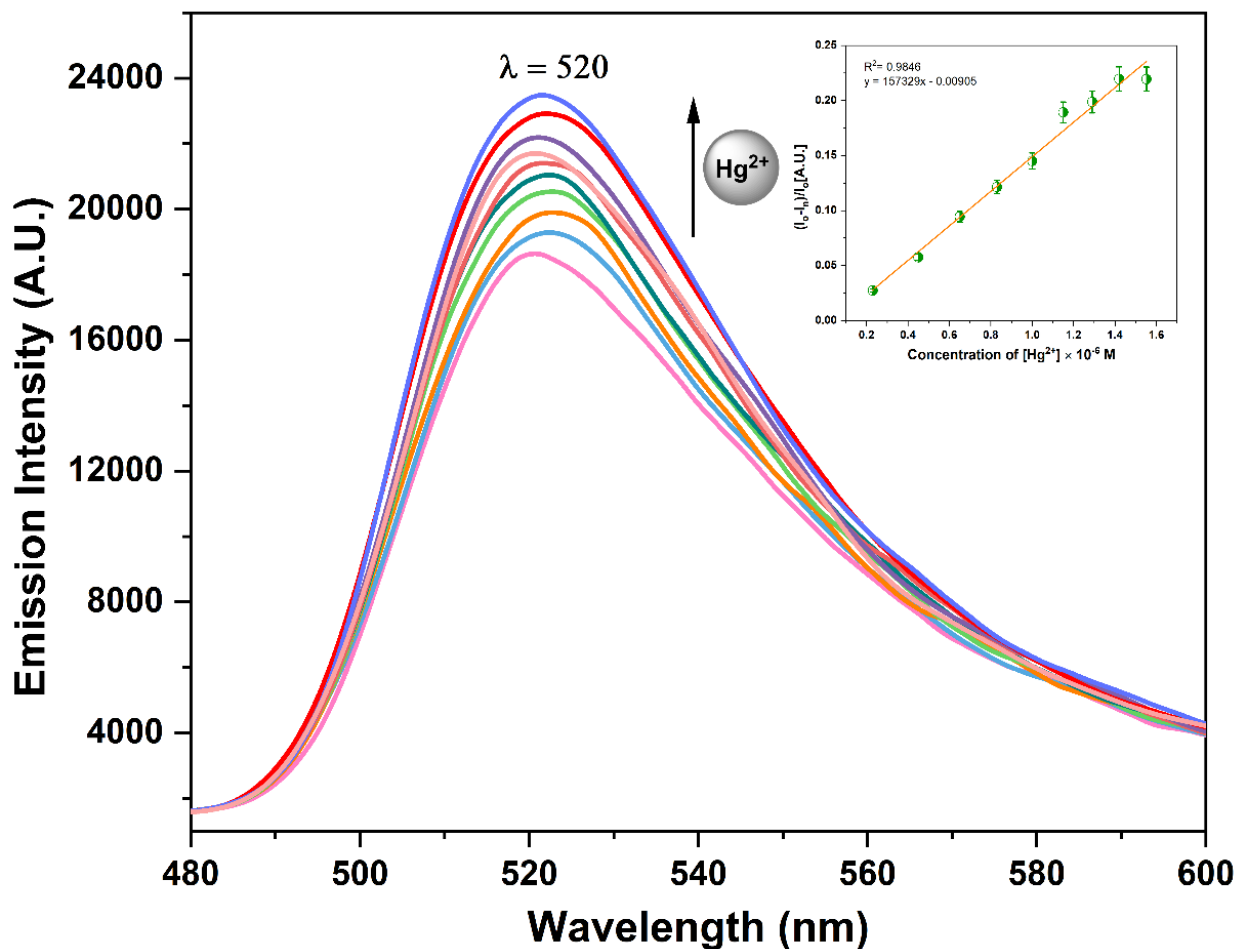


Figure S13. The fluorescence spectra of the sensor **84c** titrated against Hg^{2+} ions in $\text{ACN}:\text{H}_2\text{O}::4:1$ solution, inset exhibited the relative emission intensity with increase in conc. of Hg^{2+} ions solution

Absorption spectroscopy was employed to investigate the effect of various metal ions on the sensing capability of the ligand **85c** (0.05 mM) in ($\text{ACN}:\text{H}_2\text{O}::4:1$) solvent. When copper or lead metal ions were added into the **85c** solution, the higher energy band experienced an enhancement, while the lower energy band was reduced.

The isosbestic point was seen at 392 nm for Cu^{2+} and at 396 nm for Pb^{2+} , respectively. (Figure S14, S15)

The binding structure for the **85c** in the presence of Cu^{2+} or Pb^{2+} was postulated, from Job's plot relying on the formation of a 1:1 complex. The binding constant (K_a) values have been calculated to be 3.75×10^5 and $1.02 \times 10^5 \text{ M}^{-1}$ for Cu^{2+} and Pb^{2+} ions, respectively.

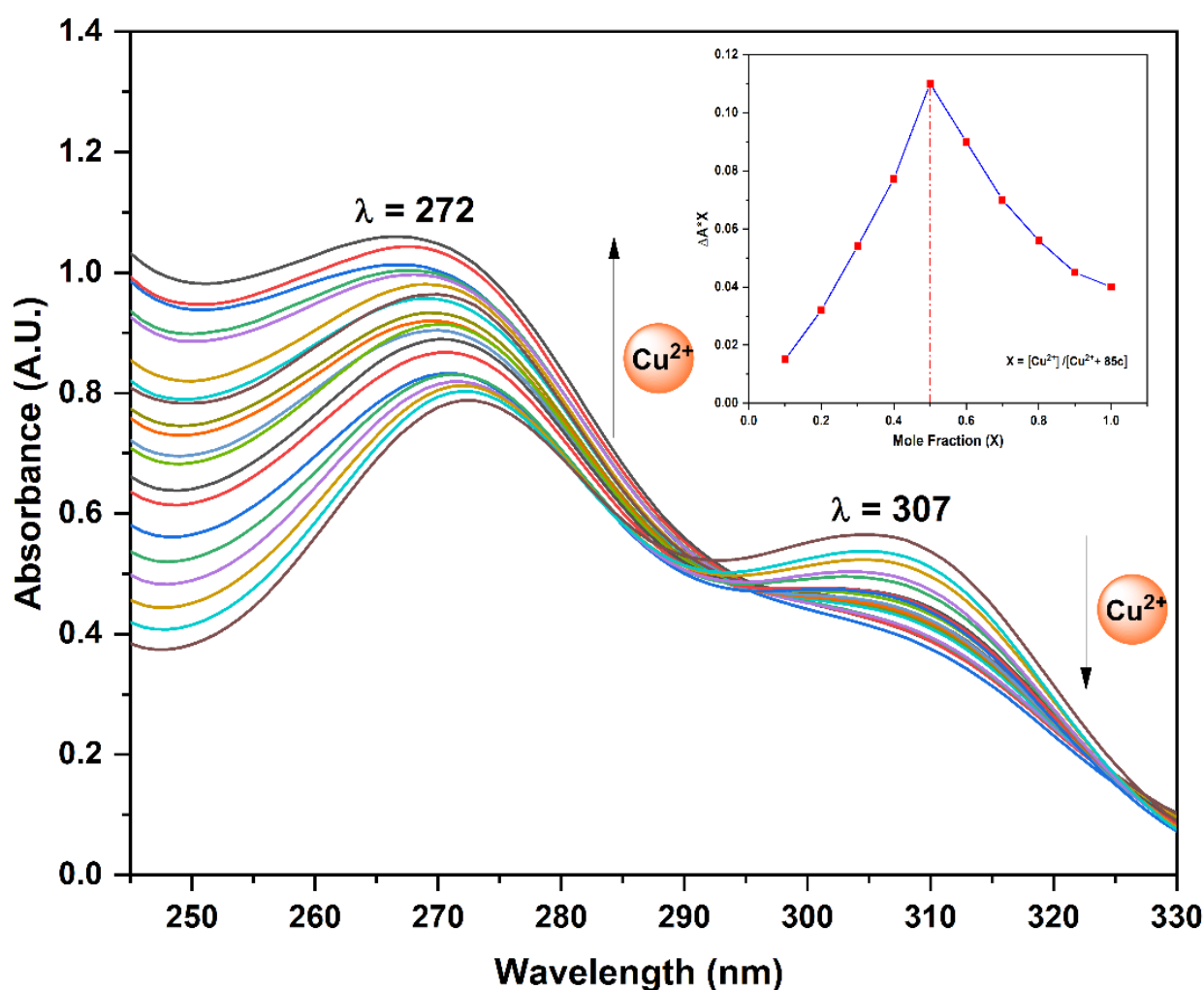
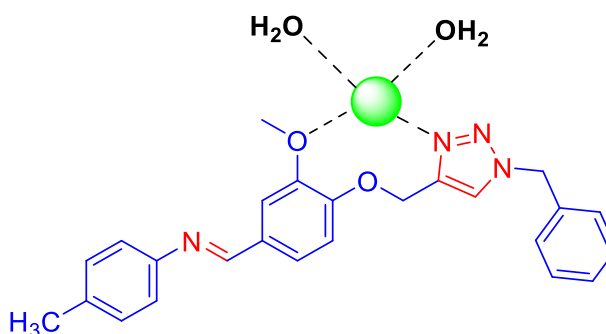


Figure S14. The UV-vis spectral variations of **85c** after incremental addition of Cu^{2+} ions in in $\text{ACN}:\text{H}_2\text{O}::4:1$ solvent, inset demonstrating job's plot (1:1) binding ratio of **85c**- Cu^{2+} complex

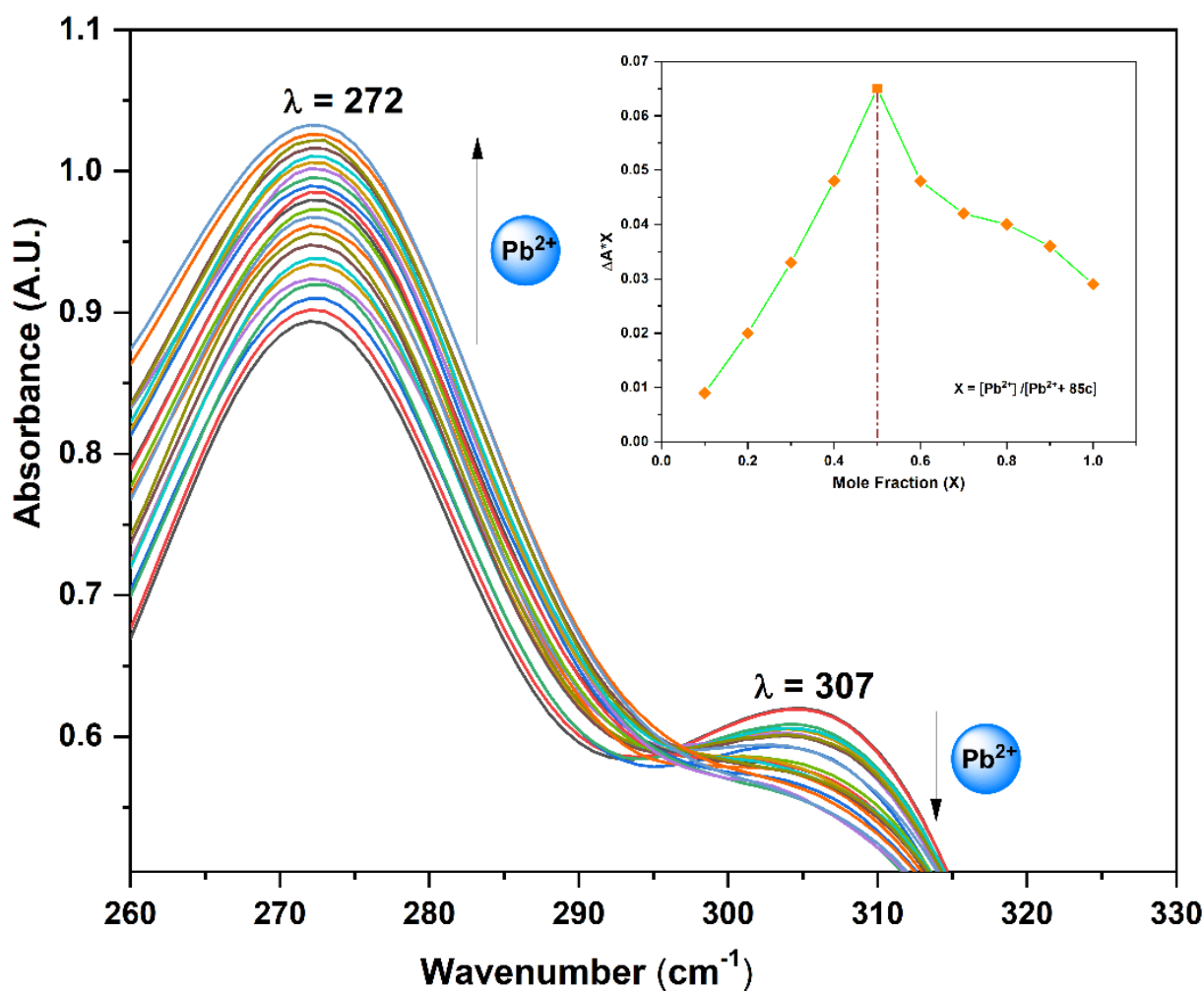


Figure S15. The absorbance spectra of **85c** displaying the spectral changes after addition of Pb²⁺ ions in ACN:H₂O::4:1 solvent, inset exhibiting binding ratio (1:1) of **85c**-Pb²⁺ complexation

Fluorescence titration studies were conducted to attain comprehensive knowledge of the molecular-level interaction between the sensor **85c** and both of the metal ions (Cu²⁺, Pb²⁺). Fluorescence emission studies were performed for probe **85c** (5 μ M) with metal Cu²⁺ and Pb²⁺ ions (100 μ M) in (ACN:H₂O::4:1) solvent.

The fluorescence emission intensity progressively increased when Cu^{2+} ions or Pb^{2+} ions were added in incremental amounts to **85c** in ACN/ H_2O (4/1, v/v) medium. (**Figure S16, S17**) The LOD values for Cu^{2+} and Pb^{2+} was calculated as 0.19 nM and 0.39 nM respectively. This suggests that the probe **85c** exhibits a high level of sensitivity towards both metal ions.

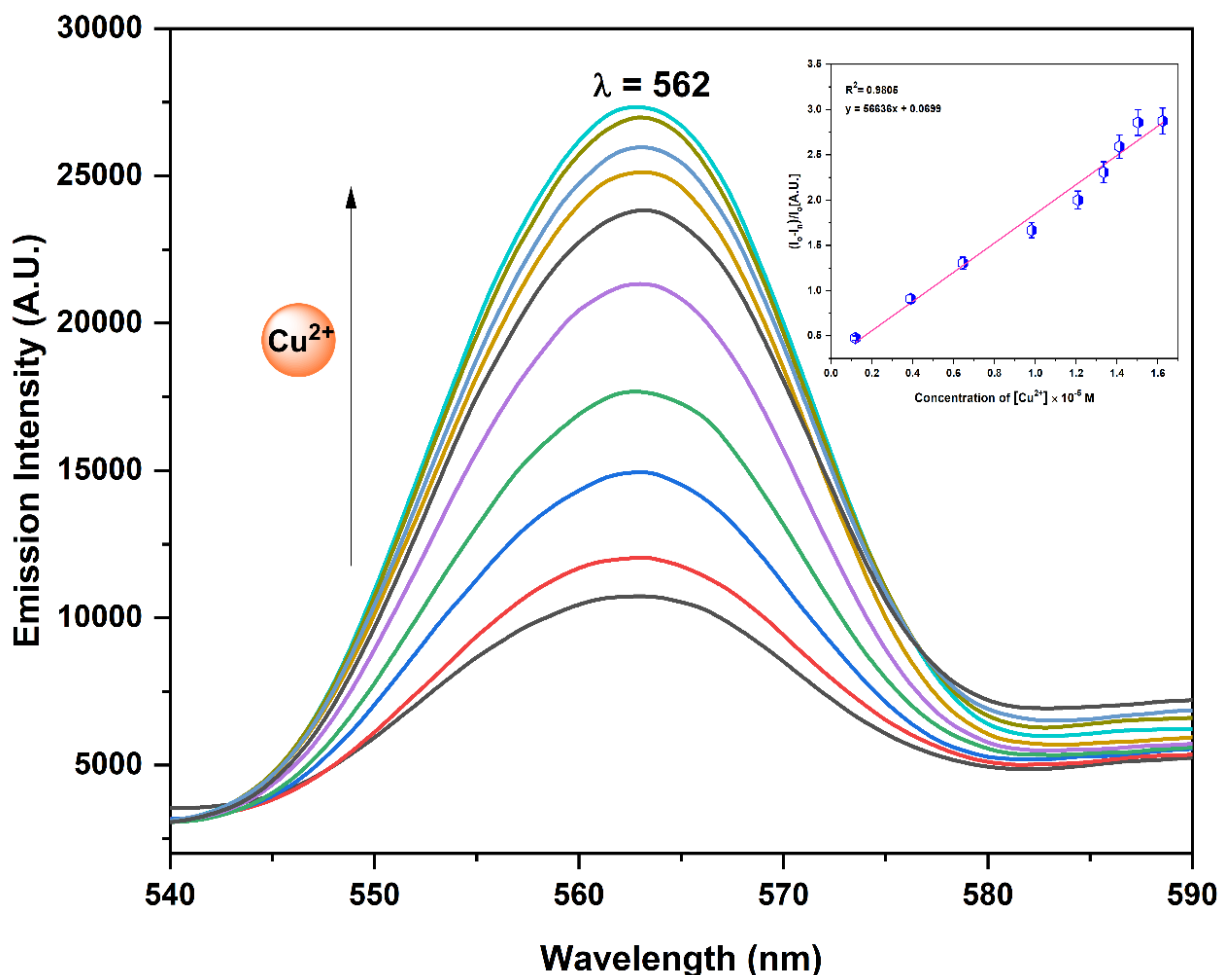


Figure S16. Fluorescence spectra of **85c** with increasing concentration of Cu^{2+} ions in (ACN: H_2O ::4:1) solvent medium, inset exhibiting relative emission against increasing conc. of Cu^{2+} ions solution

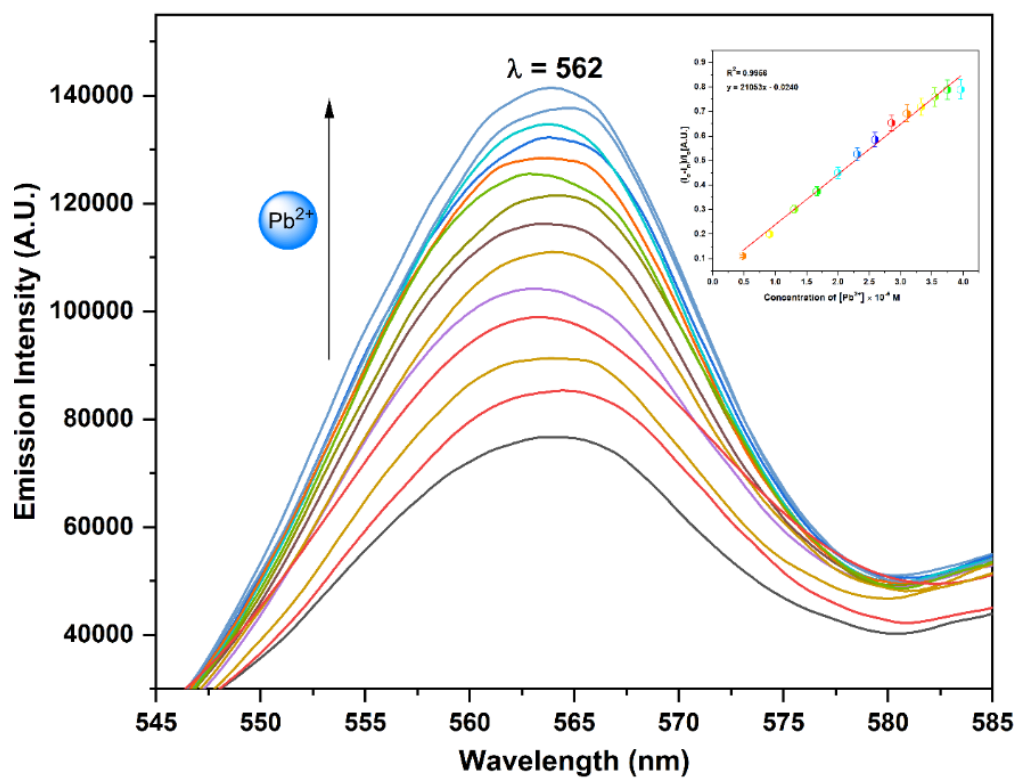


Figure S17. The Change in emission spectra of Probe **85c** upon the addition of Pb²⁺ ions in a ACN:H₂O::4:1 solvent medium, inset showing change in emission intensity with increasing conc. of Pb²⁺ ions

Annexure A



Chemicals and Instruments

Annexure A provides a comprehensive list of the chemicals, reagents, catalysts, and solvents utilised for the chemical syntheses and analytical study of the novel compounds. It also discusses the instruments utilised for different research endeavours.

Techniques for conducting general Experiments:

1. ATR-FTIR spectra

FTIR spectra of synthesized compounds were recorded in Diamond attenuated total reflection (ATR) mode from PERKIN ELMER Spectrum 2 Spectrometer (pellet accessories) covering field $4000\text{--}500\text{ cm}^{-1}$ at Central instrumentation facility, Lovely professional university, Phagwara with sensitivity including peak to peak for 1 min scan. The detector used in the record of the IR spectra was pyroelectric detector with material Lithium tantalate [LiTaO_3].

2. NMR spectra

NMR spectra were obtained on BRUKER-ADVANCE-II FT-NMR-AL 500 MHz and 126 MHz for (^1H and ^{13}C) spectrometer respectively using CDCl_3 and DMSO as solvents and the chemical shifts were recorded against tetramethylsilane as an internal standard at Sophisticated analytical instrumentation facility, Panjab University, Chandigarh.

3. Mass spectra

Gas Chromatograph-Mass spectrometer (GCMS/ MS Shimadzu TQ8040) was used for recording mass of the compounds and for few compounds the mass spectra (LCMS/MS) were acquired using the Waters Q-TOF Micro mass spectrometer.

4. UV-Visible spectra

The electronic absorption spectra were measured using a SHIMADZU UV-1800 UV-Spectrophotometer through a pair of quartz cuvettes bearing a path length of 1 cm, utilizing standard solutions at School of chemical and physical sciences, Lovely professional university, Phagwara.

5. Fluorescence spectra

Fluorescence emission spectra were generated from Perkin Elmer LS6500 Fluorescence Spectrometer at Central instrumentation facility, Lovely professional university, Phagwara.

6. CHNS Analysis

The CHN elemental analyses were conducted with Perkin Elmer Model 2400 CHNS elemental analyzer at Department of Chemistry, Panjab University, Chandigarh.

7. Melting Point

Mel Temp II device for determining melting point of the compounds using sealed capillary at School of chemical and physical sciences, Lovely professional university, Phagwara.

8. Weighing balance

The solutions were made by weighing samples using a microbalance WENSAR MAB 220 with an accuracy of ± 0.1 mg in volumetric glassware at School of chemical and physical sciences, Lovely professional university, Phagwara.

9. General materials

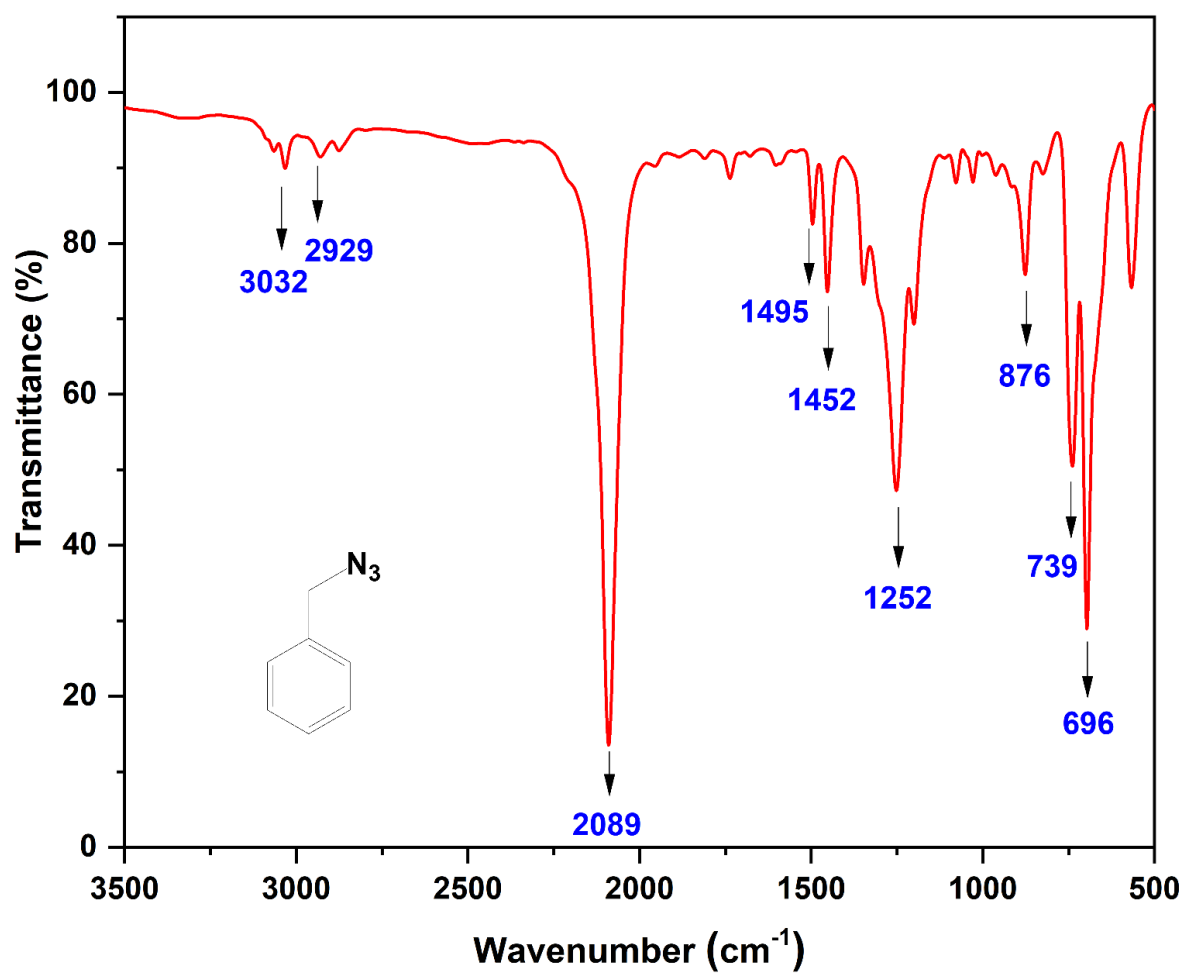
Commercially available high purity reagents and solvents such as 4-hydroxy-3-methoxy benzaldehyde (LOBA), 4-amino-phenol (LOBA), benzylamine (LOBA), 1-naphthylamine (LOBA), 2-phenylethylamine (LOBA), p-toluidine (LOBA), propargyl bromide (80% in toluene) (Spectro-chem), potassium carbonate (LOBA), dimethylformamide (DMF) (CDH), benzyl chloride (LOBA), tetrahydrofuran (THF) (CDH), triethylamine (CDH), sodium azide, bromotris(triphenylphosphine)copper(I) [CuBrPPh_3] (Merck), hexane, ethyl acetate were used as received. The Metal salts were acquired from LOBA and without any purification used for solution preparation.

Annexure B

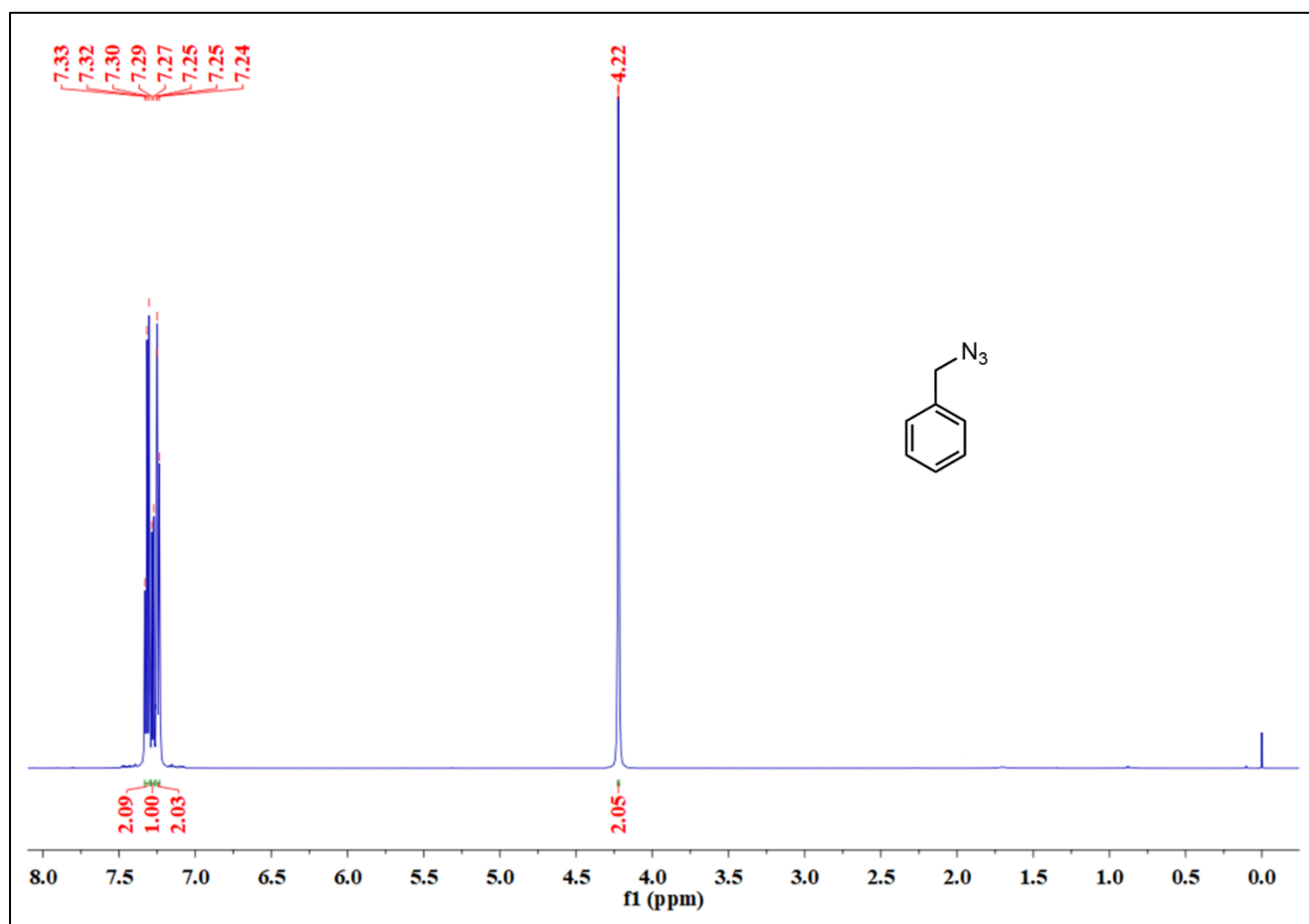
ATR-FTIR,
NMR (¹H, ¹³C),
and
MS spectra
(GCMS-MS/ LCMS-MS)

Appendix B contains all of the FTIR, NMR (¹H, ¹³C), and MS spectra of synthesized Schiff bases, Schiff base terminal alkynes, Schiff base tethered 1,2,3-triazole

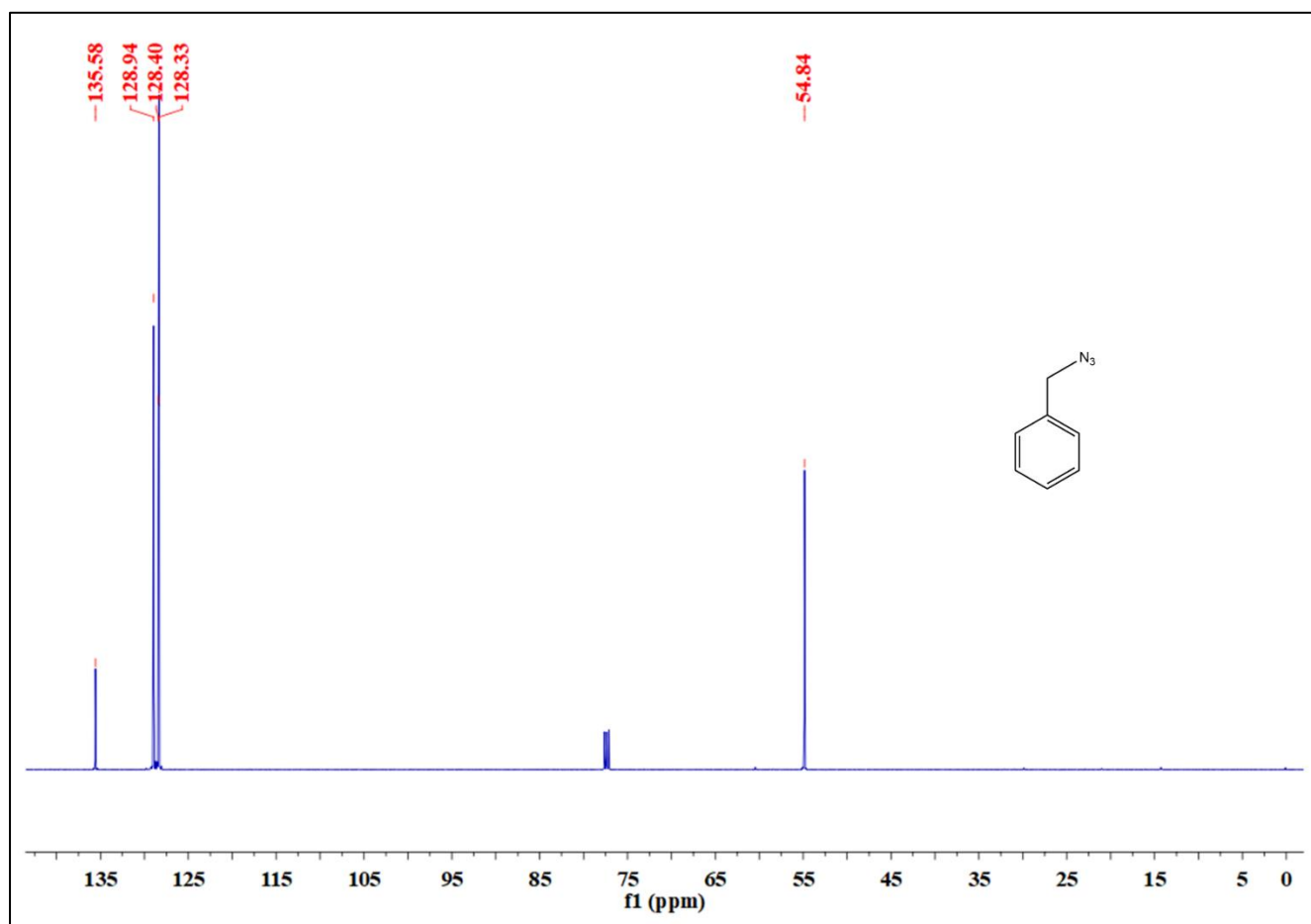
FTIR spectrum of *Azidomethylbenzene 39*



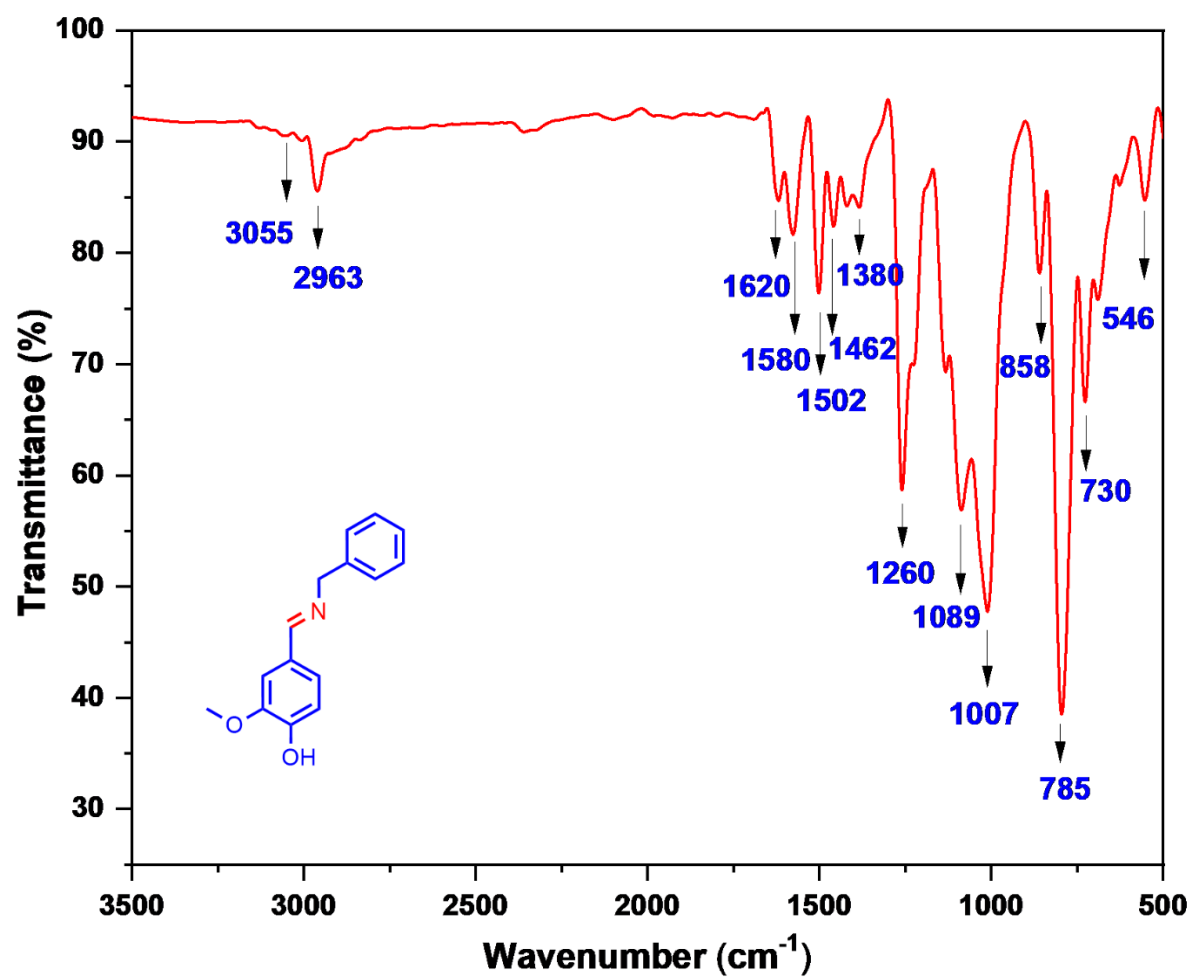
¹H NMR spectrum of Azidomethylbenzene 39



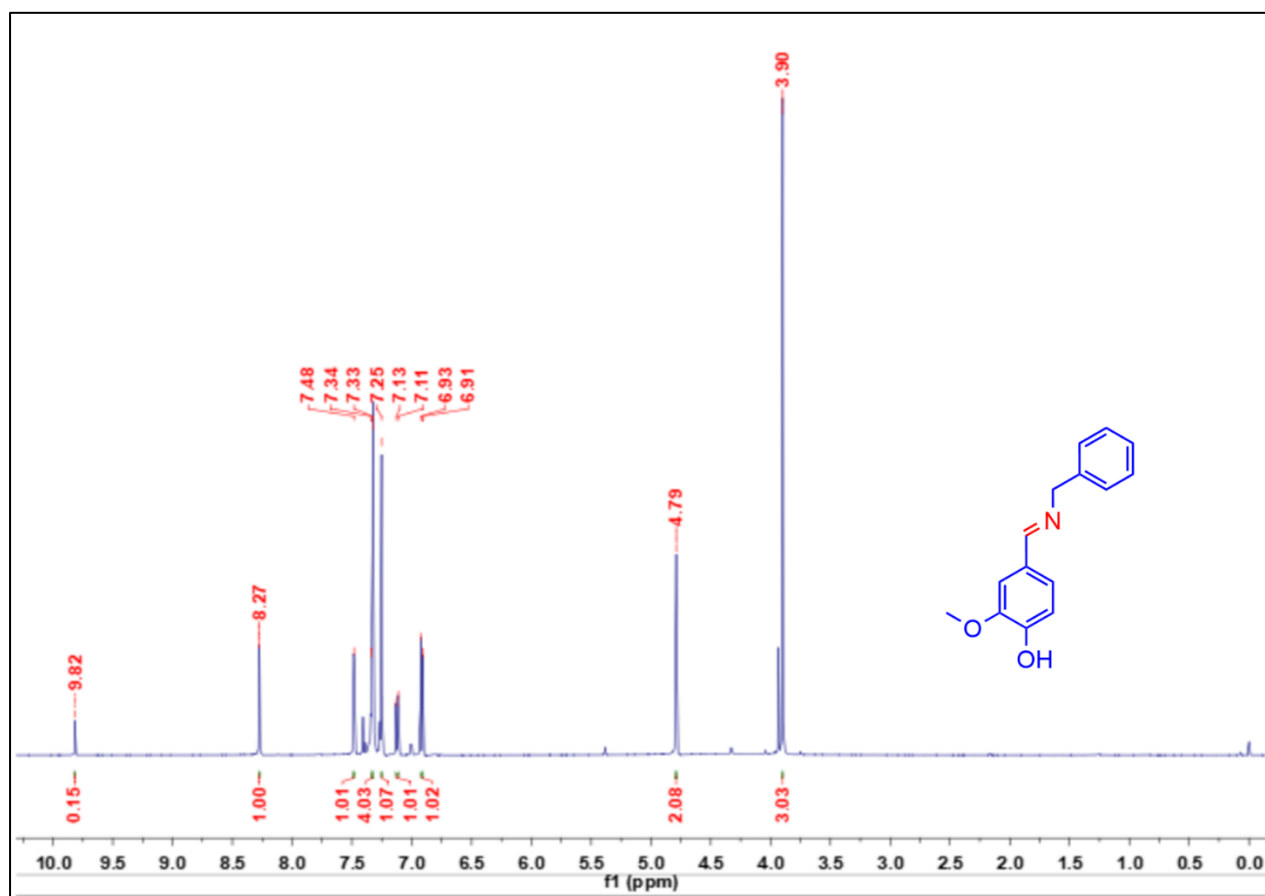
^{13}C NMR spectrum of Azidomethylbenzene 39



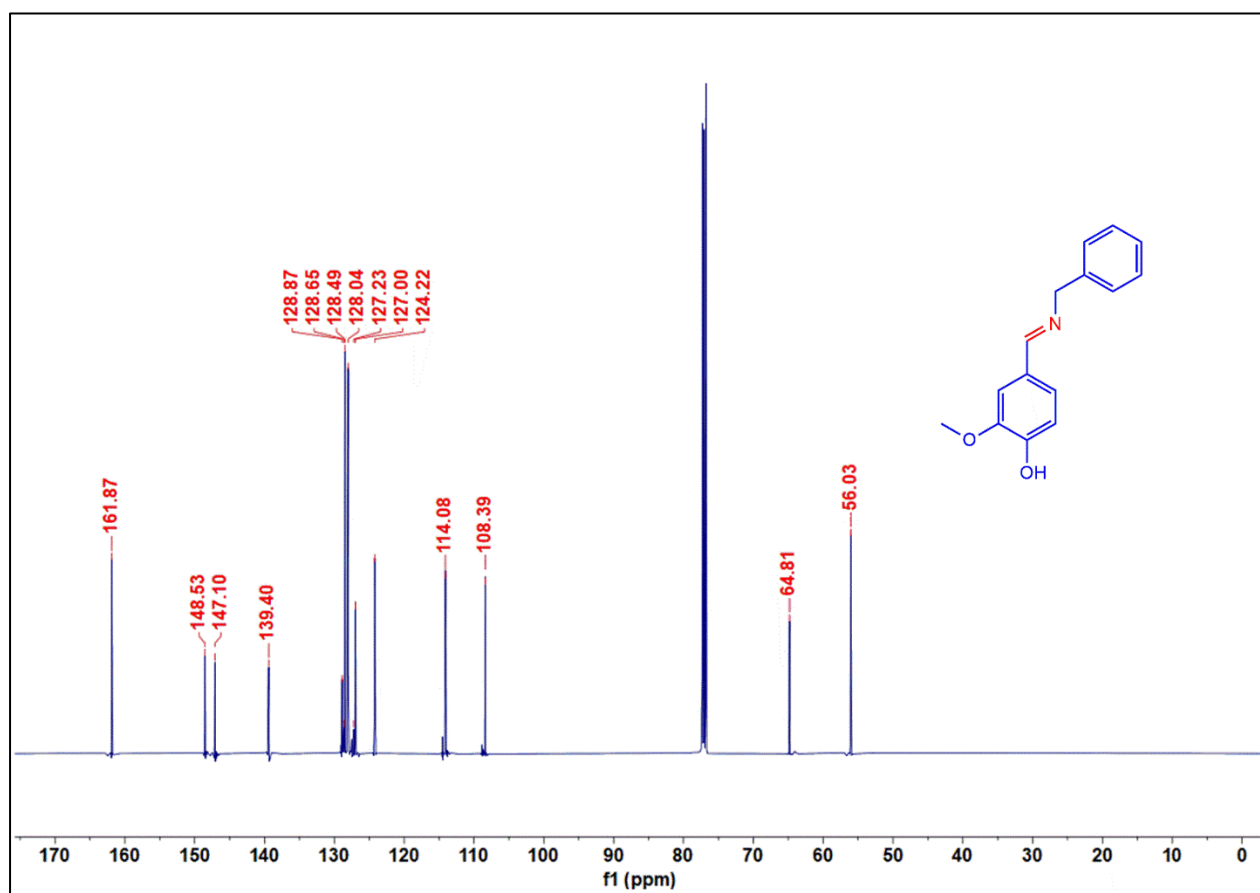
FTIR spectrum of Schiff base 81a



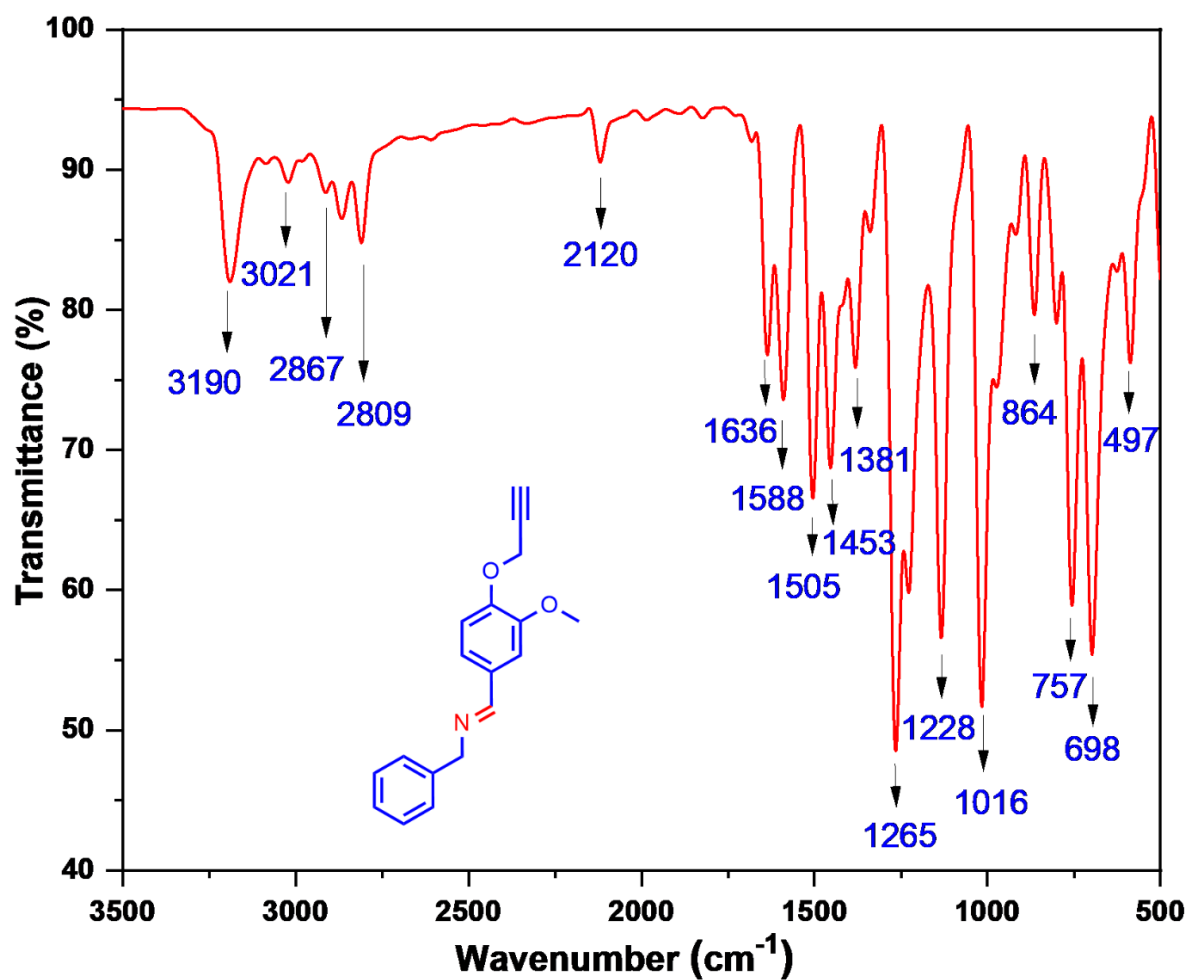
¹H NMR spectrum of Schiff base 81a



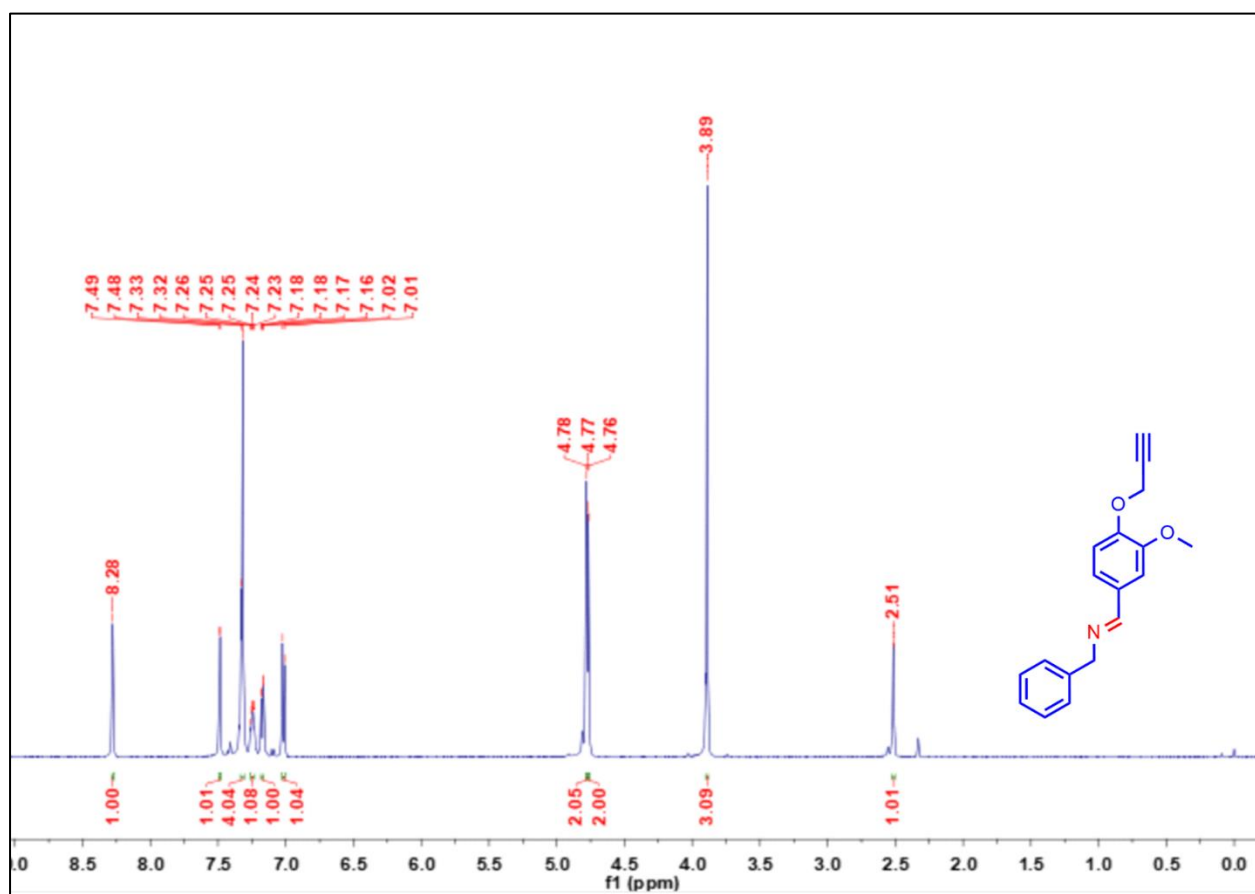
¹³C NMR spectrum of Schiff base 81a



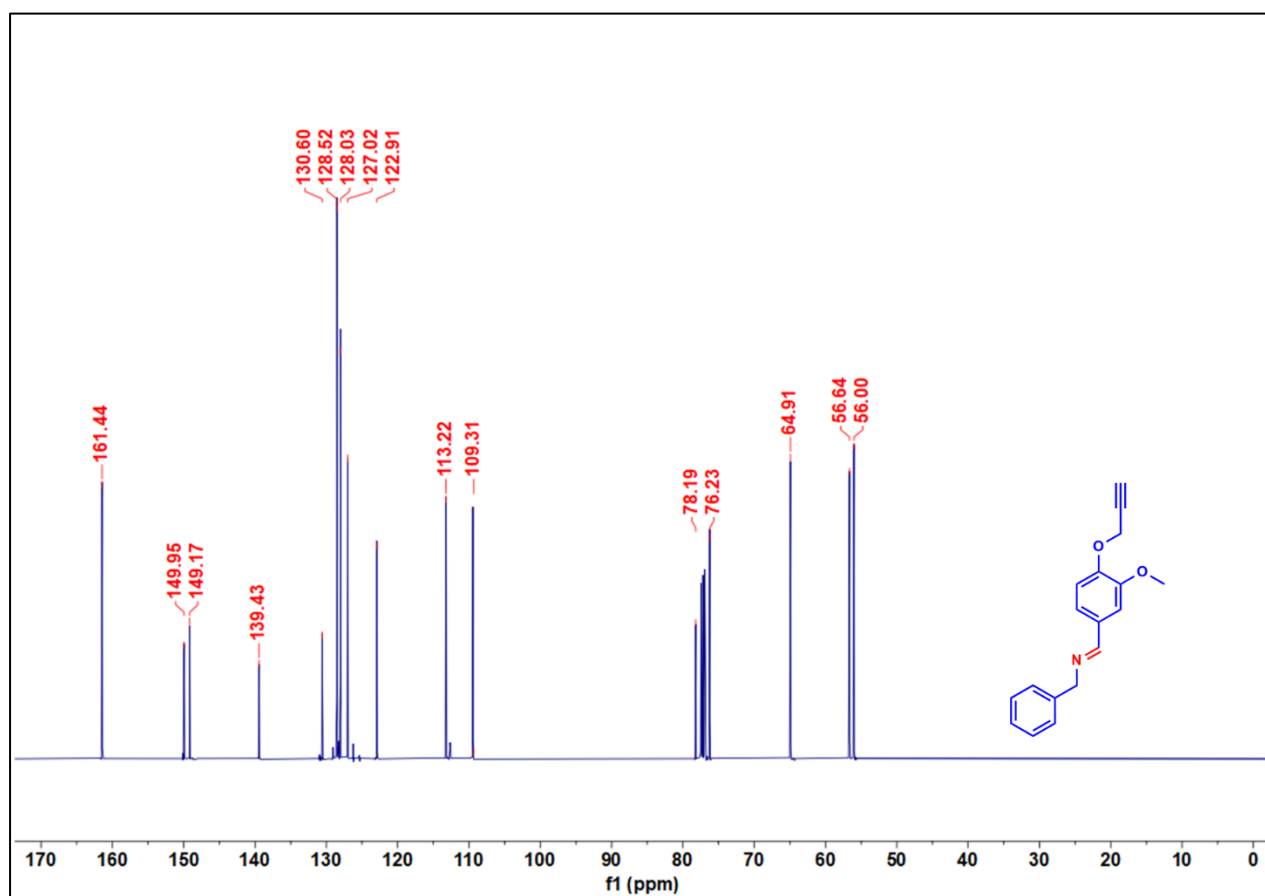
FTIR spectrum of Schiff base alkyne 81b



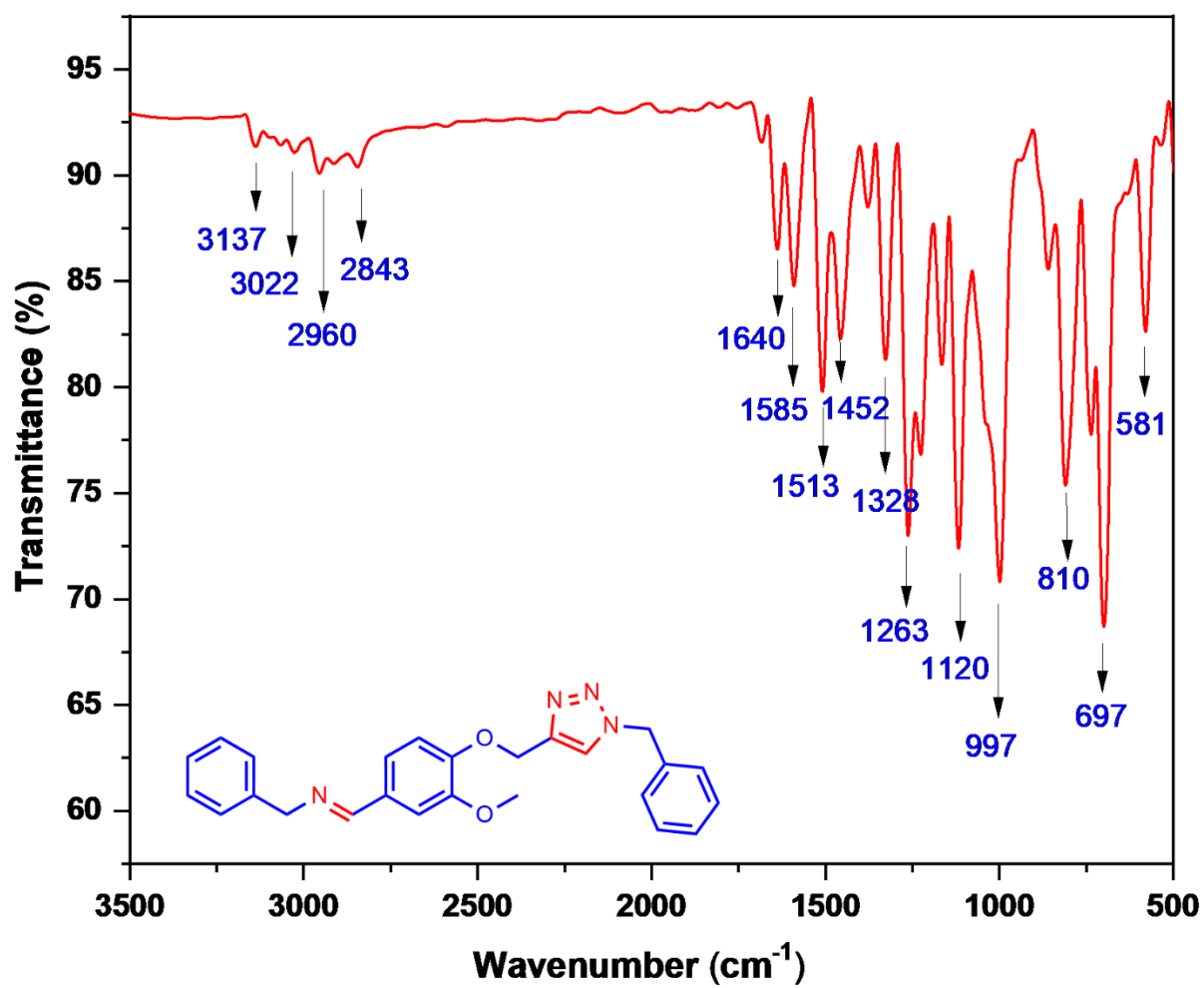
^1H NMR spectrum of Schiff base alkyne 81b



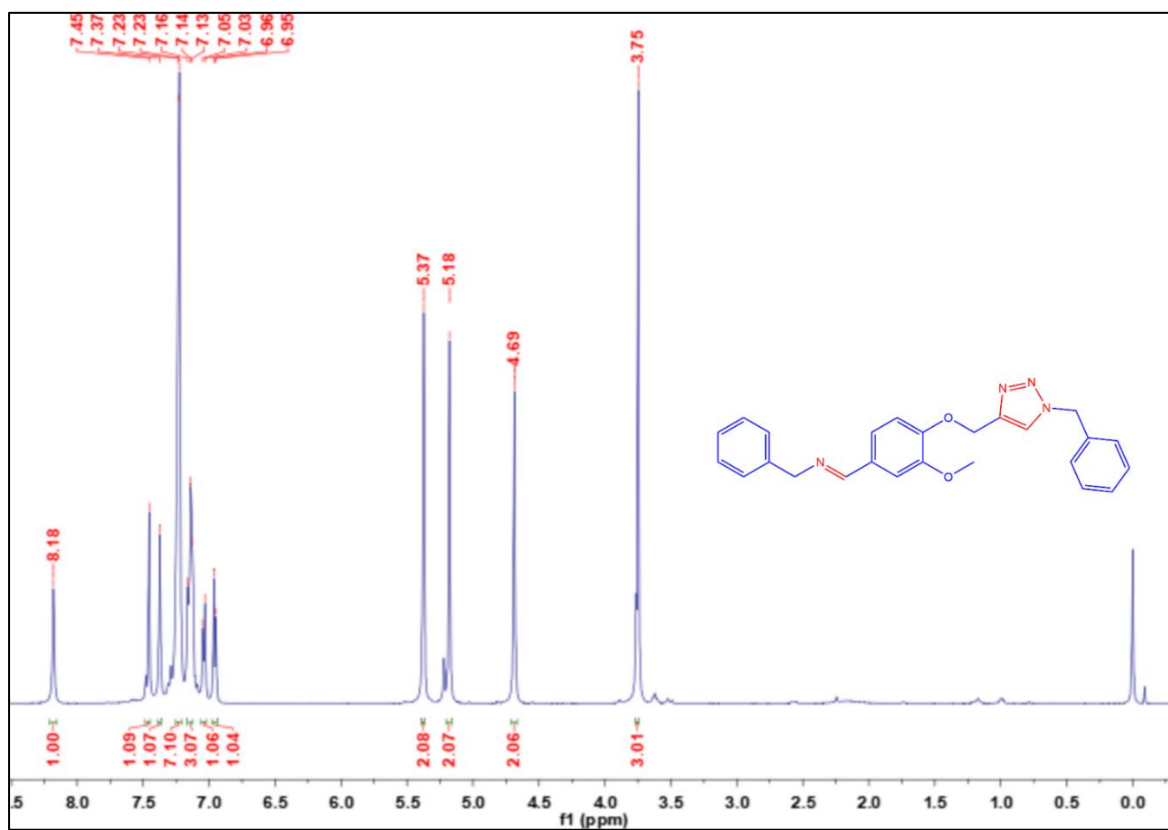
^{13}C NMR spectrum of Schiff base alkyne 81b



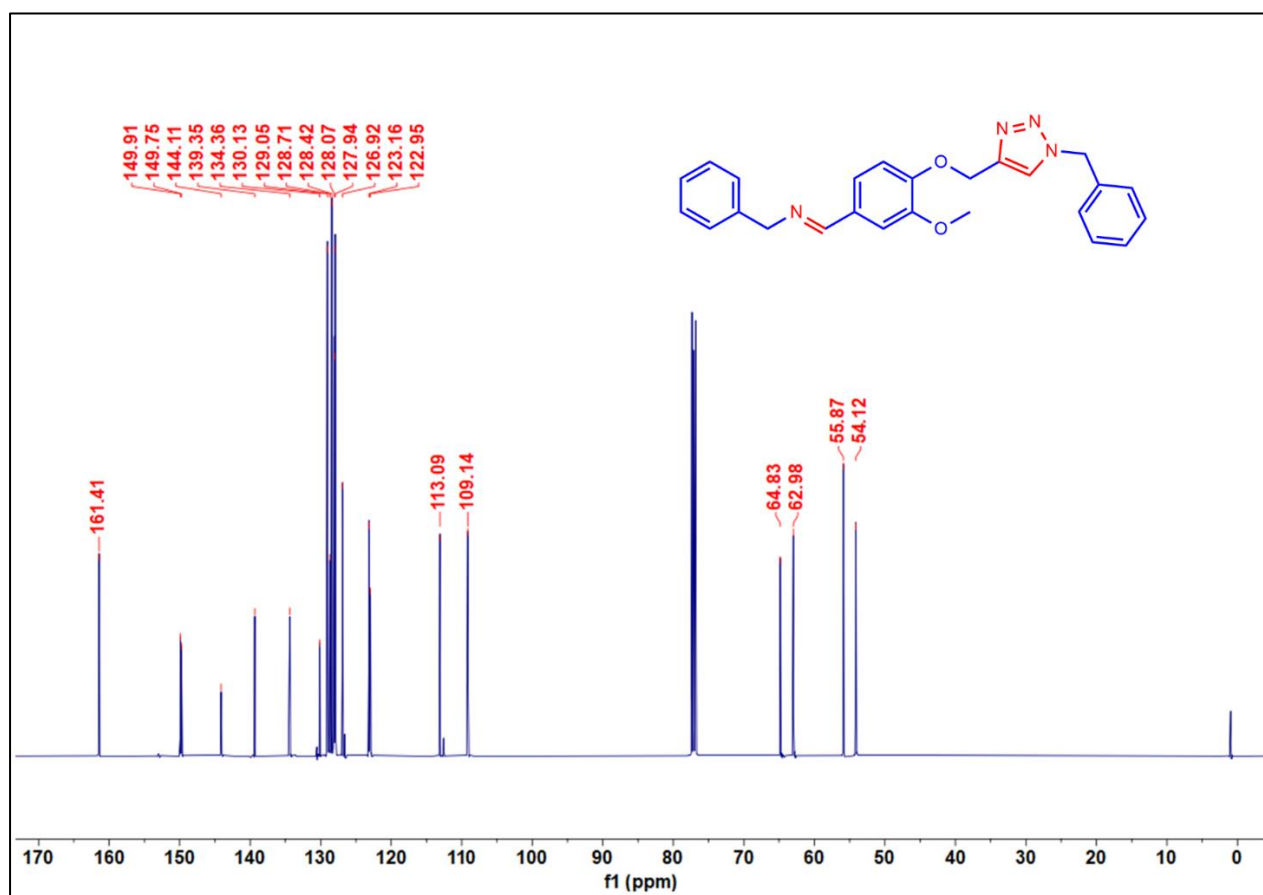
FTIR spectrum of Schiff base triazole 81c



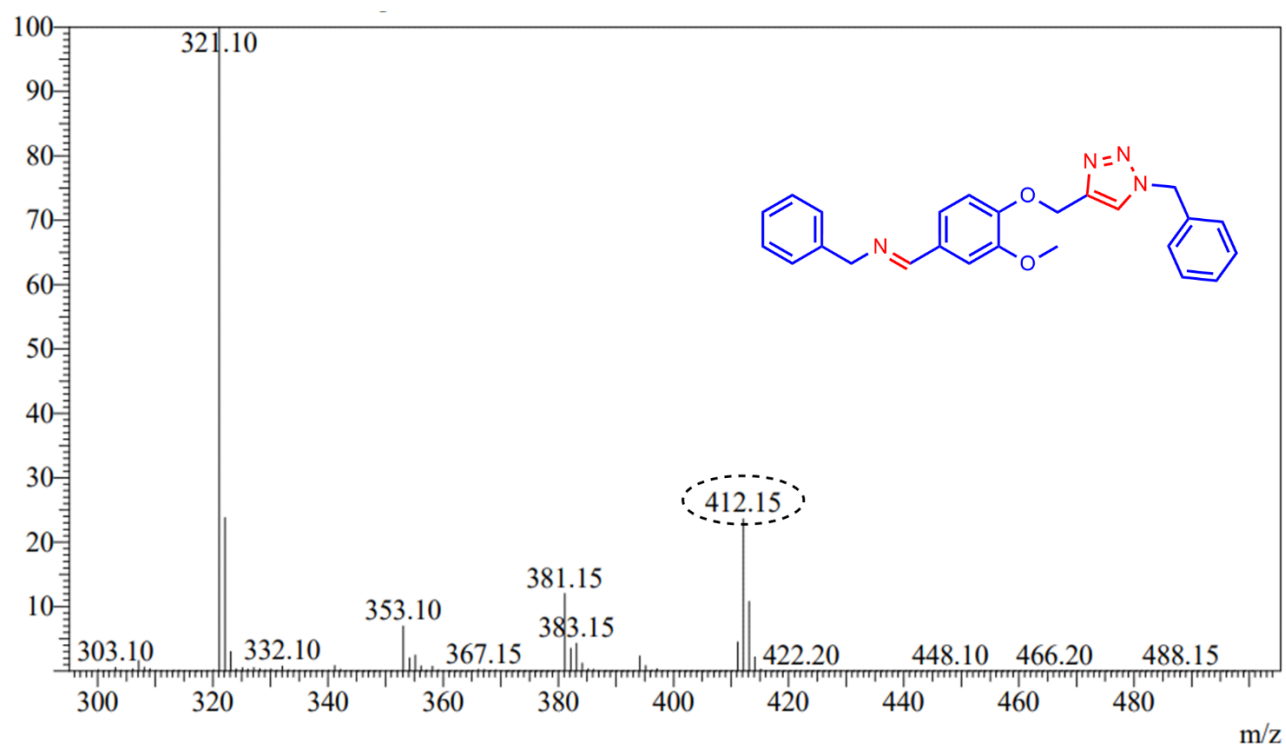
¹H NMR spectrum of Schiff base triazole 81c



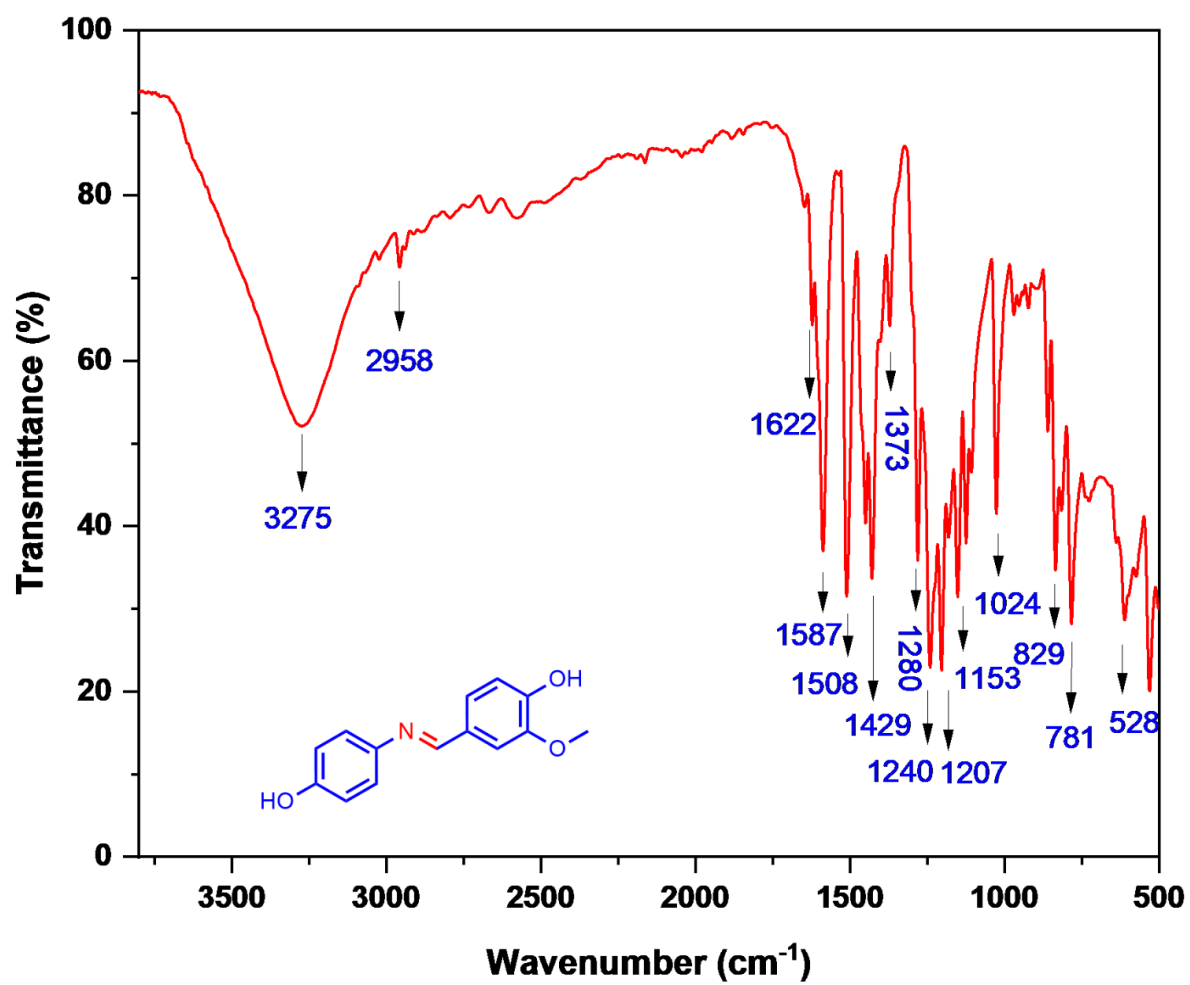
^{13}C NMR spectrum of Schiff base triazole 81c



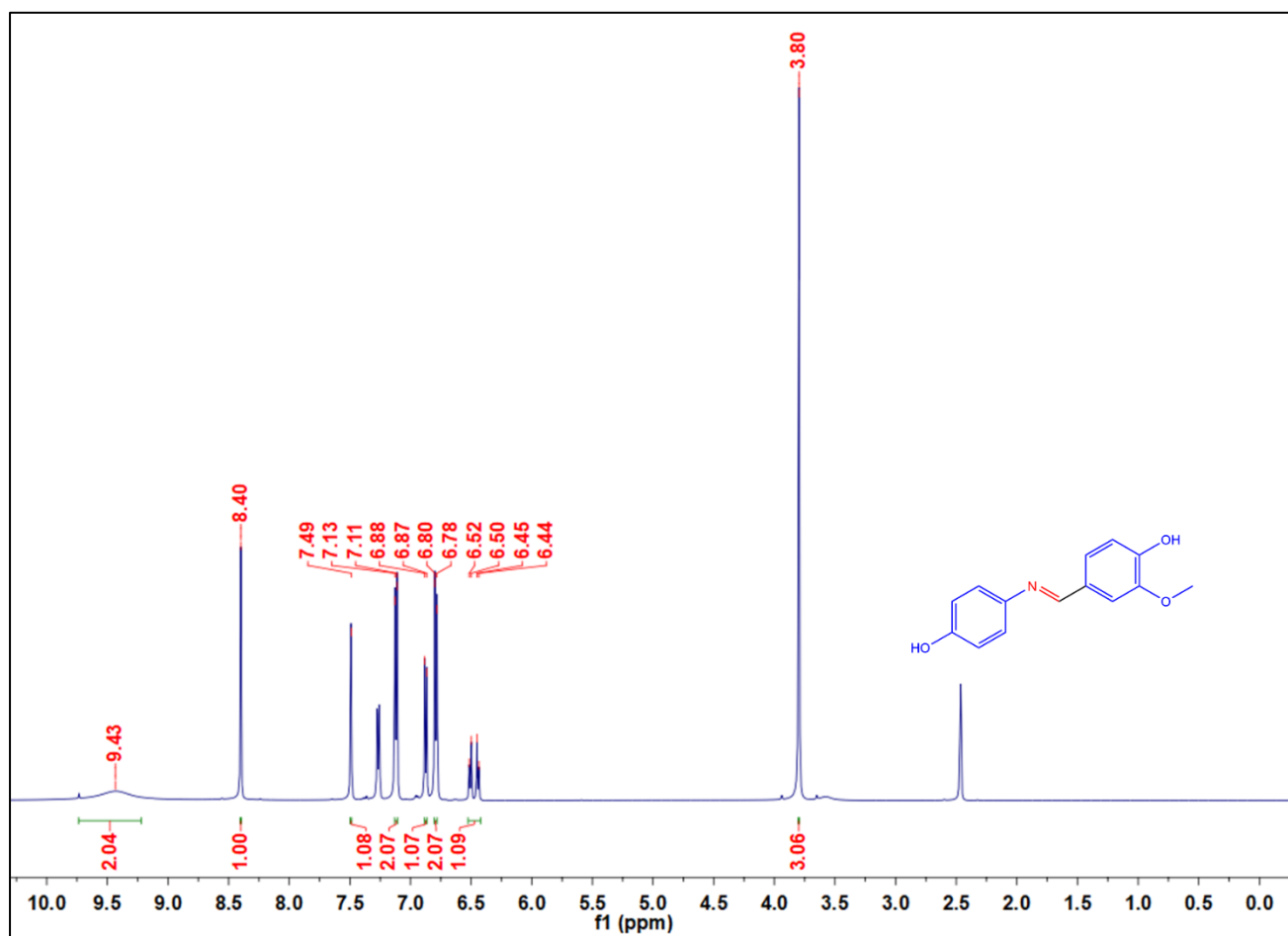
Mass spectrum of Schiff base triazole 81c



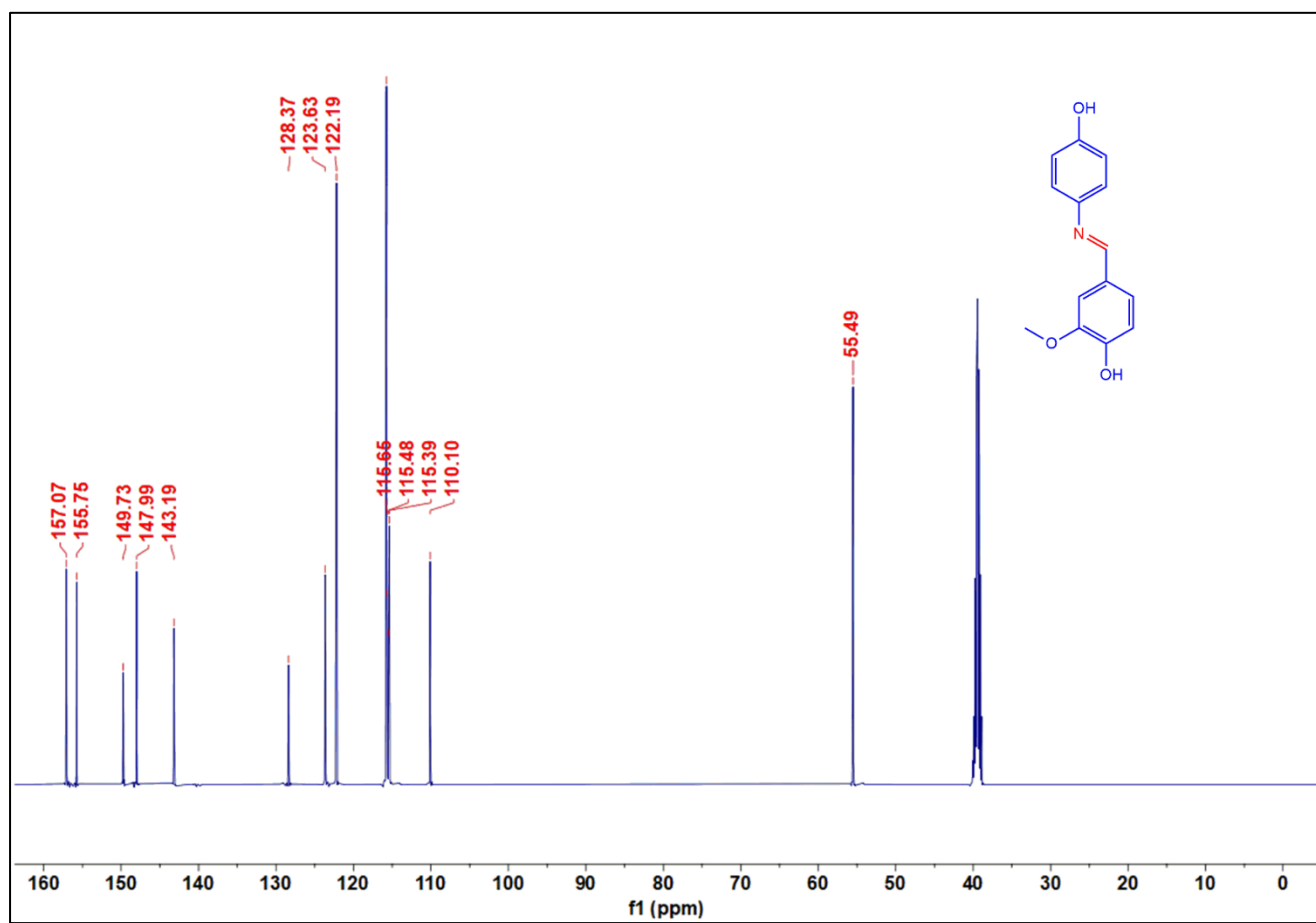
FTIR spectrum of Schiff base 82a



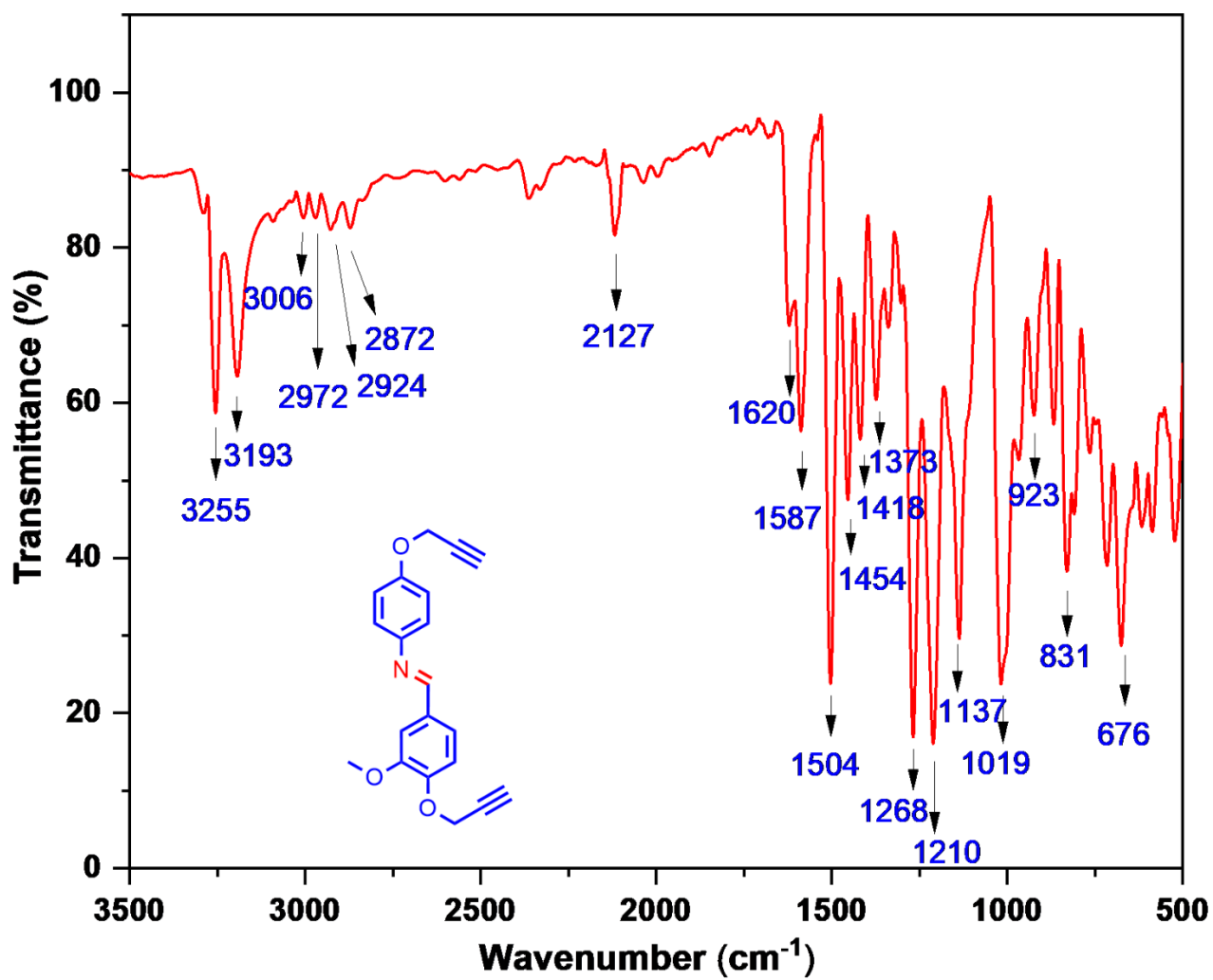
¹H NMR spectrum of Schiff base 82a



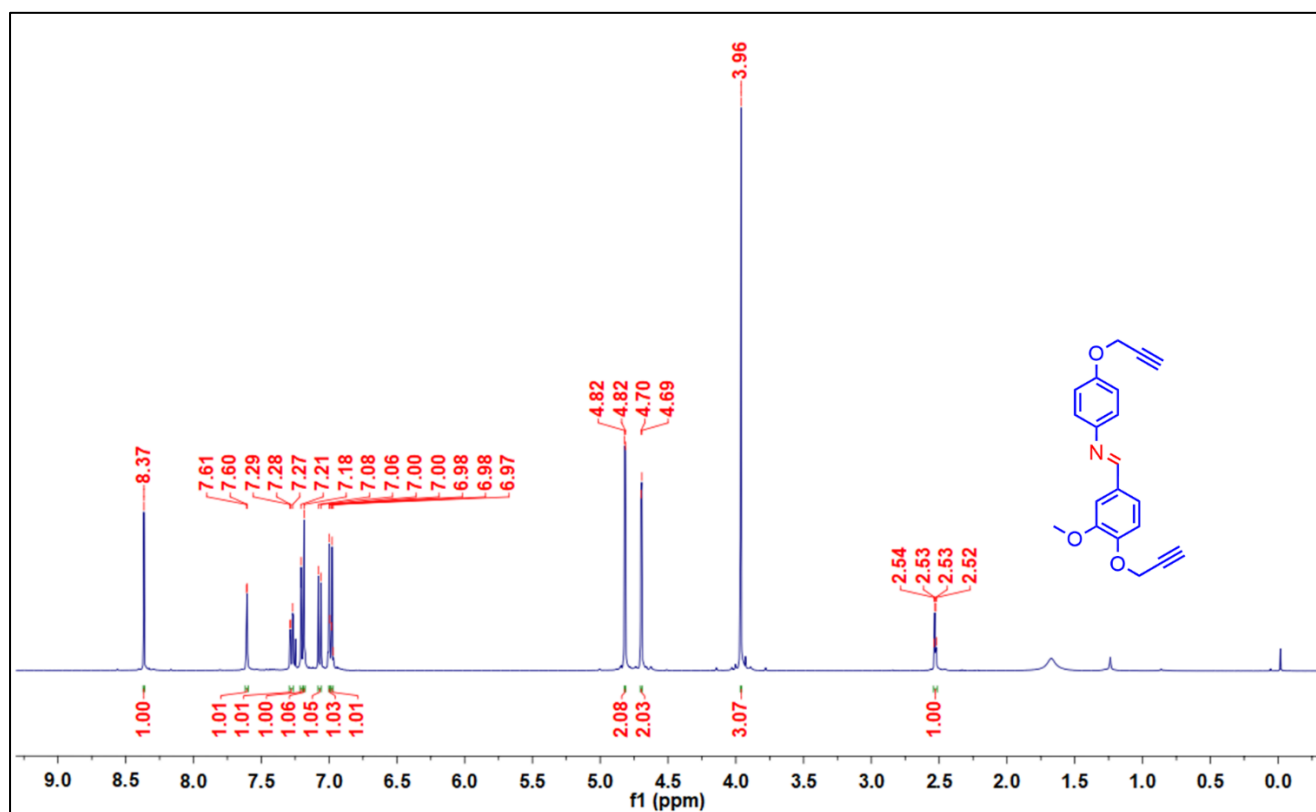
¹³C NMR spectrum of Schiff base 82a



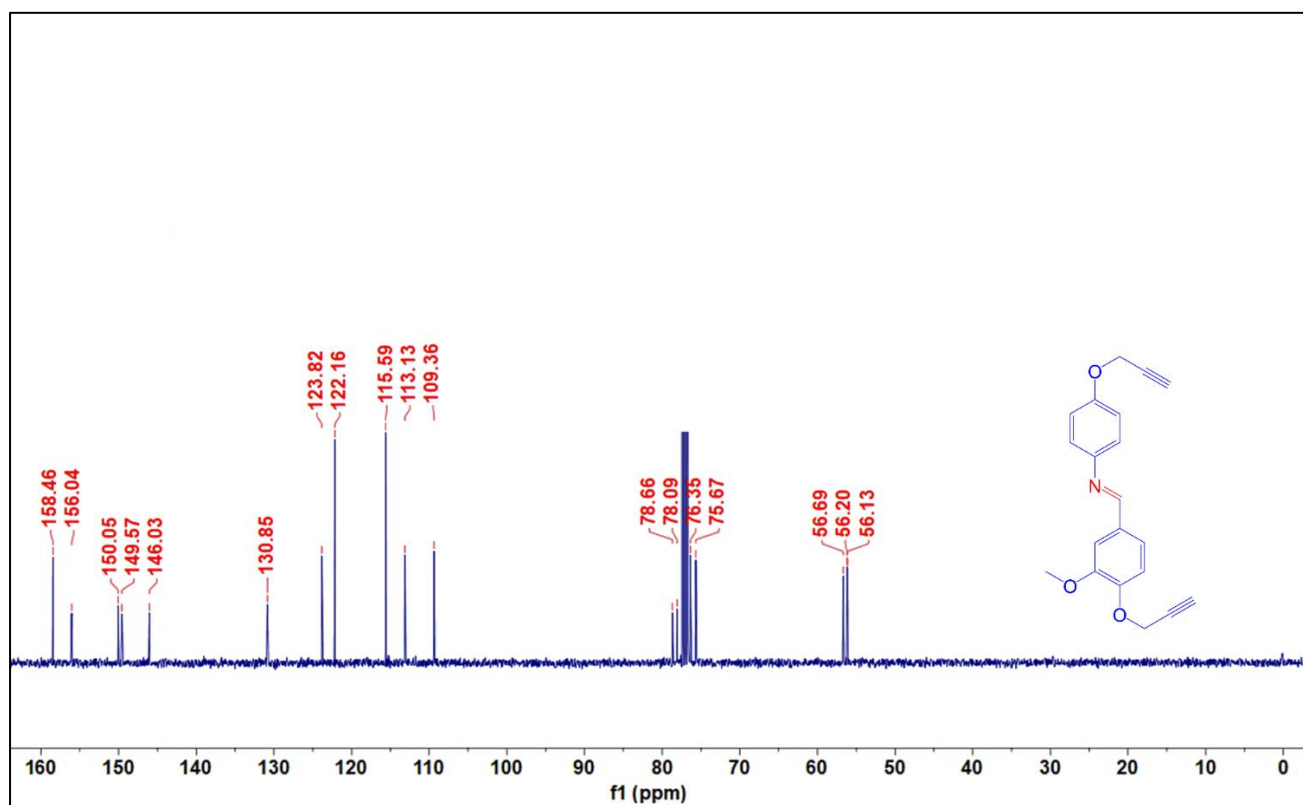
FTIR spectrum of Schiff base alkyne 82b



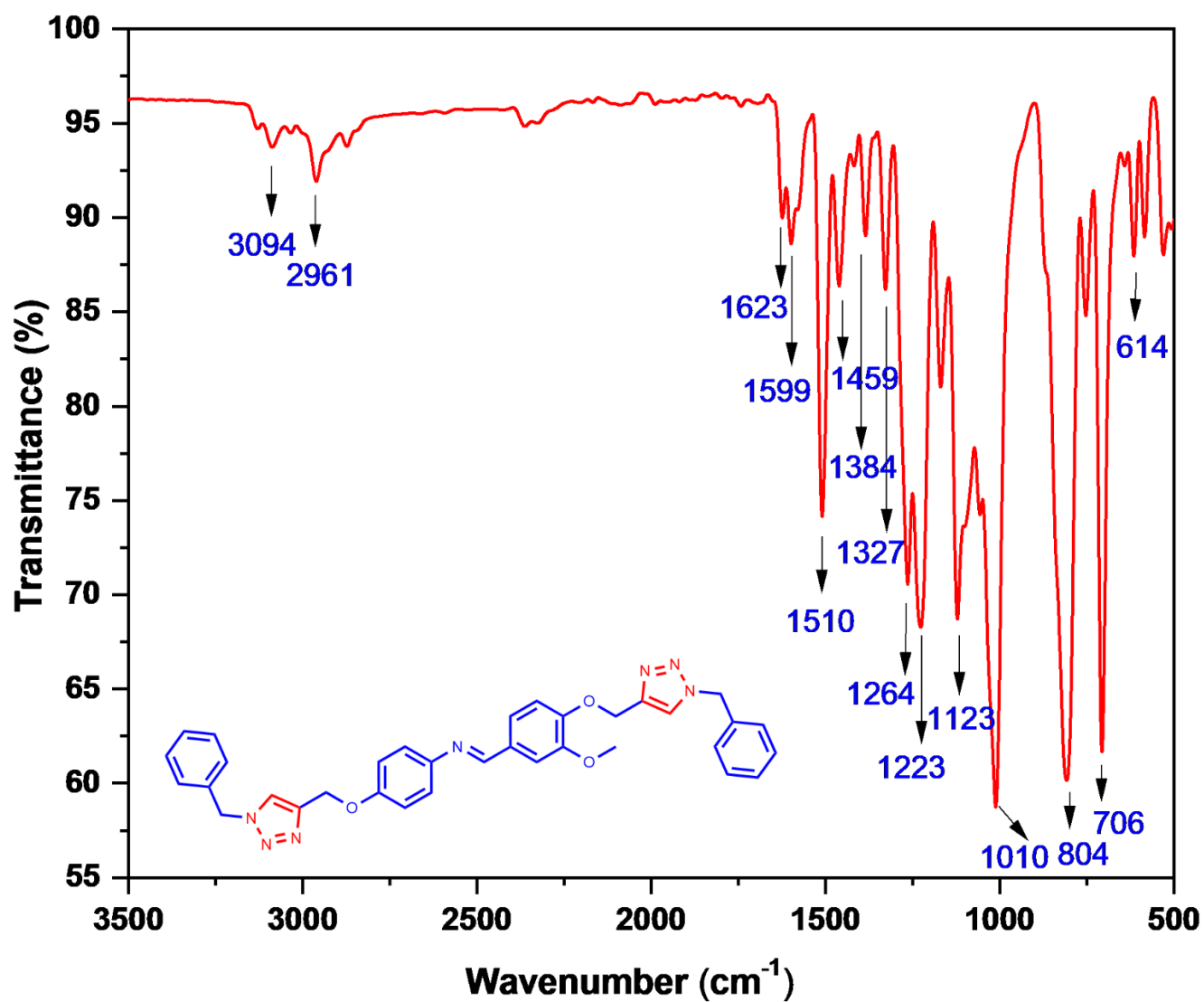
^1H NMR spectrum of Schiff base alkyne 82b



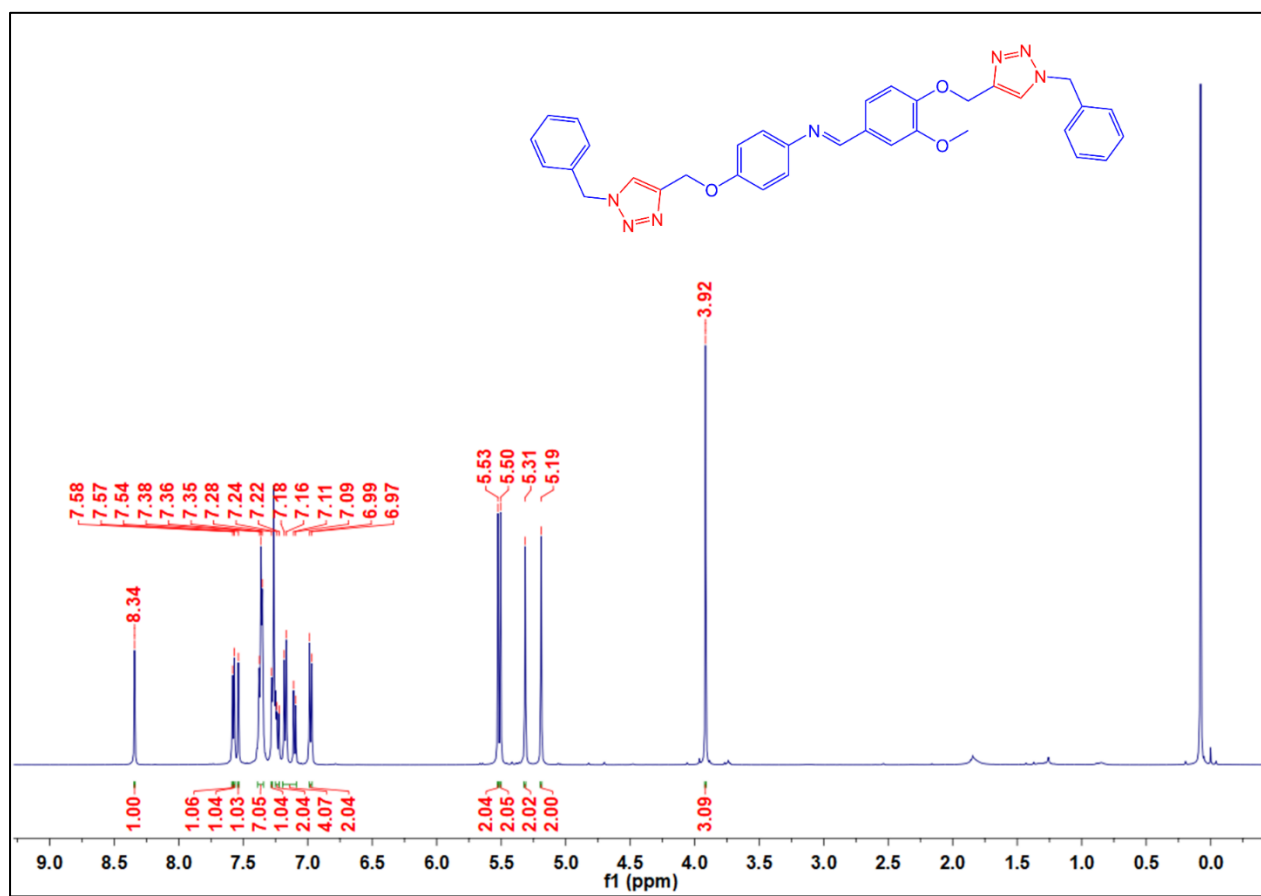
^{13}C NMR spectrum of Schiff base alkyne 82b



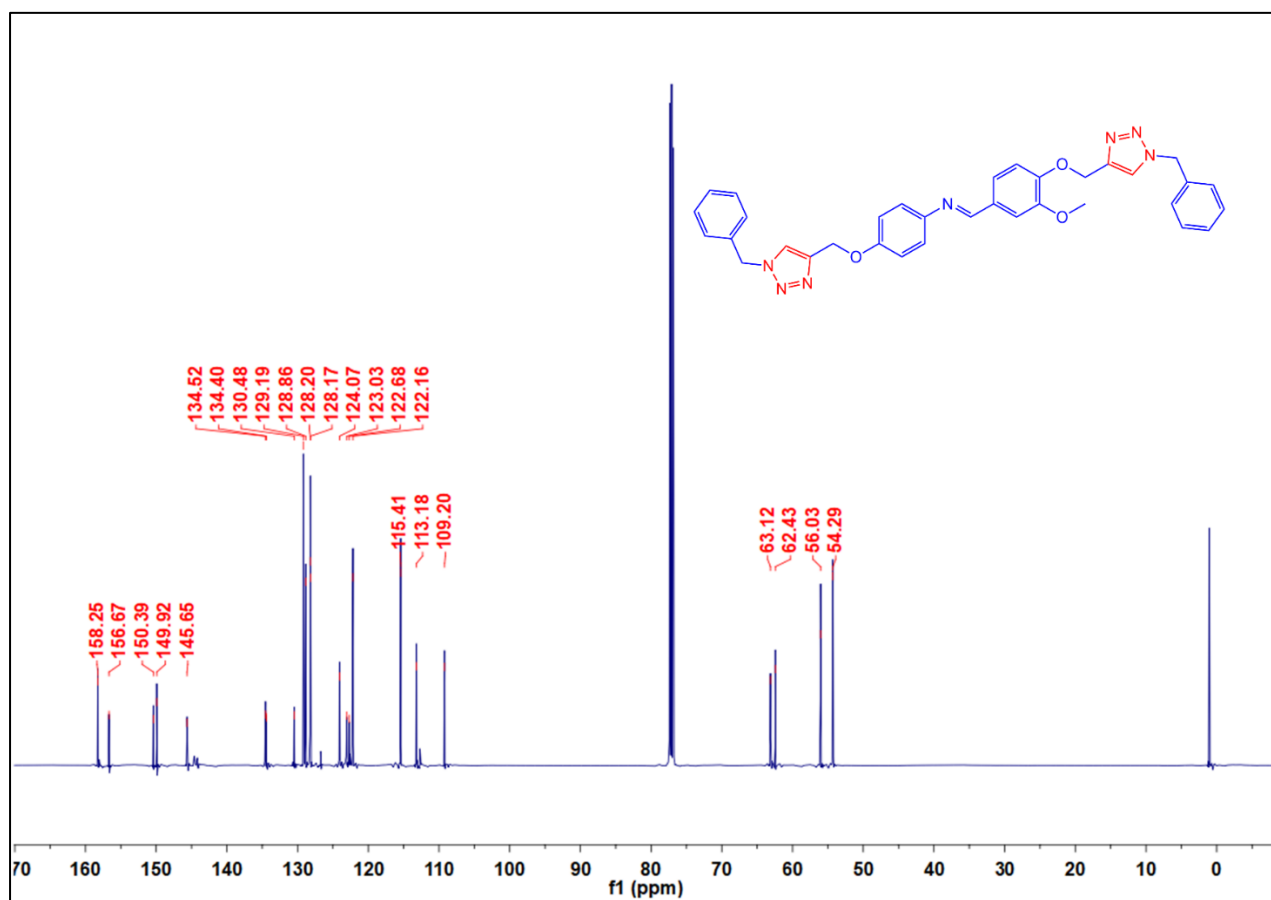
FTIR spectrum of Schiff base triazole 82c



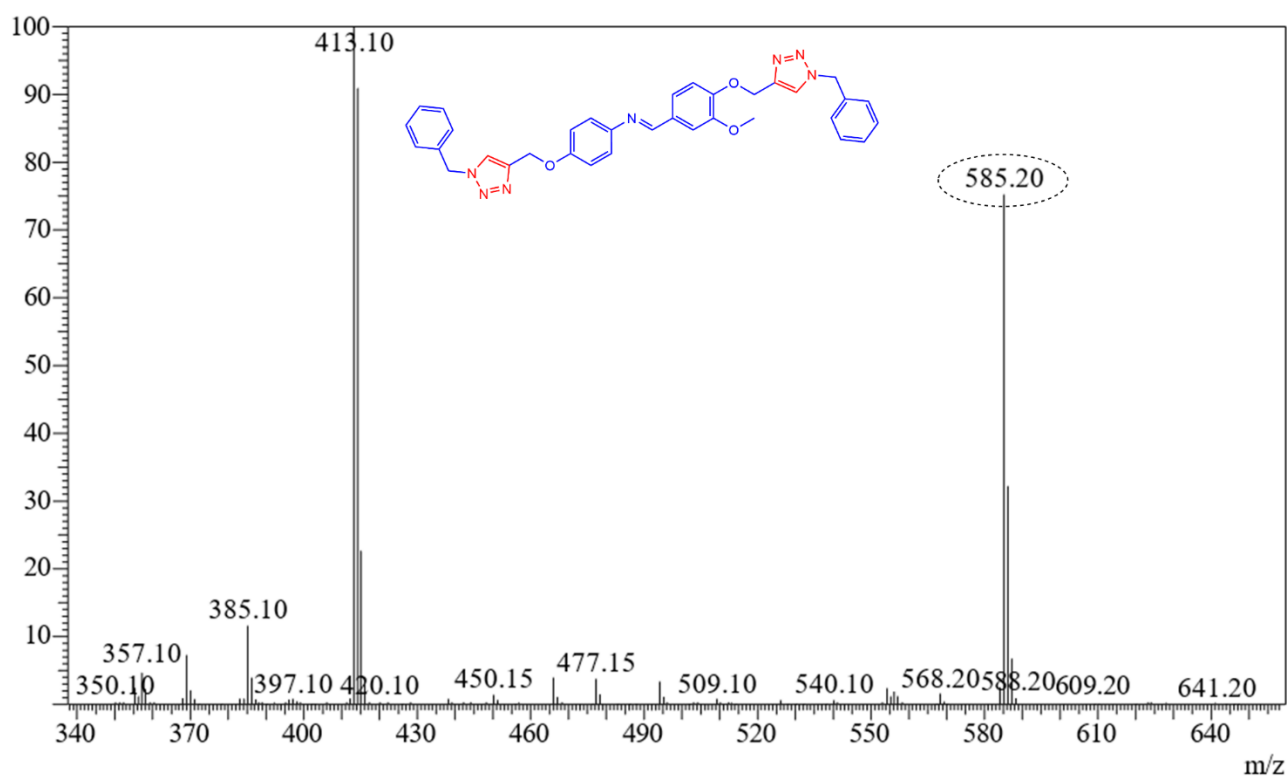
¹H NMR spectrum of Schiff base triazole 82c



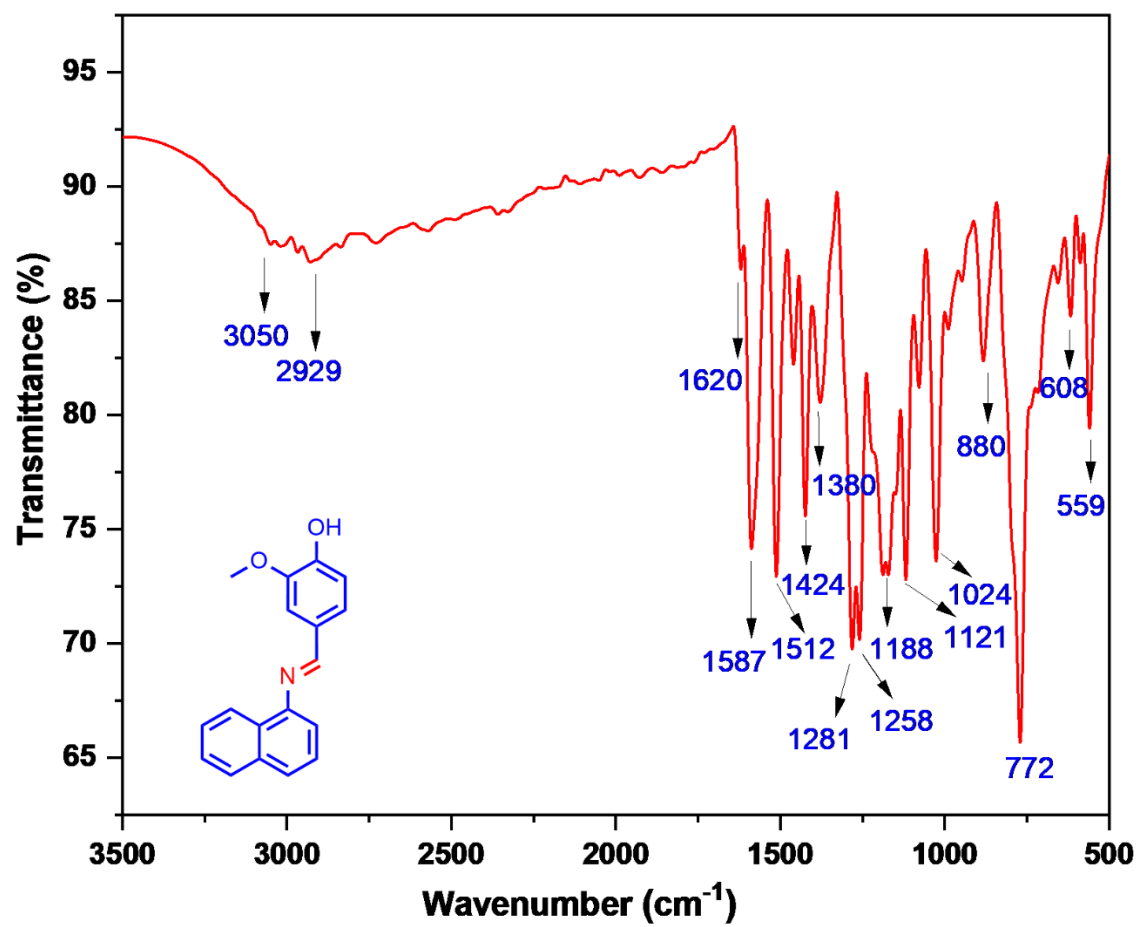
^{13}C NMR spectrum of Schiff base alkyne 82c



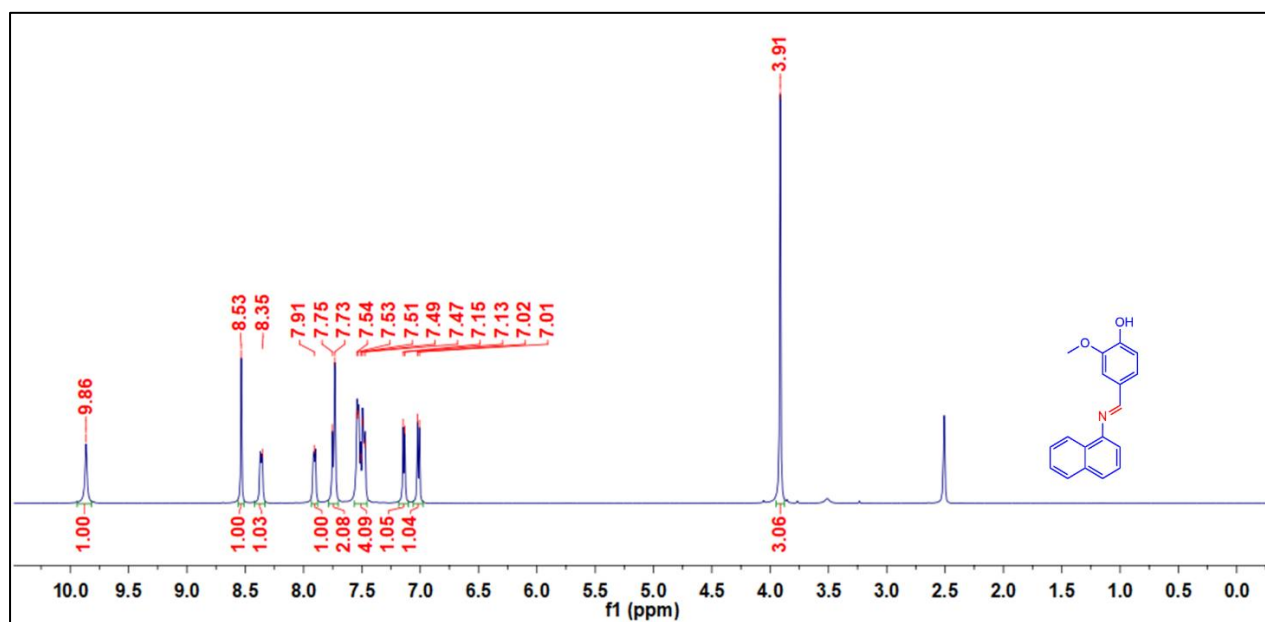
Mass spectrum of Schiff base triazole 82c



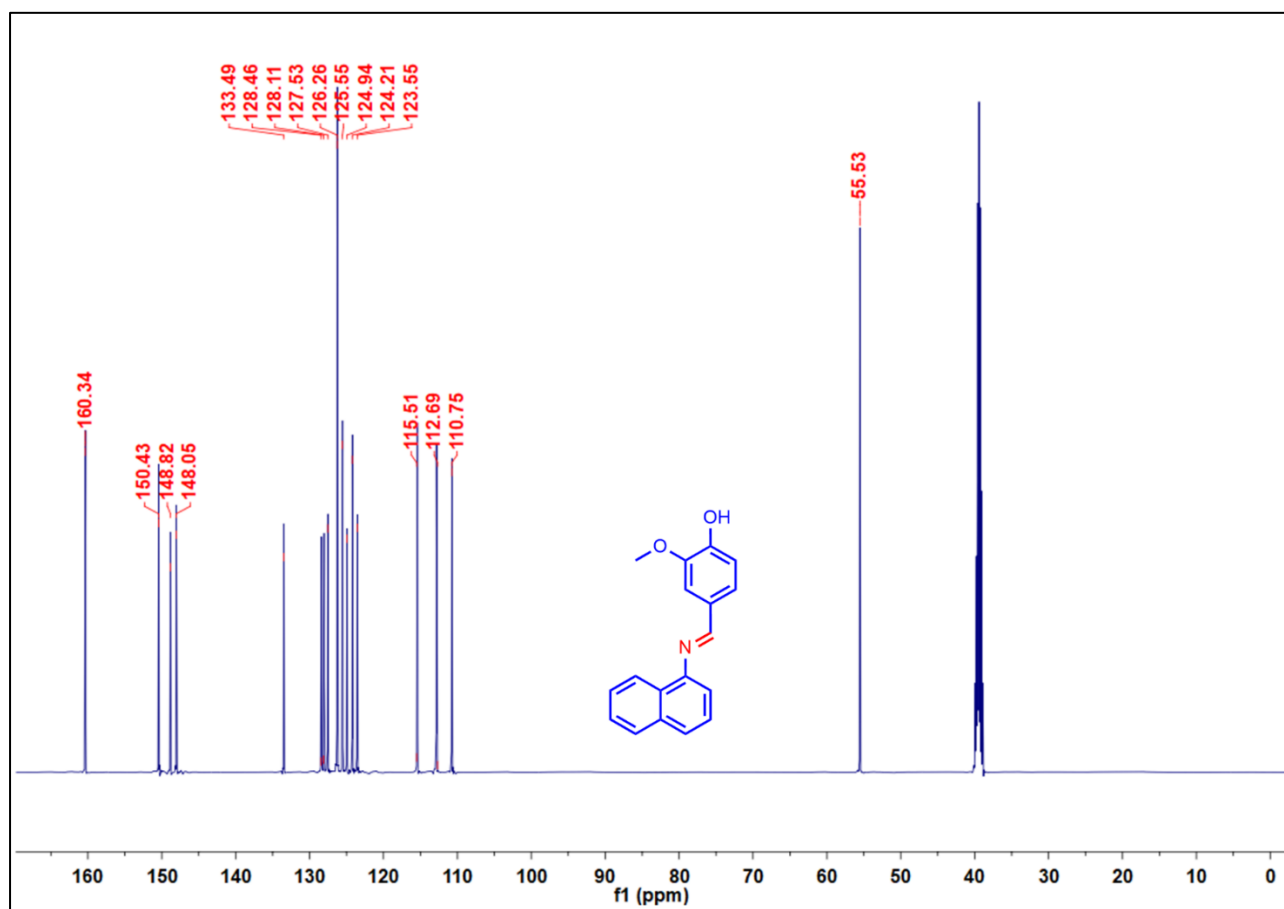
FTIR spectrum of Schiff base 83a



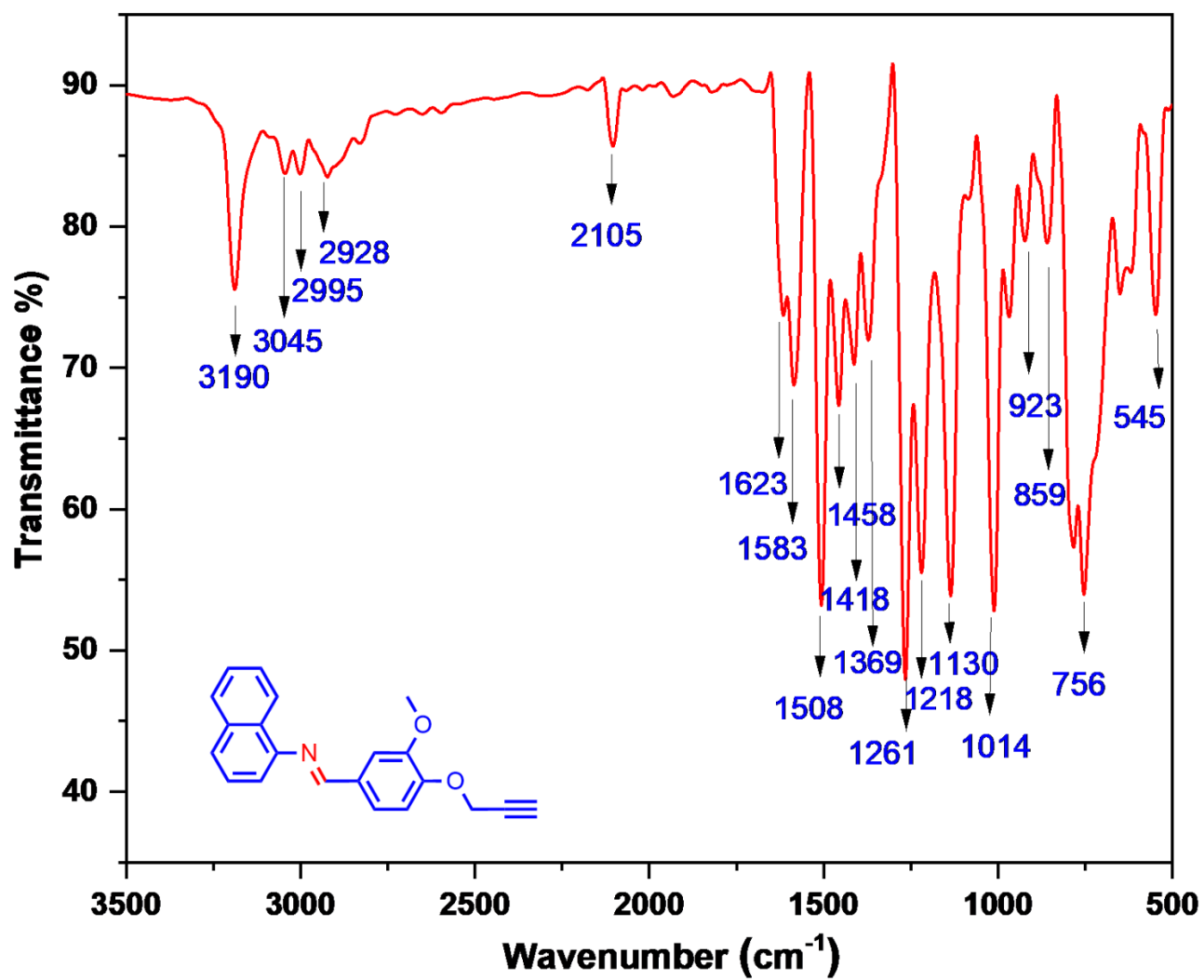
¹H NMR spectrum of Schiff base 83a



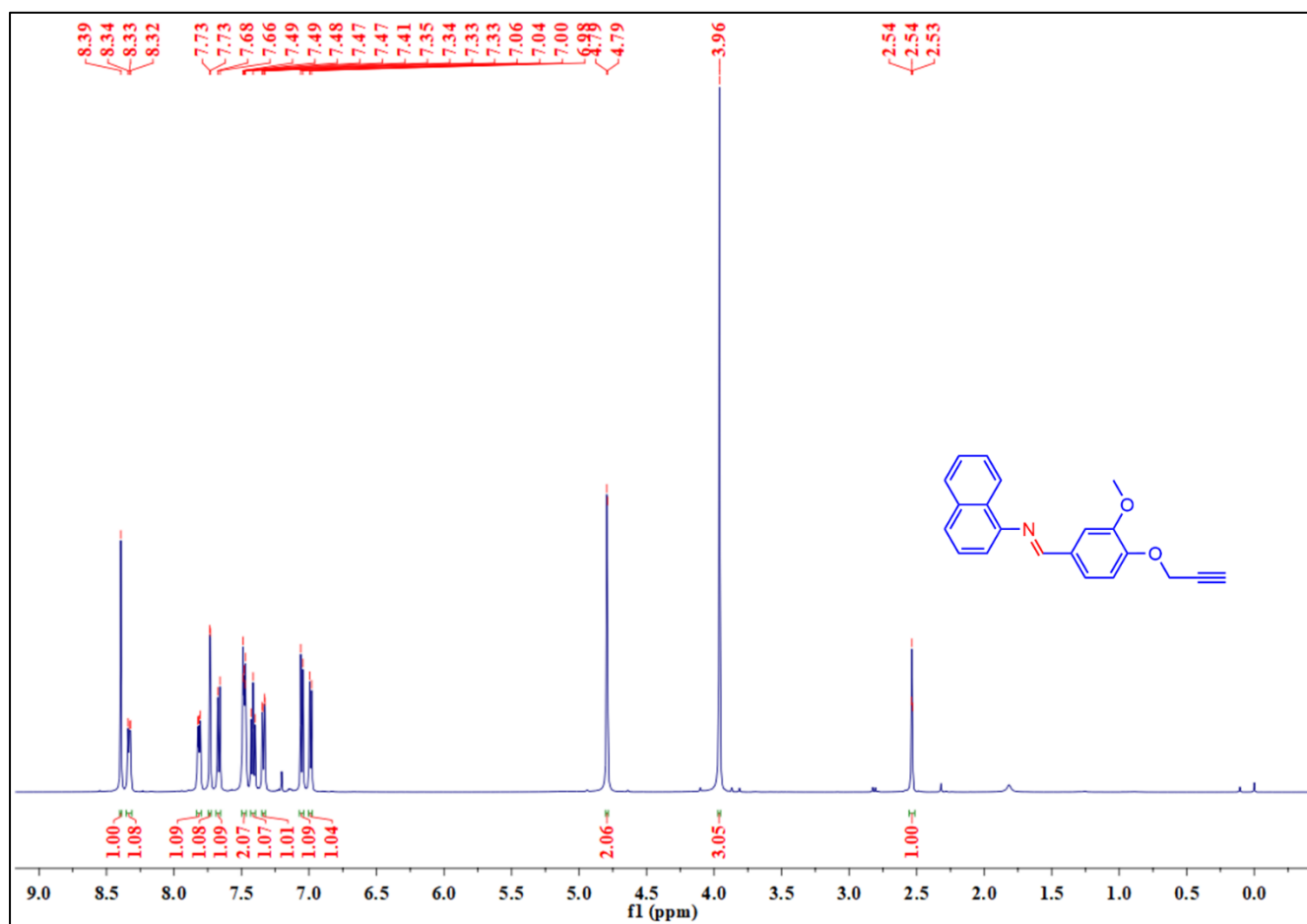
¹³C NMR spectrum of Schiff base 83a



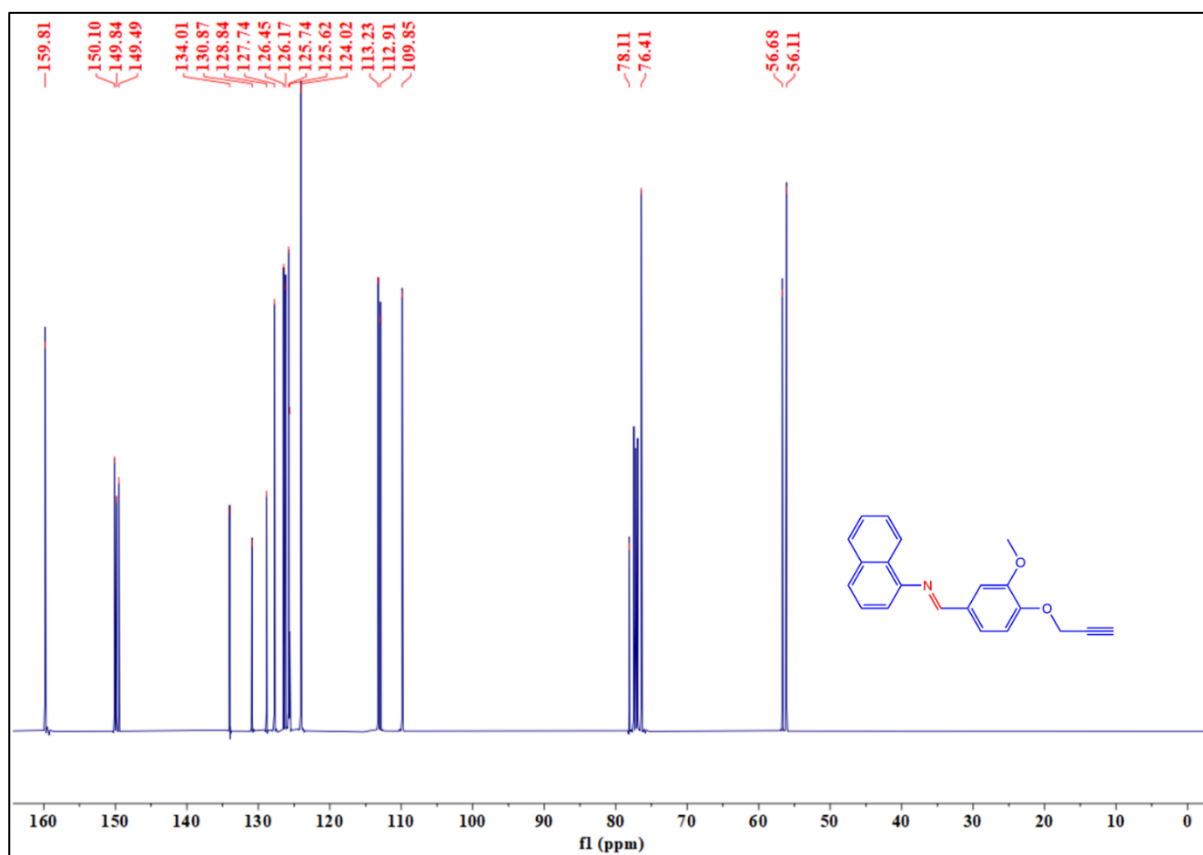
FTIR spectrum of Schiff base alkyne 83b



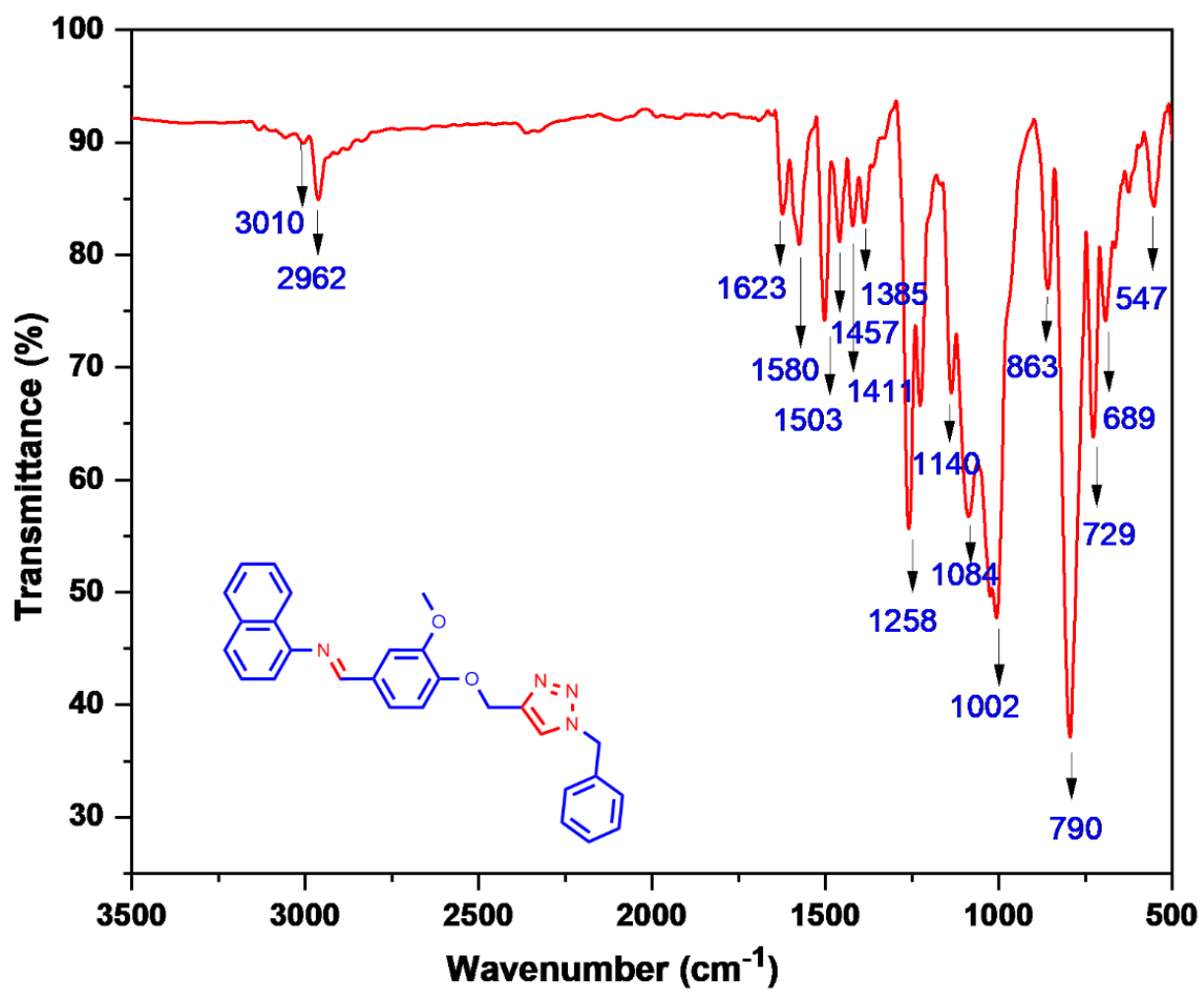
¹H NMR spectrum of Schiff base 83b



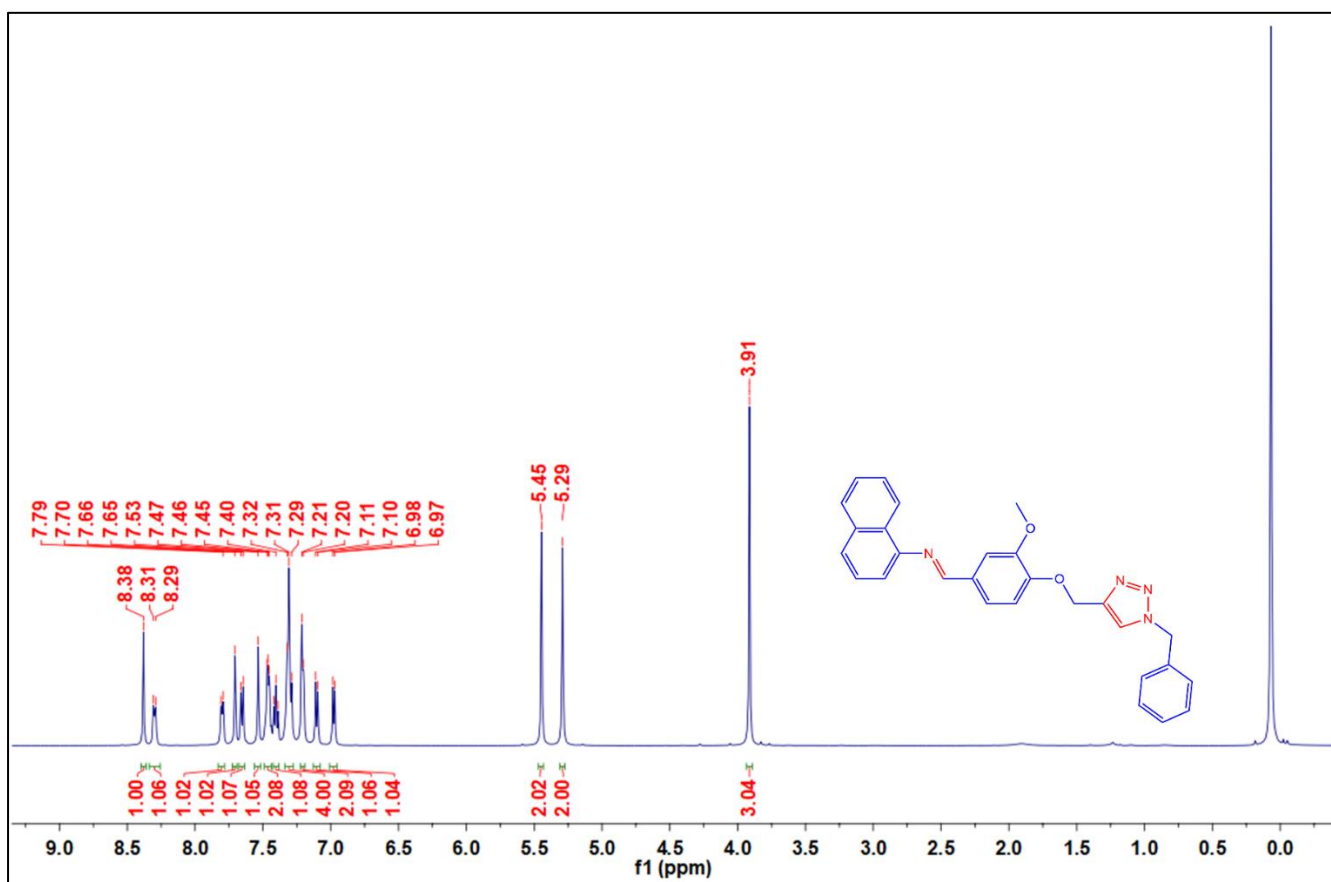
^{13}C NMR spectrum of Schiff base 83b



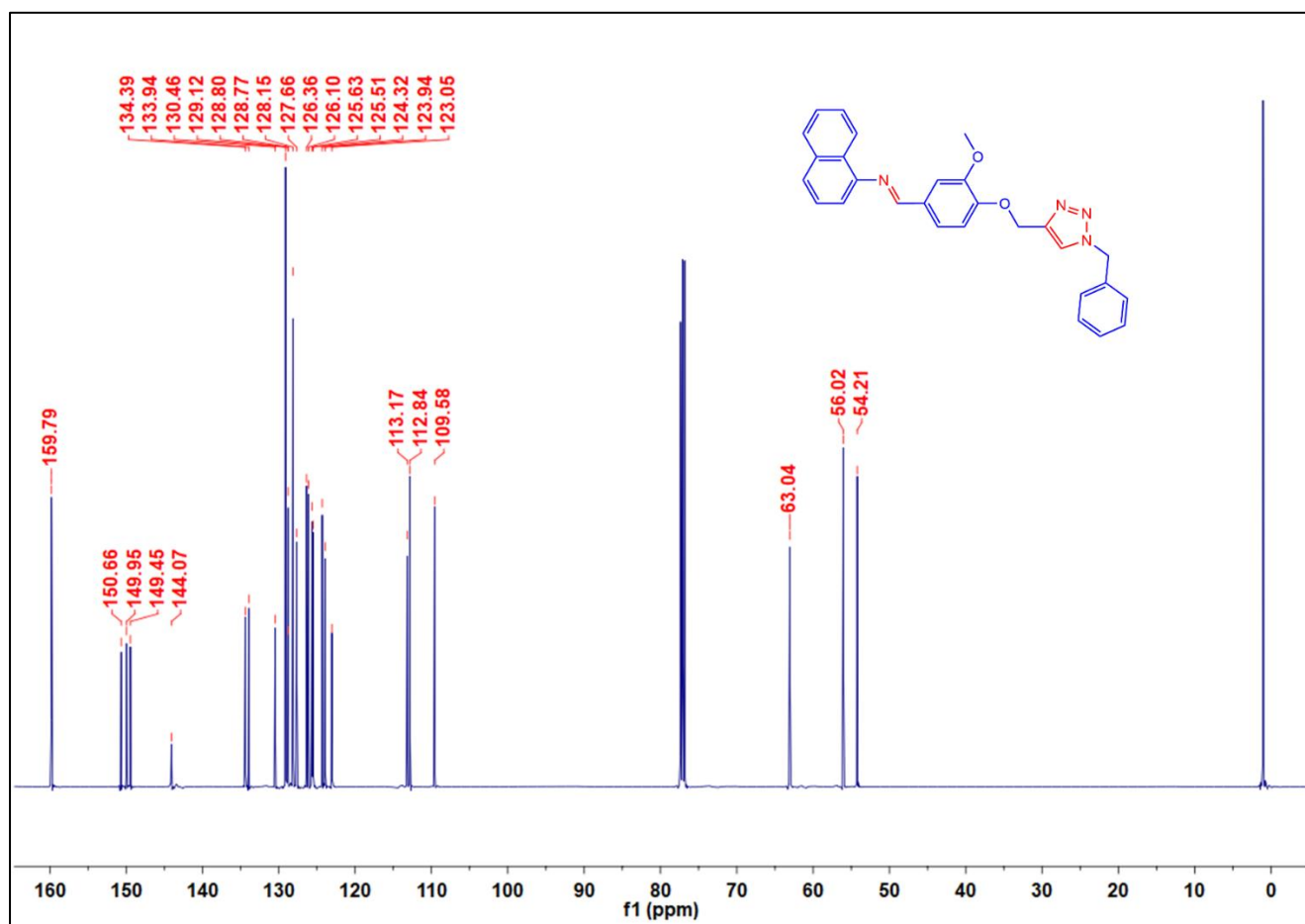
FTIR spectrum of Schiff base triazole 83c



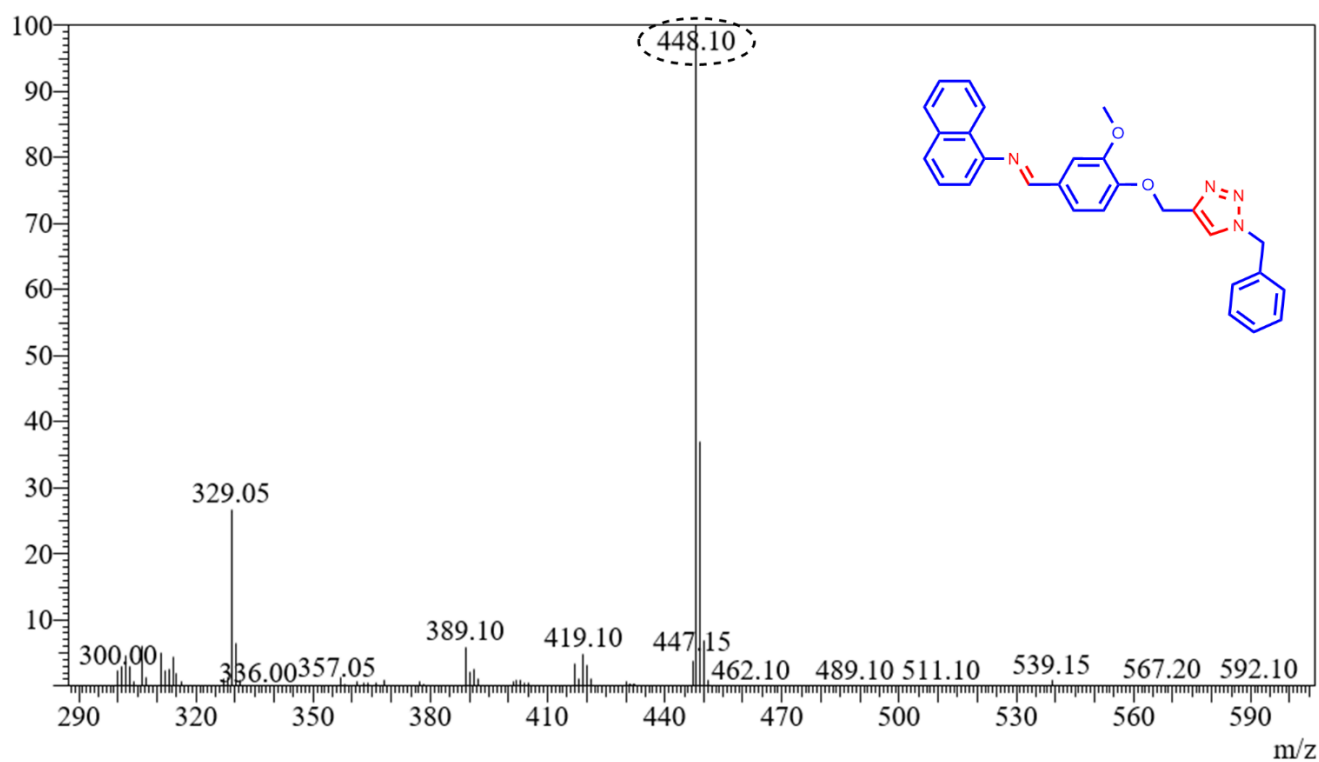
¹H NMR spectrum of Schiff base triazole 83c



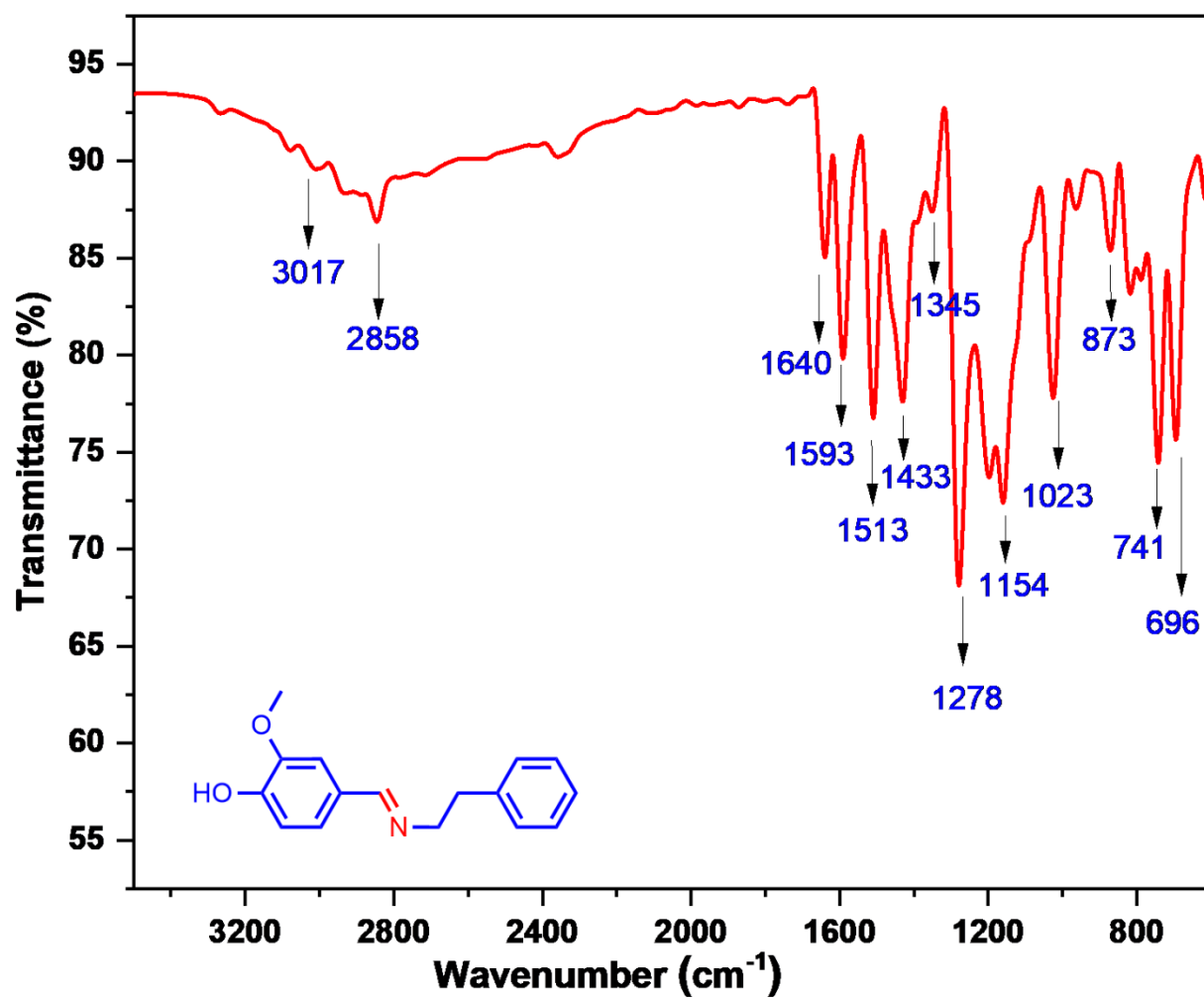
^{13}C NMR spectrum of Schiff base triazole 83c



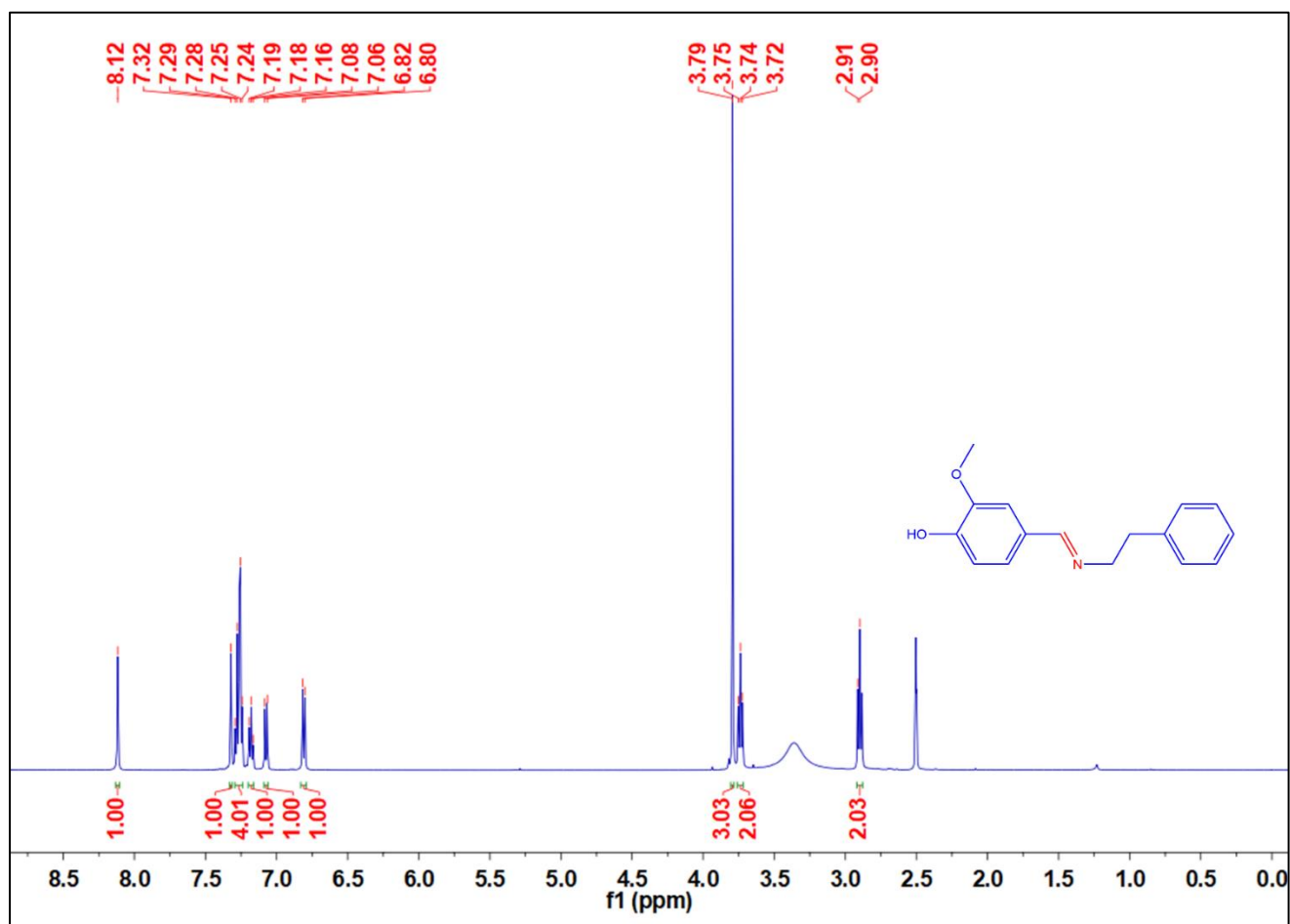
Mass spectrum of Schiff base triazole 83c



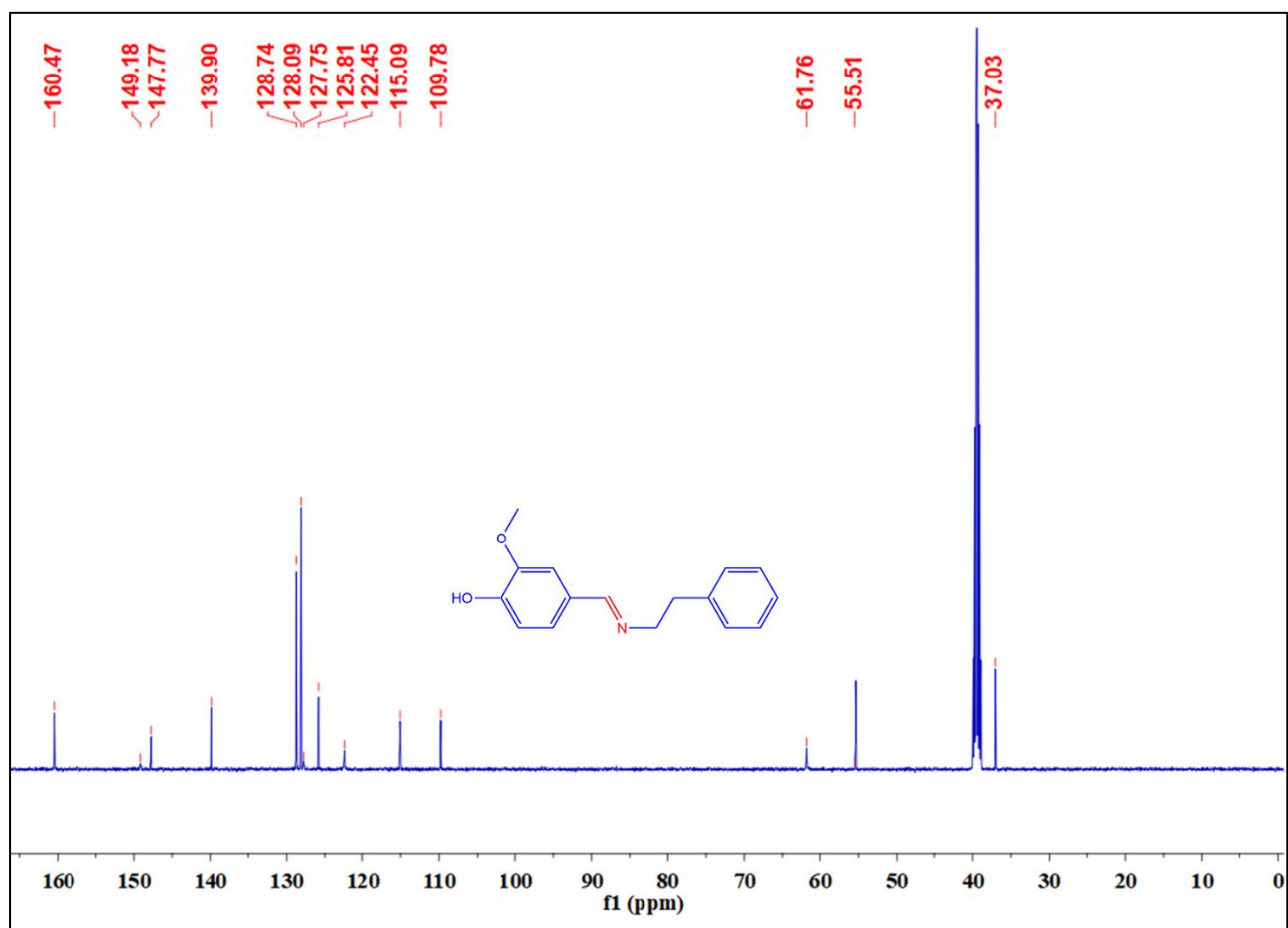
FTIR spectrum of Schiff base 84a



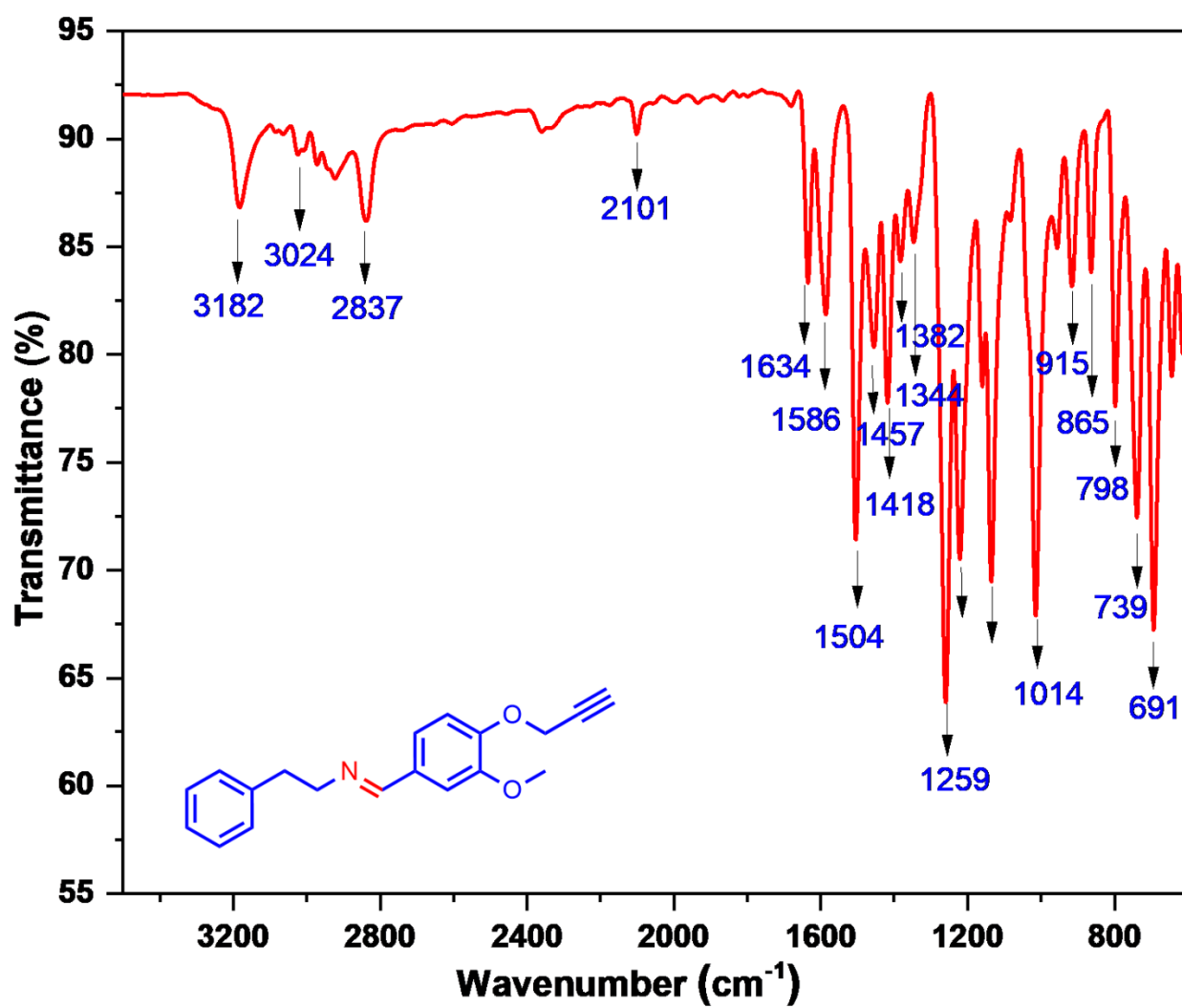
^1H NMR spectrum of Schiff base 84a



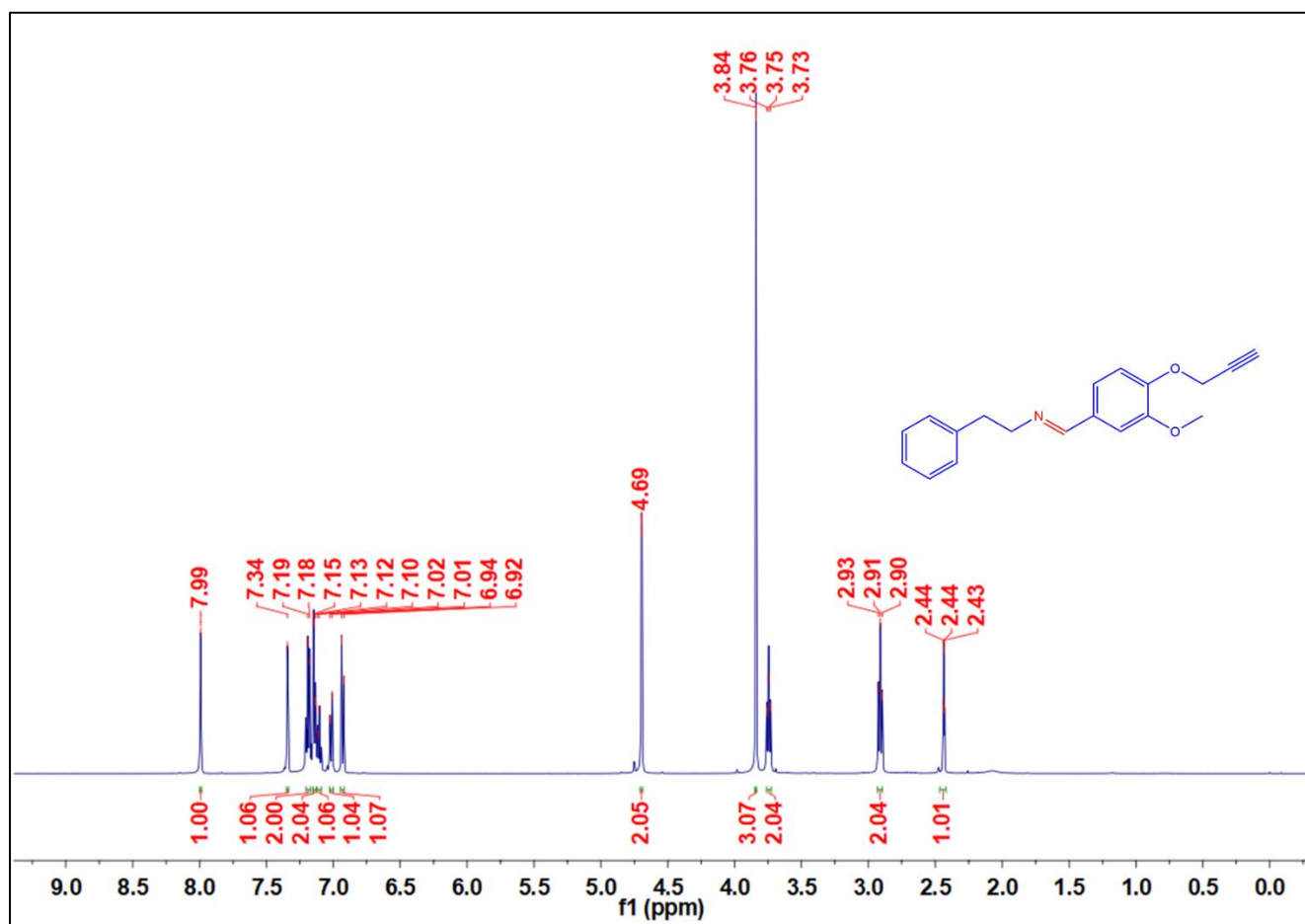
^{13}C NMR spectrum of Schiff base 84a



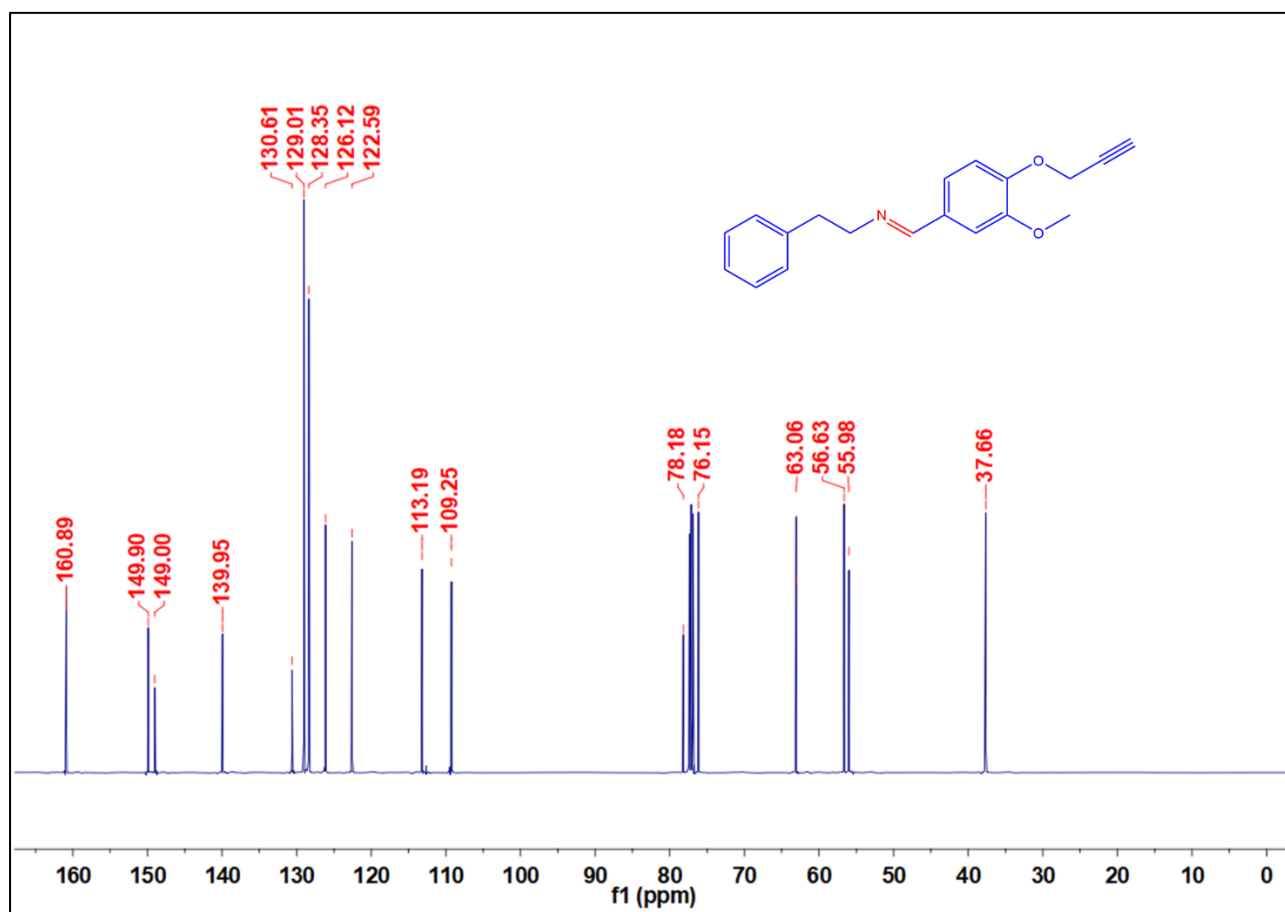
FTIR spectrum of Schiff base alkyne 84b



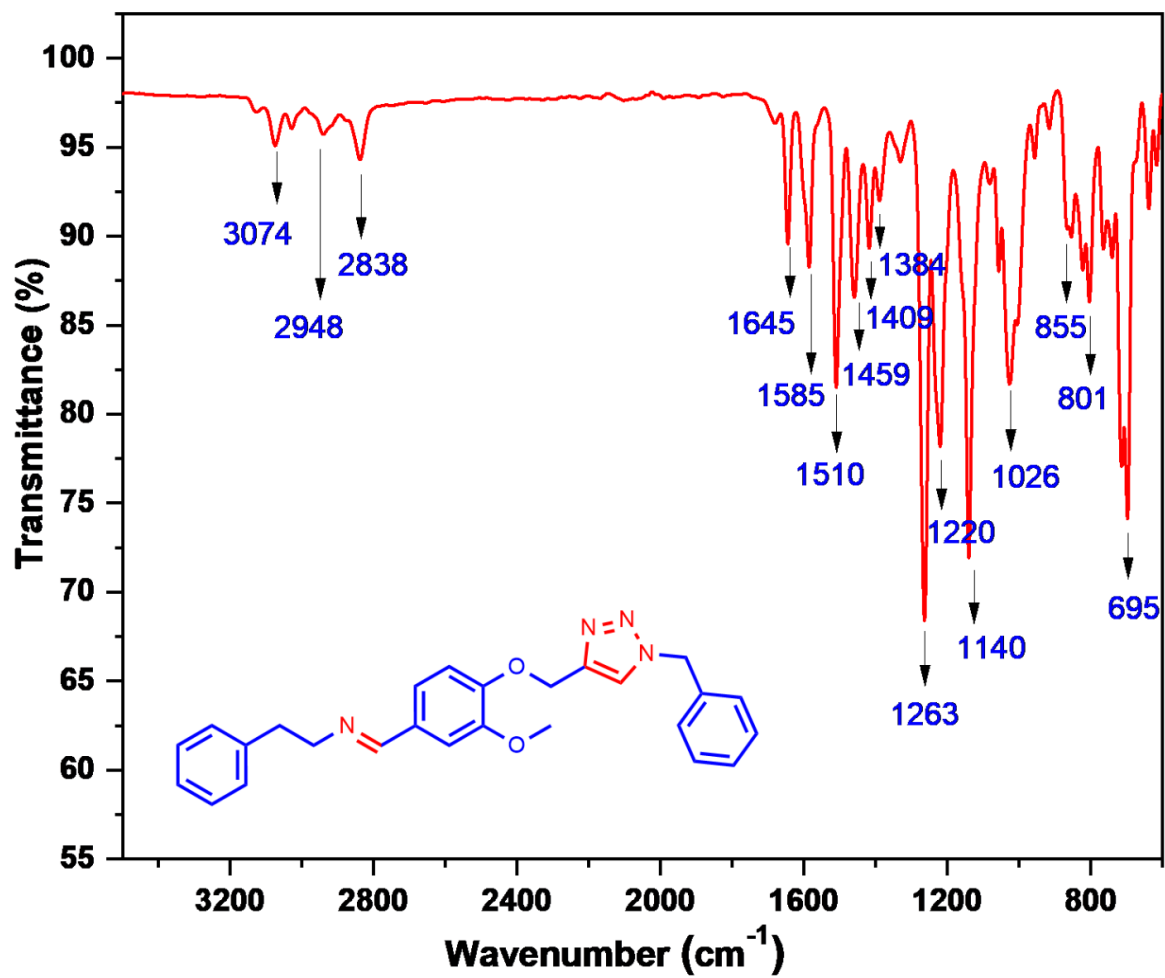
^1H NMR spectrum of Schiff base alkyne 84b



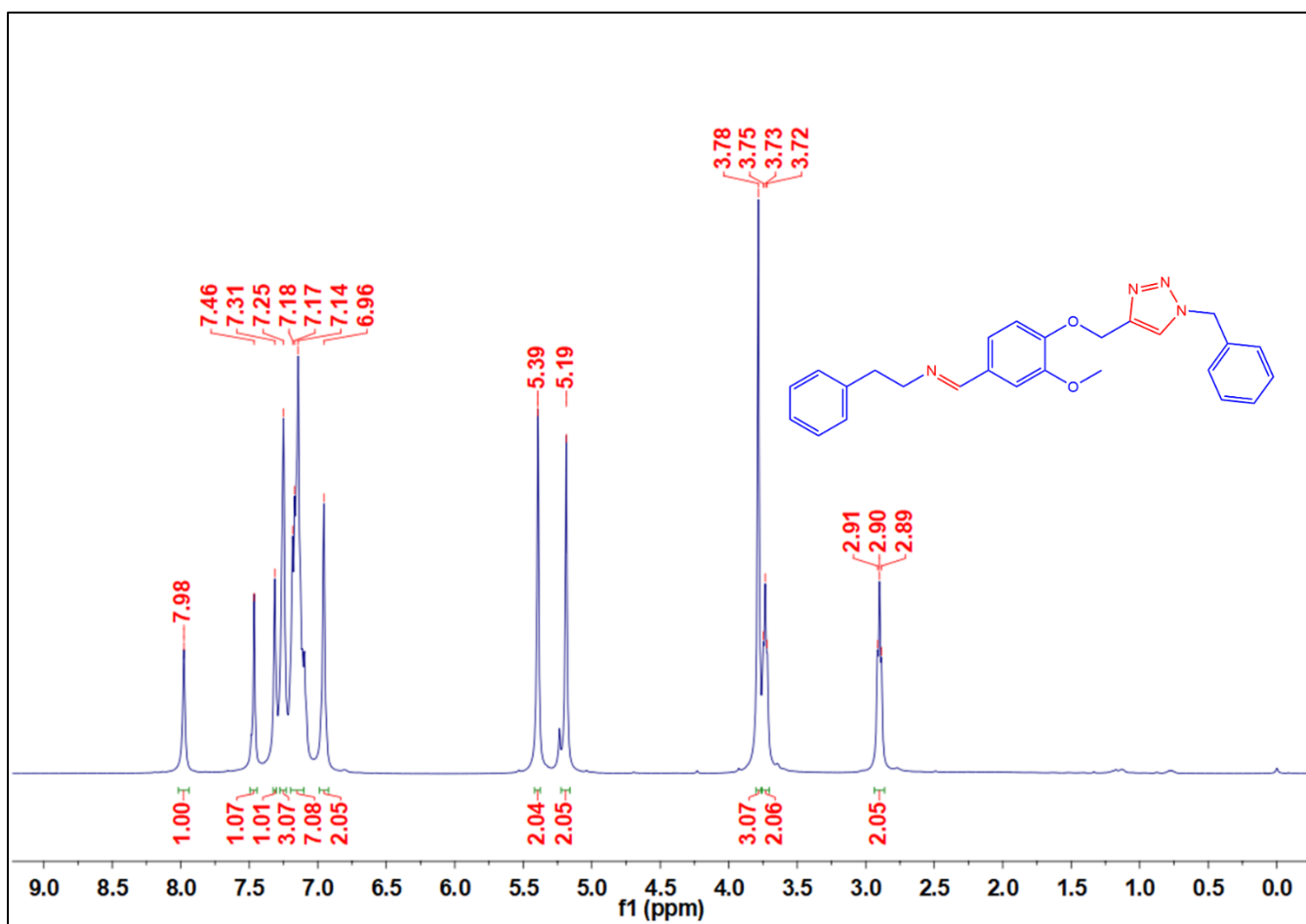
^{13}C NMR spectrum of Schiff base alkyne 84b



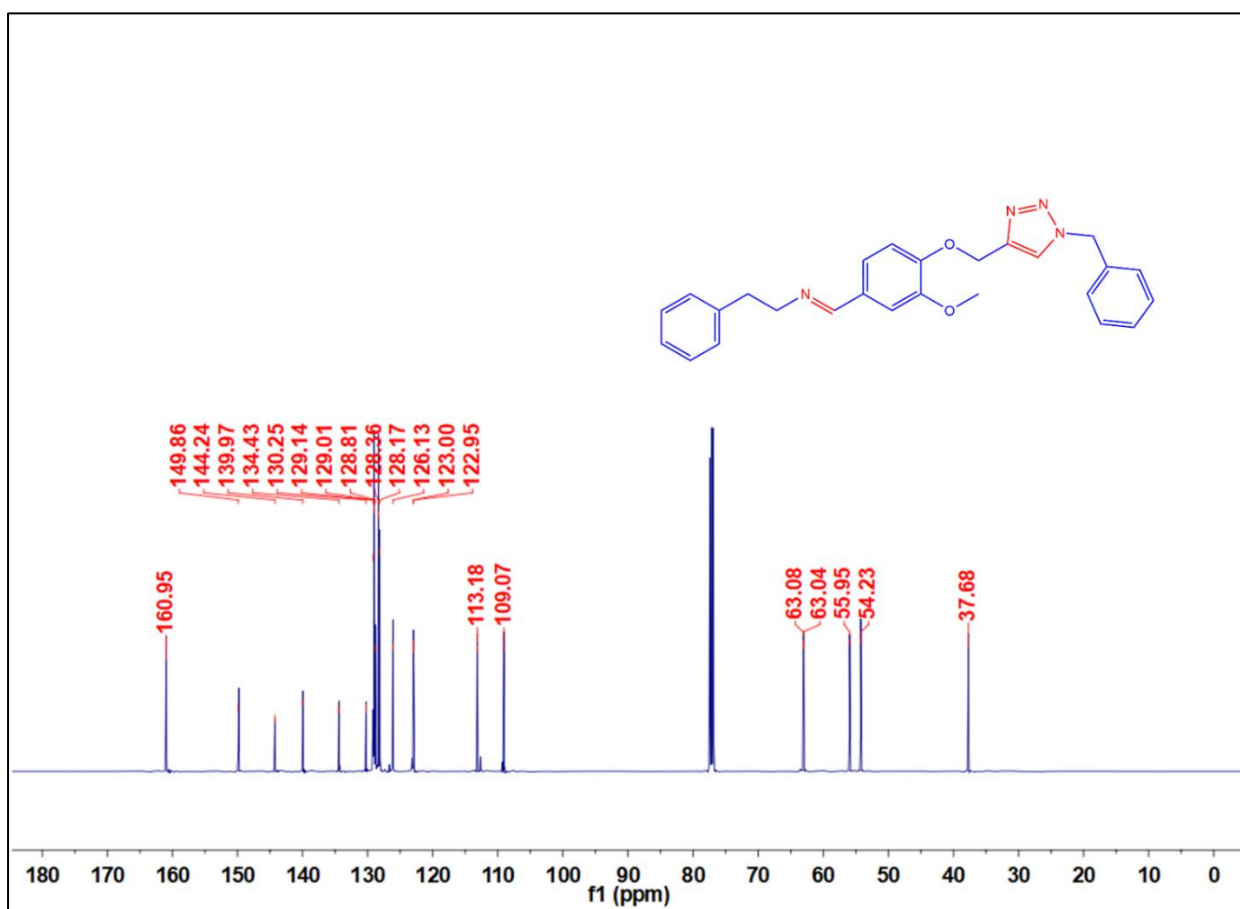
FTIR spectrum of Schiff base triazole 84c



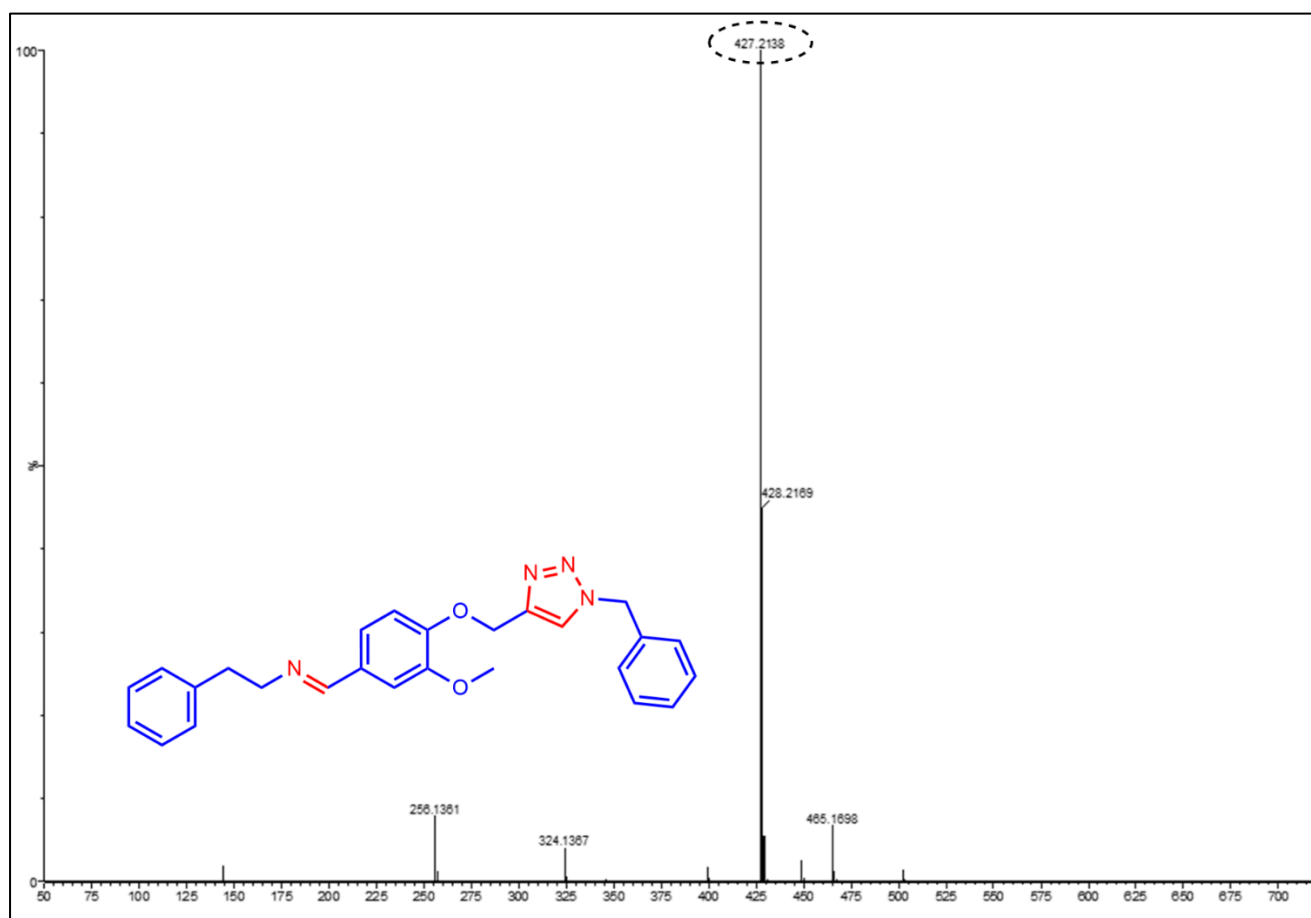
¹H NMR spectrum of Schiff base triazole 84c



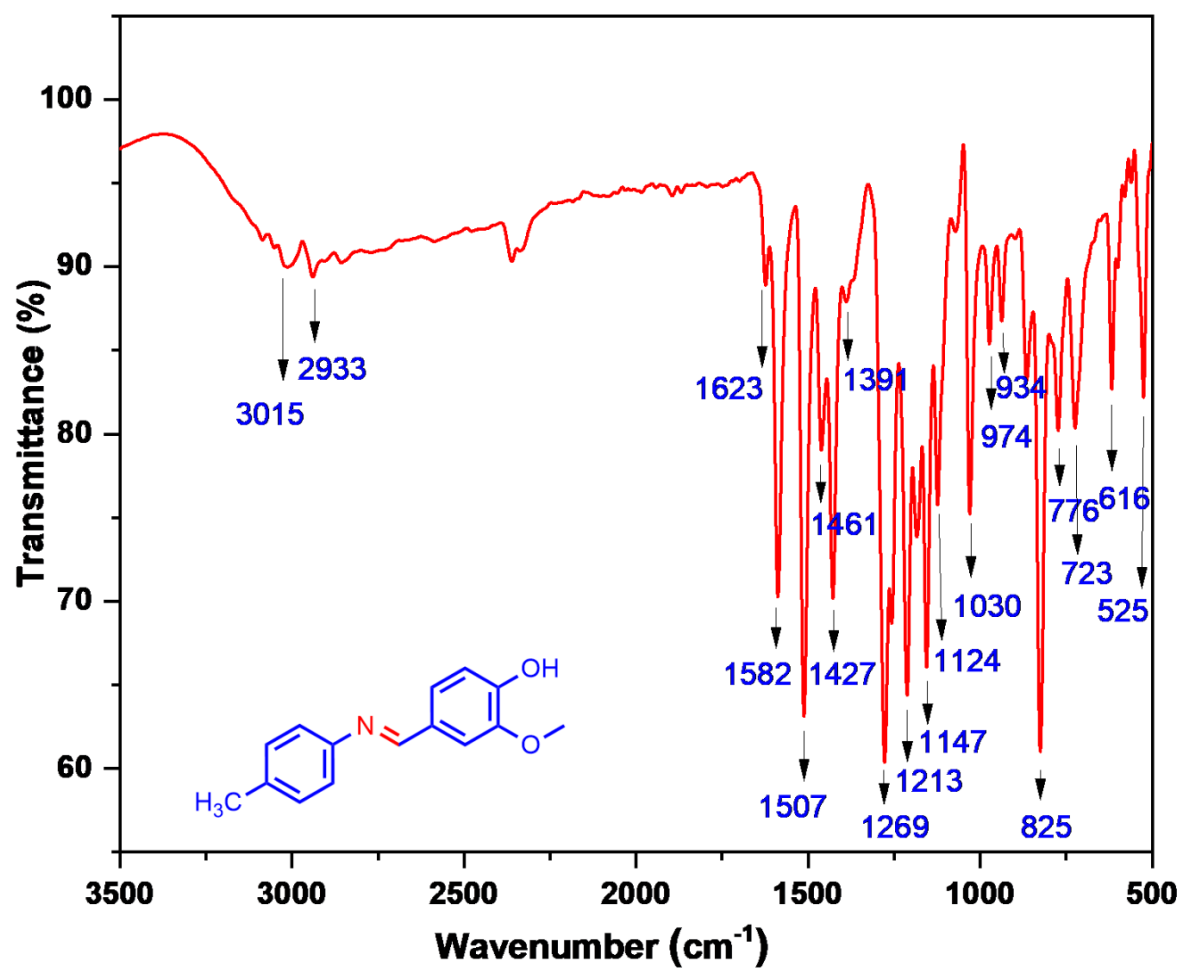
^{13}C NMR spectrum of Schiff base triazole 84c



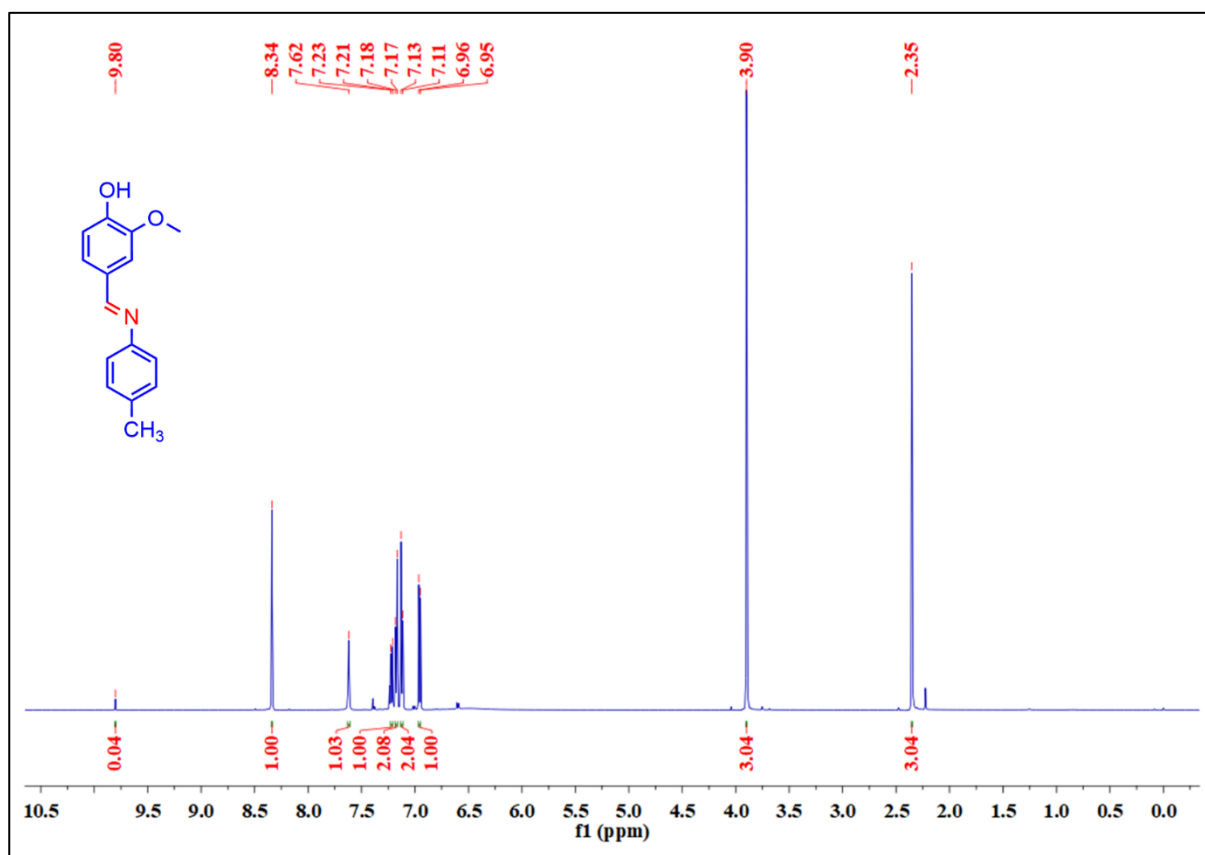
Mass spectrum of Schiff base triazole 84c



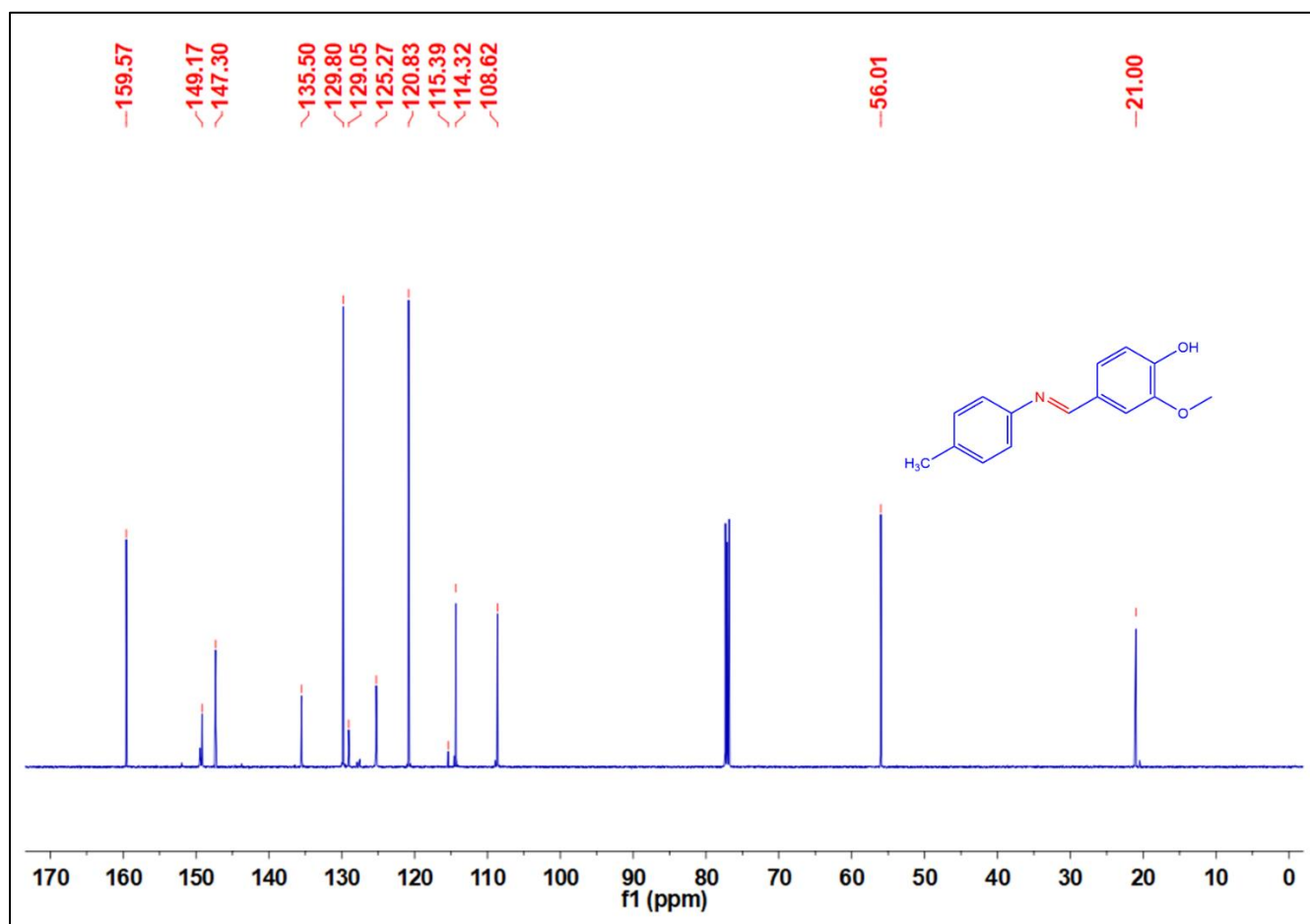
FTIR spectrum of Schiff base 85a



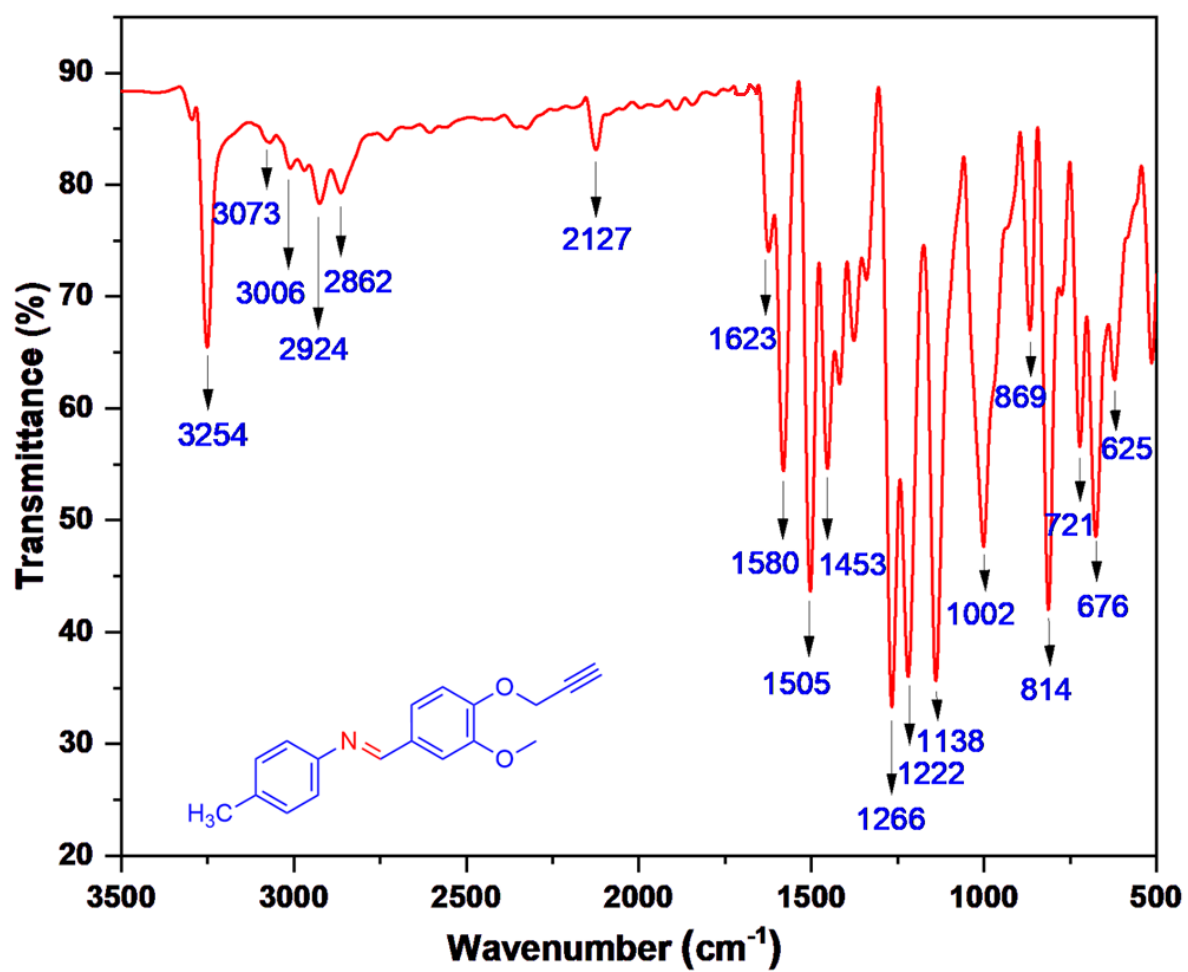
¹H NMR spectrum of Schiff base 85a



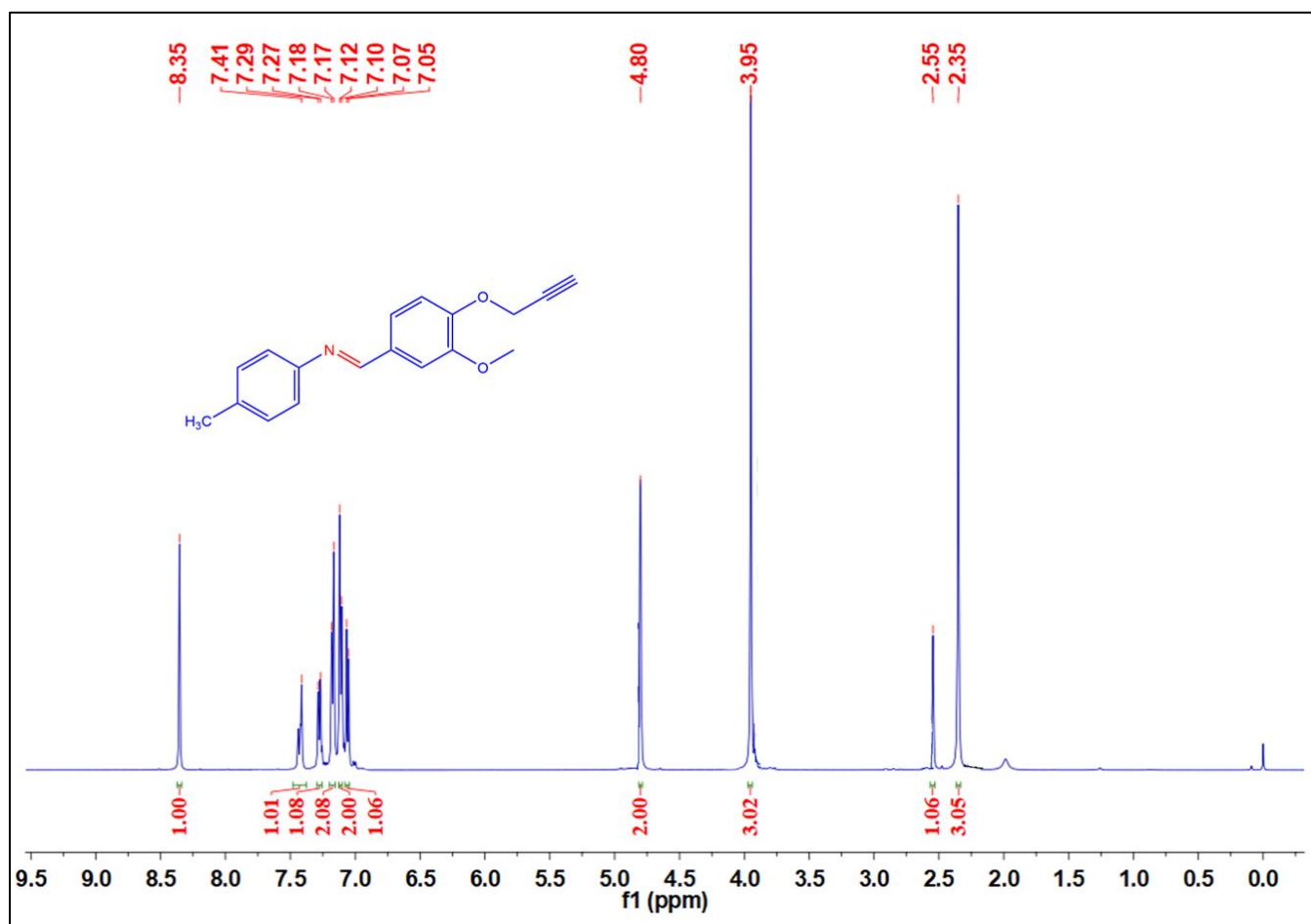
¹³C NMR spectrum of Schiff base 85a



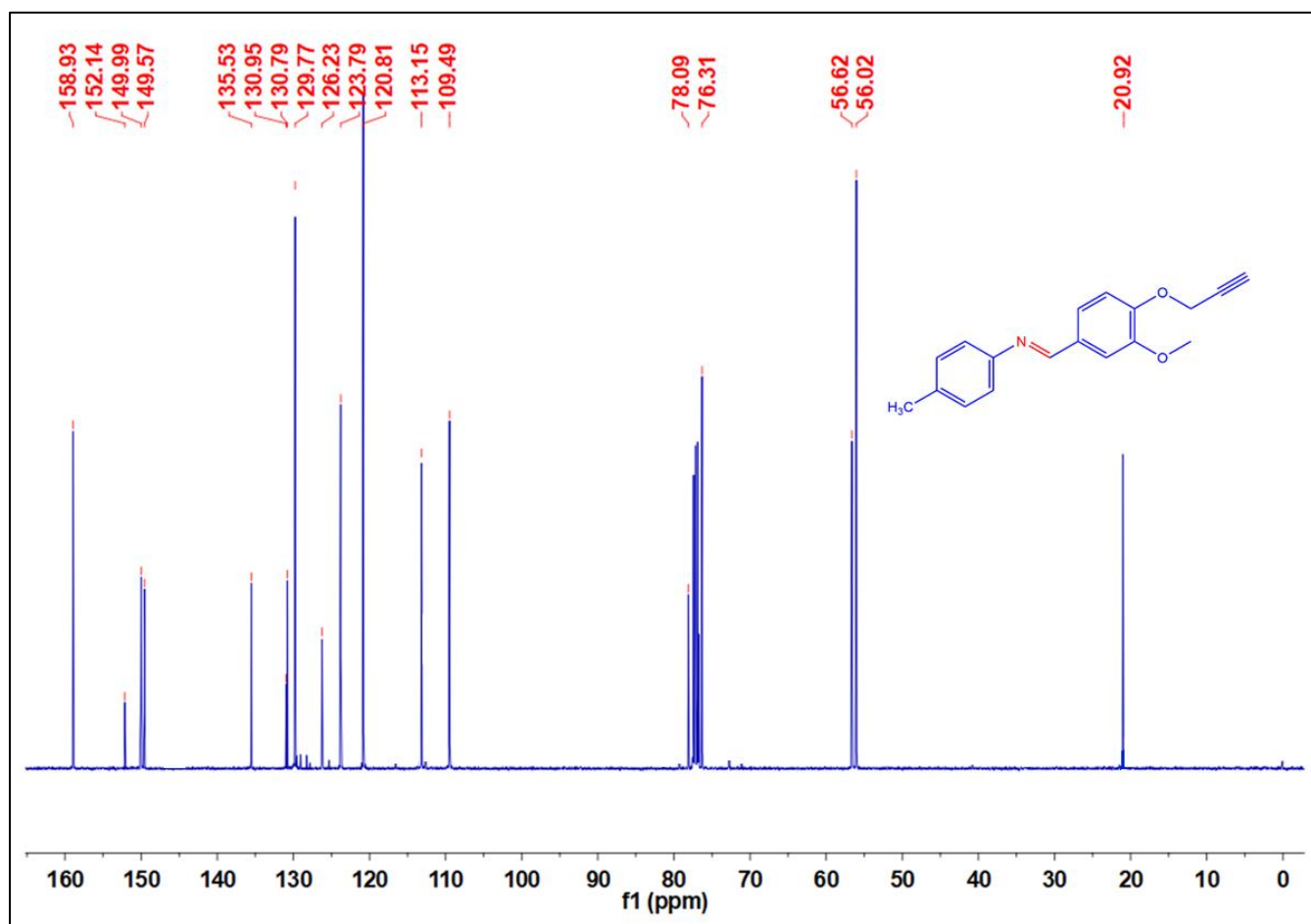
FTIR spectrum of Schiff base alkyne 85b



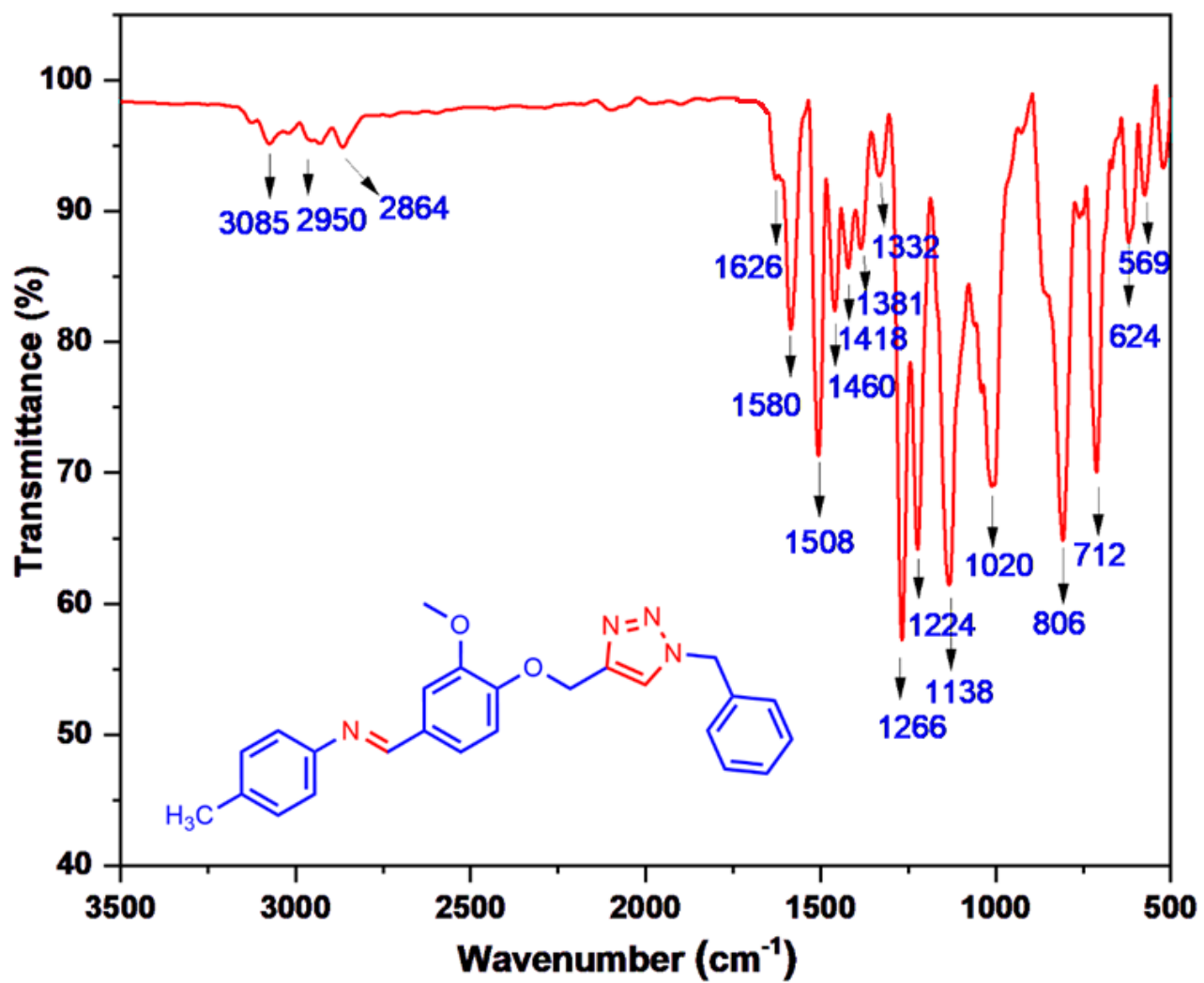
¹H NMR spectrum of Schiff base alkyne 85b



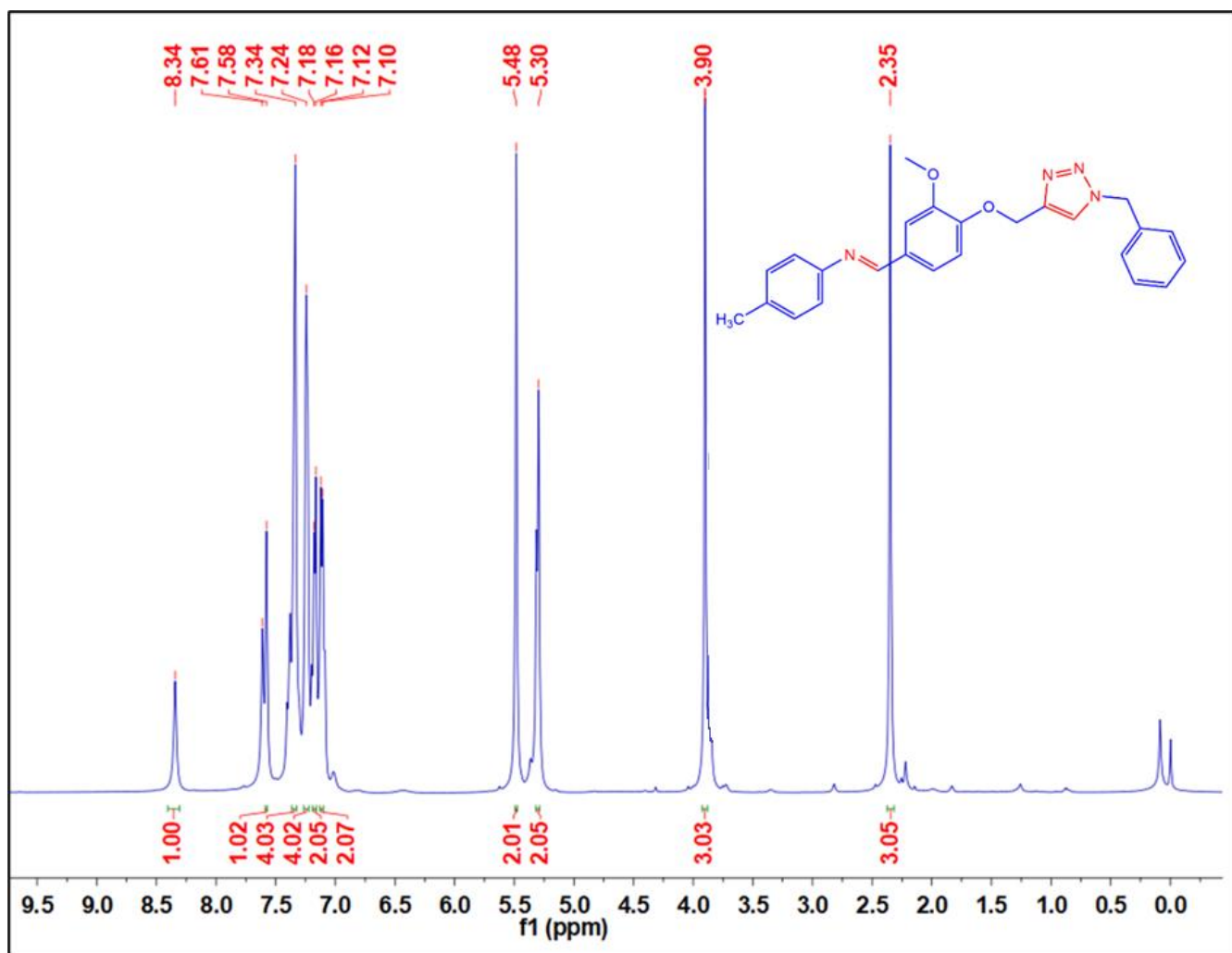
^{13}C NMR spectrum of Schiff base alkyne 85b



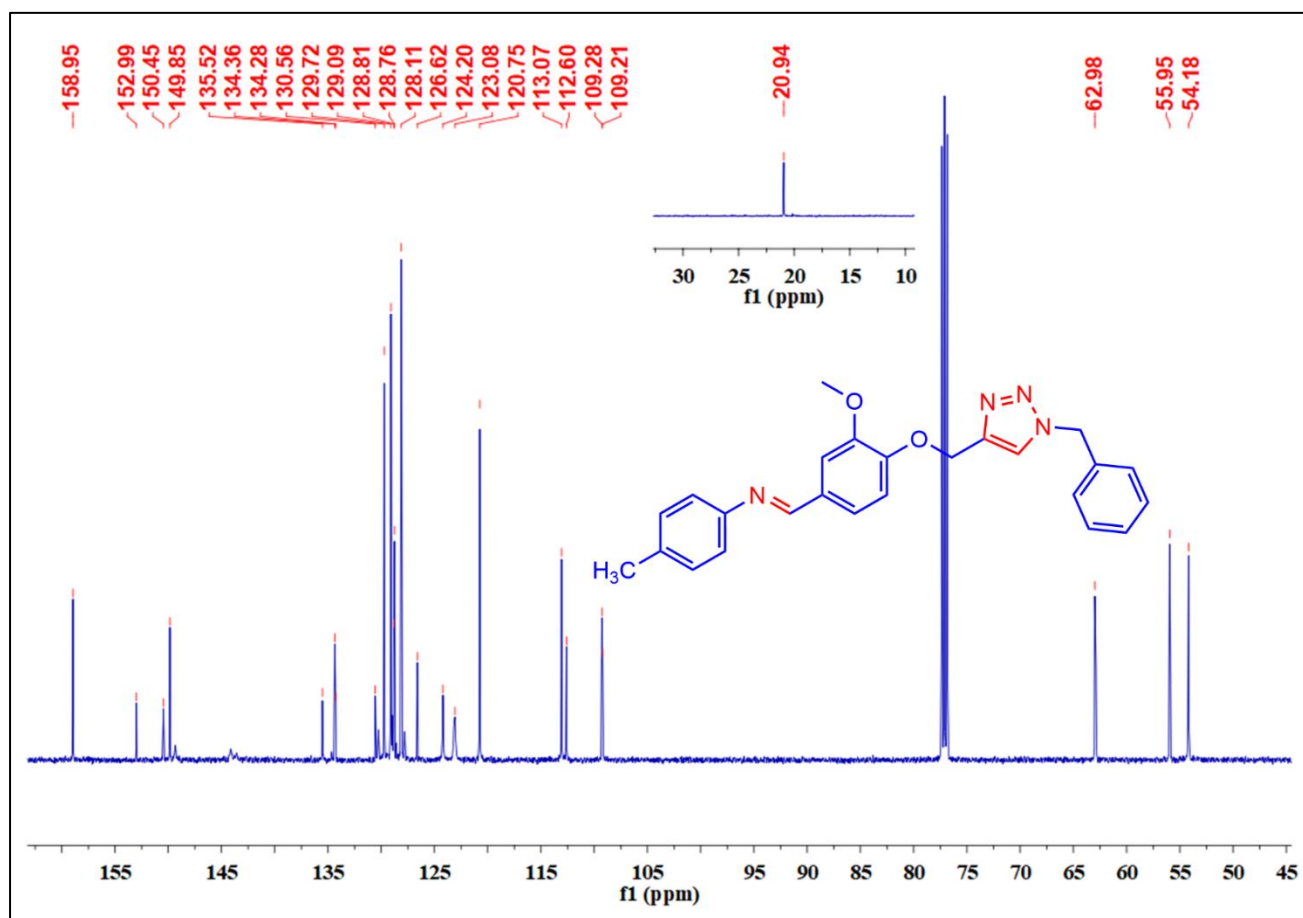
FTIR spectrum of Schiff base triazole 85c



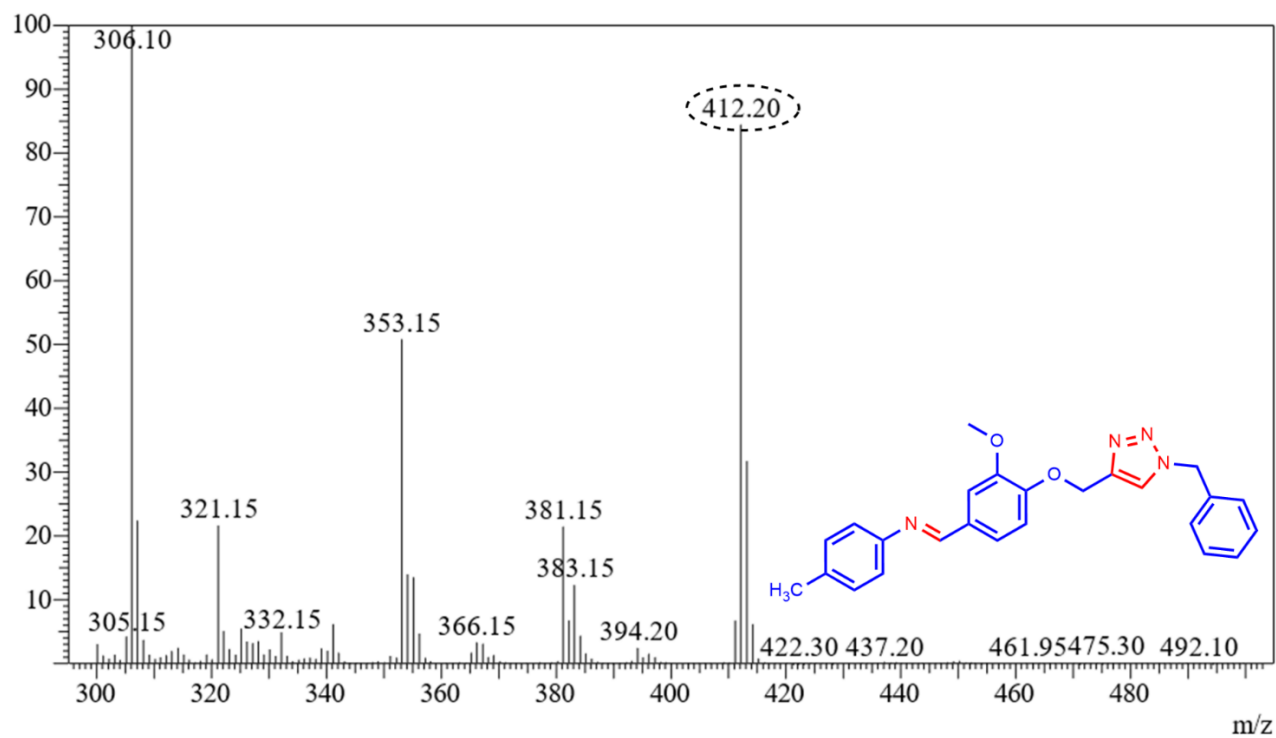
^1H NMR spectrum of Schiff base triazole 85c



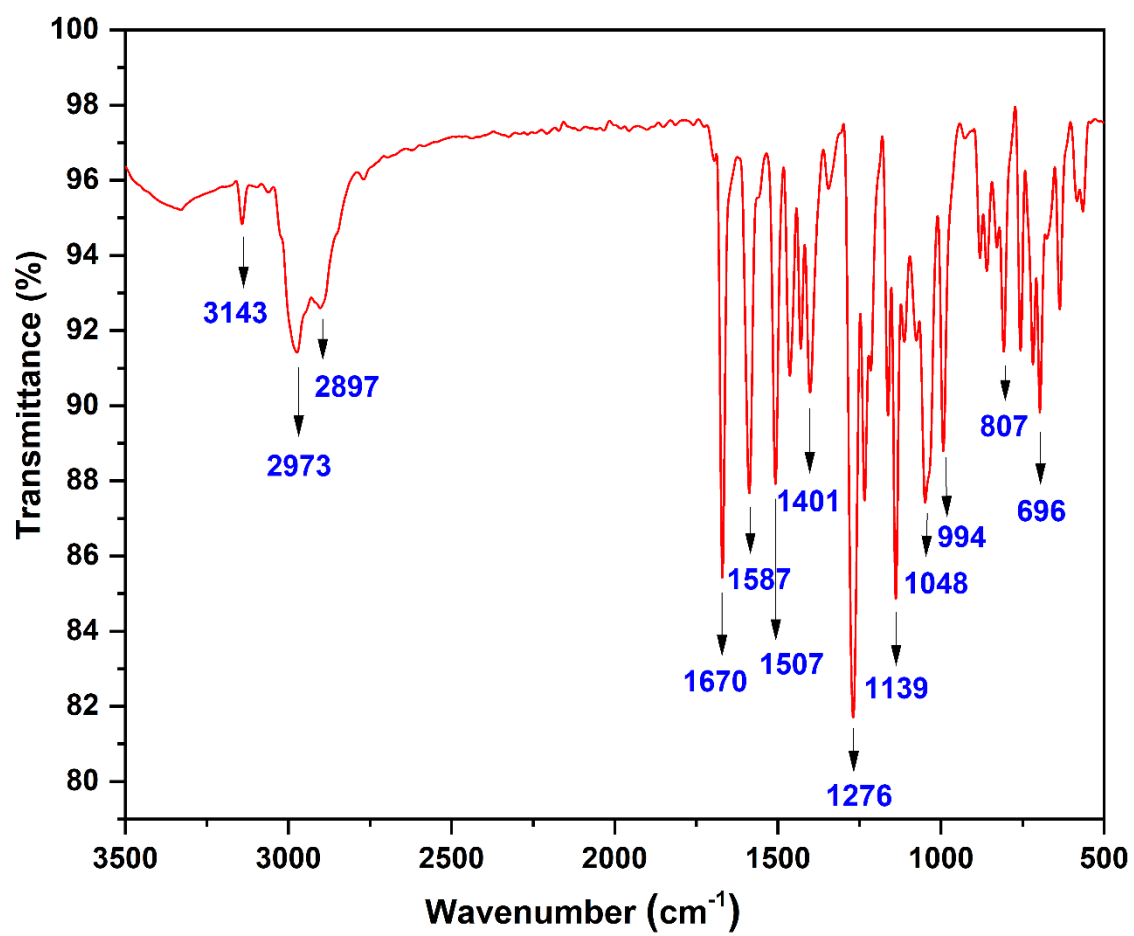
^{13}C NMR spectrum of Schiff base triazole 85c



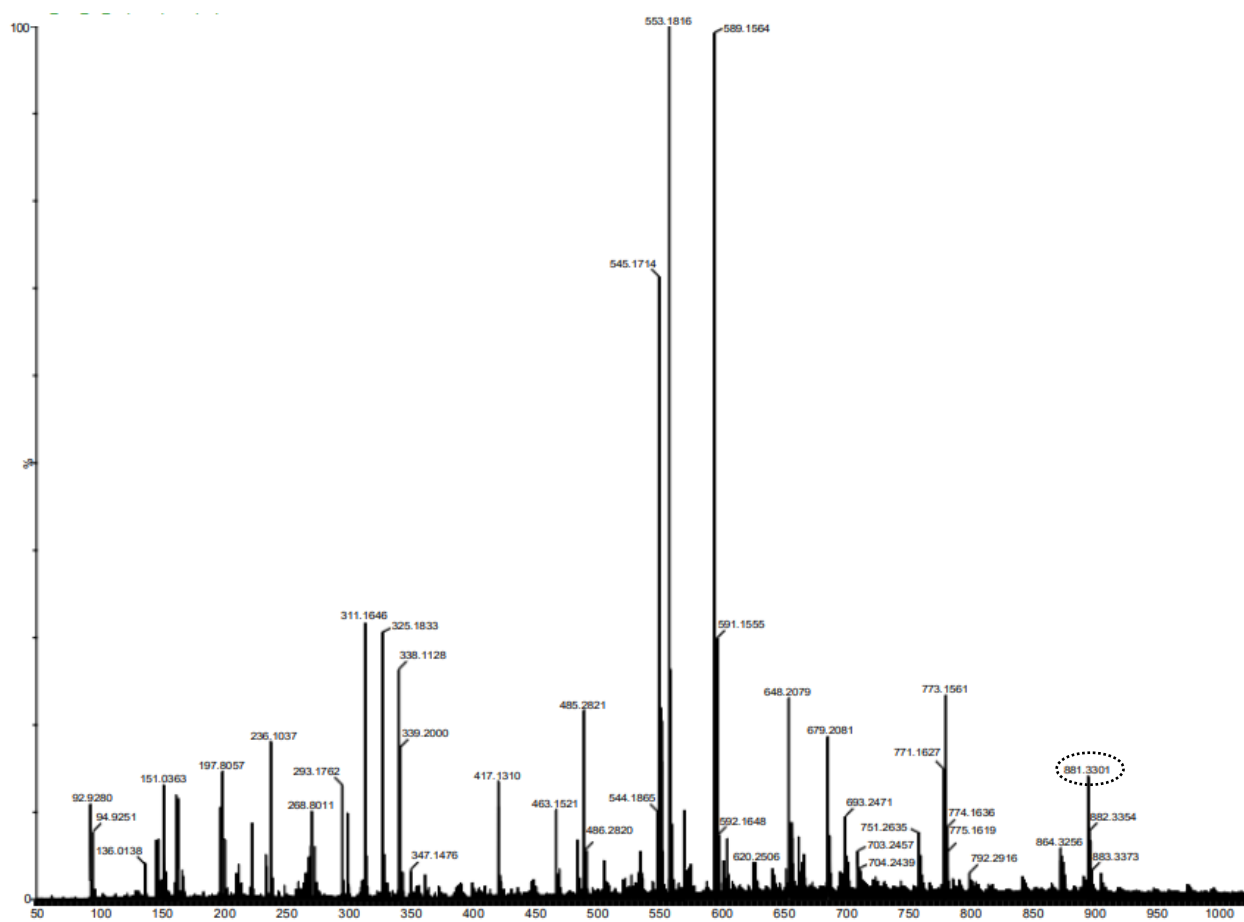
Mass spectrum of Schiff base triazole 85c



FTIR spectrum of [81c + Fe³⁺] complex



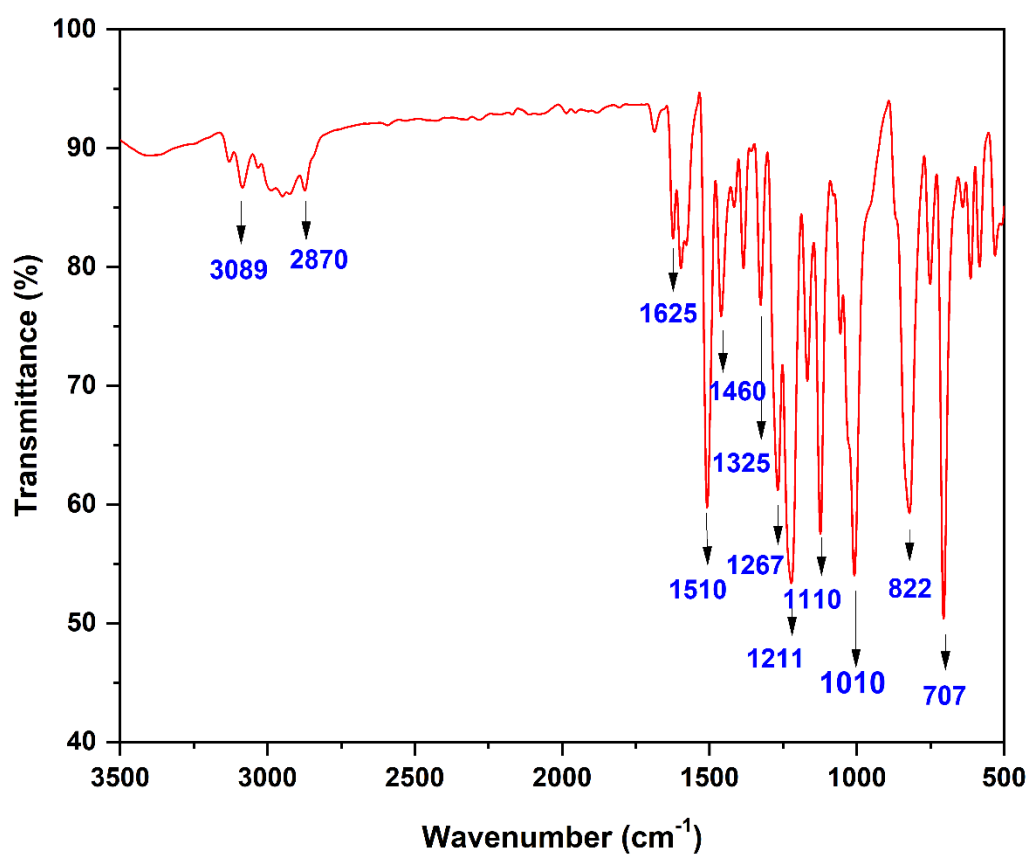
Mass spectrum of [81c + Fe³⁺] complex



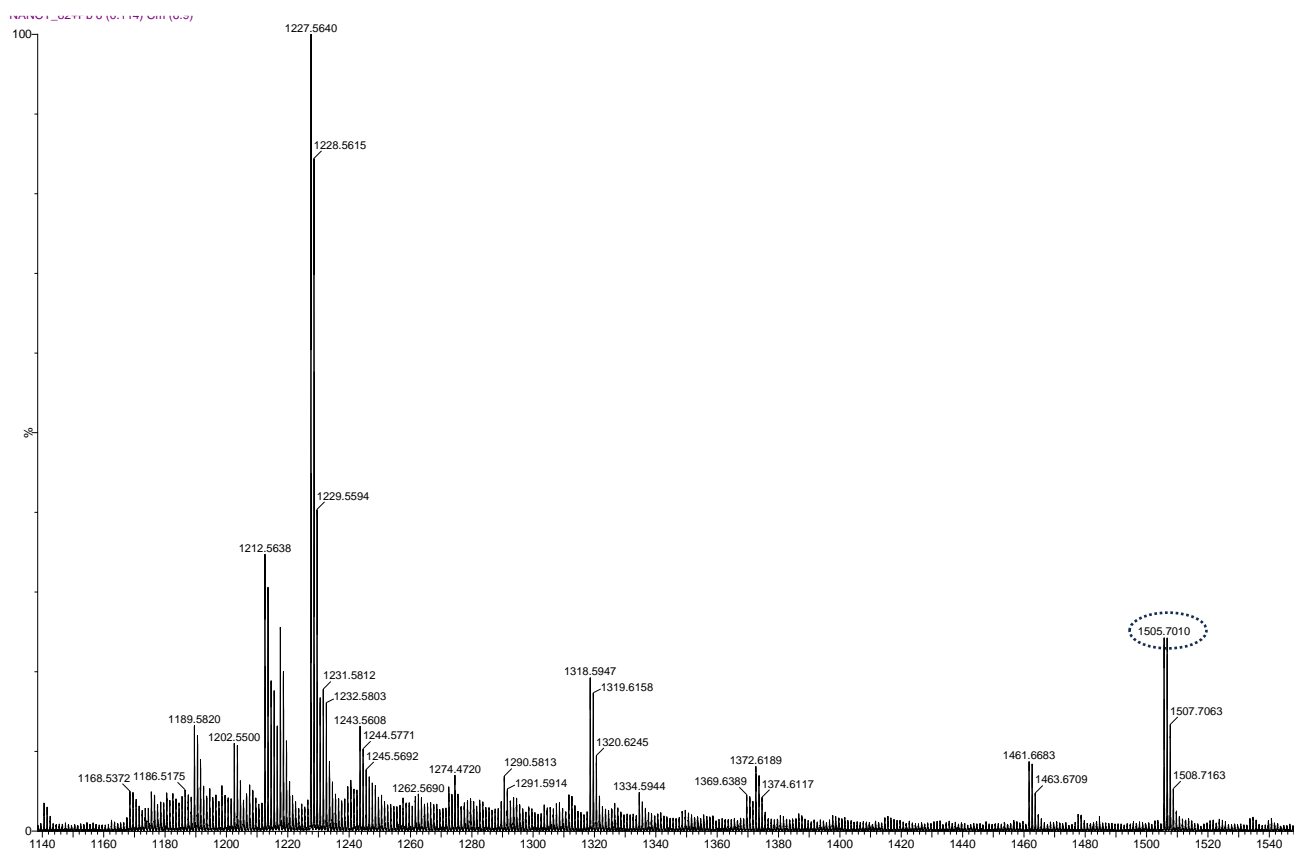
Expected m/z = 880.22

Experimental m/z = 881.33 [M+1]

FTIR spectrum of [82c + Pb²⁺] complex



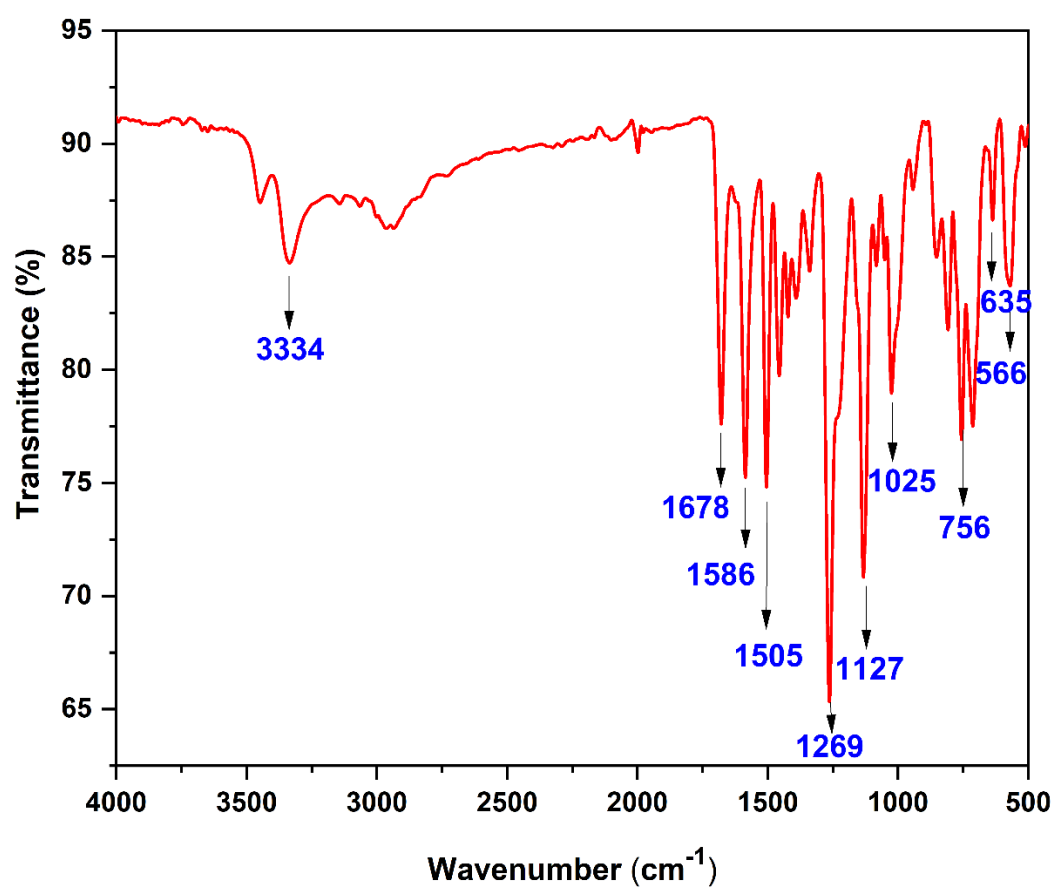
Mass spectrum of [82c + Pb²⁺] complex



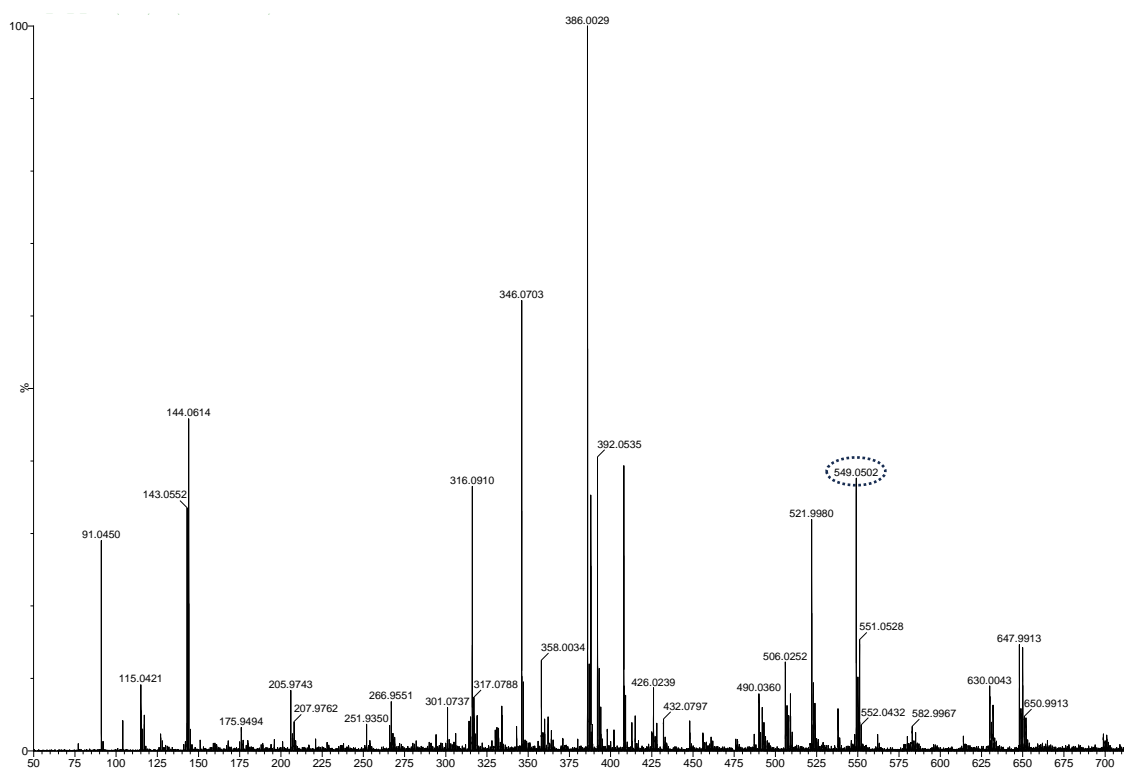
Expected m/z = 1505.09

Experimental m/z = 1505.70

FTIR spectrum of [83c + Cu²⁺] complex



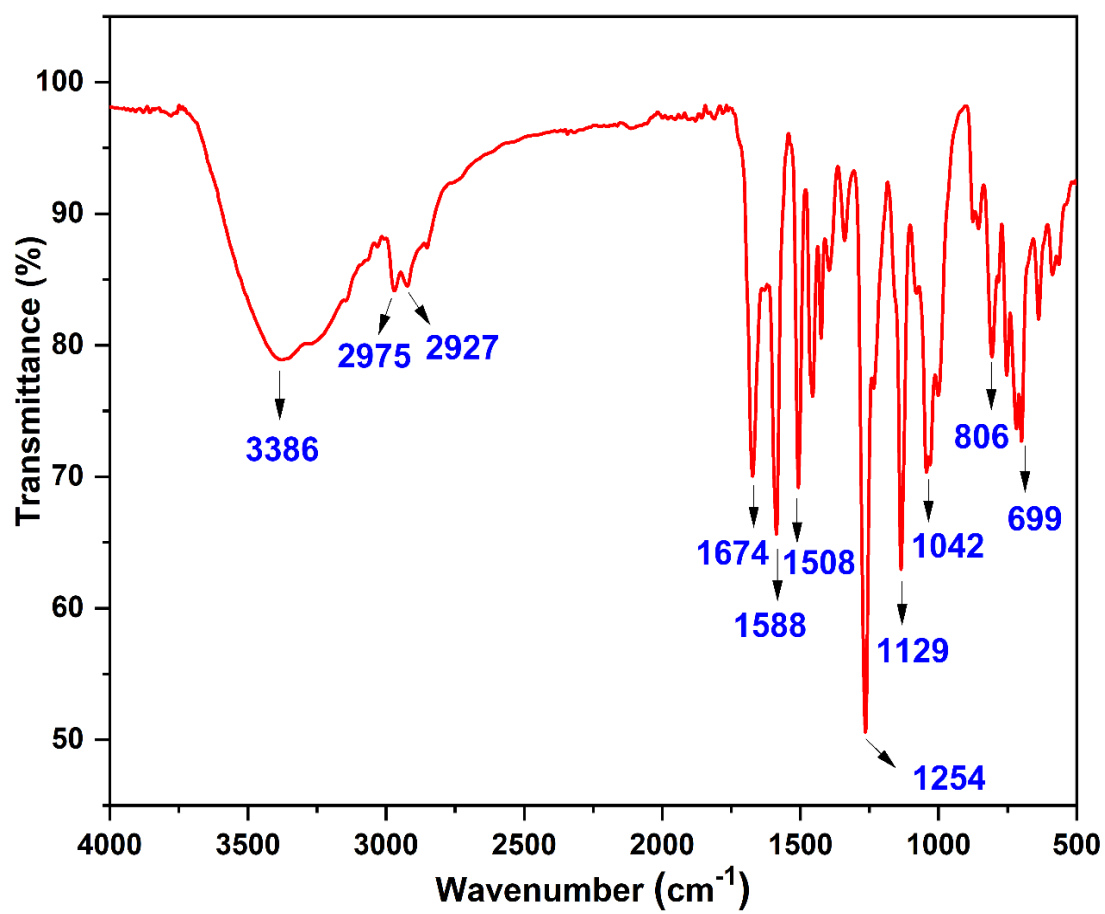
Mass spectrum of [83c + Cu²⁺] complex



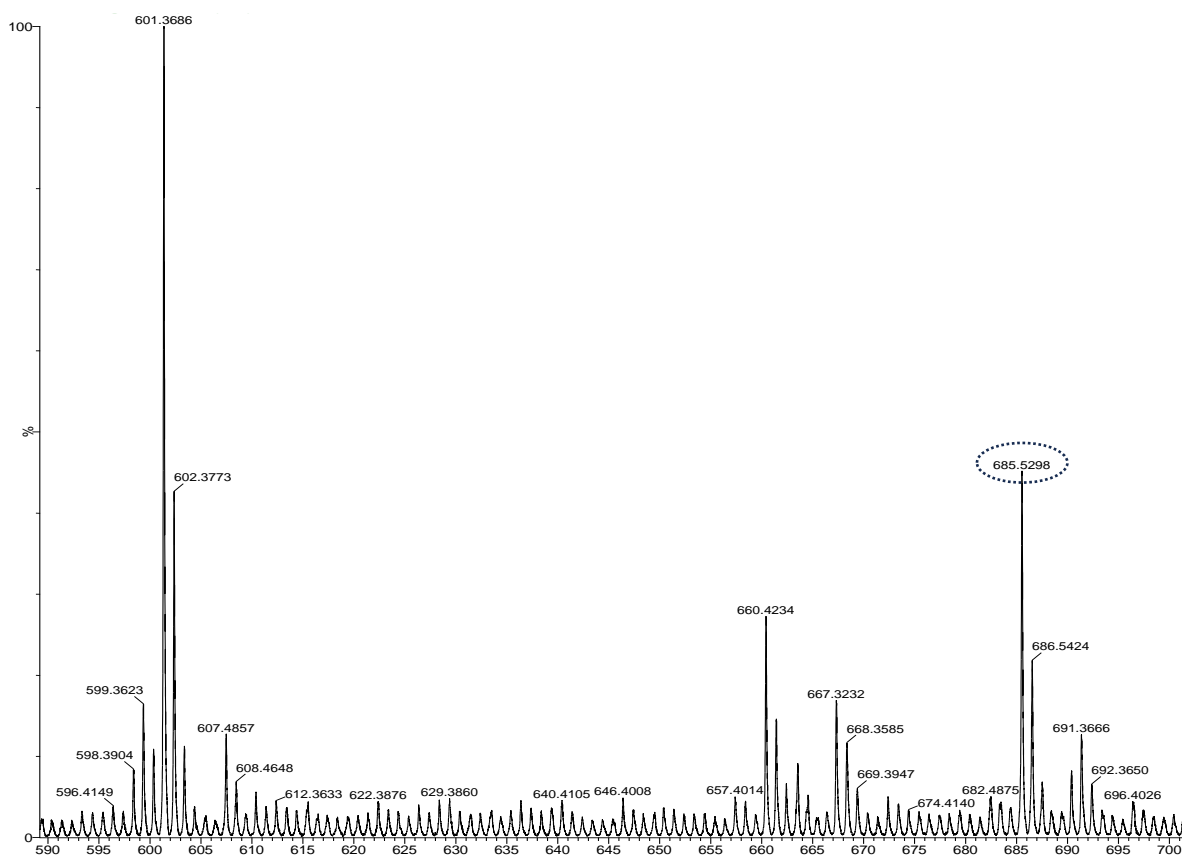
Expected m/z = 547.12

Experimental m/z = 549.05 [M+2]

FTIR spectrum of [84c + Hg²⁺] complex



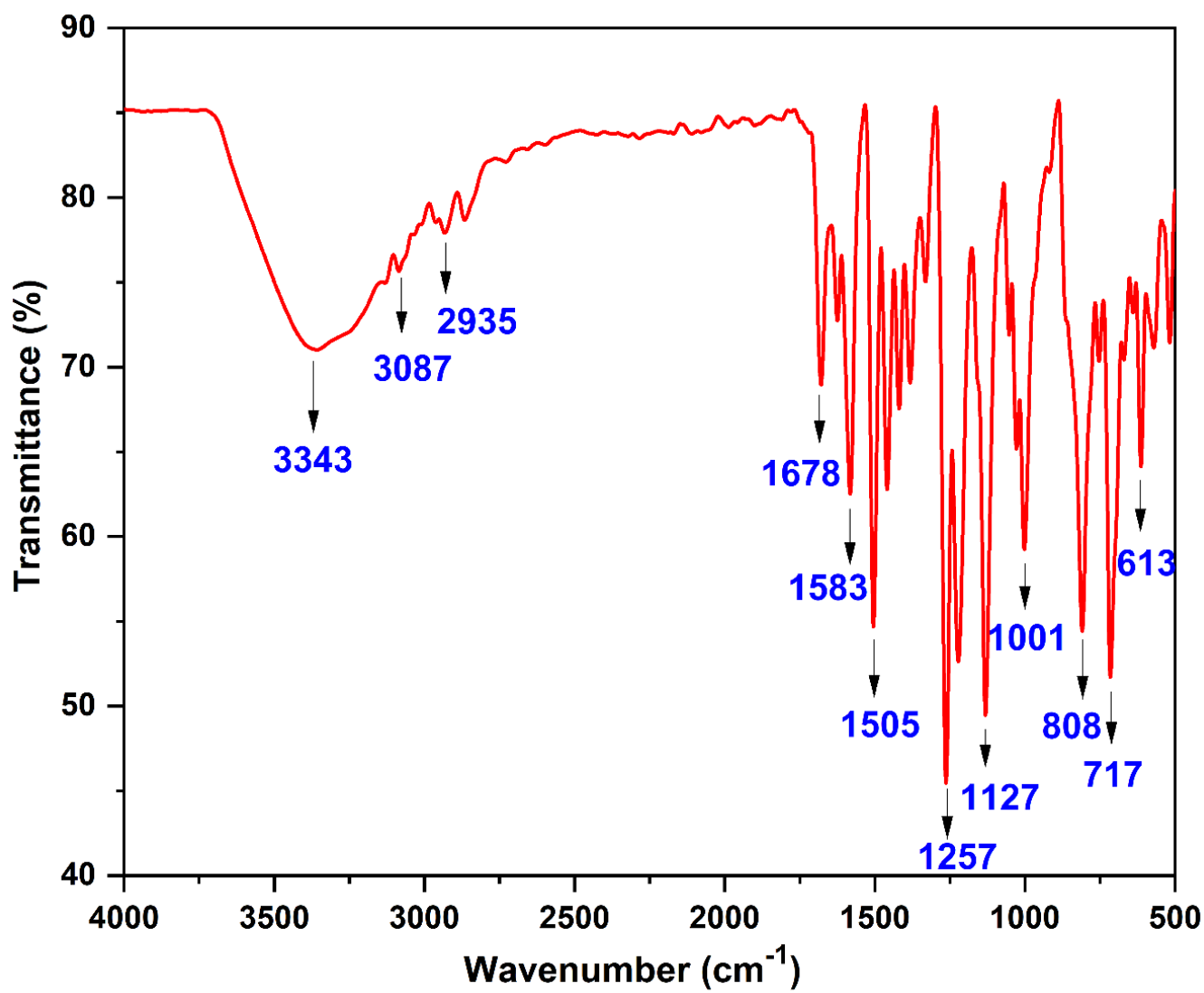
Mass spectrum of [84c + Hg²⁺] complex



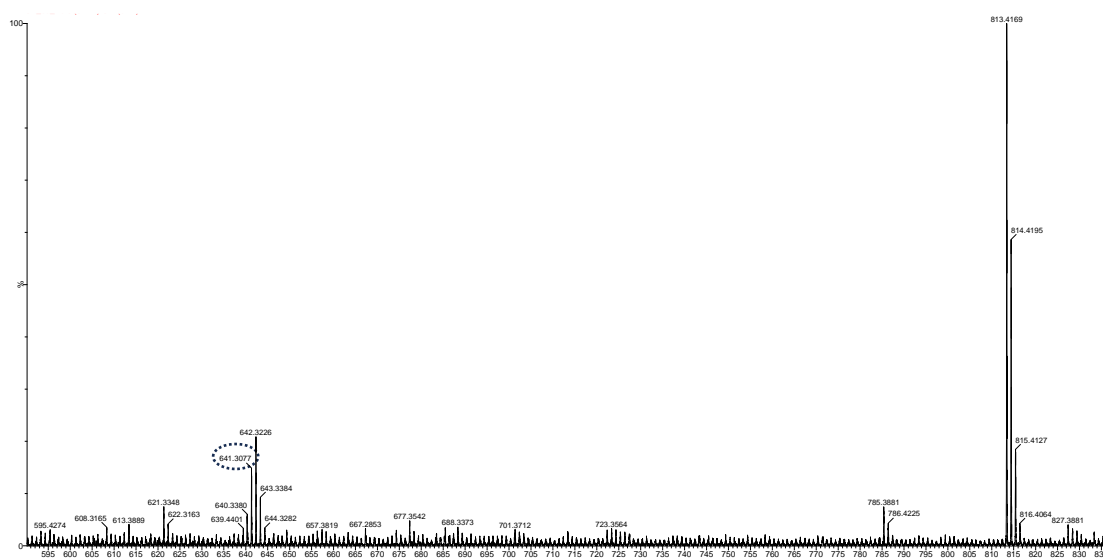
Expected m/z = 684.98

Experimental m/z = 685.52 (M+1)

FTIR spectrum of [85c + Pb²⁺] complex



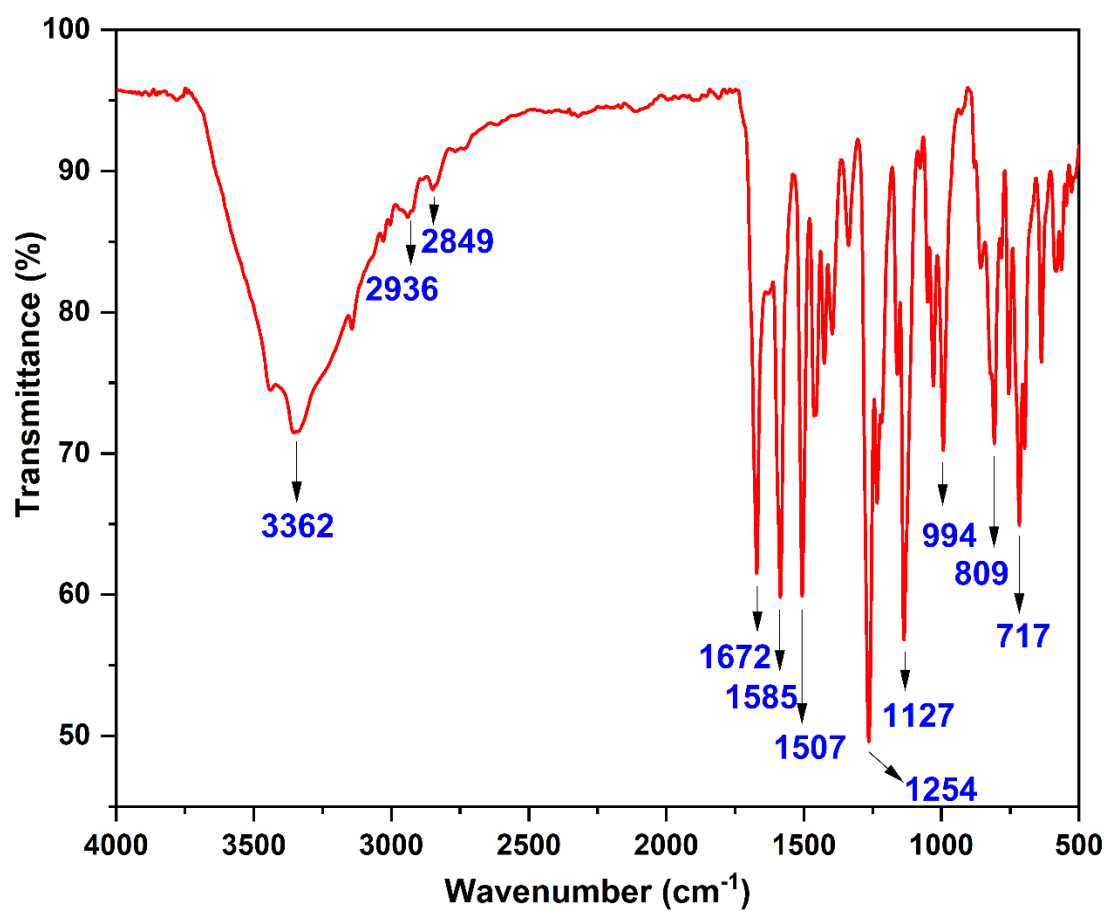
Mass spectrum of [85c + Pb²⁺] complex



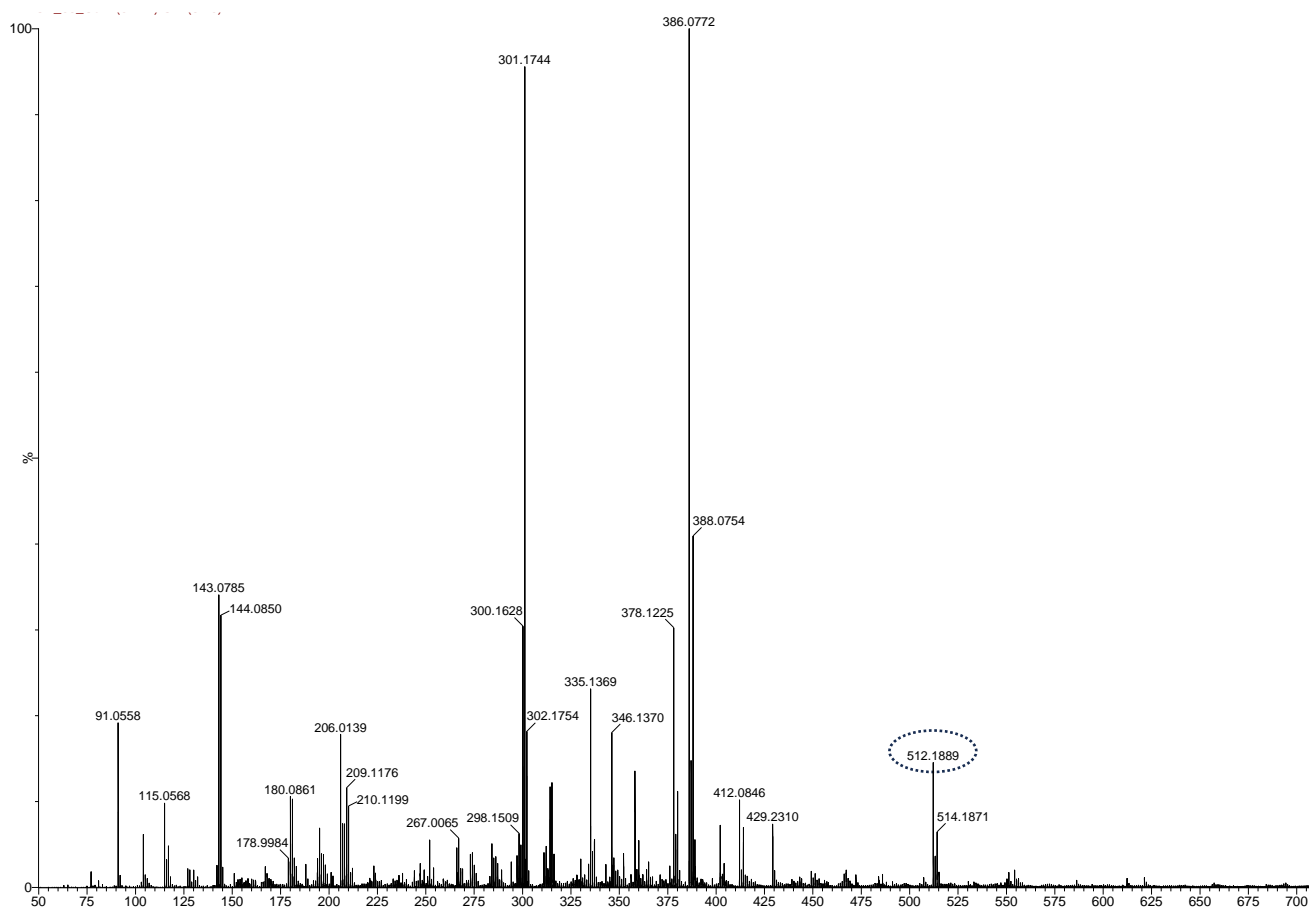
Expected m/z = 641.30

Experimental m/z = 641.39

FTIR spectrum of [85c + Cu²⁺] complex



Mass spectrum of [85c + Cu²⁺] complex



Expected m/z = 511.18

Experimental m/z = 512.18 (M+1)

List of Publications

1. Review paper

“Microwave accelerated green approach for tailored 1,2,3–triazoles via CuAAC”

Sustainable Chemistry and Pharmacy-journal-Elsevier 2022, 30, 100824

Nancy George, Gurleen Singh, Riddima Singh, Gurjaspreet Singh, Anita Devi, Harminder Singh, Gurpreet Kaur, Jandeep Singh

2. Research article

“Click modified bis-appended Schiff base 1,2,3-triazole chemosensor for detection of Pb(II) ion and computational studies”

Journal of Molecular structure, Elsevier, 2023, 1288, 135666

Nancy George, Gurleen Singh, Riddima Singh, Gurjaspreet Singh, Priyanka, Harminder Singh, Gurpreet Kaur, Jandeep Singh

3. Research manuscript

“Schiff base functionalized 1,2,3-triazole derivative for Fe(III) ion recognition, as N,O,O-Fe-O,O,N sandwich complex: DFT analysis”

Polyhedron-journal-Elsevier, 2023, 242, 116496

Nancy George, Gurleen Singh, Riddima Singh, Gurjaspreet Singh, Sushma, Harminder Singh, Gurpreet Kaur, Jandeep Singh

4. Research paper

“Detection of copper in tea and water sample: A click-oriented azomethine-based 1,2,3-triazole fluorescent chemosensor with reversible INHIBIT logic gate behavior and computational aspects”

Journal of Molecular structure, Elsevier, 2023, 1311, 138288

Nancy George, Parveen Saini, Gurleen Singh, Riddima Singh, Gurjaspreet Singh, Pooja Malik, Harminder Singh, Gurpreet Kaur, Jandeep Singh

5. Research article

“‘Turn On’ fluorescent imine linked 1,2,3-triazole based chemosensor for detection of mercuric ions”

Inorganic Chemistry Communications, *Elsevier*, 2024, 169, 113088

Nancy George, Gurleen Singh, Riddima Singh, Gurjaspreet Singh, Sudha Malik, Harminder Singh, Gurpreet Kaur, Jandeep Singh

6. Book Chapter

“Catalysts for Click Chemistry”

Click Chemistry, Taylor & Francis Group, 2024, 1, 151-171

Nancy George, Gurleen Singh, Gurpreet Kaur, Jandeep Singh

List of conferences and workshops

1. Presented **oral presentation** on “**Design and characterization of newly synthesized schiff base derived 1,2,3-triazole**” in the ICMET organized by division of research and development, Lovely Professional University on February 18-19, 2022
2. Participated in **poster presentation** on “**Development of newly schiff based 1,2,3-triazole chemosensor from azomethine group for detection of toxic lead ion**” in the EMSD-2022 organized by NTC IEEE CSIO on October 09-11, 2022
3. Participated in **oral presentation** on “**Synthesis of azomethine functionalized 1,2,3-triazole chemosensor for detection of ferric ion**” in the ICMEC organized by IGDTUW IAAM SU on December 12-14, 2022
4. Participated in **Workshop** on “**Advanced Materials Characterization Techniques**” organized by Lovely Professional University on December 19-20, 2022
5. Participated in **Workshop** on “**Gaussian Software**” organized by SIAS Research Centre on April 15- May 02, 2024
6. Participated in **Workshop** on “**Molecular Docking**” organized by SIAS Research Centre on May 06-16, 2024



Contents lists available at ScienceDirect

Sustainable Chemistry and Pharmacy

journal homepage: www.elsevier.com/locate/scp

Microwave accelerated green approach for tailored 1,2,3-triazoles via CuAAC

Nancy George^a, Gurleen Singh^a, Riddima Singh^a, Gurjaspreet Singh^b, Anita Devi^b,
Harmander Singh^a, Gurpreet Kaur^{c,*}, Jandeep Singh^{a,*}

^a School of Chemical Engineering and Physical Sciences, Lovely Professional University, Phagwara, 144411, Punjab, India

^b Department of Chemistry and Centre of Advanced Studies in Chemistry, Panjab University, Chandigarh, 160014, India

^c Department of Chemistry, Gujranwala Guru Nanak Khalsa College, Civil Lines, Ludhiana, 141001, Punjab, India

ARTICLE INFO

Keywords:

Green chemistry
Microwave-assisted synthesis
1,2,3-triazole
Click chemistry
CuAAC
Sustainability

ABSTRACT

The persistent deterioration of our environmental assets has initiated 'a push' among the scientific community for increased reliance on eco-friendly methodologies minimizing the utilization of hazardous materials. As an outcome, there is a paradigm shift in the synthetic modules of organic reactions from conventional techniques to the parameters of green principles. Therefore, the demand for microwave (μ w) tailored reactions has witnessed substantial and exponential growth in the last two decades. In accordance, the employment of green methodology in Cu(I) catalyzed alkyne-azide cycloaddition reaction (CuAAC) for the synthesis of 1,2,3-triazole derivatives have reared fruitful results with the reduction of synthetic time, superior yields without benign solvents. The use of the microwave technique has been amplified with its implementation of a range of green methodologies by contributing to solvent-less, catalyst-free, use of ionic liquids and aqueous medium. This review puts forward the microwave synthesis of 1,2,3-triazoles through Cu(I) mediated click chemistry.

1. Introduction

Heterocyclic compounds have emerged as a special class of compounds owing to their numerous medicinal properties such as DNA-virus inhibitors, anti-hepatotoxic, anti-microbial agents and industrial applications like the synthesis of dyes, cosmetics, weed killers, reprography, antioxidants, and plastics, leading to the advancement in scientific research (Mishra et al., 2021; Dharavath et al., 2020; Ashok et al., 2020a). The stitching of a terminal alkyne with an organic azide in a cycloadditive manner is one of the most extensive techniques for the synthesis of N-heterocycles (Hernández-López et al., 2020; SinghSanchita et al., 2018; M'Hamed, 2015; Kumar et al., 2021). and utilizing this methodology, particularly the 5-membered 1,2,3-triazole linked molecules can be effectively synthesized. Huisgen in the 1960's laid down the path for 1,3 dipolar cycloaddition reaction under uncatalyzed and prolonged thermal conditions giving a mixture of 1,4 and 1,5-disubstituted products. However, the reaction methodology suffered from the serious drawbacks of non-regioselectivity, long reaction time, and poor product yields (Bräse et al., 2005; T.-S. L. and Prusoff, 1978; Singh et al., 2018a; Tiwari et al., 2016; Huisgen, 1963; Huisgen et al., 1967; Kanemasa and Kanai, 2000; Bhuyan et al., 2018; Dheer et al., 2017; Hein and Fokin, 2010).

* Corresponding author.

** Corresponding author.

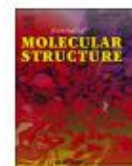
E-mail addresses: chemgurpreet5@gmail.com (G. Kaur), singhjandeep@gmail.com (J. Singh).

<https://doi.org/10.1016/j.scp.2022.100824>

Received 4 July 2022; Received in revised form 15 August 2022; Accepted 31 August 2022

Available online 30 September 2022

2352-5541/© 2022 Elsevier B.V. All rights reserved.



Click modified bis-appended Schiff base 1,2,3-triazole chemosensor for detection of Pb(II) ion and computational studies

Nancy George^a, Gurleen Singh^a, Riddima Singh^a, Gurjaspreet Singh^b, Priyanka^b, Harminder Singh^a, Gurpreet Kaur^c, Jandeep Singh^{a,*}

^a School of Chemical Engineering and Physical Sciences, Lovely Professional University, Phagwara, Punjab 144411, India

^b Department of Chemistry and Centre of Advanced Studies in Chemistry, Panjab University, Chandigarh 160014, India

^c Department of Chemistry, Gujranwala Guru Nanak Khalsa College, Civil lines, Ludhiana, Punjab 141001, India

ARTICLE INFO

Keywords:

Click chemistry

CuAAC

Lead (II) sensor

1,2,3-triazole

Chemosensors

Computational chemistry

ABSTRACT

A novel 1,2,3-triazole linked schiff base chemosensor was stitched via Cu(I) catalyzed click reaction with excellent yield, high selectivity, sensitivity and characterized using fourier transform infrared spectroscopy (FTIR), NMR (¹H and ¹³C), mass spectrometry (MS), CHN analysis, thermal gravimetric analysis (TGA) and differential scanning calorimetry (DSC). The developed chemosensor was investigated for its optical properties using UV-visible and fluorescent spectroscopy. The detected limit of the synthesized probe was estimated 0.25 μM from fluorescence spectroscopy, which is particularly below the WHO guidelines. The binding stoichiometric (2:1) of ligand was confirmed by the job's plot and the binding constant was determined to be $4.1 \times 10^6 \text{ M}^{-1}$ and $1.4 \times 10^5 \text{ M}^{-1}$ from the B-H plot and the Stern-Volmer curve, respectively. These results establish the developed chemosensor as a potent probe for analytical and practical applications. The optimized geometrical structure of the probe (4) was run on Gaussian 09 program using DFT method with (B3LYP)/6-311G++(d,p) basis set of hybrid density functional theory.

1. Introduction

Metal ion pollution has become a worldwide ecological concern in recent years due to rapid development and increasing industrialization. The pervasive use of lead ions in particular has resulted in massive environmental pollution, posing grave health concern to individuals and biological systems. Petrol, paints, pigments, lead batteries, alloys, ceramics, glass, chemicals, toys, electronics, water pipes, and other consumer items are the most prevalent anthropogenic sources of lead contamination in environmental matrices (water, soil, air, and food). Excessive lead exposure causes a variety of health problems in humans, affecting the kidneys, gastrointestinal, hematological, cardiac, reproductive, and neurological systems. Furthermore, Pb²⁺ is far more dangerous than those other metals since it is a neurotoxin that may accumulate in muscles and bones, causing nervous system damage as well as brain and blood disorders [1–5]. The United States Environmental Protection Agency (USEPA) and the World Health Organization (WHO) have precisely specified permitted concentration limits of Pb²⁺ metal ions in drinking water as 16 ppb (16 μg L⁻¹) and 10 ppb (48 nM),

respectively. Similarly, the US Food and Drug administration had established an action level of 2.5 μM for Pb²⁺ in goods intended for use by newborns and children. As a result, determining and monitoring the level of the lead metal ion is critical to ensure that heavy metal lead concentrations remain below the designated hazardous limit [6–8].

Schiff bases are widely recognized as tunable compounds with an azomethine bond, and they are developing as a prominent class in chemical and medicinal chemistry due to their distinguishing characteristics and diverse biological activities. Schiff bases have been widely explored as flexible ligands for analyte detection, and their facile interactions with metal due to changes in electrical characteristics have been intensively researched [9–13]. Synthetically achievable and structurally versatile, 1,2,3-triazole derivatives are primarily produced via 1,3-dipolar cycloaddition of organic azides and substituted alkynes [10,14]. Recently, Carolyn R. Bertozza, Morten Meldal, and K. Barry Sharpless were awarded 2022 Nobel Prize in Chemistry for discovering click chemistry, an ecologically benign approach for swiftly combining molecules to produce cancer treatments and generate materials. The potential of the generated 1,2,3-triazole system to behave as a binding

* Corresponding author.

E-mail address: singhjandeep@gmail.com (J. Singh).

<https://doi.org/10.1016/j.molstruc.2023.135666>

Received 6 January 2023; Received in revised form 24 April 2023; Accepted 25 April 2023

Available online 29 April 2023

0022-2860/© 2023 Elsevier B.V. All rights reserved.



Schiff base functionalized 1,2,3-triazole derivative for Fe(III) ion recognition, as N,O,O-Fe-O,O,N sandwich complex: DFT analysis

Nancy George^a, Gurleen Singh^a, Riddima Singh^a, Gurjaspreet Singh^b, Sushma^c,
Harmander Singh^a, Gurpreet Kaur^{d,*}, Jandeep Singh^{a,*}

^a School of Chemical Engineering and Physical Sciences, Lovely Professional University, Phagwara 144411, Punjab, India

^b Department of Chemistry and Centre of Advanced Studies in Chemistry, Punjab University, Chandigarh 160014, India

^c Chitkara College of Pharmacy, Chitkara University, Patiala 140417, Punjab, India

^d Department of Chemistry, Gujranwala Guru Nanak Khalsa College, Civil Lines, Ludhiana 141001, Punjab, India

ARTICLE INFO

Keywords:
Click Chemistry
CuAAC
1,2,3-Triazole
Iron (III) sensor
Chemosensors

ABSTRACT

The present research aims to synthesize Schiff base tethered 1,2,3-triazole derivative using Cu(I) catalyzed click reaction as a highly sensitive and selective optical chemosensor for the recognition of ferric ions. The synthesized probe was characterized using Fourier transform infrared spectroscopy (FTIR), NMR (¹H and ¹³C), mass spectrometry, CHN analysis, and Thermal gravimetric analysis (TGA). The UV-vis spectroscopy was employed in eco-friendly EtOH:H₂O (9:1 v/v) solvent media to investigate the optical properties of the developed chemosensor **SBT**, the association constant and limit of detection of Fe³⁺ was determined to be $2.6 \times 10^4 \text{ M}^{-1}$ and $1.3 \times 10^{-7} \text{ M}$ establishing the designed **SBT** as a potent probe for analytical and practical applications. Additionally, the time-dependent study and pH sensitivity of the developed probe **SBT** and metal-ligand complex were also studied via UV-visible spectroscopy. Besides, FTIR spectra and TGA curve of the synthesized (**SBT**-metal complex) confirmed the binding of the metal-ligand complex. Furthermore, the real sample application for detection of Fe³⁺ in spinach (food rich in Iron) was analysed, and the **SBT**-based sensing system yielded a recovery rate of greater than 99.07%. The synthesized probe was also explored for its computational-based DFT studies via Gaussian 09 programs using the DFT method with (B3LYP)/-311G (d,p) basis set of hybrid density functional theory.

1. Introduction

Among the most persistent challenges for scientists is to develop extremely sensitive and selective metal-ion responsive chemosensors for the effective tracking of physiologically and ecologically relevant metal ions. Although, Iron is a substantial transition metal that plays a requisite role in oxygen transport in the human body, and subsequently act as a cofactor in the enzymatic activities involved in biochemical reactions [1]. However, excessive deposition of iron in ferritin proteins can cause metabolic imbalance resulting in the disruption of cellular processes, and hinders the biosynthetic activity. Iron in a trivalent state is predominant owing to its capacity to oxidise during aerobic oxidation photosynthesis [2]. But the concomitant accumulation of Fe³⁺ can be fatal to human beings, causing respiration syndrome, convulsions, skin ailments, dysfunction of organs, Parkinson's and Alzheimer's diseases, cardiac arrest and can lead to cancer [3–5]. Meanwhile, the daily requirement of iron uptake in adult male and the female body is 9.1 and

19.6 (mg/d) respectively as recommended by the World Health Organization (WHO) and exceeding these levels can lead to deterioration of human's health if left untreated [2,6,7]. Therefore, development of versatile, precise and efficient Fe³⁺ ion responsive chemosensor, below the permissible levels, is essential [8–10]. Recently, the development of Fe³⁺ selective sensors feature drawbacks such as turn-off responses and interferences with other metal ions. Additionally, these detectors are structurally intricate and need a tedious multistep chemical synthesis, resulting in excessively expensive costs. Most of the chemosensors reported have the inability to clearly distinguish between Fe³⁺ and Fe²⁺ oxidation states. Subsequently, various oxidation states have distinct features, it is vital to identify one from the other in order to analyse their course of action [11–14]. Table 1. Table 2..

'Click chemistry' has allured enormous research attention due to the synthetic simplicity for synthesis of 1,2,3-triazole linkers, that act as binding pockets in diverse applications in chemical biology, agrochemical, dyes, pigments and so forth. The CuAAC Meldal–Sharpless

* Corresponding authors.

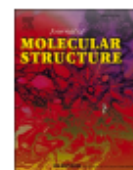
E-mail address: singhjandeep@gmail.com (J. Singh).

<https://doi.org/10.1016/j.poly.2023.116496>

Received 29 March 2023; Accepted 7 June 2023

Available online 20 June 2023

0277-5387/© 2023 Elsevier Ltd. All rights reserved.



Detection of copper in tea and water sample: A click-oriented azomethine-based 1,2,3-triazole fluorescent chemosensor with reversible INHIBIT logic gate behavior and computational aspects

Nancy George^a, Parveen Saini^b, Gurleen Singh^a, Riddima Singh^a, Gurjaspreet Singh^c, Pooja Malik^c, Harminder Singh^a, Gurpreet Kaur^{d,*}, Jandeep Singh^{a,*}

^a School of Chemical Engineering and Physical Sciences, Lovely Professional University, Phagwara 144411, Punjab, India

^b Department of Chemistry, Shanti Devi Arya Mahila College, Dinanagar 143531, Punjab, India

^c Department of Chemistry and Centre of Advanced Studies in Chemistry, Panjab University, Chandigarh 160014, India

^d Department of Chemistry, Gujranwala Guru Nanak Khalsa College, Civil lines, Ludhiana 141001, Punjab, India

ARTICLE INFO

Keywords:

1,2,3-triazole
Click chemistry
Chemosensor
Cu²⁺ ions sensor
Black Tea

ABSTRACT

A fluorescent azomethine-scaffolded-1,2,3-triazole linked chemosensor was synthesized utilizing alkyne and azidomethylbenzene via Cu(I)-catalyzed click chemistry. The compounds (3–5 and L6) were analyzed using FTIR, ¹H NMR, ¹³C NMR, and GCMS-. The exploration of ion sensing ability of L6 complex, using UV-Vis and fluorescence spectroscopy in ACN:H₂O (4:1) medium resulted in detection of Cu(II) ions, exclusively. Further L6-Cu(II) complex was characterized via FTIR, FE-SEM, LCMS and supported by DFT studies. A significant structural modification has rendered the current probe as highly selective for Cu²⁺ ions, with 'Turn-On' response. The chemical receptor (L6) establishes 1:1 molar ratio with Cu(II) ions with binding constant of $6.0 \times 10^4 \text{ M}^{-1}$ and excellent detection limit of 20 nM. In addition, the sensitive reversible behavior of probe (L6) with two chemical inputs (Cu²⁺ and EDTA) contributes to the construction of an INHIBIT logic circuit. The Copper ion detection was effectively monitored for real-world samples like Black Tea with precise quantification of Copper(II) ions.

1. Introduction

The ever-evolving field of ion-sensors, serving as selective probes for detection of charged species exemplifies a highly promising domain within applied supramolecular chemistry. Copper remains an indispensable trace element ubiquitously found in cells and organs, critical for cellular respiration, antioxidant defense, connective tissue formation, neurotransmitter biosynthesis, peptide hormone maturation, pigmentation, keratinization, and iron homeostasis [1]. Copper ions form integral microelement with occurrence in most oxidases, including cytochrome C and copper oxidase, and aids in the structural integrity and orientation of the enzymes, ensuring appropriate in vivo redox processes [2–4]. However, copper dysregulation in homo-sapiens can develop Menkes, Wilson's diseases and/or lead to neurogenetic disorders such as Alzheimer's, Huntington's, Prion, and Parkinson's syndrome, as well as amyotrophic lateral sclerosis, and metabolic disorders including diabetes mellitus and adiposity. Consequently, copper has been recognized to modulate malignancies that function via renowned

oncogenic BRAF mutations and influence tumorigenesis [5–9]. The permissible tolerable limit of copper within a human body is 1.0–1.5 ppm, with recommended dietary intake in adults of 0.9 ppm, set forth by FDA [10]. EPA has established a regulatory threshold, specifically known as the maximum contaminant level goal for copper in potable drinking water at 1.3 ppm [11]. Owing to the pivotal role of Cu²⁺ and its profound impact on metabolic pathways, it is imperative to employ a forthright, selective and highly perceptive approach for the precise quantification and identification of Cu²⁺ in various matrices such as drinking water, industrial settings, environmental contexts, and food samples [12,13].

Despite the precision and sensitivity of atomic absorption spectroscopy (AAS), inductively coupled plasma mass spectrometry (ICP-MS), mass spectroscopy (MS), and time-of-flight mass spectrometry (TOFMS), their utilization requires expensive instrumentation, meticulous sample preparation, and expertise skill [14,15]. Subsequently, fluorescent detection of metal ions is enticing a great deal of attentiveness for applications in optical imaging and analytical sensing owing to their

* Corresponding authors.

E-mail addresses: chemgurpreet5@gmail.com (G. Kaur), singhjandeep@gmail.com (J. Singh).

<https://doi.org/10.1016/j.molstruc.2024.138288>

Received 1 January 2024; Received in revised form 26 March 2024; Accepted 8 April 2024

Available online 13 April 2024

0022-2860/© 2024 Elsevier B.V. All rights reserved.



Short communication

‘Turn On’ fluorescent imine linked 1,2,3-triazole based chemosensor for detection of mercuric ions

Nancy George^a, Gurleen Singh^a, Riddima Singh^a, Gurjaspreet Singh^b, Sudha Malik^b, Harminder Singh^a, Gurpreet Kaur^{c,*}, Jandeep Singh^{a,*}^a School of Chemical Engineering and Physical Sciences, Lovely Professional University, Phagwara 144411, Punjab, India^b Department of Chemistry and Centre of Advanced Studies in Chemistry, Panjab University, Chandigarh 160014, India^c Department of Chemistry, Gujranwala Guru Nanak Khalsa College, Civil Lines, Ludhiana 141001, Punjab, India

A B S T R A C T

The exorbitant use or erroneous management of metal ions has been incurred with catastrophic pollution of our ecological system, particularly in soil and water bodies, resulting in significant repercussions. Hence, precise identification and analysis of heavy-metal ions in intricate hydrological environments is imperative. Therefore, an imine conjugated 1,2,3-triazole derivative **VPT** was synthesized, characterized via FTIR, NMR (¹H & ¹³C), LCMS spectroscopic techniques and was employed for the exclusive identification of Hg²⁺ ions in the presence of various other metal ions via UV-Visible and fluorescence spectroscopy. The sensor **VPT** exhibited binding constant (K_b) value of $2.93 \times 10^4 \text{ M}^{-1}$ and detection limit value of $0.5 \times 10^{-6} \text{ M}$ in the ACN:H₂O:4:1 medium. The stoichiometric ratio was determined using Job's plot, which revealed a (1:1) ratio of **VPT** with Hg²⁺ ions. In addition, time-dependent, temperature-dependent, and pH titration studies were conducted via U.V-Visible spectroscopy to expand the sensor's applicability. The viable configurations of probe **VPT** and its 1:1 stoichiometric with Hg²⁺ ion were optimized using the B3LYP/6-311G++(d,p)/LANL2DZ levels of theory in the Gaussian 09 program respectively and this semi-empirical quantum mechanics approach demonstrated a reduction in the energy gap confirming the stable formation of [**VPT**-Hg²⁺] complex. These insights facilitate the design of fluorescent probe **VPT** for detecting Hg²⁺ in both environmental and biological context.

1. Introduction

Mercury is a relentless bio-accumulative, hazardous metal that possesses distinct physicochemical properties, which are of significant global health concern. The natural and anthropogenic dispersal of Hg continues to pose a substantial risk to both human and environmental well-being [1,2]. Mercury finds extensive application in various sectors such as domestic items (cutlery, culinary pots, skin lotions), the electrical industry (switches, thermostats, and batteries) dentistry (dental amalgams), and numerous industrial processes, including the production of caustic soda, its use in nuclear reactors, as antifungal agents for wood processing, as a solvent for reactive and metallic substances, and as a preservative for pharmaceutical products. However, humans are exposed to several sources of mercury including accidental incidents, environmental pollution, food adulteration, orthodontic treatments, preventative healthcare measures, industrial, agricultural activities, and occupational practices [3]. Therefore, excessive mercury accumulation may cause mental retardation, cognitive impairment, and prolonged exposure may accelerate the development of disorders including Parkinson's, Alzheimer's, and multiple sclerosis, subsequently damage

the neurological system, respiratory tract, and cardiovascular system [4,5]. The World Health Organization (WHO) has established guidelines for the acceptable levels of Hg²⁺ in drinking water, stipulating that it should not exceed 6 parts per billion (30 nM) [6]. Consequently, developing a method to accurately analyze the qualitative and quantitative aspects of Hg²⁺ metal ions is crucial for studying their role in life activities and timely monitoring their prevalence in the ecological environment [7].

Photophysical mechanism such as Atomic absorption spectroscopy (AAS), Gas chromatography-mass spectrometry (GC-MS), Inductively coupled plasma atomic emission spectroscopy (ICP-AES), and X-ray or laser-induced breakdown spectrometry (LIBS) remain as well recognized, predominant techniques for heavy metal detection [8]. However, the aforementioned procedures tend to incur high costs and lack portability, since they need lengthy measurement durations, substantial sample quantities, and the expertise personnel [9,10]. Alternatively, prevalence of absorbance and emission-based techniques has surged in several fields as these approaches have attained prominence owing to their ease of implementation and their ability to provide ameliorated levels of sensitivity and specificity. Chemosensors have shown

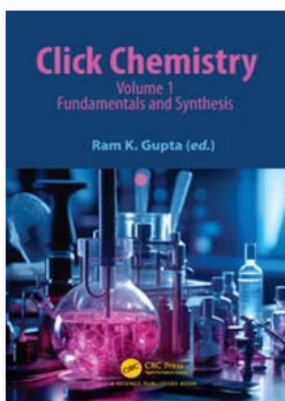
* Corresponding authors.

E-mail address: singhjandeep@gmail.com (J. Singh).<https://doi.org/10.1016/j.inoche.2024.113088>

Received 27 March 2024; Accepted 29 August 2024

Available online 2 September 2024

1387-7003/© 2024 Elsevier B.V. All rights are reserved, including those for text and data mining, AI training, and similar technologies.



Chapter

Catalysts for Click Chemistry

By Nancy George, Gurleen Singh, Gurpreet Kaur, Jandeep Singh

Book [Click Chemistry](#)

Edition	1st Edition
First Published	2024
Imprint	CRC Press
Pages	21
eBook ISBN	9781003403340



ABSTRACT

The modern era organic synthesis thrives on reactions featuring the quickest and most selective conjugation of molecules possessing extensive amenities. 'Click Chemistry' was coined to describe a set of guiding principles designed to address the challenges of contemporary chemistry and the exigencies of drug discovery [1]. The term "click" refers to the intuitive coupling of molecular building blocks, as in a seat belt locking device. A resilient thermodynamic force

DIVISION OF RESEARCH AND DEVELOPMENT

[Under the Aegis of Lovely Professional University, Jalandhar-Delhi G.T. Road, Phagwara (Punjab)]

Certificate No.240400

Certificate of Participation

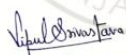
This is to certify that **Ms. Nancy George** of **Lovely Professional University, Phagwara, Punjab, India** has presented paper on **Design and characterization of newly synthesized schiff base derived 1,2,3-triazole** in the **International Conference on Materials for Emerging Technologies (ICMET-21)** held on February 18-19, 2022, organized by Department of Research Impact and Outcome, Division of Research and Development, Lovely Professional University, Punjab.

Date of Issue: 16-03-2022

Place: Phagwara (Punjab), India



Prepared by
(Administrative Officer-Records)



Dr. Vipul Srivastava
Convener
(ICMET-21)



Dr. Manish Vyas
Organizing Secretary
(ICMET-21)



Dr. Chander Prakash
Co-Chairperson
(ICMET-21)



Certification of Poster Presentation

This is to certify that Dr./Mr./Ms. *Nancy George* from *LPU* presented a poster titled "*Development of newly schiff based 1,2,3-triazole chemosensor from azomethine group for detection of toxic lead ion*" in the "**International Conference On Emerging Materials For Sustainable Development (EMSD-2022)**" Jointly organized by CSIR-CSIO, Chandigarh and IEEE AcSIR-CSIO Student Chapter during October 9th -11th, 2022 held at CSIR-CSIO, Chandigarh.



Dr. Vinod Karar
Chief Scientist, CSIR-CSIO,
Branch Counsellor,
IEEE AcSIR-CSIO SB, Chandigarh



Dr. Pooja Devi
Principal Scientist, CSIR-CSIO,
Faculty Advisor, IEEE NTC, AcSIR-CSIO
Convener, EMSD-2022



Ms. Aditi Chopra
Chair
IEEE AcSIR-CSIO SB, Chandigarh
Student Convener, EMSD-2022

CERTIFICATE

This is to certify that

Ms. Nancy George

Lovely Professional University, India

Delivered Oral Presentation

On

"Synthesis of azomethine functionalized 1,2,3-triazole chemosensor for detection of ferric ion"

In the

International Conclave on Materials, Energy & Climate,

12 December to 14 December 2022

ONSITE - ONLINE LIVE

Onsite Venue

Indira Gandhi Delhi Technical University for Women, Delhi, India

Organized by



IAAM[®]
International Association of
Advanced Materials



**Shoolini
University**

Date:
14 December 2022

Place and Country
New Delhi, India

International Association of
Advanced Materials
Org. 802503-6784

Gammalkilsvägen 18
Ulrika 590 53, Sweden

Web : www.iaamonline.org
Tel. : (+46) 1313-2424
E-mail : contact@iaamonline.org



Secretary General

HUMAN RESOURCE DEVELOPMENT CENTER

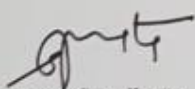
[Under the aegis of Lovely Professional University, Jalandhar-Delhi G.T. Road, Phagwara (Punjab)]



Certificate No. 258623

Certificate of Participation

This is to certify that **Ms. Nancy George** D/o Mr. George Masih participated in **Workshop on Advanced Materials' Characterization Techniques** organized by Lovely Professional University w.e.f. **December 19, 2022 to December 20, 2022** and obtained "A" Grade.



Program Coordinator
Human Resource Development Center



Program Convener
Human Resource Development Center

CERTIFICATE OF PARTICIPATION

This certificate is awarded to

nancy george

has successfully completed the **Two-Week Online Workshop on Gaussian Software** held from 15-April to 02-May 2024 organized by the SIAS Research Center.



Dr. Sabeel M Basheer
Workshop Coordinator



DIRECTOR
SIAS Research Center

director@thesias.in

<https://www.siasrf.com/>



SIAS Research Center
Kohinoor, Kerala,



SIAS Research Center

Kohinoor, Kerala, India

CERTIFICATE OF PARTICIPATION

THIS CERTIFICATE IS PRESENTED TO

Nancy George

has successfully completed the **Nine-Day Online Workshop on Molecular Docking** held during **06 - 16 May 2024** organized by the SIAS Research Center.

DR. SMA FAYAZ

Tutor, Assistant Professor
Manipal Institute of Technology (MIT),
Manipal, Karnataka, India



DIRECTOR

SIAS Research Center

director@thesias.in

<https://www.siasrf.com/>